THESIS CONTAINS

VIDEO CD DVD TAPE CASSETTE

Dielectrophoresis of colloids and polyelectrolytes

by

David John Guy Bakewell

A thesis submitted to the Faculty of Engineering

University of Glasgow

in fulfilment for

the degree of Doctor of Philosophy

Department of Electronics and Electrical Engineering,
University of Glasgow,
Scotland, United Kingdom

November, 2002

Abstract

This PhD dissertation describes experimental and theoretical investigations on the dielectrophoretic movement of colloidal particles and polyelectrolytes suspended in aqueous solution. Dielectrophoresis (DEP) is the movement of polarisable particles in non-uniform electric fields according to their induced, or effective, polarisability. The colloidal particles used in experiments were fluorescently labelled 216 nm diameter carboxyl-modified polystyrene micro-spheres (beads) and the polyelectrolyte particles were fluorescently labelled 12 kilobase pair DNA plasmids with approximately 1 μm planar diameter. The dielectrophoretic force was generated by applying electrical alternating current (AC) potentials of varying frequency to micro-fabricated electrodes covered with low conductivity aqueous suspending media. The electrodes used for quantitative particle measurements were interdigitated Ti/Pd/Au electrode arrays (10 μm width and 10 μm gap) microfabricated on glass microscope slides using standard photolithography techniques.

The frequency dependent effective particle polarisability, α_p, is a key parameter in governing the dielectrophoretic force. Time domain dielectric spectroscopic measurements of solutions of DNA gave values of α_p at 2 to 80×10^{-31} (F m^2), in the frequency range 12 MHz – 140 kHz. For latex micro-spheres, the DEP cross-over technique was used to predict α_p. Since the diameters of micro-spheres and plasmid DNA were up to a micron in size, their movement in an aqueous medium at room temperature was influenced by random, thermal Brownian motion. One and two-dimensional Fokker-Planck equation (FPE) models were constructed to predict DEP-driven collection of particles onto electrodes. The model comprised DEP-induced particle flux and thermally driven diffusion flux. The FPE computer model also predicted the diffusion of particles away from the electrode surfaces after the DEP force was switched off, called particle *relaxation*. Using the values of α_p, the FPE model was used to simulate particle collections and relaxations under the action of DEP onto a planar interdigitated electrode surface for a range of applied frequencies and voltages.

The collection of particles (beads and plasmid DNA) onto interdigitated electrodes was observed using epi-fluorescence microscopy together with video-recording of images. The images were processed using software written in MATLAB 5.0™. The processed images yielded time-dependent particle *collection* profiles representing particle accumulation on the electrodes, and particle *relaxation* profiles after the DEP potential was switched off. Theoretical predictions were used to compare DEP collection experiments of 216 nm diameter beads and DNA plasmids. Collection and relaxation profiles were measured for AC frequencies from 100 kHz to 20 MHz and applied voltages from 1 to 4.5 V (peak). The data was in broad agreement with theoretical predictions, but there were significant quantitative differences. There are a number of reasons for these discrepancies between theory and experiment. These include electrohydrodynamically induced fluid motion that can disturb particle movement, and distortion of the electric field

generated by the interdigitated electrodes due to the presence of charges associated with colloidal particles and DNA. As a first approximation, these factors were not included in the FPE model.

List of Contents

List of accompanying programs on CD-ROM

Programs referenced in dissertation and appendices (CD-ROM inside back cover)

CD-R:/FlexPDE/*fpe_1d_Co.pde*

CD-R:/FlexPDE/*Epot2D3ElTh.pde*

CD-R:/FlexPDE/*Fpe2dTh.pde*

CD-R:/FlexPDE/*Fpde2dThDNA.pde*

CD-R:/FlexPDE/*EpotPl0·5ElTh.pde*

CD-R:/FlexPDE/*Epot2D0·5ElTh.pde*

CD-R:/Mathematica/*O&PDEs.nb*

CD-R:/Mathematica/*Grd3dTh.nb*

CD-R:/Mathematica/*GrdE2NrEdgeTh.nb*

CD-R:/Mathematica/*BesFourZero.nb*

CD-R:/Matlab/*depint.m*

CD-R:/Matlab/*oruh.m*

CD-R:/Matlab/*fpex.m*

CD-R:/Matlab/*sidepth.m*

CD-R:/Matlab/*E3dth.m*

CD-R:/Matlab/*ch6flx.m*

Acknowledgements

I would like to thank my supervisor, Professor Hywel Morgan, for his encouragement, patience and genuine interest throughout the course of this work. I would also like to express my gratitude to my parents, Bill and Wilma Bakewell, and my brother, Peter, and his wife Ellie, for their kind support from abroad. I take this opportunity to thank Mr. Bill Monaghan and Mrs. Mary Robertson for their technical assistance in the bioelectronics laboratory and Drs. Edi Cecchini, Chiara Geri[1], Peter Dominy, and in particular, Joel Milner (at the Institute for Biomedical and Life Sciences), for assistance with preparation of the DNA and understanding its properties.

The postdoctoral and postgraduate students at Glasgow University were wonderful for illuminating discussions (and emotional support!) and I warmly thank them: Drs. Nic Green, Mike Hughes, Ka Lok Chan, Irina Ermolina and Erik Johannessen, and Debbie Boam, Mary Flynn, David Holmes and Mairi Sandison. I extend my thanks to other members of staff in the Department of Electronics and Electrical Engineering, Computing Services and Library, for their assistance. Finally, I express my gratitude to Dr. Keith Vass and staff at the Beatson Laboratories, Cancer Research, UK, for enabling me to print the final version of this thesis.

---

[1] On temporary leave from the Institute of Mutagenesis and Differentiation, C.N.R., Pisa, Italy.

Declaration

I hereby declare that all material presented in this thesis is my own research unless otherwise stated. To the best of my knowledge, this thesis does not contain any material previously published or written by another person, except where due reference is made in the text. Furthermore, this thesis does not contain any material that has been accepted for the award of any other degree (or diploma, etc.) in any university or institution.

Nomenclature, constants and lists of symbols

Nomenclature

Abbreviation	Full name
AC	Alternating Current
AVI	Audio Visual Interleave
BC(s)	Boundary Condition(s)
bp	base pair (of double stranded DNA)
CAD	Computer Aided Design
CCD	Charged Coupled Device
CM	Claussius-Mossotti (factor or function)
CsCl	Caesium-Chloride
DAPI	4′, 6-Diamidino-2-phenylindole
DC	Direct Current
DCF	Dipole Correlation Function
ddH_20	double distilled water (also subscripted as 'ddw')
DDS	Direct Digital Synthesiser
DEP	Dielectrophoresis (or dielectrophoretic)
DNA	Deoxyribonucleic acid
cccDNA	covalently closed-circular DNA (otherwise called supercoiled closed circular DNA (scDNA)
dsDNA	double stranded DNA
ocDNA	open circular DNA (otherwise called nicked-circular DNA)
ssDNA	single stranded DNA
EP	Electrophoresis (or electrophoretic)
EtBr	Ethidium Bromide
FFF	Field Flow Fractionation
FPE	Fokker-Planck Equation
GS	General Solution
IC	Initial Condition
kbp	kilobase pair
lhs	left hand side (of equation)
ME	Mercaptoethanol
MPEG	Motion Picture Expert Group
M-W	Maxwell-Wagner

MW_{bp}	Molecular Weight (per) base pair (for dsDNA = 662 Daltons/bp)
MW_{pTA250}	Molecular Weight of a pTA250 DNA plasmid
ODE	Ordinary Differential Equation
O-U	Ornstein-Uhlenbeck
PC	Personal Computer
PCB	Printed Circuit Board
PDE	Partial Differential Equation
PS	Particular Solution
pTA250	plasmid *Triticum aestivum* 250 (designation)
$pDNA_{TE}$	pTA250 suspended in TE buffer
$pDNA_{10\%TE}$	pTA250 suspended in 10% TE buffer
$pDNA_{ddw}$	pTA250 suspended in double distilled water
RAM	Random Access Memory
rhs	right hand side (of equation)
RNA	Ribonucleic acid
RO	Reverse Osmosis
ROM	Read Only Memory
SDE	Stochastic Differential Equation
TDR	Time Domain Reflectometry
TE	10 mM Tris-HCl, 1 mM EDTA, pH = 7.5
TIFF	Tagged Image File Format
UV	Ultra-Violet (light)
v:v	volume/volume ratio
1-D	One dimensional (or one dimension)
2-D (or 2D)	Two dimensional (or two dimensions)
3-D (or 3D)	Three dimensional (or three dimensions)

Unit name	**Symbol**	**Primary units**
Ampere	A	
degree Celsius	°C	K
Coulomb	C	A s
Farad	F	$C\,V^{-1} = m^{-2}\,kg^{-1}\,s^{4}\,A^{2}$
Hertz	Hz	s^{-1}
Joule	J	$N\,m = m^{2}\,kg\,s^{-2} = C\,V$
Kelvin	K	
Kilogram	kg	

Metre	m	
Mole	mol	
Newton	N	$m\ kg\ s^{-2}$
Ohm	Ω	$V\ A^{-1}$
Radian	rad	
Second	s	Note: sec(s) is used as abbreviation for second(s) in text
Siemen	S	Ω^{-1}
Volt	V	$J\ C^{-1} = N\ m\ C^{-1}$

Physical constants

Quantity	Symbol	Value	Units
Avogadro constant	N_{Av}	6.0221×10^{23}	mol^{-1}
elementary charge	q	1.6022×10^{-19}	C
permittivity of free space	ε_o	8.8542×10^{-12}	$F\ m^{-1}$
temperature	T	298.15 at 25.00° C	K
Boltzmann constant	k_B	1.3807×10^{-23}	$J\ K^{-1}$
molar gas constant	R	8.3145	$J\ mol^{-1}K^{-1}$
unified atomic mass {1 m_u = 1 Dalton (Da)}	m_u	$\cong1.6605\times10^{-27}$	kg

Mathematical and physical symbols frequently used

(where possible, symbols are the same as those used in the literature)

1. Symbol	Quantity
$\langle\ \rangle$	ensemble average
$\langle\ \rangle_t$	small-time average
$\bar{}$	spatial average
$\vec{\nabla}$	gradient operator with → denoting a vector quantity
•	scalar, or inner, product
$\|\ \|$	magnitude of a quantity

2. Symbol	Quantity
a	vertical position of electrode surface plane (m)
b	vertical position of cover-slip electrode plane (m) - all chs. except 2 and 4
b	average distance between phosphate groups on DNA - chs. 2 and 4 only
c	particle concentration or number density
c_V, c_A, c_L	number of particles per unit volume, area, or length, respectively
c_{ef}	ratio of the particle number density at an electrode edge with respect to far field
d	width or gap between each interdigitated electrode (m)
f_{CM}	Claussius-Mossotti factor (or function)
f_c	dielectrophoretic cross-over frequency (Hz)
f_R	dielectric relaxation frequency (Hz)
h	height of cover-slip above electrode surface (plane) $h = b - a$ (m)
j	$\sqrt{-1}$
k	coefficient for one-dimensional (1-D) Ornstein-Uhlenbeck linear, and hyperbolic DEP force profiles (J) – Chapter 5 only
k	fluorescence coefficient – chapters 3 and 7
k_1	coefficient for a 1-D exponential DEP force profile (N)
k_2	interdigitated array 1-D DEP force spatial coefficient (m^{-1})
k_f	general DEP force coefficient for a particle ($F\ m^2 = C\ V^{-1}\ m^2$)
m	mass of a particle
n_c	number of sample points for a transverse $w/2 + d/2$ *characteristic* for image processing an interdigitated electrode array
n_{cc}	number of *condensed counterions*
n_e	number of particles within a designated region surrounding an interdigitated electrode edge determined by *experiment*
n_{ed}	number of interdigitated electrode *edges* for image processing
n_p	number of particles within a designated region surrounding an interdigitated electrode edge *predicted* theoretically
n_{sp}	number of *spherical particles* in total suspension volume, V_T
n_{pr}	number of interdigitated electrode and gap *pairs* (for image processing)
$\vec{p}$	induced dipole moment (C m)
p	1-D particle probability density (m^{-1})
p_c	probability density integration constant (m^{-1})
p_{edge}	2-D particle probability density at an interdigitated electrode *edge* (m^{-2})
p_{ef}	ratio of the near and far field particle probability densities p_{edge}/p_{far}

p_{far}	2-D particle probability density in the *far* field from an interdigitated electrode array (m^{-2})
r	radius of a spherical particle (m)
$\vec{u}_x$	unit vector in the transverse x-direction parallel to the electrode plane
$\vec{u}_y$	unit vector in the vertical y-direction orthogonal to the electrode plane
$\vec{u}_z$	unit vector in the longitudinal z-direction (along each interdigitated electrode edge) parallel to the electrode plane and orthogonal to $\vec{u}_x$
v	particle velocity ($m\ s^{-1}$)
v_f	volume fraction of particle suspension
w	width of each interdigitated electrode (m)
z	ion valence

3. Symbol	**Quantity**
A	magnitude of rise, or fall, *amplitude*
A_r	relative rise *amplitude*
A_{st}	ionic stability factor
C	arbitrary integration constant
$C_{1_m}, C_{2_m}, C_{R_m}$	eigenfunction expansion integration constants for mth eigenmode
C_{DNA}	concentration of DNA suspended in solution ($kg\ m^{-3}$)
C_l	concentration of bulk and diffuse ions surrounding DNA ($mol\ m^{-3}$)
C_p	concentration of phosphate groups ($mol\ m^{-3}$)
C_m	concentration (number density) of DNA macromolecules in solution (m^{-3})
D	thermal diffusion constant = $k_B T/\zeta$ ($m^2\ s^{-1}$)
E or $\lvert\vec{E}\rvert$	magnitude of electric field $\vec{E}$ ($V\ m^{-1}$), unless otherwise stated, with $\rightarrow$ denoting a vector quantity and $\lvert\ \rvert$ magnitude
E_a or $\lvert\vec{E}_a\rvert$	magnitude of electric field ($V\ m^{-1}$) assuming the BC of a linearly interpolated potential along an inter-electrode space or gap, $\gamma = 1$, and infinite cover-slip height $h \rightarrow \infty$
$\vec{E}_{x_a}$	component of the electric field $\vec{E}_a$ in the transverse x-direction direction
$\vec{E}_{x,x_a}$	partial x-derivative of $\vec{E}_{a_x}$, $\partial\vec{E}_{a_x}/\partial x \equiv \partial_x \vec{E}_{a_x}$ ($V\ m^{-2}$)
$\vec{\nabla}\lvert\vec{E}\rvert^2$	gradient of the electric field magnitude squared (or for conciseness, electric field 'intensity' gradient) ($V^2\ m^{-3}$)
F_{DEP}	scalar dielectrophoretic (DEP) force (N)

F_{EP}	scalar electrophoretic (EP) force (N)
F	fluorescence ratio of image intensity, I
I	image intensity of interdigitated electrode array (undergoing DEP collection or relaxation) in the electrode plane orthogonal to $\vec{u}_y$
$\bar{I}$	spatial z-average of image intensity I in the longitudinal direction, $\vec{u}_z$
$\tilde{I}$	characteristic intensity of a 'cell' for $0 \le x \le \frac{w+d}{2}$ formed by a periodic and symmetric average of I in $\vec{u}_x$ transverse direction of the array
$\bar{\bar{I}}$	spatial x-average of image intensity $\tilde{I}$ for x values within a cell defined over the closed interval $x \in [0, \frac{w+d}{2}]$ in $\vec{u}_x$ direction
J	particle flux in one dimension
J_μ	Bessel function of the first kind with order μ - Chapter 5 only
K_s	surface conductance (S or Ω^{-1})
L_{bp}	DNA contour length per double helical base pair (m)
L_s	sub-unit length of macromolecule (m)
N	particle number
N_{bp}	number of double helical DNA base pairs
V	particle volume (usually for a sphere) (m^3)
V_T	total volume of particle suspension (m^3)
V_o	peak sinusoidal electrode potential - with respect to earth (V)
V_{o_e}	peak sinusoidal electrode potential measured in an *experiment* (V) when V_o , in contradistinction, is the peak potential used in a corresponding *simulation*

4. Symbol	**Quantity**
α	effective, or induced, general polarisability (F m^{-1}) - all chapters except Chapter 5
$\alpha_m = \alpha V_{1dna}$	effective polarisability for one DNA macromolecule with volume V_{1dna} (F m^2)
$\alpha_p = \alpha V$	effective particle polarisability for a particle with volume V (F m^2)
α_s	effective polarisability of a macromolecular subunit length L_s (F m^2)
α	DEP/thermal energy parameter - Chapter 5 only
β_m	mth eigenvalue
δ_e	thickness of interdigitated electrode
δ_f	fluorescence deviation
ε_r	*relative* permittivity

	$\varepsilon_{r\,m}$	*relative* permittivity of *medium*
	$\varepsilon_{r\,p}$	*relative* permittivity of *particle*
ε_m		*medium* permittivity = $\varepsilon_o\ \varepsilon_{r\,m}$ (F m^{-1})
ε_p		*particle* permittivity = $\varepsilon_o\ \varepsilon_{r\,p}$ (F m^{-1})
ε		small positive value, or error
η		viscosity of medium (kg m^{-1} s^{-1})
γ		linear interpolated potential along inter-electrode space or gap
κ_s		reciprocal of the Debye screening length
λ_e		emission wavelength of fluorescent dye (m)
λ_D		Debye screening length (m)
μ		mobility of ion or particle (m^2 V^{-1} s^{-1}) – chapters 2 and 4
μ		complement of the DEP/thermal energy parameter = 1 – α (Ch. 5 only)
ω		angular frequency (rad s^{-1})
ϕ		minimum diagonal length between polynomial electrodes (or diameter)
ϕ_c		fraction of condensed counterions
ρ_m		density of suspension *medium* (kg m^{-3})
ρ_p		*particle* density (kg m^{-3})
σ_m		conductivity of suspension *medium* (S m^{-1} or Ω^{-1} m^{-1})
σ_p		*particle* conductivity (S m^{-1})
τ		particle relaxation time (s)
τ_{MW}		Maxwell-Wagner relaxation time (s)
τ_{rise}		*rise* time (s)
τ_{fall}		*fall* time (s)
θ		phase of electric field
ξ		charge density parameter
ζ		friction or fluid drag coefficient (kg s^{-1})

5. Symbol	**Quantity**
Γ_x, Γ_y	dimensionless gradients of electric field squared (or 'intensity')
Φ	electrical potential (V)
Φ_ζ	zeta potential of the electrical double layer (V)
Θ_L, Θ_T	dimensionless parts of the gradient of electric field squared (or 'intensity')
Ξ_+, Ξ_-	dimensionless parts of the gradient of electric field squared (or 'intensity')

Dielectrophoresis of colloids and polyelectrolytes

1 Introduction

"I often say when you can measure what you are speaking about, and express it in numbers, you know something about it; but when you cannot express it in numbers, your knowledge is of a meagre and unsatisfactory kind: it may be the beginning of knowledge, but you have scarcely, in your thoughts, advanced to the stage of science."

Lord Kelvin (William Thomson), 1883, (Cran and Robertson, 1996)

1.0 Background

There is considerable scientific and engineering interest in techniques for non-contact manipulation and movement of polyelectrolytes and colloidal particles. Polyelectrolytes are macromolecules that in solution carry a large number of chemically charged groups, and one of the most important biological polyelectrolytes is deoxyribonucleic acid (DNA) (Armstrong and Strauss, 1969; Steiner and Millar, 1970; Mandel and Odijk, 1984; Mandel, 1988; Russell, 1994). Colloidal particles are classified principally by their physical size, ranging from nanometres to microns in their linear dimension (Shaw, 1992; Russel *et al.*, 1999). Many colloidal particles also possess a number of charged groups, hence both polyelectrolytes and colloids are very responsive to electric fields and are said to have a high induced (or effective) polarisability. Developments in micro-analytical devices have prompted innovations for moving these polarisable entities, particularly over sub-millimetre distances. Dielectrophoresis (DEP) is a promising electrokinetic method for moving these particles by application of non-uniform electric fields (Pohl, 1978; Jones, 1995; Cheng *et al.*, 1998).

The dielectrophoretic force arises from the application of an alternating current (AC) potential to micro-electrodes submerged within a suspension of particles in a low conducting medium. The particles move in the non-uniform field depending on their effective polarisability. The force is dependent on the gradient of the field intensity, and consequently *independent* of the instantaneous polarity of the AC potential. One of the advantages of using this AC electrokinetic method for moving particles in solutions of low to moderate conductivity, is that electrochemical damage at the electrode-solution interface can be avoided (Washizu *et al.*, 1992).

Interest in the dielectrophoretic manipulation of small, micron sized biological particles (or bioparticles), such as, blood cells and bacteria, has received increasing attention since the exposition of this technique by Pohl (1978). Other closely related electrokinetic methods, such as, electro-rotation and travelling wave dielectrophoresis have also been studied in recent years (Huang *et al.*, 1993; Becker *et al.*, 1994; Burt *et al.*, 1996; Talary *et al.*, 1996; Goater *et al.*, 1997). Advances in microfabrication methods means that electrodes of sub-micron dimensions can be

made that yield strong electric fields and enable the size of manipulated particles to be considerably reduced. New DEP techniques are currently being pursued to characterise and manipulate smaller nano-scale particles such as colloids and other biologically important entities such as viruses, DNA, and proteins (Hughes *et al.*, 1997).

An important aspect of understanding dielectrophoresis, both as a science and in terms of technological application, lies in being able to quantitatively measure particle movement. In this respect, a key measure of the dielectrophoretic force on a particle is the time-dependent accumulation of particles onto the electrode surfaces. This thesis describes the development of software for analysing images, and an experimental system for analysing collections of colloidal particles and DNA using epi-fluorescence microscopy. A theoretical model for predicting particle collections, under the action of positive DEP, onto planar electrode surfaces is also developed and comparisons are made with experimental measurements for a range of electrode potentials and frequencies (100 kHz – 20 MHz).

1.1 A short history and motivation for research

Research on DEP of DNA has been either theoretical investigations of particle trapping on microelectrodes (Ajdari and Prost, 1991) or largely qualitative experiments where DNA macromolecules have been oriented, stretched, transported and/or trapped on electrode structures or though micro-flow devices (Washizu and Kurosawa, 1990; Kabata *et al.*, 1993; Washizu *et al.*, 1994; Nishioka *et al.*, 1995, Mizuno *et al.*, 1995; Washizu *et al.*, 1995; Morishima *et al.*, 1995; Morishima *et al.*, 1996; Morishima *et al.*, 1997; Yamamoto *et al.*, 1998, Crippen *et al.*, 2000; Morishima *et al.*, 2000). These experiments have pioneered the use of DEP for novel purposes, such as field flow fractionation and molecular 'surgery' using laser radiation and enzymes. The only published quantitative study of DNA collecting onto electrode surfaces is from one group in Seattle, USA (Asbury and van den Engh, 1998; Asbury, 1999). They showed that the time course of fluorescently labelled DNA trapped by non-uniform electric fields onto planar interdigitated electrode arrays was fitted by a single or double exponential profile. They compared their results against the equivalent DEP energy required to trap DNA, from which they concluded the DEP trapping efficiency was less than predicted when using values of the effective polarisability deduced from dielectric spectroscopy studies. These quantitative results of DNA trapping were performed at low AC frequencies spanning 1 - 10 kHz (typically 30 Hz) and exhibited an interesting dependence on solvent conductivity and on molecular weight. Fluorescence profiles of DNA being released and diffusing away from electrode surfaces were also described.

The general absence of quantitative measurements of DNA dielectrophoresis, underpinned by a theoretical model that provides a comprehensive comparison with experimental results, prompted a joint theoretical and experimental investigation by the author. In terms of predicting

the DEP force from known parameters, however, the response of macromolecules with a poorly defined particle/solvent interface is not well characterised compared with colloidal particles. This means, at this stage, predictions from a model that encompasses time dependent DEP collections (or profiles) of colloidal particles can be more easily tested against experimental data. This feature, in conjunction with recent interest in the dielectrophoretic characterisation of colloidal particles (Green and Morgan, 1997a; Green and Morgan, 1997b; Green and Morgan, 1998; Hughes and Morgan, 1999), motivated investigations of the DEP collection time-profiles of colloidal particles. The colloids examined in this dissertation are latex micro-spheres that represent 'model' colloidal particles.

One of the parameters of time dependent DEP collections of particles on to electrode surfaces is the *initial time* rate of particle accumulation, generally called the DEP *collection rate* (Pohl, 1951; Pohl, 1978; Price *et al.*, 1988; Gascoyne *et al.*, 1994). In the past, DEP collection rates have been used to quantify the dielectric and dielectrophoretic properties of particles, such as, cells and micro-organisms (Inoue *et al.*, 1988; Burt *et al.*, 1989; Talary and Pethig, 1994; Markx, *et al.*, 1994). However, these particles are much larger than the nano-scale sizes of DNA or colloidal particles of interest where the effects of thermal fluctuations (Brownian motion) on particle movement need to be considered. Consequently, both the DEP induced particle flux and a diffusion flux form two essential parts of the dynamic model describing DEP collections. The governing dynamic equation, for large numbers of non-interacting particles is called the continuity equation, or Fokker-Planck equation (FPE) (Gardiner, 1985). The FPE also describes the diffusion of these sub-micron sized particles away from the electrode surfaces after the DEP force is switched off – the process is called particle *relaxation*.

1.2 The structure of this dissertation

This PhD dissertation is organised in the following manner. The theoretical basis of the polarisation mechanisms of DNA and colloidal particles, and derivation of the dielectrophoretic force is described in Chapter 2. The FPE model is also introduced in Chapter 2 together with the general relations laying the foundations for numerical simulations of DEP collection and relaxation time-profiles. The dependent variables giving spatial-temporal information about particles are inter-related; they include particle number, concentration, and probability density. The experimental apparatus for measuring DEP collections (and relaxations), purification and preparation of 12 kilobase pair (kbp) plasmid DNA and micro-spheres, and planar electrode array micro-fabrication, is described in Chapter 3. The chapter also gives a detailed account of the image processing software written in MATLAB 5.0™ for quantifying video images of fluorescently labelled DNA and micro-spheres collecting onto the planar electrode arrays under the action of DEP forces. Dielectric spectroscopy measurements of the plasmid DNA suspension, described in

Chapter 3, are described and analysed in Chapter 4. Values for the effective polarisability are determined and shown to exhibit frequency dependence in the range of interest for the DEP collections at high frequencies (100 kHz – 20 MHz).

Chapter 5 describes how the FPE model is developed for a one-dimensional (1-D) hyperbolic DEP force where point particles in a suspension confined by a cover-slip are attracted onto the electrode plane. The FPE is solved for a range of forces and cover-slip heights both by a Fourier-Bessel eigenfunction expansion and by a finite element method. These two methods are shown to concur. The chapter introduces rise (and fall) times of collection (and relaxation) time-profiles, and steady state collection probability density as important parameters for characterising DEP collections and relaxations. The 1-D FPE model is further developed in Chapter 6 for two-dimensions (2-D). This model describes particle movement over interdigitated electrode arrays that have symmetry in the third (longitudinal) dimension. In this chapter an expression is derived for the electric field non-uniformity, based on the Laplace equation, that results in the dielectrophoretic force (gradient of the electric field magnitude squared). It is shown that in the near field the field gradient approximates to a hyperbolic function, thus validating its application in Chapter 5. Chapter 6 describes analytical solutions for the 2-D electric field assuming a finite cover-slip height and predicts the particle steady state probability density (or concentration) ratio near electrode edges compared with the far field. This is a sensitive DEP metric, concisely revealing the extent to which steady state theoretical predictions concur, or disagree, with quantitative experimental observations.

Chapter 7 describes DEP collection experiments of 216 nm diameter latex micro-sphere and DNA plasmid aqueous suspensions onto planar 10 μm width 10 μm gap interdigitated electrodes for a range of AC frequencies and electrical potentials. The collection profiles are compared with those generated from the 2-D FPE model developed in Chapter 6. Data about relaxations is also included for completeness. The collection parameters of interest are the initial collection rate, rise time, and steady state values. This brings together the two strands of research, experimental and theoretical. A brief summary of the investigations together with future work concludes the dissertation in Chapter 8.

2 Theory

2.0 Introduction

The dielectrophoretic accumulation of nano-scale particles, in aqueous solutions, onto electrode surfaces encompasses several electro-kinetic and physical phenomena. These are (i) dielectrophoresis (DEP) as the principal external electro-kinetic force on each particle, (ii) the DEP dependency on the polarisability and size of particle material and non-uniform electric field strength, and (iii) the influence of random, fluctuating collisions from water molecules on the motion of these particles. To set-up a model of DEP time dependent collection (and relaxation) profiles, it is convenient to separately introduce the theoretical basis of each of these phenomena.

This chapter has the following structure. The basic theory of DEP is presented in section 2.1. This is followed by a description of the polarisation mechanisms of colloidal particles and DNA in section 2.2. These polarisation mechanisms are responsible for the dielectrophoretic movement of these particles in non-uniform AC electric fields. In addition to the DEP force, there are a number of other forces acting on a single sub-micron sized particle, in a non-uniform AC electric field, suspended in an aqueous medium. These forces are described in section 2.3 and include inertial, Stokes' drag, electrophoretic, sedimentation, and thermal fluctuations from the aqueous medium. Section 2.4 combines the most significant of the forces into models describing the motion of both a single particle and an ensemble, or population, of particles.

2.1 Theory of dielectrophoresis (DEP)

The theory of particle movement in a non-uniform electric field initially considers a particle in a one-dimensional (1-D) static electric field. This simple case is then extended to understand the general three-dimensional (3-D) force acting on a particle in a time varying electric field.

2.1.1 Elementary aspects of DEP

It is well known that an electric field applied to a neutral body composed of dielectric material causes charge[1] movement, within the material, that opposes the (original) field. The movement of these charges resulting from the external electric field, is said to cause *induced dipoles*, as shown

[1] The term 'charge' means an electron (negative charge), or absence (positive charge).

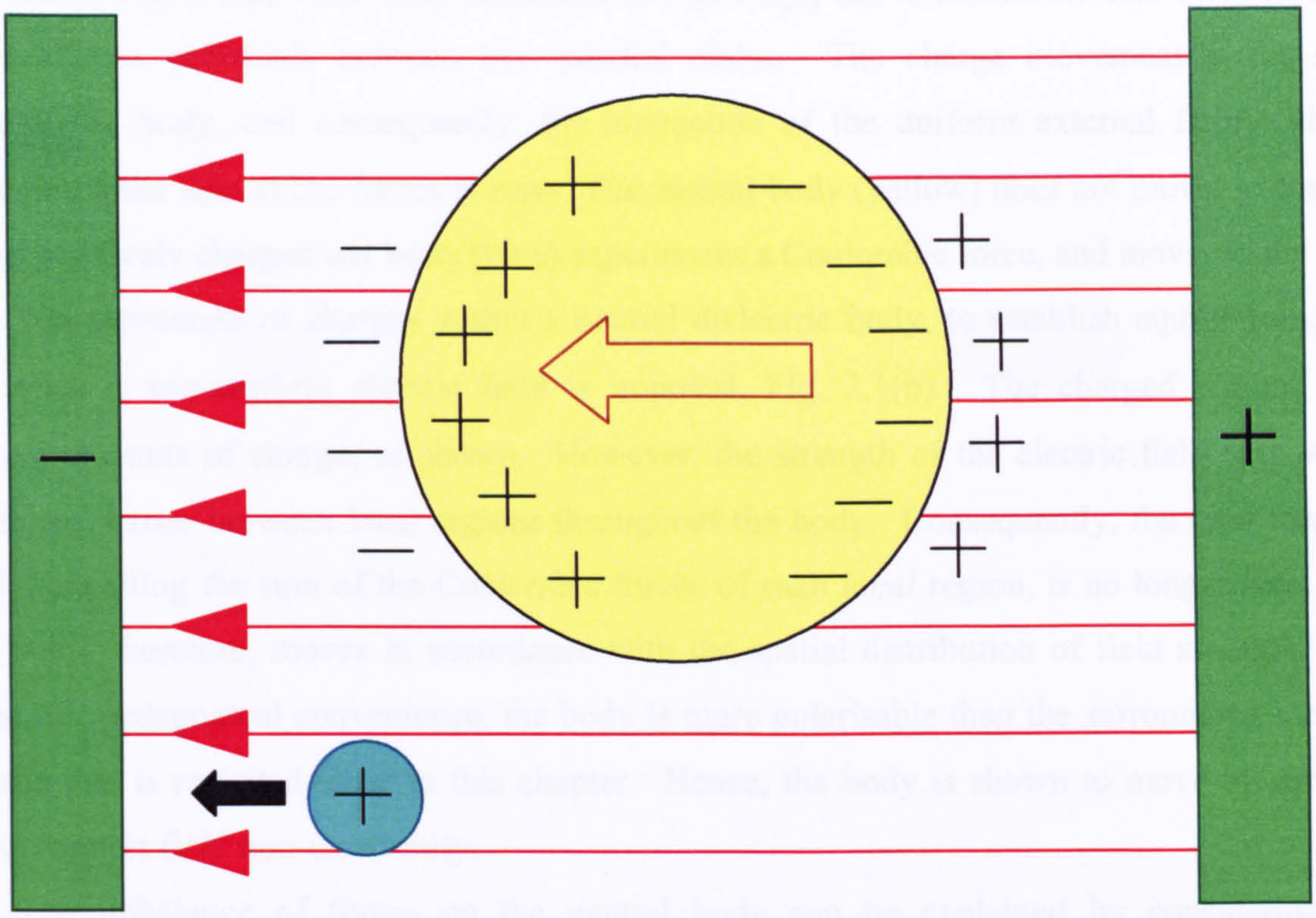

Fig. 2.1(a) Charge movement in a neutral body (yellow) in a uniform electric field (red arrows) results in induced dipoles (the sum of the induced dipoles represented by the brown, unfilled, arrow using the $- \rightarrow +$ convention adopted by Von Hippel, 1954). The sum of the forces is zero so the neutral body does not move. In contrast, a positive test charge (aqua), acting under a Coulombic force, moves to the left. In this example the polarisability of the body is greater than the surrounding medium.

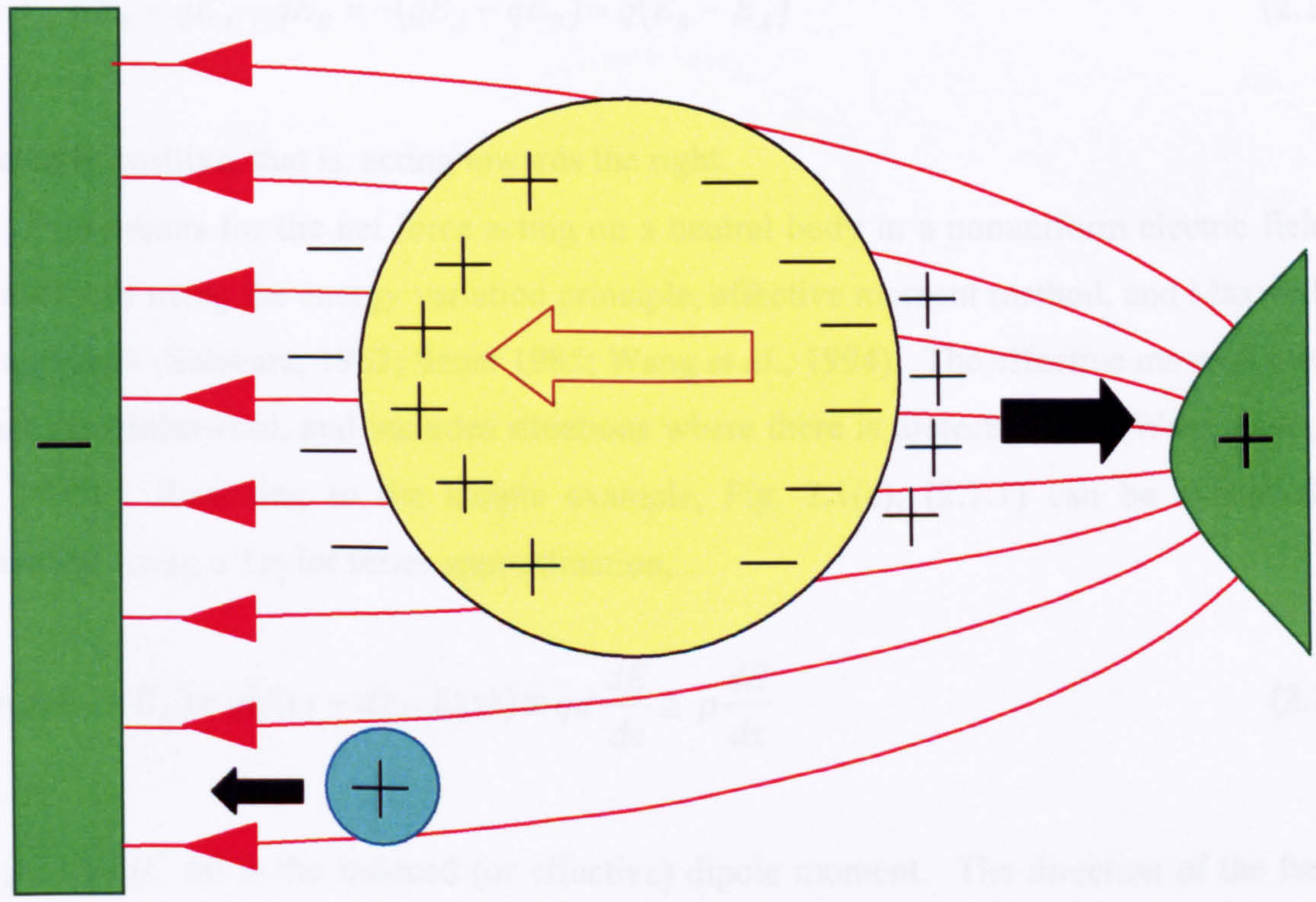

Fig. 2.1(b) Dielectrophoresis: the neutral body (yellow) in a nonuniform electric field (red arrows) experiences a net force depending on spatial distribution of electric field strength. In this example, where the polarisability of the body is greater than the surrounding medium, it moves to the right (black arrow).

schematically, Fig. 2.1(a). The body illustrated in Fig. 2.1(a) lies in a uniform field established by different electric potentials between two parallel plates. The charge movement is the same throughout the body, and consequently, the interaction of the uniform external field with the charges means the sum of the forces is zero. The neutral body (yellow) does not move; in contrast the small positively charged test body (blue) experiences a Coulombic force, and moves to the left.

The movement of charges within a neutral dielectric body, to establish equilibrium, also occurs when a *non-uniform* electric field is imposed, Fig. 2.1(b). The charged regions have equivalent amounts of charge, as shown. However, the strength of the electric field with which they interact, varies between local regions throughout the body. Consequently, the total force on the body, equalling the sum of the Coulombic forces of each *local* region, is no longer zero. The neutral body, therefore, moves in accordance with the spatial distribution of field strength. It is assumed, for pedagogical convenience, the body is more polarisable than the surrounding medium – an issue that is revisited latter in this chapter. Hence, the body is shown to move towards the region of highest field non-uniformity.

The imbalance of forces on the neutral body can be explained by considering two elementary charges $+q$ and $-q$ at A and B, distance d apart, Fig. 2.1(c). The electric field at B, E_B, is shown to be stronger than at A, E_A. The sum of the two Coulombic forces, assuming the forces are acting in the horizontal direction and using a standard convention where forces acting to the right are positive, and those to the left are negative, is written

$$\vec{F}_{body} = \vec{F}_A + \vec{F}_B = q\vec{E}_A - q\vec{E}_B = -\left(qE_A - qE_B\right) = q\left(E_B - E_A\right) \tag{2.1.1}$$

and is clearly positive, that is, acting towards the right.

Expressions for the net force acting on a neutral body in a nonuniform electric field have been developed using the energy variation principle, effective moment method, and Maxwell stress tensor approach (Schwarz, 1963; Sauer 1985; Wang *et al.*, 1994). The effective moment method is the most straightforward, and includes situations where there is dielectric loss (Wang *et al.*, 1997; Jones, 1995). Returning to the simple example, Fig. 2.1(c), (2.1.1) can be evaluated more conveniently, using a Taylor series approximation,

$$\vec{F}_{body} = q\left(E_B - E_A\right) = q\left(E(x+d) - E(x)\right) \cong qd\frac{dE}{dx} \cong p\frac{dE}{dx} \tag{2.1.2}$$

where $p = qd$ (C m) is the induced (or effective) dipole moment. The direction of the force can again be verified by realising the derivative of the electric field, as shown, is positive. Equation (2.1.2), illustrates a simple case, and introduces the more general 3-D case in a time varying electric field.

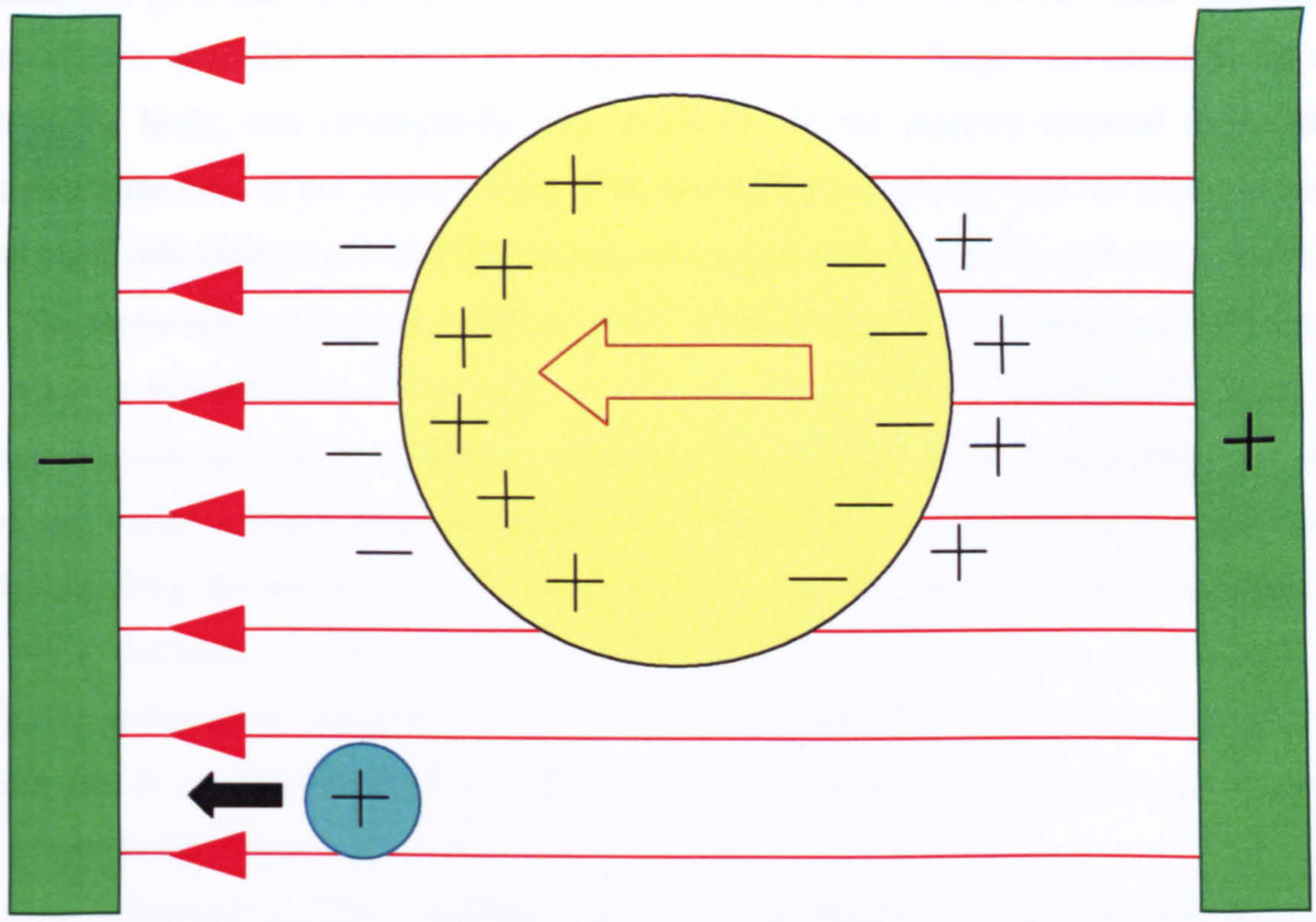

Fig. 2.1(a) Charge movement in a neutral body (yellow) in a uniform electric field (red arrows) results in induced dipoles (the sum of the induced dipoles represented by the brown, unfilled, arrow using the $- \rightarrow +$ convention adopted by Von Hippel, 1954). The sum of the forces is zero so the neutral body does not move. In contrast, a positive test charge (aqua), acting under a Coulombic force, moves to the left. In this example the polarisability of the body is greater than the surrounding medium.

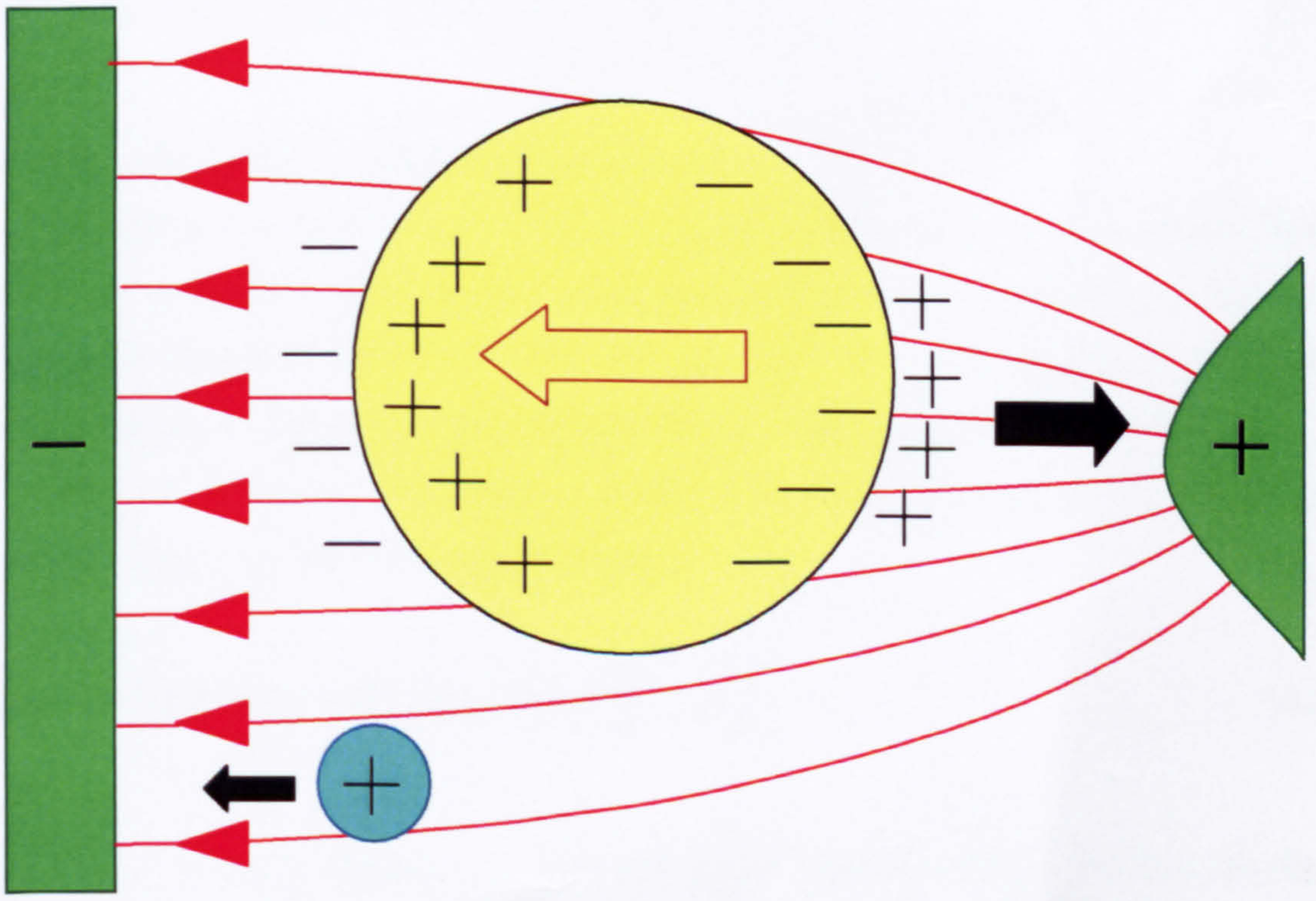

Fig. 2.1(b) Dielectrophoresis: the neutral body (yellow) in a nonuniform electric field (red arrows) experiences a net force depending on spatial distribution of electric field strength. In this example, where the polarisability of the body is greater than the surrounding medium, it moves to the right (black arrow).

schematically, Fig. 2.1(a). The body illustrated in Fig. 2.1(a) lies in a uniform field established by different electric potentials between two parallel plates. The charge movement is the same throughout the body, and consequently, the interaction of the uniform external field with the charges means the sum of the forces is zero. The neutral body (yellow) does not move; in contrast the small positively charged test body (blue) experiences a Coulombic force, and moves to the left.

The movement of charges within a neutral dielectric body, to establish equilibrium, also occurs when a *non-uniform* electric field is imposed, Fig. 2.1(b). The charged regions have equivalent amounts of charge, as shown. However, the strength of the electric field with which they interact, varies between local regions throughout the body. Consequently, the total force on the body, equalling the sum of the Coulombic forces of each *local* region, is no longer zero. The neutral body, therefore, moves in accordance with the spatial distribution of field strength. It is assumed, for pedagogical convenience, the body is more polarisable than the surrounding medium – an issue that is revisited latter in this chapter. Hence, the body is shown to move towards the region of highest field non-uniformity.

The imbalance of forces on the neutral body can be explained by considering two elementary charges $+q$ and $-q$ at A and B, distance d apart, Fig. 2.1(c). The electric field at B, E_B, is shown to be stronger than at A, E_A. The sum of the two Coulombic forces, assuming the forces are acting in the horizontal direction and using a standard convention where forces acting to the right are positive, and those to the left are negative, is written

$$\vec{F}_{body} = \vec{F}_A + \vec{F}_B = q\vec{E}_A - q\vec{E}_B = -\left(qE_A - qE_B\right) = q\left(E_B - E_A\right) \tag{2.1.1}$$

and is clearly positive, that is, acting towards the right.

Expressions for the net force acting on a neutral body in a nonuniform electric field have been developed using the energy variation principle, effective moment method, and Maxwell stress tensor approach (Schwarz, 1963; Sauer 1985; Wang *et al.*, 1994). The effective moment method is the most straightforward, and includes situations where there is dielectric loss (Wang *et al.*, 1997; Jones, 1995). Returning to the simple example, Fig. 2.1(c), (2.1.1) can be evaluated more conveniently, using a Taylor series approximation,

$$\vec{F}_{body} = q\left(E_B - E_A\right) = q\left(E(x+d) - E(x)\right) \cong qd\frac{dE}{dx} \cong p\frac{dE}{dx} \tag{2.1.2}$$

where $p = qd$ (C m) is the induced (or effective) dipole moment. The direction of the force can again be verified by realising the derivative of the electric field, as shown, is positive. Equation (2.1.2), illustrates a simple case, and introduces the more general 3-D case in a time varying electric field.

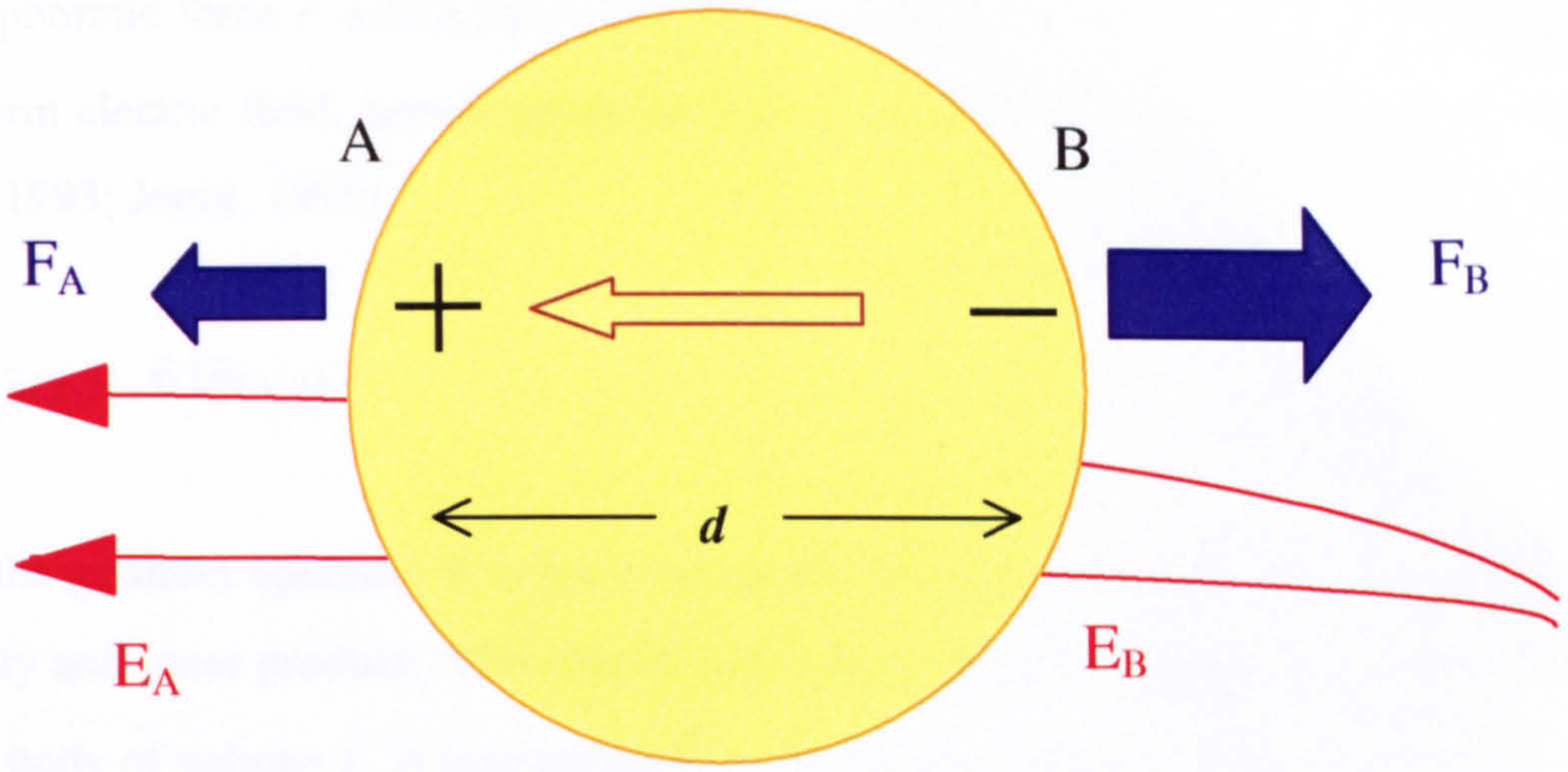

Fig. 2.1(c) The displaced charges at A and B interact with the electric field, E_A and E_B, generating Coulombic forces, F_A and F_B acting in the opposite directions, as shown. The force at B is greater than at A, $F_B > F_A$, so the neutral body moves to the right.

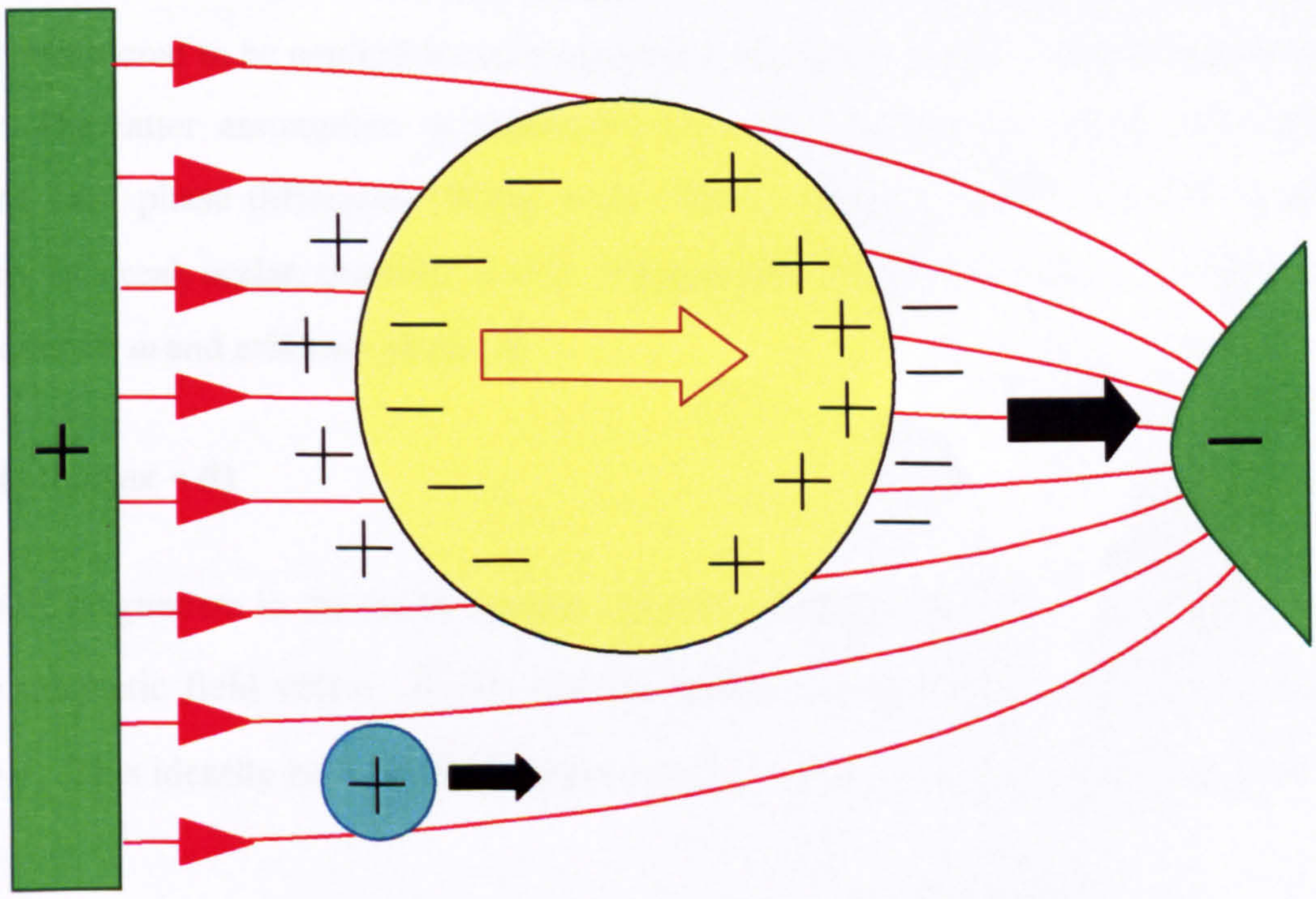

Fig. 2.1(d) The DEP movement of a neutral body is invariant to the sign of the electrode potentials and direction of the electric field.

2.1.2 General time averaged DEP force in three dimensions (3-D)

The dielectrophoretic force F acting on a small neutral particle at position $\underline{x} = (x, y, z)$ and time t, in a nonuniform electric field, approximated to first order, is written in general form (Pohl, 1978; Huang *et al.*, 1993; Jones, 1995)

$$\vec{F}_{DEP}(\underline{x},t) = \left(\vec{p}(\underline{x},t)\cdot\vec{\nabla}\right)\vec{E}(\underline{x},t) \qquad (2.1.3)$$

where ∇ is the gradient operator, E is the external electric field, and symbols $\rightarrow$ and $\bullet$ denote vector quantity and inner product. The generalised induced dipole moment, $\vec{p}$, for the case where the dielectric body of volume V, is homogeneously, linearly and isotropically polarisable, is

$$\vec{p}(\underline{x},t) = \alpha V\vec{E}(\underline{x},t) \qquad (2.1.4)$$

where α is the induced polarisability, or effective dipole moment per unit volume in unit electric field. It has dimensions Farad per metre (Fm^{-1}). The physical origin of the polarisability is discussed further in the next section 2.2. It is assumed, for the force to be proportional to the gradient of E in (2.1.2), that the dimension of the dipole p is small compared with the characteristic length of the electric field non-uniformity (Schnelle *et al.*, 1993). Any spatial electric field phase variation is considered to be negligible, and our interest lies solely in the in-phase component of the DEP force. The latter assumption is reasonable since the experiments supply electrodes with potentials of 180° phase difference (Wang *et al.* 1994). Thus, it is convenient to consider the polarisability as a real, scalar, quantity: $\alpha \in R$. Furthermore, the electric field is written in terms of angular frequency ω and arbitrary phase, θ,

$$\vec{E}(\underline{x},t) = \vec{E}(\underline{x})\cos(\omega t + \theta) \qquad (2.1.5)$$

The effects of magnetism in the entire system - particle, medium, and electrodes - can be ignored. Hence, the magnetic field vector, $B = 0$, and the differential form of Faraday's Law simplifies, $\Rightarrow \vec{\nabla}\times\vec{E} = 0$. This identity enables the combination (2.1.3), (2.1.4) and (2.1.5) to be transformed,

$$\vec{F}_{DEP}(\underline{x},t) = \frac{1}{2}\alpha V\vec{\nabla}\left|\vec{E}(\underline{x})\right|^2\cos^2(\omega t+\theta) = \underbrace{\frac{1}{4}\alpha V\vec{\nabla}\left|\vec{E}(\underline{x})\right|^2}_{\vec{F}_{DEP}(\underline{x})}\left(1+\cos(2\omega t+2\theta)\right) \qquad (2.1.6)$$

The spatial component of the DEP force can be segregated from the time varying part, and is labelled as shown. It is shown in Appendix A, for electric field frequencies above 20 kHz, that the contribution of the co-sinusoidal oscillatory term to the motion of the particle is negligible. Thus, it is convenient to view the force in terms of a 'small-time' average, denoted by $\langle\ \rangle_t$, over an oscillation period (Baygents, 1994; Wang *et al.*, 1994). Equation (2.1.6) simplifies to

$$\left\langle \vec{F}_{DEP}(\underline{x},t) \right\rangle_t = \vec{F}_{DEP}(\underline{x}) = \frac{1}{4}\alpha V \vec{\nabla} \left| \vec{E}(\underline{x}) \right|^2 = \frac{1}{2}\alpha V \vec{\nabla} \left| \vec{E}_{rms}(\underline{x}) \right|^2 \qquad (2.1.7)$$

and can be expressed in terms of the electric field root-mean-square (rms), E_{rms}. The DEP force, hereafter, is understood to be 'almost instantaneous'.

Equation (2.1.7) illustrates an important property of dielectrophoresis; the direction of the force is *invariant* to the electric field direction (or sign of the electrode potentials). This property is as illustrated in Fig. 2.1(d), where the neutral body continues to moves to the right - irrespective of the change in electric field direction. The direction of the force is, however, dependent on the *sign* of the polarisability. In terms of computing the DEP force, the electric field gradient for realistic geometric electrode designs can be determined, analytically for simple cases, or by appropriate electromagnetic simulation software. The volume of the bioparticle V is usually known or can be estimated. This leaves the polarisability α as the only value to be determined by other means, such as, dielectric measurements. Conversely, if the DEP force is known or estimated by experiment, then an approximate value of α can be determined.

2.2 Polarisation mechanisms

Polarisation is a term that describes how charges, within a dielectric, respond to an externally applied electric field. Charges that are free to move reveal their movement on a macroscopic scale as conduction. If the movement of the charges is blocked they are said to be 'polarised'. In this respect, polarisation is the 'intention' of the charges to move in response to an applied electric field.

2.2.1 Polarisation: introduction

Before detailing two key polarisation mechanisms it is useful to introduce the parameters for measuring polarisation, basic types of polarisation, and the concept of a double layer.

2.2.1.1 Polarisation parameters

The free movement of charges can be expressed, in terms of electric circuit parameters, as the in-phase conductivity; and the restricted movement, or polarisation, as the out-of-phase conductivity, (Pohl, 1978, Ch. 2). An equivalent, and frequently used alternative, is to parameterise the free movement of charges as the out-of phase permittivity ε'', and polarisation as the in-phase permittivity ε'. The complex permittivity ε is the combination of these,

$$\varepsilon(\omega) = \varepsilon' - j\varepsilon'' \tag{2.2.1}$$

Usually ε' is referred to as the real (in-phase) part of ε, or simply *permittivity*, ε'' is called the imaginary (out-of-phase) part of ε or *dielectric loss*, and $j = \sqrt{-1}$. Polarisability is a measure of response of a body to an external electric field. It is represented quantitatively by the constant α, as introduced in equation (2.1.4). A highly polarisable body, for example, features many charges that are responsive to an electric field, but their movement is in some way restricted.

The literature on dielectric properties of colloids and DNA suspended in solution, motivates an extension of equation (2.2.1) to include the conductivity (or low frequency Ohmic loss) of the ionic solution, σ (Grant *et al.*, 1978, chs. 2 and 3; Jones, 1995). In addition, the frequency dependency is also made explicit, hence the relation for the complex permittivity becomes

$$\varepsilon(\omega) = \varepsilon'(\omega) - j\left(\varepsilon''(\omega) + \sigma/\omega\right) \tag{2.2.2a}$$

An important parameter for determining the value of the polarisability of a particle, is the dielectric increment (Takashima, 1989, p. 111), or decrement, $\Delta\varepsilon' = \varepsilon'_{rl} - \varepsilon'_{rh}$ where ε_{rl} and ε_{rh} are the low and high frequency relative permittivities, or limiting dielectric constants. The decrement, $\Delta\varepsilon'$, is utilised later in Chapter 4 for determining the polarisability of DNA.

An alternative expression used in the literature for the frequency dependent dielectric complex permittivity ignores the dielectric loss ε'' since it is often small compared with Ohmic loss σ/ω. The superscript ′ notation is omitted,

$$\underline{\varepsilon}^{*} = \varepsilon - j\sigma/\omega \tag{2.2.2b}$$

where ε is the permittivity (real part of $\underline{\varepsilon}^*$) or "dielectric constant" (Takashima, 1989, p. 37-9). The form for the complex permittivity given by (2.2.2b) is useful for describing polarisation mechanisms in section 2.2.2.

2.2.1.2 Types of polarisation

There are a number of kinds of polarisation: electronic, atomic, molecular, interfacial (or space-charge), and counterion polarisation. The first three are attributed to the displacement, or orientation, of bound charges; the latter two concern movement on a larger scale. *Electronic* polarisation arises from a slight asymmetric displacement of electrons (with respect to the positive nuclei of atoms) caused by an externally applied electric field. Atoms constituting a molecule, such as sodium chloride, have different net charges due to an unequal sharing of electrons. Consequently, when an external electric field is applied, the atoms behave differently. This causes a displacement of the atoms, from their equilibrium positions, resulting in *atomic* polarisation. An example of a molecule that exhibits atomic polarisation is sodium chloride. Both electronic and atomic polarisations are *induced*, and contribute only modestly to the total polarisability.

The asymmetric distribution of electrons in molecules also gives rise to *permanent* dipoles. The interaction of such a dipole with an externally applied electric field causes a torque that attempts to orient the molecule in the field direction. The polarisation is appropriately called *orientation*, or *dipole*, polarisation (Von Hippel, 1954, Part 2, section 1). Water is an example of a molecule with a permanent dipole, and is responsible for manifesting a significant permittivity for frequencies up to 17 GHz. In summary, of the first three types of polarisation, only molecular dipole polarisation, tends to feature in the literature concerning dielectric properties of colloids and DNA. It is discussed briefly in section 2.2.4.

The last two kinds of polarisation, interfacial and counterion, are familiar in the current literature and involve large-scale charge movement. Currently, there is no universal consensus in the literature on the high frequency polarisation mechanisms for DNA. At present, the emphasis tends to favour Maxwell-Wagner interfacial polarisation for latex beads, and counterion fluctuation polarisation, along the longitudinal axis, for DNA.

Interfacial, or *space-charge*, polarisation arises from free charge accumulation across the interfaces, between different dielectric materials, when they are juxtaposed. The interfacial charge accumulation, or polarisation, results in dielectric dispersions when the aggregate of dissimilar materials is exposed to AC electric fields (Pethig, 1979; Takashima, 1989). The simplest form of interfacial polarisation is a Maxwell-Wagner type, and is discussed in the following section 2.2.2. Counterions are ions in solution that are attracted to bodies of the opposite charge. They form 'clouds' around the bodies that become distorted when an external electric field is applied. *Counterion* polarisation arises when the movement of these counterions is restricted. Counterion

movement around the surface of colloidal particles, and along the double helical axis of DNA, is discussed in 2.2.3.

2.2.1.3 Double layer formation

DNA and most latex beads, in aqueous solution, both possess a net negative charge. The former is due to the negatively charged double-helical sugar-phosphate backbone, and the latter arises from a surface that has been modified by adding carboxyl groups. In solution, counterions (in this case, cations) cluster around the surface of the bead (or DNA), so as to neutralise the negative charge. Fig. 2.2 shows a schematic of the magnitude of the electrical potential $|\Phi|$ versus transverse displacement x perpendicular to the surface of a particle, adapted from Lyklema *et al.*, (1983). Since the presence of counterions acts to neutralise the surface charge the *magnitude* of the potential decreases with transverse displacement from the body. Some of the counterions are so strongly attracted to the surface, they form a 'sub-layer' of bound charges referred to as the *bound-charge layer,* or *Stern layer* (Pethig, 1979; Russel *et al.*, 1999, p. 100). Additional counterions accumulate around the bead, or DNA double helix, resulting in an ionic concentration gradient that is counteracted by diffusion. The second 'sub-layer' is known in the literature as the *diffuse layer*, and acts to 'screen' counterions, further away from the double layer, from the negative charge of the particle. The combination of the negatively charged surface layer, and layer of counterions, is known as the electrical *double layer*.

The potential change across the thin, capacitive Stern layer is linear. The potential of the diffuse layer is described by the Poisson-Boltzmann equation (Russel *et al.*, 1999). Depending on the geometry of the particle surface and ionic conditions, $\Phi(x)$ can be described by the Debye-Hukel exponential approximation (Pethig, 1979; Russel *et al.*, 1999). The extent of the diffuse layer into the surrounding medium is described by the *Debye* screening *length* λ_D (m). The value of the screening length, λ_D plays an important part in determining the dielectric properties of the double layer and is discussed further in section 2.2.3.1.

2.2.2 *Maxwell-Wagner interfacial polarisation*

A schematic diagram of Maxwell-Wagner (M-W) interfacial polarisation for a latex bead suspended in aqueous solution, is shown in Fig. 2.3(a). It represents a similar scenario to that illustrated in Fig. 2.1(a) except ions of the opposite charge, termed *counterions*, form around the interface between the polarised bead and surrounding aqueous solution. The counterions exist in the aqueous environment, for example, Na^+, Mg^{2+}, OH^-, Cl^-. Their concentration depends on the conductivity of the solution.

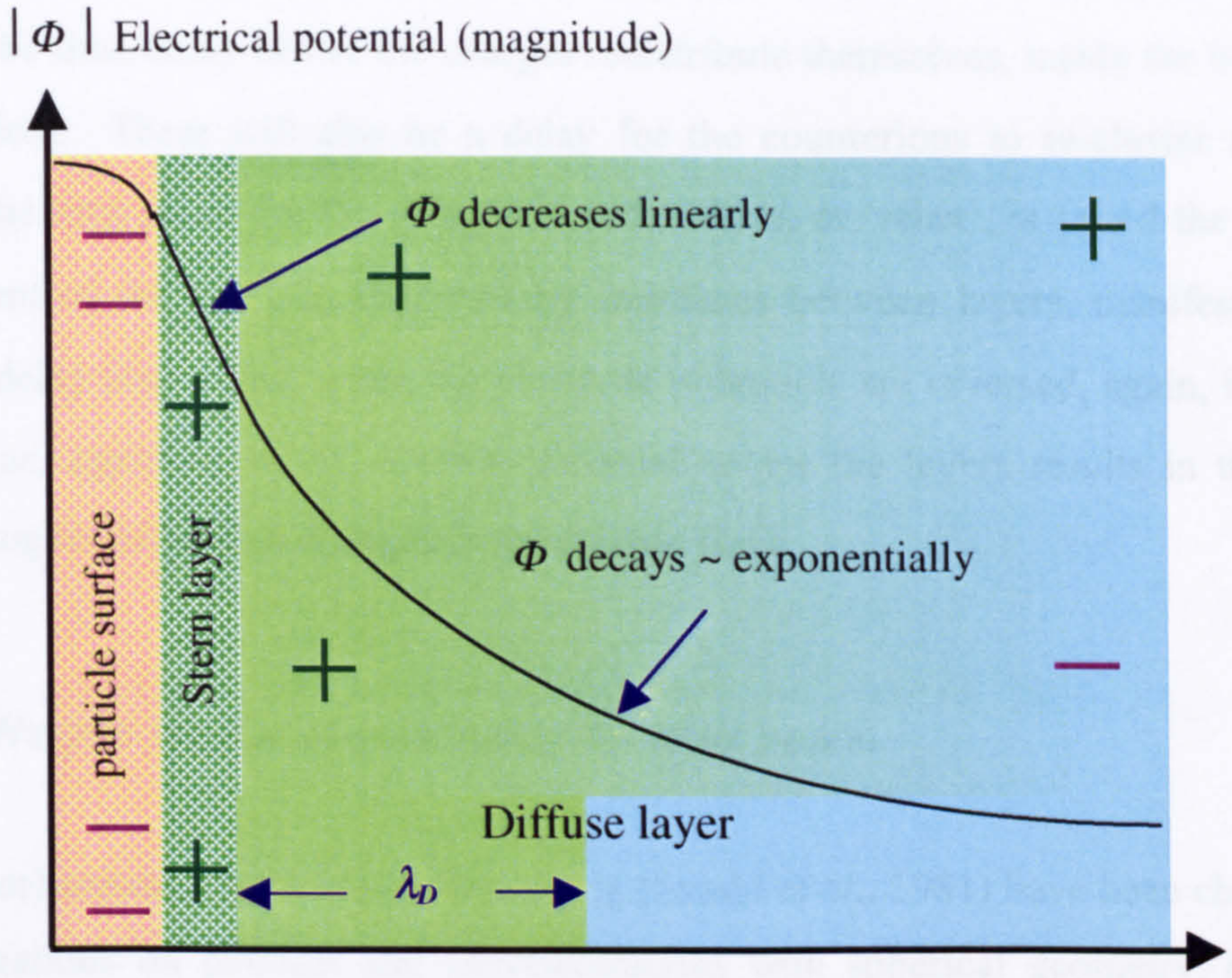

Fig. 2.2 The electrical double-layer scheme with potential magnitude Φ superposed: a layer of negative charges at the particle surface is surrounded by a positively charged counterion layer. This consists of a thin Stern layer and diffuse layer with characteristic length, λ_D (drawn not to scale).

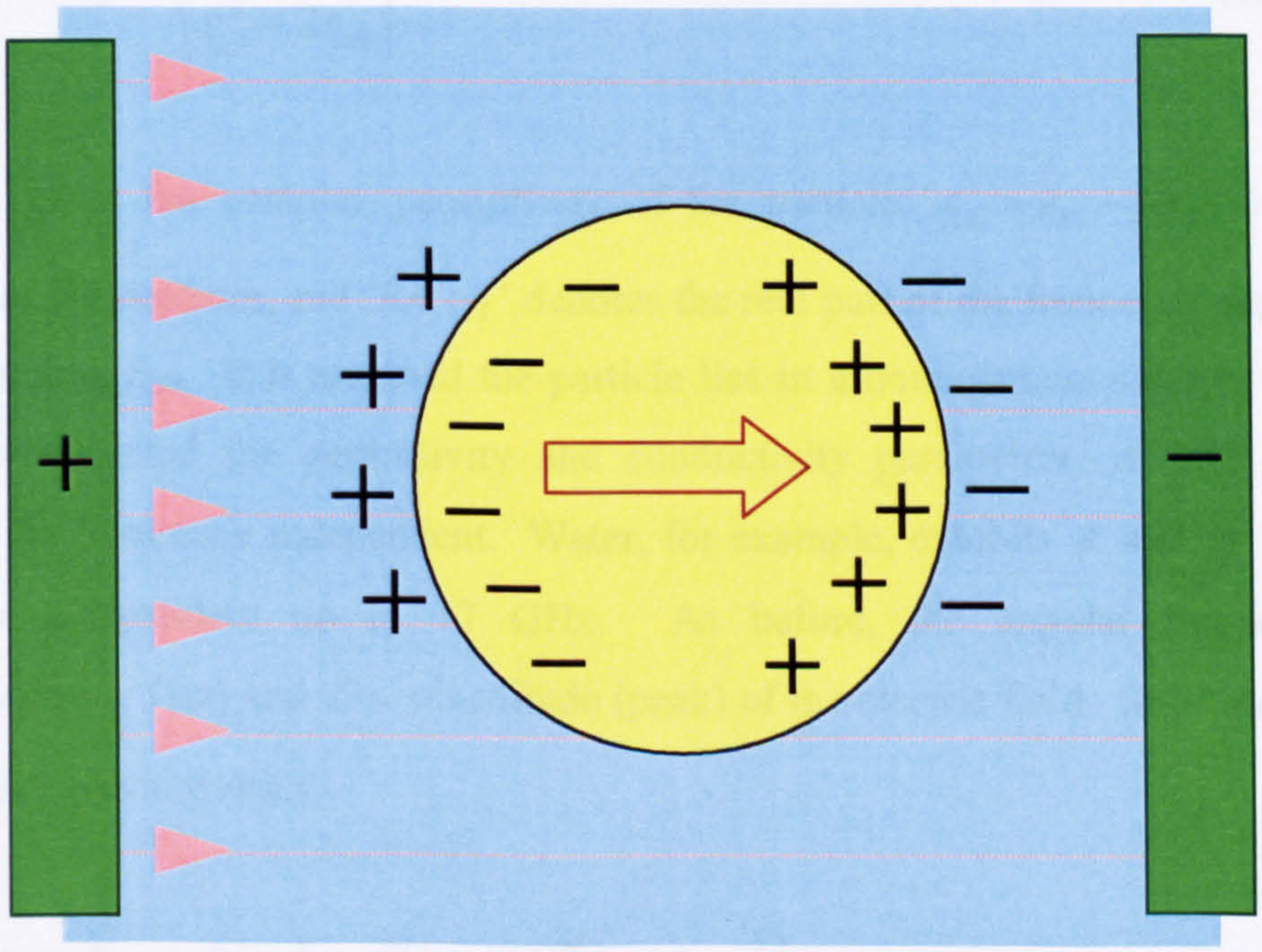

Fig. 2.3(a) Maxwell-Wagner (M-W) interfacial polarisation of a neutral dielectric body in a uniform field, similar to Fig. 2.1(a). Charges accumulate at the interface between the dielectric sphere and the aqueous medium.

Suppose the potential on the electrodes is suddenly reversed to the values shown in Fig. 2.3(a). There will be time delay before the charges redistribute themselves, inside the body, to the imposed electric field. There will also be a delay for the counterions to re-cluster around the polarised body. The time taken for the charges to redistribute, or 'relax', is called the *relaxation time*. The movement of the charges, restricted by interfaces between layers, manifests itself as polarisation. The delay also occurs when the electrode potentials are reversed, again, back to the original state. Thus, applying an AC electric potential across the layers results in the charges constantly attempting to respond to changes in the electric field.

2.2.2.1 Maxwell-Wagner interfacial polarisation for latex beads

The polarisation mechanisms applicable to latex beads (Sasaki *et al.*, 1981) have been characterised by similar investigations on colloids and polyelectrolytes with spherical geometry, (O'Konski, 1960; Schwartz *et al.*, 1962; Schwan *et al.*, 1962; Lyklema *et al.*, 1983; Springer *et al.*, 1983; Lyklema *et al.*, 1986). The expression for the effective polarisability, α, or dipole moment per unit volume per unit electric field, for interfacial polarisation of a spherical particle immersed in a medium is (Von Hippel, 1954; Jones, 1995)

$$\alpha = 3\varepsilon_m \operatorname{Re}\{f_{CM}(\omega)\} = 3\varepsilon_m \operatorname{Re}\left\{\frac{\underline{\varepsilon}_p^* - \underline{\varepsilon}_m^*}{\underline{\varepsilon}_p^* + 2\underline{\varepsilon}_m^*}\right\} \tag{2.2.3}$$

where $\underline{\varepsilon}_p^* = \varepsilon_p - j\sigma_p/\omega$ is the complex permittivity of the particle, $\underline{\varepsilon}_m^* = \varepsilon_m - j\sigma_m/\omega$ is the complex permittivity of the medium, and 'Re { }' denotes the real part of the frequency dependent Clausius-Mossotti function, f_{CM}. It is assumed the particle lies in a homogenous external electric field. Unless otherwise stated the permittivity and conductivity parameters, ε and σ, are implicitly assumed to be frequency independent. Water, for example, exhibits ε and σ that are practically frequency independent up to 17 GHz. As before, the angular frequency is $\omega = 2\pi f$ where f is frequency (Hz) and E = magnitude (peak) of the electric field. Substituting the relations for the complex permittivities,

$$\operatorname{Re}\{f_{CM}(\omega)\} = \left[\frac{(\sigma_p - \sigma_m)(\sigma_p + 2\sigma_m) + \omega^2(\varepsilon_p - \varepsilon_m)(\varepsilon_p + 2\varepsilon_m)}{(\sigma_p + 2\sigma_m)^2 + \omega^2(\varepsilon_p + 2\varepsilon_m)^2}\right] \tag{2.2.4}$$

By considering the two conditions $\sigma_p >> \sigma_m$, $\sigma_p << \sigma_m$ for the limiting case $\omega \to 0$, and $\varepsilon_p >> \varepsilon_m$, $\varepsilon_p << \varepsilon_m$ for $\omega \to \infty$, it is evident, $-0.5 \le \mathrm{Re}\{f_{CM}(\omega)\} \le 1$.

Analysis of the transient response of the sphere to an electric field reveals a M-W relaxation time constant τ_{MW} associated with free charge storage at the spherical interface (Jones, 1995),

$$\tau_{MW} = \frac{\varepsilon_p + 2\varepsilon_m}{\sigma_p + 2\sigma_m} \tag{2.2.5}$$

The relaxation time constant enables (2.2.4) to be cast (Benguigui and Lin, 1982; Jones, 1995),

$$\mathrm{Re}\{f_{CM}(\omega)\} = \left[\frac{\varepsilon_p - \varepsilon_m}{\varepsilon_p + 2\varepsilon_m} + \frac{3(\varepsilon_m\sigma_p - \varepsilon_p\sigma_m)}{\tau_{MW}(\sigma_p + 2\sigma_m)^2(1 + \omega^2\tau_{MW}^2)} \right] \tag{2.2.6}$$

and reveals two interesting features. First, it shows the conductivity parameters dominate at low frequencies, and the permittivities at high frequencies,

$$\mathrm{Re}\{f_{CM}(\omega)\} = \begin{Bmatrix} (\sigma_p - \sigma_m)/(\sigma_p + 2\sigma_m), & \tau_{MW}\omega << 1 \\ (\varepsilon_p - \varepsilon_m)/(\varepsilon_p + 2\varepsilon_m), & \tau_{MW}\omega >> 1 \end{Bmatrix} \tag{2.2.7}$$

Second, in the case $\varepsilon_m\sigma_p = \varepsilon_p\sigma_m$, the real part of the Clausius-Mossotti function is shown to be frequency independent.

Combining (2.1.7) and (2.2.3) and (2.2.4), the small-time averaged DEP force resulting from Maxwell-Wagner polarisation for a sphere with radius, r, and volume, $V = 4\pi r^3/3$ is,

$$\begin{aligned} \vec{F}_{DEP}(\underline{x}) &= \frac{1}{4}\alpha V \vec{\nabla}\left|\vec{E}(\underline{x})\right|^2 = \pi r^3 \varepsilon_m \mathrm{Re}\{f_{CM}(\omega)\}\vec{\nabla}\left|\vec{E}(\underline{x})\right|^2 \\ &= \pi r^3 \varepsilon_m \vec{\nabla}\left|\vec{E}(\underline{x})\right|^2 \left[\frac{(\sigma_p - \sigma_m)(\sigma_p + 2\sigma_m) + \omega^2(\varepsilon_p - \varepsilon_m)(\varepsilon_p + 2\varepsilon_m)}{(\sigma_p + 2\sigma_m)^2 + \omega^2(\varepsilon_p + 2\varepsilon_m)^2} \right] \end{aligned} \tag{2.2.8}$$

and is the starting point in most of the published work (Arnold *et al.*, 1993). In (2.2.8), positive DEP occurs when $\mathrm{Re}\{f_{CM}(\omega)\} > 0$, the direction of the force $\vec{F}$ is governed by $\vec{\nabla}|E|^2$, so the particle moves towards the region of maximum electric field intensity. Conversely, negative DEP occurs when $\mathrm{Re}\{f_{CM}(\omega)\} < 0$, and the direction of the force $\vec{F}$ is towards electric field minima.

The conditions for positive and negative DEP also apply to non-spherical geometry (Jones, 1995, p. 43).

The transition from positive DEP to negative DEP occurs when $\vec{F}_{DEP} = 0$. It is evident the *positive/negative* transition may, theoretically, involve any suitable combinations of σ, ε and ω values that force the numerator of (2.2.4) to be zero. In practice, however, the parameters controlled in DEP experiments are ω, σ_m, and sometimes ε_m. The other parameters remain constant. Typical values for the permittivities of water and 282 nm diameter latex bead are $\varepsilon_m = 78.4\varepsilon_o$ and $\varepsilon_p = 2.55\varepsilon_o$ (Green and Morgan, 1997a) where $\varepsilon_o = 8.854\times10^{-12}$ F/m. Applying the condition $\mathrm{Re}\{f_{CM}\} = 0$ in (2.2.4), establishes the relationship between cross-over frequency $f = f_c$ and medium conductivity for these latex beads,

$$f_c = \frac{1}{2\pi}\sqrt{\frac{(\sigma_p - \sigma_m)(\sigma_p + 2\sigma_m)}{(\varepsilon_m - \varepsilon_p)(\varepsilon_p + 2\varepsilon_m)}} = 1.635\times10^8\sqrt{(\sigma_p - \sigma_m)(\sigma_p + 2\sigma_m)} \qquad (2.2.9)$$

The conductivity of the particle (bead) σ_p, of radius r, consists of the bulk conductivity σ_b of the polystyrene and from ion movement shunted around, tangential, to the surface of the particle (O'Konski, 1960) with surface conductance, K_s (S).

$$\sigma_p = \sigma_b + 2K_s / r \qquad (2.2.10)$$

K_s can include ion movement in both parts of the double layer described in section 2.2.1.3 (Hughes *et al.*, 1999). Consider a low conductivity 1 mM potassium phosphate suspension, $\sigma_m = 0.018$ S/m with bead parameters, $r = 141$ nm, $\sigma_b \cong 0$ and $K_s = 2.2$ nS. Equation (2.2.10) yields $\sigma_p = 0.0312$ S/m, and (2.2.9) predicts $f_c = 5.23$ MHz. This is close to the experimentally observed crossover frequency (Green and Morgan, 1997a). The real and imaginary parts of the Clausius-Mossotti function for the above parameter values is plotted in Fig. 2.3(b) for the high frequency range of interest, $10^4 \le f \le 10^8$ Hz. In addition, using the above values in (2.2.5) predicts $f_{MW} = 1/(2\pi\tau_{MW}) = 3.93$ MHz. Although it is rather fortuitous τ_{MW} is so close to f_c in this example, in general, it is anticipated the DEP crossover frequency will be in the vicinity of the relaxation frequency.

There are several consequences of the above discussion. First, the transition from positive to negative DEP force, as the applied frequency f or conductivity σ_m are varied, means these parameters can be varied to explore subsequent changes in DEP collection rates. Secondly, the region of the crossover frequency can be estimated from the M-W relaxation time. Finally,

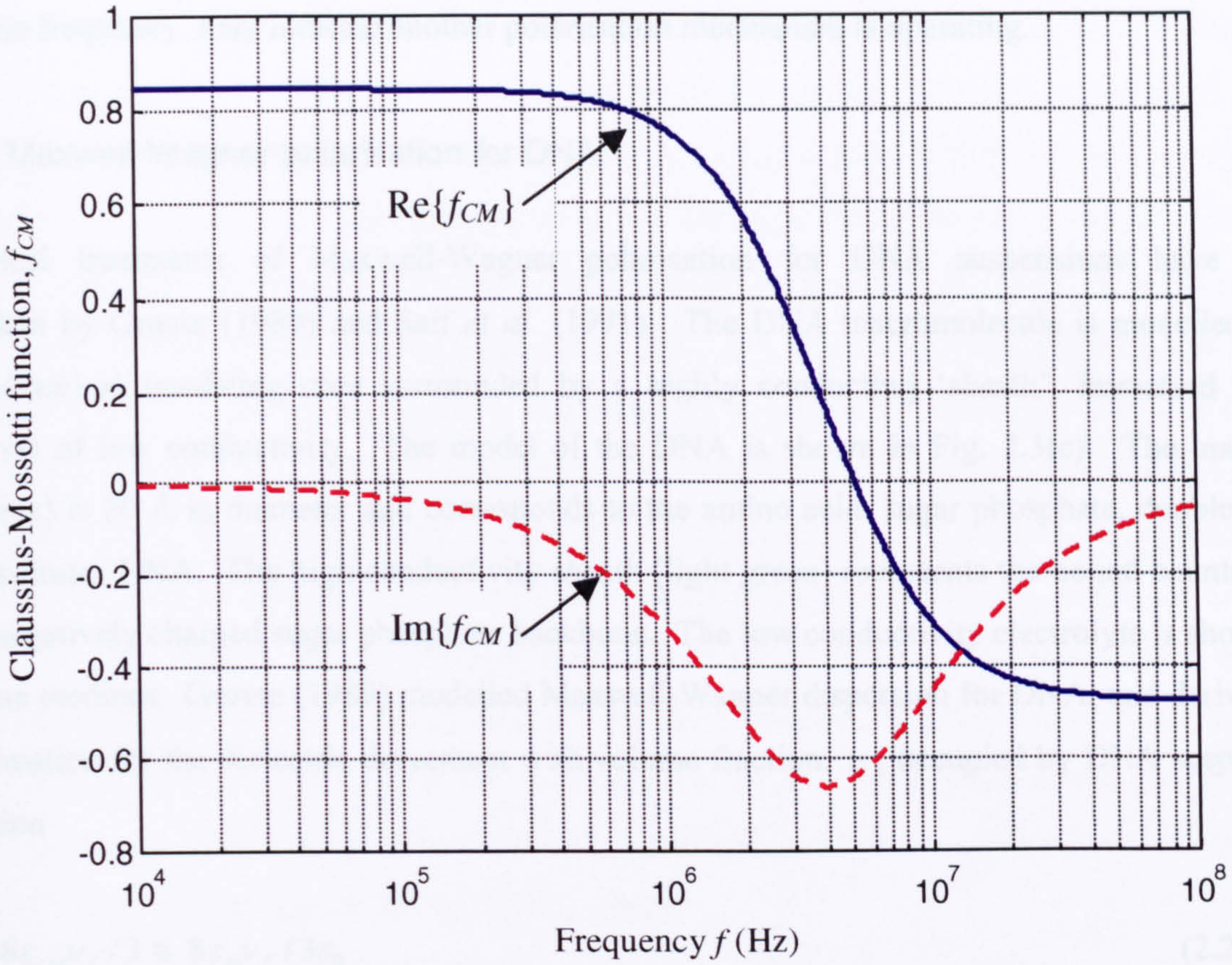

Fig. 2.3(b) Real and imaginary components of the frequency dependent Clausius-Mossotti function, Re$\{f_{CM}\}$ and Im$\{f_{CM}\}$, respectively.

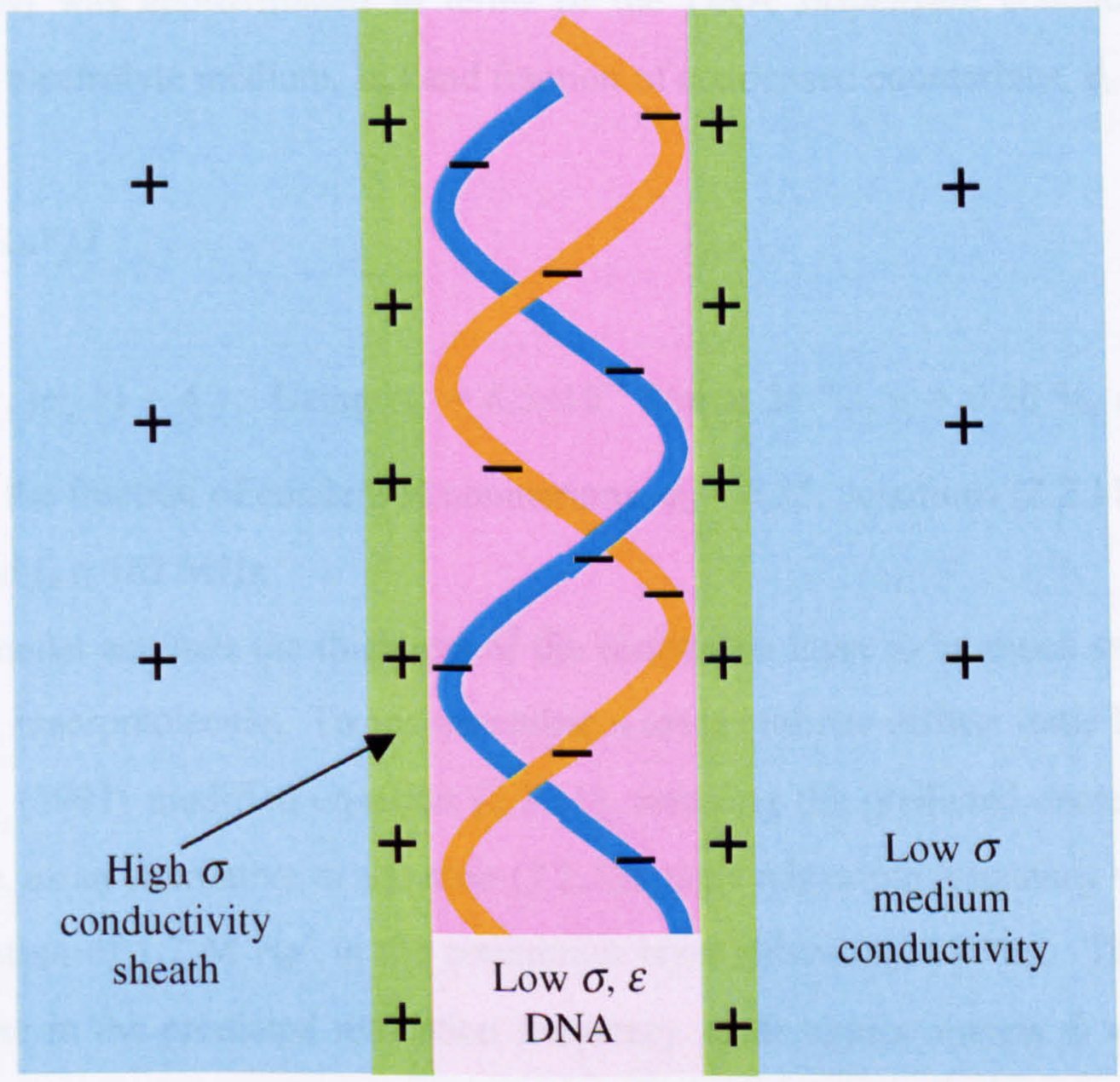

Fig. 2.3(c) Maxwell-Wagner interfacial polarisation of negatively charged DNA in aqueous solution. Counterions form a cylindrical sheath (light green) around the double helix of the DNA.

experiments exhibiting a large deviation of crossover frequency, compared with predicted relaxation frequency, may indicate another polarisation mechanism is operating.

2.2.2.2 Maxwell-Wagner polarisation for DNA

Theoretical treatments of Maxwell-Wagner polarisation for DNA suspensions have been undertaken by Grosse (1989) and Saif *et al.* (1991). The DNA macromolecule is modelled as a long cylindrical insulating core surrounded by a highly conducting 'sheath', immersed in an electrolyte of low conductivity. The model of the DNA is shown in Fig. 2.3(c). The insulator (light pink) is 20 Å in diameter and corresponds to the amino acid, sugar phosphate, double helix that constitutes DNA. The high conductivity sheath (light green) represents the bound counterions on the negatively charged sugar phosphate backbone. The low conductivity electrolyte is shown as light blue medium. Grosse (1989) modelled Maxwell-Wagner dispersion for DNA, and derived an approximation for the dielectric decrement with volume fraction, v_f, occupied by DNA suspended in solution

$$\Delta\varepsilon' \cong 8\varepsilon_{rm}v_f/3 \cong 8\varepsilon_m v_f/3\varepsilon_0 \qquad (2.2.11)$$

where ε_{rm} is the relative permittivity of the external (bulk) electrolyte medium. Similarly, the high frequency relaxation was approximated in terms of the DNA *suspension* conductivity σ_s (or conductivity of the electrolyte medium, σ_m) and fraction of condensed counterions, ϕ_c,

$$f_R = \sigma_m\phi_c/(4\pi\varepsilon_o\varepsilon_{rm}v_f) \qquad (2.2.12)$$

where $\sigma_m = (1 - v_f)\sigma_s/(1 - \phi_c)$. Using $\sigma_s = 8.5\times10^{-3}$ S/m at 25 °C, $v_f = 0.20$ %, $\varepsilon_{rm} = 78.4$ and Grosse's value for the fraction of condensed counterions, $\phi_c = 0.25$, equations (2.2.11) and (2.2.12) yield $\Delta\varepsilon' \cong 0.42$ and $f_R \cong 162$ MHz.

Grosse's model assumes the thickness of the counterion layer to be much smaller than the radius of the DNA macromolecule. To accommodate a more realistic diffuse ionic layer thickness of 7 Å, Saif *et al.* (1991) modified equation (2.2.11), reducing the predicted decrement to $\Delta\varepsilon' \cong 0.07$. Furthermore, as an alternative to equation (2.2.12), their relaxation frequency was based on a reported concentration of 1.2 M Na^+ in the counterion layer (Manning, 1978a). This amendment leads to an increase in the predicted relaxation frequency up to approximately $f_R \approx 1$ GHz. It is shown in Chapter 4 that these predictions do not coincide particularly well with values determined by dielectric experiments on pTA250 DNA, and this conclusion tends to be the same in the literature for other DNA samples.

The polarisation of DNA in solution can also be understood using a general expression for dielectric interfacial polarisation for suspensions of randomly oriented, shelled, prolate ellipsoids (Asami *et al.,* 1980). In this scenario, the geometry of the idealised rod-shaped DNA macromolecule with conducting sheath is mimicked by a shelled, prolate ellipsoid with a very short minor axes, and an extremely long major axis. Again, similar to the model by Grosse this approach predicts a very high relaxation frequency, $f_R \cong 400$ MHz (Bone *et al.*, 1995). It is reasonable to assume more realistic models should represent the DNA as a worm-like chain (Mandel and Odijk, 1984) than a rod. Although the shape of the ellipsoid is shown to have a significant effect on dielectric dispersions (Asami *et al.,* 1980), it is not clear whether an improvement in geometry would dramatically improve predicted relaxations or polarisability. At present, M-W interfacial polarisation appears to be a less successful model for explaining the dielectric behaviour of DNA than it is for latex beads. This is perhaps because relatively dilute suspensions of DNA exist as worm-like entanglements with a poorly defined interface compared with the well defined spherical boundaries of latex beads (Nagasawa, 1974; Bonincontro *et al.*, 1984). Polarisation due to charge movement along, or across, a poorly defined boundary, such as, a double-layer is possibly explained better with the counterion fluctuation model.

2.2.3 *Counterion fluctuation polarisation*

It is the response of the counterions to an externally applied AC electric field that results in counterion polarisation. Since there is Coulombic attraction between the charged body and the counterion layer, the counterions attempt to pull the charged body along with them as they follow the electric field. The double layer introduced in section 2.2.1.3 plays a key role in the movement of counterions. Although the double layer scheme, as presented in Fig. 2.2, is generally applicable for both colloidal particles and DNA, there are subtle differences in the two models (Eisenberg, 1976), and these are discussed separately.

2.2.3.1 Counterion fluctuation polarisation for latex beads

Investigations of the low frequency dispersion of colloidal particles have been undertaken by a number of groups, and was given impetus by Schwarz (1962) who derived expressions for the dielectric increment and relaxation frequency for a spherical particle. In the model proposed by Schwarz, the counterions were so strongly attracted to the surface, they could only move along the surface but not perpendicular to it. The effect of the diffuse layer, introduced in section 2.2.1.3, was included in subsequent refinements of the model (Dukhin, 1971; Fixman 1980a; Lyklema *et al.*, 1983; O'Brien, 1986) and accommodated radial and tangential ion movement, Fig. 2.4(a). There has been considerable progress in understanding counterion polarisation mechanisms but

further investigations are needed to resolve differences between theoretical predictions of dielectric dispersions and experimental data. At this stage, it is sufficient to outline the effects of the double layer on dielectric increment and relaxation frequency by way of a general example.

The thickness of the diffuse layer, illustrated in Fig. 2.2, is described by the reciprocal of the Debye screening length, given by κ_s (m^{-1}),

$$\kappa_s = \frac{1}{\lambda_D} = \left(\frac{2c_0 N_{Av} z^2 q^2}{\varepsilon_m k_B T} \right)^{0.5} \tag{2.2.13}$$

where c_o (mol m^{-3}) is the equilibrium concentration of counterions in the medium, N_{Av} is Avogadro constant (6.022×10^{23} mol^{-1}), the electronic charge is $q = 1.602\times10^{-19}$ (C), Boltzmann's constant is $k_B = 1.381\times10^{-23}$ (JK^{-1}) (Lide, 1994), absolute temperature T is nominally 298 (K), and all other symbols have been previously defined. In conjunction with the Coulombic and diffusive forces, the diffuse layer is subjected to hydrodynamic forces. The 'slip plane' designates where part of the diffuse layer moves with the body, in comparison with the remainder that tends to be dragged away by the surrounding medium. The zeta potential Φ_ζ (not shown in Fig. 2.2) is the electrical potential at the slip plane (Pethig, 1979; Russel *et al.*, 1999).

Expressions for the static dielectric increment and relaxation time arising from the movement of bound charges are given in Lyklema *et al.*, 1983 and Lyklema *et al.*, 1986,

$$\Delta\varepsilon(0) = \frac{9 r v_f q \rho_b}{4\varepsilon_o k_B T} \frac{1}{M} \tag{2.2.14}$$

$$\tau = \frac{r^2 q}{2\mu k_B T} \frac{1}{M} = \frac{r^2}{2D_b} \frac{1}{M} \tag{2.2.15}$$

where ρ_b is the bound layer charge density of the sphere, μ ($m^2\ V^{-1}\ s^{-1}$) is the counterion mobility in the double layer, D_b is diffusion coefficient of bound counterions. The dimensionless factor, M, is

$$M = 1 + \frac{q\rho_b}{k_B T \underbrace{\varepsilon_m \kappa_s \cosh(q\Phi_d / 2k_B T)}_{C_d}} \tag{2.2.16}$$

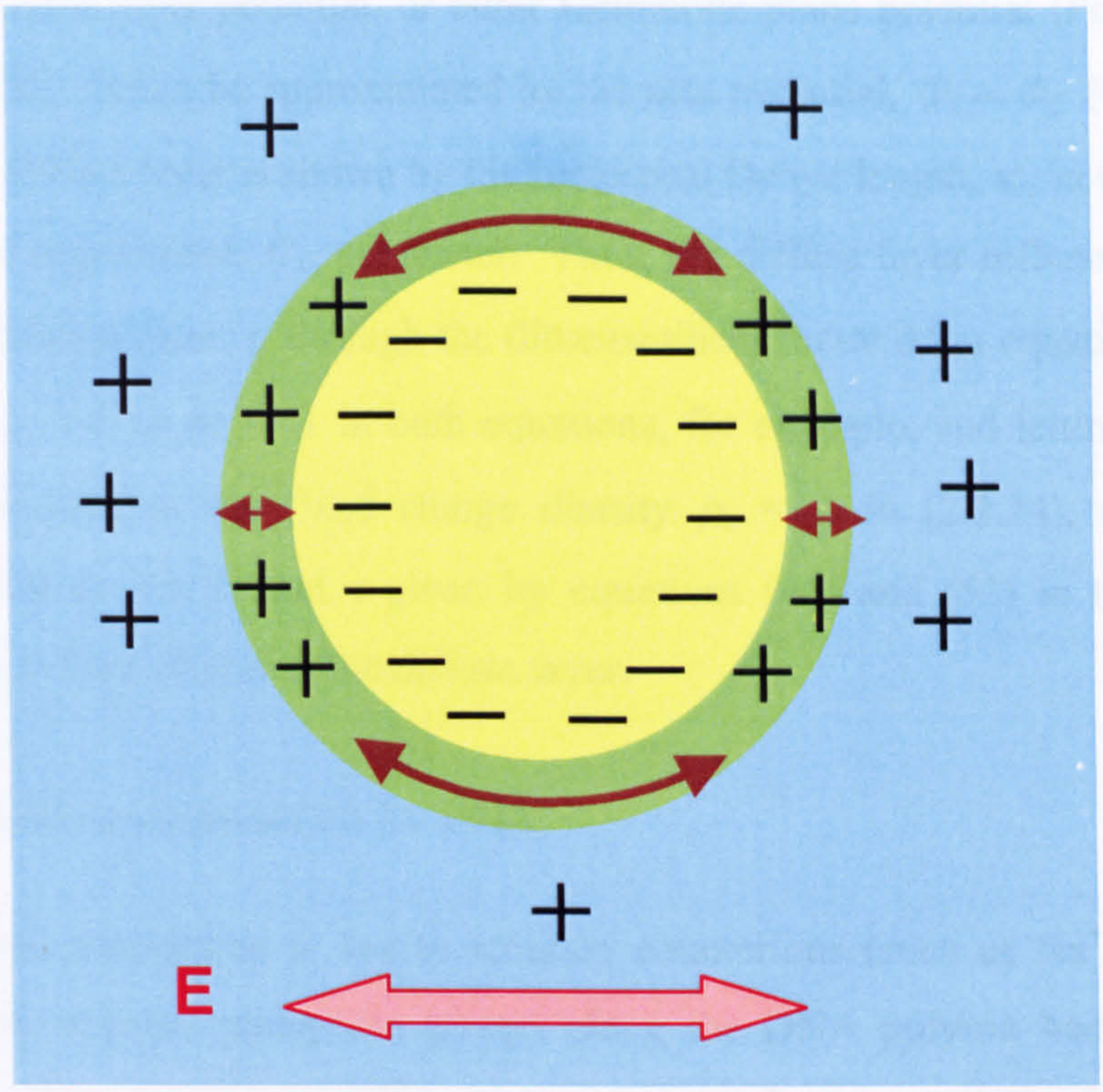

Fig. 2.4(a) Counterion polarisation: a negatively charged latex bead attracts ions of opposite (positive) charge, or counterions. Application of an AC electric field (red bi-directional arrow) causes charge movement tangential to the surface (brown, curved bi-directional arrows) within the double-layer (light green) surrounding the bead. It also causes radial counterion movement within the double-layer (shown by short, horizontal, brown bi-directional arrows).

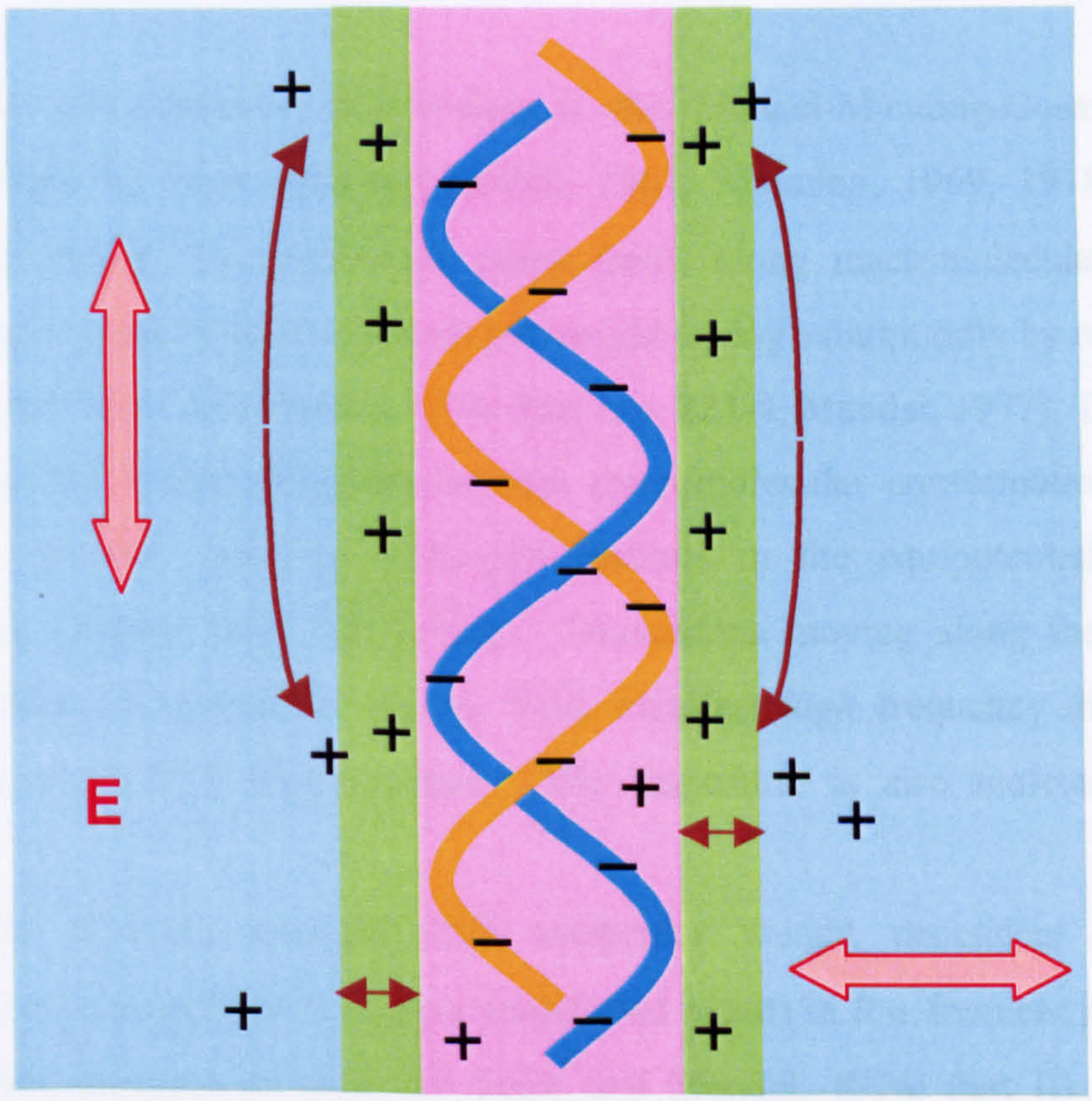

Fig. 2.4(b) Counterion polarisation on a short segment of DNA: a negatively charged sugar phosphate double helix attracts counterions. Components of an applied AC electric field (red bi-directional arrows) causes counterion movement in the longitudinal direction - along the DNA backbone, and transverse direction (brown bi-directional arrows). The counterion movement tends to be within the 'cylindrical' double-layer (light green).

where Φ_d is the diffuse double layer potential, or outer Helmholtz plane potential (Pohl, 1978, p. 275-8, Lyklema *et al.*, 1986). It can be approximated by the zeta potential, $\Phi_d \approx \Phi_\zeta$ (Green *et al.*, 1997a). The effect of the diffuse layer is shown by the reciprocal Debye length, κ_s, in (2.2.16), and included in the differential capacitance, C_d, parameter. Thus, the diffuse layer influences both the increment, $\Delta\varepsilon(0)$, and relaxation time, τ, through the dimensionless factor M in equations (2.2.15) and (2.2.16). Allowing $\lambda_D \rightarrow 0$ so $M \rightarrow 1$ in both equations, for example, and letting the bound charge density to be the same as the fixed charge density $\rho_b = \rho_f$ in (2.2.14), recovers the expressions for $\Delta\varepsilon(0)$ (with $v_f \ll 1$) and τ given by equations (46) and (51) in the paper by Schwarz (1962) that excluded the effects of the diffuse layer.

2.2.3.2 Counterion fluctuation polarisation for DNA

The counterion polarisation mechanism is due to solution counterions (such as Na^+, Mg^{2+}, etc.) interacting with negatively charged phosphate groups along the DNA polyion backbone. The counterions move freely along lengths of DNA in response to the component of the external electric field parallel to the major axis or 'backbone', Fig. 2.4(b). Their migration results in an induced dipole moment, and hence, an identifiable polarisability. To reiterate: dispersions arise when the oscillating cloud of counterions can no longer follow the alternating electric field (Oosawa, 1971), and this effect is observed in both real and imaginary parts of the complex permittivity.

A popular model of counterion polarisation is the Mandel-Manning-Oosawa model developed in various stages by these authors (Mandel, 1961; Manning, 1969, 1978a, 1978b; Oosawa, 1970). In this model, the counterions move freely along macromolecular "subunit lengths" and are permitted to cross from one subunit to a neighbouring subunit only by overcoming "potential barriers" (van der Touw and Mandel, 1974: Part I, p. 223-4; Mandel, 1977). The *subunit length* L_s is described as the length along the average macromolecular conformation between "breaks", or "potential barriers" resulting from perturbations in the equipotentials (due to conformational processes, folding, etc.), Fig. 2.4(c). Counterions moving along these *subunit* lengths, under the influence of an external electric field, manifest *high* frequency dispersion – which is of major interest to DEP investigations. The dispersion is also molecular weight independent.

This polarisation scenario contrasts with molecular weight dependent counterion movement along the entire macromolecular contour length that results in *low* frequency dispersion and accounts for the static permittivity (van der Touw and Mandel, 1974: Part II). It is also proposed (Manning 1969, 1978a, 1978b) that a proportion of the counterions are so strongly attracted to the polyelectrolyte that they are said to 'condense' onto the DNA backbone.

Essentially there are three distinct phases: (Saif *et al.*, 1991)

(i) *condensed* counterions – these are sufficiently, but non-locally, bound (or 'delocalised') to the phosphate groups of the DNA, and thereby neutralise a fraction of the DNA charge.

(ii) *diffuse* counterions which are responsible for neutralising the remainder of the DNA charge, with a density which decreases exponentially with distance from the axis.

(iii) *bulk* ions or 'added salt' ordinary aqueous solution ions.

In terms of their contribution to polarisability, the condensed counterion phase is the most important. A feature of the condensed state is that the local concentration of counterions around the DNA does not tend to zero when the bulk electrolyte concentration does (Anderson and Record, 1982). Condensation occurs when the condition $\xi \geq 1/|z|$ is satisfied (Manning, 1978a; Bone and Small, 1995) where z is the valence of each counterion and the charge density parameter, ξ, is given by

$$\xi = q^2 / 4\pi\varepsilon_m k_B T b \qquad (2.2.17)$$

where b is the average distance between charged sites, and for the B-DNA double helix, b = 1.73 Å. The fraction of condensed counterions is ϕ_c

$$\phi_c = 1 - |z^{-1}|\xi^{-1} = 1 - 4\pi\varepsilon_m k_B T b / q^2 |z| \qquad (2.2.18)$$

Using $\varepsilon_m = 78.4\varepsilon_o$ and z = 1.00, the charge density parameter at 25°C is evaluated to be ξ = 4.132, and hence for monovalent cations, ϕ_c = 0.7580 ≅ 0.76. The 'Manning-Mandel-Oosawa' model yields a generalised expression for scalar longitudinal polarisability α_s per subunit length L_s,

$$\alpha_s = \frac{z^2 q^2 L_s^{\,2} n_{cc} A_{st}}{12 k_B T} \qquad (2.2.19)$$

where n_{cc} is the number of condensed counterions, and can be predicted theoretically (Manning, 1978a; Bone and Small, 1995),

$$n_{cc} = \phi_c L_s / |z| b \qquad (2.2.20)$$

and A_{st} is the stability factor of the ionic phase and includes mutual repulsion between fixed charges on the backbone and the effect of Debye screening,

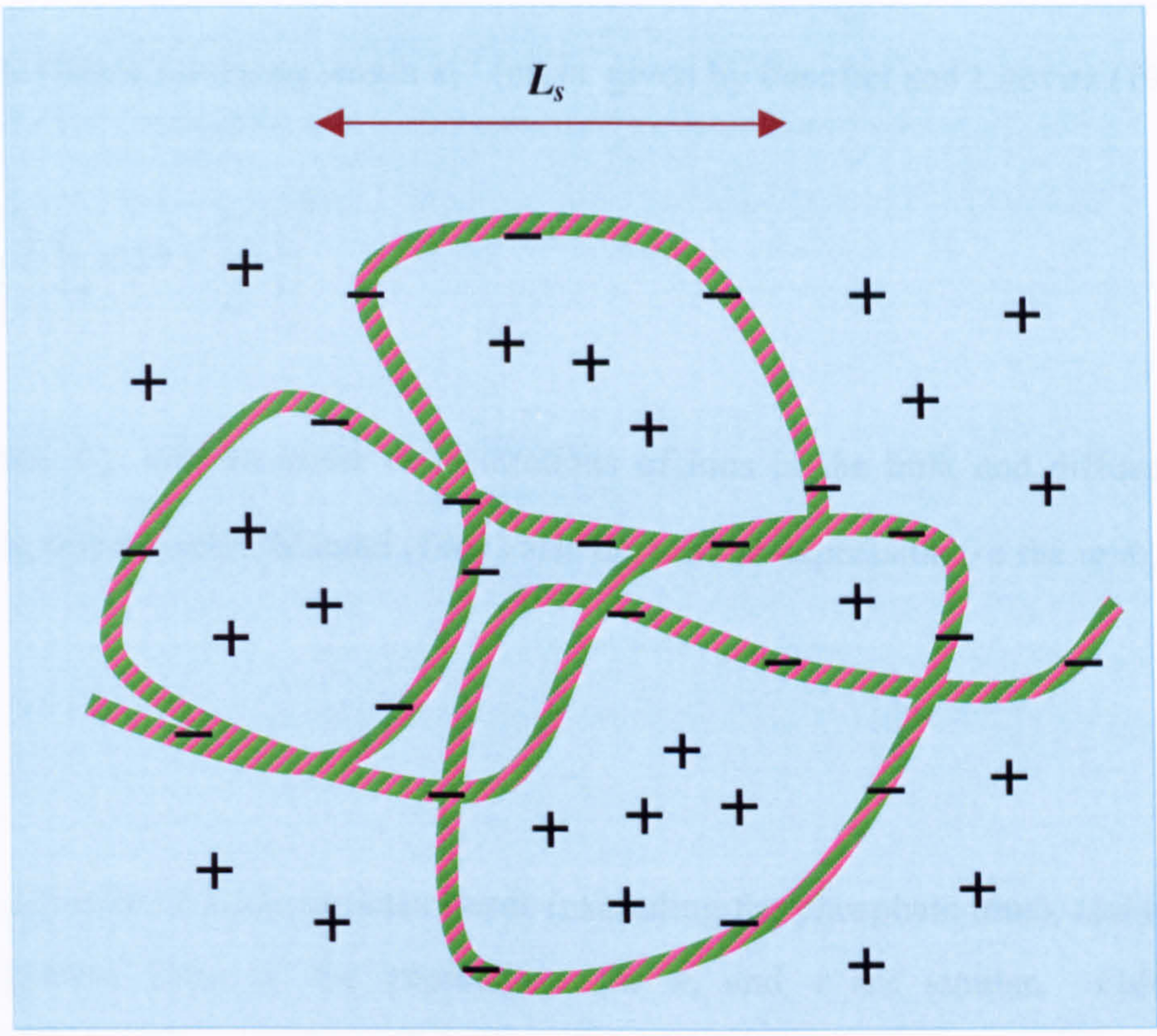

Fig. 2.4(c) Worm-like chain of DNA and double-layer sheath (patterned pink-green) is divided into sub-unit lengths, L_s, based on the distance between equipotentials.

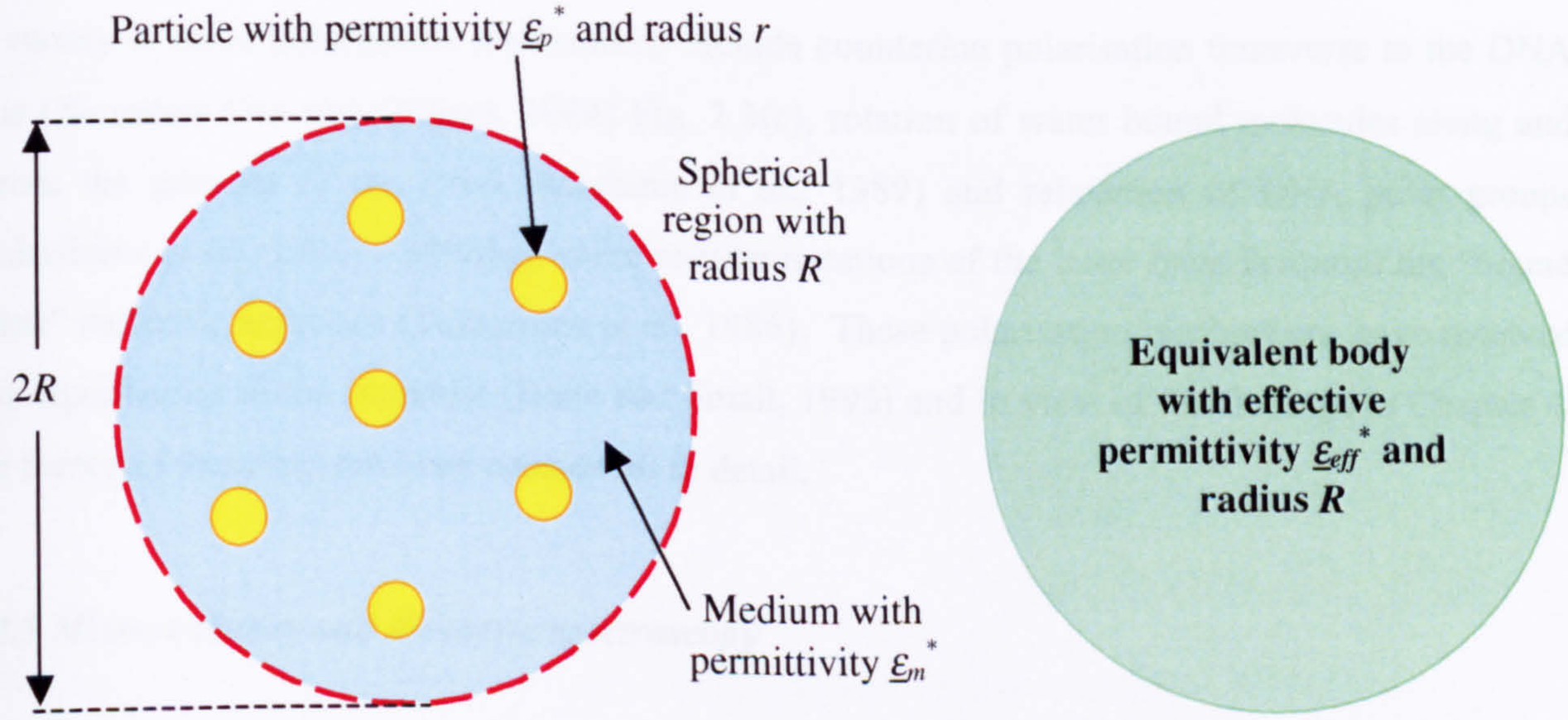

Fig. 2.5 Suspension of spherical particles. (a) n_{sp} particles enclosed in spherical volume with radius R (b) Equivalent sphere with effective permittivity $\underline{\varepsilon}_{eff}^*$ and radius R. Adapted from Jones (1995) and Asami *et al.* (1980).

$$A_{st} = \left[1 - 2(|z|\xi - 1)\ln(\kappa_s b)\right]^{-1} \tag{2.2.21}$$

and the reciprocal Debye screening length κ_s^{-1} (m) is given by Penafiel and Litovitz (1992)

$$\kappa_s = \left[\left(\frac{N_{Av} 4\pi q^2}{4\pi\varepsilon_m k_B T}\right)\left(\sum_i C_i z^2 + \frac{C_p}{\xi}\right)\right]^{0.5} \tag{2.2.22}$$

where and C_i and C_p are the molar concentrations of ions in the bulk and diffuse phase, and phosphate groups, respectively. Mandel (1961) also derived an expression for the relaxation time

$$\tau = \frac{L_s^{\,2} q}{\pi^2 \mu k_B T} \tag{2.2.23}$$

Comparing (2.2.22) with (2.2.13) for latex beads (excluding the phosphate ions), and (2.2.15) with (2.2.23), the algebraic form of the expressions for κ_s and τ are similar. Calculations of polarisability for DNA, using equations (2.2.17) – (2.2.23), are detailed in Chapter 4.

2.2.4 *Other polarisation mechanisms*

A variety of other polarisation mechanisms include counterion polarisation transverse to the DNA axis (Xammara Oro and Grigera, 1984) Fig. 2.3(c), rotation of water bound molecules along and across the grooves of the DNA (Mashimo *et al.*, 1989) and relaxation of DNA polar groups (Takashima *et al.*, 1984) - although some re-interpretations of the latter have favoured the "bound water" molecule approach (Takashima *et al.*, 1986). These polarisation mechanisms have received less significance in the literature (Bone and Small, 1995) and in view of the findings in Chapter 4, the theory of these has not been considered in detail.

2.2.5 Mixture theory and dielectric spectroscopy

In section 2.2.1 the complex dielectric parameters $\underline{\varepsilon_p}^*$ and $\underline{\varepsilon_m}^*$ were introduced for a single particle suspended in a medium. Dielectric spectroscopy enables these parameters to be determined by measuring the dielectric dispersion for a suspension, or population, of particles. Mixture theory enables the experimentally measured quantities to related to the properties of a single particle.

Consider a suspension of n_{sp} spherical particles each with volume $V = 4\pi r^3/3$, as shown in Fig. 2.5(a), encapsulated in a space with a total volume, $V_T = 4\pi R^3/3$. It is assumed the particle suspension is sufficiently dilute so the particles do not interact. Using (2.1.4) and following an analogous approach by Jones (1995), the induced dipole moment for n_{sp} particles is found by superposition,

$$\vec{p}_\Sigma(\underline{x},t) = \sum_1^{n_{sp}} \vec{p}(\underline{x},t) = n_{sp}\vec{p}(\underline{x},t) = n_{sp}\alpha V\vec{E}(\underline{x},t) \qquad (2.2.24)$$

where the subscript, Σ in $\vec{p}(\underline{x},t)$ indicates a population, or sum, of particles, and all other symbols have been previously defined. The suspension can be represented by a *single* particle with polarisability, α_Σ (dipole moment per unit volume per unit electric field with dimensions, F m^{-1}) as shown in Fig. 2.5(b). The induced dipole moment is written,

$$\vec{p}_\Sigma(\underline{x},t) = \alpha_\Sigma V_T\vec{E}(\underline{x},t) \qquad (2.2.25)$$

Equating (2.2.24) with (2.2.25),

$$\alpha_\Sigma = v_f\,\alpha \qquad (2.2.26)$$

where v_f is the volume fraction, $v_f = n_{sp}V/V_T = n_{sp}r^3/R^3$. Substituting the expression for polarisability, α, given by (2.2.3) for Maxwell-Wagner polarisation, yields the well known mixture formula in terms of the Claussius-Mossotti function f_{CM},

$$\underbrace{\frac{\underline{\varepsilon}^*_{eff} - \underline{\varepsilon}^*_m}{\underline{\varepsilon}^*_{eff} + 2\underline{\varepsilon}^*_m}}_{f_{CM_\Sigma}} = v_f \underbrace{\frac{\underline{\varepsilon}^*_p - \underline{\varepsilon}^*_m}{\underline{\varepsilon}^*_p + 2\underline{\varepsilon}^*_m}}_{f_{CM}} \qquad (2.2.27)$$

where the sphere with volume V_T in Fig. 2.5(b) has an *effective* complex permittivity, $\underline{\varepsilon}^*_{eff}$. As above, the subscript, Σ indicates the 'sum' of particles. Equation (2.2.27) indicates that the dielectric properties measured for a suspension of monodisperse particles, f_{CM_Σ}, can be used to find the dispersion for a single particle f_{CM} via the volume fraction (Asami *et al.*, 1980; Wang *et al.*, 1993b; Hilfer *et al.*, 1994; Raicu *et al.*, 1996).

Equation (2.2.26) can be alternatively written,

$$\alpha_{\Sigma} = c_V V \alpha = c_V \alpha_p \tag{2.2.28}$$

where the particle concentration or number density is $c_V = n_{sp}/V_T$ (m^{-3}) and the dipole moment per unit electric field for a particle is $\alpha_p = \alpha V$ (F m^2). The relation (2.2.28) is useful in Chapter 4 where dielectric spectroscopy is used to determine the dipole moment per unit electric field for a single DNA *macromolecule*, α_m. The term 'polarisability per macromolecule' is used for α_m in chapters 4 and 7, and it is understood to be synonymous with 'dipole moment per unit electric field'. It implicitly includes the volume of the macromolecule, i.e. $\alpha_m \equiv \alpha_p$. Note that the dimensions of the polarisabilities, α_p and α_m are (F m^2) whereas α and α_{Σ} are (F m^{-1}).

2.3 Forces acting on a particle

The dielectrophoretic motion of particles in aqueous media, with diameters ranging 10 nm to 10 μm, can be modelled adequately by Newtonian mechanics. It is convenient to consider, at this stage, a one-dimensional system similar to that of Morishima *et al.*, (1996) and Watarai *et al.*, (1997). This avoids needing to consider vector quantities. The result is easily generalised to three dimensions later. The motion of each particle is governed by four kinds of Newtonian force: inertial, external, friction and thermal. An important simplifying assumption is that the particles do not interact; this is an idealisation, but a reasonable one for this stage of DEP collection rate modelling.

2.3.1 Inertial force

The inertial force is given by product of particle mass m and acceleration,

$$F_{Inert}(x,t) = m\frac{d^2x}{dt^2} \tag{2.3.1}$$

The mass of a latex bead with radius r (and volume V) is calculated using published values (Bangs, 1997) of its density $\rho_p = 1.05$ g/cm^3 = 1.05x10^3 kg/m^3.

$$m = \rho_p V = \rho_p 4\pi r^3/3 \tag{2.3.2}$$

hence each 216 nm latex bead has mass $m = 5.54\times10^{-18}$ kg. The mass of a DNA macromolecule can be calculated from the number of base pairs, N_{bp}, using a known value for molecular weight in daltons (Da) per base pair (bp), MW_{bp}. It understood one dalton is equivalent to one (unified) atomic mass unit, $m_u = m_a(^{12}C)/12 = 1.6605 \times 10^{-27}$ kg (Lide, 1994), thus

$$m_{N_{bp}} = N_{bp} MW_{bp} m_u \tag{2.3.3}$$

Typically MW_{bp} = 662 daltons/base pair (Da/bp) for double stranded Na^+ DNA (Bloomfield *et al.*, 1974, p. 174; Coggins, 1987, p. 24; Bone and Small, 1995) although lower values are quoted in the literature, MW_{bp} = 649 Da/bp (Perbal, 1988, p. 79) and MW_{bp} = 635 Da/bp (Sambrook *et al.*, 1989, App. C.3). Using MW_{bp} = 662 in (2.3.3) the mass of a DNA macromolecule with $N_{bp} = 12\times10^3$ is $m_{12kbp} = N_{bp} MW_{bp} m_u = 12000\times662\times1.66\times10^{-27} = 1.32\times10^{-20}$ kg $\cong 1.3\times10^{-17}$ g. The abbreviation 'kbp' means kilo-base–pair. Therefore, the particle mass m for nano-scale particles, such as polystyrene latex beads and 12 kbp DNA used in DEP experiments (described later in chapters 3 and 7), is exceedingly small. As shown in the following sections, this considerably simplifies subsequent analyses of electrokinetic motion.

2.3.2 Friction force or Stokes' drag

A particle moving though a liquid medium with velocity v experiences Stokes' drag, or friction, force F_{Drag}, in a direction opposite to its movement,

$$F_{Drag} = -\zeta v = -\zeta\, dx/dt \tag{2.3.4}$$

where ζ (kg s^{-1}) is the friction, or Stokes' drag, coefficient. Unless otherwise stated, particles are assumed to be spherical bodies with radius r moving through a fluid with dynamic viscosity, η (kg m^{-1} s^{-1}). The friction coefficient for a sphere is

$$\zeta = 6\pi\eta r \tag{2.3.5}$$

The ratio m/ζ is an important parameter for understanding how quickly a particle approaches, or 'relaxes' to, steady state terminal velocity. For a simple sphere, the relaxation time τ (s)

$$\tau = m/\zeta = \rho V/\zeta = \rho 4\pi r^3/(18\pi\eta r) = 2\rho r^2/(9\eta) \qquad (2.3.6)$$

In the case where the particles are model particles, such as latex beads, the coefficient r can be interpreted as the radius of the sphere. Using a value for dynamic viscosity of water at 25 °C, $\eta = 9.0\times10^{-4}$ kg m^{-1} s^{-1}, (2.3.6) predicts a 216 nm latex bead has a relaxation time $\tau = 2.7\times10^{-9}$ s.

For a macromolecule, such as DNA, r can be interpreted as the hydrodynamic radius, and can be deduced from the literature using scaling laws applied to the Stokes-Einstein relation. An estimate of the hydrodynamic radius, for 12 kbp DNA is $r_h \approx 200$ nm (Newman, *et al.*, 1974; Viovy and Duke, 1993; Smith *et al.*, 1996). A minimum value of r_h, representing the DNA as a tightly compact sphere, is also a useful parameter. It can be calculated from the cylindrical volume the macromolecule occupies V_{cyl},

$$r_{\min} = \sqrt[3]{3V_{cyl}/4\pi} = \sqrt[3]{3r_{dh}{}^2 L_{bp} N_{bp}/4} \qquad (2.3.7)$$

where r_{dh} is the radius of the double-helix and L_{bp} is the contour length of DNA per base pair. The value of r_{dh} is 10 Å for the radius of double helix plus a nominal value of 5Å for the thickness of the counterion layer (Saif *et al.*, 1991), hence $r_{dh} = 1.5$ nm. For B-DNA, $L_{bp} = 3.46$ Å, (Bloomfield *et al.*, 1974, p. 174). Hence, for a 12 kbp DNA, (2.3.7) gives, $r_{min} \cong 19$ nm. The drag coefficient, using (2.3.5), is $\zeta = 3.2\text{x}10^{-10}$ kg s^{-1}. Using the above result for the mass of 12 kbp DNA, $m_{12kbp} = 1.3\times10^{-20}$ kg, (2.3.6) gives $\tau = m/\zeta = 4.1\times10^{-11}$ s. The relaxation time needs comment: if the value of r is interpreted as the hydrodynamic radius, ζ would be up to an order of magnitude larger. However, the effective mass of the DNA, as discussed previously, would also increase due to counterions and loosely bound water molecules.

2.3.3 Deterministic external forces

The deterministic external force $F_{Ext}(x, t)$ is the external force acting on the particle that includes electrophoresis, dielectrophoresis, and vertical resolved components of gravity and buoyancy that are constant (with respect to time). The external force is expressed,

$$F_{Ext}(x,t) = F_{DEP}(x,t) + F_{EP}(x,t) + F_{Const} \qquad (2.3.8)$$

where the subscripts *EP*, *DEP*, and *Const* denote the electrophoretic, dielectrophoretic, and constant forces. The effects of convection currents (Melcher and Taylor, 1969; Tritton, 1988; Pontiga and Castellanos, 1992) due to electrode heating and flow of ions in solution can be ignored

for the AC electric field frequency regimes of interest and low conductivity of the suspension medium.

The 1-D dielectrophoretic force, from (2.1.6), is rewritten

$$F_{DEP}(x,t)=\underbrace{\frac{\alpha V}{4}\frac{\partial E(x)^2}{\partial x}}_{F_{DEP}(x)}[1+\cos(2\omega t+2\theta)] \tag{2.3.9}$$

where all symbols are as previously defined.

The electrophoretic force can be expressed using Smoluchowski's mobility relation $\mu=\varepsilon_m\Phi_\zeta/\eta$ (Ohshima, 1997; Grattarola and Massobrio, 1998, Ch. 5; Arnold *et al.*, 1993; Reese, 1994) where, as before, Φ_ζ is the zeta potential of the electrical double layer,

$$F_{EP}(x,t)=\mu\zeta E(x)\cos(\omega t+\theta)=\underbrace{6\pi r\varepsilon_m\Phi_\zeta E(x)}_{F_{EP}(x)}\cos(\omega t+\theta) \tag{2.3.10}$$

and the other symbols are as previously defined. A description of the counterion and co-ion cloud surrounding the particle in an applied electric field is given in O'Brien and White (1978) and DeLacey and White (1981).

The force due to gravity F_g, acting in the vertical direction (adopting the convention upwards as positive), can be written as the product of particle mass m and gravitational acceleration g (that is assumed to have a constant value, $g = 9.8\ \mathrm{m\ s^{-2}}$),

$$F_g=-mg=-\rho_pVg \tag{2.3.11}$$

The particle mass m, in turn, can be expressed as the density ρ_p and volume of the particle, V. The fluid displaced by the particle, exerts a buoyancy force (upwards),

$$F_b=\rho_mVg \tag{2.3.12}$$

where ρ_m is the density of fluid medium ($1.00\times10^3\ \mathrm{kg/m^3}$). Both gravitational and buoyancy forces can be combined into a sedimentation force that is constant,

$$F_{Const}=F_b+F_g=(\rho_m-\rho_p)Vg \tag{2.3.13}$$

The constant force due to gravity and buoyancy, for example, on a 216 nm diameter spherical polystyrene latex bead with $\rho_p = 1.05\times10^3$ kg/m^3 submerged in water $\rho_m = 1.00\times10^3$ kg/m^3 is, $F_{Const} = -2.5856\times10^{-18} \cong -2.6\times10^{-18}$ (N). The minus sign indicates the direction of the net force is downwards.

2.3.4 Thermal fluctuations

Nano-sized particles in a liquid medium, at room temperature, incur incessant collisions from neighbouring molecules. The collisions of the thermally agitated molecules with each particle, are random in direction and time, and cause the particle to move in a haphazard way. This random movement is called Brownian motion, named after the botanist, Robert Brown, who in 1827 observed the irregular motion of pollen grains suspended in water (Gardiner, 1985). To fully describe the irregular motion of the nano-scale particle would require knowledge about the motion of all the colliding molecules. This is untenable, therefore, the motion of the particle is described probabilistically. At least two assumptions have been made about the nature of this probabilistic movement (Einstein, 1924, p. 12-13):

(i) the movement of each particle is *independent* of the movement of all other particles,

(ii) the movements of a particular particle in successive time intervals are *independent* processes, as long as the time intervals are chosen 'not too small'.

To enable a quantitative description of movement it is necessary to introduce two statistical parameters. First, the ensemble average, or mean, of a random variable $x_n(t)$ (Papoulis, 1984; Gardiner, 1985)

$$\langle x(t)\rangle = \lim_{N\to\infty}\left\{\frac{1}{N}\sum_{n=1}^{N}x_n(t)\right\} \cong \frac{1}{N}\sum_{n=1}^{N}x_n(t) \qquad (2.3.14a)$$

where N is sufficiently large, and is often, less formally, written as

$$\langle x(t)\rangle = \sum_n x_n(t) \qquad (2.3.14b)$$

The second parameter is the variance, and can be specified in terms of (2.3.14)

$$\mathrm{var}\{x(t)\} = \left\langle \left[x(t) - \langle x(t)\rangle\right]^2 \right\rangle \qquad (2.3.15)$$

There have been many experimental and theoretical studies of Brownian motion that indicate assumptions (i) and (ii) are essentially correct provided the suspension of particles is dilute. The force exerted on the nano-scale particle, from each thermal collision, can be expressed,

$$F_{Therm}(t) = \sqrt{2\zeta\, k_B T}\, \xi(t) \tag{2.3.16}$$

where all symbols have been previously defined. The random variable $\xi(t)$ exhibits zero mean,

$$\langle \xi(t) \rangle = \sum_i \xi(t_i) = 0 \tag{2.3.17}$$

and autocorrelation,

$$\langle \xi(t')\xi(t) \rangle = \sum_i \sum_j \xi(t_i')\xi(t_j) = \delta(t' - t) \tag{2.3.18}$$

where $\delta(t' - t)$ is the Dirac delta function (or functional) and can be defined (Haken, 1978),

$$\int_{t_0-\varepsilon}^{t_0+\varepsilon} \delta(t - t_0)\, dt = 1 \qquad \text{for any } \varepsilon > 0 \tag{2.3.19a}$$

and

$$\delta(t - t_0) = 0 \qquad \text{for } t \neq t_0 \tag{2.3.19b}$$

Furthermore, the collisions are assumed to be spatially invariant, hence $F_{Therm}(t)$ is written without x dependence.

2.4 Characterising dielectrophoretic particle movement

Applying the Second Law of Motion, the inertial force on a particle is expressed as the sum of external, friction and thermal forces,

$$F_{Inert}(x,t) = F_{Ext}(x,t) + F_{Drag}(x,t) + F_{Therm}(t) \tag{2.4.1}$$

Substituting (2.3.1) and (2.3.4) into (2.4.1),

$$m\frac{d^2x}{dt^2} = F_{Ext}(x,t) - \zeta\frac{dx}{dt} + F_{Therm}(t) \tag{2.4.2}$$

yielding a second order stochastic differential equation (SDE).

2.4.1 Development of the Langevin equation

Since the particle mass m is very small, the inertial force term in (2.4.2) can be neglected, and the left hand side (*lhs*) is set to zero. A more rigorous and satisfactory approach, discussed in Gardiner (1985), involves adiabatic elimination methods using the slaving principle (Haken, 1983). The first step is to partition (2.4.2) into two equations,

$$\begin{aligned} \frac{dx}{dt} &= v \\ m\frac{dv}{dt} &= F_{Ext}(x,t) - \zeta v + F_{Therm}(t) \end{aligned} \tag{2.4.3}$$

and allow the fast variable $v = dx/dt$ to be controlled, or 'slaved', to the slow variable x. The second equation then becomes a first order SDE and is solved for v. The derivation is given in Appendix A. Combining (2.3.9) - (2.3.10) and (2.3.13) – (2.3.19) with (2.4.3), and using the result of the approximation for the relaxation time, $\tau = m/\zeta \to 0$, yields the Langevin equation (A.4.1),

$$v(x,t) = \frac{F_{DEP}(x)}{\zeta}\left[1+\cos(2\omega t + 2\theta)\right] + \frac{F_{EP}(x)\cos(\omega t+\theta)}{\zeta} + \frac{F_{Const}}{\zeta} + \sqrt{\frac{2k_BT}{\zeta}}\xi(t) \tag{2.4.4}$$

There are several ways to establish the significance of the terms in (2.4.4). One approach is to integrate over a small-time period to yield a measure of displacement. The analysis, in Appendix A.4, shows the displacements (or excursions), of the oscillatory electrophoretic, and AC component of the DEP, forces can be ignored for high frequencies (above 20 kHz). The average and variance of a set of trial, or *ensemble*, Gedanken-experiments, shows both deterministic and stochastic velocity components, abbreviated $v_{dtm}(x)$ and $v_{stch}(t)$, should be included for a comprehensive model. Thus (2.4.4) simplifies,

$$v(x,t)=\frac{dx}{dt}=\underbrace{\frac{F_{DEP}(x)+F_{Const}}{\zeta}}_{\text{deterministic}}+\underbrace{\sqrt{\frac{2k_BT}{\zeta}}\,\xi(t)}_{\text{stochastic}} \qquad (2.4.5)$$

$$=v_{dtm}(x)+v_{stch}(t)$$

2.4.2 Single particle movement

In principle, the strength of the DEP force acting on single sub-micron sized particles can be estimated from their recorded trajectories observed in DEP experiments. Due to the effect of stochastic Brownian motion, an average of an ensemble of trajectories would be required. This is evident by taking the ensemble average of (2.4.5),

$$\langle v(x,t)\rangle=\left\langle\frac{dx}{dt}\right\rangle=\left\langle\frac{1}{\zeta}\left[F_{DEP}(x)+F_{Const}+\sqrt{2k_BT\zeta}\,\xi(t)\right]\right\rangle \qquad (2.4.6)$$

and since the ensemble average of the deterministic term is the term itself, and the ensemble average of stochastic noise, from (2.3.17) is zero, then

$$\langle v\rangle=\frac{1}{\zeta}\left[F_{DEP}(x)+F_{Const}+\sqrt{2k_BT\zeta}\,\langle\xi(t)\rangle\right]=\frac{1}{\zeta}\left[F_{DEP}(x)+F_{Const}\right] \qquad (2.4.7)$$

If F_{Const} is known, it follows that F_{DEP}, and hence, the polarisability α, can be estimated from $<v>$ by solving (2.4.7). However, the number of trajectories needed is likely to be large, and the spatial dependence of the dielectrophoretic force will also need to be incorporated in the analysis.

2.4.3 Movement of an ensemble of particles: the Fokker-Planck Equation

The rate of accumulation, under the action of positive DEP, of particles onto electrode surfaces gives an indication of the dielectrophoretic force $F_{DEP}(x)$. There is no simple method, however, for integrating the Langevin equation (2.4.5) with arbitrary $F_{DEP}(x)$ and accommodating suitable boundary conditions that adequately mimic DEP experiments. One approach could be to numerically integrate (2.4.5) and simulate trajectories of individual particles, subject to DEP forces and Brownian motion, on computer. However, this is cumbersome, and prone to accumulation of numerical errors.

An alternative route to follow is to convert the Langevin equation to a Fokker-Planck equation (FPE), and the particle position, as the dependent variable in (2.4.5), is replaced by the spatial-temporal probability distribution $p(x, t)$. Solving for $p(x, t)$ can then lead to estimates of $F_{DEP}(x)$, and therefore, effective polarisability α. Methods for algebraic integration, that enable conversion from a Langevin to a FPE, include Ito or Stratonovich techniques, as described in Gardiner (1985). A more intuitively appealing technique is described in Haken (1978). Here a less mathematically rigorous description of Haken's argument is presented, but hopefully sufficient to understand the underlying concepts.

The probability distribution $p(x,t)$ of particles expresses the probability of finding a particle at space-time coordinate (x,t); specifically, N particles in a DEP experiment. Another conceptual model, is to consider the trajectory, or path, of a single particle in a set of N DEP, Gedanken-experiments. It is assumed N is sufficiently large for the law of large numbers to apply. The models are the same assuming, in the former, the particles do not interact with each other. The probability distribution $p(x, t)$ can be written in terms of the probability distribution for the nth path, $P_n(x, t)$,

$$p(x,t) = \sum_{n=1}^{N} P_n(x,t) = \sum_{n=1}^{N} p_n \delta\left(x - x_n(t)\right) = \left\langle \delta\left(x - x(t)\right) \right\rangle \qquad (2.4.8a)$$

where p_n is the probability of occurrence of path n, and the Dirac delta function states with certainty the path n is described by $x_n(t)$ and is given by (2.3.14). Comparing with the definition of the summation notation <...> in (2.3.14), the definitions are in this respect, analogous. It is understood the p_n factor is implicated when a Dirac delta function lies in the argument of the brackets. It should be noted the probability axioms require,

$$\int_{-\infty}^{+\infty} p(x,t)\,dx = 1 \;\; \forall t,\; p(x,t) \geq 0 \qquad (2.4.8b)$$

The aim is to express the development of $p(x, t)$ in terms of a differential equation. This circumvents evaluating (2.4.8a) by introducing a probability distribution for the stochastic Brownian motion. To set-up the differential equation, the increment in the probability distribution $p(x, t)$, for time interval Δt, is

$$\Delta p(x,t) \equiv p(x,t+\Delta t) - p(x,t)$$
$$= \sum_{n=1}^{N} p_n \delta\big(x - x_n(t+\Delta t)\big) - \sum_{n=1}^{N} p_n \delta\big(x - x_n(t)\big) \qquad (2.4.9a)$$
$$= \sum_{n=1}^{N} p_n \big[\delta\big(x - x_n(t+\Delta t)\big) - \delta\big(x - x_n(t)\big)\big]$$

By writing $\Delta x(t) \equiv x(t+\Delta t) - x(t)$, then

$\Delta p(x,t) = \sum_{n=1}^{N} p_n \big[\delta\big(x - x_n(t) - \Delta x_n(t)\big) - \delta\big(x - x_n(t)\big)\big]$, or using < .... > notation

$$\Delta p(x,t) = \big\langle \delta\big(x - x(t) - x(\Delta t)\big) - \delta\big(x - x(t)\big) \big\rangle \qquad (2.4.9b)$$

The right hand side (*rhs*) of (2.4.9) can be approximated by a Taylor series,

$$\therefore \Delta p(x,t) = \sum_{n=1}^{N} p_n \left[-\Delta x_n(t) \frac{d\,\delta\big(x - x_n(t)\big)}{dx} + \frac{\Delta x_n{}^2(t)}{2} \frac{d^2\,\delta\big(x - x_n(t)\big)}{dx^2} \right]$$
$$= \sum_{n=1}^{N} \left[-\Delta x_n(t) p_n \frac{d\,\delta\big(x - x_n(t)\big)}{dx} \right] + \sum_{n=1}^{N} \left[\frac{\Delta x_n{}^2(t)}{2} p_n \frac{d^2\,\delta\big(x - x_n(t)\big)}{dx^2} \right]$$

or,

$$\Delta p(x,t) = \left\langle -\Delta x(t) \frac{d\,\delta\big(x - x(t)\big)}{dx} \right\rangle + \frac{1}{2} \left\langle \Delta x^2(t) \frac{d^2\,\delta\big(x - x(t)\big)}{dx^2} \right\rangle \qquad (2.4.10)$$

Returning to the Langevin equation (2.4.5) and integrating over the time interval Δt,

$$\int_t^{t+\Delta t} \frac{dx}{dt'} dt' = \int_t^{t+\Delta t} v_{dtm}(x)\, dt' + \int_t^{t+\Delta t} v_{stch}(t')\, dt' \qquad (2.4.11)$$

and it has been assumed the changes in x changes are small compared with interactions from Brownian motion. Hence, the *lhs* of (2.4.5) can be written in terms of an increment,

$$\Delta x \equiv x(t+\Delta t) - x(t) = v_{dtm}(x)\Delta t + \Delta v_{stch}(t)$$

or, explicitly showing t dependence

$$\Delta x(t) = v_{dtm}\big(x(t)\big)\Delta t + \Delta v_{stch}(t) \qquad (2.4.12)$$

Substituting (2.4.12) into (2.4.10),

$$\Delta p(x,t) = \underbrace{\left\langle -\left[\left(v_{dtm}(x(t))\Delta t + \Delta v_{stch}(t)\right)\right]\frac{d\,\delta(x-x(t))}{dx}\right\rangle}_{term\,1} + \underbrace{\frac{1}{2}\left\langle \left[v_{dtm}(x(t))\Delta t + \Delta v_{stch}(t)\right]^2 \frac{d^2\,\delta(x-x(t))}{dx^2}\right\rangle}_{term\,2} \tag{2.4.13}$$

Each of the two *rhs* terms is evaluated separately. The analysis is detailed in Appendix B and follows the approach by Haken (1978, p. 158-164). To evaluate (2.4.13), it is helpful to recall the statistical assumption for Brownian motion: the events leading up to $x(t)$ are *independent* of the events *after* t, within the increment Δt. This enables, for example, sums of products $\langle v_{dtm}(x(t))\ \Delta v_{stch}(t)\rangle$ to be split into $\langle v_{dtm}(x(t))\rangle \langle \Delta v_{stch}(t)\rangle$. The final step (B.8) leads to the FPE,

$$\frac{\partial p(x,t)}{\partial t} = -\frac{\partial\left(p(x,t)v_{dtm}(x)\right)}{\partial x} + \frac{k_B T}{\zeta}\frac{\partial^2 p(x,t)}{\partial x^2} \tag{2.4.14}$$

Comparing the form of the Langevin equation (2.4.5) with the FPE (2.4.14), a few comments may be insightful. On the *rhs* of (2.4.14) the first order spatial partial-derivative arises from 'deterministic' *term 1* in (2.4.13) - a linear term arising from the Taylor series with the *sign* of v_{dtm} in (2.4.5) reversed. The second order partial-derivative in (2.4.14) arises from the 'stochastic' *term 2* in (2.4.13) with the Taylor series manifesting the v_{stch} term in (2.4.5) that is squared and the factor of 2 eliminated. This yields the coefficient, $k_B T/\zeta$, in front of the second order partial-derivative in (2.4.14). The final step involves dividing both sides by Δt and taking the limit $\Delta t \to 0$. The *rhs* is linearised, and on the *lhs*, the probability increment becomes a temporal partial-derivative.

The FPE is also called the Smoluchowski, or Kolmogorov, generalised diffusion, or continuity equation (van Holde, 1971; Risken, 1989; Doi and Edwards, 1986; Gardiner, 1985),

$$\frac{\partial p}{\partial t} = -\frac{\partial(pv)}{\partial x} + \frac{k_B T}{\zeta}\frac{\partial^2 p}{\partial x^2} = -\frac{\partial}{\partial x}\left(pv - D\frac{\partial p}{\partial x}\right) = -\frac{\partial J(x,t)}{\partial x} \tag{2.4.15}$$

where the diffusion coefficient is $D = k_B T/\zeta$ and it is understood $p = p(x, t)$ and $v = v_{dtm}(x)$. The latter title is not surprising since the expression can be developed from continuity considerations in a similar manner as Fick's Second Law (Berg, 1983, Ch. 2). It is also useful to render the equation in terms of the "probability flux", $J(x, t)$.

2.4.4 Generalising particle collections for two and three dimensions

The one dimensional (1-D) FPE (2.4.15) can be generalised for two and three dimensions and it is assumed the 2-D and 3-D spaces are specified by unit vectors $\vec{u}_x$, $\vec{u}_y$ and $\vec{u}_z$ that are orthogonal to each other. The arrangement of the coordinate bases, in relation to an experimental DEP device is described further in Chapter 3. The 3-D spatial notation adopted is $\underline{x} = (x, y, z)$, for example, the joint probability density, $p(x, y, z, t) = p(\underline{x}, t)$.

2.4.4.1 3-D Fokker-Planck Equation

The FPE (2.4.15) can be generalised for three-dimensions,

$$\frac{\partial p(\underline{x},t)}{\partial t} = -\vec{\nabla}\cdot\vec{J}(\underline{x},t) = -\vec{\nabla}\cdot\left(p(\underline{x},t)\vec{v}(\underline{x})\right) + D\,\vec{\nabla}\cdot\left(\vec{\nabla}p(\underline{x},t)\right) \tag{2.4.16}$$

where the velocity vector is given by $\vec{v}(\underline{x}) = v_x(\underline{x})\vec{u}_x + v_y(\underline{x})\vec{u}_y + v_z(\underline{x})\vec{u}_z$. When the probability density no longer changes with time and the *lhs* = 0, $p(\underline{x}, t)$ is said to have reached *steady state*, or become *stationary*, and the system of particles remains at equilibrium. The divergence of the probability flux $J(\underline{x},t)$ is zero,

$$\vec{\nabla}\cdot\vec{J}(\underline{x},t) = 0 \tag{2.4.17}$$

Specifically, in one dimension, steady state means the probability flux is constant. Physically, particle movement caused by deterministic force is counterbalanced by diffusion. Generally, equilibrium in a system occurs when the spatial gradient of the total potential - chemical (diffusion), electrostatic, sedimentation (buoyancy and gravity) - remains constant, and independent of the spatial dimension (van Holde, 1971, p. 83-5).

2.4.4.2 Probability density and particle concentration

The axioms of probability imply (2.4.8b) is extended for three dimensions,

$$\iiint_{V_T} p(\underline{x},t)\,d\underline{x} = 1 \;\forall\; t \;,\; p(\underline{x},t) \geq 0 \qquad (2.4.18a)$$

where the volume integral over V_T encompasses the entire probability space or *total volume*. This includes the steady state case, $p(\underline{x},t)\big|_{t\to\infty} = p(\underline{x})$. In a situation where the volume integral encompasses only *part* of the probability space, the indefinite integral of $p(\underline{x},t)$ results in the cumulative distribution $P(t)$ (Papoulis, 1984, ch. 4.2),

$$\iiint p(\underline{x},t)\,d\underline{x} = P(t) \;\forall\; t \;,\; p(\underline{x},t) \geq 0 \,,\; 0 \leq P(t) \leq 1 \qquad (2.4.18b)$$

Furthermore, a reduction in the dimension of the density occurs when $p(\underline{x},t)$ is integrated over the entire interval in that probability space. For example, if V_T is specified entirely by $z_1 \leq z \leq z_2$ in the direction $\vec{u}_z$ then

$$p(x,y,t) = \int_{z_1}^{z_2} p(x,y,z,t)\,dz \quad \forall\; t \;,\; p(\underline{x},t) \geq 0 \qquad (2.4.18c)$$

The density is said to be *marginal* (Papoulis, 1984, p. 125) and some authors use a subscript to denote this, i.e. $p_z(x,y,t)$. However, to avoid over-use of subscripts for the probability density, this is omitted.

Similar relations apply to particle concentration (or number density) $c(\underline{x},t)$ for a closed system where particles are not added, or do not escape, during the course of the experiment. This means the total number of particles N within V_T remains constant, and by definition

$$\iiint_{V_T} c(\underline{x},t)\,d\underline{x} = N \;\forall\; t \;,\; c(\underline{x},t) \geq 0 \qquad (2.4.19a)$$

For a partial volume enclosure (written as an indefinite volume integral),

$$\iiint c(\underline{x},t)\,d\underline{x} = n(t) \;\forall\; t \;,\; c(\underline{x},t) \geq 0 \,,\; 0 \leq n(t) \leq N \qquad (2.4.19b)$$

where $n(t)$ is the number particles within the designated enclosure. Furthermore, the volumetric concentration $c(\underline{x},t)$ can be reduced in a similar way to the probability density, for example,

$$c(x,y,t) = \int_{z_1}^{z_2} c(x,y,z,t)\,dz \quad \forall\, t\ ,\ p(\underline{x},t) \geq 0 \tag{2.4.19c}$$

The x and y variables indicate the *lhs* quantity is an 'area' concentration (or number of particles per unit *area*), and where the independent variables are *not* explicitly stated the subscript A distinguishes this, $c_A \equiv c(x,y)$ from a volumetric concentration $c_V \equiv c(\underline{x})$. An example of the use of a number density c_V is shown in equation (2.2.28). Similarly, the number of particles per unit *length*, is written $c_L \equiv c(x)$. Equations (2.4.18a) and (2.4.19a) are related numerically by,

$$c(\underline{x},t) = Np(\underline{x},t) \tag{2.4.20}$$

and the total number of particles, N, therein acts as a normalisation constant.

2.4.4.3 Predictions of particle collections

The above relations can be used for theoretical prediction and experimental analysis of particle collections into a specified volume V. A key step for comparing predictions with measurements is relating the model describing the experiment with the actual simulation model. Due to computation limitations the later is often simplified. A simple example of comparing models, particularly relevant for chapters 6 and 7, is to consider a DEP system exhibiting symmetry in z-direction. Specifically, there is no component of the DEP force acting in the direction $\vec{u}_z$ and the probability density is invariant, $p(x,y,z,t) = p(x,y,z+\Delta z,t)$ at arbitrary $z \Rightarrow \dfrac{\partial p(\underline{x},t)}{\partial z} = 0 = \dfrac{\partial^2 p(\underline{x},t)}{\partial z^2}$. The 3-D FPE (2.4.16) is simplified to a 2-D FPE representing a 3-D system with z-invariance,

$$\frac{\partial p(\underline{x},t)}{\partial t} = -\left(\frac{\partial[p(\underline{x},t)v_x(\underline{x})]}{\partial x} + \frac{\partial[p(\underline{x},t)\,v_y(\underline{x})]}{\partial y}\right) + D\left(\frac{\partial^2 p(\underline{x},t)}{\partial x^2} + \frac{\partial^2 p(\underline{x},t)}{\partial y^2}\right) \tag{2.4.21}$$

In effect it is a pseudo-three dimensional model. Multiplying both sides by N and using (2.4.20), yields the model of the experiment with particle concentration,

$$\frac{\partial c(\underline{x},t)}{\partial t} = -\left(\frac{\partial [c(\underline{x},t) v_x(x,y)]}{\partial x} + \frac{\partial [c(\underline{x},t)\, v_y(x,y)]}{\partial y} \right) + D\left(\frac{\partial^2 c(\underline{x},t)}{\partial x^2} + \frac{\partial^2 c(\underline{x},t)}{\partial y^2} \right) \qquad (2.4.22)$$

Integrating (2.4.22) with respect to time gives $c(\underline{x},t)$, and the number of particles $n(t)$ collected within a specified 3-D volume can be evaluated using (2.4.19b),

$$n(t) = \int_{z_1}^{z_2} \int_{y_1}^{y_2} \int_{x_1}^{x_2} c(\underline{x},t)\, d\underline{x} = \int_{y_1}^{y_2} \int_{x_1}^{x_2} c(x,y,t)\, dx\, dy \qquad (2.4.23)$$

This means data about $c(\underline{x},t)$ in a 3-D DEP experimental system can be used to compare with predictions from a FPE model (2.4.21). In terms of *predicting* $n(t)$ from simulation, however, (2.4.21) is too cumbersome to compute. It is convenient to simplify (2.4.21) using (2.4.18c), and the integration over $z_1 \le z \le z_2$ reduces $p(x,y,z,t) \rightarrow p(x,y,t)$,

$$\frac{\partial p}{\partial t} = -\left(\frac{\partial [p\, v_x(x,y)]}{\partial x} + \frac{\partial [p\, v_y(x,y)]}{\partial y} \right) + D\left(\frac{\partial^2 p}{\partial x^2} + \frac{\partial^2 p}{\partial y^2} \right) \qquad (2.4.24)$$

where it is understood, $p \equiv p(x,y,t)$. The predicted number of particles $n(t)$ is

$$n(t) = N \int_{y_1}^{y_2} \int_{x_1}^{x_2} p(x,y,t)\, dx\, dy \qquad (2.4.25)$$

It is numerically the same as (2.4.23) thus enabling comparison with $n(t)$ evaluated from experimental data.

2.5 Concluding remarks

This chapter has presented the theoretical foundations for DEP and introduced the polarisation mechanisms resulting in the effective polarisability of colloidal particles and DNA. The two important polarisation mechanisms responsible for the dielectrophoretic movement of these particles are Maxwell-Wagner and counterion fluctuation polarisation. The forces acting on a single sub-micron sized particle, in a non-uniform AC electric field, suspended in aqueous solution are described. The dominant forces for high AC frequencies of interest are Stokes' drag, DEP, and fluctuations from the random thermal motion of the aqueous medium.

The motion of a single particle under the action of these dominant forces is described by the Langevin equation. The motion of an ensemble of particles is described by the Fokker-Planck equation, and the connection between these two models is described. The FPE is generalised to three dimensions and rendered in probabilistic form. All together, the material in this chapter forms the theoretical basis for the ensuing chapters 3, 4, 5, 6 and 7.

3 Materials and methods

3.0 Introduction

The dielectrophoretic collection of nano-scale particles onto electrode surfaces is measured using fluorescence microscopy. This is the usual technique for visualising DEP experiments and enables real-time video recording of fluorescent particle movement. The video images are later processed and provide quantitative measurements of particle collection. Broadly speaking, there are three stages of DEP measurement. The first is preparatory: the set-up of experimental apparatus, fabrication and mounting of micro-electrodes, and preparation of sub-micron colloidal particles and DNA in aqueous solution. The second stage is experimental: performing the DEP experiment itself, and monitoring and recording images of particle movement. The third stage is processing and interpretation: image processing of video frames and data visualisation and visualization.

This chapter describes the first and third stages; these can be viewed as 'materials and methods' in terms of laboratory 'hardware' and 'software', respectively. The first stage, electrode fabrication and DNA preparation, etc., is described in sections 3.1 to 3.4. The third stage, development of image processing software and data interpretation, is described in sections 3.5 and 3.6. The second stage, detailing the DEP experiments, is relatively straightforward and is described in Chapter 7 in conjunction with the processed time-dependent collection and relaxation profiles.

3.1 DEP experimental apparatus and set-up

A schematic diagram of the experimental apparatus used for performing and recording DEP collections is shown in Fig. 3.1(a). Fig. 3.1(b) illustrates an example of the DEP electrode arrays that were microfabricated on a glass microscope slide and (in turn) mounted on a Printed Circuit Board (PCB). Each array receives an AC potential via microfabricated bus-bars and pads on the glass slide. The pads have been bonded with electrical (silver) conductive paint (RS components, USA) to wires that were soldered onto PCB supply rails. The rails are in-turn supplied with an AC signal (via PCB sockets, as shown) usually from a computer controlled Direct Digital Synthesiser (DDS) illustrated in Fig. 3.1(a). The DDS, that was built in the Department, provides a command driven AC signal with variable peak potential Φ (V), $0 \le \Phi \le 12$ and frequency f (Hz), $100 < f \le 2\times10^7$. Alternative sources for preliminary experiments included a Hewlett Packard (HP) (USA) HP3314A and HP 8656B signal generators.

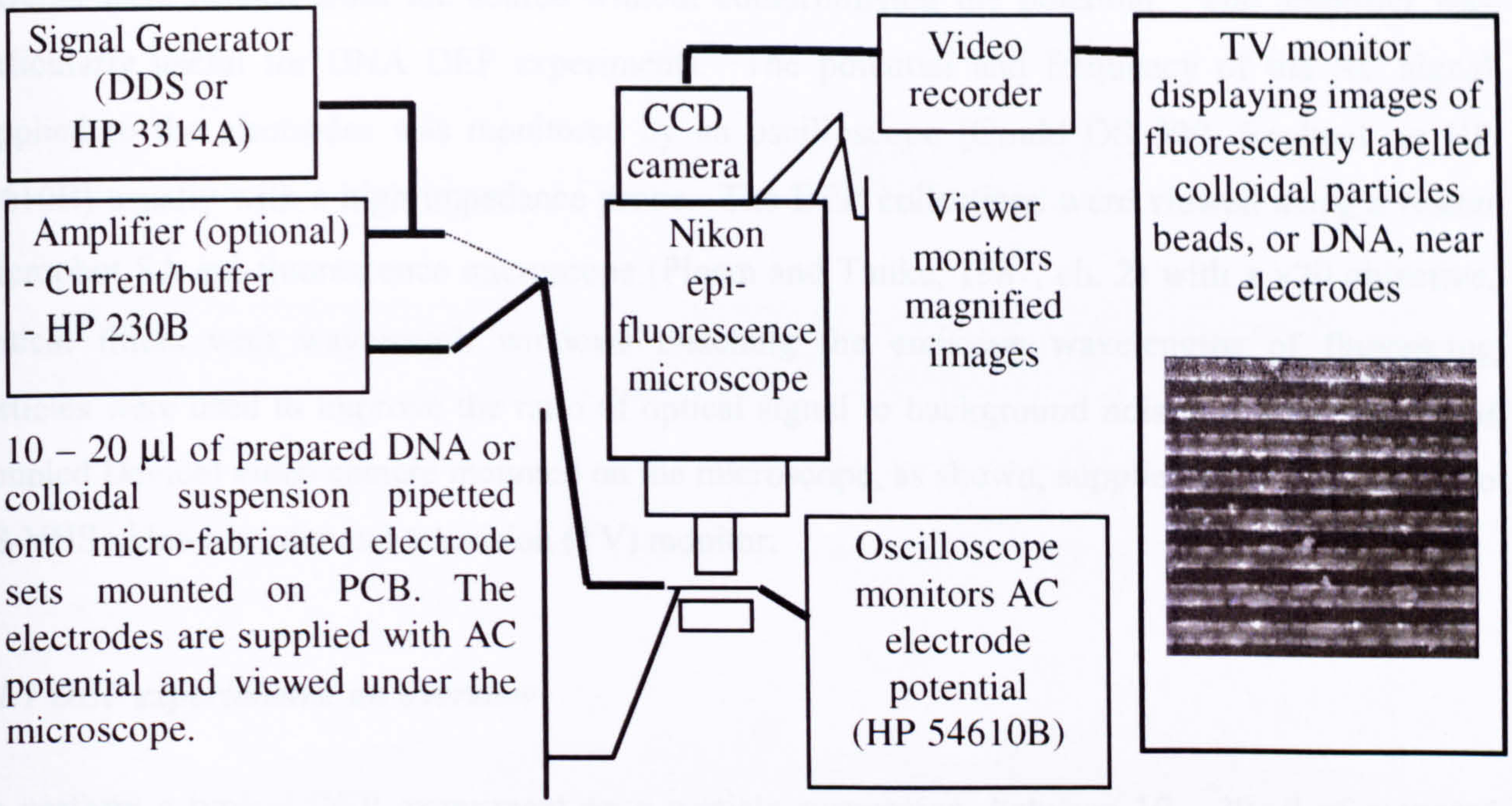

Fig. 3.1 (a) Scheme of DEP experimental apparatus showing AC signal source, amplifier, monitoring oscilloscope, epi-fluorescence microscope, CCD camera, video recorder and television monitor.

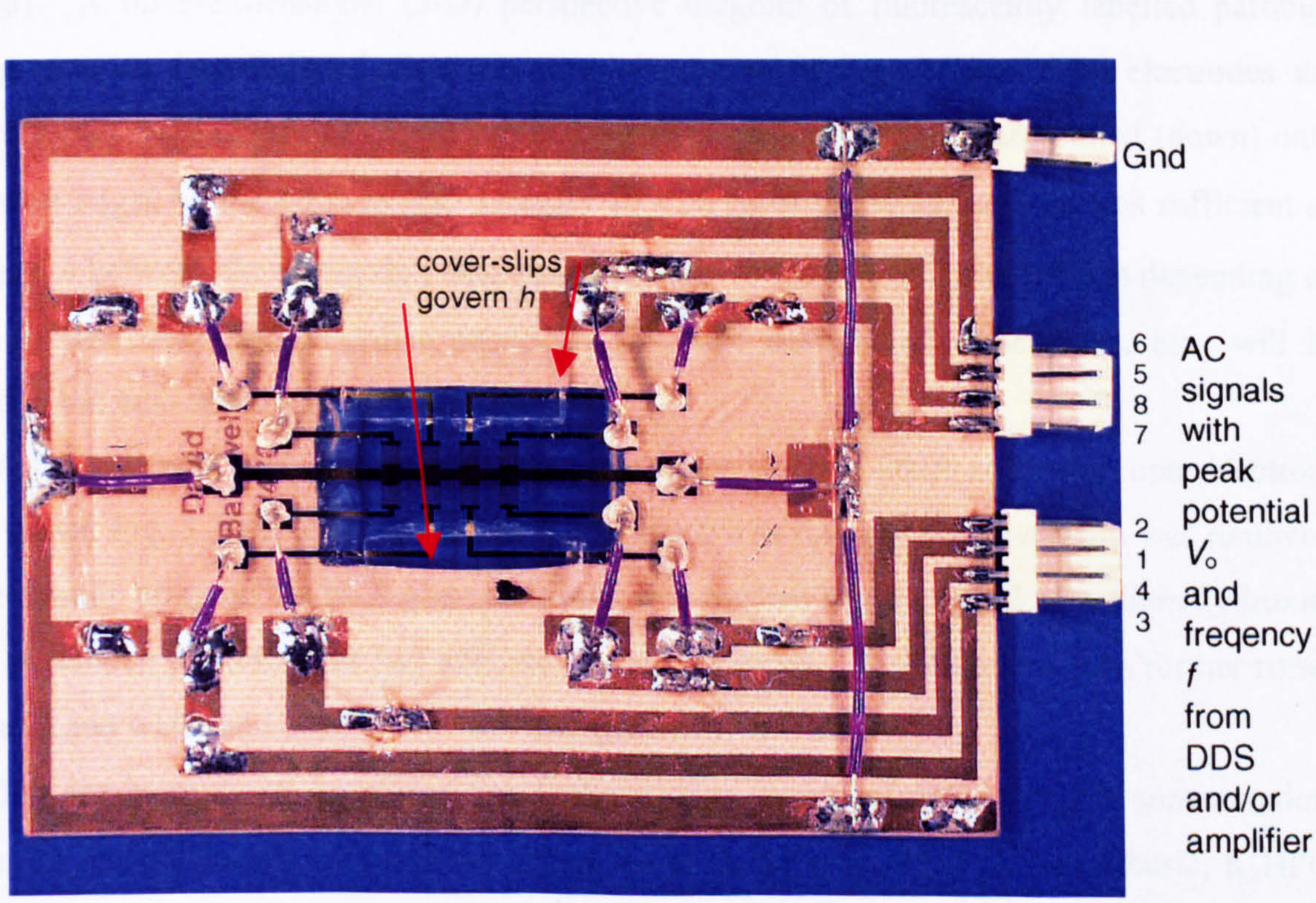

Fig. 3.1 (b) Separately addressable {channels: 1, … , 8} 8 array interdigitated electrodes fabricated on a glass slide and mounted onto a PCB with supply buses. The 160 µm thickness of two narrow cover-slips, adhered to the slide as shown, governs the minimum possible height h between the surface of the array and the 18 × 18 mm cover-slip (not shown) used to reduce evaporation.

A current (buffer) amplifier, also built in the Department, was used when relatively large currents were needed from the source without compromising the potential. The amplifier was particularly useful for DNA DEP experiments. The potential and frequency of the AC signal supplied to the electrodes was monitored by an oscilloscope (Gould OS 300, England; or HP 54610B) usually with a high impedance probe. The DEP collections were viewed using a Nikon Microphot SA epi-fluorescence microscope (Ploem and Tanke, 1987, ch. 2) with a ×20 objective. Optical filters with wavelength windows matching the emission wavelengths of fluorescing particles were used to improve the ratio of optical signal to background noise. A CCD (Charged Coupled Device) video camera mounted on the microscope, as shown, supplied real-time images to a S-VHS video recorder and television (TV) monitor.

3.1.1 DEP experiments: an overview

To perform a typical DEP experiment on a particle suspension, between 10 - 20 μl of prepared solution (medium) was micropipetted onto the electrode array as indicated in Fig. 3.1(b). A glass cover-slip was placed on the droplet to prevent evaporation of the solvent. The PCB (with mounted electrode array and enclosed prepared solution) was then placed on the microscope for viewing and video recording, and connected to AC variable frequency source, as described above, Fig. 3.1(a). A three-dimensional (3-D) perspective diagram of fluorescently labelled particles collecting onto an interdigitated electrode array is shown in Fig. 3.2(a). The electrodes are connected to alternate phases of the AC source. The suspended particles are pulled (down) onto the electrode edges by the DEP forces. Usually 10 - 20 μl of prepared medium was sufficient so the distance h between the electrode plane and cover-slip ranged from 20 to 150 μm depending on the size of the cover-slip. Further details of electrode design and dimensions, etc., will be discussed in the next section 3.2.1.

A typical (plan view) image of the fluorescently labelled DNA collecting onto electrode edges is shown Fig. 3.2(b). After each DEP experiment was finished the cover-slip was removed, and the electrode array on the PCB glass slide area was washed briefly with 2 M sodium hydroxide (NaOH) to remove particles that had adhered to the electrodes. The slide area was further rinsed with ethanol and water and blow-dried with nitrogen.

The conductivity of the preparation (solvent) was controlled using variable concentrations of potassium phosphate salt – equal molar amounts of monobasic, KH_2PO_4 and dibasic, K_2HPO_4 (Sigma™ P-0662 and P-3786, Sigma, USA) or, for DNA, using buffers of different dilution strengths.

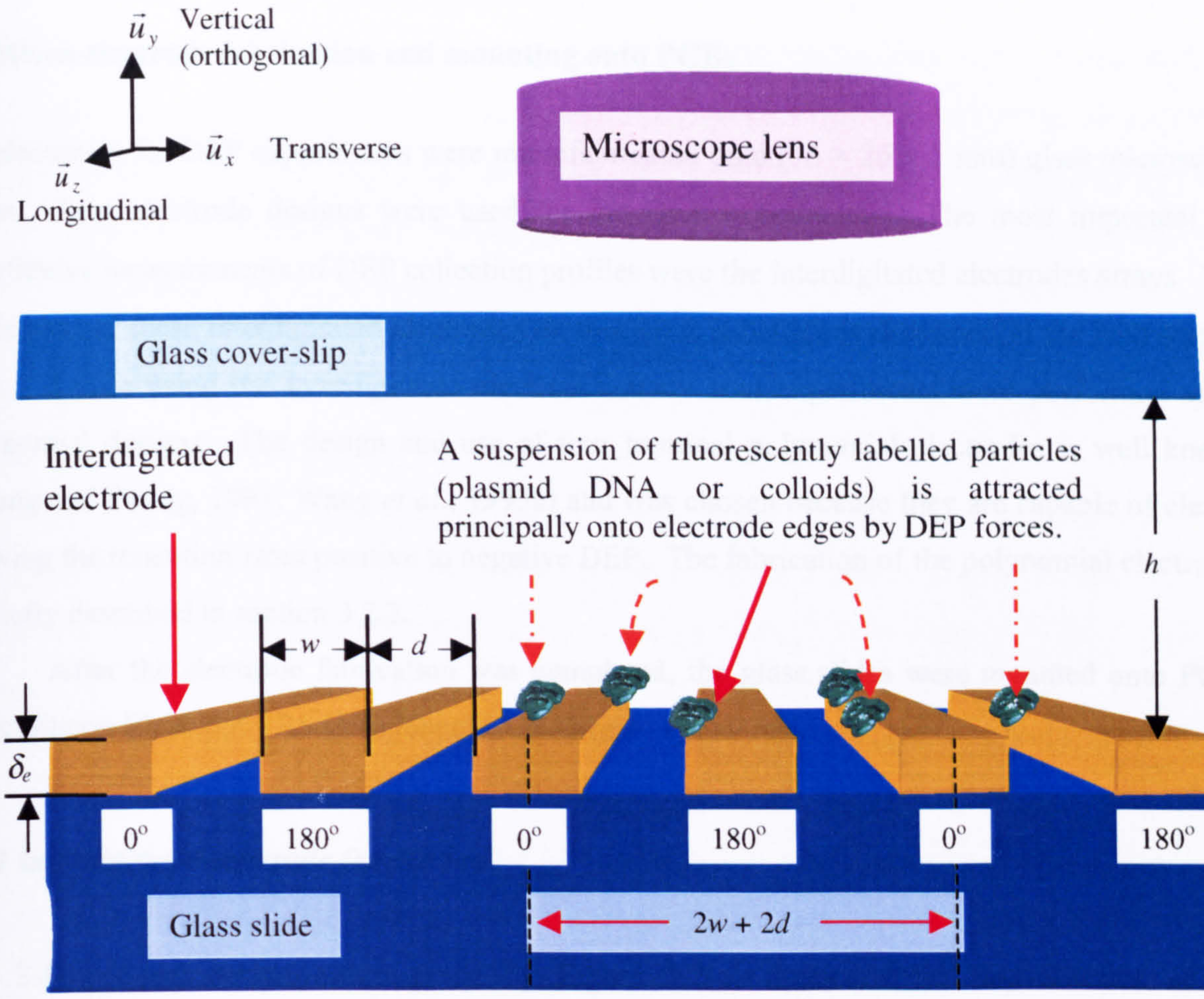

Fig. 3.2(a) Diagram of a DEP collection experiment (using interdigitated electrodes fabricated on glass with width w, interelectrode space d, and thickness δ_e) *not* to scale. The movement of the fluorescently labelled particles, suspended in aqueous medium, is monitored with a microscope.

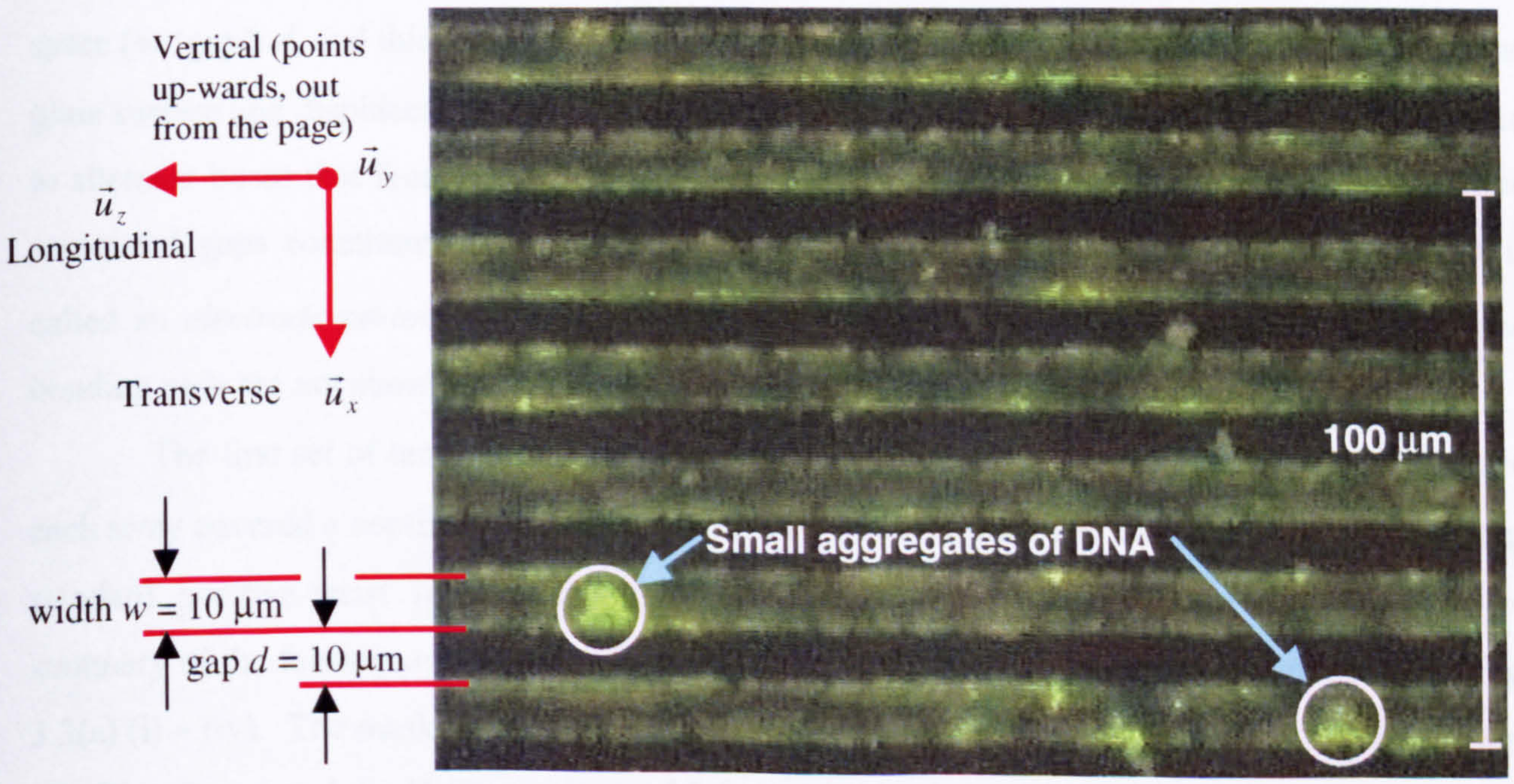

Fig. 3.2(b) A video frame of planar interdigitated electrodes fabricated on glass ($w = d = 10$ µm). The frame shows DAPI labelled DNA dielectrophoretically collecting onto the electrode edges.

3.2 Micro-electrode fabrication and mounting onto PCBs

All electrodes for DEP experiments were microfabricated onto (76 × 26 × 1 mm) glass microscope slides. Two electrode designs were used for the DEP experiments. The most important for quantitative measurements of DEP collection profiles were the interdigitated electrodes arrays. The fabrication of these interdigitated electrodes on to a glass substrate is described in the next section 3.2.1. Before using the interdigitated electrodes many trial experiments were performed using polynomial designs. The design and use of four terminal polynomial electrodes is well known (Huang and Pethig, 1991; Wang *et al.*, 1993a) and was chosen because they are capable of clearly showing the transition from positive to negative DEP. The fabrication of the polynomial electrodes is briefly described in section 3.2.2.

After the electrode fabrication was completed, the glass slides were mounted onto PCBs using Silicon Elastomer (RS Components, USA) or an epoxy resin.

3.2.1 Interdigitated electrode fabrication

The 3-D perspective projection given by Figure 3.2(a) illustrates the key features of the interdigitated electrode array. The 3-D co-ordinate reference axes, shows the *longitudinal* direction with unit vector $\vec{u}_z$ along the length of each electrode and the orthogonal, *transverse* direction ($\vec{u}_x$) that lies in the same plane as the glass surface. Since the glass surface is horizontal, the direction orthogonal to this plane is the *vertical* direction $\vec{u}_y$. All electrodes have width w, interelectrode space (or 'gap') d, and thickness δ_e. The plane of the upper surface of the electrodes, parallel to the glass surface and displaced by δ_e, is defined as the 'electrode plane'. The electrodes are connected to alternate buses that feed 0° and 180° signals. A pair of electrodes with phases 0° and 180° and associated gaps constitutes a transverse displacement $2w+2d$ as shown. This displacement is called an *electrode period* and is a useful measure of transverse displacement. The buses and bonding pads are not shown in this close-up view, but are depicted in the example, Fig. 3.1(b).

The first set of ten interdigitated electrodes had transverse dimensions $w = d = 10$ μm and each array covered a continuous area approximately 1.0×0.95 cm. The electrodes were made using standard positive-resist lift-off photolithography techniques (Pacansky and Lyerla, 1979). A summary of the fabrication stages is given in Appendix C and four key steps are illustrated in Fig. 3.3(a) (i) – (iv). The mask pattern was drawn by Mr. W. Monaghan using Computer Aided Design (CAD) software and the Cr/Fe mask was fabricated using electron beam lithography (EBPG 5-HR, Leica-Cambridge, England).

To facilitate an even surface contact during Ultra-Violet (UV) exposure, Fig. 3.3(a) step (i), the microscope slides were cut to half-length (38 mm). The slides were acid cleaned, and the S1818 resist coating process included a 15 minute chlorobenzene soak, between 15 minute oven-baking periods, to improve resist edge definition quality. The mask pattern was exposed onto positive photo-resist coated glass microscope slides using the mask aligner, developed, and inspected for defects and edge definition quality. Optimal double-exposure mask aligner times were found to be 5.5 to 6.0 seconds for the electrode array and a total of 13.0 seconds for the contact pads. Optimal development times depended on the amount of exposed resist being removed, and were approximately 120 – 150 seconds.

Metallic films of approximate thickness 10 nm titanium (Ti), 10 nm palladium (Pd), and 100 nm gold (Au), were consecutively vapour-deposited using a Plassys MEB 450 evaporator onto each of the patterned resist coated glass slides, as shown in Fig. 3.3(a) steps (ii) – (iii). Acetone was used to 'lift-off' areas of resist coating that had not been radiated with UV light. The lift-off was assisted by sonication and rubbing with cotton buds (viewed under a microscope). Anticipating short-circuits occurring due to the large fabrication (1.0 × 0.95 cm) area, the electrode array was resistance tested during the final stage, before the electrodes were taken out of acetone.

Often, small debris of metal, still connected to electrode surfaces, caused short-circuits after removal from the acetone bath. This problem was overcome by re-immersing the electrode structure in an acetone bath, sweeping suspected surfaces of gold with a cotton wool bud (combed into a soft 'broom') and resistance testing. Fig. 3.3(a) step (iv) illustrates the array after the acetone lift-off showing the electrodes with width w, gap d and thickness δ_e fabricated on glass. The inset shows the Ti – Pd – Au layers amounting to total thickness, δ_e = 120 nm.

3.2.1.1 Separately addressable interdigitated electrodes

The use of the large area interdigitated electrode array was adequate for measuring the DEP collections of model nano-scale particles, such as, latex beads. The same array, however, tended to be problematic for plasmid DNA that tended to aggregate and adhere to the electrodes after the AC signal was switched off. The non-homogeneity of DNA samples imaged using fluorescence microscopy is discussed later in sections 3.3.4 and 3.3.5. These problems impeded the investigations of the dependency of DEP collections on variables, such as, applied AC frequency and/or medium conductivity.

Attempting to alleviate these problems, three large area electrode arrays were divided, in the transverse direction, into seven separately addressable arrays. A schematic of a microfabricated separately addressable interdigitated electrode array is exhibited in Fig. 3.3(b). A glass scribe was

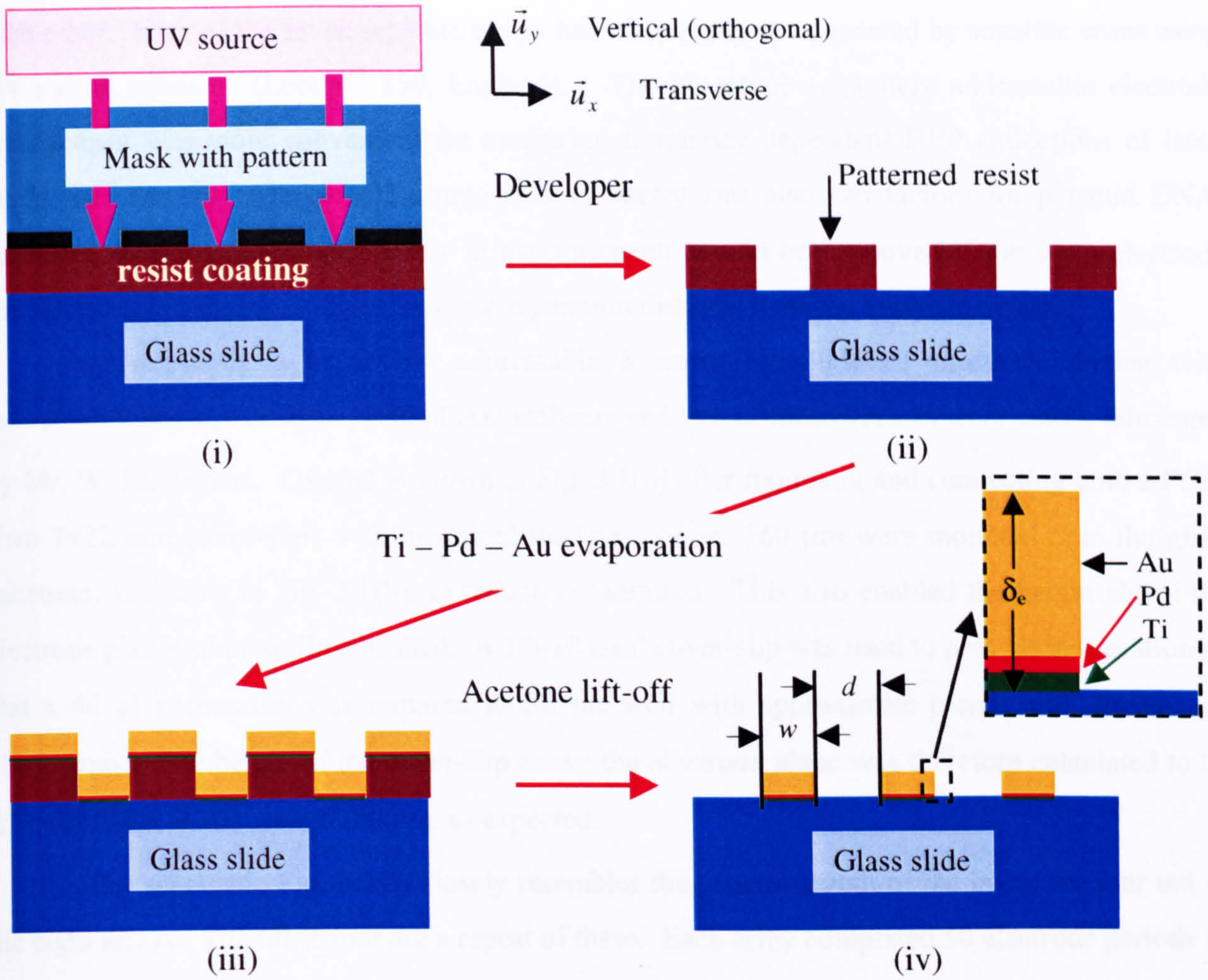

Fig. 3.3(a) Key steps in electrode micro-fabrication (cross-section or transverse plane view): (i) UV pattern exposure through mask onto resist coated glass microscope slide, (ii) application of developer removes irradiated (positive) resist, (iii) Ti – Pd – Au consecutively evaporated on to patterned resist/slide, and (iv) application of acetone lifts off metal layers leaving electrodes firmly bonded onto glass.

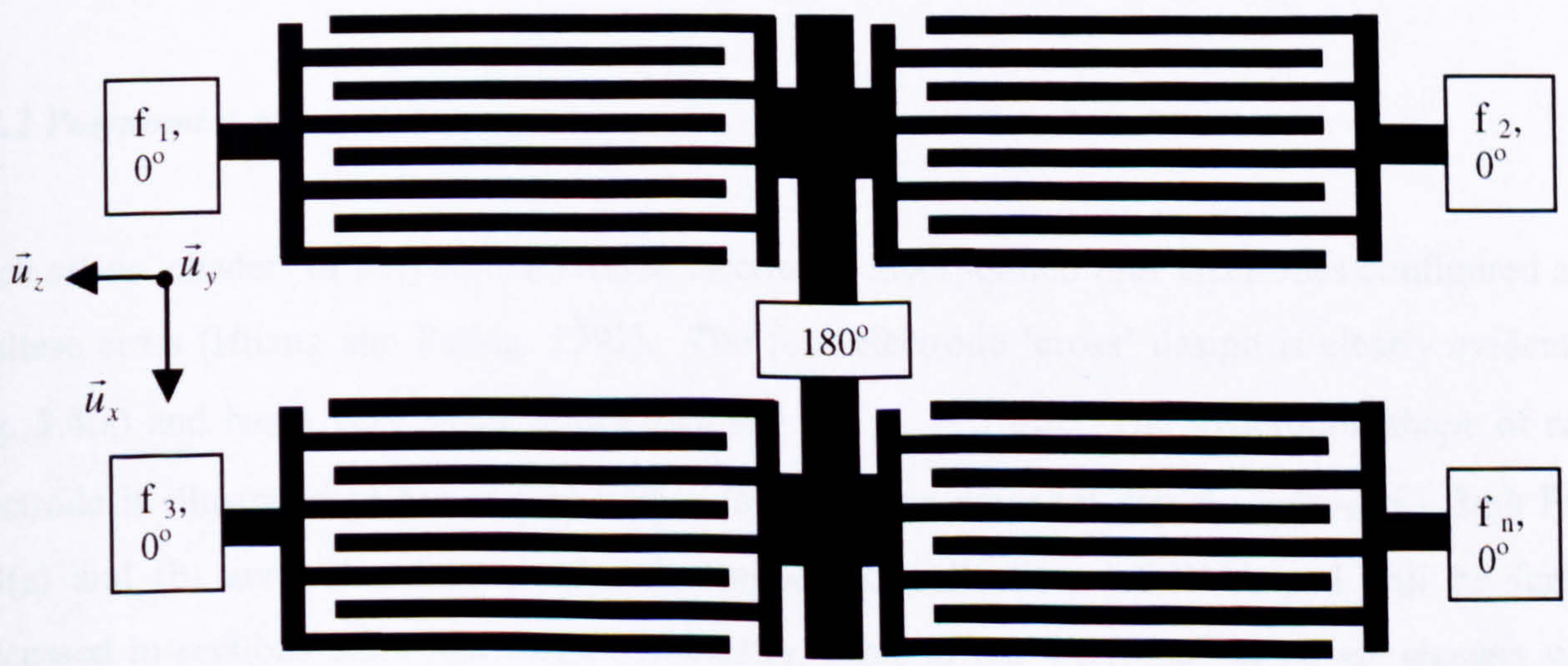

Fig. 3.3(b) Schematic diagram of separately addressable interdigitated electrode arrays (plan view).

used to incise the array buses and gouge a gap between the arrays to electrically isolate them from each other. Each of the seven separate arrays was electrically re-connected by separate wires using UV curing adhesive (Loctite® 350, England). The prototype separately addressable electrode arrangement was more convenient for measuring frequency dependent DEP collections of latex beads than the single large area array. The geometry was also satisfactory for plasmid DNA. However, it was thought consistency in measurements would be improved if the 1 cm electrode lengths were shortened and the transverse separation distance between arrays increased.

Consequently a separately addressable 8 array interdigitated electrode device with $w = d = 10$ μm was designed using CAD software and two of these devices were kindly fabricated by Mr. W. Monaghan. One set is shown in Fig. 3.1(b) after mounting and connecting onto a PCB. Two 7×22 mm cover-slips with measured thickness of *ca.* 160 μm were mounted onto the glass substrate, as shown in Fig. 3.1(b), to reduce evaporation. This also enabled the height above the electrode planes to be well controlled. A 18×18 mm^2 cover-slip was used to prevent evaporation so that a 40 μl suspension was required to fill the well with approximate planar area dimensions 18×11 mm^2. The height of the cover-slip above the electrode plane was therefore calculated to be $h = 40/198 = 0.202$ mm $\cong 200$ μm, as expected.

The schematic Fig. 3.3(b) closely resembles the general layout of the buses for four out of the eight arrays. The other four are a repeat of these. Each array comprised 50 electrode periods so the total transverse array width was $50(2w+2d) = 50\times 40\mu$m $= 2000$ μm or 2 mm. The (longitudinal) length of each array was 1.8 mm and the transverse spacing between each array was 2 mm. For convenience only 3.5 periods for each array is shown in Fig. 3.3(b). The common bus is labelled with the 180° phase and each array is separately connected via 0° phase as shown. Since frequency was an important variable for DEP collection rates, the four separate connections are labelled f_1, f_2, f_3, f_n.

3.2.2 Polynomial electrodes

Each set or 'cluster' of polynomial shaped electrodes incorporated four electrodes configured as a Maltese cross (Huang and Pethig, 1991). The four electrode 'cross' design is clearly evident in Fig. 3.4(a) and has a very small centre diagonal gap ϕ = 5 μm. The hyperbolic shape of each electrode is illustrated in Fig. 3.4(b) with a larger centre diagonal gap ϕ = 46 μm. Both Figs. 3.4(a) and (b) are video frames of dielectrophoretic collections of DNA and will be further discussed in sections 3.3.4 and 3.3.5. Generally, three to ten 4-terminal electrode clusters were fabricated on each slide using the same fabrication methods as described for the interdigitated design, section 3.3.1. Most slides had several different sizes in order to investigate possible

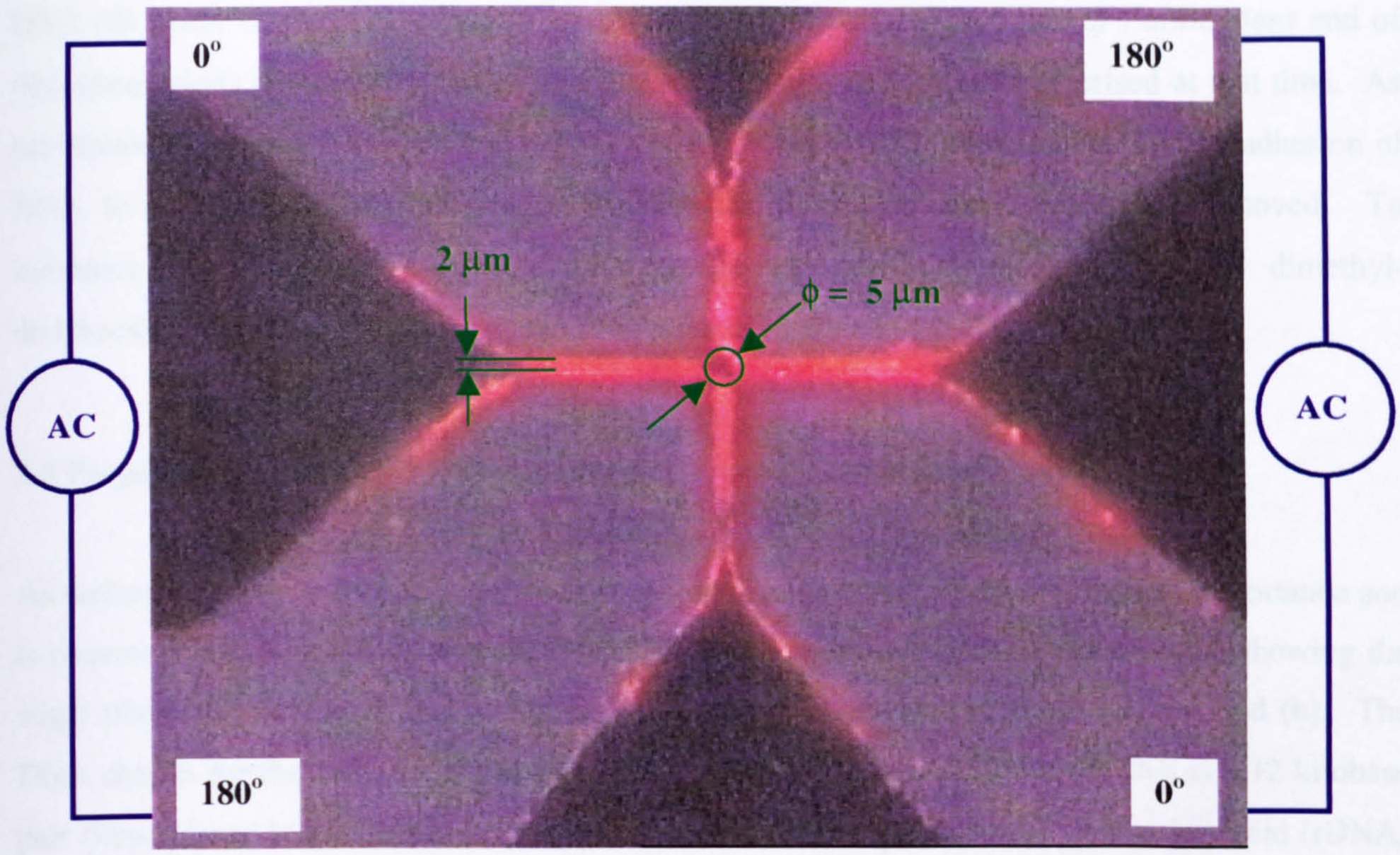

Fig. 3.4(a) DEP of plasmid DNA using polynomial electrodes configured as a Maltese cross (centre diagonal ϕ = 5 μm). The electrodes have been connected to an AC potential source with phases as shown. The plasmid DNA was labelled with ethidium bromide.

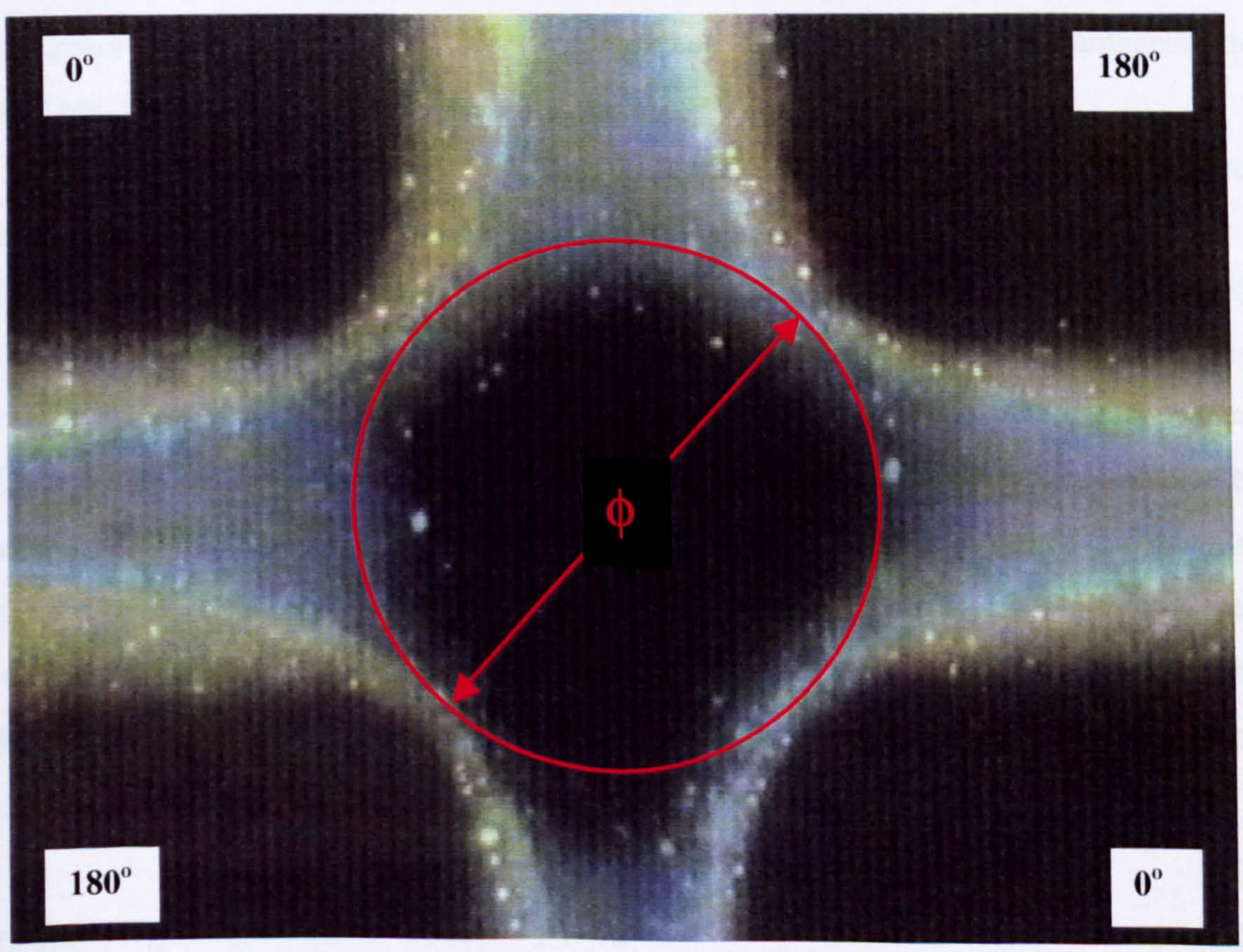

Fig. 3.4(b) DEP of plasmid DNA using polynomial electrodes (configured as a Maltese cross with centre diagonal ϕ = 46 μm) using DAPI as a fluorescent label.

transitions from positive to negative DEP. One should remark that although stable trapping of DNA did occur in some experiments investigating negative DEP (see *List of Publications* end of this dissertation) it was attributed to fluid motion that was not well characterised at that time. As mentioned in the previous section a problem encountered in DEP experiments was the adhesion of DNA to electrodes and/or glass surfaces after the dielectrophoretic force was removed. To minimise this adhesion several devices were treated with a surface repellent, dimethyl-dichlorosilane, but the reductions in adhesion were not very effective.

3.3 Preparation of DNA for DEP and dielectric spectroscopy experiments

As outlined in chapters 1 and 2, DNA is a macromolecule of significant biological importance and is responsive to non-uniform electric fields (DEP). A 3-D molecular model of DNA showing the sugar phosphate backbone and nucleotide base pairs is illustrated in figures 3.5(a) and (b). The DNA chosen for the DEP dielectric spectroscopy experiments was pTA250. This is a 12 kilobase pair (kbp) plasmid that contains a single repeat of the 8.9 kbp ribosomal ribonucleic acid (rDNA) coding unit from wheat (*Triticum aestivum* var. Chinese Spring, clone designation 250) subcloned into the *Eco*RI site of pUC19 (Gerlach and Bedbrook, 1979). Generally, plasmids are double-stranded, closed circular DNA macromolecules, ranging from 1 kbp to more than 200 kbp in size, and are extra chromosomal genetic elements found in a variety of bacterial species. Often they contain genes coding for enzymes that, under certain circumstances, are advantageous to the bacterial host (Maniatis *et al.*, 1982, p. 3).

Plasmid DNA prepared from *E. Coli* bacteria is typically 6% negatively supercoiled (Calladine and Drew, 1997, Ch. 6). A schematic of supercoiled covalently closed-circular DNA (cccDNA) is shown in Fig. 3.5(c). The inter-wound structure generally makes the macromolecule more compact than if it was the relaxed circular topological form. Assuming an axial length of 0.34 nm per base pair, the calculated contour length of this pTA250 plasmid is approximately $12\times0.34\mu m \approx 4.1\mu m$. Comparing the sizes of relaxed circular and supercoiled circular human mitochondrial DNA (Stryer, 1995, p. 88) a planar length of $\approx 1\ \mu m$ is expected for this plasmid. Atomic Force Microscope images (not shown) of a sample of dried pTA250 DNA plasmid indicated an inter-wound structure spanning a region $\approx 1\ \mu m \times 1.5\ \mu m$. Assuming molecular weight (MW) per base pair, $MW_{bp} = 662$ Da/bp, as adopted in equation (2.3.3), and number of base pairs, $N_{bp} = 12\times10^3$, then the MW of each 12 kbp plasmid (Da),

$$MW_{pTA250} = N_{bp}MW_{bp} = 12\times10^3\times662 = 7.94\times10^6 \qquad (3.3.1)$$

or $MW_{\mathrm{pTA250}} \cong 8$ MDa.

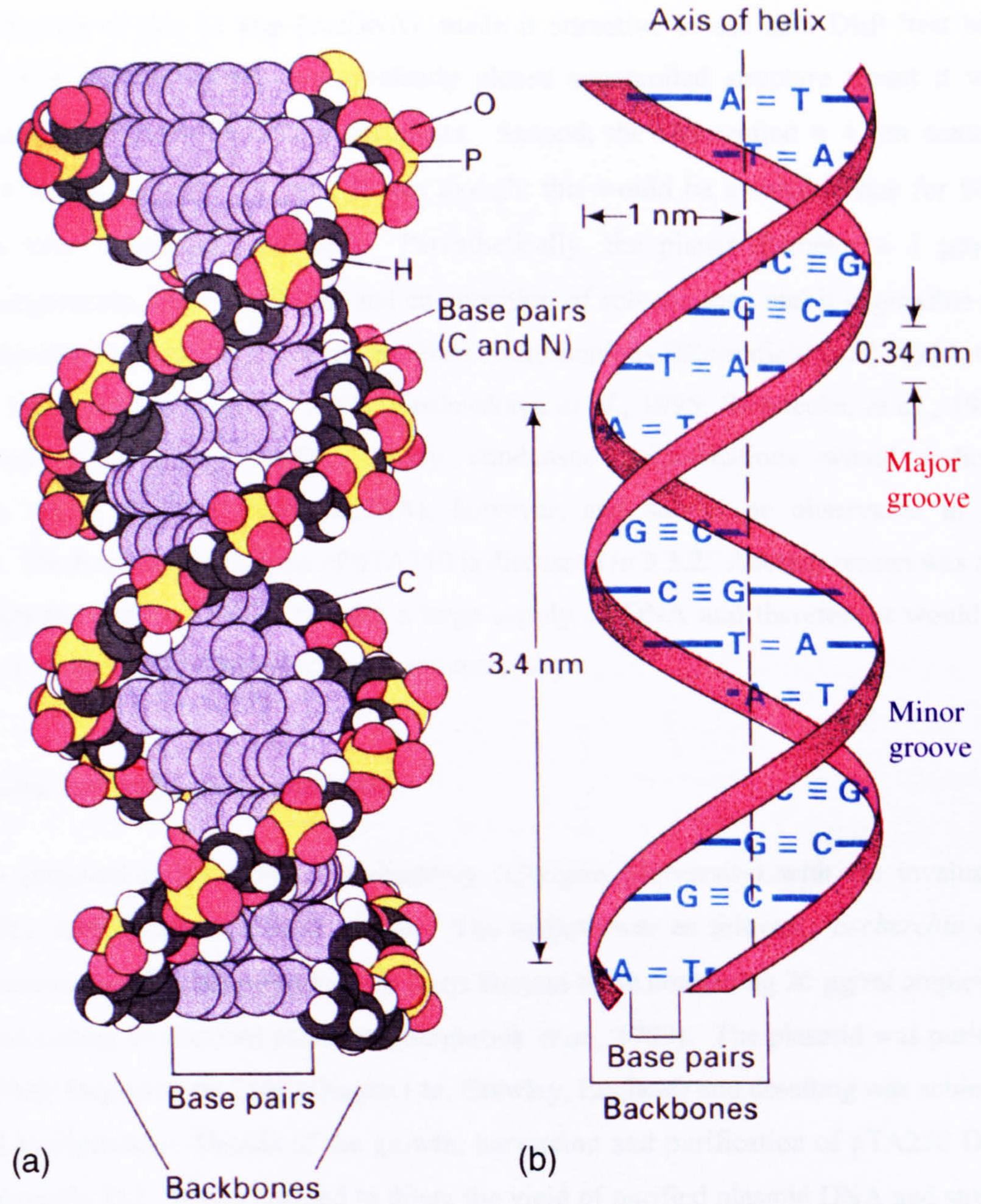

Fig. 3.5 A three dimensional structure of 'Watson and Crick' DNA (a) Molecular model with symbols: H = Hydrogen, O = Oxygen, C = Carbon, N = Nitrogen, P = Phosphorus (b) Stylised diagram with bases: A = Adenine, G = Guanine, C = Cytosine, T = Thymine (adapted from Russell, 1994, p. 181).

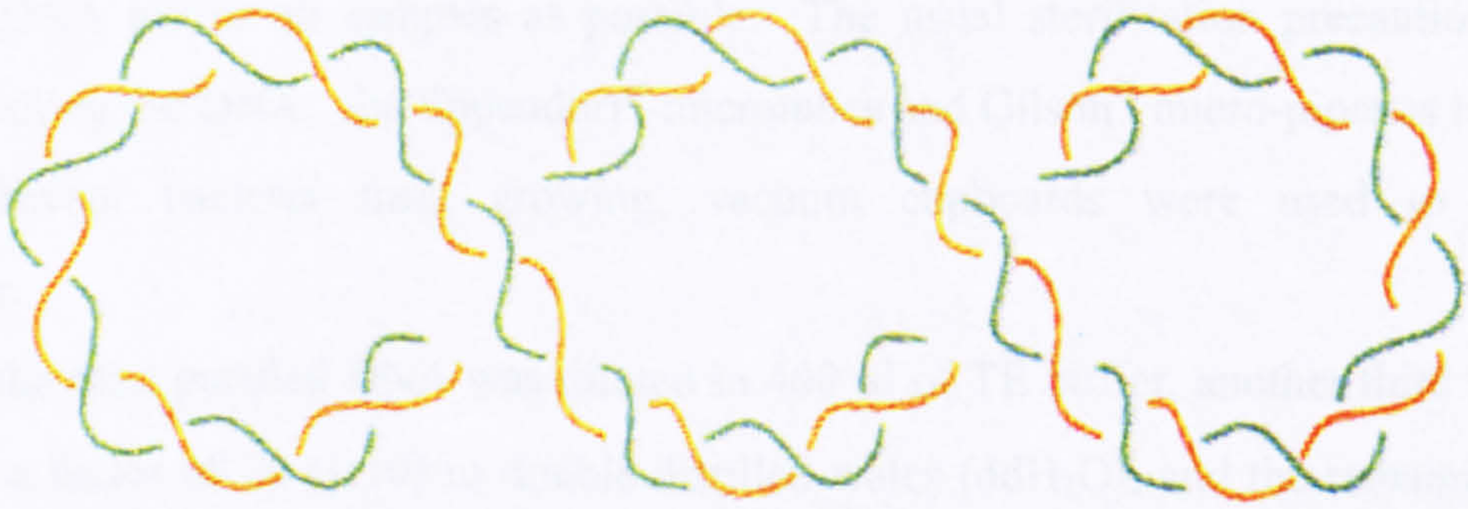

Fig. 3.5(c) Schematic diagram of negatively supercoiled plasmid DNA with 20 helical turns and 2 superhelical turns (from Russell, 1994, p. 189).

The properties of this 12 kbp (cccDNA), made it attractive to use as a DEP 'test bio-particle' for several reasons. First, the covalently closed supercoiled structure meant it was relatively mechanically robust for DEP experiments. Second, the supercoiled ≈ 4 μm contour length implied a planar diameter ≈ 1 μm. It was thought this would be a suitable size for DEP experiments on micro-fabricated electrodes. Parenthetically, the planar diameter ≈ 1 μm is contingent on temperature, ionic conditions and composition of solvent, etc., and it is possible for DNA macromolecules to condense into more compact conformations (Bloomfield *et al.*, 1974, Ch. 5; Bloomfield, 1991; Mel'nikov *et al.*, 1995; Vasilevskaya *et al.*, 1995; Strzelecka, *et al.*, 1988; Lyubchenko and Shlyakhtenko, 1997). Very condensed conformations would indicate denaturation to single stranded DNA (ssDNA), however, and should be observable in gel electrophoresis. Electrophoresis analysis of pTA250 is discussed in 3.3.2. Another reason was that the DEP experiments were envisaged to need a large supply of DNA and therefore it would be better to purify it on-site, rather than purchase it commercially.

3.3.1 DNA growth, harvesting and purification

The DNA was prepared at the Wolfson Laboratory (Glasgow University) with the invaluable assistance of Drs. Joel Milner and Edi Cecchini. The method was as follows: *Escherchia coli* (strain DHα), containing pTA250 was grown in Luria Bertani broth containing 20 μg/ml ampicillin and harvested according to standard protocols (Sambrook *et al.*, 1989). The plasmid was purified using a QIAGEN® Megaprep tip 2500 (Qiagen Ltd, Crawley, England) and desalting was achieved by isopropanol precipitation. Details of the growth, harvesting and purification of pTA250 DNA are given in Appendix D.1. It was decided to dilute the yield of purified plasmid DNA and store it at –20 °C in solutions of three different conductivities. The reason for using three different conductivities is that there is a trade-off between unwanted conductivity in DEP experiments and DNA stability during storage that tends to improve with the presence of stabilising buffer such as TE (10 mM Tris-HCl, 1 mM EDTA, pH 7.5). Care was taken to ensure a homogenous concentration of DNA across all samples as possible. The usual sterilisation precautions were adopted when handling the DNA: the Eppendorf® microtubes and Gilson® micro-pipettes had been autoclaved to prevent bacteria from growing, vacuum cupboards were used to prevent contamination, etc.

One third of the total purified DNA was diluted in 400 μl of TE buffer, another third into 400 μl TE diluted by a factor of 10 (1:10) in double distilled water (ddH_2O), and the remaining third into 400 μl of ddH_2O. The 400 μl preparations were labelled accordingly:

- $pDNA_{TE}$ - pTA250 DNA in TE buffer
- $pDNA_{10\%TE}$ - pTA250 DNA in 10% TE buffer
- $pDNA_{ddw}$ - pTA250 DNA in double distilled water

Each of the three 400 µl solutions was divided into 40 × 10 µl aliquots and stored at –20 °C.

3.3.2 DNA spectrophotometry and gel electrophoresis

Measurements of the UV absorption ratio for three randomly selected aliquots were undertaken by the author under the direction of Dr. Peter J. Dominy (Arnott Laboratory). The UV absorption ratio was calculated A_{260}/A_{280} = 1.8 and indicated the preparation was relatively free from protein (Wissenburg *et al.*, 1995). The plasmid concentration was estimated to be approximately 2.7 µg/µl. The details of the sample test results are given in Appendix D.2.1.

Samples of plasmid DNA were also analysed by electrophoresis on a non-denaturing agarose gel stained with Ethidium Bromide (EtBr) (2,7-diamino-10-ethyl-9-phenyl phenanthridinium bromide; $C_{21}H_{20}N_3Br$, Sigma™ E1510; Brown, 1995, p. 42) and prepared according to standard methods described in Appendix D.2.2. Viewing the gel under UV illumination at 30 minute intervals, showed the presence of two bands consistent with a mixture of catenated[1] cccDNA (Bloomfield *et al.*, 1974, p. 282-3, Adams, 1991, p. 12). Smears that would indicate the presence of low MW nucleic acids (such as degraded RNA), protein, or lipid contaminants, were not observed. Two photographs of gels are shown in figures 3.6(a) and (b) and are discussed in the following sections. It appears that a significant proportion of the plasmids are in fact linked to each other, in addition to being single entities. The presence of two bands interestingly contrasts with an initial batch of plasmid DNA pTA250 (kindly prepared by Dr. J. Milner) that exhibited only one band.

3.3.2.1 Use of restriction enzymes and DNA electrophoresis

An interesting way of investigating the geometric and topological structure of pTA250 cccDNA was to cut or incise it using enzymes and analyse the cut DNA with gel electrophoresis. The application of restriction endonuclease enzymes for cutting DNA at recognised base sequences is well documented (Brown 1995, Ch. 4). One experiment using *Bam*H1, *Eco*R1, and *Hin*dIII to cut pTA250 plasmids, was performed with the assistance of Dr. E. Cecchini and Ms. Maria Giannakou, Wolfson Laboratory. The details of the preparations are given in Appendix D.2.3 and a UV photograph of the electrophoresis results (100V, 1 hour) is exhibited in Fig. 3.6(a). Marker DNA was loaded into the first, far left, lane (lane 1), the control (or uncut sample) was loaded into lane 2, and samples digested with *Bam*H1, *Eco*R1, and *Hin*dIII were loaded into lanes 3, 4 and 5, respectively.

---

[1] The term 'catenated', referred to in the technical literature, is understood to be synonymous with 'concatenated'.

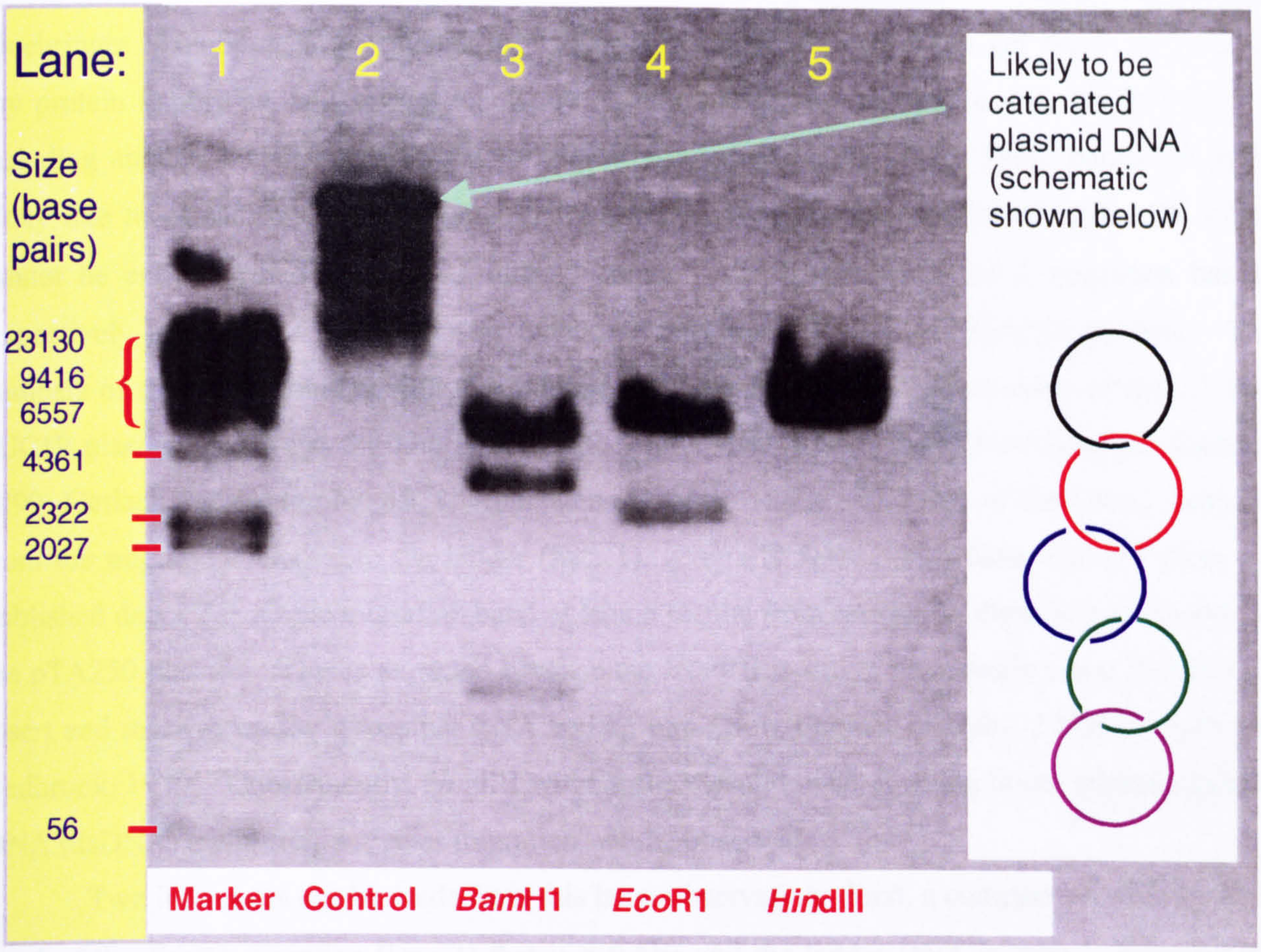

Fig. 3.6(a) Agarose non-denaturing EtBr gel of restriction digested pTA250 (with control and marker).

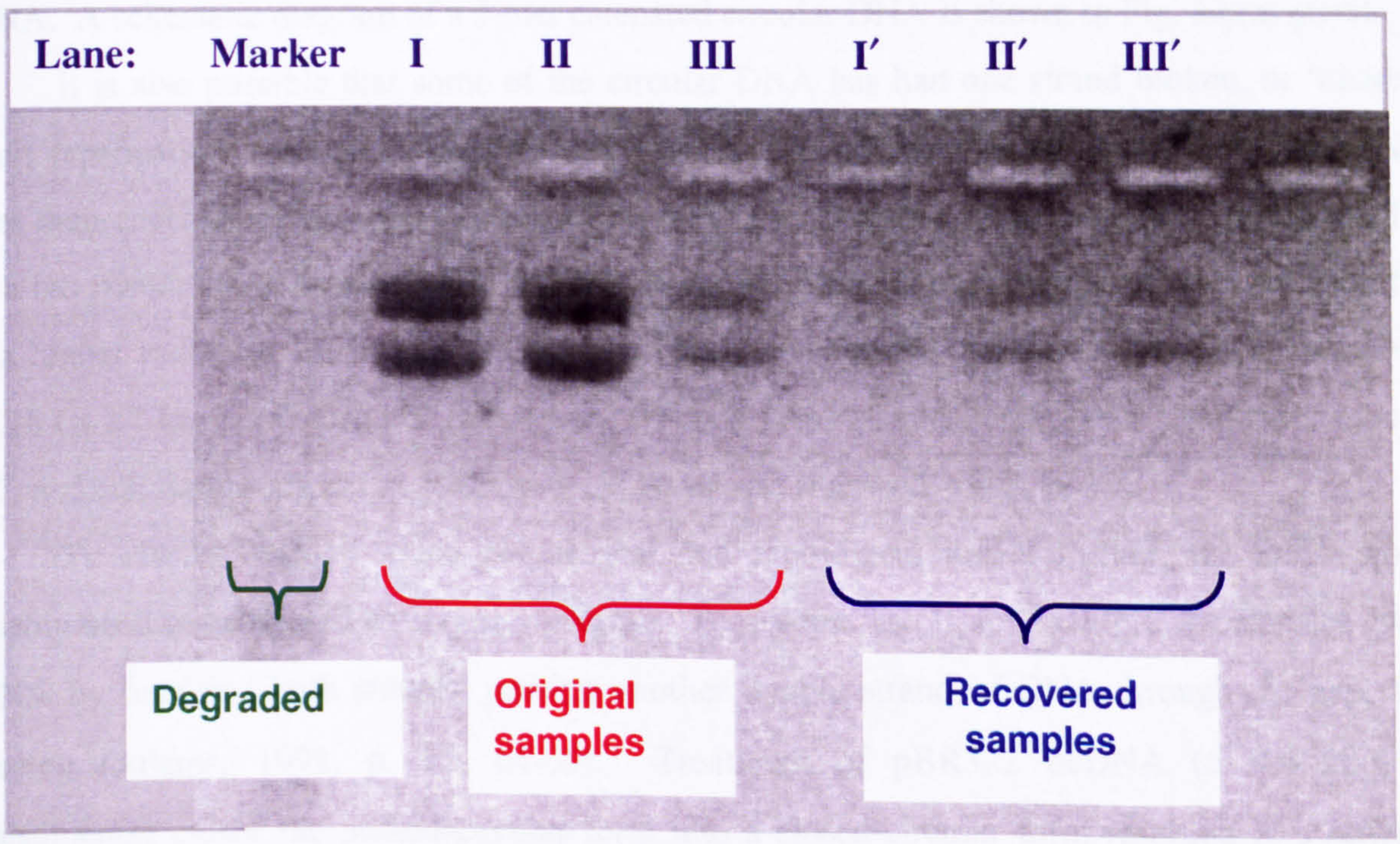

Fig. 3.6(b) Agarose non-denaturing EtBr gel of three pTA250 samples and the same samples recovered from DEP experiments (EtBr was used as a fluorescent label).

The sizes of the *Hin*dIII λ Marker bands in lane 1 have been estimated from published data (Boehringer Mannheim, 1996) though the ladder is not well resolved. The gel shows absence of any protein impurities, and several bands are discernable for the control (uncut) DNA in lane 2 including another which appeared not to migrate from the loading well. These bands are most likely due to catenated cccDNA bands that aggregate, though the presence of high MW DNA cannot be entirely ruled out for the latter. Lanes 3 and 4 exhibit 3 and 2 migration bands, respectively, revealing the digestion activity of *Bam*H1 and *Eco*R1 on pTA250 plasmid. The numbers of the bands concurs with those deduced from published restriction maps of the 2.7 kbp pUC19 plasmid insert and 8.9 kbp pTA250 ribosomal RNA coding unit (New England Biolabs, 1999; Gerlach and Bedbrook, 1979; Appels and Dvořák, 1982). The size of the bands, deduced from the migration relative to the ladder (lane 1), generally agrees with those inferred from the published data. The single migration band in lane 5 results from restriction digestion of *Hin*dIII on the pTA250 plasmid. This is expected because the *Hin*dIII is active on a single site in the pUC19 insert and inactive on the ribosomal RNA coding unit (New England Biolabs, 1999; Gerlach and Bedbrook, 1979). Consequently, *Hin*dIII will cut the plasmid once, forming linear double stranded DNA (dsDNA) and a single species migration will be observed.

Two inferences can be made from this latter observation. First, a comparison with the slow band of the *Eco*R1 digestion (lane 4) that is ≅ 9 kbp and the ladder DNA in lane 1, indicates the size of cut dsDNA is 10 to 12 kbp, as expected. Second, comparing with the slower migration of uncut DNA in lane 2, suggests those bands (in lane 2) are catenated circular DNA and not linear dsDNA. A schematic diagram of a 5-mer catenated circular DNA is shown in Fig. 3.6(a) insert.

It is also possible that some of the circular DNA has had one strand broken, or 'nicked', during purification - in which case its conformation would be relaxed open-circular (ocDNA) rather than cccDNA (Bloomfield *et al.*, 1974, p. 272-3; Coggins, 1987, p. 12). Usually ocDNA that a has planar circle conformation exhibits lower mobility in a gel compared with cccDNA that has a higher mobility due to its compact, negatively supercoiled structure. This is the case with pUC18 (≅ 2.7 kbp) and pBR322 (≅ 4.4 kbp) (QIAGEN® Plasmid Purification Handbook, January 1997, p. 52-3; Sambrook *et al.*, 1989, p. 1.13; Bates and Maxwell, 1993, p. 31).

To clarify both of these geometrical and topological issues further, the DNA would probably need to be treated with topoisomerase. Topoisomerase II, for example, decatenates cyclic dsDNA by breaking both strands, passing another double strand of DNA through the gap, then resealing (Adams, 1991, p. 12, 64-65). Treatment of pBR322 ocDNA (≅ 4.4 kbp) by topoisomerase closes the nicked-circular form into a closed-circular form resulting in a series of bands between ocDNA and cccDNA forms (Bates and Maxwell, 1993, p. 32). Another option would to use the properties of intercalating drugs, such as, EtBr that intercalate and unwind DNA macromolecules thereby distinguishing ocDNA from cccDNA (Bloomfield *et. al.*, 1974; Brown, 1995, ch. 3).

3.3.3 Staining DNA for fluorescence microscopy

The pTA250 DNA samples were stained (or labelled) by mixing with a sufficient amount of fluorescent dye dissolved in aqueous media. Two dyes were used. The first was Ethidium Bromide (Sigma™ E1385) with stock concentration 500 μg/ml (or equivalent) and optical emission wavelength, λ_e = 600 nm. The second dye was 4′, 6-Diamidino-2-phenylindole (DAPI) (Molecular Probes, D-1306; Morikawa and Yanagida, 1981; Kapuscinski, 1995) with λ_e = 457 nm. Stock solutions of DAPI consisted of ≈ 0.5 mg lyophilised DAPI dissolved in ≈ 5 ml distilled reverse osmosis (RO) water to give a nominal concentration of 1 mg/ml.

These respective dyes were then used to stain the DNA shown in Fig. 3.4(a) and (b). Typically, a 10 μl aliquot was selected from stored (– 20 °C) plasmid ($pDNA_{TE}$, $pDNA_{10\%TE}$, or $pDNA_{ddw}$ c.f. section 3.3.1), thawed, and 1 - 2 μl drawn and micro-pipetted into an Eppendorf® microtube containing 10 – 15 μl of suitable medium (RO water for lowest conductivity). To avoid variations in DNA content, care was taken to gently move the Gilson® micropipette tip around, within the volume of thawed DNA, when small aliquots were being drawn. In addition, the tip was carefully 'flushed' to ensure the correct amount (as possible) of plasmid was transferred from the tip and diluted. The diluted DNA (typically ≈ 300 ng/μl) was labelled with fluorescent dye by micropipetting 1 – 2 μl of EtBr, or DAPI, stock into the microtube. The mixture was gently stirred (with the Gilson® tip), shaken, and left at least for a few minutes for the dye to bind. The microtubes were often wrapped in foil to prevent ambient light from activating the dye. The resulting concentrations of EtBr or DAPI were ≈ 100 μg/μl. The dye concentrations were varied by two orders of magnitude (10 to 1000 μg/μl) to optimise the fluorescent signal. The plasmid concentrations were also varied ≈ 1 - 300 ng/μl. The reason is that, in principle, very low concentrations of DNA should be visible using fluorescent microscopy.

Suppose, for example, only 10 ng of DNA was drawn into a pipetted 10 μl (10^{-8} m^3) sample; which would be visible by gel analysis. The mass of a 12 kbp macromolecule of DNA, from section 2.3.1, equation (2.3.3), is $m_{12kbp} \cong 1.3\times10^{-17}$ g. Assigning the total mass of DNA, m_{DNA} = 10 ng, and the total volume (of DNA plus solvent), V_T = 10 μl, the sample concentration, c_V (or number density) is

$$c_V = \frac{m_{DNA}}{m_{12kbp}V_T} = \frac{10\times10^{-9}}{1.3\times10^{-17}\,10\times10^{-6}\times10^{-3}} = 7.7\times10^{16}\ \text{m}^{-3} \qquad (3.3.2)$$

or $c_V = 0.077\ (\mu\text{m})^{-3}$.

Viewing though microscope the number of fluorescently labelled plasmids clearly visible is limited by the vertical depth-of-focus that is typically about 1 μm (Piller, 1977). Consequently, the number of macromolecules per unit area in the horizontal plane with thickness Δy is the area concentration,

$$c_A = c_V \Delta y \tag{3.3.3}$$

Using $c_V = 0.077\ (\mu m)^{-3}$ and $\Delta y = 1\ \mu m$, $c_A = 0.077\ (\mu m)^{-2}$. Equation (3.3.3) can be extended to evaluate the average number of plasmids n viewed in a rectangular strip of transverse width Δx and length Δz (or per unit longitudinal length c_L),

$$n = c_A \Delta x \Delta z = c_L \Delta z \tag{3.3.4}$$

Hence, choosing a planar square area with side lengths the same as the electrode widths and gaps, $\Delta x = \Delta z = 10\ \mu m$, $n = 7.7$ plasmids. Alternatively, on average one plasmid should be observable (in-focus) for a planar horizontal square viewing area with lengths $\sqrt{1/0.077} = 3.6\,\mu m$. This concentration predicts that a very large number of particles should be clearly visible. However, these low dilutions were not particularly satisfactory and labelled plasmid sample concentrations two orders of magnitude higher (~ 100 ng/μl) were preferable.

3.3.4 Viewing DNA on microfabricated electrodes using fluorescence microscopy

The solutions of stained DNA diluted into 10 – 20 μl aliquots were placed on microscope slides or microfabricated electrodes (mounted on glass slides). The latter were easier to visualize under the microscope because the reflectivity of the gold tended to increase the illumination. Fluorescent particles or 'specs' of the order of 1 μm were often observed suspended in aqueous medium. All three figures 3.2(b), 3.4(a) and 3.4(b) showing stained DNA illustrate the specs. This is expected from the size of the cccDNA pTA250 plasmids that are ≈ 1 μm which is about the same as the resolution limit of the optical microscope. The ×20 microscope objective used in experiments, for example, had a numerical aperture, NA = 0.75. Using $\lambda = 500$ nm, the limit of resolution is approximately $\lambda/\mathrm{NA} = 0.67$ μm (Piller, 1977; Hiemenz, 1986; Born and Wolf, 1999). Finer resolution of the conformational shape of the plasmids was not expected, particularly when fluorescent labelling tends to optically distort shapes of objects.

Isolated strands directly corresponding to cut dsDNA ≈ 4 μm were not obvious but entanglements from several microns to hundreds of microns were regularly observed. Some of

these entanglements are likely to stem from catenation of cccDNA and their presence complicated the quantification of DEP collection profiles. A distinction is made, therefore in the type of DNA observed, between (a) 'single' or isolated cccDNA plasmids and small catenations up to a few microns in size, and (b) large scale 'conglomerates' extending up to hundreds of microns. Small conglomerates are labelled in Fig. 3.2(b).

Frequently, however, there was a frustrating, entire absence of recognisable plasmids in solution. In many respects this is not altogether surprising since the presence of large conglomerates indicates the concentration of DNA is not uniformly distributed. In an ideal situation, without entanglements, a reasonably uniform concentration of DNA would be expected to occur particularly in a low salt solvent – as is the case with most DEP DNA preparations. This is due to the polyelectrolyte properties of DNA, as described in Chapter 2. In a low salt solution, only a small number of counterions are available to screen the negative charge of each DNA macromolecule. Consequently, each macromolecule would be strongly repelled from each other. This results in an almost equal distance between neighbouring DNA macromolecules, and hence a reasonably uniform concentration (Oosawa, 1971, ch. 9; van Holde, 1971, ch. 2.2; Tanford, 1961, p. 488-9)[2]. On the contrary, in a high salt solution the negatively charged DNA is screened so fluctuations in concentration are expected.

Epi-fluorescence microscopic imaging of DNA movement over micro-fabricated electrodes was generally more problematic than first envisaged. Some preparations of EtBr stained DNA did not exhibit the presence of any plasmids until sufficient AC potentials were applied to the electrodes. Plasmids then accumulated near the electrode edges due to positive DEP. Particle 'clouds' formed across the interelectrode gap on polynomial electrode regions where the interelectrode spacing was about 2 μm, and this is shown in Fig. 3.4(a).

Some plasmid preparations with the two dyes did not show their presence either in suspension, or when AC potentials were applied to the electrodes. Occasionally, plasmids were observed in solution but did not exhibit collections when appropriate AC potentials were applied to the electrodes. This was rare, and occurred when very high medium conductivity was used that suppressed the potential of the electrodes (c.f. Appendix D.2.3.3).

Generally, there were compromises with regards to optimal choice of dye and plasmid concentration. For example, reducing the EtBr concentration to 10 μg/ml tended to improve visualisation of DNA plasmids using epi-fluorescence microscopy. However, their brightness appeared to fade more rapidly (probably due to photo-bleaching). On the other hand, very high concentrations of EtBr tended to increase the background light intensity so isolated plasmids were more difficult to identify. The same features applied to the DAPI stained plasmid DNA.

---

[2] A strictly uniform concentration is unlikely due to several effects including excluded volume.

Reducing the DNA concentration also tended to improve visualisation of single plasmids but at the expense of poorer DEP collections. Generally, the clarity of the DNA plasmids using DAPI was clearer compared with the images resolved using EtBr as a comparison of figures 3.4(a) and (b) suggests.

3.3.5 Observing DNA DEP movement

A number of investigations were undertaken to remedy the large variation in amount of plasmid DNA that was observed with epi-fluorescence microscopy. These were undertaken in the context of DEP experiments with the ultimate goal of producing quantitative measurements of plasmid accumulation.

3.3.5.1 Verifying the presence of DNA plasmids

Initial investigations confirmed that plasmid DNA was being collected, and not contaminants or precipitates of the dyes. For example preparations without plasmid DNA, that is, EtBr diluted solely with TE and/or distilled RO water never exhibited accumulation at electrode edges when AC potentials were applied to the electrodes. Furthermore, accumulation at electrode edges occurred only when DNA plasmids were added. This was performed mid-way though a DEP experiment by turning off the electrode potential and lifting the cover-slip, micropipetting 1 – 2 μl plasmid suspension into the existing droplet on the electrode surface, and replacing the cover-slip. The same confirmation applied for the preparations using DAPI.

DNA DEP experiments were short in duration (up to 20 minutes). Often there was sufficient un-evaporated sample remaining that 2 – 5 μl was recovered (after removing the cover-slip) using a micropipette. This *recovered* preparation was then analysed by agarose gel electrophoresis. The procedure was particularly useful for EtBr preparations because the same dye was used for gel electrophoresis. An example of gel electrophoresis analysis of three plasmid DNA samples taken directly from storage and compared with those recovered after a DEP experiment, is shown in Fig. 3.6(b). The details of the preparation, and loading of recovery DNA are presented in Appendix D.3. The lanes are labelled I, II, and III - corresponding to samples taken from $pDNA_{TE}$, $pDNA_{10\%TE}$, or $pDNA_{ddw}$ stored at – 20 °C. Lanes labelled I′, II′ and III′ correspond to the samples *recovered* from each DEP experiment where respective samples I, II, and III were used. The 'dash' ′ denotes the *recovered* sample.

It is clear I′, II′ and III′ exhibit the same band structure as for lanes I, II, and III. The only visible difference is the dullness of the bands, which is probably due to the *recovered* DNA being diluted further by 1/7 to about 40 ng per lane [3]. The gel electrophoresis analysis indicates that it is quite possible for plasmid DNA to be present in an experiment and not be visible under epi-fluorescence microscopy, or not until DEP begins to collect the plasmids at the electrode edges. Furthermore, if the plasmids are stained with EtBr, their existence can be verified by recovering and comparing with the original sample by gel electrophoresis. Generally, particles observed under the microscope that appeared as EtBr stained DNA plasmids, when later recovered and analysed using electrophoresis, were confirmed to be DNA. Unfortunately the recovery technique for DAPI labelled DNA produced large smears in the gel and therefore no conclusion could be reached.

3.3.5.2 DNA homogeneity

The precautions for ensuring homogenous (uniformly distributed) plasmid concentrations during purification, storage, and fluorescent labelling have been described in sections 3.3.1 and 3.3.3. Ideally, if clumping or aggregation did not occur, the concentration of plasmid DNA suspended in medium should be uniformly distributed across all 120 10 µl aliquots (stored at – 20 °C). Moreover, consecutive 1 – 2 µl aliquots that were diluted and labelled with fluorescent dye should yield the same content of suspended plasmid (viewed under the microscope).

However, aggregation occurred so, for example, consecutive viewings of prepared samples from a single 10 µl aliquot showed considerable variation in DNA content: varying from a preponderance of single or small catenated cccDNA plasmids, to large conglomerates, to complete absence of any particles at all. There did not appear to be any significant variation attributed to the type of medium used to store the DNA. That is, there was no significant general variation in plasmid content of Eppendorf microtubes containing $pDNA_{TE}$, $pDNA_{10\%TE}$, or $pDNA_{ddw}$.

Different methods of dilutions and labelling were tried without any consistent improvement in DNA content or type (single micron sized macromolecules or large conglomerates). Fortunately, many sample preparations yielded practicable amounts of single plasmids that enabled substantial DEP collections of DNA on polynomial and interdigitated electrodes. The main difficulty with quantitative measurements of DEP collection profiles was the unpredictability in content. This was helped to some extent by previewing prepared 10 – 20 µl stained DNA samples under UV light prior to micropipetting onto the electrodes (for viewing under the microscope).

---

[3] It is not known why the both bands in lane III, corresponding to sample 3, are dull compared with the bands in lanes I and II.

The prepared sample was micropipetted onto a stretch of clean Nescofilm® (Azwell Inc., Japan) and viewed for a few seconds underneath a portable UV lamp (Blak-Ray® 366 nm, UVP Inc., CA, USA). Usual precautions were taken to avoid UV irradiation! The sample droplet on Nescofilm® was then drawn back into the Gilson® tip and pipetted onto the electrodes. Large conglomerates were clearly visible without magnification, especially with DAPI labelling. If necessary, these could be moved away from the sample droplet using a Gilson® tip. Frequently, when viewed under the microscope, conglomerates tended to coexist with single or micron sized catenated cccDNA plasmids. Hence, the presence of these large visible structures during previewing moderately guaranteed there would be enough single plasmids in the sample for DEP collections. On the other hand, prepared samples that appeared dull under the portable UV lamp almost certainly meant an absence of plasmids when later viewed under the microscope.

3.3.5.3 Use of parallel DEP electrode arrays

It is clear that homogeneity was difficult to attain and single micron sized catenated cccDNA plasmids were often accompanied by conglomerates that complicated DEP measurements. Furthermore, as described in section 3.2, DNA that was attracted to electrodes frequently adhered after the DEP force had been removed. This made serial DEP measurements (investigating the dependency on variables such as AC frequency) extremely unreliable. This was the motivation for the design and fabrication of eight separately addressable arrays – as described in section 3.2.1.1.

3.3.6 Reduction in oxidation and photo-bleaching

Both EtBr and DAPI stained DNA exhibited photo-bleaching when illuminated by UV for periods more than about a quarter of a minute. As previously mentioned DAPI stained DNA was generally more clearer than EtBr and became the preferred dye of use. However, DAPI not only bleaches but also causes DNA filament cutting or strand breakage (Bustamante 1991; Houseal *et al.*, 1989; Yanagida *et al.*, 1983). In fact, initial DEP trials using high concentrations of plasmid DNA labelled with DAPI, exhibited extraordinary spindle structures. Consequently, a stock solution of reducing agent 10 % volume:volume (v:v) 2-Mercaptoethanol (ME) (Sigma, M3148) was added to the dye aliquots during sample preparation to decrease photo-bleaching and strand breakage. The final dilution was typically 1% v:v. An alternative to ME, used by (Matsumoto *et al.*, 1981), is sodium cacodylate.

Adding the 2-Mercaptoethanol anti-fade agent reduced the photobleaching effect so the fading was insignificant over the duration of each collection experiment of up to a minute.

3.4 Preparation of colloidal particles for DEP experiments

The model colloidal particles used for most DEP experiments were yellow-green fluorescently labelled carboxy-polystyrene micro-spheres (or 'beads') purchased from Molecular Probes, Eugene, USA. The two sizes used were 93 nm and 216 nm diameter FluoSpheres® (Molecular Probes, L-5221 and F-8811). Both sizes had a specified emission wavelength λ_e = 515 nm and excitation wavelengths 490 nm and 505 nm, respectively. The spheres were supplied as 2 % solids (w/w) in aqueous solution (2 mM sodium azide in distilled water).

An expression for the number of spheres per unit volume, or concentration c_v' (m^{-3}) can be written in terms of the weight S % solids, density of polystyrene $\hat{\rho}_s$ = 1.05 g/cm^3 and diameter of each sphere $\hat{d}_s$ (μm) (Bangs, 1997). The dash ' denotes this concentration applies to the sample supplied,

$$c_V' = \frac{6\times10^{18}\,\hat{S}}{\pi\hat{d}_s^3[\hat{\rho}_s - \hat{S}(\hat{\rho}_s - 1)]} \tag{3.4.1}$$

where 2% solids means $\hat{S} = 0.02$. The inverted v (∧) indicates (3.4.1) is applicable for the quantities scaled as stated. Equation (3.4.1) can be derived by combining expressions for the volume, density and % solids of each sphere $V_s = 4\pi r^3/3 = \pi d_s^3/6$, $\rho_s = m_s/V_s$, and $\hat{S} = m_s/(m_s + m_w)$. The density of the suspending medium is assumed to be unity, which is the case for water $\hat{\rho}_w$ = 1.00 (g/cm^3) to two decimal places at 25 °C.

For DEP experiments the sample was diluted by a volume ratio, V_r. Typically, a 1 μl 2% micro-sphere suspension was added to 1 ml distilled RO water (or 1:1000 dilution) so V_r = 1/1000. Hence, the final micro-sphere concentration is written,

$$c_V = c_V' V_r = \frac{6\times10^{18}\,\hat{S}V_r}{\pi\hat{d}_s^3[\hat{\rho}_s - \hat{S}(\hat{\rho}_s - 1)]} \tag{3.4.2}$$

Substituting the above values for the parameters and $\hat{d}_s$ = 0.216 μm (3.4.2) yields a typical value for the volumetric concentration used in a DEP experiment c_V = 3.613×10^{15} m^{-3} or $c_V \cong$ 3.61×10^{-3} (μm)$^{-3}$. The planar area concentration, from (3.3.3), is $c_A = c_V \Delta y$. Assuming, as before with the plasmid DNA, the microscope has 1 μm vertical depth-of-focus, Δy = 1 μm then c_A = 3.61×10^{-3} (μm)$^{-2}$. Hence for a transverse strip of width Δx = 10 μm, the average number of beads viewed per unit longitudinal length from (3.3.4) is $c_L = c_A \Delta x$ = 0.036 μm^{-1}.

Comparing, for example, with the viewable electrode lengths in Fig. 3.7(a) where $\Delta z \cong 117$ μm, the expected number of beads to be seen for each 117 × 10 μm strip is $n = c_L \Delta z = 117 \times 0.036 \cong 4.2$ beads. Inspecting Fig. 3.7(a), about one bead is visible over the (darker) 10 μm gaps and an average of about 10 are visible over the 10 μm width electrodes. Clearly, the reflectivity of the gold surface of the electrodes influences the visibility as well as image brightness. Nonetheless, the calculated value of 4 beads per strip generally agrees with the number visible in Fig. 3.7(a).

3.5 Development of video image processing software

An overview of DEP experiments of sub-micron particles collecting onto interdigitated electrodes has been given in section 3.1.1. The quantitative measurement of fluorescently labelled particles collecting onto the electrode edges required sequential processing of microscope images recorded on videotape throughout the course of each experiment. The time dependent fluorescence intensity of images is represented symbolically as $I(x,z,t)$ where I denotes the intensity of the image that is located optically at the camera detector. The 2-D image plane is assumed to be parallel to the plane of the electrodes and spans directions $\vec{u}_x$ and $\vec{u}_z$.

An example of two recorded video (frame) images of a 216 nm latex bead suspension before and approximately 5 seconds after the onset of DEP is shown in figures 3.7(a) and (b). Both images are approximately half-length frame size (540 x 360 pixels) and have been cropped and juxtaposed for illustrative purposes. Fig. 3.7(b) shows the tendency for beads to accumulate, in response to DEP forces, at the electrode edges and is similar to that for DNA plasmids illustrated in Fig. 3.2(b). Both images also show the fluorescence is generally higher over the electrodes than over the gaps. This is attributed to the gold surface of the electrodes that reflects light emitted from the beads more than the glass substrate under the gaps.

The processing of video images consisted of two stages. The first stage involved capturing (or 'grabbing') 25 frames sec^{-1} and converting these to individual TIFF (Tagged Image File Format) image files, or an MPEG (Motion Picture Expert Group) movie file (Haskell *et al.*, 1997). The second stage consisted of spatially integrating the fluorescence intensity of the sequential TIFF/MPEG images to give a time dependent fluorescence profile representing particle collection about an electrode edge. The profile for each collection experiment was then compared with other profiles under different experimental conditions, such as, applied AC frequency. The same processing of images applied for particle *relaxations* – that is, for particles already dielectrophoretically accumulated onto the electrodes that diffused into solution once the AC potential to the electrodes had been switched off.

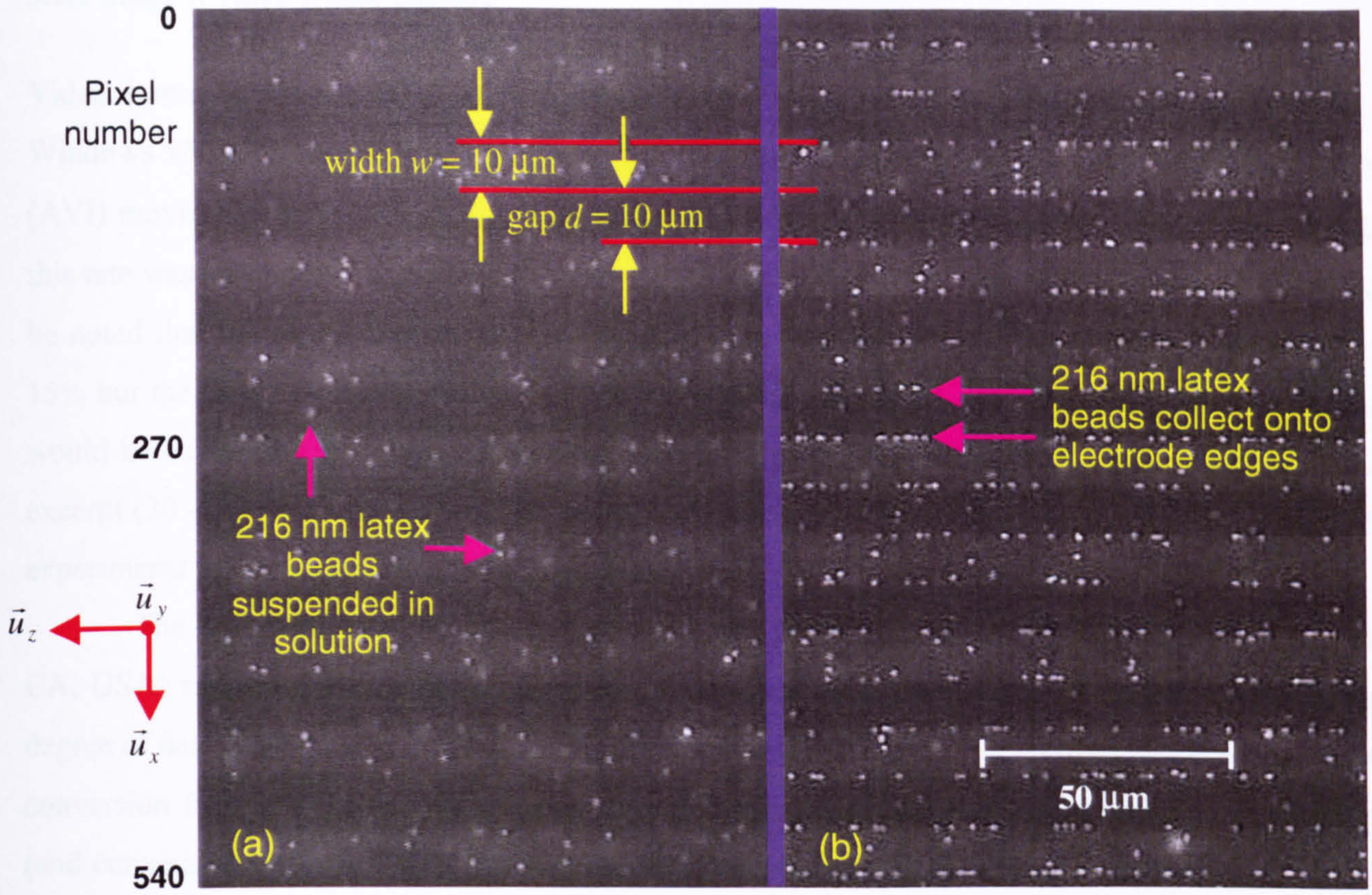

Fig. 3.7 Positive DEP collection of 216 nm diameter latex beads onto $d = w$ = 10 µm interdigitated electrodes (a) ~ 1 second before DEP force applied (b) ~ 5 seconds after DEP force applied.

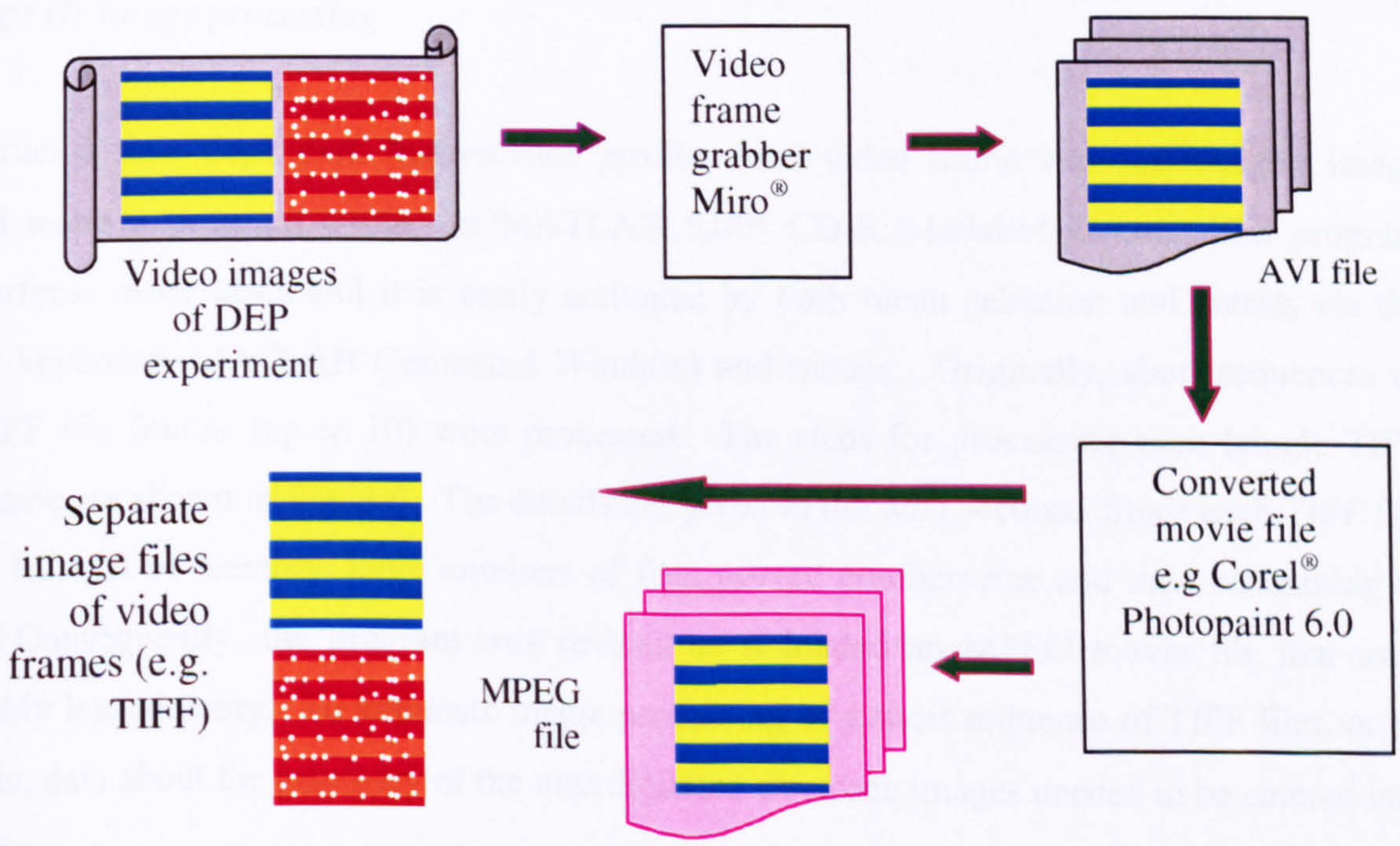

Fig. 3.8 Video frame grabbing leading to TIFF files, or an MPEG movie file, for automated processing.

3.5.1 Stage I: video frame capture

Video frames were captured using a miroVIDEO® DC 30 (CA, USA) frame grabber on a Windows 95® (Microsoft, USA) platform and stored automatically as an Audio Visual Interleave (AVI) movie file, as shown in Fig. 3.8. The capture rate was usually set at 1 frame sec^{-1} though this rate was a minimum and could be much higher (up to the video rate 25 frames sec^{-1}). It should be noted that the actual capture rate appeared to vary slightly about 1 frame sec^{-1} by as much as 15% but the effect on the final fluorescence profile was not significant. Typically 30 – 50 frames would be captured for a video excerpt (or clip) from each DEP experiment. The duration of the excerpt (30 – 50 seconds) was verified using a stop-watch. A microphone was used in many DEP experiments to simultaneously record comments.

The AVI files were viewed using commercial software, such as, Photo-Paint 6.0® (Corel, CA, USA) and were stored as MPEG movie files. One of the attributes of MPEG coding is the degree of data compression involved that can minimise the memory needed to store the movie. The conversion from AVI to MPEG files involved a compromise between image quality and memory (and conversion time) and most conversions were set to maintain high image quality (set to '5' on Photo-Paint 6.0® display menu). Typically a 40 frame MPEG file required only 1.8 megabytes (MB) of memory. A few important frames from each AVI file were selected and stored separately as TIFF files. These were used to set up the automated processing of the MPEG files.

3.5.2 Stage II: Image processing

To construct a time dependent fluorescence profile, each video frame was sequentially image processed using a program written in MATLAB 5.0™ CD-R:/Matlab/*depint.m*. The program *depint* perfoms many tasks and it is easily activated by both menu selection and entries via the computer keyboard (MATLAB Command Window) and mouse. Originally, short sequences of stored TIFF file frames (up to 10) were processed. The steps for processing each (single TIFF image) frame are shown in Fig. 3.9. The details are given in the next section. Since each TIFF file occupied 1.2 MB of memory, large numbers of files proved cumbersome and time consuming to process. Consequently, the program was revised so it loaded an MPEG movie file that used considerably less memory. To automate image processing of a short sequence of TIFF files, or an MPEG file, data about the geometry of the interdigitated electrode images needed to be entered into the program.

This data was compiled and stored by loading a *single* 'representative' frame into the program and processing the image on a step-by-step basis. Information about the image geometry was entered by the operator in response to image displays and requests by the program. This data

was applicable for all images to be later automatically processed, and the program was thus 'set-up' or 'trained' for this purpose. An illustration of single image processing and program 'training' is summarised in Fig. 3.9. In most cases two separate images would be used as representative samples and the data compared for consistency.

3.5.2.1 Stage II(a): single image processing and program training

The initial steps for constructing a time dependent fluorescent intensity profile about an electrode edge required summation of the pixel intensities along the longitudinal direction $\vec{u}_z$ of the electrodes shown in Fig. 3.7. This takes advantage of the longitudinal invariance (or symmetry) of interdigitated electrodes and required $\vec{u}_z$ to be aligned with the (horizontal) pixel column axis of the image. Before most DEP experiments commenced, the CCD camera on the microscope was aligned with the horizontal (pixel column) axis of the TV monitor. Usually this was performed using the UV filter since gold on glass substrate has a good contrast. This ensured that for most video excerpts, the images of electrode edges were almost parallel with the horizontal axis of the image. This is evident in Fig. 3.7(b) where beads have accumulated on the electrode edges with almost horizontal alignment (with respect to the image axis).

A closer inspection of Fig. 3.7(b), however, shows the electrode edges $\vec{u}_z$ are slightly misaligned and need to be rotated clockwise by a small angle. In fact it turned out (later) a clockwise rotation of 0.1° (or -0.1° using conventional polar coordinate geometry) achieved an excellent alignment for this frame (and others) in this video clip. Correction of this misalignment was important because an angular error of 0.1° over 720 pixels results in a mismatch of 1 pixel in the vertical axis of the image ($720\tan 0.1^\circ \cong \frac{2\pi}{5} \cong 1.3$). Achieving fine rotations of order of a tenth of a degree was not successful using Photo-Paint® 6.0, so the first main task of the MATLAB program *depint* was to check the alignment of the electrode array with a horizontal/vertical cross-hair that could be positioned over the image by using a mouse. This is shown as diagram (i) inside the hashed blue box in Fig. 3.9. Angles for rotation were successively entered into the MATLAB Command Window until the re-displayed, rotated electrode edges were correctly aligned with the cross-hair, diagram (ii). An actual half-frame length image displayed by *depint* is shown in Fig. 10(a) that was rotated -0.1°. This frame is from the same video clip as those two in Fig. 3.7 and it is clear the longitudinal direction $\vec{u}_z$ of the electrode edges is aligned with the pixel column axis of the image.

Once the image was correctly oriented, the average longitudinal intensity, for each pixel location (row r) in the transverse direction, was calculated. This is expressed (in general continuous integral form) as,

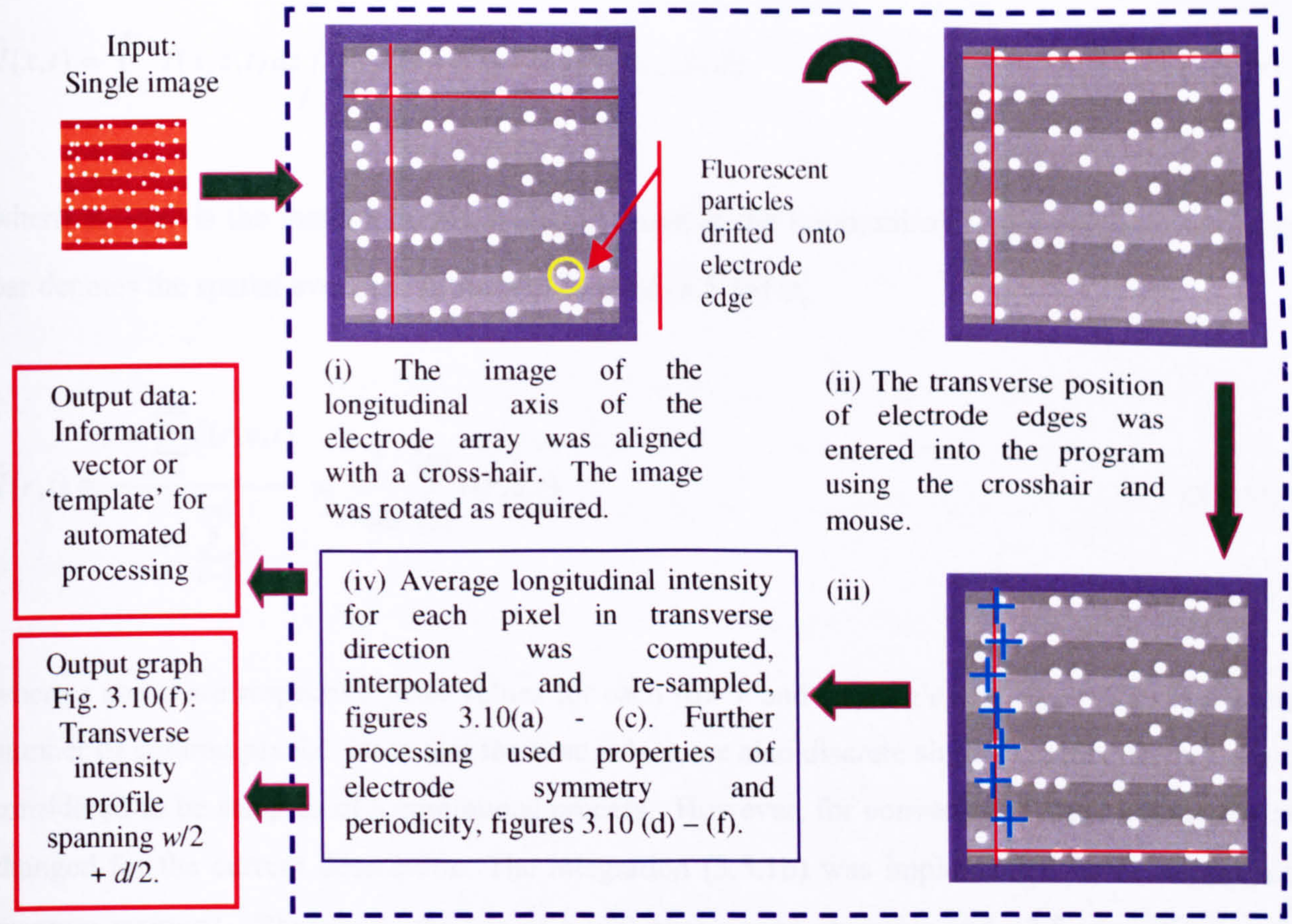

Fig. 3.9 Single image processing and set-up, or 'training', program for automated image processing. The steps are (i) to (iv) as labelled above.

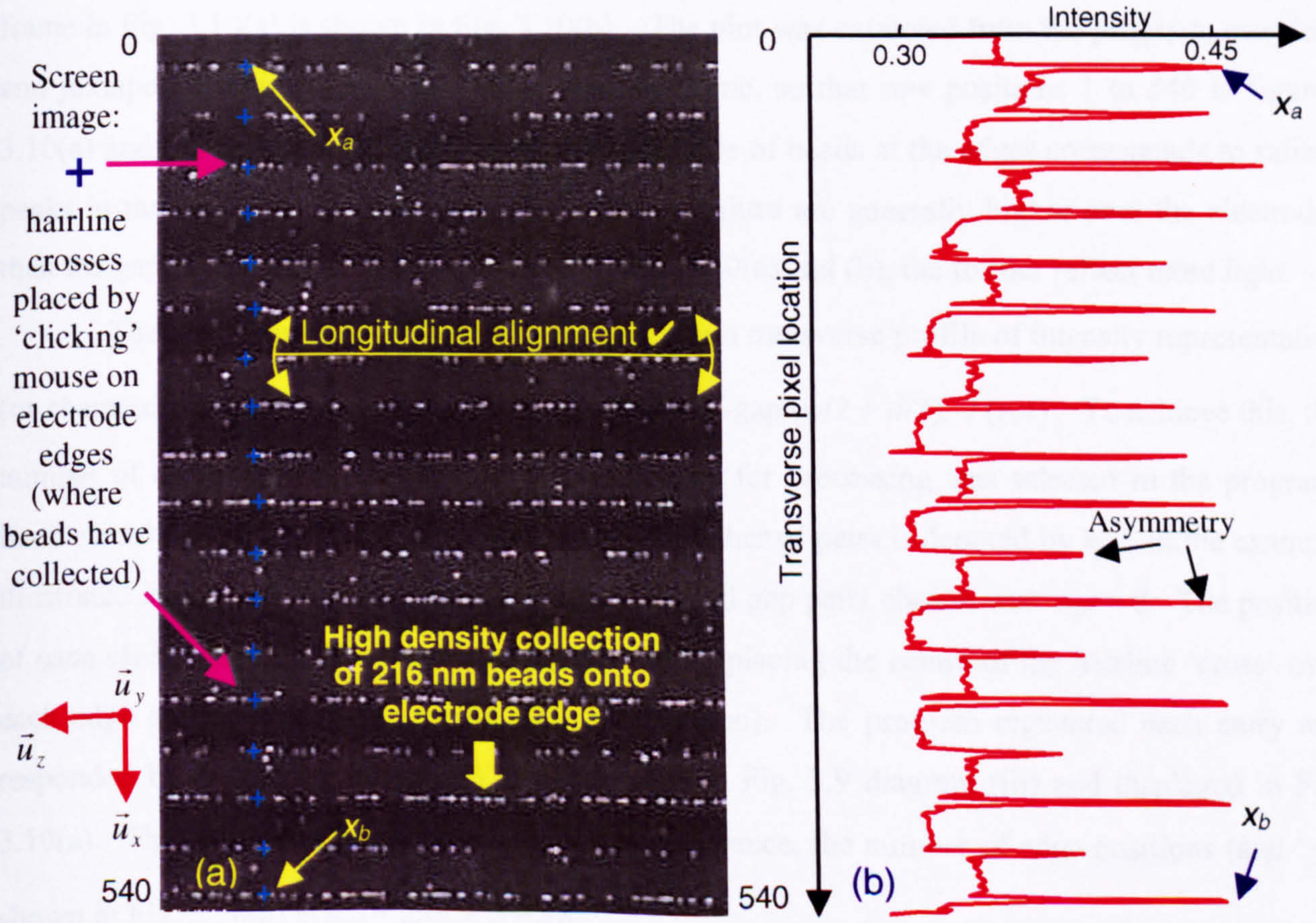

Fig. 3.10 (a) Positive DEP collection image processed frame (37 seconds after DEP force applied) with (b) associated average longitudinal greyscale intensity for each transverse pixel.

$$\bar{I}(x,t) = \int_{z_1}^{z_2} I(x,z,t)\,dz \Big/ \int_{z_1}^{z_2} dz = \frac{1}{z_2 - z_1} \int_{z_1}^{z_2} I(x,z,t)\,dz \qquad (3.5.1a)$$

where $z_2 - z_1$ is the maximum image displacement in the longitudinal $\vec{u}_z$ direction and the over-bar denotes the spatial average. A discrete form of (3.5.1a) is,

$$\bar{I}(r,t) \cong \frac{\Delta z \sum_{c=1}^{c_{max}} I(r,c,t)}{\Delta z \sum_{c=1}^{c_{max}} 1} = \frac{1}{c_{max}} \sum_{c=1}^{c_{max}} I(r,c,t) \qquad (3.5.1b)$$

where r and c are respective pixel values for each row r and column c and $c_{max} = 720$ is the total number of column pixels. Note that the time values are also discrete since the video frames can be considered to be samples of a continuous process. However, for convenience, the t notation is not changed for the current description. The integration (3.5.1b) was implemented in the *depint* sub-program *tralong1*. Physically, the use of a ×20 microscope objective and ×2.5 magnification for the CCD camera means for 720 pixels, the size of the electrode array image is $z_2 - z_1 \cong 251$ μm.

A plot of the average intensity $\bar{I}(r,t_i)$ in the longitudinal $\vec{u}_z$ direction, for the grayscale frame in Fig. 3.10(a) is shown in Fig. 3.10(b). The plot was extracted from the program, rescaled, and juxtaposed with cropped grayscale intensity frame, so that row positions 1 to 540 in figures 3.10(a) and (b) coincide. The plot shows the presence of beads at the edges corresponds to salient peaks in the intensity. It also shows the intensity values are generally higher over the electrodes than the gaps since, as previously observed in Fig. 3.10(a) and (b), the former reflect more light.

The next steps were to construct from $\bar{I}(r,t)$ a transverse profile of intensity representative (or characteristic) for an electrode half-width and half-gap ($w/2 + d/2$), $\tilde{I}(r,t)$. To achieve this, the number of electrodes and neighbouring gaps chosen for processing was selected in the program. Each electrode and gap is called a 'pair', and the number of pairs is denoted by n_{pr}. In the example illustrated in Fig. 3.10(a), the number of electrode and gap pairs chosen was $n_{pr} = 8$. The position of each electrode edge was consecutively entered by placing the centre of the hairline 'cross' over each edge and activating the mouse (left hand button). The program registered each entry and responded by displaying a cross '+' as illustrated in Fig. 3.9 diagram (iii) and displayed in Fig. 3.10(a). The number of edges is $n_{ed} = 2n_{pr} + 2$. Hence, the number of edge positions (and '+') shown in Fig. 3.10(a) is $n_{ed} = 2\times8 + 2 = 18$.

The program provided an option for renewing the entered values of edges if the displayed crosses '+' did not line up with the electrode edges. Only the ordinate in the transverse direction

was needed and the longitudinal ordinate was essentially redundant. The transverse position of the first and last '+' electrode edge markers, at x_a and x_b, is shown in both figures 3.10(a) and 3.10(b).

The precise transverse position of each marker '+' was limited to positive integer plus half-integer values: $x_+ = (m + ½)$, $m \in J^+$, as specified for pixel inputs in MATLAB 5.0™. For example, in Fig. 3.10(a) the entries for the electrode edges input from the mouse were $x_+ = 20.5, 50.5, 81.5, 110.5, 141.5, \ldots, 502.5, 530.5$. The difference between these values varied slightly about 30 pixel units: 30, 31, 29, 31, ..., 28 and so forth. Since the electrode dimensions are known to remain constant $w = d = 10$ μm this means there was a small quantization error in the values assigned for the edges in addition to possible misjudgements by the operator. The combined error is called an *entry error*. Although the error is itself is not significant, it made construction of a $w/2 + d/2$ characteristic intensity difficult.

The pixel count problem was circumvented by interpolating $I(r, t)$ and re-sampling such that each electrode width and gap between x_a and x_b received the same number of samples. Since the width and gap of the interdigitated electrodes was the same, the number of samples for each $w/2 = d/2$ was given by $n_{1/2}$. The number of sample points for each *characteristic* ($w/2 + d/2$) was therefore $n_c = 2n_{1/2}$ where n_c is a positive even number. Fig. 3.10(c) illustrates the re-sampled interpolated profile of Fig. 10(b) between x_a and x_b where $n_{1/2} = 50 \Rightarrow n_c = 100$. These values are high, and smaller values, for example, $n_{1/2} = 30$ are sufficient.

The process is expressed by the following two algorithms and mapping coupled together using i and j as vector indices, $i = \{1,2,\ldots,n_c\}$, $k = \{1,2,\ldots,n_{ed} - 1\}$

$$j = n_c(k-1) + i \tag{3.5.2a}$$

$$x_s(j) = x_+(k) + i[x_+(k+1) - x_+(k)]/n_c \quad \forall \quad j = \{1,2,\ldots, n_c(n_{ed} - 1)\} \tag{3.5.2b}$$

$$\underbrace{\bar{I}(r,t)}_{\textit{Intensity}} \rightarrow \underbrace{\bar{I}(x,t)}_{\textit{Interpolate}} \rightarrow \underbrace{\bar{I}(x_s,t)}_{\textit{Resample}} \rightarrow \underbrace{\bar{I}(j,t)}_{\substack{\textit{Reconstructed} \\ \textit{Intensity}}} \tag{3.5.2c}$$

Essentially, $x_s(j)$ assigns (or 'points to') transverse locations where the interpolated intensity $I(x,t)$ is re-sampled, thus reconstructing the intensity profile $\bar{I}(j,t)$. In the example shown in Fig. 3.10(c), $j = \{1,2, \ldots, 1700\}$.

Since the prime goal for constructing a $w/2 + d/2$ characteristic intensity was to evaluate the fluorescence over the electrode edges, the profile between x_a and x_b was segmented into two types. The transverse j values were segmented, as shown by the alternatively shaded oblongs on the left side of Fig. 3.10(c). The first segment labelled red /// are transverse values lying within the

transition from electrode half-width → half-gap (moving down the figure from x_a to x_b), and the second segment labelled green \\\ are values lying within the transition from half-gap → electrode half-width.

Algebraically, the j index was segmented by implementing the relations,

$$j_{red} = i + n_{1/2} + 2n_c(k-1)\ ,\ i = \{1,2,...,n_c\}\ ,\ \forall\ k = \{1,2,...,n_{pr}\} \tag{3.5.3a}$$

$$j_{green} = j_{red} + n_c \tag{3.5.3b}$$

where subscripts 'red' and 'green' correspond to the colour code in Fig. 3.10(c). The $n_{1/2}$ end segments were not included (as shown).

The intensities along each of the two segment types were summed and divided by the number of electrode and gap pairs n_{pr},

$$\underbrace{\tilde{I}(i,t)}_{\tilde{I}_{red}} = \frac{1}{n_{pr}} \sum_{k=1}^{n_{pr}} \underbrace{\bar{I}(i + n_{1/2} + 2n_c(k-1), t)}_{I_{red\ segments}}\ \forall\ i = \{1,2,...,n_c\} \tag{3.5.4a}$$

$$\underbrace{\tilde{I}(i+n_c,t)}_{\tilde{I}_{green}} = \frac{1}{n_{pr}} \sum_{k=1}^{n_{pr}} \underbrace{\bar{I}(i + n_{1/2} + 2n_c(k-1) + n_c, t)}_{I_{green\ segments}}\ \forall\ i = \{1,2,...,n_c\} \tag{3.5.4b}$$

This formed a 'periodic' *average* profile spanning the interval $w/2 + d + w/2$ (one electrode width and gap) and is denoted by the *tilda* symbol (~). The example of averaging Fig. 3.10(c) is exhibited in Fig. 3.10(d). The transverse positions are shown in terms of the discrete physical displacement $\{x_i : 0 \le x_i \le w + d\}$ as well as the i index $i = \{1,2,...,2n_c\}$, $n_c = 100$.

An interesting feature of figures 3.10(b) and (c) is the variation in the peak intensities that are approximately proportional to the number of beads accumulated at each of the electrode edges. In particular, some of the intensities at the edges showed a marked asymmetry as depicted in Fig. 3.10(b). The asymmetry is clear in Fig. 3.10(d). This is not expected from theory that predicts the DEP force, and hence particle collection (for positive DEP), on both sides of any electrode edge should be the same. That is they should be symmetrical, or exhibit even symmetry about $i = n_c = 100$ axis.

Fluctuations similar to these have been reported by other workers (Asbury and van den Engh, 1998). In order to achieve the prime goal of characterising particle accumulation at *one* edge, the asymmetry was not analysed (though it could be interesting and worthwhile to do so).

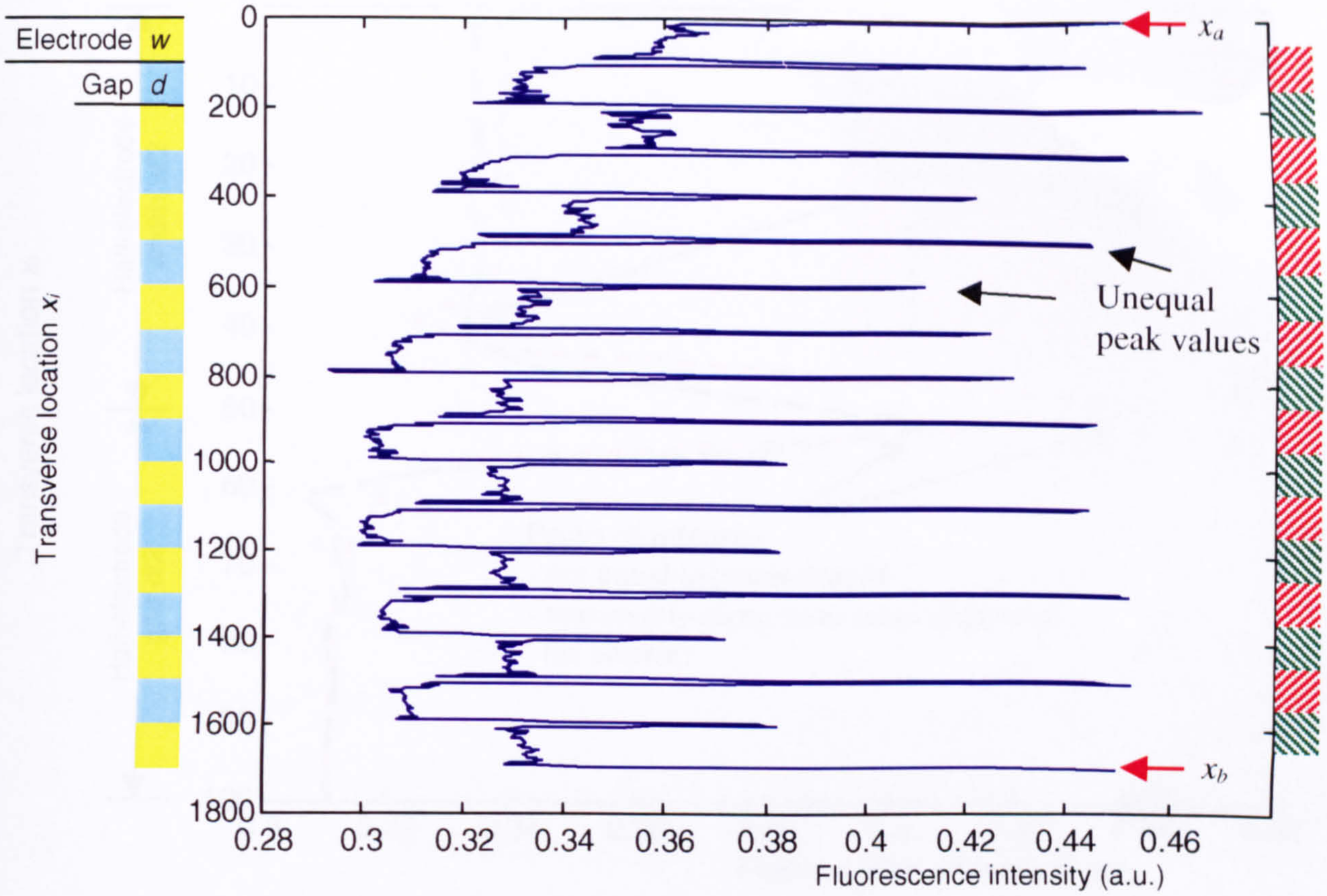

Fig. 3.10(c) Interpolated fluorescence intensity $\bar{I}(x,t)$ re-sampled at 100 points for $w = d = 10$ μm. The position of electrode and gaps are as shown on the left. The transverse displacement between x_a and x_b was divided into two segment categories (shown on the right) labelled red //// and green \\\\.

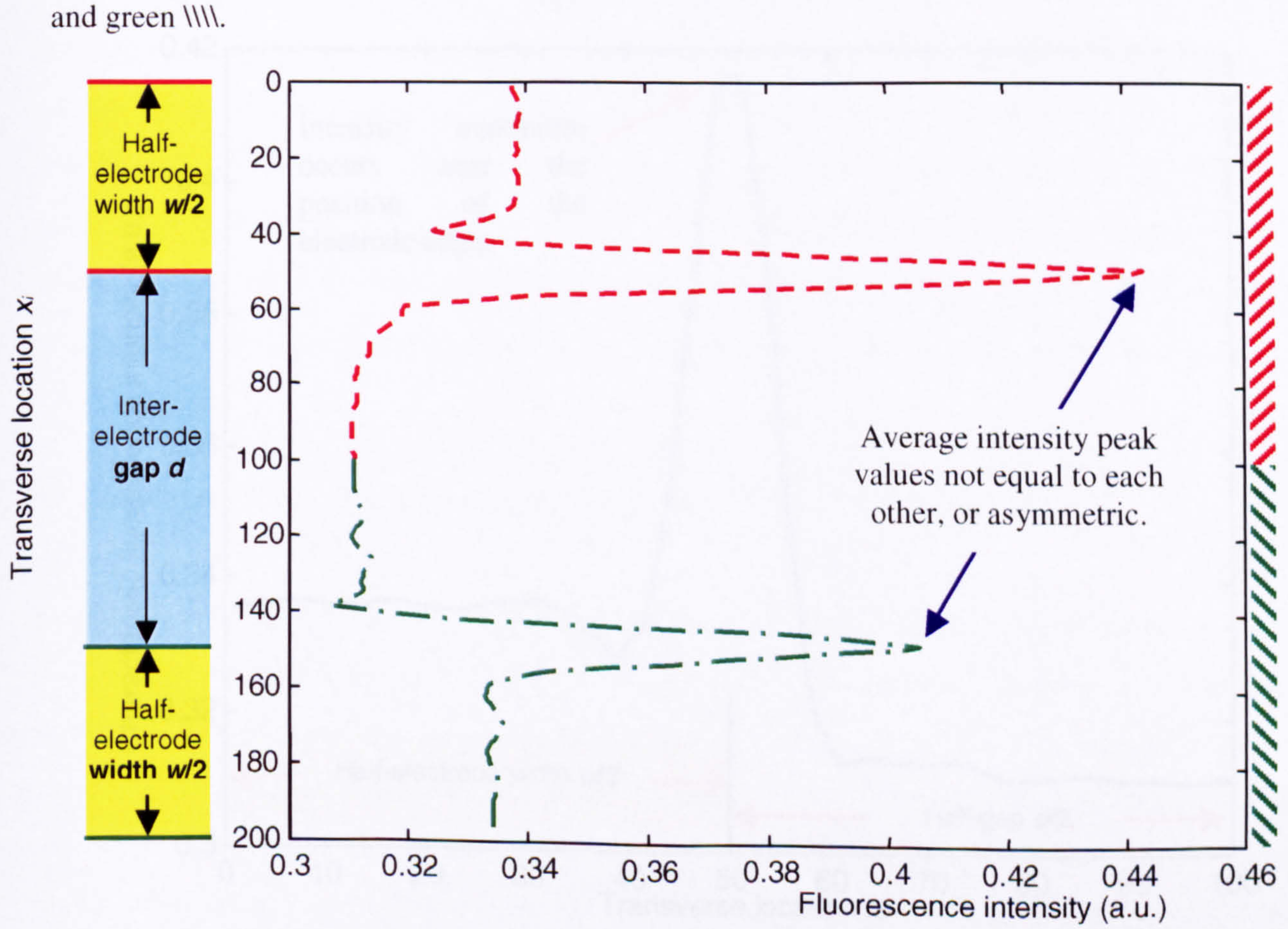

Fig. 3.10(d) Average of the fluorescence intensity $\tilde{I}(x,t)$ along each of the two segment types in Fig. 3.10(c) above: red ///// - - - - and green \\\\\ - · - · - .

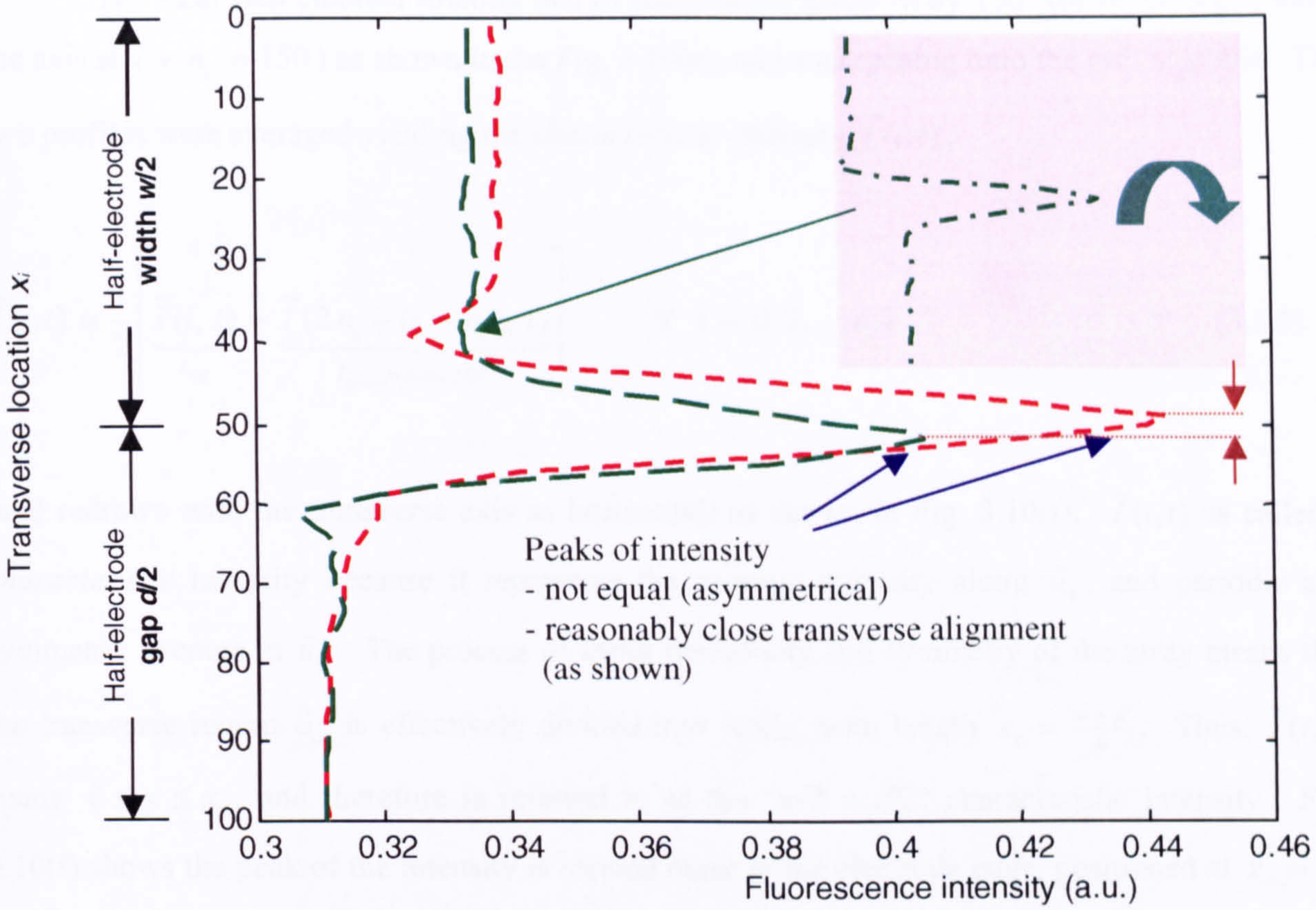

Fig. 3.10(e) Superposition of two segment fluorescence intensity profiles: green intensity profile (- · - · -) of Fig. 3.10(d) (insert top right) rotated 180° and superimposed with red profile (- - - -).

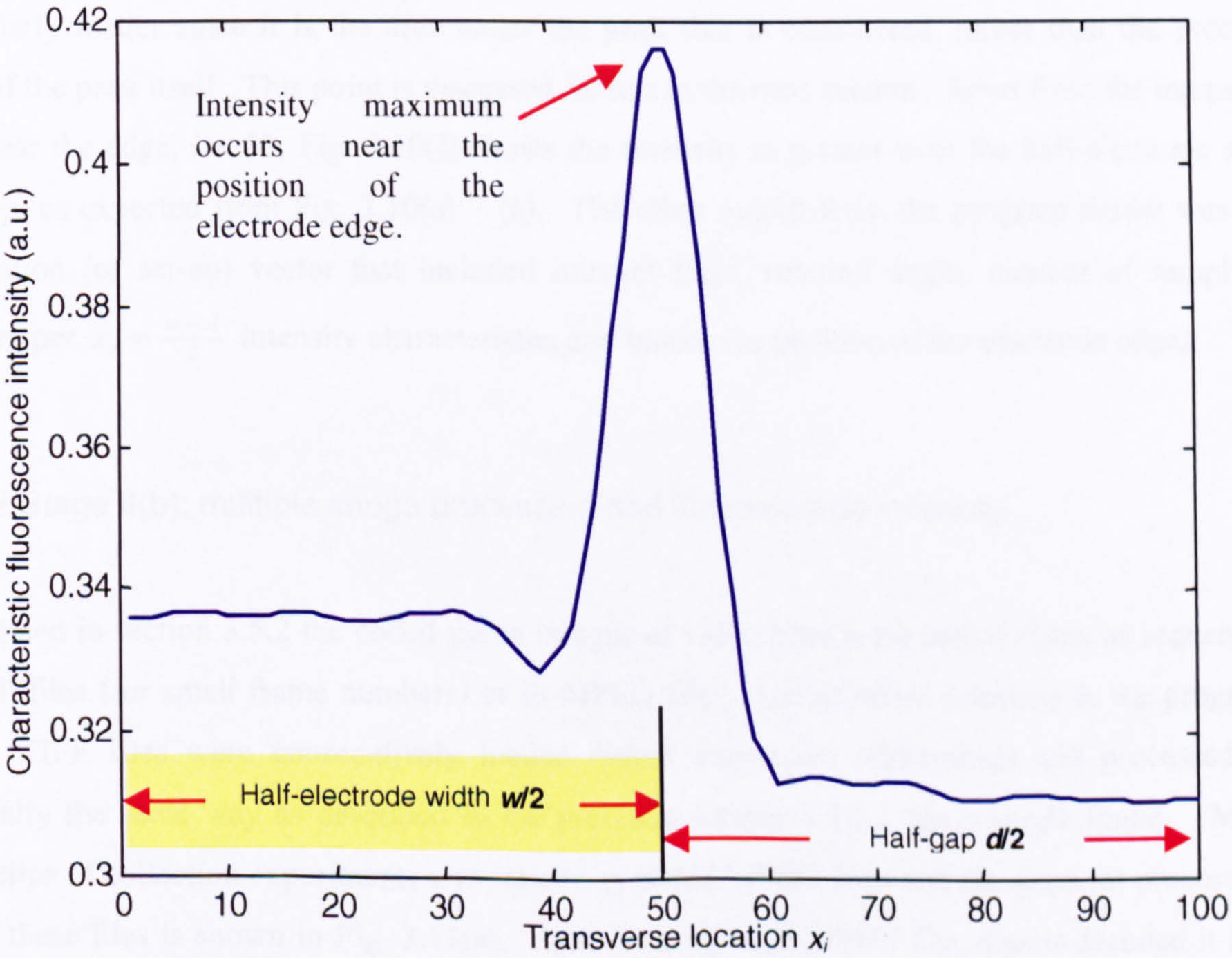

Fig. 3.10(f) Average of the two-segment fluorescence intensity profiles from Fig. 3.10(e) above forms the *characteristic* intensity $\tilde{I}(x,t)$ spanning a half-electrode width and half gap.

The final step entailed rotating one of the profiles green \\\ by 180° (or reflecting it about the axis at $i + n_c = 150$) as shown in the Fig. 3.10(e), and superposing onto the red /// profile. The two profiles were averaged yielding the *characteristic* intensity $\tilde{I}(i,t)$,

$$\tilde{I}(i,t) = \frac{1}{2}\left[\underbrace{\tilde{I}(i,t)}_{I_{red}} + \underbrace{\tilde{I}(2n_c - (i+n_c), t)}_{I_{green}\,rotated\,180^o}\right] \qquad \forall \;\; i = \{1,2,...,n_c\} \tag{3.5.5}$$

(and redrawn with the transverse axis as horizontal) as shown in Fig. 3.10(f). $\tilde{I}(i,t)$ is called a *characteristic* intensity because it represents the average intensity along $\vec{u}_z$, and periodic and symmetric average in $\vec{u}_x$. The process of using periodicity and symmetry of the array means that the transverse region $\vec{u}_x$ is effectively divided into 'cells' with length $x_c = \frac{w+d}{2}$. Thus, $\tilde{I}(i,t)$ spans $0 \le x \le x_c$, and therefore is referred to as the '$w/2 + d/2$' characteristic intensity. Fig. 3.10(f) shows the peak of the intensity is located close to the electrode edge, positioned at $x_e = \frac{w}{2}$. Effectively, x_e represents the edges of the array x_+ as described above.

It should be noted that the peaks of the (transverse) profiles in Fig. 3.10(e) do not coincide as they should in an ideal DEP collection image processing case. However, this does not particularly matter since it is the area under the peak that is considered, rather than the precise value of the peak itself. This point is discussed further in the next section. Apart from the intensity peak near the edge, $i = 50$, Fig. 3.10(f) shows the intensity is greater over the half-electrode and half-gap, as expected from Fig. 3.10(a) – (e). The other output from the program *depint* was an information (or set-up) vector that included internal flags, rotation angle, number of sampling points n_c per $x_c = \frac{w+d}{2}$ intensity characteristic, and transverse position of the electrode edges.

3.5.2.2 Stage II(b): multiple image processing and fluorescence intensity

As outlined in section 3.5.2 the coded frame images of video clips were coded either as sequences of TIFF files (for small frame numbers) or in MPEG files. Using menu selection in the program *depint*, TIFF files were consecutively loaded (using automated addressing) and processed in essentially the same way as described in the previous section 3.5.2.1 for a single frame. Most video clips of collection experiments were stored as coded MPEG files and the steps for processing one of these files is shown in Fig. 3.11(a). After loading each MPEG file, *depint* decoded it into

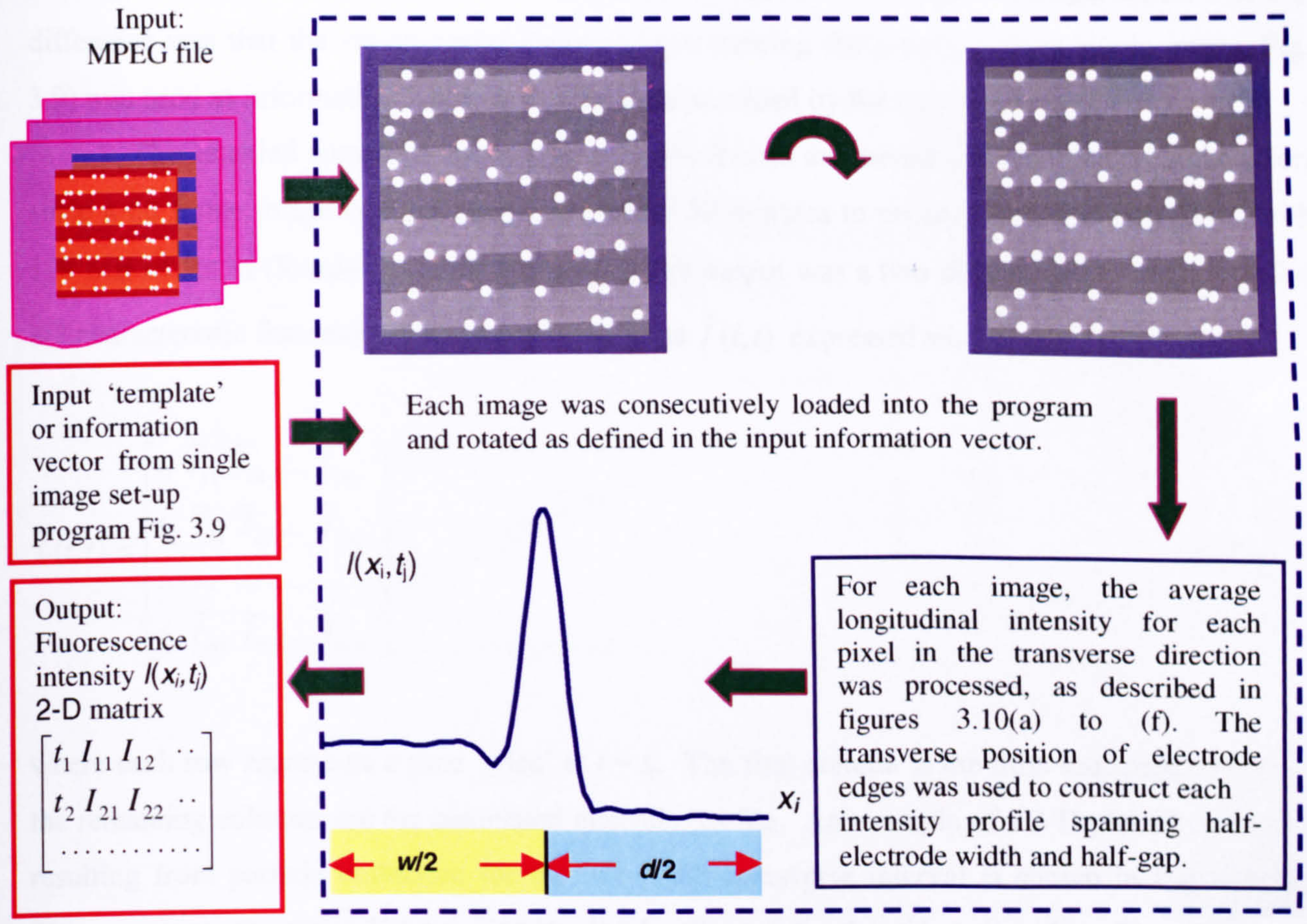

(a)

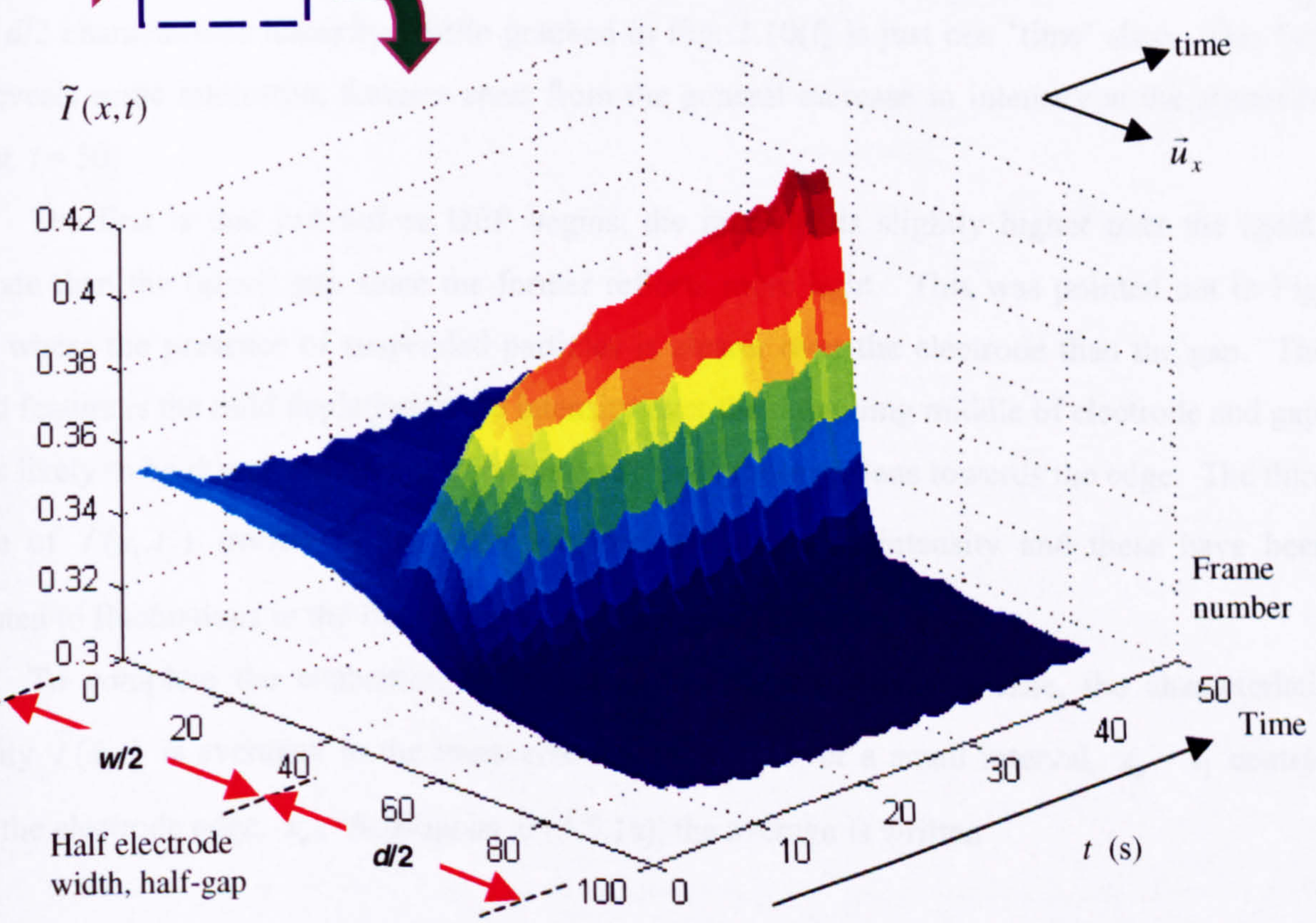

(b)

Fig. 3.11 Imaging DEP collection on interdigitated electrodes (a) automated image processing of an MPEG file, (b) 3-D plot of fluorescence characteristic intensity versus time (s) (or frame number).

individual frames and each of these was processed as described above for a single frame. The key difference was that the set-up vector (created from training the program for a single image, Fig. 3.9) was used as information input rather than data provided by the user/viewer.

This enabled automatic processing of video frames and saved considerable time and effort since a 60 frame image could take approximately 30 minutes to process on a Pentium II PC with 128 MB of RAM (Random Access Memory). The output was a two dimensional matrix of $w/2 + d/2$ characteristic fluorescent intensities verses time $\tilde{I}(i,t)$ expressed as,

$$\tilde{I}(i,t) = \begin{bmatrix} t_1 & \tilde{I}_{11} & \tilde{I}_{12} & \cdots & \tilde{I}_{1n_c} \\ t_2 & \tilde{I}_{21} & \tilde{I}_{22} & \cdots & \tilde{I}_{2n_c} \\ \cdots & \cdots & \cdots & \cdots & \cdots \\ t_m & \tilde{I}_{m1} & \tilde{I}_{m2} & \cdots & \tilde{I}_{mn_c} \end{bmatrix} \tag{3.5.6}$$

where each row represents a time 'slice' at $t = t_j$. The first column is the time sequence (secs) and the remaining columns are the associated intensity profile. An example of a 3-D plot of the matrix resulting from particle collection for the $w/2 + d/2$ transverse interval is shown in Fig. 3.11(b). This represents the entire 216 nm diameter bead collection for the video clip where Figs. 3.7(a) and (b), and Fig. 3.10(c) were separate half-length frame images. In the context of Fig. 3.11(b), the $w/2 + d/2$ characteristic intensity profile graphed in Fig. 3.10(f) is just one 'time' slice. The 3-D plot reveals some interesting features apart from the general increase in intensity at the electrode edge at $i = 50$.

The first is that just before DEP begins, the intensity is slightly higher over the (gold) electrode than the (glass) gap since the former reflects more light. This was pointed out in Fig. 3.7(a) where the presence of suspended particles is clearer over the electrode than the gap. The second feature is the mild depletion in the intensity over the remaining middle of electrode and gap. This is likely to be due to movement of beads away from these regions towards the edge. The third feature of $\tilde{I}(x_i,t_j)$ profile is the small temporal variations in intensity and these have been attributed to fluctuations in the fluorescence microscope light source.

To complete the evaluation of the time dependent intensity profile, the characteristic intensity $\tilde{I}(x,t)$ is averaged in the transverse direction $\vec{u}_x$ over a small interval, $x_u - x_l$ centred about the electrode edge, x_e. Analogous to (3.5.1a), the average is written

$$\bar{\tilde{I}}_E(t) = \int_{x_l}^{x_u} \tilde{I}(x,t)\,dx \Big/ \int_{x_l}^{x_u} dx = \frac{1}{x_u - x_l} \int_{x_l}^{x_u} \tilde{I}(x,t)\,dx \tag{3.5.7a}$$

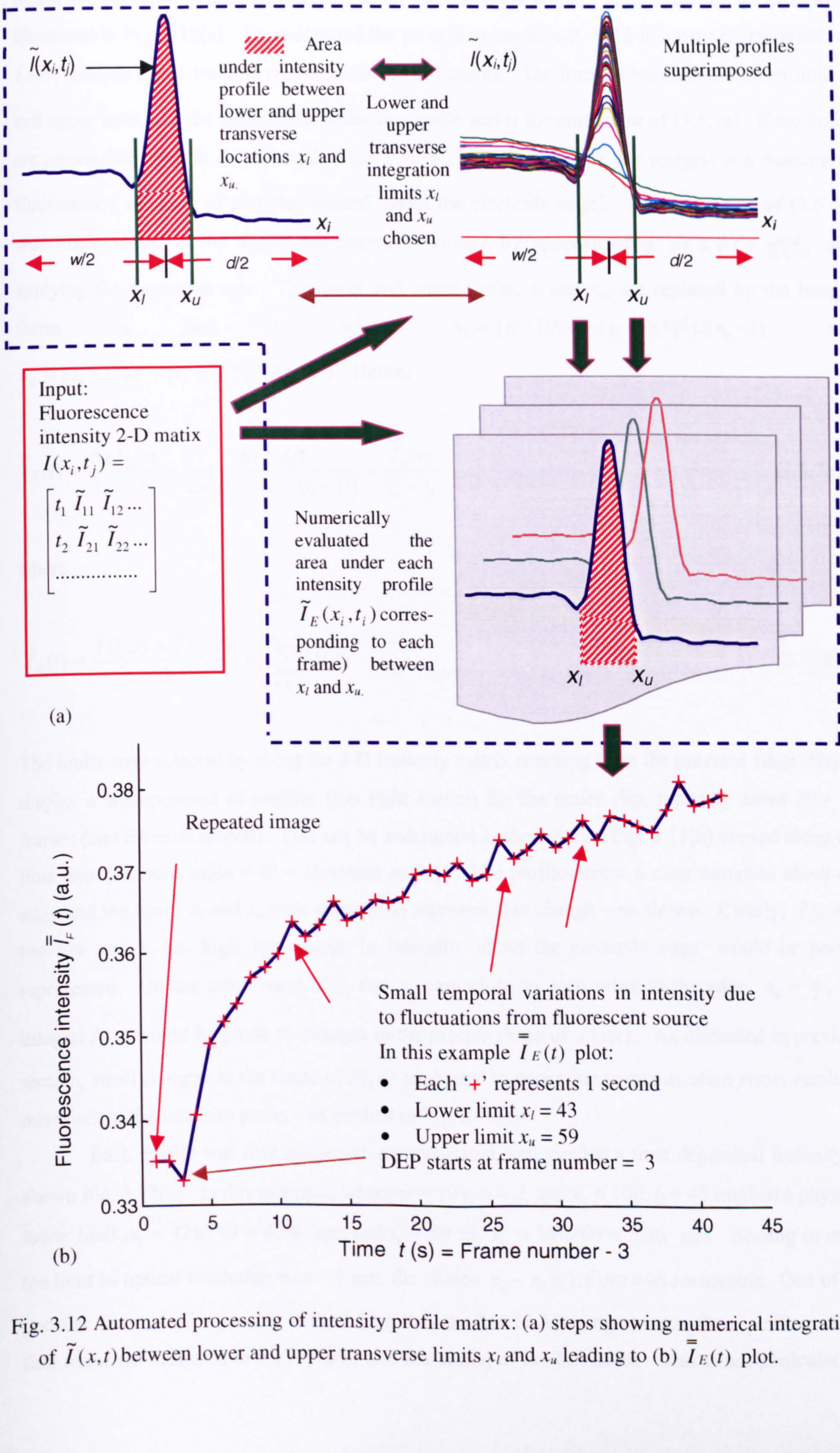

Fig. 3.12 Automated processing of intensity profile matrix: (a) steps showing numerical integration of $\tilde{I}(x,t)$ between lower and upper transverse limits x_l and x_u leading to (b) $\bar{\bar{I}}_E(t)$ plot.

where the subscript E denotes interval 'about the electrode edge'. The evaluation of (3.5.7a) is illustrated in Fig. 3.12(a). To understand the process, a single $w/2 + d/2$ intensity characteristic at $t = t_j$ such as Fig. 3.10(f), is shown in the top left corner. The integral between the lower limit x_l and upper limit x_u is the shaded area under the profile and is the numerator of (3.5.7a). If the limits are reasonably close to the electrode edge $x_e = \frac{w}{2}$, but not too close, the integral is a measure of fluorescence intensity of particles located 'about the electrode edge'. The integration of (3.5.7a) was implemented in the *depint* sub-program *tralong1* by approximating $dx \cong \Delta x = \frac{w+d}{2(n_c-1)}$ and applying the trapezium rule. The lower and upper limits, x_l and x_u, are replaced by the integer forms i_l and i_u where $x_l = (i_l - 1)\Delta x = (i_l - 1)(\frac{w+d}{2})/(n_c - 1)$ and $x_u = (i_u - 1)\Delta x = (i_u - 1)(\frac{w+d}{2})/(n_c - 1)$. Hence,

$$\bar{\bar{I}}_E(t) = \frac{\Delta x \hat{I}_E(t)}{x_u - x_l} = \frac{\Delta x \hat{I}_E(t)}{\Delta x[(i_u - 1) - (i_l - 1)]} = \frac{\hat{I}_E(t)}{i_u - i_l} \qquad (3.5.7b)$$

where

$$\hat{I}_E(t) = \frac{\tilde{I}(i_l,t) + \tilde{I}(i_u,t)}{2} + \sum_{i=i_l+1}^{i_u-1} \tilde{I}(i,t) \qquad (3.5.7c).$$

The limits were selected by using the 2-D intensity matrix resulting from the previous stage II(a) to display a superposition of profiles (top right corner) for the entire clip, typically about 30 - 50 frames (one for each second). This can be understood as the 3-D plot Fig. 3.11(b) viewed along the time axis (azimuth angle = 0° = elevation angle). The profiles show a clear variation about the edge and the limits x_l and x_u were selected to represent this change – as shown. Clearly, if x_l was too low and x_u too high, the change in intensity 'about the electrode edge' would be poorly represented. On the other hand, if x_l and x_u were close to each other at the edge, $x_e = \frac{w}{2}$, the integral $I_E(t_i)$ would be prone to changes in the precise shape of $\tilde{I}(x,t)$. As discussed in previous section, small changes in the shape of $I(i, t_j)$ are bound to occur due to quantization errors resulting mismatch of the intensity peaks – as evident in Fig. 3.10(e).

Each profile was then consecutively integrated, and yielded a time dependent intensity as shown Fig. 3.12(b). In this example, where $w = 10\ \mu m = d$, and $n_c = 100$, $i_l = 43$ implied a physical lower limit $x_l = 420/99 = 4.24\ \mu m$ and $i_u = 59 \Rightarrow x_u = 580/99 = 5.86\ \mu m$. Bearing in mind the limit of optical resolution was ~ 1 μm, the choice $x_u - x_l \cong 1.6\ \mu m$ was reasonable. One of the peculiar features of importing MPEG files into the MATLAB program was the repetition of the first frame (as indicated in Fig. 3.12(b) and discarding of the last frame. This is not particularly a

problem provided one is aware of the feature and is thought to arise during MPEG decoding. As noted in Fig. 3.11(b), the other interesting feature about the $I_E(t)$ profile was the small-time variations and these have been attributed to fluctuations in the fluorescent light source that is not uncommon with mercury lamps (Ploem and Tanke, 1987, p.39). A means of smoothing these fluctuations and checking for long term variations in intensity was to average the intensity $\tilde{I}(i,t)$ over the entire $w/2 + d/2$ transverse interval. This yields the *total* intensity, $\bar{\bar{I}}_T(i,t)$ and is found by applying $i_l = 1$ and $i_u = n_c$ into (3.5.7b) and (3.5.7c),

$$\bar{\bar{I}}_T(t) = \frac{\hat{I}_T(t)}{n_c - 1}, \quad \hat{I}_T(t) = \frac{\tilde{I}(1,t) + \tilde{I}(n_c,t)}{2} + \sum_{i=2}^{n_c-1} \tilde{I}(i,t) \tag{3.5.8}$$

Using the same matrix data as Fig. 3.12(b), $\bar{\bar{I}}_T(t)$ is shown in Fig. 3.13(a). The fluctuations coincide with those in Fig. 3.12(b) and the general trend of the intensity is roughly constant as one would expect.

3.5.2.3 Post-processing: normalised fluorescence intensity

Thus, by dividing (3.5.7b) by (3.5.8) the total intensity can be used to smooth $\bar{\bar{I}}_E(t)$ and is called the normalised intensity,

$$I_N(t) = \frac{\bar{\bar{I}}_E(t)}{\bar{\bar{I}}_T(t)} \tag{3.5.9}$$

One issue about this definition is that since $\bar{\bar{I}}_T(t)$ includes $\bar{\bar{I}}_E(t)$ then normalisation tends to 'flatten' the rise profile of the DEP collection. In fact, in the extreme case where $i_l \to 1$ and $i_u \to n_c$ are used in $\bar{\bar{I}}_E(t)$ then $I_N(t) \to 1$. Conversely when the $i_u - i_l << n_c - 1$ then (3.5.9) is satisfactory. However, the *depint* program and resultant profiles are then more sensitive to misalignment (or *entry* errors) described in the previous section.

An alternative definition is found by *excluding* $\bar{\bar{I}}_E(t)$ from $\bar{\bar{I}}_T(t)$. This is the definition used particularly for colloidal particles, such as the above example, where $i_l = 43$ and $i_u = 59$. In this case, the normalised fluorescence intensity $F(t)$ is

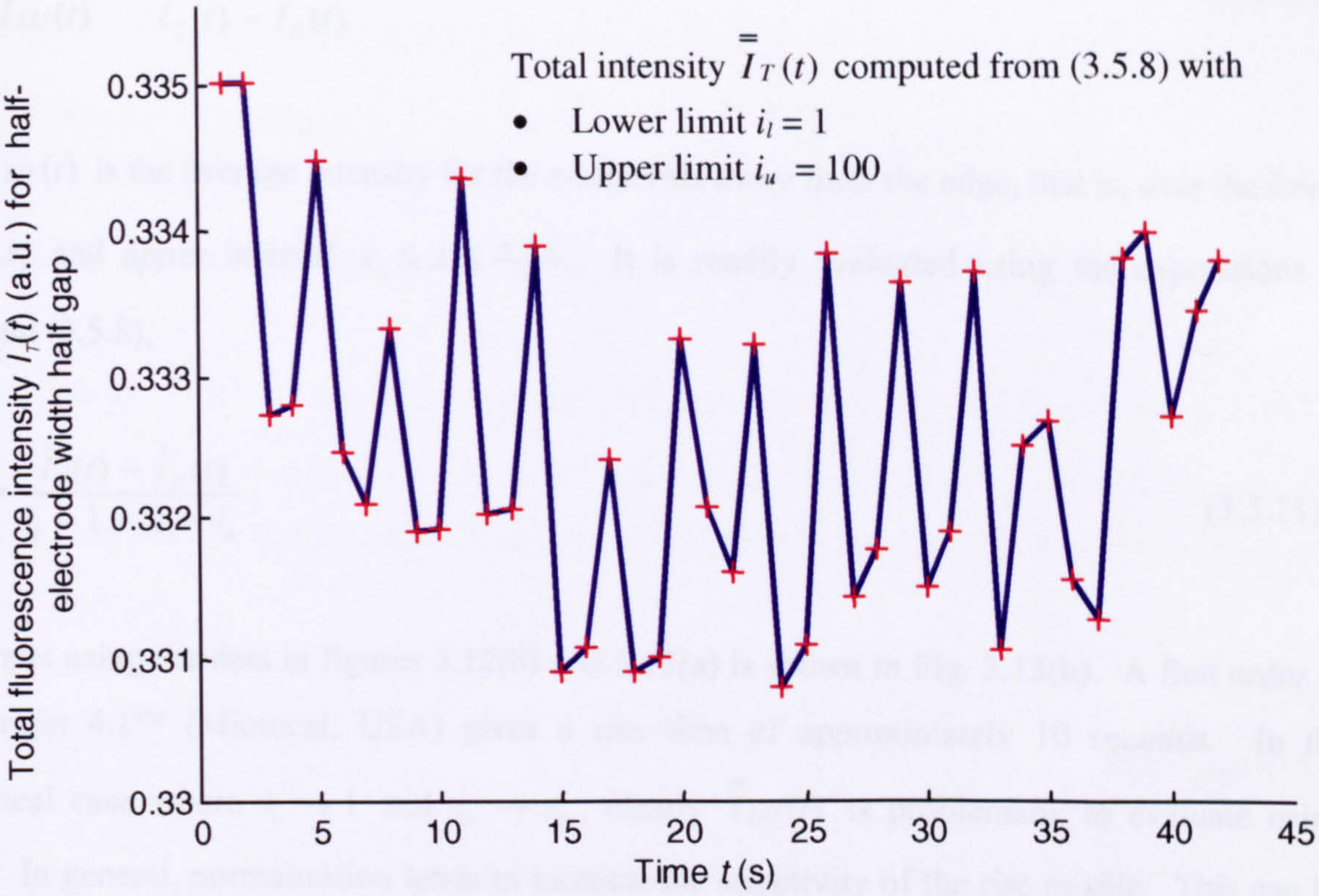

Fig. 3.13(a) Small-scale temporal fluctuations in total spatially averged fluorescence intensity $\bar{\bar{I}}_T(t)$ evaluated using the charactersitc intensity, $\tilde{I}(x,t)$ illustrated in Fig. 3.11.

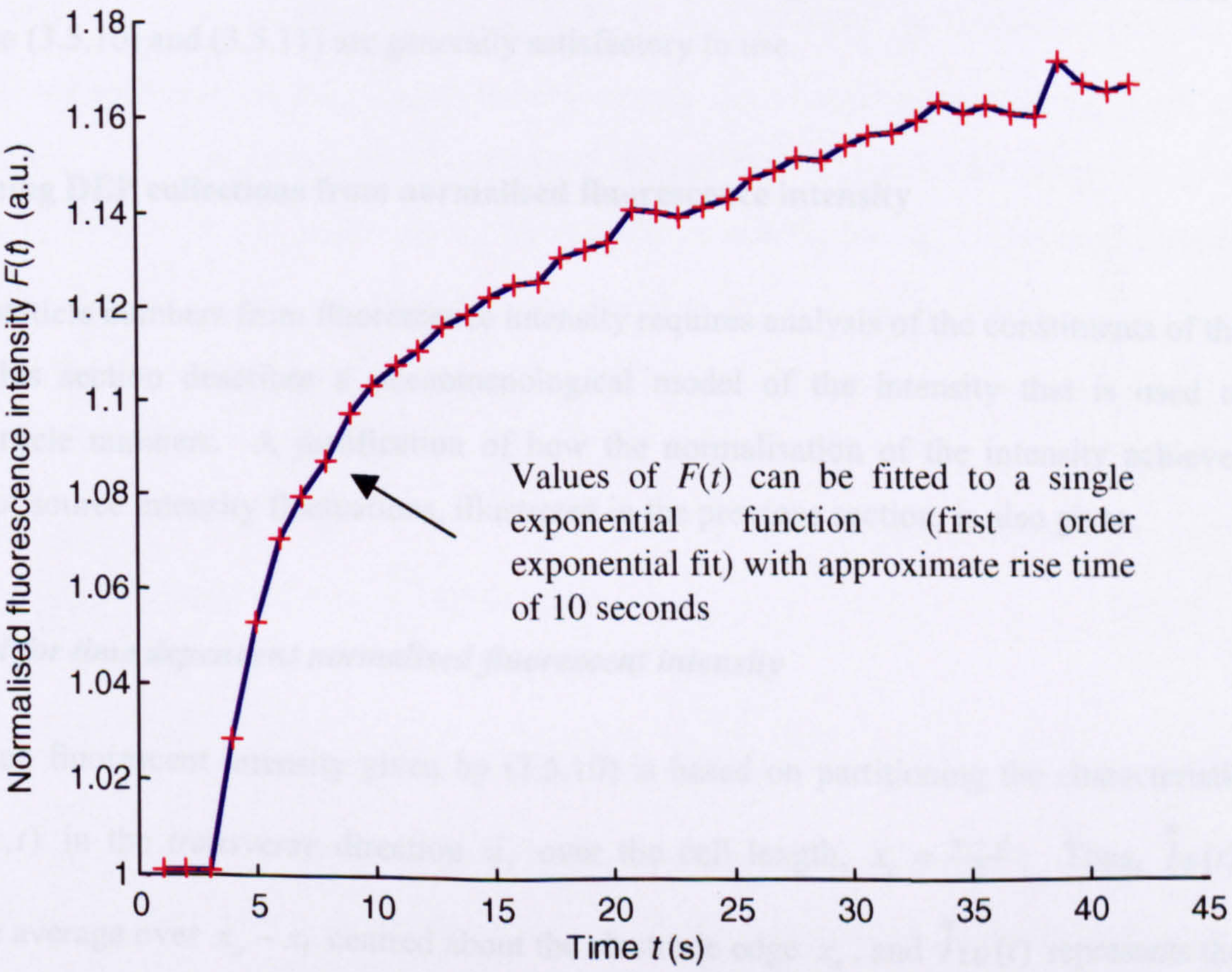

Fig. 3.13(b) Plot of the normalized fluorescence intensity $F(t)$ representing the time-profile of a typical DEP collection (evaluated using 3.5.10).

$$F(t) = \frac{\bar{\bar{I}}_E(t)}{\bar{\bar{I}}_{LU}(t)} = \frac{\bar{\bar{I}}_E(t)}{\tilde{\bar{I}}_T(t) - \tilde{\bar{I}}_E(t)} \tag{3.5.10}$$

where $\bar{\bar{I}}_{LU}(t)$ is the average intensity for the x-intervals *away* from the edge, that is, over the *lower* $0 \le x \le x_l$ and *upper* interval $x_u \le x \le \frac{w+d}{2}$. It is readily evaluated using the expressions in (3.5.7) and (3.5.8),

$$\bar{\bar{I}}_{LU}(t) = \frac{\hat{I}_T(t) - \hat{I}_E(t)}{i_l - 1 + n_c - i_u} \tag{3.5.11}$$

An example using the data in figures 3.12(b) and 3.13(a) is shown in Fig. 3.13(b). A first order fit using Origin 4.1™ (Microcal, USA) gives a rise time of approximately 10 seconds. In the hypothetical case where $i_l \to 1$ and $i_u \to n_c$, clearly $\bar{\bar{I}}_{LU}(t)$ is problematic to evaluate using (3.5.11). In general, normalisation tends to increase the sensitivity of the rise profile. This can be seen in the extreme case where particle collection onto the electrode edge causes almost entire particle depletion elsewhere, so that $\bar{\bar{I}}_E(t) \neq 0$ and $\bar{\bar{I}}_{LU}(t) \to 0$ hence $F(t) \to \infty$. Clearly, in this situation (3.5.10) would be inappropriate to use. In practice, DEP experiments do not exhibit extreme particle depletion, except when the aqueous suspending medium has almost entirely evaporated, so (3.5.10) and (3.5.11) are generally satisfactory to use.

3.6 Determining DEP collections from normalised fluorescence intensity

To estimate particle numbers from fluorescence intensity requires analysis of the constituents of the intensity. This section describes a phenomenological model of the intensity that is used to determine particle numbers. A justification of how the normalisation of the intensity achieves 'smoothing' of source intensity fluctuations, illustrated in the previous section, is also given.

3.6.1 A model for time dependent normalised fluorescent intensity

The normalised fluorescent intensity given by (3.5.10) is based on partitioning the characteristic intensity $\tilde{I}(x,t)$ in the *transverse* direction $\vec{u}_x$ over the cell length, $x_c = \frac{w+d}{2}$. Thus, $\bar{\bar{I}}_E(t)$ represents the average over $x_u - x_l$ centred about the electrode edge x_e, and $\bar{\bar{I}}_{LU}(t)$ represents the average the *lower* and *upper* intervals, $0 \le x \le x_l$ and $x_u \le x \le x_c$.

In this section, the intensities $\bar{\bar{I}}_E(t)$ and $\bar{\bar{I}}_{LU}(t)$ are further partitioned (or decomposed) in the vertical direction $\vec{u}_y$. This enables changes in fluorescent intensity to characterise particle collections near the electrodes.

3.6.1.1 Fluorescence from transverse positions about an electrode edge

An expression for $\bar{\bar{I}}_E(t)$ is derived in Appendix E.1 that distinguishes between fluorescence from particles within a small displacement ΔL within the plane of focus (located close to the electrode plane), and fluorescence from particles above the focal plane in the bulk solution. The expression is given by (E.1.13),

$$\bar{\bar{I}}_E(t) = \underbrace{k_l \bar{\bar{c}}_E(t) I_s(t)}_{focal\ \Delta L} + \underbrace{\bar{\bar{B}}_E(t) I_s(t)}_{bulk} \tag{3.6.1}$$

where k_l is a fluorescence constant, $\bar{\bar{c}}_E(t)$ is the spatially averaged particle concentration about the electrode *edge*, $\bar{\bar{B}}_E(t)$ accounts for *background* fluorescence from particles in the bulk, and $I_s(t)$ is the source intensity. The double bar on both $\bar{\bar{c}}_E(t)$ and $\bar{\bar{B}}_E(t)$ indicates spatial averages in both directions $\vec{u}_x$ and $\vec{u}_z$. The constant $k_l = k_{op}\, k_{ra}\, \eta_q\, k_a\, k_{ea}\, \Delta L$ accounts for a number of optical processes detailed in Appendix E.1. These include optical microscope parameters k_{op} (such as, numerical aperture of the objective), re-absorption of emitted light k_{ra}, quantum efficiency η_q of the fluorophore, absorption and scattering k_a, and excitation absorbance k_{ea}. The concentration $\bar{\bar{c}}_E(t)$, averaged over $x_l \le x \le x_u$ in the transverse direction $\vec{u}_x$, is weighted by the constants r_{el} and r_{gp} that describe the reflectivity of the electrode and glass interface to the aqueous solvent. It is given by (E.1.11b),

$$\bar{\bar{c}}_E(t) = \frac{1}{x_u - x_l}\left(r_{el} \int_{x_l}^{x_e} \tilde{c}(x,t)\, dx + r_{gp} \int_{x_e}^{x_u} \tilde{c}(x,t)\, dx \right) \tag{3.6.2}$$

where the *characteristic* concentration $\tilde{c}(x,t)$ is a *periodic* average over n_{pr} electrode and gap pairs of $\bar{c}(x,t)$, $\tilde{c}(x,t) \leftarrow \bar{c}(x,t)$. This is analogous to $\tilde{I}(x,t)$ given by (3.5.2) to (3.5.5). $\bar{c}(x,t)$ is the spatial average of $c(x,z,t)$ over a displacement $z_2 - z_1$ in the longitudinal $\vec{u}_z$ direction as stated in (E.1.9b).

Similarly, as described in Appendix E.1, the background fluorescence is a 2-D spatial average of $B(x,z,t)$ in directions $\vec{u}_x$ and $\vec{u}_z$, and is written as (E.1.12b),

$$\overline{\overline{B}}_E(t) = \frac{1}{x_u - x_l}\left(r_{el} \int_{x_l}^{x_e} \tilde{B}(x,t)\, dx + r_{gp} \int_{x_e}^{x_u} \tilde{B}(x,t)\, dx \right) \tag{3.6.3}$$

where $\tilde{B}(x,t) \leftarrow \overline{B}(x,t)$ and $\overline{B}(x,t)$ is the spatial average of $B(x,z,t)$ over a displacement $z_2 - z_1$ in the longitudinal $\vec{u}_z$ direction as stated in (E.1.9c). The variable $B(x,z,t)$ includes the particle concentration in the bulk suspension above the focal plane and incorporates optical processes described by k_l.

3.6.1.2 Fluorescence from lower and upper transverse positions

An expression for the intensity $\overline{\overline{I}}_{LU}(t)$ is given by (E.2.3a) in Appendix E.2

$$\overline{\overline{I}}_{LU}(t) = \left(k_l \overline{\overline{c}}_{LU}(t) + \overline{\overline{B}}_{LU}(t) \right) I_s(t) \tag{3.6.4}$$

where from (E.2.3b) and (E.2.3c)

$$\overline{\overline{c}}_{LU}(t) = \frac{r_{el} \int_0^{x_l} \tilde{c}(x,t)\, dx + r_{gp} \int_{x_u}^{x_c} \tilde{c}(x,t)\, dx}{x_c - x_u + x_l} \tag{3.6.5}$$

and

$$\overline{\overline{B}}_{LU}(t) = \frac{r_{el} \int_0^{x_l} \tilde{B}(x,t)\, dx + r_{gp} \int_{x_u}^{x_c} \tilde{B}(x,t)\, dx}{x_c - x_u + x_l} \tag{3.6.6}$$

and all other symbols have been previously defined.

3.6.1.3 Reducing the effect of light source intensity fluctuations by normalisation

Clearly, $\overline{\overline{I}}_E(t)$ and $\overline{\overline{I}}_{LU}(t)$ are both dependent on the source intensity $I_s(t)$ that is prone to fluctuations. However, by taking ratio of $\overline{\overline{I}}_E(t)$ and $\overline{\overline{I}}_{LU}(t)$ which is the normalised intensity, $I_s(t)$ is eliminated. Substituting (3.6.1) and (3.6.4) into (3.5.10),

$$F(t) = \frac{\bar{\bar{I}}_E(t)}{\bar{\bar{I}}_{LU}(t)} = \frac{[k_l \bar{\bar{c}}_E(t) + \bar{\bar{B}}_E(t)]I_s(t)}{[k_l \bar{\bar{c}}_{LU}(t) + \bar{\bar{B}}_{LU}(t)]I_s(t)} = \frac{k_l \bar{\bar{c}}_E(t) + \bar{\bar{B}}_E(t)}{k_l \bar{\bar{c}}_{LU}(t) + \bar{\bar{B}}_{LU}(t)} \tag{3.6.7}$$

This gives a simple explanation for Fig. 3.13(b) being much smoother than Fig. 3.12(b).

3.6.2 Determining DEP collections from changes in normalised fluorescence

The background fluorescence can be eliminated by considering the difference in normalised fluorescence over a given time interval $t - t_0$.

3.6.2.1 General expression

Defining $\Delta F(t) = F(t) - F(t_0)$, equation (E.3.2) in Appendix E.3 shows,

$$\Delta F(t) = F(t) - F(t_0) = \frac{k_l}{\underbrace{k_l \bar{\bar{c}}_{LU}(t_0) + \bar{\bar{B}}_{LU}(t_0)}_{constant}}[(1+\delta_f)\bar{\bar{c}}_E(t) - \bar{\bar{c}}_E(t_0)] \tag{3.6.8}$$

where the fluorescence deviation, δ_f, accounts for small variations in background fluorescence, and is typically 10% or less, $0 \le \delta_f \le 0.1$. This means the difference in normalised fluorescence about the electrode edge is approximately proportional to the difference in particle concentration near the edge. Introducing $n_E(t)$ given by (E.3.4b) as the number of particles at an electrode edge of a representative cell weighted by the reflection constants,

$$n_E(t) = r_{el} \underbrace{\int_{x_l}^{x_e}\int_{z_1}^{z_2}\int_{a}^{a+\Delta L} c(x,y,z,t)\,dydzdx}_{particle\ number\ from\ x_l\ to\ edge} + r_{gp} \underbrace{\int_{x_e}^{x_u}\int_{z_1}^{z_2}\int_{a}^{a+\Delta L} c(x,y,z,t)\,dydzdx}_{particle\ number\ from\ edge\ to\ x_u} \tag{3.6.9}$$

Appendix E.3 shows (3.6.8) can be re-cast as (E.3.5),

$$\Delta F(t) = F(t) - F(t_0) = k[n_E(t) - n_E(t_0)] + \varepsilon_f(t) = k\Delta n_E(t) + \varepsilon_f(t) \tag{3.6.10}$$

where $k = \dfrac{k_{op}\, k_{ra}\, \eta_q\, k_a\, k_{ea}}{(x_u - x_l)(z_2 - z_1)[k_l \bar{\bar{c}}_{LU}(t_0) + \bar{\bar{B}}_{LU}(t_0)]}$ and the small error is $\varepsilon_f(t) = k\delta_f\, n_E(t)$.

This means measurements of normalised fluorescence change $\Delta F(t)$ tend to slightly *overestimate* changes in particle collections at the electrode edges. Applying the same argument as above to the difference in the *un-normalised* intensity changes $\bar{\bar{I}}_E(t) - \bar{\bar{I}}_E(t_0)$, indicates they slightly *underestimate* changes in particle collections. Since the error in most cases is small, (3.6.10) can be approximated,

$$\Delta n_e(t) = \frac{1}{k}[\Delta F - \varepsilon_f(t)] \cong \frac{\Delta F}{k} \tag{3.6.11}$$

where the 'E' subscript in $\Delta n_E(t)$ has been exchanged for lower case 'e' to indicate the particle number, $\Delta n_e(t)$, is determined by *experiment* via ΔF. This contrasts with change in particle number $\Delta n_p(t)$ that signifies it is *predicted* by computer simulation of the FPE model described in Chapter 6.

3.6.2.2 Initial particle collection rate from normalised fluorescence

The incremental change in fluorescence can be used to determine the initial rate of particle accumulation. Letting $t = t_0 + \Delta t$ in (3.6.11) and dividing both sides by Δt,

$$\frac{n_e(t_0 + \Delta t) - n_e(t_0)}{\Delta t} = \frac{1}{k}\frac{F(t_0 + \Delta t) - F(t_0)}{\Delta t} \tag{3.6.12}$$

Taking the *rhs* or *upper* limit $\Delta t \to 0^+$,

$$\left.\frac{dn_e}{dt}\right|_{t=t_0} = \lim_{\Delta t \to 0^+}\left\{\frac{n_e(t_0 + \Delta t) - n_e(t_0)}{\Delta t}\right\} = \frac{1}{k}\lim_{\Delta t \to 0^+}\left\{\frac{F(t_0 + \Delta t) - F(t_0)}{\Delta t}\right\} = \frac{1}{k}\left.\frac{dF}{dt}\right|_{t=t_0} \tag{3.6.13}$$

One should remark that since the DEP collection process starts at $t = t_0$, $F(t)$ is piecewise continuous at this point[4] (for example, Fig. 3.13(b) at $t = t_0 = 3$ s). This means the limit operations $\Delta t \to 0^+$ and $\Delta t \to 0^-$ may lead to different rates of change. Hence, the 'derivative' at this point is understood to be in the $+t$ direction about t_0. For convenience let $t_0 = 0$, (3.6.13) is concisely written

---

[4] In reality, $F(t)$ is a discrete time process since it is constructed from video sampled images.

$$\dot{n}_e(0) = \frac{\dot{F}(0)}{k} \tag{3.6.14}$$

The above expressions can be generalised for other $t > 0$ values, but the t_0 dependence of k should be kept in mind.

3.6.2.3 Relative changes in normalised fluorescence

Correct comparisons of $\Delta F(t)$, over the same time interval $t - t_0$, for sets of DEP experiments where values of $F(t_0)$ are *different*, is facilitated by considering the *relative* change in normalised fluorescence $\Delta F_r(t)$,

$$\Delta F_r(t) = \frac{F(t) - F(t_0)}{F(t_0)} = k_r \Delta n_E(t) + \varepsilon_r(t) \tag{3.6.15}$$

where the *rhs* stems from (E.3.6), and the *relative* fluorescent constant k_r is given by

$$k_r = \frac{k_{op}\, k_{ra}\, \eta_q\, k_a\, k_{ea}}{(x_u - x_l)(z_2 - z_1)[k_l \overline{\overline{c}}_E(t_0) + \overline{\overline{B}}_E(t_0)]} \quad \text{and the small error is } \varepsilon_r(t) = k_r \delta_f\, n_E(t)$$

The initial normalised fluorescence $F(t_0)$ can vary from one image processed experiment to another, for example, if the lower and upper limits, x_l and x_u, are chosen so that the $x_e - x_l$ varies considerably from $x_c - x_e$. The reason for this, as pointed out in section 3.5.2.2, is that $\tilde{I}(x, t_0)$ is slightly higher over the electrode than the gap, and asymmetric about the edge. This is due to the light reflections from the gold electrode, r_{el}, and glass gap, r_{gp}, being different. Therefore, $F(t_0)$ is dependent on x_l and x_u.

In cases where the lower and upper limits, x_l and x_u, are chosen such that they are approximately equidistant from x_e, i.e. $x_e - x_l \cong x_c - x_e$ then $\overline{\overline{I}}_E(t_0) \cong \overline{\overline{I}}_{LU}(t_0)$ in (3.6.7). This means processed images of DEP experiments yield values of $F(t_0)$ that are all close to unity. An example is shown in Fig. 3.13(b). Consequently, for these cases it is sufficient to consider just $\Delta F(t)$.

3.7 Concluding remarks

This chapter has described the materials and methods needed for DEP experiments including laboratory apparatus, fabrication of planar micro sized electrodes using standard photolithography, and preparation of 12 kbp pTA250 DNA using standard protocols. The latter is important for the next chapter that describes dielectric spectroscopic measurements of suspensions of this DNA. The techniques used to circumvent variations in DNA concentration viewed using fluorescence microscopy have also been discussed.

The chapter has also described the development of MATLAB 5.0™ based software for processing fluorescence microscope video images of dielectrophoretic particle collection onto interdigitated electrode arrays. The software utilizes the periodic and symmetric properties of the interdigitated array design. Fluorescence light intensity data from the processed images is used to visualise particle accumulation over a representative half-electrode width and half-gap. Using data based on a typical collection experiment, this leads to a time-profile of particle collection with light source fluctuations smoothed using a normalisation technique. The materials and methods described in terms of laboratory 'hardware' and 'software' supports the DEP experiments on latex micro-spheres and pTA250 DNA described in Chapter 7.

4 Dielectric relaxation measurements of pTA250 DNA

4.0 Introduction

In Chapter 2, equation (2.1.7), the DEP force was shown to be dependent on the effective polarisability, α (F m^{-1}), which is the induced dipole moment per unit volume in a unit electric field. Several polarisation mechanisms responsible for the induced dipole moment of DNA were discussed (sections 2.2.1.2, 2.2.2.2 and 2.2.3.2), in particular, Maxwell-Wagner and counterion fluctuation processes. The polarisability of DNA depends on a number of parameters including the conductivity and permittivity of the macromolecule and suspending medium, temperature, and AC frequency of the applied electric field. This dependence of the polarisability α, particularly for high AC frequencies of interest (100 kHz to 20 MHz), motivated an investigation into polarisation mechanisms most likely to account for the dielectrophoretic movement of pTA250, as illustrated in the previous chapter, figures 3.2(b), 3.4(a) and 3.4(b). The investigation involved the use of dielectric spectroscopy that yields quantitative information about the response of a system of DNA macromolecules, and surrounding counterions, to AC electric fields.

This chapter describes the dielectric measurements of 12 kbp pTA250 plasmid DNA suspended in a low conductivity medium, for a range of temperatures, 5°C to 40°C. The measurements were performed by Drs. Irina Ermolina and Yuri Feldman at the Department of Applied Physics, The Hebrew University of Jerusalem, Israel. The measurements and analysis is referenced in *List of Publications* at the end of this dissertation. The Time-Domain Reflectometry (TDR) technique, well described in the literature (Grant *et al.*, 1978), has been used over the frequency range 100 kHz to 5 GHz. Values of the frequency dependent polarisability per DNA macromolecule, a key parameter for DEP investigations, are determined from the TDR measurements. Possible mechanisms that could give rise to dielectric dispersion are also discussed, in particular with respect to the counterion fluctuation model of Manning-Mandel-Oosawa introduced in section 2.2.3.2.

4.1 Dielectric spectroscopic measurements

The dielectric properties of the DNA were determined by a commercial time-domain dielectric spectrometer (TDS-2.1®, Dipole TDS, Jerusalem, Israel). This spectrometer determines dielectric properties of materials by measuring the response of a sample to a voltage step with a fast rise time

(Ermolina *et al.*, 1991; Feldman *et al.*, 1995; Feldman *et al.*, 1996). In the framework of the lumped capacitance approximation, the complex dielectric permittivity is written as follows:

$$\varepsilon^*(\omega) = \frac{1}{j\omega C_0} \cdot \frac{L\{I(t)\}}{L\{V(t)\}} \qquad (4.1.1)$$

where *I(t)* is the current flowing through the sample, *V(t)* is the voltage applied to the sample, *L* is the operator of the Laplace transform and C_0 is the capacitance of the empty sample holder terminated to the end of the coaxial line ($C_0 = 0.2$ pF).

4.1.1 DNA preparation for dielectric measurements

The growth, harvesting and purification of pTA250 plasmid DNA has been described in the previous chapter, section 3.3. It will be recalled 10 µl stock solutions of DNA were stored at – 20 °C with concentration 2.7µg/µl. The absorbance ratio, A_{260}/A_{280} = 1.8 and gel analyses indicated the DNA was free from protein and other contaminants. To achieve a low direct current (DC), or zero frequency, conductivity for TDR measurements, 20 separate stock 10 µl samples suspended in distilled RO water ($pDNA_{ddw}$) were thawed and dialysed against RO water using Millipore® 25 nm pore size membrane flotation filters (Millipore Corp., Bedford, USA) for two hours. During dialysis the total volume of aqueous DNA increased from 200 µl to 600 µl, hence the final concentration of pTA250 DNA prepared for the measurements was C_{DNA} = 0.9 µg/µl.

4.1.2 Time domain spectroscopy measurements

A small sample (about 150 µl) of DNA solution was injected into the sample holder, and the time domain response of the sample was determined from the accumulation of 25600 individual scans. Non-uniform sampling of the time window (5 µs) for each pulse enables the generation of spectra in the frequency range from 100 kHz up to 5 GHz. Measurements were taken as a function of increasing temperature from 5 °C to 40 °C, at intervals of 5 °C. The measurement accuracy of the dielectric permittivity and loss was better than 5% (Feldman *et al.*, 1996). The accuracy of fitting (i.e. the mean square deviation) was less than 10^{-3}.

4.2 Results of time domain spectroscopy

Time Domain Reflectometry measurements were performed, under both heating and cooling cycles, for temperatures in the range 5 – 40°C. The data treatment was carried out directly in the time domain in terms of the decay function, $\psi(t)$, of the dielectric polarisation (Feldman and Kozlovich, 1995; Kamyshny *et al.*, 2000). The decay function is approximated by macroscopic dipole correlation function $\Gamma(t)$ (DCF):

$$\psi(t) \approx \Gamma(t) = \frac{\left\langle \bar{M}(0) \cdot \bar{M}(t) \right\rangle}{\left\langle \bar{M}(0) \cdot \bar{M}(0) \right\rangle} \qquad (4.2.1)$$

where $\bar{M}(t)$ is the macroscopic fluctuation dipole moment of the sample volume unit, which is equal to the vector sum of all the molecular dipoles; the symbol $\langle\ \rangle$ denotes averaging of the ensemble.

The velocity and laws governing the decay function $\psi(t)$ are directly related to the structural and kinetic properties of the sample and characterise the macroscopic properties of the system under investigation. The least square fitting procedure based on the simplex method was used. Within the limit of experimental errors the DCF may be described by the sum of three exponential components corresponding to several dielectric relaxation processes. The optimal number of the exponents was obtained by the routine of sequential subtraction of relaxation components from the DCF (Ermolina *et al.*, 1997; Kamyshny *et al.*, 2000). Figure 4.1 shows a graph of voltage signals recorded in a typical TDS experiment. The plot shows three signals: (1) is that of the reference sample (air); (2) the DNA solution (at 15°C); and (3) the short circuit. The signal differences are proportional to the current following through the sample $I(t)$ and the voltage applied to the sample $V(t)$.

The analysis identified and resolved three temperature dependent dielectric dispersions. Results of the temperature dependent dielectric decrement $\Delta\varepsilon$ and relaxation time τ, for each of the three identifiable dispersions are shown in Figs. 4.2 and 4.3, respectively. The figures show the heating cycle; the results for the cooling cycle were essentially the same, but not as comprehensive. The first dispersion, labelled with subscript 1 occurs at a frequency, f_1 = 137 kHz at 25°C. Similarly, the second and third dispersions are at f_2 = 2.01 MHz and f_3 = 11.6 MHz at 25°C.

In Fig. 4.2, the major dielectric decrement (the first dispersion, $\Delta\varepsilon_1$) shows a marked increase with temperature with gradient, $\delta(\Delta\varepsilon_1)/\delta T \cong 0.25$/°C. By contrast, the second and third (minor) dispersions exhibit decrements that decrease with temperature, with gradients –0.01/°C and

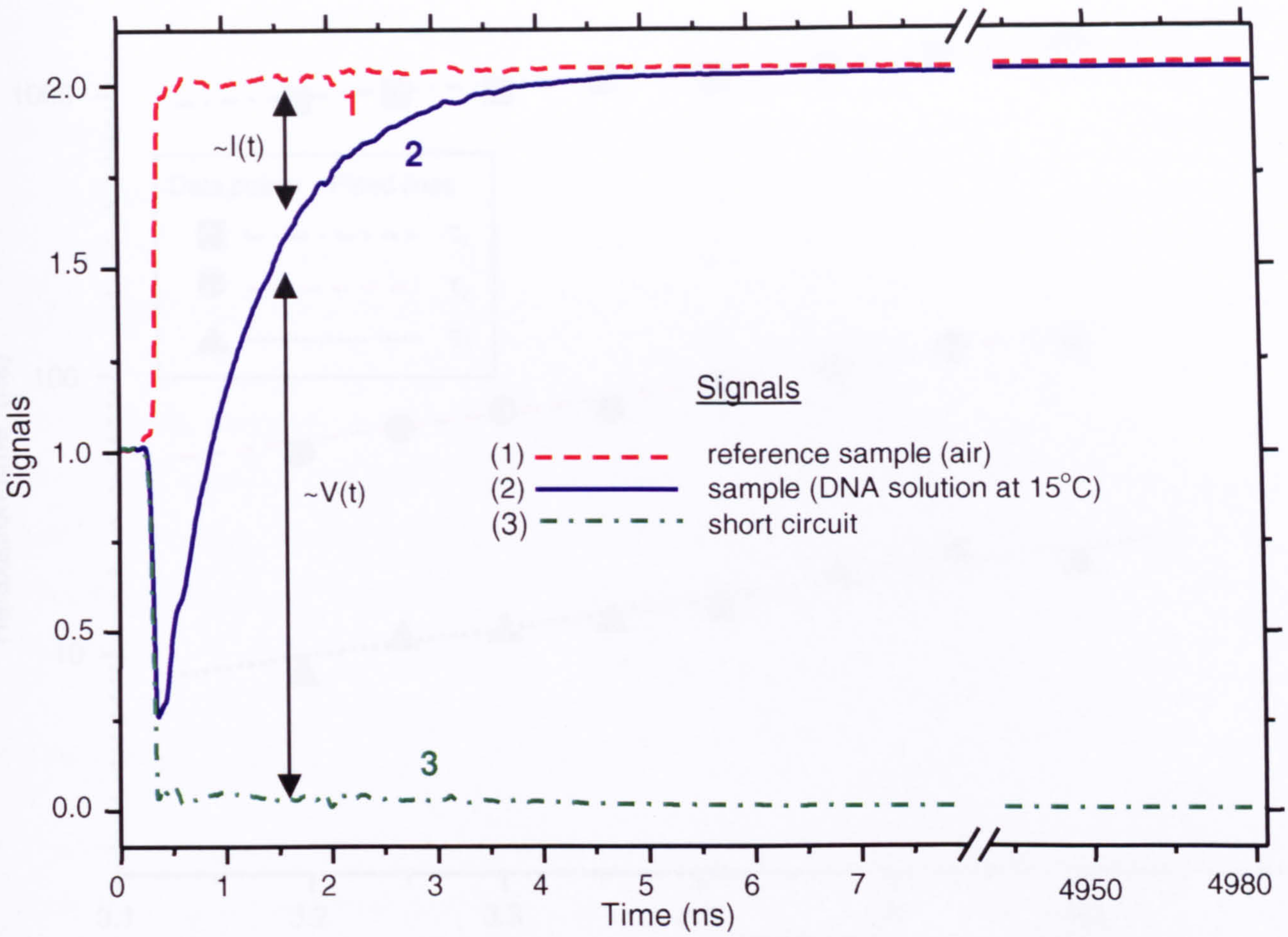

Fig. 4.1 Signals recorded in a typical TDS experiment: reference, DNA sample, and short circuit.

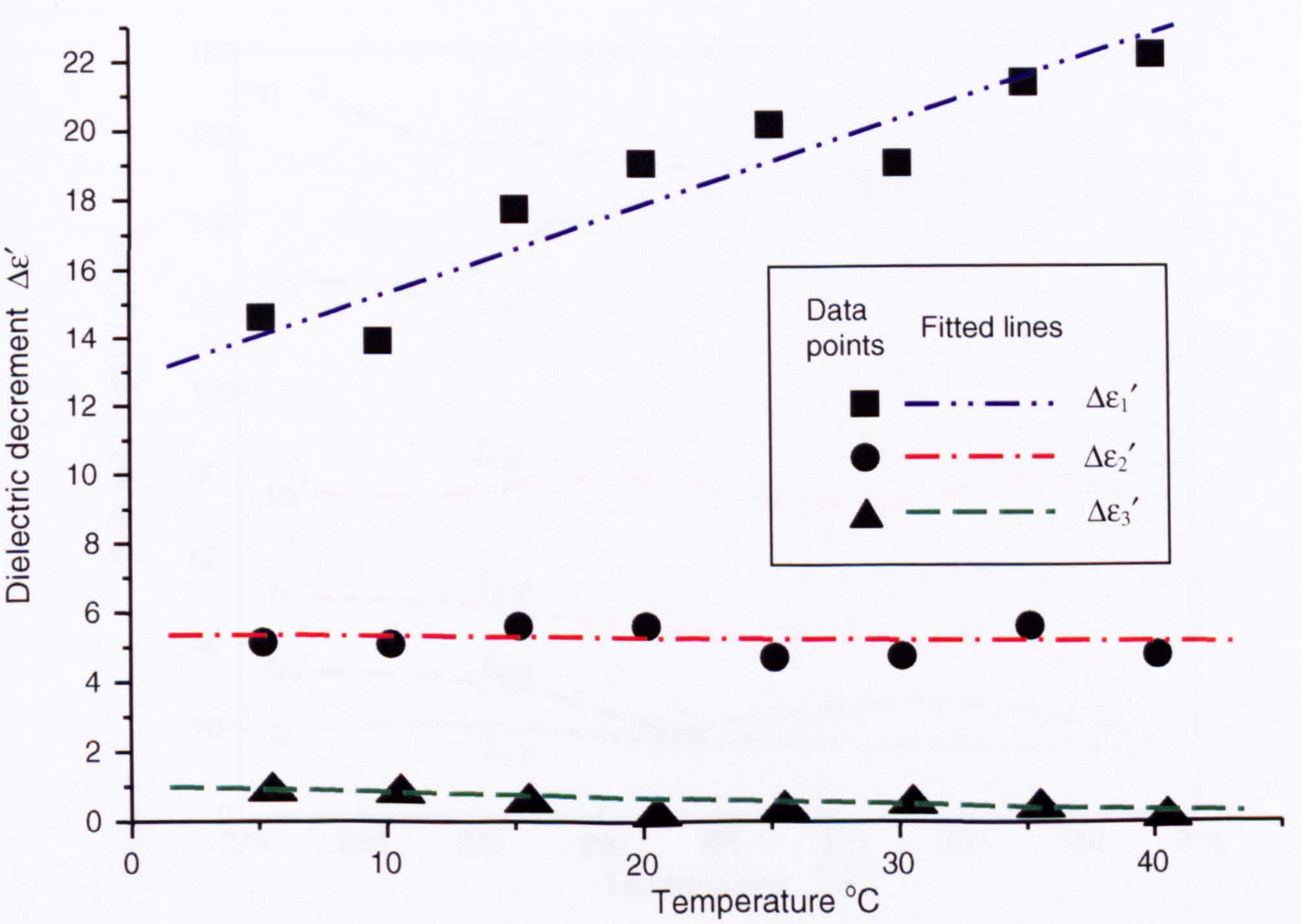

Fig. 4.2 Variation in dielectric decrement for each relaxation process as a function of temperature for pTA250 DNA. Measurements were made with a DNA concentration, C_{DNA} = 0.9 μg/μl.

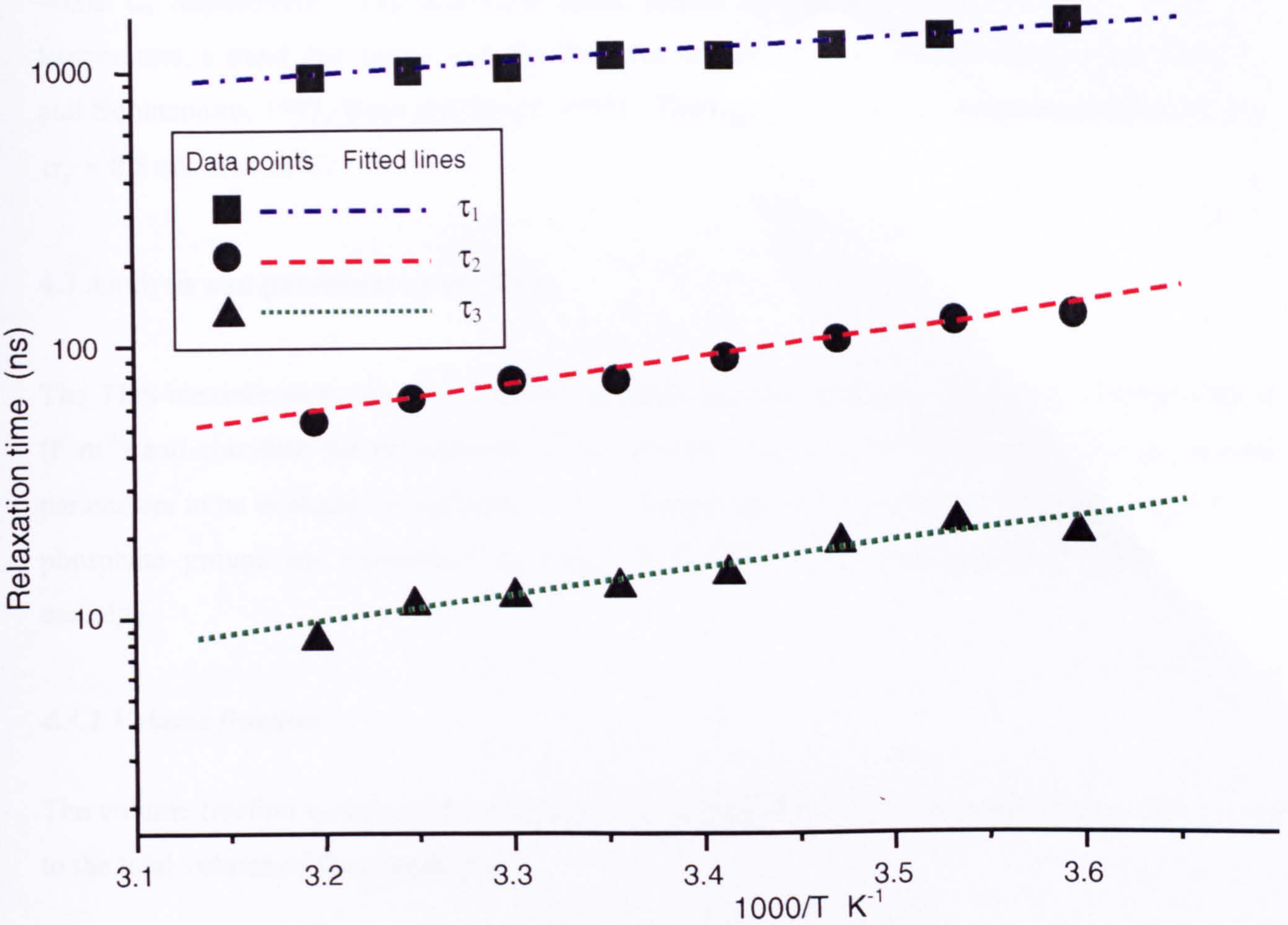

Fig. 4.3 Variation in relaxation times of the three dispersions as a function of temperature.

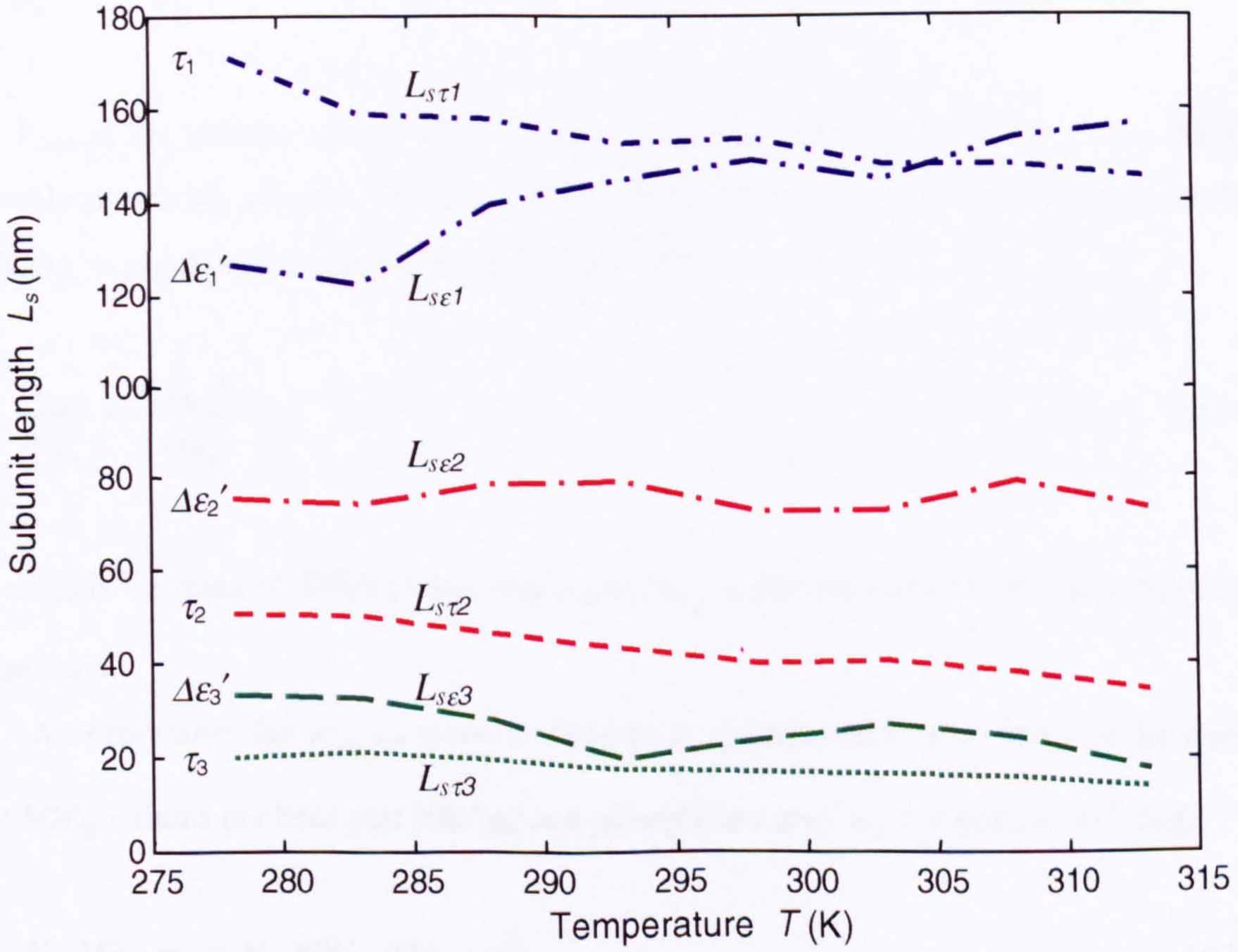

Fig. 4.4 Predicted subunit lengths from temperature dependent dielectric decrements and relaxation times.

–0.02/°C, respectively. The relaxation times, shown in Fig. 4.3, all decrease with increasing temperature, a trend that agrees with the literature for solutions of low salt concentration (Pedone and Bonincontro, 1991; Bone and Small, 1995). The measured DNA *suspension* conductivity was $\sigma_s = 8.5\,\text{mS/m}$ at 25°C.

4.3 Analysis and parameter evaluation

The TDS measurements are now analysed to determine the frequency dependent polarisability α (F m^{-1}) and elucidate the mechanisms of polarisation. To perform these tasks, there are several parameters to be evaluated in addition to α. These are the volume fraction, concentration of DNA phosphate groups (or monomers) and ions surrounding each macromolecule, and activation enthalpy.

4.3.1 Volume fraction

The volume fraction v_f is the ratio of volume V_{DNA} occupied by DNA macromolecules with respect to the total volume of the sample, V_T,

$$v_f = \frac{V_{DNA}}{V_T} = \frac{V_{1dna}\, n_{dna}}{V_T} \tag{4.3.1}$$

where V_{1dna} is the volume occupied by a *single* DNA macromolecule and n_{dna} is the number of macromolecules in the sample. The latter can be expressed in terms of DNA solution concentration C_{DNA} (kg/m^3 ≡ μg/μl) and molecular weight (Segel, 1976),

$$n_{dna} = \frac{m_{DNA}}{m_{N_{bp}}} = \frac{C_{DNA} V_T}{m_{N_{bp}}} \tag{4.3.2}$$

where m_{DNA} is the mass of DNA in the sample and $m_{N_{bp}}$ is the mass of a DNA macromolecule with N_{bp} base pairs.

An expression for $m_{N_{bp}}$ is given in Chapter 2, equation (2.3.3), in terms of the molecular weight MW_{bp} daltons per base pair (Da/bp) and atomic mass unit, $m_u = 1.6605 \times 10^{-27}$ (kg)

$$m_{N_{bp}} = N_{bp} MW_{bp} m_u = N_{bp} MW_{bp} / (N_{Av} \times 10^3) \tag{4.3.3}$$

and is also expressed, for application in the next section, using Avogadro's number N_{Av} = 6.022× 10^{23} mol^{-1} (Lide, 1994, p. 1-1). The 10^3 term is a g/kg conversion factor. Substituting (4.3.3) into (4.3.2),

$$n_{dna} = \frac{C_{DNA} V_T}{N_{bp} MW_{bp} m_u} = \frac{C_{DNA} V_T N_{Av} 10^3}{N_{bp} MW_{bp}} \tag{4.3.4}$$

In (4.3.1) the volume occupied by a DNA macromolecule, V_{1dna} can be estimated by assuming a cylindrical geometry for each DNA macromolecule with double helical radius r_{dh},

$$V_{1dna} = \pi r_{dh}^{\ 2} L = \pi r_{dh}^{\ 2} L_{bp} N_{bp} \tag{4.3.5}$$

where the length L is the product of the number of base pairs N_{bp} and contour length per base pair L_{bp}. Substituting (4.3.4) and (4.3.5) into (4.3.1),

$$v_f = \frac{\pi r_{dh}^{\ 2} L_{bp} N_{bp}}{V_T} \frac{C_{DNA} V_T}{N_{bp} MW_{bp} m_u} = \frac{\pi r_{dh}^{\ 2} L_{bp} C_{DNA}}{MW_{bp} m_u} \tag{4.3.6}$$

Using the same values as (2.3.3) and (2.3.7), r_{dh} = 1.5 nm, MW_{bp} = 662 Da/bp and L_{bp} = 3.46 Å and the DNA concentration for this sample, C_{DNA} = 0.9 μg/μl, equation (4.3.6) yields a value for the volume fraction v_f = 2.002×10^{-3} or v_f = 0.20 %.

The 0.2 % volume fraction is close to values adopted in Saif *et al.* (1991) for approximately the same DNA concentration. The calculation is in essence, independent of the size of the macromolecule, thus enabling a comparison with volume fractions in other dielectric spectroscopy studies. It is interesting to recall the calculation in section 2.3.2 using (2.3.7) that revealed that each 12 kbp DNA plasmid, if packed into a tight sphere, would have a radius of approximately 19 nm.[1]

4.3.2 Concentration of DNA monomers

Another parameter for determining polyelectrolyte polarisability is the concentration of monomers, or for DNA, the number concentration of phosphate groups C_p,

---

[1] This value concurs with an estimate of 30 nm by Washizu *et al.* (1994), for λ-phage DNA that is four times longer.

$$C_p = \frac{n_{pg}}{V_T} = \frac{L}{b}\frac{n_{dna}}{V_T} = \frac{L_{bp}N_{bp}}{b}\frac{n_{dna}}{V_T} \qquad (4.3.7)$$

where n_{pg} is the number of phosphate groups in the sample, b is the average distance between charged sites (phosphate groups), and all other symbols are as previously defined. The number of phosphate groups per DNA is L/b and on average $b = L_{bp}/2 = 1.73$ Å. Substituting this relation and (4.3.4) into (4.3.7),

$$C_p = \frac{L_{bp}N_{bp}}{V_T L_{bp}/2}\frac{C_{DNA}V_T N_{Av}10^3}{N_{bp}MW_{bp}} = \frac{2\times10^3 C_{DNA}N_{Av}}{MW_{bp}} \qquad (\mathrm{m^{-3}}) \qquad (4.3.8a)$$

or, in terms of molar concentration for application in section 4.6.3,

$$C_p = \frac{2\times10^3 C_{DNA}}{MW_{bp}} \qquad (\mathrm{mol/m^3}) \qquad (4.3.8b)$$

Using C_{DNA} = 0.9 μg/μl and MW_{bp} = 662 in (4.3.8b) yields C_p = 2.719 mol/m^3 or 2.72 mM (millimol/litre).

4.3.3 Concentration of ions surrounding the DNA

The concentration of ions is a useful parameter for understanding polarisability and in section 2.2.3.2 three phases of ions were distinguished, namely, (i) *condensed* counterions that are bound (non-locally) to the phosphate groups of the DNA thereby neutralising a fraction of the DNA charge, (ii) *diffuse* counterions which are responsible for neutralising the remainder of the DNA charge, with a density which decreases exponentially with distance from the axis, and (iii) *bulk* ions or 'added salt' ordinary aqueous solution ions

The low frequency conductivity of the suspension is σ_s = 8.5 mS/m (at 25°C) and is significantly larger than the conductivity of the RO water which was used for dialysis (0.2 mS/m). It is, however, comparable with the low frequency (100 Hz) conductivity measured by Saif *et al.*, (1991) who reported σ_s = 5 mS/m at 25°C, after their DNA solution had been dialysed for a week to eliminate bulk ions from the sample. Following their argument, it is possible to attribute the low frequency σ to the diffuse ionic phase surrounding the DNA, rather than the bulk ion phase. However, in the absence of conclusive evidence, it will suffice to designate C_l (mol/m^3) as the combined concentration of *bulk* and *diffuse* phase ions surrounding the DNA macromolecules.

Using the relation,

$$C_i = \frac{\sigma_s}{q\mu N_{Av}} \tag{4.3.9}$$

where typically (for potassium ions) the ion mobility $\mu = 8\times10^{-8}$ ($m^2\ V^{-1}s^{-1}$), the elementary (or electronic) charge is $q = 1.602\times10^{-19}$ (C), and other symbols are as previously stated. Ignoring the effect of the electrophoresis of DNA on the DC conductivity, C_i is calculated to be 1.101 mol/m^3 or 1.10 mM.

4.3.4 Dielectric relaxation times and activation enthalpy

The relaxation time τ varies with temperature T (K) according to the Arrhenius expression (Takashima, 1989; Grant *et al.*, 1978)

$$\tau = \tau_o \exp\left(-\frac{\Delta H}{RT}\right) \tag{4.3.10}$$

where τ_o is the nominal relaxation time, ΔH is the activation enthalpy (J mol^{-1}), and is the R molar gas constant, R = 8.315 J mol^{-1} K^{-1} (Lide, 1994, p. 1-1). Rearranging equation (4.3.10), and differentiating with respect to $1/T$, it can easily be shown that a plot of $\ln(\tau)$ *vs* $1/T$ yields a straight line with gradient $\Delta H/R$. The temperature dependent relaxation times shown in Fig. 4.3 for each of the three dispersions were computed as Arrhenius plots and the resulting activation enthalpy, ΔH for each dispersion, is listed in Table 4.1. All three ΔH values agree with published values in the range 1-4 kCal/mol (Pedone and Bonincontro, 1991), where the dispersions are attributed to counterion fluctuation.

4.4 Polarisability

The polarisability α (F m^{-1}) is related to the dielectric decrement $\Delta\varepsilon'$ (Von Hippel, 1954; van der Touw *et al.*, 1973) and can be expressed in several ways. The polarisability per macromolecule α_m (F m^2), introduced previously in section 2.2.5, can be written as

$$\alpha_m = 3\varepsilon_o \Delta\varepsilon' / C_m \tag{4.4.1}$$

where C_m (m^{-3}) is the number density of DNA macromolecules and ε_o is the permittivity of free space (as defined previously in Chapter 2). Using (4.3.4),

$$C_m = \frac{n_{dna}}{V_T} = \frac{C_{DNA}}{N_{bp} MW_{bp} m_u} = \frac{C_{DNA} N_{Av} 10^3}{N_{bp} MW_{bp}} \qquad (4.4.2)$$

Hence, for the sample values with C_{DNA} = 0.9 μg/μl, $N_{bp} = 12\times10^3$, and MW_{bp} = 662 Da/bp, (4.4.2) gives $C_m = 6.823\times10^{19}$ macromolecules/m^3. Values of α_m, calculated using equation (4.4.1), for each of the three $\Delta\varepsilon'$ values are listed in Table 4.1.

An alternative way of expressing the polarisability is in terms of the macromolecular subunit length L_s, an important parameter where counterion fluctuation models are used to describe the polarisability. In this case the polarisability α_s (F m^2) per subunit length, is determined from measurements of the decrement $\Delta\varepsilon'$ via the number density of subunits C_s (Penafiel and Litovitz, 1992; Saif *et al.*, 1991)

$$\alpha_s = \frac{3\varepsilon_o \Delta\varepsilon'}{C_s} = \frac{3\varepsilon_o \Delta\varepsilon'}{N_{Av} C_p (b/L_s)} \qquad (4.4.3)$$

This definition enables α_s to be compared with other dielectric studies of DNA with different molecular weights. Using for example, a subunit length L_s = 30 nm in (4.4.3), the values of α_s are calculated for each of the three $\Delta\varepsilon'$ decrements. The α_s values are listed in Table 4.1 and show agreement with polarisability values measured by Saif *et al.* (1991) for comparable values of $\Delta\varepsilon'$.

The study by Saif *et al.* (1991) of calf thymus DNA resolved three dielectric dispersions with characteristic frequencies higher than those described in section 4.2, but with an average decrement (for their dialysed solution) of $\Delta\varepsilon'$ = 1.94 (normalised to 1 g/l) giving[2] $\alpha_s = 5.3\times10^{-33}$ (F m^2). They compare favourably with those calculated by Suzuki *et al.* (1995) using measurements of fluorescence anisotropy of DNA in AC electric fields. These authors obtained $\alpha_p = 1\times10^{-32}$ (F m^2) for pUC18 (2.7 kbp) which is 4.5 times smaller than the pTA250 DNA, and therefore their polarisability should be increased by the same amount for a comparison with our values. However, the origin of the polarisability has not been resolved, and the differences in experimental methodologies between Suzuki *et al.* (1995) and those described in this chapter prevent an exact comparison.

---

[2] In Saif *et al.* (1991) the value 5.3×10^{33} is assumed to have a typographical error and the value of 5.3×10^{-33} (F m^2) is used.

Dispersion (at 25°C)			Activation enthalpy ΔH (kCal mol^{-1})	Polarisability per macromolecule α_m (F m^2) at 25°C	Polarisability for 30 nm subunit α_s (F m^2) at 25°C
No.	$\Delta\varepsilon'$	f(MHz)			
1	20.3	0.137	1.4	7.90×10^{-30}	5.71×10^{-32}
2	4.82	2.01	3.8	1.88×10^{-30}	1.36×10^{-32}
3	0.507	11.7	4.0	1.97×10^{-31}	1.43×10^{-33}

Table 4.1 DNA pTA250 dielectric decrement, relaxation frequency, activation energy and polarisabilities, determined from experimental data, for each of the three dispersions.

4.5 Discussion of polarisation mechanisms

Previous dielectric spectroscopic investigations of polyelectrolyte solutions, including DNA, have proposed a number of mechanisms for the dispersions. These include Maxwell-Wagner interfacial polarisation (described in section 2.2.2.2), rotation of bound water molecules (Mashimo *et al.*, 1989) and polar groups (Takashima *et al.*, 1984) associated with the DNA, and fluctuations of counterions along the longitudinal (described in section 2.2.3.2) and transverse (Xammar Oro and Grigera, 1984) axes of the DNA. Although it is difficult to draw a definitive conclusion about the mechanism(s), the evidence tends to favour counterion fluctuation along the longitudinal DNA axis, in particular concerning the low frequency relaxation around 140 kHz.

4.5.1 Rotation of bound water molecules and polar groups

The characteristics of water molecule clusters bound along and across DNA grooves were shown by Mashimo *et al.* (1989) to have an activation energy of 17 kCal/mol accompanied with a relaxation time $\tau = 1.4$ ns (relaxation frequency $f = 113$ MHz). This data was obtained for B-DNA below the melting point. Reports of dispersions around 100 MHz, for example, by Takashima *et al.* (1984) have also attributed this high frequency dispersion to the motion of polar groups inside the DNA macromolecule.

The dispersions exhibited by the pTA250 DNA sample, prepared as described in section 4.1.1, have considerably lower activation energies (1.4 – 4 kCal/mol) and relaxation frequencies (lower by an order of magnitude) - values that do not agree with the τ and ΔH values expected for this type of mechanism. A similar conclusion can be drawn for the motion of DNA sugar-phosphate groups. The analysis of Bone and Small (1995) showed that for DNA concentrations

and dielectric increments comparable to this investigation, the dipole moment per base pair exceeded expected values by more than two orders of magnitude.

4.5.2 Maxwell-Wagner interfacial polarisation

As described in section 2.2.2.2 Maxwell-Wagner interfacial polarisation for DNA arises from the rod-like, macromolecular insulating core being surrounded by a highly conducting 'sheath', immersed in an electrolyte. The 2 nm diameter, amino acid - sugar phosphate double helix acts as the insulator and is surrounded by the high conductivity layer that represents the bound counterions on the negatively charged sugar phosphate backbone.

The low frequency polarisation of this charge has been identified with the classical α-dispersion with a higher frequency relaxation corresponding to an interfacial polarisation (Maxwell-Wagner) mechanism. Predictions by Grosse (1989) for the dielectric decrement $\Delta\varepsilon'$ and relaxation frequency f_R arising from Maxwell-Wagner polarisation are given in equations (2.2.11) and (2.2.12). Assuming a typical value used by Grosse (1989) for the fraction of counterions $\phi_c = 0.25$ and substituting values for the sample, volume fraction $v_f = 0.20$ %, relative permittivity of the bulk medium $\varepsilon_{rm} = 78.4$, and measured DNA suspension conductivity $\sigma_s = 8.5\text{x}10^{-3}$ S/m at 25°C, (2.2.11) and (2.2.12) yield values, $\Delta\varepsilon' \cong 0.42$ and $f_R \cong 162$ MHz.

These predicted values markedly differ with those listed in Table 4.1, albeit less for the 12 MHz dispersion. As discussed in section 2.2.2.2, Saif *et al.* (1991) modified the model by Grosse (1989) to accommodate a thicker sheath of counterions around the DNA macromolecule. However, the predicted decrement, $\Delta\varepsilon' \cong 0.07$ deviates further from the original prediction of equation (2.2.11). Consequently, Maxwell-Wagner interfacial polarisation is unlikely to be the cause of the observed dispersions described in section 4.2. However, it cannot be entirely ruled out, particularly regarding the third, high frequency, relaxation around 12 MHz.

4.5.3 Counterion fluctuation

The third possible cause of dispersions is attributed to counterion polarisation along segments (or subunit lengths L_s) of the DNA longitudinal axis. This mechanism is detailed in section 2.2.3.2 and an important feature of the Manning-Mandel-Oosawa counterion model is the non-locally bound, or condensed, counterion phase. The relationship between the polarisability α_s per subunit length, number of condensed counterions n_{cc}, and fraction of condensed counterions ϕ_c is given by equations (2.2.18) - (2.2.20). Combining these together,

$$\alpha_s = \frac{z^2 q^2 L_s{}^2 n_{cc} A_{st}}{12 k_B T} = \frac{z^2 q^2 L_s{}^2 \{\phi_c L_s/(|z|b)\} A_{st}}{12 k_B T} = \frac{z^2 q^2 L_s{}^3 A_{st}(|z|\xi - 1)}{12 k_B T z^2 b \xi} \tag{4.5.1}$$

where z is the ion valency, k_B is Boltzmann's constant (1.381×10^{-23} J K^{-1}), A_{st} is the stability factor, and ξ is the charge density parameter given by (2.2.17),

$$\xi = q^2/(4\pi \varepsilon_{rm} \varepsilon_o k_B T b) \tag{4.5.2}$$

It is understood $\varepsilon_m = \varepsilon_{rm} \varepsilon_o$ where ε_{rm} is the relative permittivity of the medium.

Substituting (4.5.2) into (4.5.1),

$$\alpha_s = \frac{\pi \varepsilon_o \varepsilon_{rm} L_s{}^3 A_{st}(|z|\xi - 1)}{3} \tag{4.5.3}$$

Equating the predicted α_s for counterion fluctuation (4.5.3) with α_s determined using the experimentally measured dielectric decrement $\Delta\varepsilon'$ (4.4.3) yields an expression for L_s,

$$L_s = \sqrt{\frac{9\Delta\varepsilon'}{\pi\varepsilon_{rm}(|z|\xi - 1)A_{st} N_{Av} C_p b}} \tag{4.5.4}$$

This is the general expression for the subunit length based on the dielectric decrement $\Delta\varepsilon'$. Values for L_s are found by using the expression for stability factor A_{st} given by (2.2.21)

$$A_{st} = [1 - 2(|z|\xi - 1)\ln(\kappa_s b)]^{-1} \tag{4.5.5}$$

where the Debye screening length, κ_s^{-1} is stated in (2.2.22)

$$\kappa_s = \left[\left(\frac{N_{Av} q^2}{\varepsilon_{rm} \varepsilon_o k_B T}\right)\left(\sum_i C_i z^2 + \frac{C_p}{\xi}\right)\right]^{0.5} \tag{4.5.6}$$

For example, selecting the temperature, $T = 298.2$ K (25.0 °C) and substituting $C_p = 2.72$ mol/m^3, $C_i = 1.10$ mol/m^3 and previous values for the other parameters, (4.5.2), (4.5.5) and (4.5.6) simplify,

$\xi|_{25\,^{\circ}C} = 4.132$, $\kappa_s|_{25\,^{\circ}C} = 9.754\times10^{7}$ and $A_{st}|_{25\,^{\circ}C} = 3.764\times10^{-2} \cong 0.038$ Thus, at 25.0 °C (4.5.4) simplifies,

$$L_s = 3.308\times10^{-8}\sqrt{\Delta\varepsilon'} \qquad (4.5.7)$$

Hence, for the first dispersion with $\Delta\varepsilon_1' = 20.3$, equation (4.5.7) gives L_s = 149 nm. Values of L_s calculated from the other two dispersions are listed in Table 4.2.

An alternative method of estimating L_s uses an expression developed by Mandel (1961) for the relaxation time given in (2.2.23). Rearranging,

$$L_s = \sqrt{\frac{\pi^2 k_B T \mu \tau}{q}} \qquad (4.5.8)$$

where all other symbols are as previously defined. Selecting again a 25°C temperature, and assuming the mobility remains at a constant value, $\mu = 8.00\times10^{-8}$, (4.5.8) simplifies,

$$L_s = 1.424\times10^{-4}\sqrt{\tau} \qquad (4.5.9)$$

Predictions of subunit length L_s for each of the three resolved relaxation times are listed in Table 4.2. It can be seen that they generally agree with those determined by the dielectric decrement and are within the range quoted in the literature.

Dispersion (at 25°C)			Subunit length L_s (nm) determined from $\Delta\varepsilon'$	Subunit length L_s (nm) determined from τ
No.	$\Delta\varepsilon'$	τ (ns)		
1	20.3	1165	149	154
2	4.82	79.1	72.6	40.1
3	0.507	13.7	23.6	16.7

Table 4.2. Subunit lengths determined from measured dielectric decrements and relaxation times (all at 25°C).

The relatively high values of L_s, particularly for the *first* dispersion, are consistent with conditions of low ionic strength where vary little electrostatic screening of the negative phosphate charges occurs. Each DNA macromolecule can be conceived of as a 'worm-like chain' consisting of freely

jointed, relatively straight segments, or 'links' (Smith and Bendich, 1990). Each link has a length equal to the Kuhn length L_k (twice the persistence length), a statistical measure of DNA rigidity with respect to thermal energy that tends to randomise its macromolecular shape (Bloomfield *et al.*, 1974; Viovy and Duke, 1993). In very low salt solutions (e.g. 1mM Na^+), the persistence length has been measured in most studies to be 80-100 nm, though some have been as low as 50 nm (Hagerman, 1998). Hence, typical values of the Kuhn length are approximately $L_k \approx 160$ nm.

In this respect the subunit length ~ 150 nm, calculated for the first (major) dispersion (from $\Delta\varepsilon'_1$ and τ_1) is remarkably close the Kuhn length, i.e. $L_{s1} \approx L_k$. This gives a physical interpretation to the most significant dispersion exhibited by the plasmid DNA suspended in the low salt electrolyte. Counterions are envisaged to move unhindered along each subunit, in the direction of the AC electric field, until they reach a potential barrier. These barriers result from 'breaks' in the average conformational shape (van der Touw and Mandel, 1974; Mandel, 1977), and it is reasonable to attribute these to structural features of the macromolecule, such as kinks or bends.

The temperature dependence of the predicted subunit length L_s values from the three resolved dielectric decrements and relaxation times is plotted in Fig. 4.4. The temperature dependent L_s values were determined from the decrements $\Delta\varepsilon'$ by combining (4.5.4) – (4.5.6) and from relaxation times τ using (4.5.8). It is assumed to a first approximation the mobility μ remains constant over the temperature range considered. In Fig. 4.4 the L_s subscripts are labelled according to the parameter they were determined from (listed near the left vertical axis). The L_s plots are also color/mark coded consistent with figures 4.2 and 4.3. Thus, $L_{s\varepsilon 1}$ (blue, – ·· – ··) is the predicted L_s where the ε_1 subscript indicates that the dispersion is calculated from $\Delta\varepsilon'_1$ as shown, etc. Generally the subunit lengths decrease with increasing temperature, except $L_{s\varepsilon 1}$ that increases with temperature.

This feature of $L_{s\varepsilon 1}$ questions the relationship of the counterion model L_{s1} to structural parameter L_k because it is known L_k should decrease as the temperature increases since the macromolecule becomes more flexible (Bloomfield *et al.*, 1974; Hagerman, 1998). At this stage, it is not clear whether this 'opposite' temperature dependence for $L_{s\varepsilon 1}$ is a second order effect, with respect to L_k, that is not accounted for in the counterion model. However, over the measured temperature range $\{5 \le T \le 40\ ^\circ C\}$ the variation in $L_{s\varepsilon 1}$ $\{126 \le L_{s\varepsilon 1} \le 156$ nm$\}$ lies within the range of values listed for L_k $\{120 \le L_k \le 200$ nm$\}$.

The temperature dependence of subunit length $L_{s\tau 1}$ in Fig. 4.4 (predicted from the relaxation time τ_1, as indicted) is shown to follow the same trend as L_k, and lies within the same range of values, $\{145 \le L_{s\tau 1} \le 171$ nm$\}$. This could be fortuitous, however, because of the uncertainty in the temperature dependence of condensed counterion mobility μ that was assumed to remain invariant to temperature changes. The subunit lengths calculated from the second and third

dispersions ($L_{s\varepsilon 2}$, $L_{s\varepsilon 3}$ and $Ls_{\tau 3}$) tend to decrease with increasing temperature. Although this trend is expected if the subunit length corresponds to macromolecular structural features, such as the Kuhn length, the values are smaller than the published L_k values at this very low salt concentration.

Another interpretation of the subunit length may be attributed to DNA strands crossing over each other from plasmid supercoiling, catenation, or from neighbouring macromolecules where strong electrostatic interactions between chains imposes some form of order as discussed by Odijk (1979), Bone *et al.* (1996), and Lee and Bone (1998). It is likely the significant presence of large conglomerates, as discussed in Chapter 2, would have some effect on counterion movement. In this case, the subunit length is equal to the mean correlation length L_c between contact points, that is, $L_s = L_c$.

4.6 Concluding remarks

The dielectric spectroscopy study of pTA250 DNA used for DEP experiments has resolved three dispersions at 140 kHz, 2 MHz and 12 MHz. The mechanism responsible for the polarisability is understood to be counterion fluctuation along subunits of the double-helical axis, although Maxwell-Wagner interfacial polarisation cannot be ruled out for the third dispersion. The subunit length for the first (major) dispersion concurs with the Kuhn length, although the temperature dependence is not as expected. An alternative interpretation of subunit length is attributed to DNA entanglements. This correlates with observations of DNA entanglements made by fluorescence microscopy. The measured polarisabilities for the first, second, and third dispersions are 80, 20, and 2×10^{-31} (F m^2) per DNA macromolecule.

5 Modelling DEP collections (I): solving the one-dimensional (1-D) Fokker-Planck Equation

5.0 Introduction

The one dimensional Fokker-Planck equation (1-D FPE) was introduced in Chapter 2 for modelling the spatial-temporal probability density function (or distribution) $p(x, t)$ of nano-scale particles moving under the influence of DEP forces and diffusion. Recalling (2.4.15), the FPE was cast including the probability flux $J(x, t)$,

$$\frac{\partial p(x,t)}{\partial t} = -\frac{\partial J(x,t)}{\partial x} = -\frac{\partial \left(p(x,t)v(x)\right)}{\partial x} + D\frac{\partial^2 p(x,t)}{\partial^2 x} \qquad (5.0.1)$$

where the diffusion coefficient is $D = k_B T/\zeta$, $k_B T$ is the Boltzmann temperature and the drag coefficient ζ was introduced previously in equation (2.3.5). For most purposes, the (deterministic) velocity is comprised solely of the DEP force $v(x) = F_{DEP}(x)/\zeta$. Equation (5.0.1) is a second order, parabolic, 1-D Partial Differential Equation (PDE), and can be solved analytically if reasonably simple appropriate boundary conditions (BCs) and initial conditions (ICs) are applied. Otherwise, numerical integration methods are needed.

This chapter describes analytical and numerical techniques used to find the solution for the probability density $p(x, t)$. This enables simulations of DEP collections and these are further developed for the two dimensional situation in Chapter 6. The simulations, in conjunction with experimental DEP collection rate characteristics (chapters 3 and 7), in turn can be used provide values for the frequency dependent polarisability of a particle. The nano-scale test particles are pTA250 plasmid DNA and 216 nm diameter polystyrene latex beads. Values of the polarisability are then compared with those determined previously by dielectric measurements and theoretical relations (chapters 2 and 4).

The simple form of the 1-D FPE (5.0.1) is applicable to a number of experimental DEP collection models, or scenarios. The first scenario that justifies reduction to a 1-D FPE involves a rectangular coordinate system where the interdigitated DEP electrode array, described in Chapter 3, is approximated as a planar surface. A second possible scenario is a cylindrical coordinate system where the edge of one electrode is approximated as a wire. Advantage can be taken of longitudinal symmetry along the axis, so the 1-D model would comprise particles being attracted in the radial direction orthogonal to the longitudinal axis. The third possible scenario is one that uses a

spherical coordinate system applied to castellated electrode geometry – a design that is often used in DEP investigations (Pethig *et al.*, 1992). In this scenario, a corner of a castellation is approximated to a tiny 'sphere' that attracts particles from a surrounding hemi-spherical region in radial directions. Advantage is taken of spherical symmetry so the problem is simplified to solving a 1-D FPE.

Only the first scenario is considered in this chapter, the second and third are candidates for further investigation beyond the scope of this dissertation. Generally, there appears considerable choice in terms of the dimension of the FPE, coordinate geometry, representation of the DEP force, and constraining BCs. In many respects, the central issue is one of scale and the kinds of approximations that experiments justify. Before considering the first scenario, it is instructive to consider the general solution to one of the simplest kinds of 1-D FPE, the Ornstein-Uhlenbeck process (Gardiner, 1985, p. 75-77; Uhlenbeck and Ornstein, 1930).

5.1 The Ornstein-Uhlenbeck (O-U) process

The Ornstein-Uhlenbeck (O-U) process describes the dynamics of a harmonically (or elastically) bound particle in a potential well Φ influenced by Brownian motion. The potential has a parabolic form $\Phi = kx^2/2$, as shown in Fig. 5.1(a), where k is a positive real constant. The O-U process is important for understanding stochastic behaviour because it treats the particle velocity as a random quantity, rather than its position *per se*. This circumvents differentiability problems encountered with other models of Brownian motion, such as, the Wiener process, and the resultant particle statistics are different (Horsthemke and Lefever, 1984, p. 49 –53; Gardiner, 1985, Ch. 3.8).

In the usual case where the particle exhibits a very short relaxation time $\tau = m/\zeta$, and considering times $t >> \tau$, the particle velocity is expressed in terms of the (deterministic) force F and potential Φ

$$v = \frac{F}{\zeta} = -\frac{1}{\zeta}\frac{d\Phi}{dx} = -\frac{kx}{\zeta} \tag{5.1.1}$$

where the same standard convention is used as adopted in (2.1.1), i.e. displacements, velocities, forces, etc., acting to the right are positive, and those to the left are negative.

Substituting the relation for v given by (5.1.1) into (5.0.1) the O-U equation is

$$\frac{\partial p}{\partial t} = \frac{k}{\zeta}\frac{\partial (px)}{\partial x} + \frac{k_B T}{\zeta}\frac{\partial^2 p}{\partial x^2} = -\frac{\partial}{\partial x}\left(-p\frac{kx}{\zeta} - D\frac{\partial p}{\partial x}\right) = -\frac{\partial J(x,t)}{\partial x} \tag{5.1.2}$$

where it is understood $p = p(x,t)$. Equation (5.1.2) can be solved analytically to find time dependent and steady state General Solutions (GSs). A number of methods can be used, particularly using Fourier transformations and the method of characteristics (Gardiner, 1985; Williams, 1980).

5.1.1 The O-U process: steady state solution

The steady state probability is found by setting $lhs = 0$ in (5.1.2), integrating the DE to find the GS, and normalising to satisfy the axiomatic condition (2.4.18b),

$$\int_{-\infty}^{+\infty} p(x)dx = 1 \tag{5.1.3}$$

The result is a Gaussian distribution with width and height governed by the ratio of parabolic potential coefficient to thermal energy, $k/(k_BT)$

$$p(x)=\frac{1}{\sqrt{2\pi k_BT/k}}\exp\left(\frac{-kx^2}{2k_BT}\right) \tag{5.1.4}$$

As expected, the steady state solution is independent of the drag coefficient ζ.

5.1.2 The O-U process: time dependent solution

In this section the time dependent solution is described for two ICs illustrated in Fig. 5.1(a). The first is a 'textbook' Dirac delta function IC, the second is a rectangular function IC. The latter is more realistic in terms of the initial uniform distribution of particles observed at the start of experiments that involve particle collection.

5.1.2.1 O-U time dependent solution: delta function IC

Applying the Dirac delta function IC,

$$p(x,0)=\delta(x-x_0) \tag{5.1.5}$$

yields the Particular Solution (PS), $p_\delta(x,t)$ (the subscript δ denotes the IC used)

$$p_\delta(\mathrm{x},\mathrm{t})=\frac{1}{\sqrt{2\pi\sigma^2(t)}}\exp\left(\frac{-(x-\bar{x}(t))^2}{2\sigma^2(t)}\right) \tag{5.1.6}$$

where the time dependent mean is $\bar{x}(t)=x_0\exp(-kt/\zeta)$, and time dependent variance is $\sigma^2(t)=k_BT\left(1-\exp(-2kt/\zeta)\right)/k$ (Gardiner, 1985, p. 76). As $t\to\infty$ the mean $\bar{x}(t)\big|_{t\to\infty}\to 0$ and variance $\sigma^2(t)\big|_{t\to\infty}\to k_BT/k$, thus becoming time independent. By inspection, the density reaches steady state yielding the same PS as (5.1.4), i.e. $p_\delta(x,t)\big|_{t\to\infty}=p(x)$.

Physically, the thermal motion of the particles, that would otherwise cause them to diffuse throughout space, is counteracted by the parabolic potential well that forces particles towards the centre as shown in Fig. 5.1(a). Hence, there is no requirement to impose additional BCs, such as impenetrable (or reflecting) barriers, to constrain particle movement. The PDE alone, ensures the solution is stationary, i.e. $p(x, t)$ tends to a non-zero, finite, value as $t\to\infty$. This contrasts with the PDE describing an ordinary diffusion (or Wiener) process, or diffusion under a constant, spatially invariant force, such as gravity. In these cases, the PDE alone is insufficient to provide a stationary solution. Additional BCs, corresponding to reflecting barriers in the physical world, are needed to prevent particles from drifting to 'infinite regions'. The PDEs can be solved using eigenfunction expansions, but the technique is more complicated than for the O-U case as presented [1].

The deterministic force in the O-U process is similar to the DEP force for a polynomial *negative* DEP trap (Huang and Pethig, 1991; Wang *et al.*, 1993a), though not so for *positive* DEP collections onto planar interdigitated arrays discussed in the following sections. In general the O-U equation is a convenient and simple 1-D FPE model for understanding particle movement and it is insightful to examine the behaviour of $p(x, t)$. An improved model of the O-U process can adopt an IC mimicking the spatial distribution of particles typical of most experiments. Often it is more realistic to assume, for a 1-D system, the particles are uniformly distributed over a given length L at $t=0$, than a Dirac δ-function!

5.1.2.2 O-U time dependent solution: rectangular function IC

The IC $p(x,0)$ is written as a normalised rectangular function, centred at $x=x_0$, from $x=x_0-L/2$ to $x=x_0+L/2$,

$$p(x,0)=\frac{1}{L}\mathrm{rect}\left(\frac{x-x_0}{L}\right)=\frac{1}{L}\left[\mathrm{u}(x-x_0+L/2)-\mathrm{u}(x-x_0-L/2)\right] \tag{5.1.7}$$

---

[1] The O-U process is also solved using eigenfunction expansions where BCs are imposed (Gardiner, 1985, p. 134-5).

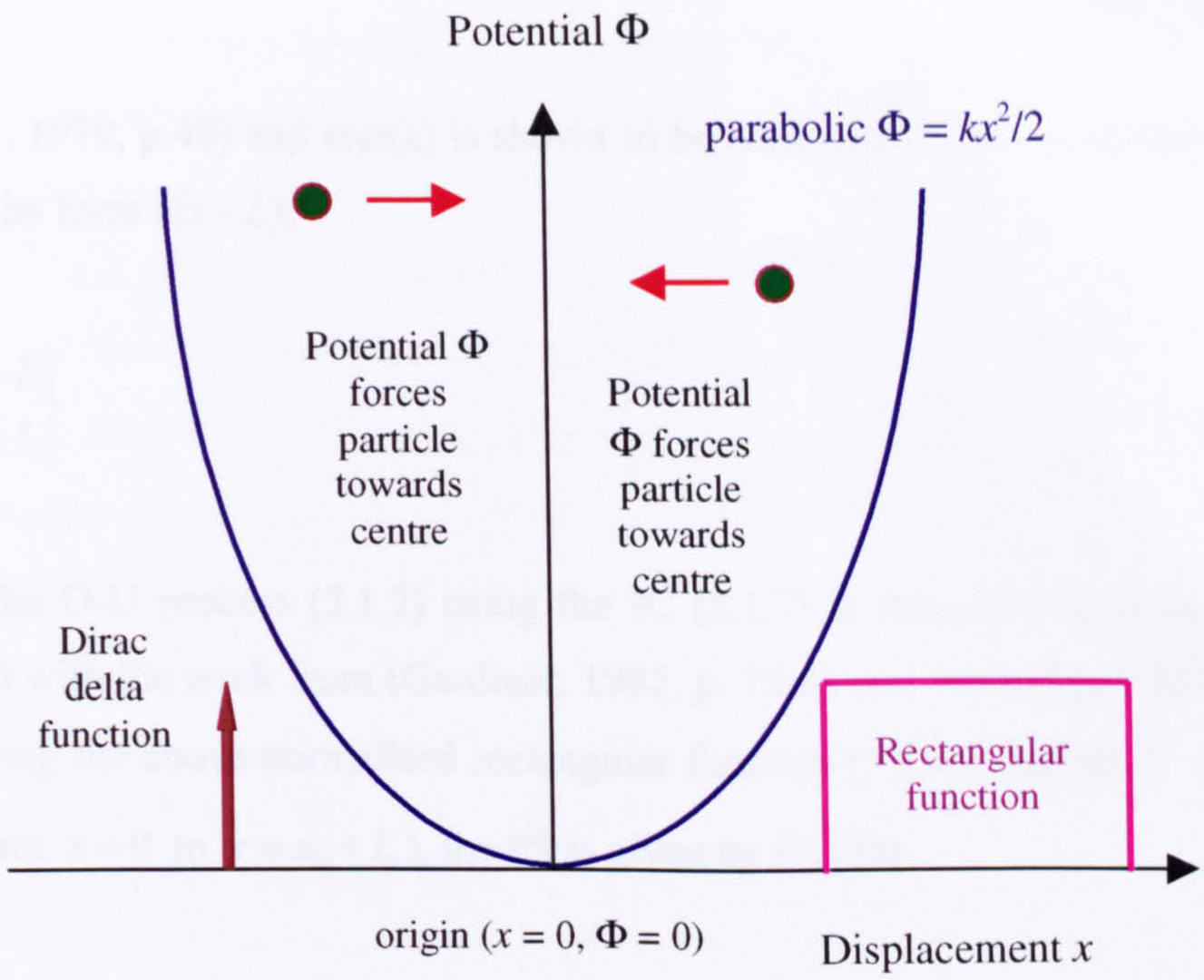

Fig. 5.1(a) Schematic of the Ornstein-Uhlenbeck process showing particles being attracted to the centre located at the origin, $x = 0$. Examples of initial conditions include rectangular and Dirac delta functions as shown (positioned arbitrarily for convenience).

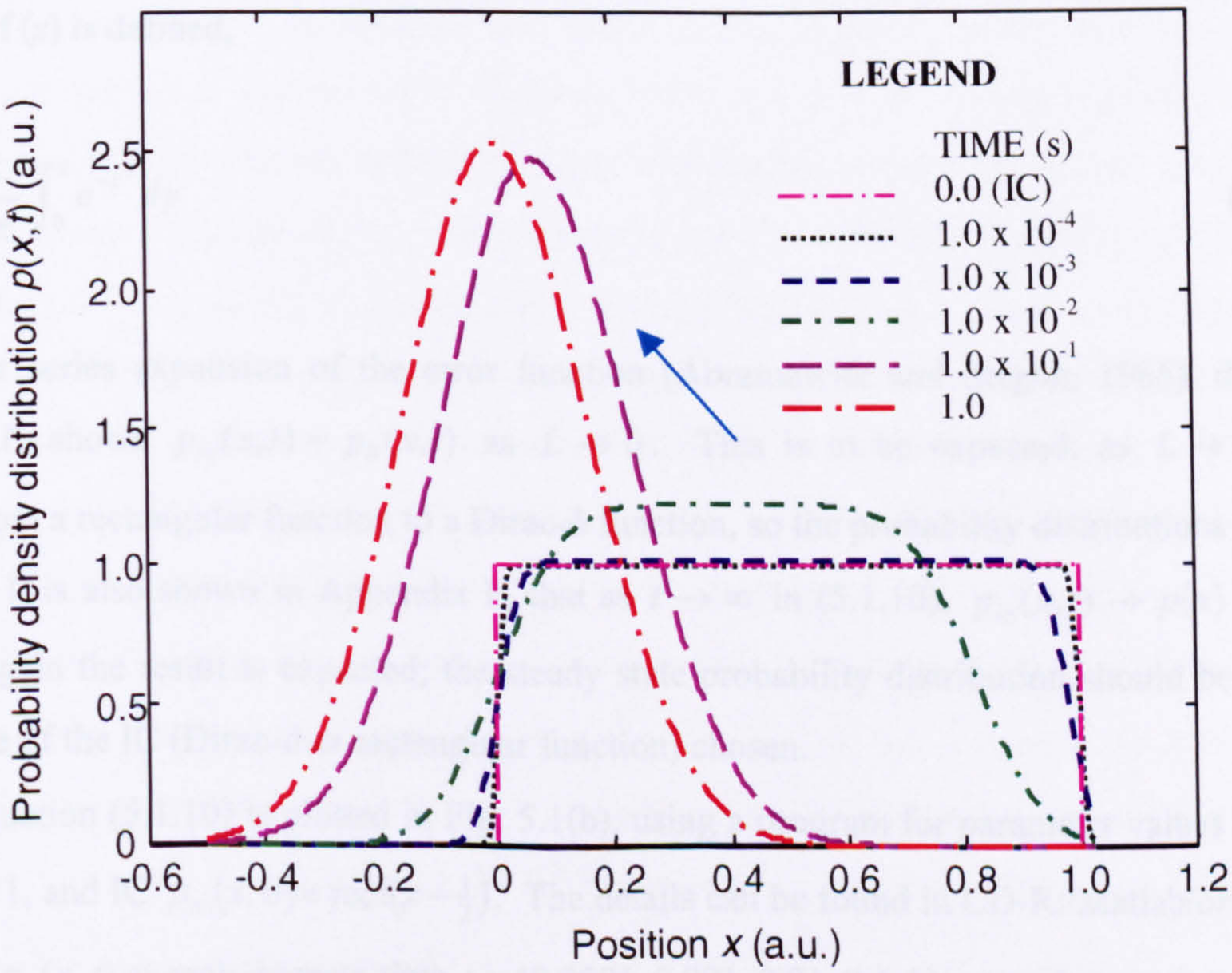

Fig. 5.1(b) Evolution of the probability density for the Ornstein-Uhlenbeck process at discrete times using a rectangular function for the initial condition (IC).

$$\text{where } \text{rect}(x/L)=\begin{cases}1, & |x|<L/2\\ 0, & |x|>L/2\end{cases} \tag{5.1.8}$$

(Stark and Tuteur, 1979, p.48) and rect(x) is shown to be constructed from a superposition of two step functions of the form u(x - L),[2]

$$\text{u}(x-L)=\begin{cases}1, & x>L\\ 0, & x<L\end{cases} \tag{5.1.9}$$

The solution of the O-U process (5.1.2) using the IC (5.1.7) is described in Appendix F. The method is assisted with the work from (Gardiner, 1985, p. 75-6) and exploiting Fourier Transform relationships. Using the above normalised rectangular function (5.1.8), centred at $x_0 = L/2$ (that is, $p(x,0) = 1/L$ from $x=0$ to $x=x_0+L$), the PS is given by (F.17b),

$$p_{\text{rc}}(x,t)=\frac{e^{kt/\zeta}}{2L}\left[\text{erf}\left(\frac{x}{2\sqrt{\frac{D}{2k/\zeta}\left(1-e^{-2kt/\zeta}\right)}}\right)-\text{erf}\left(\frac{x-Le^{-kt/\zeta}}{2\sqrt{\frac{D}{2k/\zeta}\left(1-e^{-2kt/\zeta}\right)}}\right)\right] \tag{5.1.10}$$

where the subscript *rc* denotes normalised rectangular function (5.1.7) as the IC. The error function erf (z) is defined,

$$\text{erf}(z)=\frac{2}{\sqrt{\pi}}\int_0^z e^{-\gamma^2}d\gamma \tag{5.1.11}$$

The Taylor series expansion of the error function (Abramowitz and Stegun, 1965), detailed in Appendix F, shows $p_{rc}(x,t) = p_{\delta}(x,t)$ as $L\to 0$. This is to be expected: as $L\to 0$ the IC changes from a rectangular function to a Dirac-δ function, so the probability distributions should be the same. It is also shown in Appendix F, that as $t\to\infty$ in (5.1.10), $p_{rc}(x,t)\to p(x)$ given by (5.1.4). Again the result is expected; the steady state probability distribution should be the same irrespective of the IC (Dirac-δ or rectangular function) chosen.

Equation (5.1.10) is plotted in Fig. 5.1(b), using a program for parameter values $k/\zeta = 20$, $D = 1, L = 1$, and IC $p_{\text{rc}}(x,0)=\text{rect}\left(x-\frac{1}{2}\right)$. The details can be found in CD-R:/Matlab/*oruh.m*. The profiles of $p_{\text{rc}}(x, t)$ at each discrete time $t=\{0.0001, 0.001, 0.01, 0.1, 1\}$ seconds reveals at least two

---

[2] Some definitions of the unit step function state u(0) = ½. For the applications needed in this dissertation, this equality condition is not required. The equality has also been omitted, for consistency, from the definition of the rectangular function.

interesting features. The first concerns the rapid change from the 'almost rectangular' shape of the probability density $p_{rc}(x)$ at $t=10^{-4}$ seconds to the 'nearly Gaussian' (or 'bell') shape at t = 0.1 seconds. This contrasts with the relatively small change in the bell shape in the interval from 0.1 to 1 second (and t > 1 second – not shown). This is a common feature of a diffusion limited transport process. The second feature is the movement of the centre of the density at x = ½ (rectangular) to x = 0 (bell shape). This is a consequence of the parabolic potential that forces the particles to the centre, x = 0. The width of the bell shape and temporal evolution of the density is governed by the constants k, ζ and D. Increasing the drag coefficient ζ, for example, slows the temporal evolution, and increasing $k/(k_BT)$ narrows the width of the stationary bell shape.

These features of the O-U process are useful to bear in mind since quite similar characteristics will be shown in the following sections for particle collections onto planar surfaces using positive DEP forces. This is interesting because the positive DEP force on a particle is very different to the linear increase of force with displacement, $F = -kx$ (in the O-U process). Typically the magnitude of positive DEP force *decreases* with displacement perpendicular from the electrode plane.

5.2 1-D DEP collection onto an impenetrable boundary

The interdigitated electrode geometry, as described in Chapter 3, is horizontal, and planar symmetric. Advantage can be taken of this design in that it covers a relatively large area with respect to the transverse dimensions of electrode width w and inter-electrode spacing (or gap) d. Interdigitated electrodes that are sufficiently long, with respect to w and d, imply the electric field is invariant in this longitudinal, $\vec{u}_z$, dimension and the 3-D DEP model can be reduced to two dimensions (2-D). Figure 5.2 illustrates a side view (in the transverse plane) of the interdigitated array (with particle suspension capped by a cover-slip) shown in Fig. 3.2(a). In the 2-D model, the DEP force can be represented as an exponential function – as shown in Chapter 6 (section 6.3.2). Furthermore, at a distance above the surface, $y = w + d$, the electric field profile from the interdigitated electrode array tends to become invariant in transverse direction, $\vec{u}_x$.

The first approximation is to allow transverse invariance to be valid for y values, $0 \le y \le h$ between electrode array and cover slip. This is an idealization, but it enables the 2-D collection rate model to be simplified to a 1-D model, where particle movement is considered only in the direction $\vec{u}_y$ as shown in Fig. 5.2. In the following sections, the 1-D FPE model simulating the DEP collection rate experiment will adopt y as the independent variable. Therefore, the independent variable x in the FPE (5.0.1) is replaced by y,

$$\frac{\partial p(y,t)}{\partial t} = -\frac{\partial J(y,t)}{\partial y} = -\frac{\partial \left(p(y,t)v(y)\right)}{\partial y} + D\frac{\partial^2 p(y,t)}{\partial^2 y} \qquad (5.2.1)$$

and the flux is also re-written, $J(y,t) = p(y,t)v(y) - D\frac{\partial p(y,t)}{\partial y}$.

The 1-D FPE modelling of DEP collection rates poses an interesting problem in terms of finding an elegant analytical solution for the probability density function, $p(y, t)$. This is because the magnitude of DEP force is very large near the electrode array (or boundary), thereby strongly attracting particles nearby towards it, as shown in Fig. 5.2. The actual electrode array surface, however, is impenetrable to particles; so although the particles are increasingly attracted as they approach the boundary, their movement is ultimately reversed, or reflected. The barrier itself is needed to guarantee a stationary solution. In view of the elegant O-U model presented in the previous section, it may be tempting to 'design' a drift force (or velocity) term in the FPE that mimics this situation. However, it appears to be very difficult to 'design' such a form for the DEP force that increases (in magnitude) as y decreases, accommodates the effect of an impenetrable barrier, and enables the PDE to be solved analytically.

The O-U model has an 'advantage' in the sense that the parabolic potential automatically causes particle drift towards the centre and results in a stationary, or steady state, solution. It appears the 1-D FPEs suitable for modelling DEP experiments, have a form that requires imposing BCs in order to obtain stationary analytical solutions. As a consequence, it seems the reflecting barrier needs to be imposed onto the PDE solution set via a BC, it cannot be modelled into the FPE DEP force term *per se*.

The experimental arrangement described in Chapter 3 (of particles suspended in a small aqueous volume) also means that another boundary must be imposed at a plane parallel and above the planar electrode array. In practice a cover-slip is used to reduce evaporation, so this forms the upper barrier. Thus, there are two impenetrable barriers in the 1-D model: the planar array lower barrier at $y = a$, and upper barrier at $y = b$, as shown in Fig. 5.2. The height h of the cover-slip is taken with respect to the planar array, so $h = b - a$ [3]. The two impenetrable barriers mean the particle flux J defined in (5.2.1) is zero at $y = a$ and $y = b$ (Gardiner, 1985, p. 121). This yields two BCs for the 1-D model,

$$J(a,t)=0=J(b,t)\ \forall\ t \qquad (5.2.2)$$

As a consequence of the BCs being imposed as discussed above, the time dependent 1-D FPE is analytically solved in section 5.2.2 by the eigenfunction expansion method (Kreyszig, 1967, chs. 8 and 9; Tolstov, 1962).

---

[3] The lower boundary can be set $a = 0$, so $b = h$ but this depends on how parameters, such as the DEP force, are defined.

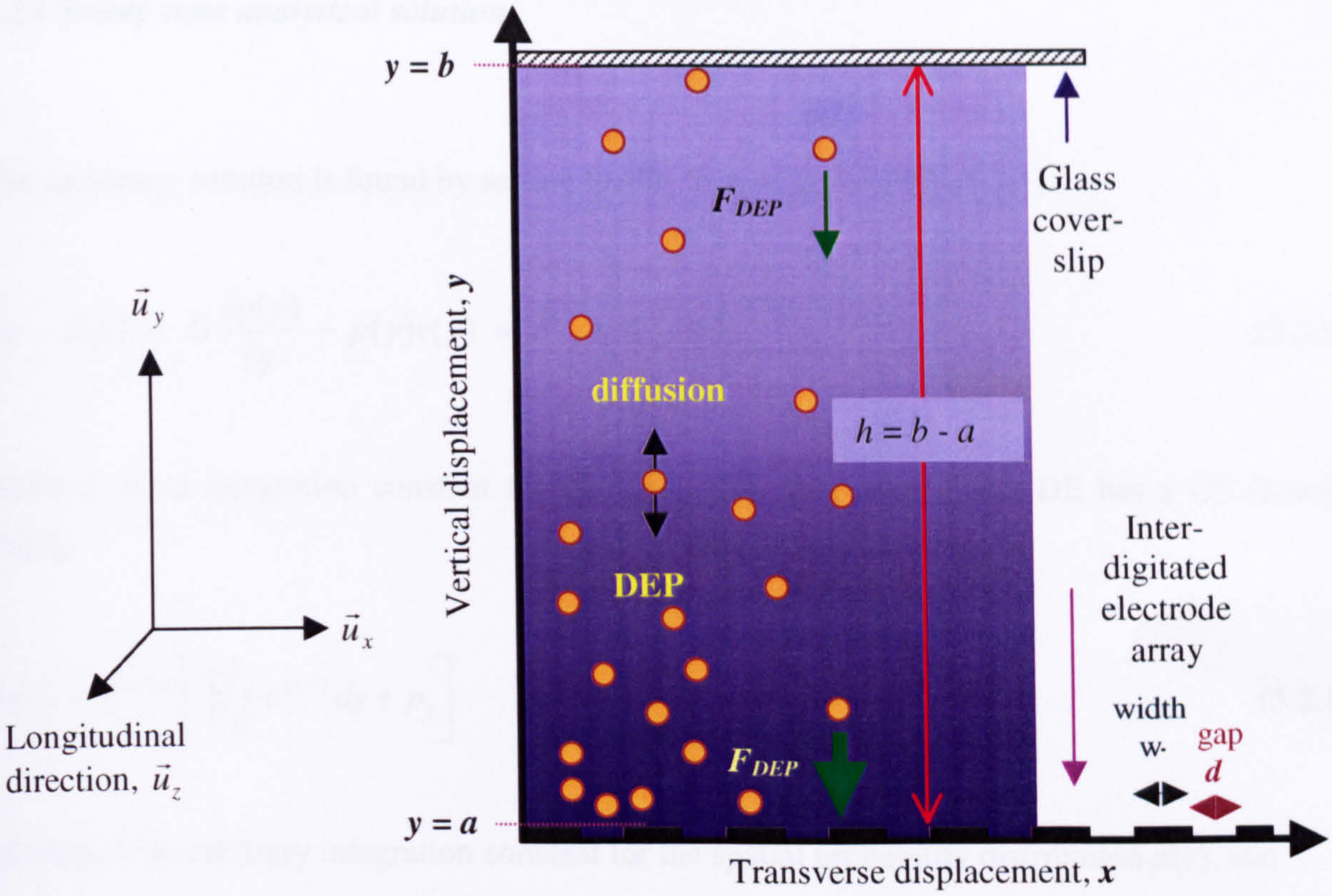

Fig. 5.2 One dimensional (1-D) movement of particles between glass cover-slip (upper boundary) and planar interdigitated electrode array (lower boundary) - side-view.

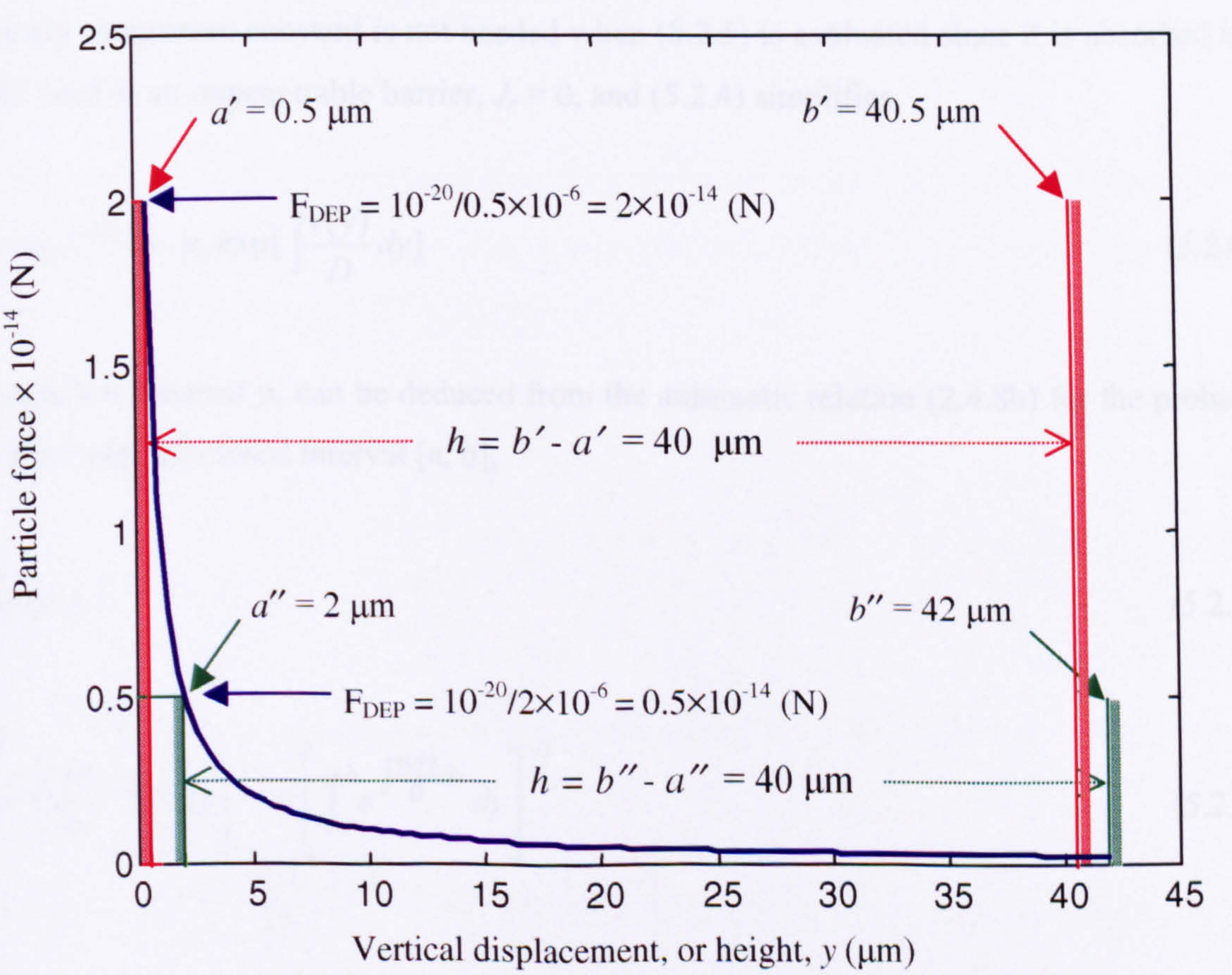

Fig. 5.3 Hyperbolic force profile with a value for the DEP force coefficient $k = 10^{-20}$ (J). The illustration shows how choices for lower and upper boundary values a and b (keeping h constant) governs the DEP force imposed on a particle located at the lower boundary.

5.2.1 Steady state analytical solution

The stationary solution is found by setting the *lhs* to zero in the FPE (5.2.1)

$$\Rightarrow -J(y) = D\frac{dp(y)}{\partial y} - p(y)v(y) = J_c,\ a \le y \le b \tag{5.2.3}$$

where J_c is an integration constant for the flux. The first order linear DE has a GS (Kreyszig, 1967),

$$p(y) = e^{-\xi(y)}\left[\int\frac{J_c}{D}e^{\xi(y)}\,dy + p_c\right] \tag{5.2.4}$$

where p_c is an arbitrary integration constant for the spatial probability distribution $p(y)$, and

$$\xi(y) = \int\frac{-v(y)}{D}dy \tag{5.2.5}$$

An arbitrary integration constant is not needed when (5.2.5) is evaluated since it is absorbed by p_c. For a BC such as an impenetrable barrier, $J_c = 0$, and (5.2.4) simplifies,

$$p(y) = p_c e^{-\xi(y)} = p_c \exp[\int\frac{v(y)}{D}dy] \tag{5.2.6}$$

The integration constant p_c can be deduced from the axiomatic relation (2.4.8b) for the probability density $p(y)$ over the closed interval [a, b],

$$\int_a^b p(y)\,dy = 1 \tag{5.2.7}$$

$$\therefore\ p_c = \left[\int_a^b e^{-\xi(y)}\,dy\right]^{-1} = \left[\int_a^b e^{\int\frac{v(y)}{D}dy}\,dy\right]^{-1} \tag{5.2.8}$$

5.2.2 Time dependent analytical solution: eigenfunction expansion

Expanding the probability density $p(y, t)$ in a series product of separate functions $g(y)$ and $h(t)$,

$$p(y,t) = \sum_{m=0}^{\infty} g_m(y) h_m(t) \tag{5.2.9}$$

(5.2.1) can be written in product form,

$$\frac{\partial\left(\sum_{m=0}^{\infty} g_m(y)h_m(t)\right)}{\partial t} = -\frac{\partial\left(v(y)\sum_{m=0}^{\infty} g_m(y)\,h_m(t)\right)}{\partial y} + \frac{k_B T}{\zeta}\frac{\partial^2\left(\sum_{m=0}^{\infty} g_m(y)h_m(t)\right)}{\partial y^2} \tag{5.2.10}$$

$$\therefore \sum_{m=0}^{\infty} g_m(y)\frac{dh_m(t)}{dt} = \sum_{m=0}^{\infty} h_m(t)\left(-\frac{d\left(v(y)g_m(y)\right)}{dy} + \frac{k_B T}{\zeta}\frac{d^2 g_m(y)}{dy^2}\right) \quad \text{or,}$$

$$g_m(y)\frac{dh_m(t)}{dt} = h_m(t)\left(-\frac{d\left(v(y)g_m(y)\right)}{dy} + \frac{k_B T}{\zeta}\frac{d^2 g_m(y)}{dy^2}\right) \tag{5.2.11}$$

The second line, written in abbreviated from, is understood to mean the PDE pertains to the mth eigenmode. Equation (5.2.11) is separable. Integrating each side of (5.2.11) separately, using ρ as an integration constant, the *lhs* GS for $h(t)$ is

$$\frac{1}{h_m(t)}\frac{dh_m(t)}{dt} \equiv -\rho_m^2 \;\Rightarrow \int\frac{1}{h_m}dh_m = -\rho_m^2\int dt$$

$$\Rightarrow h_m(t) = e^{-\rho_m^2 t} \tag{5.2.12}$$

and the *rhs* of (5.2.11) becomes a second order DE for $g(y)$,

$$\frac{k_B T}{\zeta}\frac{d^2 g_m(y)}{dy^2} - \frac{d\left(v(y)g_m(y)\right)}{dy} + g_m(y)\rho_m^2 = 0 \tag{5.2.13}$$

The system (5.2.9) (5.2.12) and (5.2.13) can be analytically solved to find a GS if $v(y)$ has the appropriate form.

Consider, now, the probability flux $J(y, t)$. Writing (5.2.1) in expanded form it is

$$J(y,t) = \sum_{m=0}^{\infty} h_m(t)\left(g_m(y)v(y) - D\frac{dg_m(y)}{dy} \right) \tag{5.2.14}$$

For a BC such as a reflecting, or impenetrable, barrier the flux is zero. Consider, for example, the barrier at $y = a$. For each m

$$J_m(a,t) = h_m(t)\left(g_m(y)v(y) - D\frac{dg_m(y)}{dy} \right)\Bigg|_{y=a} = 0 \tag{5.2.15}$$

If $h_m(t) \neq 0$ (which is the case for $\rho, t \neq \infty$) then,

$$g_m(y)v(y) - D\frac{dg_m(y)}{dy}\Bigg|_{y=a} = 0 \text{ or}$$

$$Dg'_m(a) = g_m(a)v(a) \tag{5.2.16}$$

The steady state solution is reached as time $t \to \infty$ and can be checked with the steady state solution determined in section 5.2.1 (as was described in section 5.1 for the Ornstein-Uhlenbeck process).

5.2.3 Numerical solution

The FPE (5.2.1) can be solved using finite difference, or finite element, methods (Ames, 1969; Smith, 1978; Zienkiewicz and Taylor, 1989; Strang, 1986, Ch. 5). Both techniques transform the PDE, which is a continuous problem, into a discrete one. To find the solution, the finite element difference method approximates the partial derivatives by differences (or gradients), whereas the finite element method fits trial functions into the geometry of the PDE. The finite element method has become increasingly popular for solving many PDEs and software packages are commercially available. The software purchased for solving 1-D and 2-D FPEs was FlexPDE (PDE Solutions, CA, USA) version 2.15. This software uses a specific programming language that enables users to solve a wide range of PDEs without needing an intimate knowledge of finite element techniques. The finite element method is essentially set up for solving 2-D surfaces. The 1-D FPE (5.2.1) was solved by representing the 1-D interval $a \le y \le b$ as a thin 2-D strip $a \le y \le b$ and

$-\frac{c}{2} \le x \le \frac{c}{2}$ where typically $c \le \frac{b-a}{20}$. FlexPDE discretized the solution space (x, y) into a mesh of small triangles and fitted a quadratic polynomial trial function for each triangular area.

The literature on finite elements (Zienkiewicz and Taylor, 1989; Mathworks PDE User's Guide, 1997) describes the extensive methods for finding the solutions to PDEs. One of the initial steps finite element solvers perform is recasting the PDE in integral form. In this context, the most important (and initially, problematic) step for obtaining a satisfactory solution was defining the boundary conditions in an appropriate form. As stated in the previous section the impenetrable boundaries at $y = a$ and $y = b$ requires the particle flux at both boundaries to be zero for all time (5.2.2), $J(a,t)=0=J(b,t)\ \forall\ t$. In addition, since the 1-D problem is modelled as a 2-D PDE, then

$$J(x,a,t)=0=J(x,b,t)\ \forall\ t \qquad \text{and} \qquad J(-\tfrac{c}{2},y,t)=0=J(+\tfrac{c}{2},y,t)\ \forall\ t$$

or

$$p(x,y,t)v(x,y)-D\frac{\partial p(x,y,t)}{\partial x}-D\frac{\partial p(x,y,t)}{\partial y}\bigg|_{\substack{x=-\frac{c}{2},\frac{c}{2}\\ y=a,b}}=0\forall t \tag{5.2.17}$$

Satisfying this requirement means the probability density integral condition (2.4.18a) over the entire region $x \in [\frac{-c}{2},\frac{c}{2}]$, $y \in [a,b]$ should remain at unity,

$$\int_a^b \int_{-c/2}^{+c/2} p(x,y,t)\,dxdy = 1\ \forall t \tag{5.2.18}$$

However, it was not possible to implement the zero flux relations, as written in (5.2.17), directly using FlexPDE code. Attempting to do so resulted in the probability density integral being far from unity as t became very large, thus violating (5.2.18). Physically this meant the boundaries were *not* impenetrable thus allowing particles to 'leak' into the abovementioned 2-D region! The leakage was pronounced when simulations used high DEP forces (resulting in large particle fluxes). The reason for this 'leakage', as pointed out by the staff at PDE Solutions, is that the finite element method does not allow the BC (5.2.17) to be imposed on the dependent variable $p(x,y,t)$ precisely at the stipulated boundaries. To implement BCs, FlexPDE provides a command called a 'natural' BC that integrates by parts the *second* order spatial derivatives of the PDE. However, this does not address the *first* order spatial derivative velocity (or drift) term of the FPE (5.2.1). The leakage problem was remedied by using FlexPDE command 'firstparts' that explicitly integrates the *first* order spatial derivative thus enabling the BCs (5.2.17) to be satisfactorily implemented.

It should be noted that (5.2.18) is an idealization in the sense that some numerical error is practically inevitable. A more practical condition is

$$\int_a^b \int_{-c/2}^{+c/2} p(x,y,t)\,dx\,dy = 1 \pm \varepsilon(t) \qquad (5.2.19)$$

where the time dependent error $|\varepsilon(t)| \leq \varepsilon_{max}$ never exceeds ε_{max}, the maximum tolerable error. Typically $\varepsilon_{max} = 0.1$ or 10% relative error, and was minimised by stipulating an error limit and using a 'feature' command to force a finer mesh near boundaries where high DEP forces were applied. The program error limit and feature commands are listed in each FlexPDE program. The error was easily monitored and in most simulations $|\varepsilon(t)|$ exceeded not more than 0.01%.

5.2.4 DEP collection measures

There are two important parameters that describe the temporal evolution of the particle probability density, $p(y, t)$. These are rise amplitude and rise time. These are used in the following sections and have practical relevance in terms of experimental measurements.

5.2.4.1 Rise amplitude and time

The change in probability density from initial state at $t = 0$ to steady state at $t \to \infty$, is written as $\Delta p(y) = p(y,\infty) - p(y,0)$ for any y over the closed interval $[a, b]$. In this chapter, our interest lies in DEP collections at $y = a$ where $p(a, \infty) > p(a, 0)$, so that the increase or 'rise amplitude' is expressed as $\Delta p(a) = p(a, \infty) - p(a, 0)$. In addition to particle collections on the boundary at $y = a$, our interest also lies in particle movement away from the boundary after the DEP force is switched off. The process is called particle *relaxation* and is characterised by the *fall* amplitude. The following sections analyse collections followed by relaxations that are equal in magnitude. Consequently, for convenience, the rise and fall amplitudes are defined by their *magnitude*. The *rise amplitude* is written as,

$$A = |p(a,\infty) - p(a,0)| \qquad (5.2.20)$$

To maintain notational consistency with the previous sections, $p(y,\infty)$ and $p(y)$ are the same, i.e. $p(y,\infty) \equiv p(y)$. The corresponding parameter observed experimentally is the particle concentration that is related to the density by (2.4.20), so $\Delta c(a) = c(a, \infty) - c(a,0) = N\,\Delta p(a)$ where N is the number of particles within the system. In the situation where two experiments are being compared and N remains *constant*, then the ratio of the changes in concentration is

$$\frac{|\Delta c_2(a)|}{|\Delta c_1(a)|} = \frac{N|\Delta p_2(a)|}{N|\Delta p_1(a)|} = \frac{A_2}{A_1} \tag{5.2.21}$$

In subsequent sections, 5.3 – 5.5, where collection and relaxation time profiles are described and amplitudes are compared, it is helpful to understand their direct relation to the concentration changes.

The second parameter for describing time profiles of $p(a, t)$ is the *rise time* τ_{rise}. This is the time for $p(a, t)$ to increase by about 63% of the final value, or t such that

$$p(a,t) = [p(a,\infty) - p(a,0)](1 - e^{-1}) + p(a,0) \tag{5.2.22}$$

The parameter is based on approximating the collection characteristic with a single exponential rise. This is crude but given the experimental profile in Fig. 3.13(b) and simulations in the following sections, it is quite reasonable. A related parameter for relaxations is the *fall time*, τ_{fall}, and is detailed further in section 5.3.3.3.

5.2.4.2 Relative amplitude

If the collections of two more Gedanken experiments are being compared and have different values of the IC, $p(a,0)$ then an alternative and useful parameter is the rise amplitude relative to $p(a,0)$, or *relative amplitude*,

$$A_r = \frac{A}{p(a,0)} = \frac{|p(a,\infty) - p(a,0)|}{p(a,0)} \tag{5.2.23}$$

The IC can vary, for example, if the cover-slip height $h = b - a$, as illustrated in Fig. 5.2, is different for each experiment. This is a consequence of the axiomatic condition (2.4.18a) that requires the integral of $p(y, t)$ over $[a, b]$ to be unity.

In the experimental situation where h is proportional to the volume of solvent used in the DEP experiment and the number of particles within the system, N, remains *constant* for all experiments, then

$$\frac{\Delta c_2(a)/c_2(a,0)}{\Delta c_1(a)/c_1(a,0)} = \frac{\Delta p_2(a)/p_2(a,0)}{\Delta p_1(a)/p_1(a,0)} = \frac{A_{r2}}{A_{r1}} \tag{5.2.24}$$

where the modulus sign has been dropped for convenience because all quantities are positive. In addition, if N is allowed to vary from one experiment to another, such that, $N = \hat{N} / p(a,0)$ where $\hat{N}$ and $c(y, 0)$ remain constant, then

$$\frac{\Delta c_2(a)}{\Delta c_1(a)} = \frac{N_2 \Delta p_2(a)}{N_1 \Delta p_1(a)} = \frac{\hat{N}\,\Delta p_2(a) / p_2(a,0)}{\hat{N}\,\Delta p_1(a) / p_1(a,0)} = \frac{A_{r2}}{A_{r1}} \tag{5.2.25}$$

A practical example of this situation is where two different volumes of the same particle concentration are micropipetted on the electrode array so that the cover-slip height h changes proportionally to the volume. Consequently, due to the usefulness of the relative rise amplitudes, A_r, their values are also compared and tabulated adjacent to the A values in the following sections, 5.3 to 5.5.

5.3 1-D DEP collection: hyperbolic force model

The use of a hyperbolic spatial force for investigating DEP movement is convenient because it provides a solution that is analytically tractable. This also enables verification of the time dependent numerical solution for same parameter values. The hyperbolic velocity is written as

$$v(y) = \frac{F_{dep}(y)}{\zeta} = \frac{-k / y}{\zeta} \tag{5.3.1}$$

where k is the hyperbolic force coefficient with units of energy (J). Substituting (5.3.1) into (5.2.1) gives the 1-D FPE describing the spatial-temporal evolution of the probability density $p(y, t)$,

$$\frac{\partial p(y,t)}{\partial t} = \frac{k}{\zeta} \frac{\partial (p(y,t) / y)}{\partial y} + \frac{k_B T}{\zeta} \frac{\partial^2 p(y,t)}{\partial^2 y} \tag{5.3.2}$$

The use of a hyperbolic profile is justified in Chapter 6 where the DEP force is shown to be approximately hyperbolic in the near field, (6.3.19). In this section the hyperbolic profile is used in both the near and far field. This is a simplification. As will become clearer later, the hyperbolic profile tends to overestimate the DEP force in the far field for typical parameter values used. This highlights the important effect of the collection rate rise time dependence on the cover-slip height.

Equations (5.3.1) and (5.3.2) are valid over restricted domain $\{y : a \le y \le b\}$, $a > 0$, where a and b are respective lower and upper limits of the vertical displacement y. The hyperbolic force profile is defined by values of a and b. The effects of changing these values but maintaining

constant cover-slip height above the electrode surface $h = b - a$, is shown in Fig. 5.3 (p. 114). Choosing a convenient and realistic value of $k = 10^{-20} \cong 2.5k_BT$, the hyperbolic force profile is plotted for $0.5 \leq y \leq 42\ \mu$m. Selecting $y = a' = 0.5\ \mu$m leads to DEP force $F_{DEP} = 2\text{x}10^{-14}$ (N) at this lower boundary. This is four times higher than the force resulting from selecting $y = a'' = 2\ \mu$m. On the other hand, selecting for the upper boundary $y = b' = 40.5\ \mu$m leads to a marginally larger force than arising from $y = b'' = 42\ \mu$m. Therefore, the judicious choice of interval $[a, b]$ has an important influence on the DEP force profile, in particular, the force acting on particles located near the lower reflecting barrier $y = a$. The implications for the collection and relaxation profiles is discussed further in following sections, especially 5.3.3.1.

5.3.1 Hyperbolic DEP force: steady state analytical solution

The steady state probability distribution is found by imposing BCs at $y = a$ or $y = b$ that require steady state probability flux, $J(a) = J(b) = 0$. Hence, (5.2.6) is justified. Substituting (5.3.1) into (5.2.6), gives the steady state GS,

$$p(y) = p_c \exp[\int \frac{-k/\zeta}{yD} dy] = p_c \exp[\frac{-k}{k_BT} \ln|y|] = p_c \exp[\frac{-k}{k_BT} \ln y] \tag{5.3.3}$$

Substituting (5.3.1) into (5.2.8),

$$p_c = \left[\int_a^b e^{-\frac{k}{k_BT}\ln y}\, dy\right]^{-1} = \left[\int_a^b y^{\left(-\frac{k}{k_BT}\right)} dy\right]^{-1} = \left[\int_a^b y^{(2\alpha-1)} dy\right]^{-1} \tag{5.3.4a}$$

$$\Rightarrow \frac{1}{p_c} = \int_a^b y^{(2\alpha-1)} dy = \begin{cases} \left[\frac{y^{2\alpha}}{2\alpha}\right]_a^b = \frac{b^{2\alpha} - a^{2\alpha}}{2\alpha}, & \alpha \neq 0 \\ [\ln(y)]_a^b = \ln(b) - \ln(a), & \alpha = 0 \end{cases} \tag{5.3.4b}$$

where $\alpha = \frac{1}{2} - \frac{k}{2k_BT}$ (the reason for using α becomes clear in the next section). Substituting (5.3.4b) into (5.3.3), the steady state PS is

$$p(y) = p_c y^{(2\alpha-1)} = \begin{cases} \frac{2\alpha y^{2\alpha-1}}{b^{2\alpha} - a^{2\alpha}}, & \alpha \neq 0 \\ \frac{1}{y\ln(b/a)}, & \alpha = 0 \end{cases} \tag{5.3.5}$$

5.3.2 Hyperbolic DEP force: time dependent analytical solution

The 1-D FPE with hyperbolic DEP force profile, (5.3.2) is solved for $p(y, t)$ using the eigenfunction expansion method. Substituting (5.3.1) into the ODE for $g(y)$ given by (5.2.13), and rearranging,

$$g_m''(y) + \frac{k}{k_B T}\frac{g_m'(y)}{y} + \left(\frac{\zeta \rho_m^2}{k_B T} - \frac{k}{k_B T}\frac{1}{y^2}\right) g_m(y) = 0 \qquad (5.3.6a)$$

and is re-written in a form that has an identifiable GS (Gradshteyn and Ryzhik, 1994, p. 985),

$$g_m''(y) + \frac{(1-2\alpha)}{y} g_m'(y) + \left(\beta_m{}^2 + \frac{\alpha^2 - \mu^2}{y^2}\right) g_m(y) = 0 \qquad (5.3.6b)$$

where the coefficients are,

$$\alpha \equiv \frac{1}{2} - \frac{k}{2k_B T},$$

$$\beta_m \equiv \sqrt{\frac{\rho_m{}^2 \zeta}{k_B T}}, \text{ and} \qquad (5.3.7)$$

$$\mu^2 \equiv \alpha^2 + \frac{k}{k_B T} \Rightarrow \mu = \pm\left(\frac{1}{2} + \frac{k}{2k_B T}\right)$$

The most convenient GS of (5.3.6b) is expressed in terms of the linear superposition of two Bessel functions of the first kind $J_\mu(z)$ with order μ that is real, $\mu \in R$ and non-integer value, $\mu \notin J$, to guarantee linear independence of the Bessel functions (Lebedev, 1965, p. 104-5, 112-113; Tolstov, 1962, chs. 8 and 9). The GS is written,

$$g_m(y) = y^\alpha \left(C_{1_m} J_{-\mu}(y\beta_m) + C_{2_m} J_{+\mu}(y\beta_m)\right) \qquad (5.3.8a)$$

where C_{1_m} and C_{2_m} are arbitrary integration constants, and the order $\mu \geq 0$

$\Rightarrow \mu = \frac{1}{2} + \frac{k}{2k_B T}$ and the relation holds

$$\alpha + \mu = 1 \qquad (5.3.8b)$$

Differentiating (5.3.8a) twice, and using recursion formulae, verifies it is a GS of (5.3.6b). To find the PS, two BCs and the IC are needed to determine particular values for β_m, C_{1_m} and C_{2_m}. The two BCs are found from the flux being zero at bottom electrode plane (lower boundary $y = a$) and the cover-slip (upper boundary $y = b$). Substituting (5.3.1) into (5.2.16),

$$J_m(y)\big|_{y=a,b} = \left[-\frac{k_B T}{\zeta}\frac{dg_m(y)}{dy} + g_m(y)\left(\frac{-k/y}{\zeta}\right)\right]\Bigg|_{y=a,b} = 0 \qquad (5.3.9)$$

$$\therefore \ \left[g'_m(y) + (1-2\alpha)g_m(y)/y\right]\big|_{y=a,b} = 0 \ \text{ or, expressing the two BCs separately}$$

$$g'_m(a) + (1-2\alpha)g_m(a)/a = 0 \quad \text{and} \quad g'_m(b) + (1-2\alpha)g_m(b)/b = 0 \qquad (5.3.10)$$

Using the GS (5.3.8), the two BC equations (5.2.10) are solved – the details are in Appendix G. The procedure for finding the PS is to evaluate the eigenvalues β_m, the ratio of the constants $C_{R_m} = C_{2_m}/C_{1_m}$, and finally C_{1_m}. A schematic outline of the procedure is shown in Fig. 5.4(a).

The eigenvalues β_m are specified when the following relation, derived from the expression for the eigenvalue determinant (G.10-12), holds

$$J_{1-\mu}(b\beta_m)J_{\mu-1}(a\beta_m) - J_{1-\mu}(a\beta_m)J_{\mu-1}(b\beta_m) = 0 \qquad (5.3.11)$$

Equation (5.3.11) is typically nonlinear and β_m eigenvalues were determined by iteration in a MATLAB 5.0™ program developed by the author for this purpose (details in CD-R:/Matlab/*fpex.m*). An example plot of the *lhs* of (5.3.11) is shown in Fig. 5.4(b), for the case $k = 2k_BT \ \therefore \ \mu = 3/2$ or $\alpha = -1/2$. The β_m eigenvalues are shown as '+' signifying the roots where the eigenvalue determinant, or *lhs* of (5.3.11), is zero. In this example, the set of β_m eigenvalues $\{\beta_0, \beta_1, \beta_2, \beta_3, ...\} = \{0, 1.65\times10^5, 3.31\times10^5, 4.96\times10^5, ...\}$. Typically only 10 - 30 eigenvalues are needed, but the number depends on accuracy required, value of DEP energy k, etc. Once the set of β_m eigenvalues is determined, the ratio of the constants is computed (G.13),

$$C_{R_m} \hat{=} \frac{C_{2_m}}{C_{1_m}} = \frac{J_{1-\mu}(a\beta_m)}{J_{\mu-1}(a\beta_m)} = \frac{J_{1-\mu}(b\beta_m)}{J_{\mu-1}(b\beta_m)} \qquad (5.3.12)$$

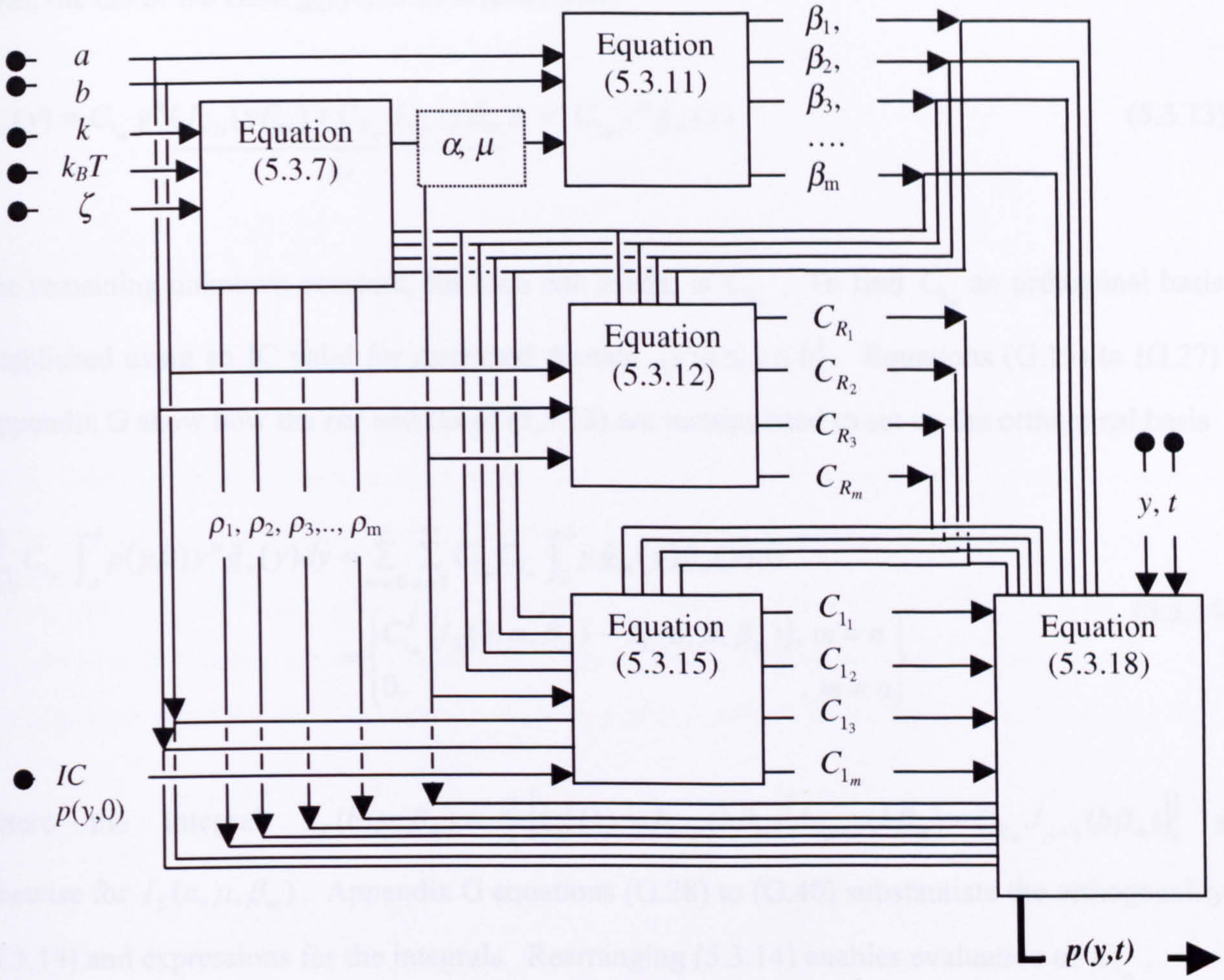

Fig. 5.4(a) Schematic for determining particle probability density $p(y,t)$ assuming hyperbolic force profile. The solution $p(y,t)$ is governed by parameters a,b, k, k_BT, ζ and IC $p(y,0)$.

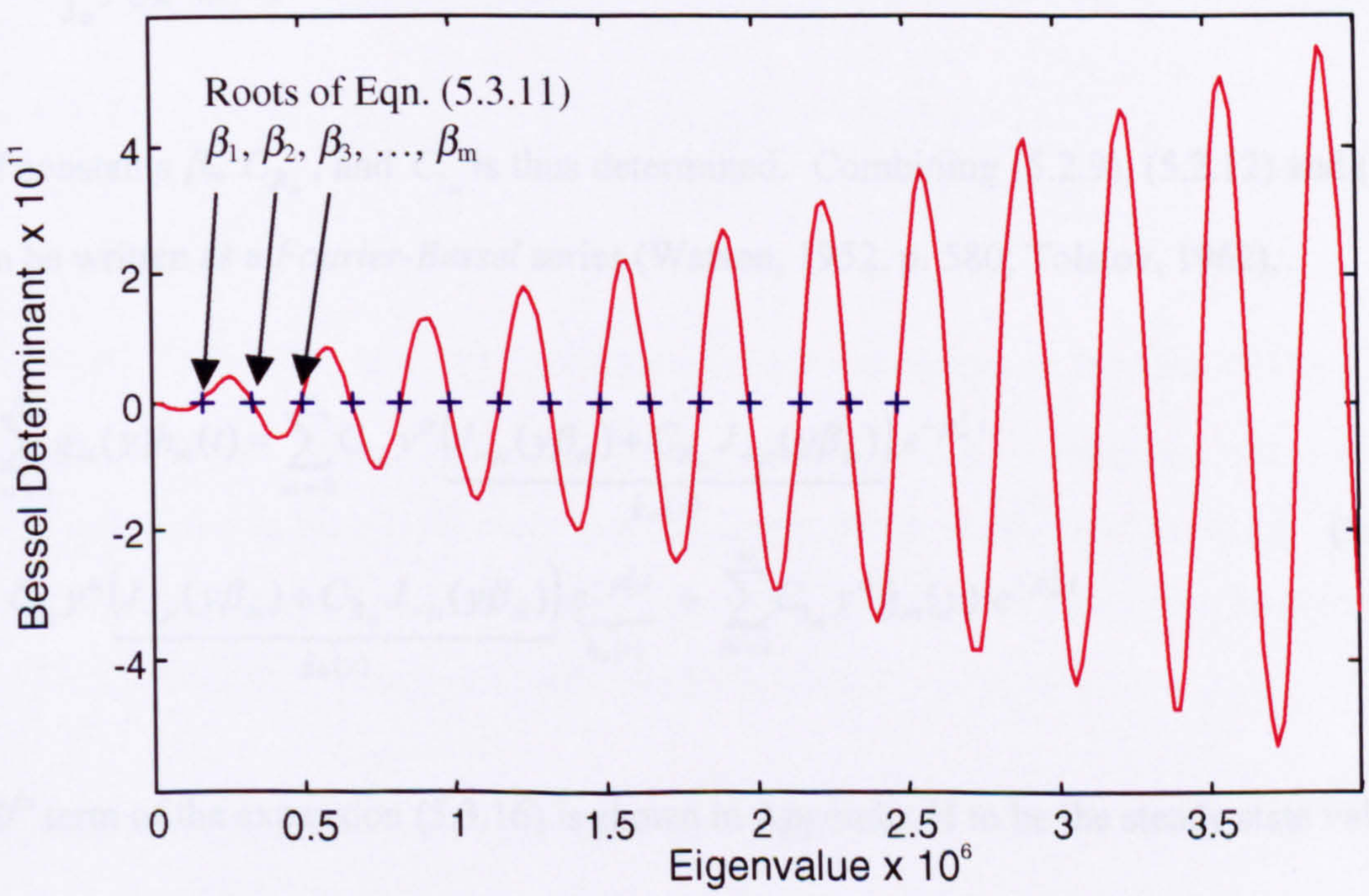

Fig. 5.4(b) Plot of the determinant equation (5.3.11) verses eigenvalue (a = 1 μm, b = 20 μm, and $k = 2\ k_BT$ or $\alpha = -1/2$).

Thus, the GS of the ODE $g(y)$ (5.3.6) is re-written,

$$g_m(y) = C_{1_m} y^{\alpha} \underbrace{(J_{-\mu}(y\beta_m) + C_{R_m} J_{+\mu}(y\beta_m))}_{\hat{g}_m} = C_{1_m} y^{\alpha} \hat{g}_m(y) \tag{5.3.13}$$

The remaining unknown constant, for each mth mode, is C_{1_m}. To find C_{1_m} an orthogonal basis is established using an IC valid for restricted domain $\{y : a \le y \le b\}$. Equations (G.15) to (G.27) in Appendix G show how the *rhs* and *lhs* of (5.3.13) are manipulated to set up the orthogonal basis

$$\begin{aligned} \sum_{n=0}^{\infty} C_{1_n} \int_a^b p(y,0) y^{\mu} \hat{g}_n(y) dy &= \sum_{m=0}^{\infty} \sum_{n=0}^{\infty} C_{1_m} C_{1_n} \int_a^b y\, \hat{g}_m(y) \hat{g}_n(y) dy \\ &= \begin{Bmatrix} C_{1_m}^2 \left(I_{\Sigma}(b,\mu,\beta_m) - I_{\Sigma}(a,\mu,\beta_m) \right), & m = n \\ 0, & m \neq n \end{Bmatrix} \end{aligned} \tag{5.3.14}$$

where the integral $I_{\Sigma}(b,\mu,\beta_m) = \frac{b^2}{2}\left[\hat{g}_m^{\,2}(b) + J_{1-\mu}(b\beta_m)\left(J_{-\mu-1}(b\beta_m) - C_{R_m} J_{\mu+1}(b\beta_m)\right)\right]$ and likewise for $I_{\Sigma}(a,\mu,\beta_m)$. Appendix G equations (G.28) to (G.40) substantiate the orthogonality of (5.3.14) and expressions for the integrals. Rearranging (5.3.14) enables evaluation of C_{1_m},

$$\therefore\ C_{1_m} = \frac{\int_a^b p(y,0)\, y^{\mu} \hat{g}_m(y) dy}{\int_a^b y\, \hat{g}_m^{\,2}(y) dy} = \frac{\int_a^b p(y,0)\, y^{\mu} \hat{g}_m(y) dy}{I_{\Sigma}(b,\mu,\beta_m) - I_{\Sigma}(a,\mu,\beta_m)} \tag{5.3.15}$$

The set of constants β_m C_{R_m}, and C_{1_m} is thus determined. Combining (5.2.9), (5.2.12) and (5.3.13) the PS can be written as a *Fourier-Bessel* series (Watson, 1952, p. 580; Tolstov, 1962),

$$\begin{aligned} p(y,t) &= \sum_{m=0}^{\infty} g_m(y) h_m(t) = \sum_{m=0}^{\infty} C_{1_m} y^{\alpha} \underbrace{\left(J_{-\mu}(y\beta_m) + C_{R_m} J_{+\mu}(y\beta_m)\right)}_{\hat{g}_m(y)} e^{-\rho_m^2 t} \\ &= C_{1_0} y^{\alpha} \underbrace{\left(J_{-\mu}(y\beta_m) + C_{R_m} J_{+\mu}(y\beta_m)\right)}_{\hat{g}_0(y)} \underbrace{e^{-\rho_0^2 t}}_{h_0(t)} + \sum_{m=1}^{\infty} C_{1_m} y^{\alpha} \hat{g}_m(y)\, e^{-\rho_m^2 t} \end{aligned} \tag{5.3.16}$$

The $m = 0^{\text{th}}$ term of the expansion (5.3.16) is shown in Appendix H to be the steady state value,

$$g_0(y) = \lim_{\beta_0 \to 0} \left\{ C_{1_0} y^{\alpha} \left(J_{-\mu}(y\beta_0) + C_{R_0} J_{+\mu}(y\beta_0) \right) \right\} = \frac{2\alpha y^{2\alpha-1}}{b^{2\alpha} - a^{2\alpha}},\ \alpha \neq 0 \tag{5.3.17}$$

As expected, it is shown to be independent of the IC and concurs with the expression for the steady state derived in (5.3.5) for the case $\alpha \neq 0$. The Fourier-Bessel expansion for the probability density, (5.3.16), is therefore written,

$$p(y,t)=\frac{2\alpha y^{2\alpha-1}}{b^{2\alpha}-a^{2\alpha}}+\sum_{m=1}^{\infty}C_{1_m}y^{\alpha}\underbrace{\left(J_{-\mu}(y\beta_m)+C_{R_m}J_{+\mu}(y\beta_m)\right)}_{\hat{g}_m(y)}e^{-\rho_m^2 t},\ \alpha\neq 0,\ \mu\notin J \qquad (5.3.18)$$

The relationships between equations (5.3.7) – (5.3.18) and information flow is summarized in Fig. 5.4(a). Before considering a number of special cases, a final note needs to be added regarding the evaluation of C_{1_m}, in particular, the numerator of (5.3.15). For DEP collections, it is sensible to assume an IC exhibiting a uniform probability distribution. The BCs at $y = a$, $(a > 0)$, and $y = b$, impose $p(y,0) = 0$ outside the region $y < a$ and $y > b$. Therefore a rectangular function is not necessary (in comparison with the O-U process) and it is sufficient to stipulate an IC simply as,

$$p(y,0)=1/(b-a) \qquad (5.3.19)$$

Hence, the numerator of (5.3.15) is

$$\int_a^b p(y,0)\,y^{\mu}\hat{g}_m(y)dy\Big|_{uniform}=\frac{1}{b-a}\int_a^b y^{\mu}\hat{g}_m(y)dy$$

$$=\frac{1}{b-a}\int_a^b y^{\mu}\left(J_{-\mu}(y\beta_m)+C_{R_m}J_{+\mu}(y\beta_m)\right)dy=\frac{\beta^{-\mu-1}}{b-a}\int_{\beta_m a}^{\beta_m b}y^{\mu}\left(J_{-\mu}(y)+C_{R_m}J_{+\mu}(y)\right)dy \qquad (5.3.20)$$

$$=\frac{\beta^{-\mu-1}}{b-a}\left[\frac{y\,{}_1F_2(\frac{1}{2};\frac{3}{2},1-\mu;\frac{-y^2}{4})}{2^{-\mu}\Gamma(1-\mu)}+C_{R_m}\frac{y^{2\mu+1}\,{}_1F_2(\mu+\frac{1}{2};\mu+\frac{3}{2},1+\mu;\frac{-y^2}{4})}{2^{-\mu}(2\mu+1)\Gamma(1+\mu)}\right]_{\beta_m a}^{\beta_m b}$$

where ${}_pF_q(\delta_1,\delta_2,...,\delta_p;\gamma_1,\gamma,...,\gamma_q;z)$ is a generalized hypergeometric function (Rainville,1960, ch. 5; Prudnikov *et al.*, 1986, Vol. I, p. 788). Hypergeometric functions are not always conveniently supported in high level computer languages (Press *et al.*, 1986) and the integrals in (5.3.20) were more conveniently evaluated using powerful built-in Gaussian Quadrature integration routines in MATLAB 5.0™ (details in CD-R:/Matlab/*fpex.m*).

5.3.3 Analytical solution: hyperbolic DEP force special cases

In this section, the 1-D FPE solution (5.3.18) is evaluated for special values of the hyperbolic force coefficient k. The values of k are chosen to facilitate simplification of the solution and yield insights about the dynamics of particle movement due to DEP-type forces and diffusion.

5.3.3.1(a) Hyperbolic DEP force with coefficient $k = 2k_BT$

A simple and interesting case occurs when the DEP force is related to thermal fluctuations by the simple relation $k = 2k_BT$ so that from (5.3.7) and (5.3.8b), $\alpha = -\frac{1}{2}$ and $\mu = 1\frac{1}{2}$. Using the definition of the Bessel function of the first kind J

$$J_{1-\mu}(y\beta_m)\Big|_{\mu=3/2} = \sqrt{\tfrac{2}{\pi y\beta_m}}\cos(y\beta_m) \tag{5.3.21a}$$

$$J_{\mu-1}(y\beta_m)\Big|_{\mu=3/2} = \sqrt{\tfrac{2}{\pi y\beta_m}}\sin(y\beta_m) \tag{5.3.21b}$$

and the recursion relation (Lebedev, 1965, p. 111; Gradshteyn and Ryzhik, 1994, p. 977-9),

$$J_{\nu-1}(z) + J_{\nu+1}(z) = \frac{2\nu}{z} J_\nu(z) \tag{5.3.22}$$

$$\Rightarrow J_{-\mu}(y\beta_m)\Big|_{\mu=3/2} = J_{-3/2}(y\beta_m) = -\sqrt{\frac{2}{\pi y\beta_m}}\left(\sin(y\beta_m) + \frac{\cos(y\beta_m)}{y\beta_m}\right) \tag{5.3.23a}$$

$$\Rightarrow J_{+\mu}(y\beta_m)\Big|_{\mu=3/2} = J_{+3/2}(y\beta_m) = \sqrt{\frac{2}{\pi y\beta_m}}\left(\frac{\sin(y\beta_m)}{y\beta_m} - \cos(y\beta_m)\right) \tag{5.3.23b}$$

Substituting (5.3.21a) and (5.3.21b) into zero flux condition BCs (5.3.10) at $y=a$ and $y=b$, (5.3.11) and (5.3.12) yield $\beta_m = \frac{\pi m}{b-a}$ and $C_{R_m} = \cot(\frac{\pi ma}{b-a}) = \cot(\frac{\pi mb}{b-a})$. The second step arises from $\sin(\frac{\pi mb}{b-a}) = \cos(m\pi)\sin(\frac{\pi ma}{b-a})$ and $\cos(\frac{\pi mb}{b-a}) = \cos(m\pi)\cos(\frac{\pi ma}{b-a})$. Hence, substituting these results in (5.3.13), for $m \neq 0$,

$$\hat{g}_{m,\frac{3}{2}}(y) = \sqrt{\frac{2}{\pi y\beta_m}}\left(-\frac{1}{y\beta_m}\cos(y\beta_m) - \sin(y\beta_m) + \cot(a\beta_m)\left[\frac{1}{y\beta_m}\sin(y\beta_m) - \cos(y\beta_m)\right]\right) \tag{5.3.24}$$

where the additional subscript '3/2' in $\hat{g}_{m,\frac{3}{2}}$ specifies the expression (5.3.24) is applicable for the case $\mu = \frac{3}{2}$. The extra '3/2' subscript is retained in the following relations. From (5.3.15)

$$C_{1_{m,\frac{3}{2}}} = \frac{\int_a^b p(y,0)\, y^{\frac{3}{2}} \hat{g}_{m,\frac{3}{2}}(y)dy}{\int_a^b y\, \hat{g}_{m,\frac{3}{2}}{}^2(y)dy} = \frac{\int_a^b p(y,0)\, y^{\frac{3}{2}} \hat{g}_{m,\frac{3}{2}}(y)dy}{[I_\Sigma(y,\frac{3}{2},\frac{\pi n}{b-a})]_a^b} \tag{5.3.25}$$

The denominator in (5.3.25) is evaluated either by substituting (5.3.24) or using the integral relations defined in (5.3.14). After some algebra,

$$\left[I_{\Sigma}(y,\tfrac{3}{2},\beta_{m\neq 0})\right]_a^b = \frac{(b-a)^2}{\pi^2 m}\operatorname{cosec}^2\left(\frac{\pi m a}{b-a}\right) \tag{5.3.26}$$

Substituting (5.3.24), (5.3.25) and (5.3.26) into (5.3.18), for an arbitrary IC $p(y,0)$

$$p(y,t)\big|_{\mu=\frac{3}{2}} = \frac{aby^{-2}}{b-a} + \frac{2}{b-a}\sum_{m=1}^{\infty}\left[\frac{1}{y^2}\int_a^b p(y,0)\,\tilde{g}_{m,\frac{3}{2}}(y)\,dy\,.\,\tilde{g}_{m,\frac{3}{2}}(y)\right]e^{-\rho^2_{m,\frac{3}{2}}t} \tag{5.3.27}$$

where $\tilde{g}_{m,\frac{3}{2}}(y) = \dfrac{\sin[\beta_m(y-a)]}{\beta_m} - y\cos[\beta_m(y-a)]$ and $\rho^2_{m,\frac{3}{2}} = \dfrac{\pi^2 m^2}{(b-a)^2}\dfrac{k_B T}{\zeta}$.

Choosing an IC with uniform distribution, $p(y,0) = 1/(b - a)$, (5.3.27) becomes

$$p(y,t)\Big|_{\substack{\mu=\frac{3}{2}\\ 1/(b-a)}} = \frac{aby^{-2}}{b-a} + \frac{2}{y^2}\sum_{m=1}^{\infty}\frac{\sin^2(m\pi/2)}{(m\pi/2)^2}\,\tilde{g}_{m,\frac{3}{2}}(y)\,e^{-\rho^2_{m,\frac{3}{2}}t} \tag{5.3.28}$$

The probability distributions given by (5.3.28) at discrete times are shown in Fig. 5.5(a). The parameter values are: $a = 1$ μm, $b = 20$ μm, and $k_BT/\zeta = 4.11\times10^{-21}/1.83\times10^{-9} = 2.24\times10^{-12}$ m^2 s^{-1}. The value of the thermal temperature and dynamic drag coefficients correspond to experimental values for 216 nm diameter spheres collecting in water at 25 °C. The height of the cover-slip $h = b-a = 19$ μm above the electrode surface is low but not unreasonable, and illustrates the essential features of DEP collection. The simulation used 15 eigenvalues (m = 1, 2, ... , 15) commencing at $t = 0$ seconds. One of the consequences of truncating the series to 15 terms is the IC, $p(y, 0)$, is shown to be not exactly uniform about $y = 1 - 2$ μm (shown by magenta - - - profile). Since the analytic form for IC is known to be uniform, this anomaly is easily compensated (shown as the black ····· profile), and the effect is not important. Elsewhere the error arising from the series truncation is negligible.

The $p(y,t)$ distribution shows a progressive increase in particle density near the lower impenetrable barrier at $y = a = 1$ μm in response to the hyperbolic DEP force that attracts the particles towards the boundary. As the particles move towards the lower boundary, there is a subsequent depletion of particle density from y > 4 μm to the upper boundary at $y = b = 20$ μm. The particle accumulation near the lower boundary is initially rapid and is shown to reach about half the final value by t = 10 seconds. The temporal evolution of particle density is nearly

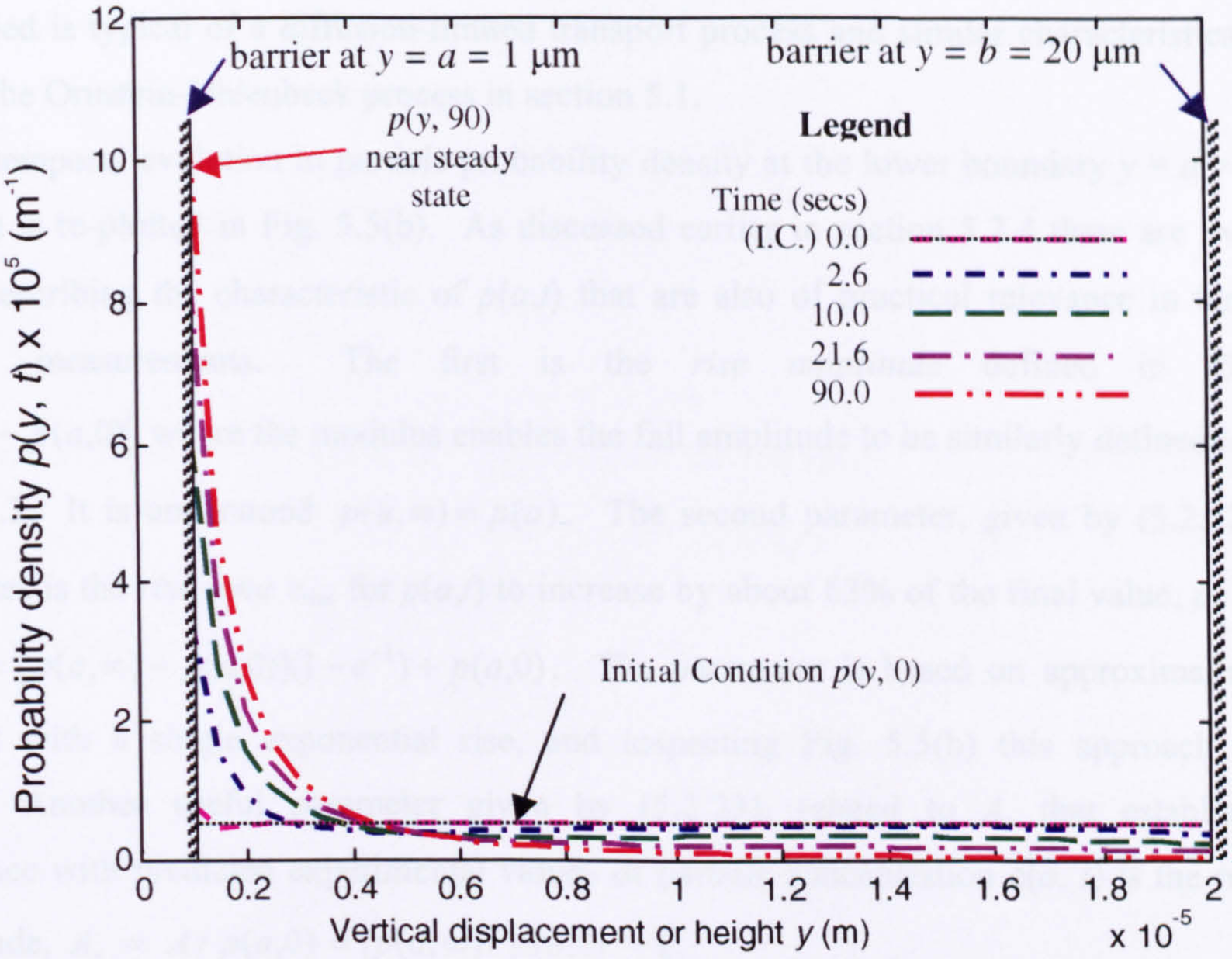

Fig. 5.5(a) Particle probability density at discrete times simulating 1-D DEP collection (assuming hyperbolic force profile).

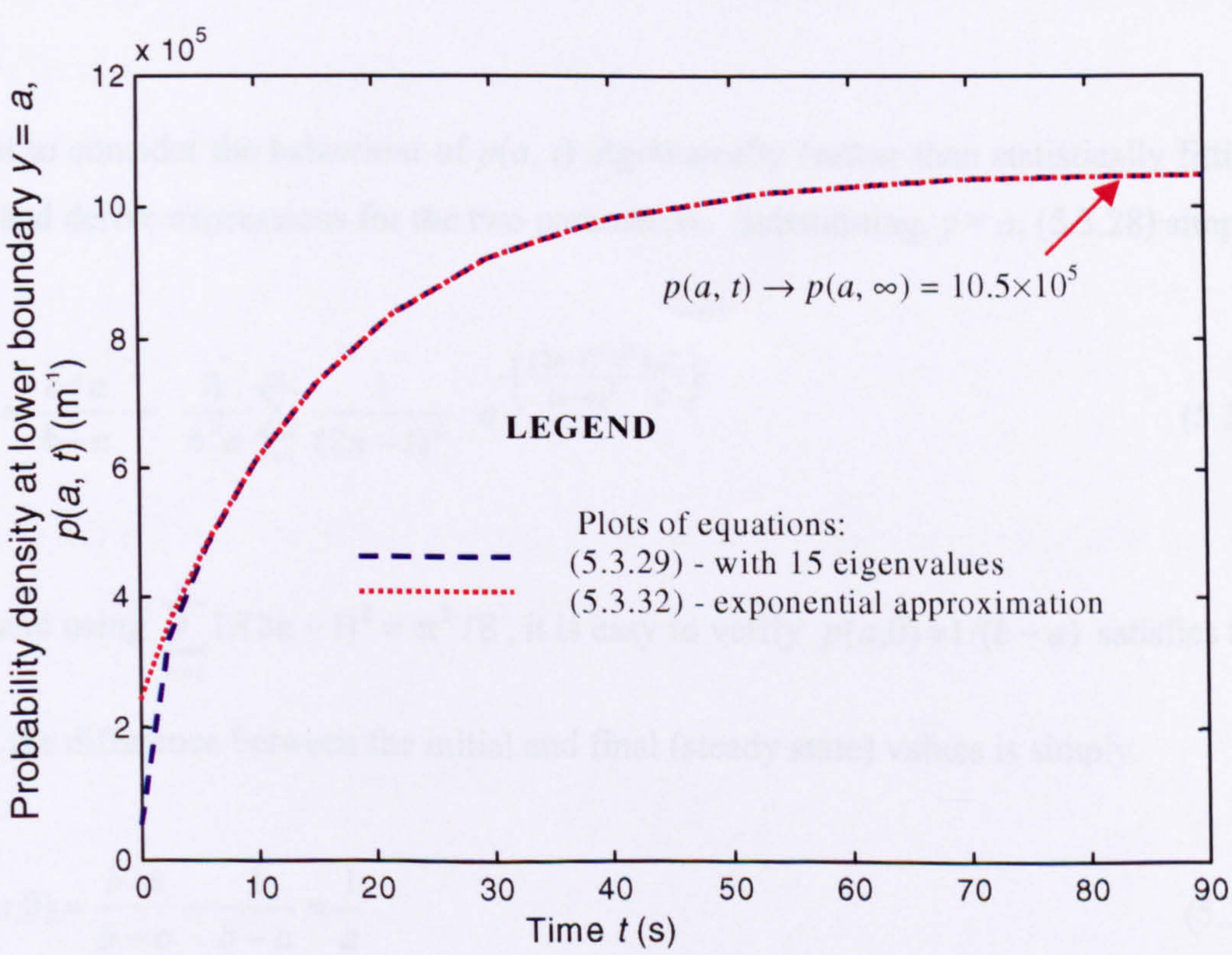

Fig. 5.5(b) Time dependent particle probability density at $y = a$ corresponding to Fig. 5.5(a).

stationary (or steady state) at t = 90 seconds. The decreasing rate of accumulation after the DEP force is applied is typical of a diffusion-limited transport process and similar characteristics were revealed for the Ornstein-Uhlenbeck process in section 5.1.

The temporal evolution in particle probability density at the lower boundary $y = a = 1$ μm in Fig. 5.5(a) is re-plotted in Fig. 5.5(b). As discussed earlier in section 5.2.4 there are two key parameters describing the characteristic of $p(a,t)$ that are also of practical relevance in terms of experimental measurements. The first is the *rise amplitude* defined in (5.2.20) $A = |p(a,\infty) - p(a,0)|$ where the modulus enables the fall amplitude to be similarly defined later in section 5.3.3.3. It is understood $p(a,\infty) = p(a)$. The second parameter, given by (5.2.22), for collection rates is the *rise time* τ_{rise} for $p(a,t)$ to increase by about 63% of the final value, or t such that $p(a,t) = [p(a,\infty) - p(a,0)](1 - e^{-1}) + p(a,0)$. The parameter is based on approximating the characteristic with a single exponential rise, and inspecting Fig. 5.5(b) this approach seems reasonable. Another useful parameter given by (5.2.23), related to A, that establishes a correspondence with predicted experimental values of particle concentration $c(a, t)$ is the relative (rise) amplitude, $A_r = A / p(a,0) = |p(a,\infty) / p(a,0) - 1|$.

5.3.3.1(b) Hyperbolic DEP force $k = 2k_BT$: approximations

It is insightful to consider the behaviour of $p(a, t)$ algebraically (rather than statistically fitting the time profile) and derive expressions for the two parameters. Substituting, $y = a$, (5.3.28) simplifies,

$$p(a,t)\Big|_{\substack{\mu=\frac{3}{2} \\ 1/(b-a)}} = \frac{b/a}{b-a} - \frac{8}{\pi^2 a}\sum_{n=1}^{\infty}\frac{1}{(2n-1)^2}\; e^{-\left(\frac{(2n-1)^2\pi^2 k_B T}{(b-a)^2\ \zeta}\right)t} \tag{5.3.29}$$

Setting $t = 0$ and using $\sum_{n=1}^{\infty} 1/(2n-1)^2 = \pi^2/8$, it is easy to verify $p(a,0)=1/(b-a)$ satisfies the IC. Furthermore, the difference between the initial and final (steady state) values is simply

$$p(a,\infty) - p(a,0) = \frac{b/a}{b-a} - \frac{1}{b-a} = \frac{1}{a} \tag{5.3.30}$$

so that (5.3.29) is rewritten

$$p(a,t)\Big|_{\substack{\mu=\frac{3}{2}\\ 1/(b-a)}} = p(a,0) + \frac{1}{a}\left(1-\frac{8}{\pi^2}\sum_{n=1}^{\infty}\frac{1}{(2n-1)^2}\; e^{-\left(\frac{(2n-1)^2\pi^2}{(b-a)^2}\frac{k_BT}{\zeta}\right)t}\right)$$

$$= p(a,0) + \frac{1}{a}\left(1-\frac{8}{\pi^2}e^{-\left(\frac{\pi^2}{(b-a)^2}\frac{k_BT}{\zeta}\right)t}\left(1+\frac{e^{-\left(\frac{8\pi^2}{(b-a)^2}\frac{k_BT}{\zeta}\right)t}}{9}+\ldots\right)\right) \qquad (5.3.31)$$

Since each term in the series decreases as n increases, for not too small $t > 0$, (5.3.31) approximates

$$p(a,t)\Big|_{\substack{\mu=\frac{3}{2}\\ 1/(b-a)}} \cong p(a,0) + \frac{1}{a}\left(1-\frac{8}{\pi^2}e^{-\left(\frac{\pi^2}{(b-a)^2}\frac{k_BT}{\zeta}\right)t}\right) \qquad t>0$$

$$\cong p(a,0) + \frac{1}{a}\left(1-\frac{8}{\pi^2}e^{-t/t_{rise1}}\right) \qquad t>0 \qquad (5.3.32)$$

where $\tau_{rise1} = \dfrac{(b-a)^2\zeta}{\pi^2 k_BT}$. Using above values for the parameters, $\tau_{rise1} = 16.3$ seconds. Equation (5.3.32) is plotted in Fig. 5.5(b) and clearly agrees with (5.3.29) for t > 16.3 s. The difference in rise amplitude $|p(a,\infty) - p(a,0)|$, estimated at $t = 0$, is in error by 19%.

An alternative approach is to equate (5.3.32) with the general equation for a single exponential rise,

$$p(a,t)\Big|_{\substack{\mu=\frac{3}{2}\\ 1/(b-a)}} = p(a,0) + A\left(1-e^{-t/t_{rise2}}\right) \qquad (5.3.33)$$

where A is the arbitrary 'rise' amplitude and τ_{rise2} is the 'adjusted' rise time for $p(a, t)$ to increase by $A(1 - e^{-1}) \cong 0.63A$. Rearranging (5.3.32) and equating with (5.3.33), $A = 1/a$

$$\tau_{rise2} = \frac{(b-a)^2}{\pi^2}\frac{\zeta}{k_BT}\left(1+\ln\left(\frac{8}{\pi^2}\right)\right) \cong 0.79\frac{(b-a)^2}{\pi^2}\frac{\zeta}{k_BT} \qquad (5.3.34)$$

$$\cong 0.79\,\tau_{rise1}$$

Deciding to use either (5.3.32) or (5.3.33) to fit a characteristic is a matter of choice. Suppose, for example, the characteristic was measured experimentally and the algebraic form was not known prior to the analysis. It is likely the approach would be to use (5.3.33) and the error would reside in the rise time (5.3.34). The expression (5.3.34) highlights some important features in collection

time-profiles where the DEP force is reasonably strong (such as for $k = 2\ k_BT$) and diffusion plays a key role. The first feature is the square law dependency of the rise time on the difference $b-a$ (or the physical height of the cover-slip above the electrode since $h = b-a$). The second feature exemplified by (5.3.34) is that small changes in the value of a can result in large changes in the rise amplitude, $|p(a,\infty) - p(a,0)|$. As expected, the rise time is reciprocally dependent on the particle diffusion constant $D = k_BT/\zeta$. Equations (5.3.32) and (5.3.34) are an approximation and it should be pointed out that the same features apply for the exact multiple exponential model (5.3.31).

5.3.3.1(c) Hyperbolic DEP force $k = 2k_BT$: example collections

An example of the effect of changing the localised DEP force (via parameter a) and cover-slip height, $h = b - a$, is shown in Fig. 5.6. Four collection profiles of $p(a, t)$ are shown using combinations of parameter values in (5.3.31), $a = \{0.5, 2.0\}$ and $b-a = \{20.0, 40.0\}$ (dimensions are μm). The profiles have also been generated numerically using the finite element method in FlexPDE 2.15 (introduced in section 5.2.3), and exhibit close agreement with the results from the eigenfunction expansion (5.3.29) implemented in MATLAB 5.0™. The program is listed in file CD-R:/FlexPDE/*fpe_1d_Co.pde*. Profiles I and II show the effect of doubling the height h of the cover-slip from $b-a = 20$ μm to 40 μm while a is held constant, $a = 0.5$ μm. This results in a four-fold increase in the rise time (from $\tau_{rise} \cong 14.3$ to 57.3 seconds). In contrast, the rise amplitude, A, remains the same, $A = 2 \times 10^6$ and the relative A_r amplitude doubles. The values of A, A_r and τ_{rise} are listed in Table 5.1 (located near the end of this section 5.3). It is helpful to remember that the relative amplitude $A_r = A/p(a, 0)$ doubles because $p(a, 0) = 1/h$ so for this example, $A_r = A \times h$. As mentioned in section 5.2.4, comparing A_r for two experiments where h is different enables a comparison of concentrations particularly for uniform initial concentrations, $c_1(y, 0) = c_2(y, 0)$. This highlights another interesting feature of this strong DEP force, $k = 2k_BT$ that accumulates particles from $t = 0$ to steady state: doubling the height, $h_2 = 2 \times h_1$ with $c_2(a,0) = c_1(a, 0)$, results in doubling the change in concentration at a, $\Delta c_2(a,0) = 2 \times \Delta c_1(a, 0)$. The particles in the 'extra h_1' are moved by the strong DEP force towards the boundary a. The increase in rise time is attributed to the extra time required for particles to move across a longer distance before the entire system reaches steady state. Comparing profile III with IV also shows that doubling the cover-slip height increases the rise time by a factor of four.

The effect of changing the boundary a while allowing the cover-slip height $h = b - a$ to remain *constant* is shown by comparing collection profile I with III, and II with IV. A four fold increase in $a = 0.5$ to $a = 2$ μm results in a reciprocal decrease in the rise amplitude of the probability density from $A = 2 \times 10^6$ to 5×10^5. In both cases, the rise time remains constant. The rise amplitude decreases because the boundary a, which specifies the minimum value of y, governs

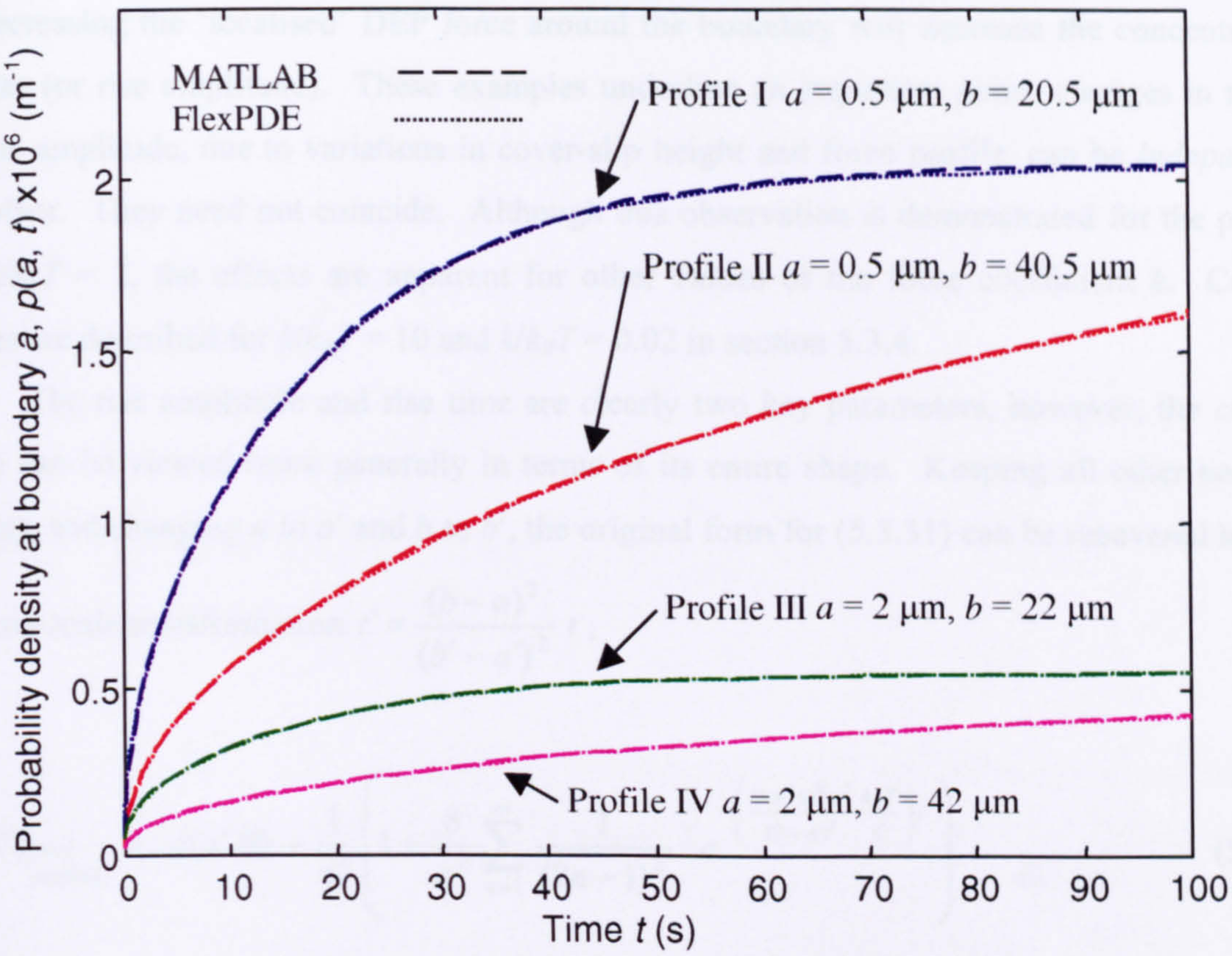

Fig. 5.6 Probability density $p(a, t)$ versus time t for a hyperbolic force value $k = 2k_BT$ with different lower and upper boundary values, a and b.

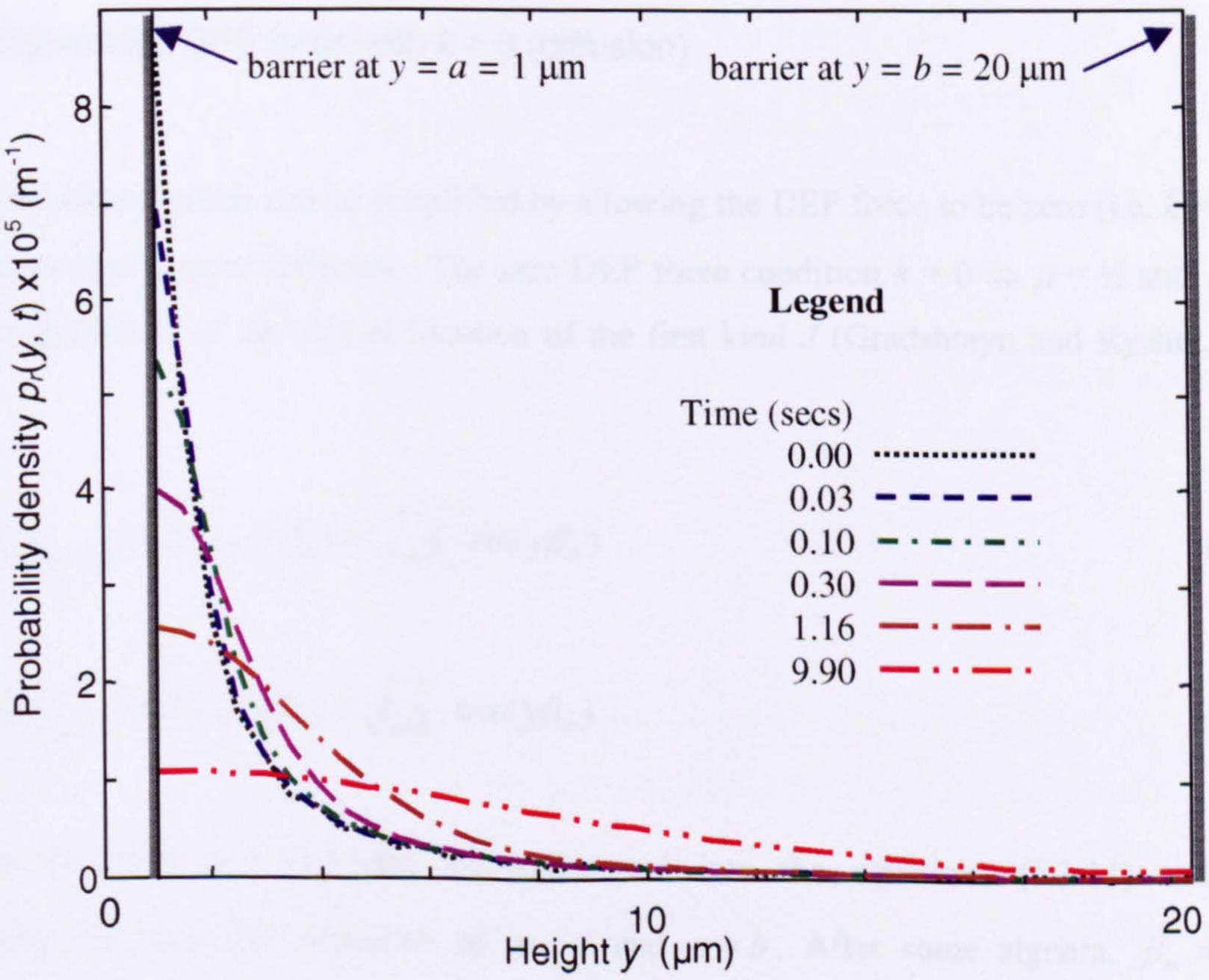

Fig. 5.7(a) Particle probability density at discrete times simulating 1-D relaxation from steady state collection (using equation 5.3.45). See text for details.

the maximum permissible DEP force via the hyperbolic relation (5.3.1). Physically, it is expected that decreasing the 'localised' DEP force around the boundary will decrease the concentration of particles (or rise amplitude). These examples underline an important point: changes in rise time and rise amplitude, due to variations in cover-slip height and force profile, can be *independent* of each other. They need not coincide. Although this observation is demonstrated for the particular case $k/k_BT = 2$, the effects are apparent for other values of the force coefficient k. Collection profiles are described for $k/k_BT = 10$ and $k/k_BT = 0.02$ in section 5.3.4.

The rise amplitude and rise time are clearly two key parameters, however, the collection profile can be viewed more generally in terms of its entire shape. Keeping all other parameters constant, and changing a to a' and b to b', the original form for (5.3.31) can be recovered by means of a time-scale transformation $t' = \dfrac{(b-a)^2}{(b'-a')^2}\, t$,

$$p(a',t')\Big|_{\substack{\mu=\frac{3}{2}\\ uniform}} = p(a',0) + \frac{1}{a'}\left(1 - \frac{8}{\pi^2}\sum_{n=1}^{\infty}\frac{1}{(2n-1)^2}\; e^{-\left(\frac{(2n-1)^2\pi^2}{(b-a)^2}\frac{k_BT}{\zeta}\right)t'}\right) \qquad (5.3.35)$$

and the IC $p(a',0) = 1/(b'-a')$ is merely shifted.

5.3.3.2 Hyperbolic DEP force with $k = 0$ (diffusion)

The Fourier-Bessel series can be simplified by allowing the DEP force to be zero (i.e. $k = 0$) so the only process operating is diffusion. The zero DEP force condition $k = 0 \Rightarrow \mu = ½$ and $\therefore\ \alpha = ½$. Using the definition of the Bessel function of the first kind J (Gradshteyn and Ryzhik, 1994, p. 977),

$$J_{1-\mu}(y\beta_m)\Big|_{\mu=1/2} = J_{+1/2}(y\beta_m) = \sqrt{\tfrac{2}{\pi y\beta_m}}\sin(y\beta_m) \qquad (5.3.36a)$$

$$J_{\mu-1}(y\beta_m)\Big|_{\mu=1/2} = J_{-1/2}(y\beta_m) = \sqrt{\tfrac{2}{\pi y\beta_m}}\cos(y\beta_m) \qquad (5.3.36b)$$

Equations (5.3.36a) and (5.3.36b) are substituted into the equations (5.3.11) and (5.3.12) representing the zero flux condition at $y = a$ and $y = b$. After some algebra, $\beta_m = \frac{\pi m}{b-a}$ and $C_{R_m} = \tan(\frac{\pi m a}{b-a}) = \tan(\frac{\pi m b}{b-a})$. Hence, from (5.3.13), (5.3.36a) and (5.3.36b) for $m \neq 0$,

$$\hat{g}_{m,\frac{1}{2}}(y) = \sqrt{\frac{2(b-a)}{\pi^2 ym}}\left(\cos\left(\frac{\pi my}{b-a}\right) + \tan\left(\frac{\pi ma}{b-a}\right)\sin\left(\frac{\pi my}{b-a}\right)\right) \tag{5.3.37}$$

and from (5.3.15)

$$C_{1_m} = \frac{\int_a^b p(y,0)\, y^{\frac{1}{2}} \hat{g}_{m,\frac{1}{2}}(y)dy}{\int_a^b y\, \hat{g}_{m,\frac{1}{2}}{}^2(y)dy} \tag{5.3.38}$$

$$= \frac{\sqrt{\frac{2(b-a)}{\pi^2 m}} \int_a^b p(y,0)\left(\cos\left(\frac{\pi my}{b-a}\right) + \tan\left(\frac{\pi ma}{b-a}\right)\sin\left(\frac{\pi my}{b-a}\right)\right)dy}{I_\Sigma(b,\frac{1}{2},\frac{\pi m}{b-a}) - I_\Sigma(a,\frac{1}{2},\frac{\pi m}{b-a})}$$

The denominator of (5.3.38) is evaluated by substituting (5.3.37) into the integrand and integrating by parts, or alternatively, using the integral relations I_Σ defined in (5.3.14). The result is,

$$\left[I_\Sigma(y,\mu,\beta_{m\neq 0})\right]_a^b = \frac{(b-a)^2}{\pi^2 m}\sec^2\left(\frac{\pi ma}{b-a}\right) \tag{5.3.39}$$

Substituting (5.3.39), (5.3.38) and (5.3.37) into (5.3.18), after further algebra

$$p(y,t)\big|_{\mu=\frac{1}{2}} = \frac{1}{b-a} + \frac{2}{b-a}\sum_{m=1}^{\infty}\left[\int_a^b p(y,0)\cos\left(\frac{\pi m(y-a)}{b-a}\right)dy.\cos\left(\frac{\pi m(y-a)}{b-a}\right)\right]e^{-\rho^2_{m,\frac{1}{2}}t} \tag{5.3.40}$$

where $\rho^2_{m,\frac{1}{2}} = \frac{\pi^2 m^2}{(b-a)^2}\frac{k_B T}{\zeta}$ and $p(y,0)$ is an arbitrary IC.

Choosing an IC $p(y,0) = \delta(y-y_0)$ and using the properties of the Dirac-δ function,

$$p(y,t)\big|_{\substack{\mu=\frac{1}{2}\\ \delta(y-y_0)}} = \frac{1}{b-a} + \frac{2}{b-a}\sum_{m=1}^{\infty}\cos\left(\frac{\pi m(y_0-a)}{b-a}\right)\cos\left(\frac{\pi m(y-a)}{b-a}\right)e^{-\rho^2_{m,\frac{1}{2}}t} \tag{5.3.41}$$

Letting $a = 0$ (which is permissible when the DEP force coefficient $k = 0$) and $b = 1$, (5.3.41) agrees with equation (5.2.107) in Gardiner (1985) that was solved for the specific diffusion case using a Fourier series. This agreement substantiates (5.3.41) and assists validation of (5.3.40).

If a uniform distribution is assumed for the IC, $p(y,0) = 1/(b - a)$, the system of particles is at equilibrium. Therefore the probability density should be time invariant. Substituting this IC into (5.3.40),

$$p(y,t)\Big|_{\substack{\mu=\frac{1}{2}\\ 1/(b-a)}} = \frac{1}{b-a} + \frac{2}{b-a}\sum_{m=1}^{\infty}\frac{1}{\pi m}\left[\sin\left(\frac{\pi m(y-a)}{b-a}\right)\right]_a^b \cos\left(\frac{\pi m(y-a)}{b-a}\right)e^{-\rho^2_{m,\frac{1}{2}}t}$$
$$= \frac{1}{b-a} + \frac{2}{b-a}\sum_{m=1}^{\infty} 0 = \frac{1}{b-a} = p(y,0) \qquad (5.3.42)$$

The probability distribution, as expected, is time invariant and remains as the IC, $p(y,0)$.

5.3.3.3(a) Hyperbolic DEP force with $k = 0$ (relaxation by diffusion)

Of particular interest is the diffusion case for an IC corresponding to a *previous steady state* solution for particle accumulation or collection. Suppose particles have dielectrophoretically collected near the electrode surface and the system is, for practical purposes, at steady state. When the DEP force is switched *off*, the system of particles 'relaxes' by diffusion eventually to a uniform distribution. In this relaxation process about-to-occur, the IC is the steady state solution of the previous DEP collection (Gedanken) experiment. To distinguish the relaxation process from DEP collection, a subscript '*r*' is used to denote the relaxation probability density. Note that there is no change in the definition of the probability density – for convenience, there is no subscript used for the collection process. The subscript '*r*' simply allows $t = 0$ to signify the moment the relaxation is to commence (to avoid confusion with the collection process). As a consequence of the above statements, the IC from (5.3.5) is

$$p_r(y,0) = p(y,\infty) = 2\alpha y^{2\alpha-1}/(b^{2\alpha}-a^{2\alpha}),\ \alpha \neq 0 \qquad (5.3.43a)$$

and

$$p_r(y,\infty) = p(y,0) = 1/(b-a) \qquad (5.3.43b)$$

Substituting the relaxation IC (5.3.43a) into (5.3.40), relaxation-by-diffusion is described by

$$p_r(y,t)\Big|_{\mu=\frac{1}{2}} = \frac{1}{b-a} +$$
$$\frac{2}{b-a}\sum_{m=1}^{\infty}\frac{2\alpha}{b^{2\alpha}-a^{2\alpha}}\int_a^b y^{2\alpha-1}\cos\left(\frac{\pi m(y-a)}{b-a}\right)dy.\cos\left(\frac{\pi m(y-a)}{b-a}\right)e^{-\rho^2_{m,\frac{1}{2}}t} \qquad (5.3.44)$$

There is no simple closed-form expression for the definite integral for arbitrary α, $\alpha \notin \mathrm{J}$. Normally it can be evaluated numerically or using integration by parts and exponential integral functions. Half-integer values of α are more convenient to use and standard formulae exist for IC cases where $k = 2nk_BT$, or $\alpha = (1-2n)/2$, where $n \in \mathrm{J}^+$ (Prudnikov *et al.*, 1986, Vol. I, p. 225; Gradshteyn and

Ryzhik, 1994, p. 219-20). In the previous section 5.3.3.1 collection rates were examined for the simple DEP case, $k = 2k_BT \Rightarrow \alpha = -½$, so it is insightful to use an IC that is the same as the steady state probability density for collection. Setting $\alpha = -½$ in (5.3.43) and (5.3.44) the IC is $p_r(y,0) = aby^{-2}/(b-a)$, and

$$p_r(y,t)\Big|_{\substack{\mu=\frac{1}{2}\\ \alpha=-\frac{1}{2}}} = \frac{1}{b-a} + \frac{2ab}{(b-a)^2}\sum_{m=1}^{\infty}\int_a^b y^{-2}\cos\left(\frac{\pi m(y-a)}{b-a}\right)dy.\cos\left(\frac{\pi m(y-a)}{b-a}\right)e^{-\rho^2_{m,\frac{1}{2}}t} \qquad (5.3.45a)$$

The lower subscript on $p_r(y,t)$ denotes the α value used for the IC. The definite integral in (5.3.45a) can be evaluated using integration by parts,

$$\int_a^b y^{-2}\cos\left(\frac{\pi m(y-a}{b-a}\right)dy = \frac{1}{a} - \frac{\cos(\pi m)}{b} + \frac{\pi m}{b-a}\left[\begin{array}{l} -\cos\left(\frac{\pi ma}{b-a}\right)\mathrm{si}\left(\frac{\pi my}{b-a}\right) \\ +\sin\left(\frac{\pi ma}{b-a}\right)\mathrm{ci}\left(\frac{\pi my}{b-a}\right)\end{array}\right]_a^b \qquad (5.3.45b)$$

where the cosine and sine integral functions $\mathrm{ci}(x)$ and $\mathrm{si}(x)$ are defined (Abramowitz and Stegun, 1965, Ch. 5; Gradshteyn and Ryzhik, 1994, p. 936)

$$\begin{Bmatrix}\mathrm{ci}(x)\\ \mathrm{si}(x)\end{Bmatrix} = \begin{Bmatrix}-\mathrm{Re}\{E_1(jx)\}\\ +\mathrm{Im}\{E_1(jx)\}\end{Bmatrix} = -\int_x^{\infty}\begin{Bmatrix}\cos(t)/t\\ \sin(t)/t\end{Bmatrix}dt \qquad (5.3.46)$$

and are readily evaluated in MATLAB 5.0™ using a form of the exponential integral function $E_1(jx)$ (Abramowitz and Stegun, 1965, Ch.5).

5.3.3.3(b) Hyperbolic force $k = 0$ (relaxation by diffusion): example

An example of DEP relaxation by diffusion $p_r(y, t)$ is shown in Figs. 5.7(a) (p. 134) and 5.7(b) for the same parameter values as the collection profile 5.3.3.1 ($a = 1$, $b = 20$). The simulation code lies in the same program as the DEP collection, CD-R:/Matlab/*fpex.m*, and is activated by menu selection. The probability density is shown in Fig. 5.7(a) for discrete times $t =$ {0.00, 0.026, 0.10, 0.30, 1.16, 9.90} seconds and shows the relaxation of particles away from the boundary at $y = a$ towards a uniform distribution as $t \to \infty$. Note that at $t = 0$, the spatial density profile $p_r(y, 0)$ in

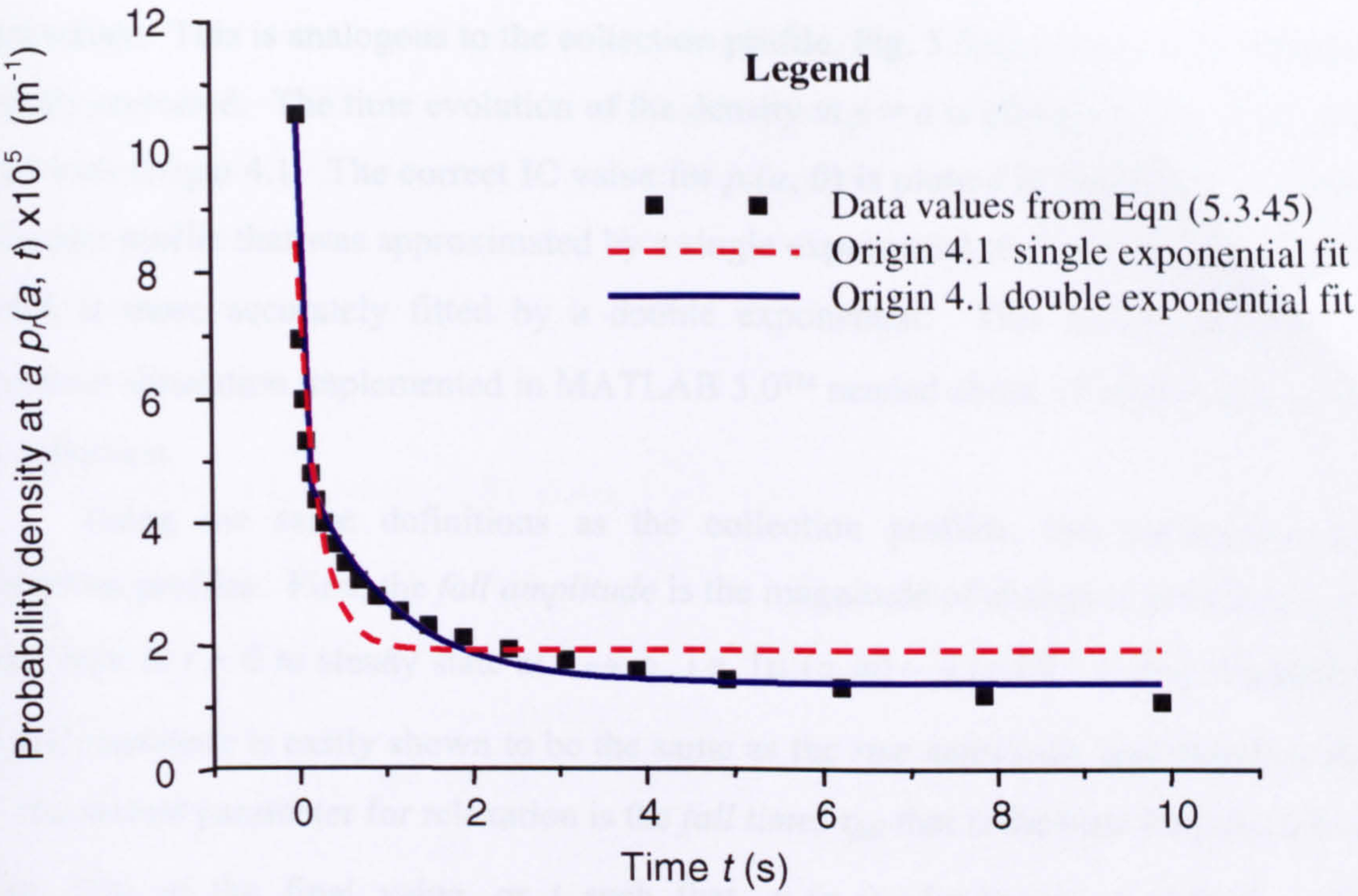

Fig. 5.7(b) Particle probability density at barrier $y = a$ corresponding to Fig. 5.7(a). Curve fitting by Origin 4.1 indicates the data is more accurately described by a double exponential. See text for details.

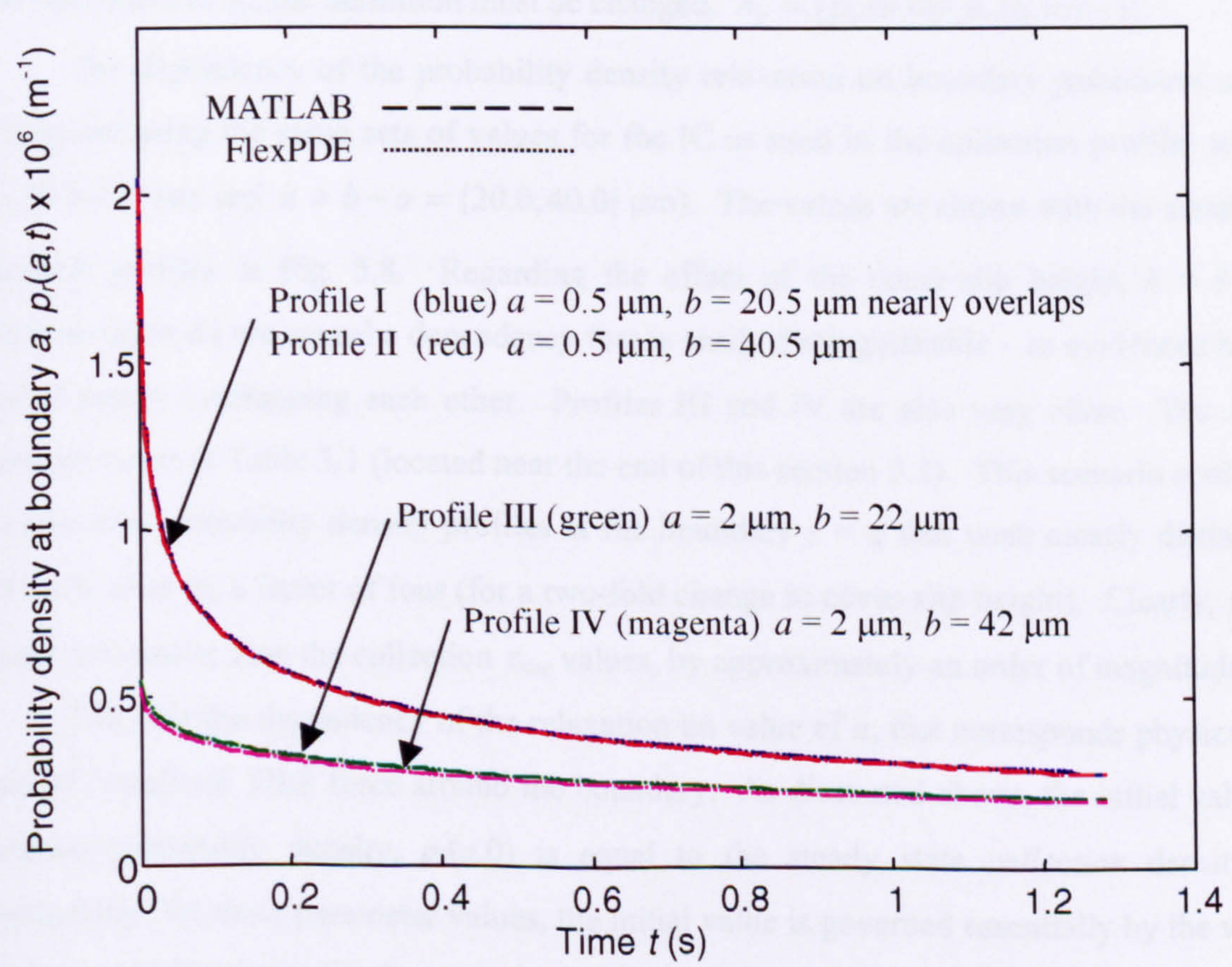

Fig. 5.8 Probability density relaxation profiles for initial condition $k = 2k_BT$ with different lower and upper boundary values a and b. See text for further details.

Fig. 5.7(a) deviates from the IC due to the truncation of the infinite series given by (5.3.45a) to 200 eigenvalues. This is analogous to the collection profile, Fig. 5.5(a) described in section 5.3.3.1 and is easily corrected. The time evolution of the density at $y = a$ is plotted in Fig. 5.7(b) and has been fitted with Origin 4.1. The correct IC value for $p_r(a, 0)$ is plotted in Fig. 5.7(b). In contrast to the collection profile that was approximated by a single exponential (for t not too small), the relaxation profile is more accurately fitted by a double exponential. This is not unexpected since the relaxation simulation implemented in MATLAB 5.0™ needed about ×7 eigenvalues compared with the collection.

Using the same definitions as the collection profiles, two parameters describe the relaxations profiles. First, the *fall amplitude* is the magnitude of change in probability density from initial state at $t = 0$ to steady state at $t \to \infty$, i.e. $|p_r(a,\infty) - p_r(a,0)|$. Using relations in (5.3.43), the *fall amplitude* is easily shown to be the same as the *rise amplitude*, and therefore is denoted as A. The second parameter for relaxation is the *fall time*, τ_{fall} that is the time for $p_r(a, t)$ to decrease to about 63% of the final value, or t such that $p_r(a,t) = [p_r(a,\infty) - p_r(a,0)](1 - e^{-1}) + p_r(a,0)$. Arguably, there could be two *fall time* parameters given the relaxation (5.3.45a) is a series consisting of multiple exponential functions. However, a single τ_{fall} serves as a useful comparison with τ_{rise} and will suffice for the present. It is also possible to specify a relative (fall) amplitude but to be equivalent to A_r, the definition must be changed, $A_r = [p_r(a,0) / p_r(a,\infty) - 1]$.

The dependency of the probability density relaxation on boundary parameters a and b is investigated using the same sets of values for the IC as used in the collection profiles in Fig. 5.6, ($a = \{0.5, 2.0\}$ μm and $h = b - a = \{20.0, 40.0\}$ μm). The values are shown with the accompanying relaxation profiles in Fig. 5.8. Regarding the effect of the cover-slip height, $h = b - a$, the relaxation times do not reveal a dependency that is easily distinguishable – as evidenced by profiles I and II nearly overlapping each other. Profiles III and IV are also very close. The A and τ_{fall} values are listed in Table 5.1 (located near the end of this section 5.3). This scenario contrasts with the *collection* probability density profiles at the boundary $y = a$ that were clearly distinguishable from each other by a factor of four (for a two-fold change in cover-slip height). Clearly, τ_{fall} values are also far smaller than the collection τ_{rise} values, by approximately an order of magnitude.

Consider the dependency of the relaxation on value of a, that corresponds physically to the nature of 'localised' DEP force around the boundary. As discussed above, the initial value for the relaxation probability density, $p_r(a,0)$ is equal to the steady state *collection* density $p(a,\infty)$. Consequently, for these parameter values, the initial value is governed essentially by the value of a. Examining profiles I and III, they are clearly distinguishable in terms of their initial value and this is expected. However, it is interesting they are also distinguishable in terms of their relaxation times. This scenario contrasts with the *collection* profiles I and III that exhibited the *same* rise times and were only distinguishable in terms of their rise amplitude (or final steady state value). A

similar feature is observed for profiles II and IV. Their relaxation times are radically different, whereas their rise times were observed to be the same. The point is that the data suggests relaxation times are essentially governed by the value of a or the extent the particles were concentrated around the boundary at the beginning of the relaxation-by-diffusion process. In the next section relaxations are shown for ICs (corresponding to collection steady state probability density profiles) for the cases $k = 10k_BT$ and $k = 0.02k_BT$.

5.3.4 Variations in hyperbolic DEP force

The collection rate characteristics can be examined for other higher and lower values of the hyperbolic force coefficient than the single case $k = 2k_BT$ considered in 5.3.3.1. The highest value considered is $k = 10k_BT$ and has been chosen for two reasons. First, this coefficient means the maximum $A_r = p(a,\infty)/p(a,0) - 1 \cong 72000$ % (c.f. Table 5.1) is very high and estimating from experiments (discussed in Chapter 7), is likely to be beyond the value found in practice. The second reason is that the performance of the program, *fpex.m*, implemented in MATLAB 5.0 is compromised for $k > 10k_BT$ and would require further software development. Therefore, $k = 10k_BT$ is the upper limit of being able to verify the characteristics generated by the Fourier-Bessel series with those produced numerically from the FlexPDE 2.15 finite element program *fpe_1d_Co.pde*. The lowest coefficient considered is $k = 0.02$ since values less than that would be comparable to collections resulting from gravity and buoyancy forces for the domain of a and b parameter values considered. The latter scenario is discussed in section 5.5. Since the relaxation-by-diffusion characteristics are of interest, these are shown for the same k values with the collection rates.

5.3.4.1. Hyperbolic DEP force coefficient $k = 10k_BT$

Collection profiles, $p(a, t)$, for $k = 10k_BT$ are shown in Fig. 5.9(a) with the same boundary parameter values considered previously, i.e. $a = \{0.5, 2.0\}$ and $b - a = \{20.0, 40.0\}$ (μm). In general, the four profiles exhibit rise times that are much shorter (a third to a quarter) than those for the $k = 2\ k_BT$ case, as listed in Table 5.1. However, they exhibit almost as strong dependence on cover-slip height (b - a). The ratio of rise times of profiles I and II, for example, is approximately 3.9 compared with 4.0 for the $k = 2\ k_BT$ case. Similarly, the ratio of rise times for profiles III and IV is 3.5 compared with 4.0. Furthermore, the rise times are not entirely independent of the value of a value as in the $k = 2\ k_BT$ example, so there are small differences in their values. Profiles I and III exhibit $\tau_{rise} = 3.7$ and 4.5 s, for example, and profiles II and IV, exhibit $\tau_{rise} = 14.4$ and 15.5 seconds, respectively.

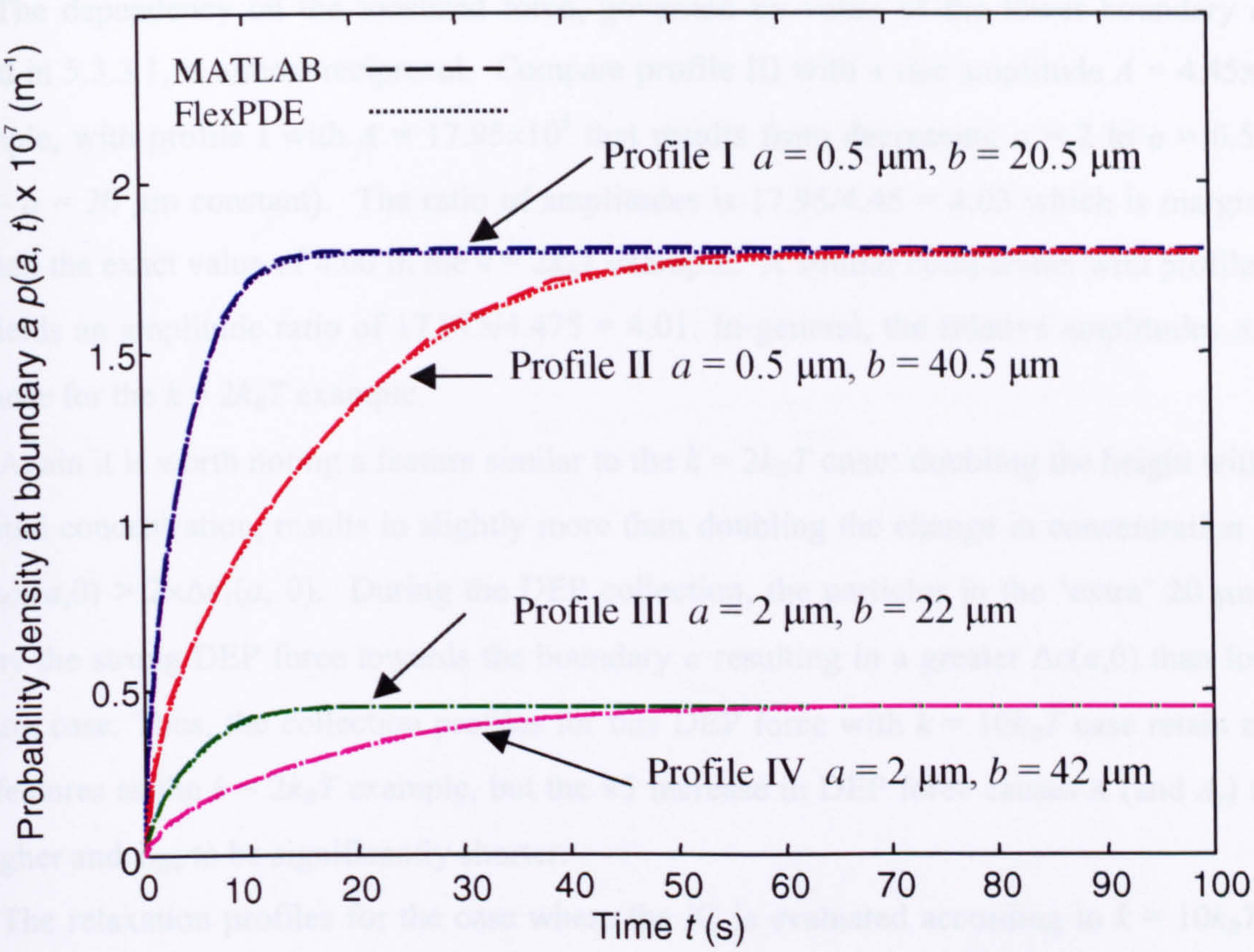

Fig. 5.9(a) Probability density collection profiles for a DEP hyperbolic force value $k = 10k_BT$ with different lower and upper boundary values a and b.

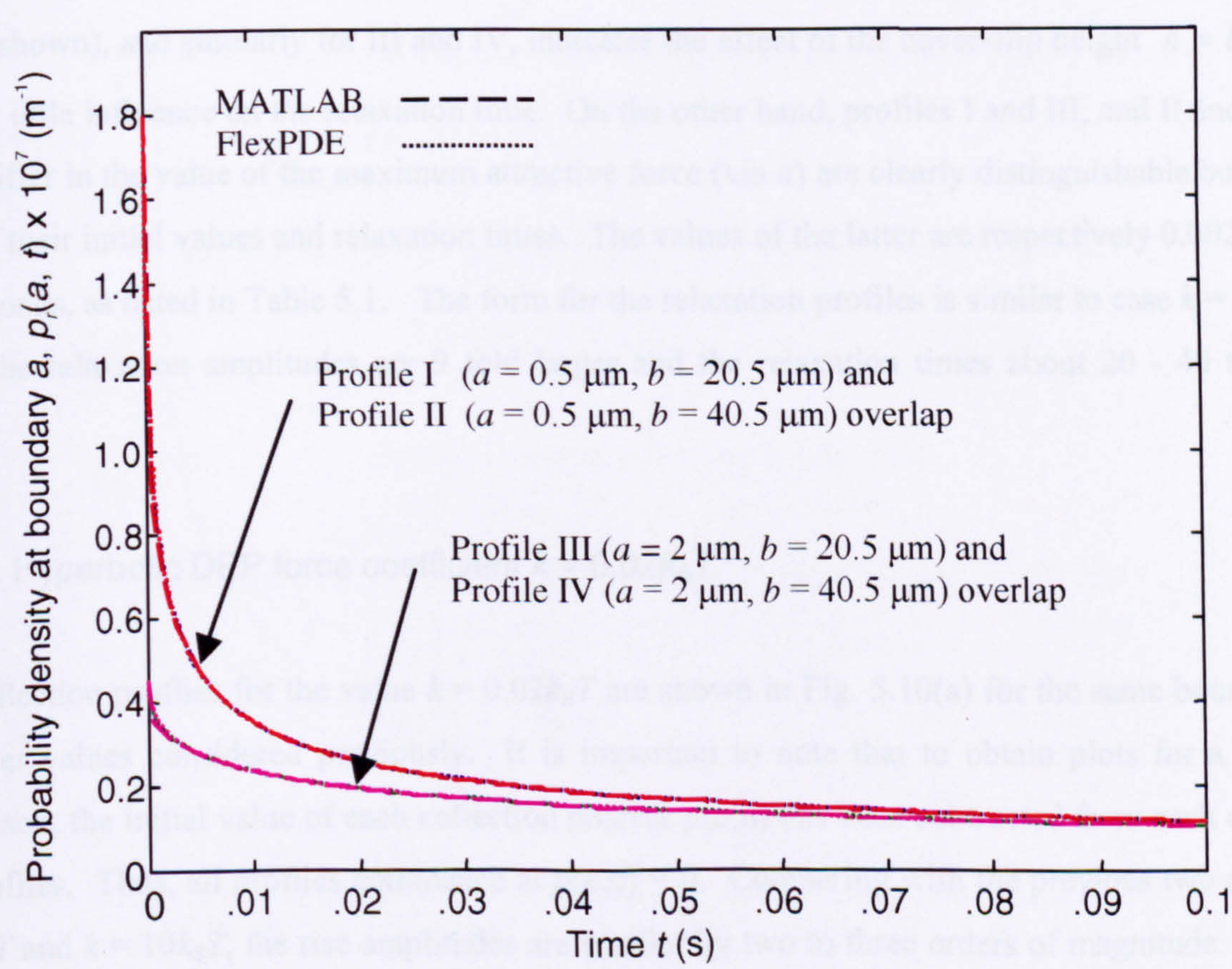

Fig. 5.9(b) Probability density relaxation profiles for initial condition $k = 10k_BT$ with different lower and upper boundary values a and b.

The dependency on the localized force, governed by value of the lower boundary a as explained in 5.3.3.1, is almost reciprocal. Compare profile III with a rise amplitude $A = 4.45\text{x}10^6$, for example, with profile I with $A = 17.95\times10^6$ that results from decreasing $a = 2$ to $a = 0.5$ μm (with $b - a = 20$ μm constant). The ratio of amplitudes is 17.95/4.45 = 4.03 which is marginally higher than the exact value of 4.00 in the $k = 2k_BT$ example. A similar comparison with profiles IV and II yields an amplitude ratio of 17.975/4.475 = 4.01. In general, the relative amplitudes A_r are *ca.* ×9 those for the $k = 2k_BT$ example.

Again it is worth noting a feature similar to the $k = 2k_BT$ case: doubling the height with the same initial concentration, results in slightly more than doubling the change in concentration at a, that is $\Delta c_2(a,0) > 2\times\Delta c_1(a, 0)$. During the DEP collection, the particles in the 'extra' 20 μm are moved by the strong DEP force towards the boundary a resulting in a greater $\Delta c(a,0)$ than for the $h = 20$ μm case. Thus, the collection profiles for this DEP force with $k = 10k_BT$ case retain many similar features as the $k = 2k_BT$ example, but the ×5 increase in DEP force causes A (and A_r) to be much higher and τ_{rise} to be significantly shorter.

The relaxation profiles for the case where the IC is evaluated according to $k = 10k_BT$ can also be compared. The profiles are for the same boundary values as the other cases and are shown in Fig. 5.9(b). The initial values of $p_r(a,0)$ for profiles I and II are essentially the same (for three significant figures), and likewise for III and IV. The overlap of profiles I and II (for the time interval shown), and similarly for III and IV, indicates the effect of the cover-slip height $h = b-a$ has very little influence on the relaxation time. On the other hand, profiles I and III, and II and IV, which differ in the value of the maximum attractive force (via a) are clearly distinguishable both in terms of their initial values and relaxation times. The values of the latter are respectively 0.002 and 0.03 seconds, as listed in Table 5.1. The form for the relaxation profiles is similar to case $k = 2k_BT$ except the relaxation amplitudes are 9 fold larger and the relaxation times about 20 - 40 times shorter.

5.3.4.2. Hyperbolic DEP force coefficient $k = 0.02k_BT$

Four collection profiles for the value $k = 0.02k_BT$ are shown in Fig. 5.10(a) for the same boundary parameter values considered previously. It is important to note that to obtain plots for a clear comparison, the initial value of each collection process $p(a,0)$ has been subtracted from each of the four profiles. Thus, all profiles commence at $p(a,0) = 0$. Comparing with the previous two cases, $k = 2k_BT$ and $k = 10k_BT$, the rise amplitudes are smaller by two to three orders of magnitude. This is expected since the value of k has been reduced by two to three orders of magnitude, and the DEP force is proportionally weaker. However, it is interesting the rise times τ_{rise} do not significantly change in the same way, lying within the range 3 to 22 seconds. Comparing profiles in the same

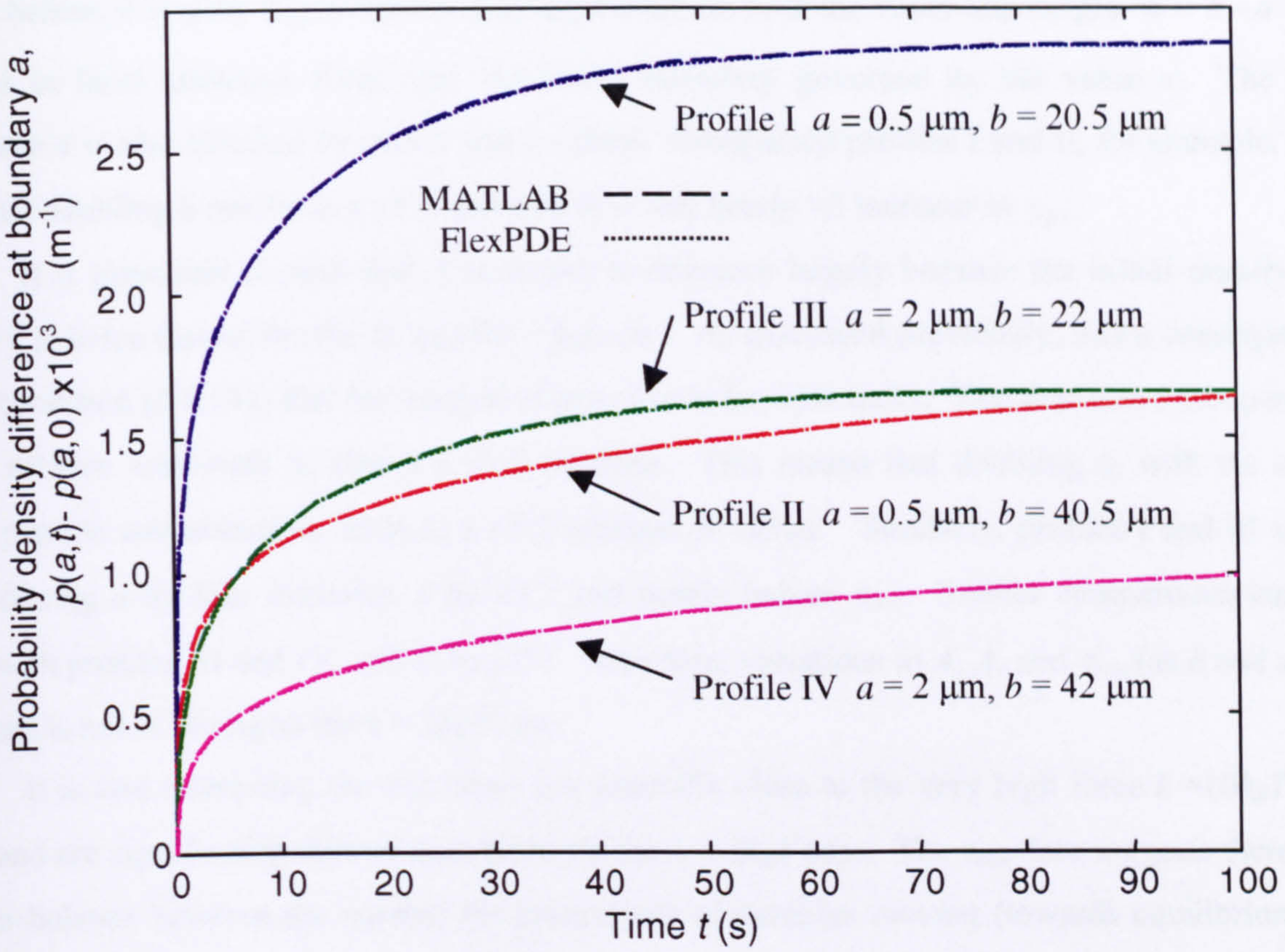

Fig. 5.10(a) Probability density collection profiles for a DEP hyperbolic force value $k = 0.02k_BT$ with different lower and upper boundary values a and b.

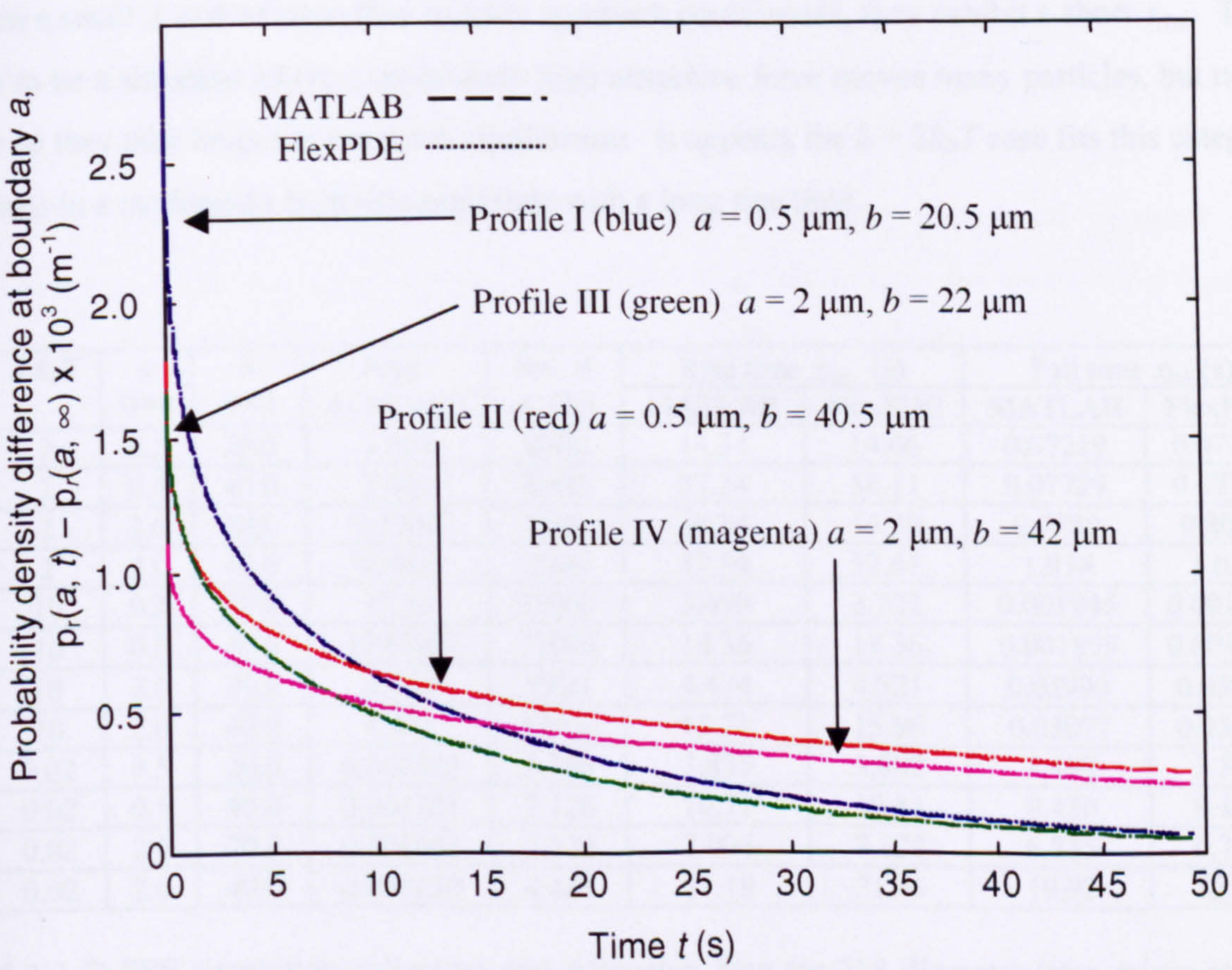

Fig. 5.10(b) Probability density relaxation profiles for initial condition $k = 0.02k_BT$ with different lower and upper boundary values a and b.

way as before, it is clear τ_{rise} is significantly dependent on both the cover-slip height $h = b - a$ and changes in local attractive force near the lower boundary governed by the value a. The rise amplitude A is also affected by both h and a values. Comparing profiles I and II, for example, it is clear that doubling h results in a ×1.6 decrease in A and nearly ×3 increase in τ_{rise}.

It is important to note that A is shown to decrease largely because the initial density for profile I is twice that of Profile II, $p_I(a,0) = p_{II}(a,0)$. As discussed previously, this a consequence of the condition (2.4.18a) that the integral of $p(y, t)$ over $[a, b]$ is unity. The alternative comparison of the relative amplitude A_r shows a ×1.2 increase. This means that doubling h, with the same initial particle concentration, leads to a ×1.2 increase in $\Delta c(a)$. Similarly, profiles I and III show that reducing a by four increases A by ×1.7 and nearly halves τ_{rise}. Similar comparisons can be made with profiles III and IV, and II and IV. Therefore, variations in A, A_r and τ_{rise} (as h and a are changed) is not as strong as the $k = 2k_BT$ case.

It is also interesting the rise times are generally close to the very high force $k = 10k_BT$ rise times and are significantly shorter than those for the $k = 2k_BT$ case. The τ_{rise} data suggests there is a counter-balance between the number (or proportion) of particles moving (towards equilibrium) in the system and the velocity at which they move. An extremely high attractive force results in many particles being moved very quickly towards the lower boundary, resulting in a high A amplitude and short τ_{rise}. On the other hand, a low attractive force slowly moves only a few particles. This results in a small A and because they quickly approach equilibrium, they exhibit a short τ_{rise}. There appears to be a situation where a moderately high attractive force moves many particles, but not so quickly so they take longer to approach equilibrium. It appears the $k = 2k_BT$ case fits this category, and results in a moderately high rise amplitude with a long rise time.

Pr.	k/k_BT	a (μm)	h (μm)	Amp. $A\times10^6$ (m^{-1})	Rel. A A_r (%)	Rise time τ_{rise} (s)		Fall time τ_{fall} (s)	
						MATLAB	FlexPDE	MATLAB	FlexPDE
I	2	0.5	20.0	2.000	4000	14.34	14.46	0.07219	0.07266
II	2	0.5	40.0	2.000	8000	57.34	58.11	0.07729	0.07777
III	2	2.0	20.0	0.5000	1000	14.34	14.39	0.7989	0.8047
IV	2	2.0	40.0	0.5000	2000	57.34	57.61	1.014	1.021
I	10	0.5	20.0	17.95	35900	3.690	3.722	0.001945	0.001961
II	10	0.5	40.0	17.97(5)	71900	14.36	14.36	0.001899	0.001966
III	10	2.0	20.0	4.450	8900	4.474	4.521	0.02993	0.03011
IV	10	2.0	40.0	4.475	17900	15.71	15.96	0.03077	0.03096
I	0.02	0.5	20.0	0.002880	5.760	3.835	3.882	3.499	3.520
II	0.02	0.5	40.0	0.001781	7.126	10.71	10.81	9.430	9.491
III	0.02	2.0	20.0	0.001661	3.322	7.004	7.122	6.733	6.770
IV	0.02	2.0	40.0	0.001220	4.481	21.19	21.46	19.92	20.10

Table 5.1 1-D FPE simulation collection and relaxation data for 216 diameter latex micro-spheres assuming hyperbolic DEP force with k, a, and cover-slip height, $h = b - a$, as listed.

The four relaxation profiles I – IV for the case where the IC is evaluated according to $k = 0.02k_BT$ are also compared using the same a and b - a values as above, Fig. 5.10(b). To enable a clear comparison, the final steady state relaxation density, $p_r(a, \infty)$, has been subtracted from each of the four profiles (so their steady state values are zero). It is clear the relaxation times, τ_{fall} are longer than those for the two previous cases $k = 2k_BT$ and $k = 10k_BT$ by up to one to two orders of magnitude. In fact, the τ_{fall} for each of the profiles is comparable to τ_{rise}, as shown in Table 5.1.

The physical reason for this is likely to stem from the fact that the distribution of the IC $p_r(y,0)$ (which is the steady state probability density of the collection process) is far more spatially graduated than the previous cases. The number of particles near the upper boundary at $y = b$, for example, is no longer depleted, and $p_r(b,0)$ comparable to $p_r(a,0)$. Essentially, the system is relaxing from a collection that can be viewed as a small *perturbation* from a uniform distribution. This means the behaviour of $p_r(a, t)$ is governed by the value of upper boundary b (as well as a), so the effect of the cover-slip height is observable when profile I is compared with II, and III with IV.

This scenario of a *perturbation* from a uniform distribution contrasts with the previous cases, $k = 2k_BT$ and $k = 10k_BT$, which can be considered as a large *state transition* - particularly as the particles are depleted near the upper boundary, so $p_r(b,0) \cong 0$. This means $p_r(a, t)$, for times up to and in the vicinity of the τ_{fall}, tend to be governed by the diffusion of particles away from the lower boundary at a and the influence of b is not observed until much later.

5.4 1-D DEP collection: exponential force model

In section 6.3.2 it is shown that the DEP force profile above an interdigitated electrode array approximates to an exponential profile in the far field. This agrees with the general form given by Markx *et al.* (1997) and Cui *et al.* (2000) and is also described in recently published work – see *List of Publications* at the end of this dissertation. Analogous to the approach with hyperbolic profile, this profile is extended to include the near field. The exponential model tends to underestimate the strength of the DEP force in the near field, it is nonetheless, a useful model. Since the DEP force is significantly stronger than the resultant force from gravity and buoyancy (Chapter 2) for most of y, the (deterministic) velocity is approximated as,

$$v(y) = \frac{F_{dep}(y)}{\zeta} = \frac{-k_1 \exp(-k_2 y)}{\zeta} \quad , \; 0 \le y \le h \tag{5.4.1}$$

where the constant $k_2 = 2\pi/(w + d)$ is dependent on the electrode dimensions with (transverse) width w and inter-electrode spacing (or gap) d, and the force coefficient k_1 expresses the magnitude of the DEP force at the surface of the electrode plane. For positive DEP $k_1 > 0$, the negative sign

in front of k_1 indicates the force is acting downwards towards the lower boundary. Substituting (5.4.1) into (5.2.1), the 1-D FPE describing the spatial-temporal evolution of $p(y, t)$, assuming an exponential force profile, is

$$\frac{\partial p(y,t)}{\partial t} = \frac{k_1}{\zeta}\frac{\partial\left(p(y,t)e^{-k_2 y}\right)}{\partial y} + \frac{k_B T}{\zeta}\frac{\partial^2 p(y,t)}{\partial^2 y} \tag{5.4.2}$$

where all other constants have been previously defined.

Assuming $w = d$, an expression for the constant k_1 is found from equations (6.0.2b) and (6.3.21),

$$k_1 = 32V_o^2 r^3 \varepsilon_m \,\mathrm{Re}\{f_{CM}\}/d^3 \tag{5.4.3}$$

where all parameters have been previously defined in Chapter 2. The peak electrode potential, V_o, is made a variable for simulations in section 5.4.3. The value of k_1 for a 216 nm diameter homogeneous sphere suspended above an interdigitated array with d = 10 μm in an aqueous medium, $\varepsilon_m = 78.4\varepsilon_o = 6.94\text{x}10^{-10}$ (F/m) assuming the real part of the frequency dependent Clausius-Mossotti factor $\mathrm{Re}\{f_{CM}\} = +1$, is $k_1 = 2.798V_0^2 \times 10^{-14}$ (N).

5.4.1 Exponential DEP force: steady state analytical solution

The steady state probability distribution is found by solving (5.4.2). Imposing BCs for the steady state probability flux at the electrode surface $y = 0$, $J(0) = 0 \Rightarrow J_c = 0$. Substituting (5.4.1) into (5.2.5)

$$\xi(y) = \int \frac{\frac{k_1}{\zeta}\exp(-k_2 y)}{D} dy = -\frac{k_1}{k_2 D\zeta}\exp(-k_2 y) = -\lambda\exp(-k_2 y) \tag{5.4.4}$$

where $\lambda = k_1/(k_2 k_B T)$. From (5.2.6)

$$p(y) = p_c e^{-\xi(y)} = p_c e^{\lambda\exp(-k_2 y)} \tag{5.4.5}$$

where the integration constant p_c is found by substituting (5.4.4) into (5.2.8)

$$p_c = \left[\int_a^b e^{\lambda \exp(-k_2 y)}\, dy\right]^{-1} = \frac{-k_2}{\mathrm{Ei}(\lambda e^{-k_2 b}) - \mathrm{Ei}(\lambda e^{-k_2 a})} \tag{5.4.6}$$

and Ei(x) is the exponential integral function (Abramowitz and Stegun, 1965, Ch.5; Prudnikov *et al.*, 1986, Vol. I, p. 138). From (5.4.5) and (5.4.6), the steady state solution is

$$\therefore\ p(y) = \frac{k_2 \exp(\lambda e^{-k_2 y})}{\mathrm{Ei}(\lambda e^{-k_2 a}) - \mathrm{Ei}(\lambda e^{-k_2 b})} \tag{5.4.7}$$

5.4.2 Exponential DEP force: time dependent analytical solution

The probability density $p(y, t)$ can be solved using the eigenfunction expansion. Substituting (5.4.1) into the decoupled spatial function given by (5.2.13), and rearranging,

$$\frac{k_B T}{\zeta}\frac{d^2 g_m(y)}{dy^2} + \frac{d\left(\frac{k_1}{\zeta} e^{-k_2 y} g_m(y)\right)}{dy} + g_m(y)\rho^2 = 0$$

$$\Rightarrow \frac{k_B T}{\zeta} g''(y) + \frac{k_1}{\zeta} e^{-k_2 y} g'(y) + \left(\rho^2 - \frac{k_1 k_2}{\zeta} e^{-k_2 y}\right) g(y) = 0 \tag{5.4.8}$$

where g′ and g″ denote first and second derivatives with respect to the independent variable, y, and for conciseness in the second equation, the m subscript notation has been omitted. The GS of (5.4.8) is expressed, using Mathematica 4.0™ , in terms of modified Bessel functions of the first kind with complex order $\nu \in Z$, or using the confluent hypergeometric function ${}_1F_1$ (Wolfram, 1996),

$$g(y) = C_{1_m}\left(e^{k_2 y}\rho_m^2\right)^{+j\lambda_m} {}_1F_1\left(1 - j\lambda_m; 1 - 2j\lambda_m; \frac{k_1 e^{-k_2 y}}{k_2 k_B T}\right) + C_{2_m}\left(e^{k_2 y}\rho_m^2\right)^{-j\lambda_m} {}_1F_1\left(1 + j\lambda_m; 1 + 2j\lambda_m; \frac{k_1 e^{-k_2 y}}{k_2 k_B T}\right) \tag{5.4.9}$$

where $\lambda_m = \frac{\rho_m \sqrt{\zeta}}{k_2 \sqrt{k_B T}}$. The solution is listed in the program CD-R:/Mathematica/*O&PDEs.nb*. Since parameters lie in the complex domain, the solution is likely to be more complicated than for the preceding hyperbolic case where the eigenfunction expansion involved Bessel functions of the first kind with real coefficients. In view of this, it is questionable whether a similar procedure should be undertaken for the exponential case. Experience gained in solving the time dependent solution has

to be weighed with the availability of numerical solutions to the FPE (5.2.1) using FlexPDE software. The exponential and hyperbolic profiles are simplifications, and the numerical approach is far more flexible in terms of the DEP force profiles it can accommodate. In addition, the steady state solution (5.4.7) provides a means of independently verifying the numerical solution as t tends to infinity. Parenthetically, alternative BCs could be applied that simplify the solution of the ODE (5.4.9). For example, it could be assumed that the number of particles that collect on the electrodes is small compared with the number in solution and the source of particles is an infinite reservoir. Although experimental observations indicate this assumption would be reasonable, it is not clear at this stage if such an approach is justified.

5.4.3 Exponential DEP force: numerical solution

The collection and relaxation profiles are investigated in a similar manner to those for the hyperbolic force profile in the previous section 5.3. The exponential force profile requires values for k_1 and k_2 and upper boundary value b. The lower boundary is set $a = 0$ and it is useful to select $d = 10$ μm since this is the electrode dimension used in experiments. The values for the thermal temperature and dynamic drag coefficients are chosen to be the same as for the hyperbolic profile, $k_BT/\zeta = 2.24\times10^{-12}$ m^{2}s^{-1} that corresponds to 216 nm diameter spheres collecting in water at 25 °C. Since the exponential force is applicable in the far field, the collection profiles are extended beyond 40 μm up to nominally 160 μm. The collection profiles are simulated for the same heights as the hyperbolic case, $h = 20$ μm and $h = 40$ μm, and consecutively doubled to 160 μm. Since $a = 0$ in the exponential model, then $b = h = \{20, 40, 80, 160\}$ (μm) yielding four profiles for comparison.

5.4.3.1 Low value for the exponential force coefficient k_1

Using $V_0 = 0.1$ (V) and substituting (5.4.3) into (5.4.1), at the lower boundary $y = a = 0$, the magnitude of the DEP force $F_{DEP} = k_1 = 2.8\times10^{-16}$ (N). This is comparable to the force at the lower boundary $y = a = 0.5$ μm for the hyperbolic model using $k = 0.02k_BT \cong 8.23\text{x}10^{-23}$ (J) described in section 5.3.4.1. The hyperbolic relation (5.3.1) yields, $F_{DEP} = 1.65\times10^{-16}$ (N). Four collection and relaxation profiles are shown in Figs. 5.11(a) and (b) for the above b values. Values for the rise (or fall) amplitude A, relative amplitude, A_r, and rise and fall times, τ_{rise} and τ_{fall} are listed in Table 5.2. The effect of increasing b ×8, from 20 μm to 160 μm, only doubles τ_{rise} by a modest 3.9 to 8.1 seconds. The τ_{fall} are less effected, increasing from 3 to 5.6 seconds. The amplitudes exhibit a decrease as b increases but it is important to remember (as discussed for the hyperbolic model) that much of this is due to the IC values being smaller as h increases due to the condition (2.4.18a) that the integral of $p(y, t)$ over $[a, b]$ is unity.

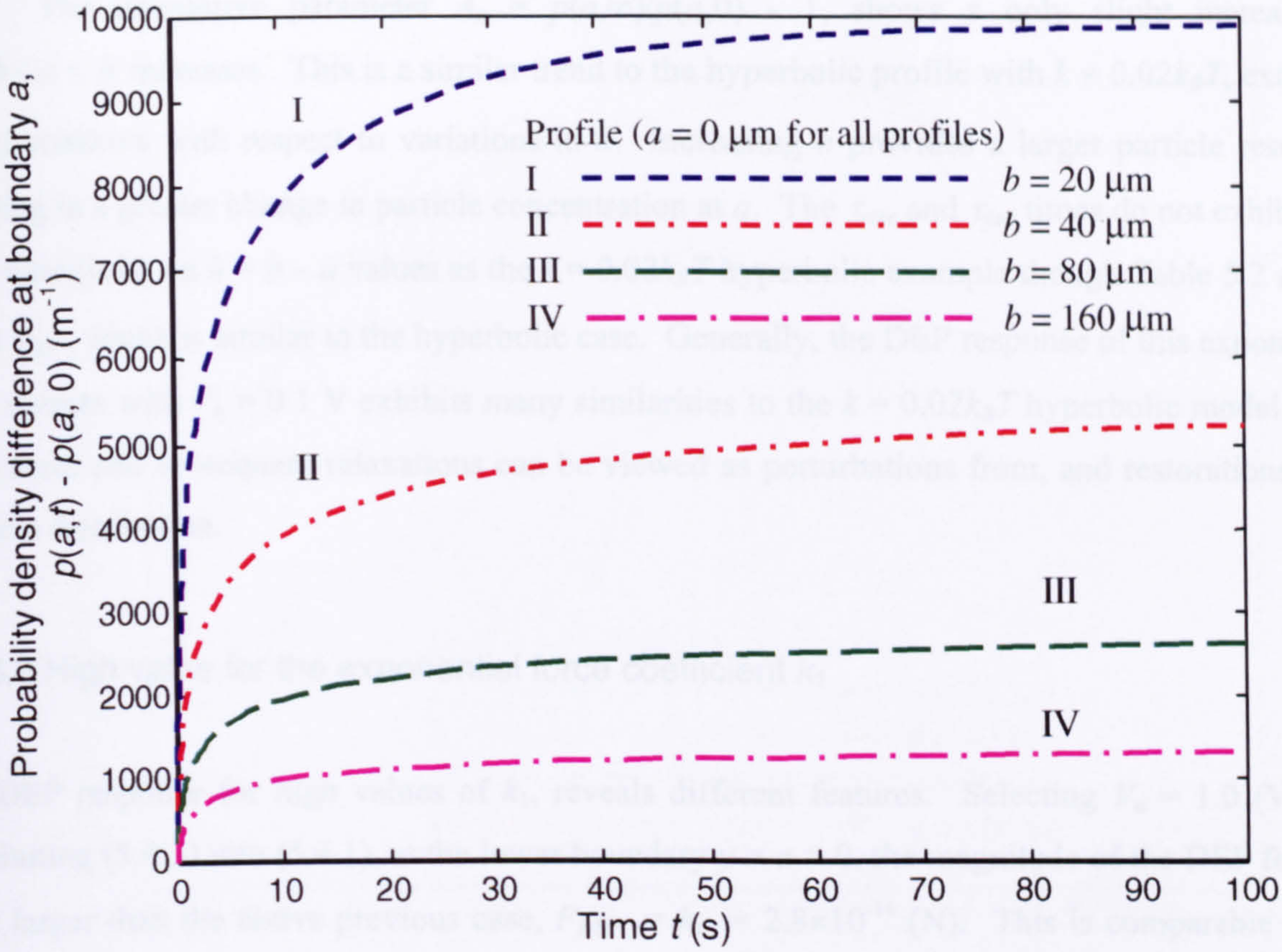

Fig. 5.11(a) Probability density collection profiles $p(a, t)$ for the DEP exponential force given by (5.4.1) with $k_1 = 2.798\times10^{-16}$ (N) and $k_2 = \pi/10$ (μm^{-1}) for different values of the upper boundary at b.

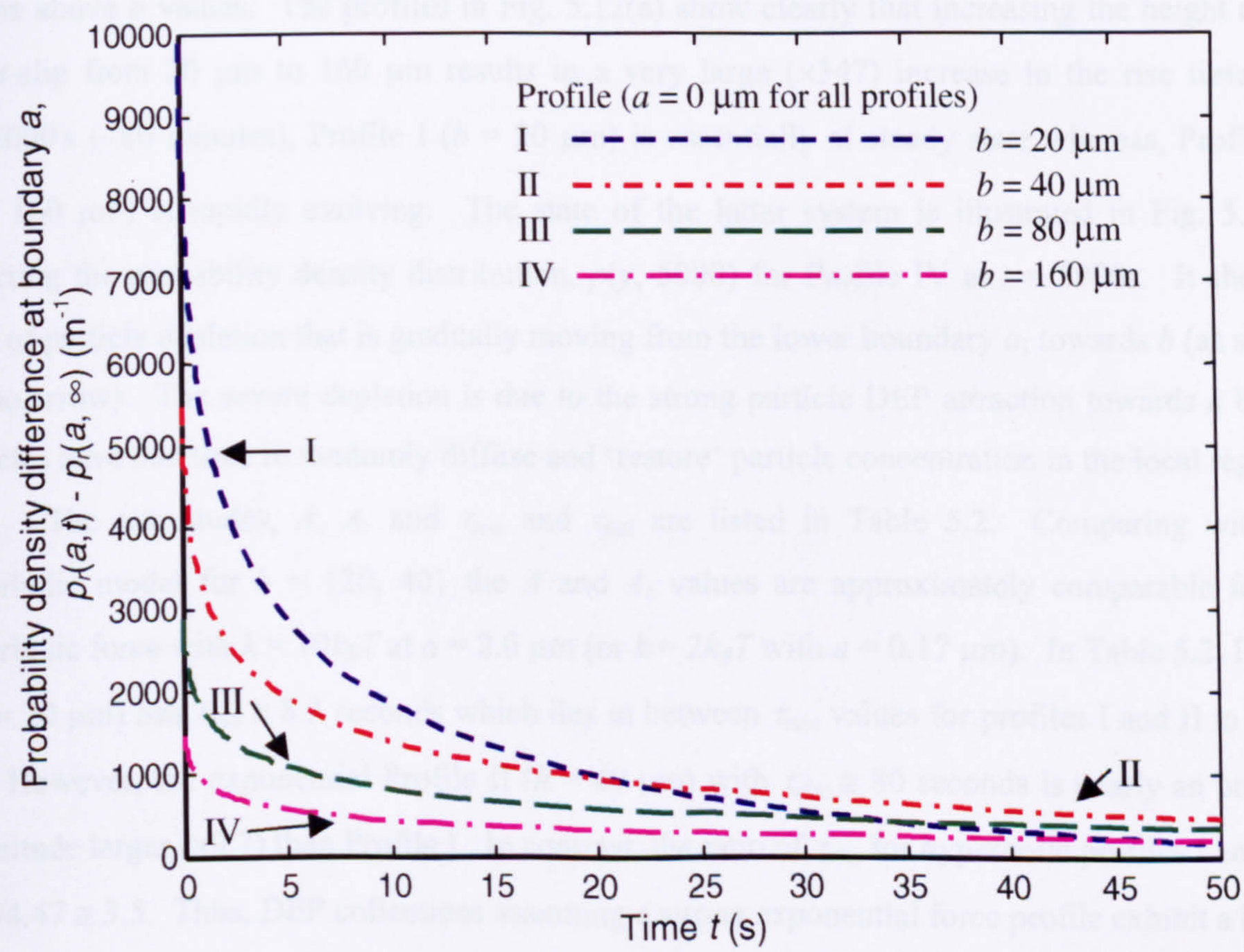

Fig. 5.11(b) Probability density relaxation profiles $p_r(a, t)$ for the initial condition given by (5.4.7) with $k_1 = 2.798\times10^{-16}$ (N) and $k_2 = \pi/10$ (μm^{-1}) for different values of the upper boundary at b.

The alternative parameter $A_r = p(a,\infty)/p(a,0) - 1$, shows a only slight increase as $h = b-a = b$ increases. This is a similar trend to the hyperbolic profile with $k = 0.02k_BT$, except it is less sensitive with respect to variations in h. Increasing h provides a larger particle reservoir resulting in a greater change in particle concentration at a. The τ_{rise} and τ_{fall} times do not exhibit the same sensitivity on $h = b - a$ values as the $k = 0.02k_BT$ hyperbolic example though Table 5.2 shows $\tau_{rise} \cong \tau_{fall}$, which is similar to the hyperbolic case. Generally, the DEP response of this exponential force system with $V_o = 0.1$ V exhibits many similarities to the $k = 0.02k_BT$ hyperbolic model. The collections and subsequent relaxations can be viewed as perturbations from, and restorations to, a uniform distribution.

5.4.3.2 High value for the exponential force coefficient k_1

The DEP response for high values of k_1, reveals different features. Selecting $V_o = 1.0$ (V) and substituting (5.4.3) into (5.4.1), at the lower boundary $y = a = 0$, the magnitude of the DEP force is 100× larger than the above previous case, $F_{DEP} = k_1 = 2.8\times10^{-14}$ (N). This is comparable to the force at the lower boundary $a = 0.5$ μm for the hyperbolic model with $k = 2k_BT$ and $F_{DEP} = 1.65\times10^{-14}$ (N). Four collection and relaxation profiles are shown in Figs. 5.12(a) and (c) for the above b values. The profiles in Fig. 5.12(a) show clearly that increasing the height of the cover-slip from 20 μm to 160 μm results in a very large (×347) increase in the rise time. At $t = 5000$ s (~80 minutes), Profile I ($b = 20$ μm) is essentially at steady state whereas, Profile IV ($b = 160$ μm) is rapidly evolving. The state of the latter system is illustrated in Fig. 5.12(b) depicting the probability density distribution, $p(y, 5000)$ for Profile IV at $t = 5000$s. It shows a zone of particle depletion that is gradually moving from the lower boundary a, towards b (as shown by the arrow). The severe depletion is due to the strong particle DEP attraction towards a before particles have had time to randomly diffuse and 'restore' particle concentration in the local region.

The amplitudes, A, A_r and τ_{rise} and τ_{fall} are listed in Table 5.2. Comparing with the hyperbolic model for $h = \{20, 40\}$ the A and A_r values are approximately comparable for the hyperbolic force with $k = 10k_BT$ at $a = 2.0$ μm (or $k = 2k_BT$ with $a = 0.17$ μm). In Table 5.2, Profile I ($h = 20$ μm) has $\tau_{rise} \cong 8.3$ seconds which lies in between τ_{rise} values for profiles I and II in Table 5.1. However, the exponential Profile II ($h = 40$ μm) with $\tau_{rise} \cong 80$ seconds is nearly an order of magnitude larger (×9.7) than Profile I. In contrast, the ratio of τ_{rise} for hyperbolic profiles I and II is $15.7/4.47 \cong 3.5$. Thus, DEP collections assuming a strong exponential force profile exhibit a higher τ_{rise} dependency on h than the equivalent hyperbolic force model. This is reasonable considering that particles far away from the lower boundary, say > 40 μm, will experience a stronger attractive force with the hyperbolic profile compared with the exponential profile. In general terms, the

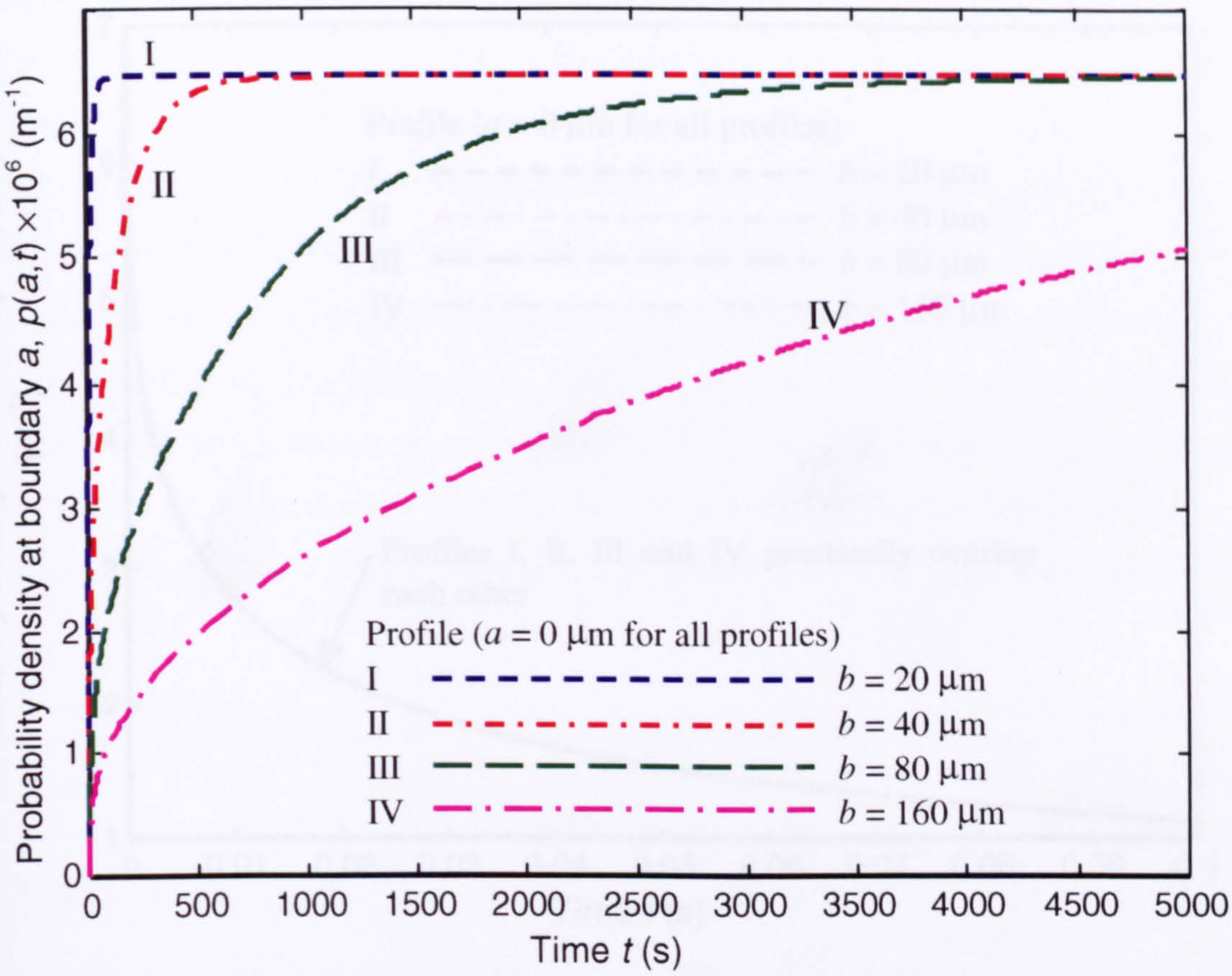

Fig. 5.12(a) Probability density collection profiles $p(a, t)$ for the DEP exponential force given by (5.4.1) with $k_1 = 2.798\times10^{-14}$ (N) and $k_2 = \pi/10$ (μm^{-1}) for different values of the upper boundary at b.

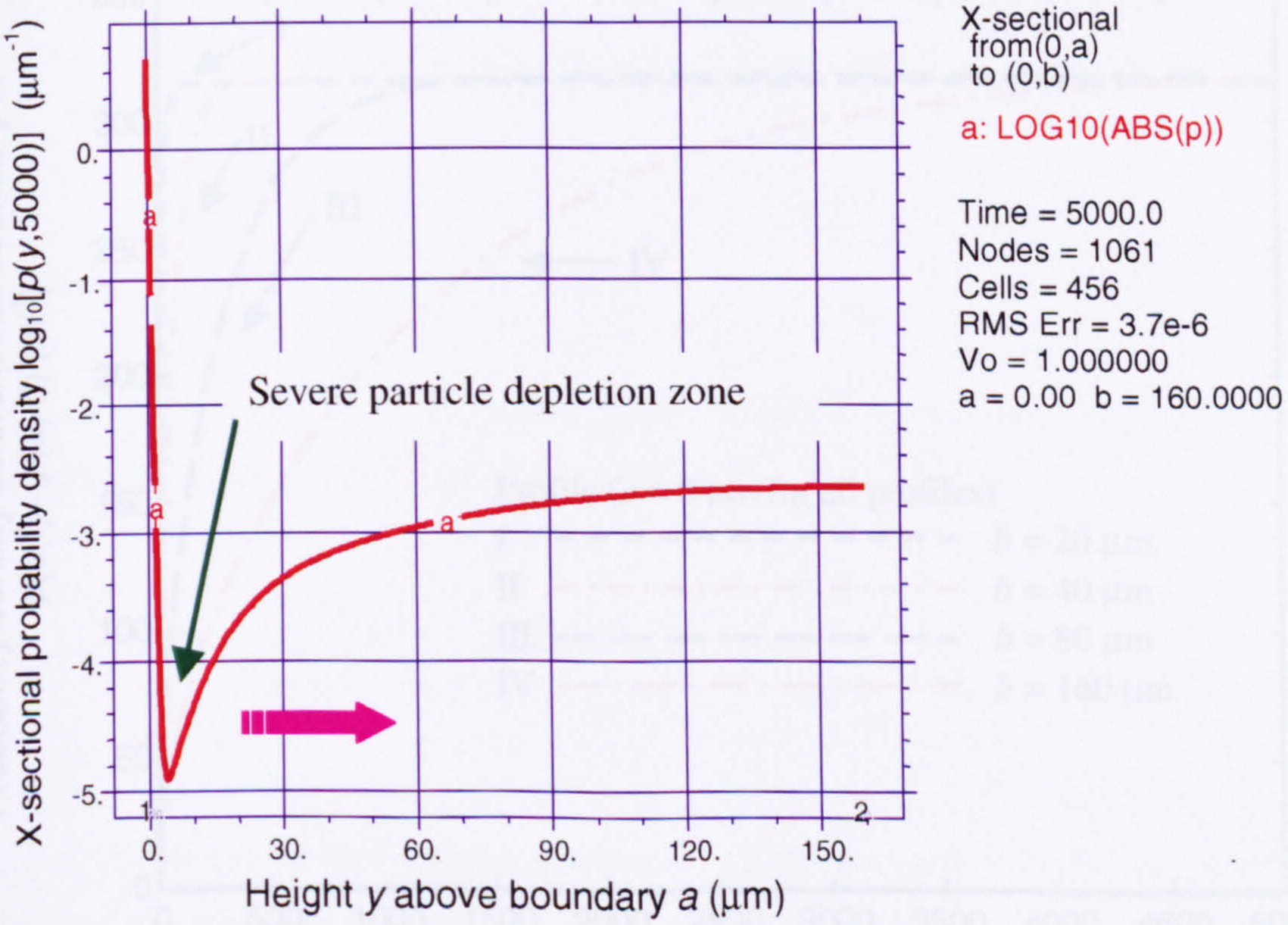

Fig. 5.12(b) Probability density along $\vec{u}_y$ at t = 5000 secs, $\log_{10}$ [$p(y,5000)$] for the DEP exponential force given by (5.4.1) with $k_1 = 2.798\times10^{-14}$ (N) and $k_2 = \pi/10$ (μm^{-1}).

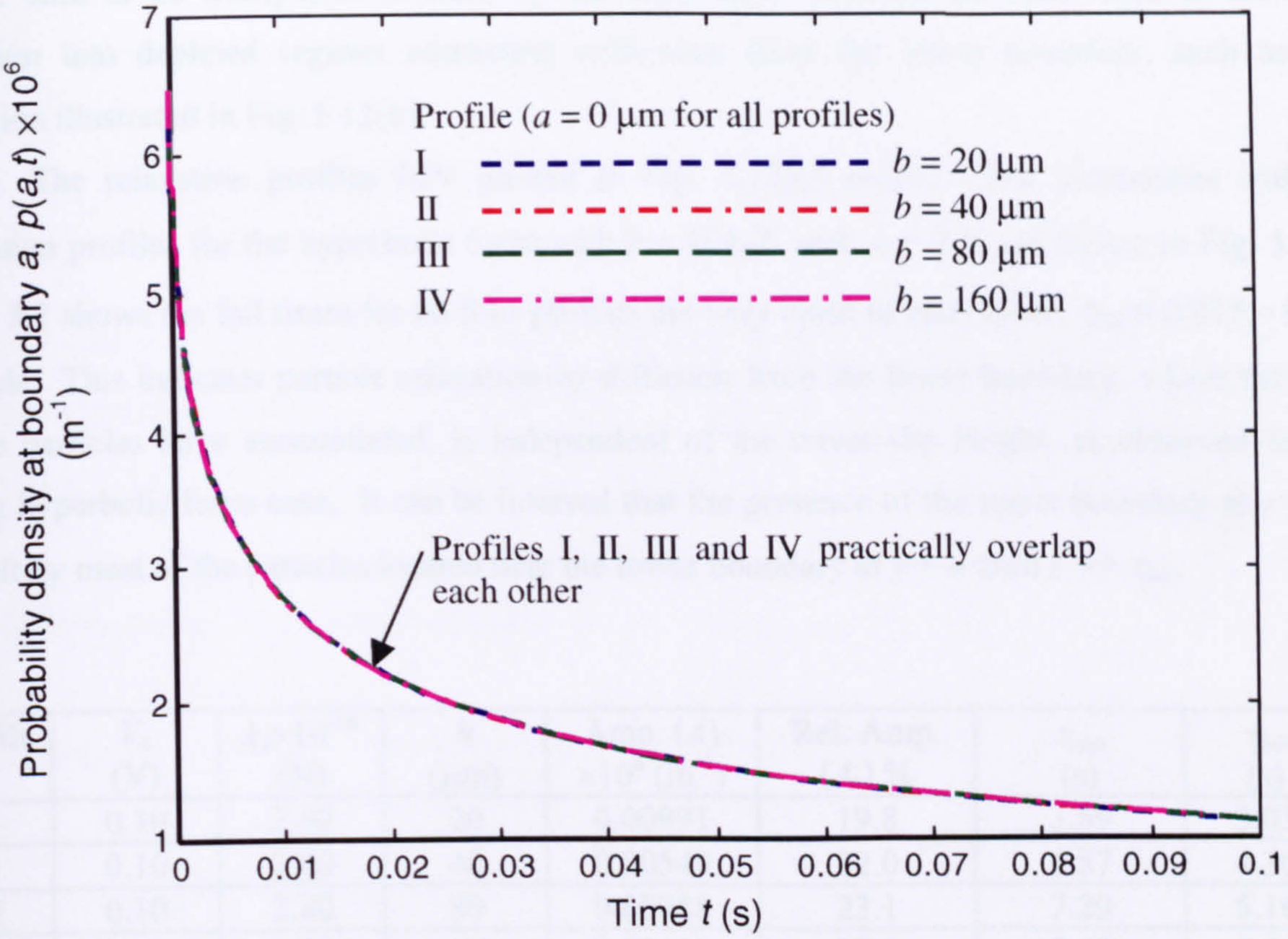

Fig. 5.12(c) Probability density relaxation profiles $p_r(a, t)$ for the initial condition given by (5.4.6) with $k_1 = 2.798\times10^{-14}$ (N) and $k_2 = \pi/10$ (μm^{-1}) for different upper boundary values b.

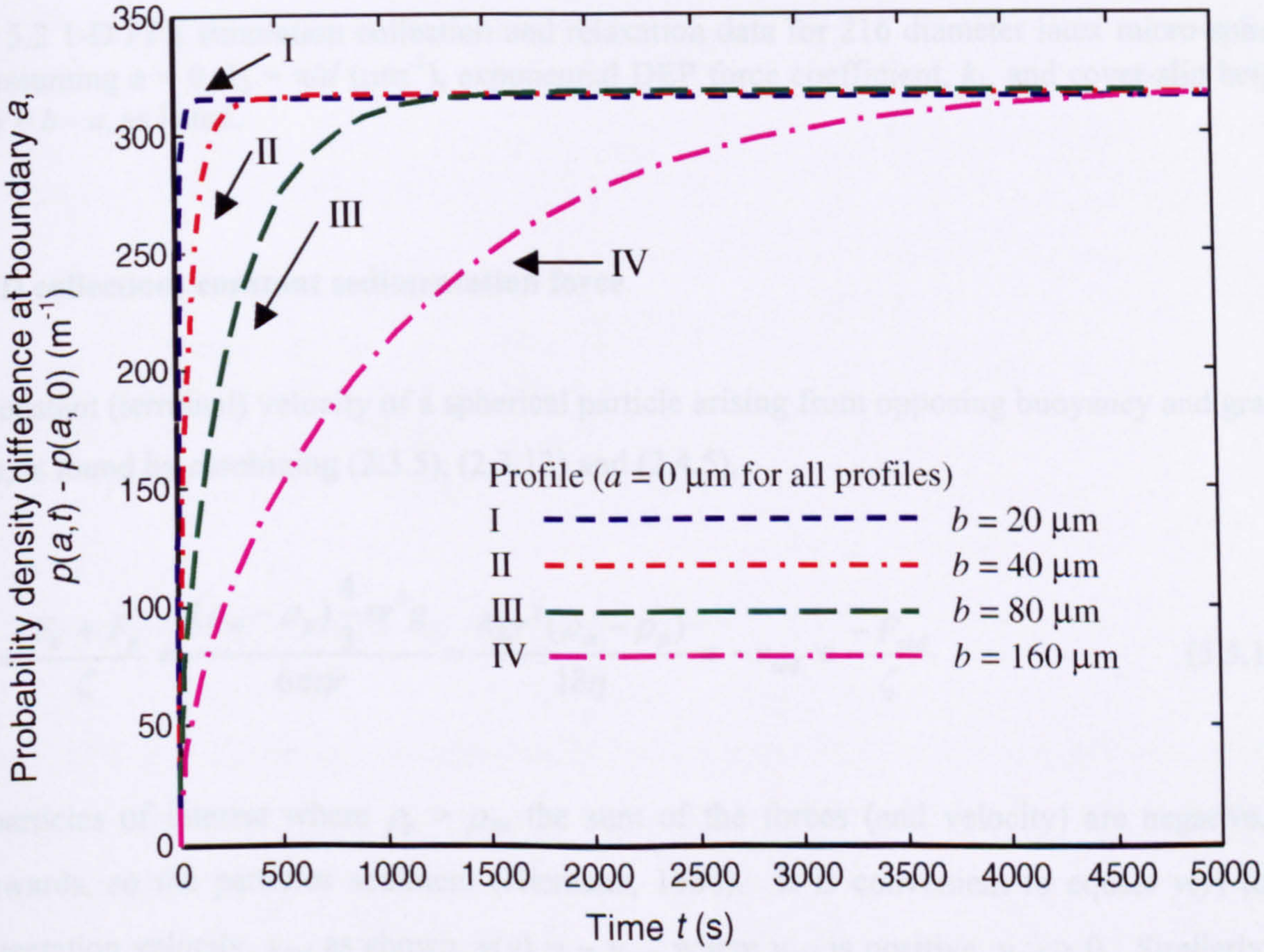

Fig. 5.13 Probability density collection profiles $p(a, t)$ for 216 nm diameter spheres sedimenting under a constant gravitational force for different upper boundary values b.

former tend to be transported directly by the DEP force whereas the latter tend to move by diffusion into depleted regions emanating with time from the lower boundary, such as, the depletion illustrated in Fig. 5.12(b).

The relaxation profiles I-IV plotted in Fig. 5.12(c) exhibit close similarities with the relaxation profiles for the hyperbolic force with $k = 10k_BT$ and $a = 2.0$ μm shown in Fig. 5.9(b). Table 5.2 shows the fall times for all four profiles are very close to each other, $\tau_{fall} \cong 0.015 - 0.016$ seconds. This indicates particle relaxation-by-diffusion from the lower boundary, where the most of the particles have accumulated, is independent of the cover-slip height, as observed for the strong hyperbolic force case. It can be inferred that the presence of the upper boundary at $y = b$ is not felt by most of the particles located near the lower boundary at $y = a$ until $t >> \tau_{fall}$.

Profile	V_o (V)	$k_1 \times 10^{-16}$ (N)	h (μm)	Amp. (A) $\times 10^6$ (m^{-1})	Rel. Amp. (A_r) %	τ_{rise} (s)	τ_{fall} (s)
I	0.10	2.80	20	0.00991	19.8	3.89	3.03
II	0.10	2.80	40	0.00549	22.0	5.87	4.30
III	0.10	2.80	80	0.00288	23.1	7.29	5.16
IV	0.10	2.80	160	0.00148	23.6	8.13	5.64
I	1.0	280	20	6.42	12800	8.29	0.0154
II	1.0	280	40	6.45	25800	80.3	0.0157
III	1.0	280	80	6.46	51700	554	0.0158
IV	1.0	280	160	6.47	103500	2875	0.0159

Table 5.2 1-D FPE simulation collection and relaxation data for 216 diameter latex micro-spheres assuming $a = 0$, $k_2 = \pi/d$ (μm^{-1}), exponential DEP force coefficient, k_1, and cover-slip height, $h = b - a$, as listed.

5.5 1-D collection: constant sedimentation force

The constant (terminal) velocity of a spherical particle arising from opposing buoyancy and gravity forces, is found by combining (2.3.5), (2.3.13) and (2.4.5),

$$v(y) = \frac{F_b + F_g}{\zeta} = \frac{(\rho_m - \rho_p)\frac{4}{3}\pi r^3 g}{6\pi\eta r} = \frac{4gr^2(\rho_m - \rho_p)}{18\eta} \equiv -v_{sed} \equiv \frac{-F_{sed}}{\zeta} \qquad (5.5.1)$$

For particles of interest where $\rho_p > \rho_m$, the sum of the forces (and velocity) are negative, i.e. downwards, so the particles sediment (Hiemenz, 1986). It is convenient to equate $v(y)$ to the sedimentation velocity, v_{sed} as shown, $v(y) = -v_{sed}$, where v_{sed} is positive, $v_{sed} > 0$. Similarly, the sum of the buoyancy and gravity forces, $F_b + F_g = -F_{sed}$. Substituting into (5.5.1) into (5.2.1), the 1-D FPE describing the spatial-temporal evolution of the probability density $p(y, t)$, is

$$\frac{\partial p(y,t)}{\partial t} = -\frac{(F_b + F_g)}{\zeta}\frac{\partial p(y,t)}{\partial y} + \frac{k_B T}{\zeta}\frac{\partial^2 p(y,t)}{\partial^2 y} = \frac{F_{sed}}{\zeta}\frac{\partial p(y,t)}{\partial y} + \frac{k_B T}{\zeta}\frac{\partial^2 p(y,t)}{\partial^2 y}$$
$$= v_{sed}\frac{\partial p(y,t)}{\partial y} + D\frac{\partial^2 p(y,t)}{\partial^2 y} \qquad (5.5.2)$$

The sedimentation force and velocity constant predicted by (5.5.1) for a 216 nm diameter spherical polystyrene latex bead with $\rho_p = 1.05\times10^3$ kg/m^3 submerged in water with $\rho_m = 1.00\times10^3$ kg/m^3, assuming $g = 9.80$ ms^{-2}, is $F_{sed} = 2.5856\times10^{-18}$ (N) and $v_{sed} = 1.4112\times10^{-9} \cong 1.41\times10^{-9}$ (m s^{-1}).

5.5.1 Sedimentation: steady state solution

Substituting (5.5.1) into (5.2.6), the steady state GS of (5.5.2) is

$$p(y) = p_c \exp[\int\frac{v(y)}{D}dy] = p_c \exp[-\frac{v_{sed}}{D}y] \qquad (5.5.3)$$

Substituting (5.5.1) into (5.2.8) the integration constant p_c is,

$$p_c = \left[\int_a^b \exp(-v_{sed}/D)\,dy\right]^{-1} = \frac{-v_{sed}}{D}\left[\exp(-\frac{v_{sed}b}{D}) - \exp(-\frac{v_{sed}a}{D})\right]^{-1} \qquad (5.5.4)$$

Combining (5.5.3) and (5.5.4),

$$p(y) = \frac{-\frac{v_{sed}}{D}\exp(-\frac{v_{sed}}{D}y)}{\exp(-\frac{v_{sed}}{D}b) - \exp(-\frac{v_{sed}}{D}a)} = \frac{\frac{v_{sed}}{D}e^{-\frac{v_{sed}}{D}(y-a)}}{1-e^{-\frac{v_{sed}}{D}(b-a)}} \qquad (5.5.5)$$

5.5.2 Sedimentation: time dependent numerical solution

The 1-D FPE (5.5.2) was solved numerically for the example of a 216 nm diameter spherical polystyrene latex bead with ρ_p and ρ_m as above with $v_{sed} = 1.41\times10^{-9}$ (ms^{-1}). The value for the diffusion coefficient was, $D = k_B T/\zeta = 2.24\times10^{-12}$ m^{2}s^{-1} which is the same as for the hyperbolic and exponential deterministic force profiles. The solution for the probability density $p(y, t)$ was written in FlexPDE 2.15 and implemented in CD-R:/FlexPDE/*fpe_1d_Co.pde*. The lower boundary was set, $a = 0$, and the collection profiles were simulated for heights, $h = b = \{20, 40, 80, 160\}$ (μm).

These were the same values as the exponential case. The simulation yielded four collection profiles at $y = a$ and these are illustrated in Fig. 5.13. Values for the rise amplitude, A, and relative rise amplitude, A_r, are listed in Table 5.3. Similar to the weak hyperbolic and exponential cases, for clarity, the dependent variable plotted is $p(a, t)$ - $p(a, 0)$. Values for the rise time show practically a square law dependence on the cover-slip height, h, i.e. $\tau_{rise} \propto h^2$.

The simulations show the A and A_r values are much smaller over the time scales considered than the collections which assumed weak hyperbolic and exponential deterministic (DEP) force profiles. Consider, for example, the amplitudes for hyperbolic profile with a = 0.5 μm, $h = b - a = 40$ μm, $k = 0.02k_BT$ and the exponential profile with h = 40 μm and V_o = 0.1 V. The respective A values listed in tables 5.1 and 5.2, are $A_{hyp} = 1781$ and $A_{exp} = 5490$ (m^{-1}). Both of these are considerably higher than $A_{sed} = 316$ (m^{-1}) (the subscript on the A's denotes the deterministic force). The comparison is the same for A_r. The τ_{rise} values are also much shorter: $\tau_{rise\ hyp} \cong 11$ (s) and $\tau_{rise\ exp} \cong 6$ (s) compared with $\tau_{rise\ sed} \cong 57$ (s). The cases where $\tau_{rise\ sed}$ is comparable with $\tau_{rise\ hyp}$ and $\tau_{rise\ exp}$ occur for strong hyperbolic and exponential forces where both A_{hyp} and $A_{exp} >> A_{sed}$. This means unless the DEP forces are extremely weak, to a first approximation the particle collections from sedimentation can be ignored.

Profile	b (μm)	Amp. (A) (m^{-1})	Rel. Amp. (A_r) %	τ_{rise} (s)
I	20	315.0	0.630	14.3
II	40	315.7	1.26	57.2
III	80	317.0	2.54	230
IV	160	319.6	5.11	925

Table 5.3 1-D FPE simulation collection data for 216 diameter latex micro-spheres assuming $a = 0$, constant sedimentation force $F_{sed} = 2.586\times10^{-18}$ (N), and b, as listed.

5.6 Discussion

Probability density time-profiles, $p(a, t)$, of collections for deterministic hyperbolic, exponential and constant force profiles highlight important features about the dynamics of particle accumulation onto a boundary. The first is the dependency of the collection time τ_{rise}, at the lower boundary at $y = a$, on the cover-slip height, $h = b - a$. The values for τ_{rise} for strong hyperbolic and exponential forces exhibit an approximate square law dependency on height. The effect of h is much less evident with low DEP force strengths at the lower boundary. The effect of the upper barrier is also dependent on the functional variation of force with height. Sedimentation, for

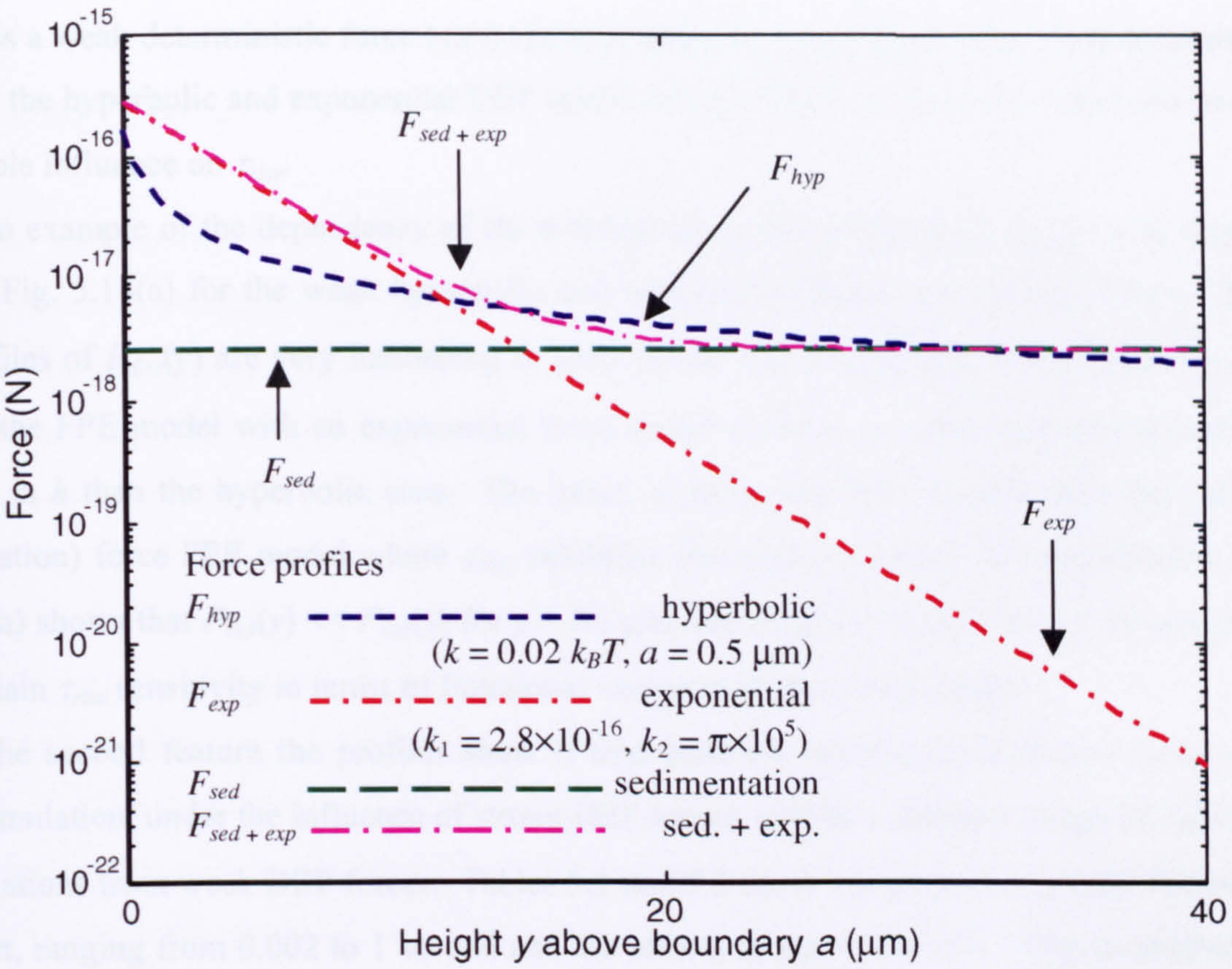

Fig. 5.14(a) Deterministic force profiles versus displacement y above boundary a (electrode plane): profiles are hyperbolic, exponential, sedimention, and sum of sedimentation and exponential.

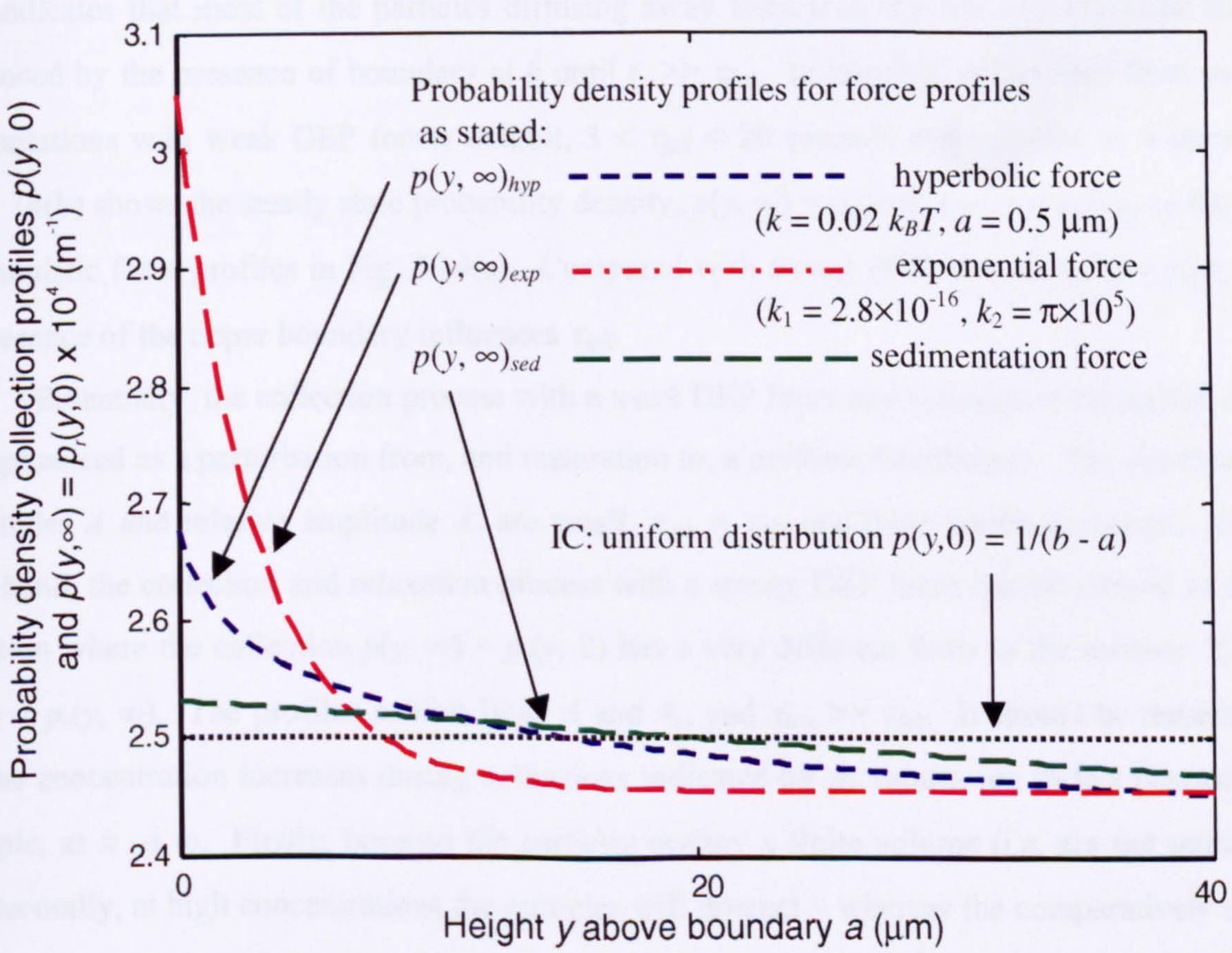

Fig. 5.14(b) Probability density collection profiles for weak DEP hyperbolic and exponential, and constant sedimentation forces corresponding to Fig. 5.14(a) above, including the uniform IC.

example, is a weak deterministic force but it remains constant with height rather than deceasing as it does for the hyperbolic and exponential DEP model forces. This results in the value of h bearing considerable influence on τ_{rise}.

An example of the dependency of the deterministic force magnitude $F_{dtm}(y)$ with height is shown in Fig. 5.14(a) for the weak hyperbolic and exponential forces and sedimentation. These weak profiles of $F_{dtm}(y)$ are very interesting in view of the τ_{rise} comparison in section 5.4.3.1 that indicated the FPE model with an exponential force model yielded τ_{rise} that were less sensitive to variations in h than the hyperbolic case. The latter, in turn, was less sensitive than the constant (sedimentation) force FPE model where τ_{rise} exhibited practically a square law dependency on h. Fig. 5.14(a) shows that $F_{exp}(y) << F_{sed}(y)$ for $y > 20$ μm, and $F_{hyp}(y) < F_{sed}(y)$ for $y > 40$ μm, which helps explain τ_{rise} sensitivity in terms of functional variation of force with height.

The second feature the profiles show is that particles relaxing-by-diffusion from steady state accumulation, under the influence of strong DEP forces, exhibit a different range of τ_{fall} values than relaxations from weak DEP forces. Tables 5.1 and 5.2 show τ_{fall} from strong DEP forces tend to be short, ranging from 0.002 to 1 second and are almost independent of h. This is attributed to most of the particles being located near the lower boundary $y = a$ at the start of the relaxation process whereas particles are almost completely absent near the upper boundary, i.e. $p_r(b,0) \cong 0$. This indicates that most of the particles diffusing away from a at the start of relaxation are not influenced by the presence of boundary at b until $t >> \tau_{fall}$. In contrast, relaxations from particle accumulations with weak DEP forces exhibit, $3 < \tau_{fall} < 20$ seconds and increase as h increases. Fig. 5.14(b) shows the steady state probability density, $p(y, \infty) = p_r(y, 0)$ corresponding to the three deterministic force profiles in Fig. 5.14(a). Compared with strong DEP case, $p_r(a, 0) \approx p_r(b, 0)$ so the presence of the upper boundary influences τ_{fall}.

Essentially, the collection process with a *weak* DEP force and subsequent relaxation can be conceptualised as a perturbation from, and restoration to, a uniform distribution. The rise (and fall) amplitudes A and relative amplitude A_r are small, $\tau_{rise} \approx \tau_{fall}$ and have moderate values. On the other hand, the collection and relaxation process with a *strong* DEP force can be viewed as a state transition where the collection $p(y, \infty) = p_r(y, 0)$ has a very different form to the uniform IC with $p(y,0) = p_r(y, \infty)$. The profiles exhibit large A and A_r, and $\tau_{rise} >> \tau_{fall}$. It should be remembered that the concentration increases during collections indicated by A_r values, are in fact bounded, for example, as $h \rightarrow \infty$. Firstly, because the particles occupy a finite volume (i.e. are not point size) and, secondly, at high concentrations the particles will interact – whereas the comparatively simple FPE model, as presented, assumes they do not interact with each other [4] (Doi and Edwards, 1986).

---

[4] The FPE (or Smoluchowski equation) can be modified to include particle-particle interactions in the diffusion term, D, and set-up in matrix form (Doi and Edwards, 1986, chs. 3.3 and 3.6; Russel *et al.*, 1999, Ch. 13; Green *et al.*, 2000b).

5.7 Concluding remarks

This chapter has introduced 1-D diffusion-limited particle transport and developed analytical and numerical methods for predicting particle collections, under the action of deterministic forces within two impenetrable boundaries. The two boundaries are the lower planar electrode array and the upper cover-slip that are typical of DEP experiments. The Fokker-Planck Equation model uses hyperbolic and exponential (decay) spatial force profiles to mimic the DEP force that attracts particles away from the upper, towards the lower, impenetrable boundary. The relaxation-by-diffusion of accumulated particles, after the DEP force is switched off, away the lower boundary is subsequently investigated for both hyperbolic and exponential spatial force profiles. Particle collection onto the boundary, under the action of sedimentation, is also examined.

The 1-D FPE model developed for predicting time-profiles of collections and relaxations is generally applicable to colloidal particles of different shapes and size. However, for conciseness the particles considered were 216 nm diameter micro-spheres relevant to experiments discussed in Chapter 7. Measures of the time profiles include the rise and fall amplitude and time, and variations in these parameter values have been studied in responses to changes in the height of the upper boundary (cover-slip). The time profiles of particle collections under the action of strong and weak deterministic forces, and subsequent relaxation profiles, show distinguishing characteristics that can be compared with experimental observations. These characteristics broadly classify DEP collection/relaxation responses as being as perturbations or transitions. The 1-D FPE model is very simple, and underlines general principles about DEP collections indispensable for understanding the behaviour of more complex 2-D systems (or quasi-3D systems) discussed in chapters 6 and 7.

6 Modelling DEP collections (II): numerical solutions to the 2-D Fokker-Planck Equation

6.0 Introduction

A more comprehensive model, than the 1-D FPE developed in Chapter 5, of dielectrophoretic collection rates onto planar, interdigitated electrode arrays is made possible by considering the solution of a three-dimensional Fokker-Planck equation (3-D FPE). A three dimensional perspective view of a planar interdigitated electrode array described in Chapter 3, is shown in Fig. 6.1(a). In most cases of practical interest the electrode length (along the longitudinal z-axis, $\vec{u}_z$) is much greater than the width and thickness - typically by about two orders of magnitude or more. Consequently, the electrode geometry is invariant in the longitudinal z-direction. As mentioned in section 2.4.4.3, particle movement can therefore be adequately described in the x-y plane, orthogonal to $\vec{u}_z$, by a two-dimensional (2-D) FPE. Recalling (2.4.24) the 2-D FPE is written,

$$\frac{\partial p(x,y,t)}{\partial t} = -\vec{\nabla}\cdot\vec{J}(x,y,t) = -\vec{\nabla}\cdot\left(p(x,y,t)\vec{v}(x,y)\right) + D\vec{\nabla}\cdot\vec{\nabla}p(x,y,t) \tag{6.0.1}$$

where the (deterministic) particle velocity is assumed to arise solely from the small-time averaged DEP force given by (2.1.7),

$$\vec{v}(x,y) = \frac{\left\langle \vec{F}_{DEP}(x,y,t)\right\rangle_t}{\zeta} = \frac{\vec{F}_{DEP}(x,y)}{\zeta} = \frac{\frac{1}{4}\alpha V\,\vec{\nabla}\left|\vec{E}(x,y)\right|^2}{\zeta} \tag{6.0.2a}$$

and all other symbols have been previously defined. Assuming for convenience the polarisability, α, can be expressed by (2.2.3), then for a sphere with volume $V = 4\pi r^3/3$,

$$\vec{v}(x,y) = \frac{\frac{1}{4}\alpha V\,\vec{\nabla}\left|\vec{E}(x,y)\right|^2}{\zeta} = \frac{\pi r^3 \varepsilon_m \,\mathrm{Re}\{f_{CM}\}\vec{\nabla}\left|\vec{E}(x,y)\right|^2}{\zeta} \tag{6.0.2b}$$

Thus, in addition to the vertical direction, $\vec{u}_y$, modelled in the 1-D case in Chapter 5, this model takes into account particle movement in the transverse direction, $\vec{u}_x$, parallel to the planar array.

A key term for determining the force via (6.0.2) is the gradient of the electric field intensity, $\vec{\nabla}\left|\vec{E}(x,y)\right|^2$. This changes markedly near the electrode edges so values generated by numerical solution of the electric potential equation tend to be prone to error compared with those made available by analytical solution (albeit with simplifications). Consequently, a major part of this chapter, (sections 6.1 to 6.3), is devoted to finding expressions for $\vec{\nabla}\left|\vec{E}(x,y)\right|^2$ that provides the basis for determining time dependent collection and relaxation profiles using (6.0.1). Solutions for the steady state and time dependent particle probability densities are developed in sections 6.4 and 6.5. The form of the steady state probability density $p(x,y)$ can be determined, for the most part, by analytical means. The time dependant density $p(x,y,t)$ is less straightforward. The form of $\vec{\nabla}\left|\vec{E}(x,y)\right|^2$, and application of reflecting flux BCs means the 2-D FPE system (6.0.1) – (6.0.2) is formidable to solve analytically, and therefore it was solved numerically using FlexPDE 2.15 (PDE Solutions, CA, USA) introduced in the previous chapter. The solutions to $p(x,y,t)$ reveals a dependency on an number of parameters that can vary with experiment, including the electrode potential and frequency, electrode width, cover-slip height, and particle radius.

6.1 Determining the electric potential

To find an expression for $\vec{\nabla}\left|\vec{E}(x,y)\right|^2$ requires a solution to the electric field that extends between the planar interdigitated electrode array and cover-slip, as illustrated in Fig. 6.1(a). The electrodes are alternately connected to two signals with respective phases, $\theta=0^\circ$ and $\theta=180^\circ$ (with peak potential V_o and angular frequency ω – not shown for conciseness). The array is considered to be infinitely periodic in the transverse x-direction $\vec{u}_x$ in terms of its electric potential applied to each electrode pair ($\theta = 0^\circ$ and $\theta = 180^\circ$) and accompanying pair of inter-electrode spaces or 'gaps'. In the following sections a solution for the electric field is found by solving Laplace's equation. The electric field exhibits periodicity and this enables the 2-D region, between the electrode array and cover-slip, to be divided into smaller compartments in the transverse direction that repeat themselves.

Each compartment is comprised of one pair of electrodes each with width w and an accompanying pair of inter-electrode spaces, or 'gaps', (width d). Parenthetically, in the next section 6.1.2, each compartment is further sub-divided into *cells* - referred to in earlier work (see *List of Publications* at the end of this dissertation). To assist with the analysis, the partitions are placed as shown in Fig. 6.1(b) at the mid-point of the electrodes with phase $\theta=0^\circ$. The transverse displacement at the left partition for the mth compartment is $x = 2m(d + w)$ where $m \in$ J.

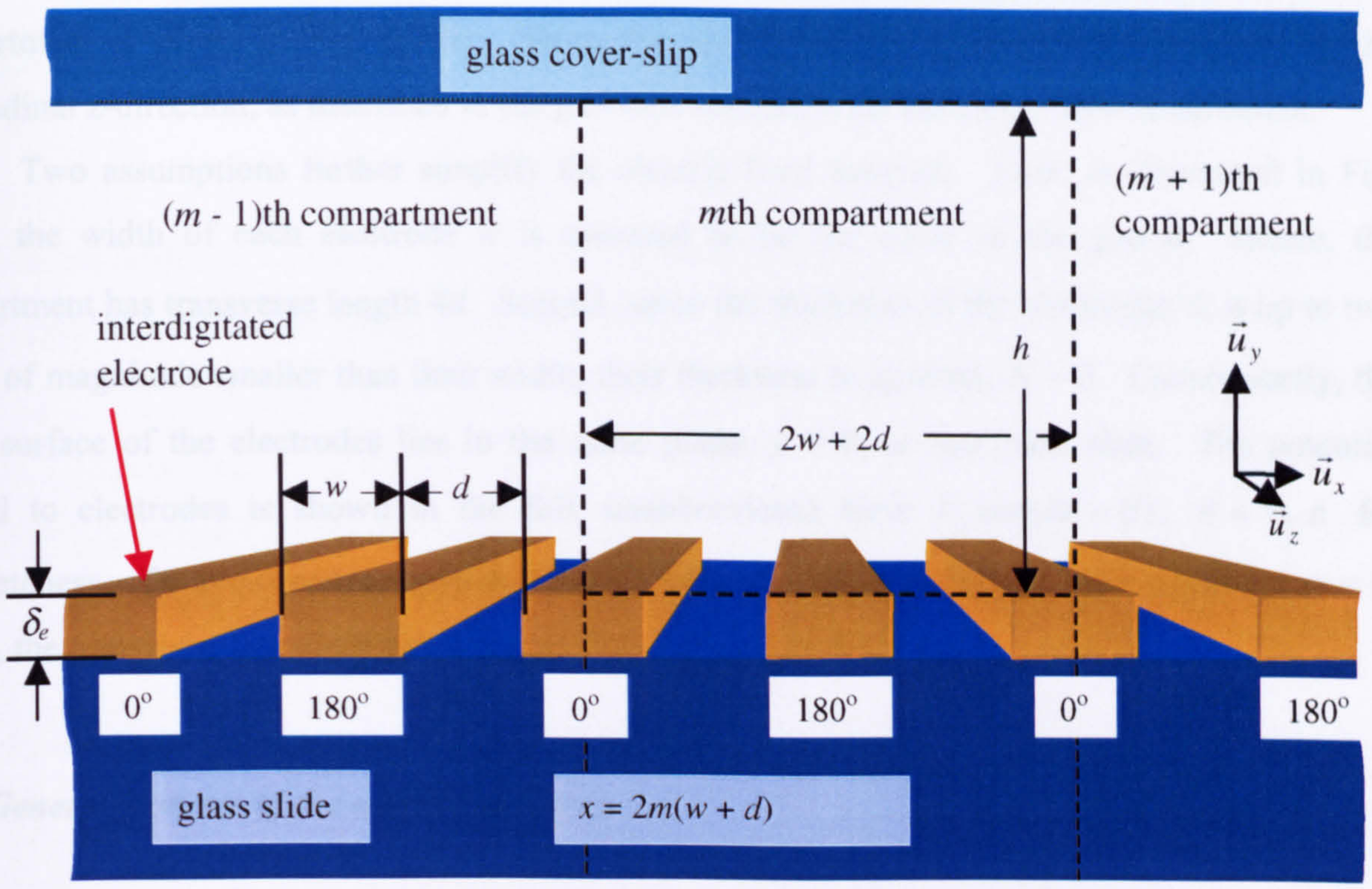

Fig. 6.1(a) A 3-D perspective view of a planar interdigitated electrode array (*not* to scale) divided into compartments in the transverse direction $\vec{u}_x$.

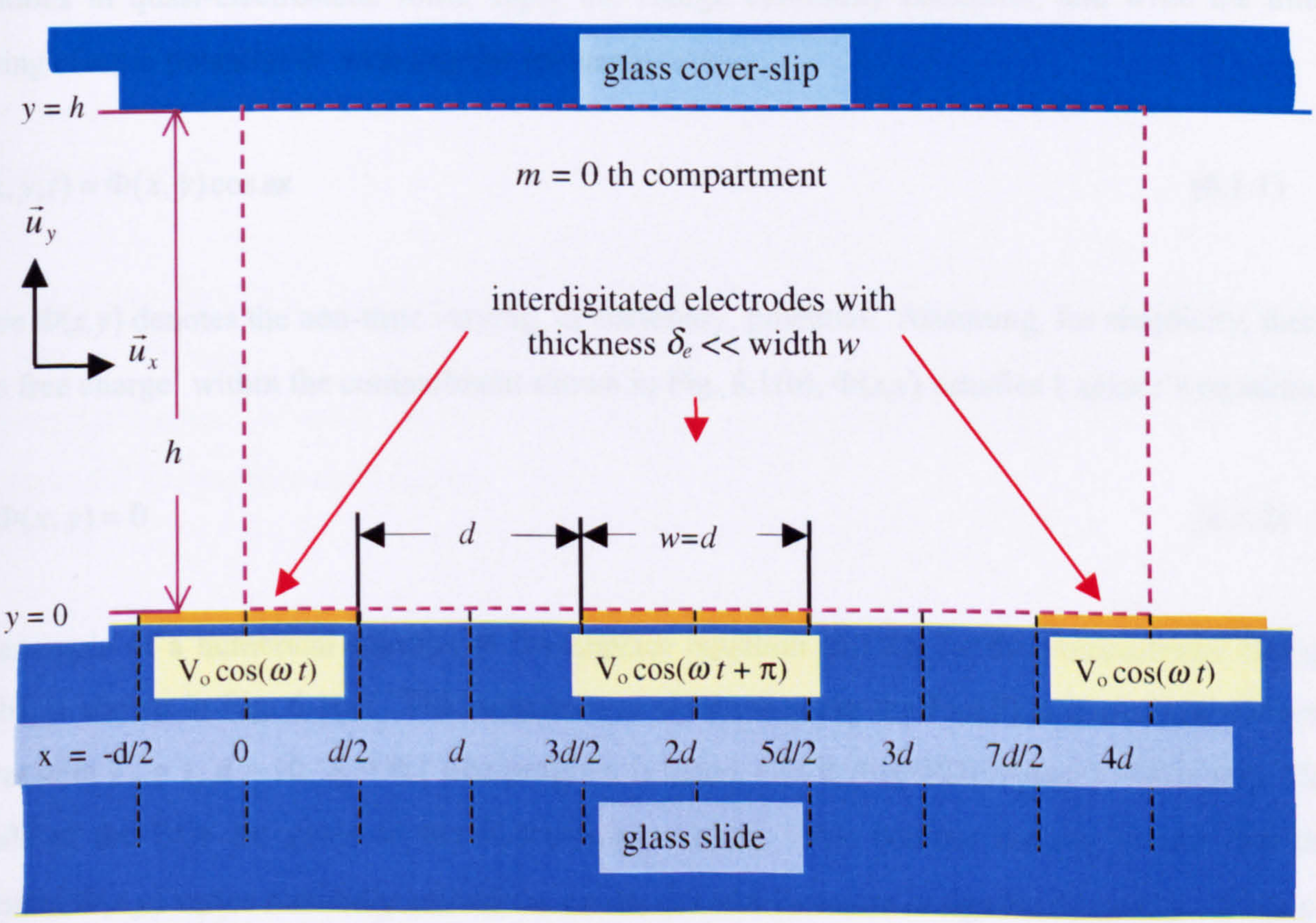

Fig. 6.1(b) An enlarged, elevation view of the $m = 0^{th}$ compartment (*not* to scale) in Fig. 6.1(a). The thickness of the interdigitated electrodes, δ_e is very small compared with their width w and the height of cover-slip, h.

One of these compartments – the mth compartment is outlined in Fig. 6.1(a). A detail of the compartment is given in Fig. 6.1(b). Since the electrodes are geometrically invariant in the longitudinal z-direction, as described in the previous section, a 2D elevation view is sufficient.

Two assumptions further simplify the electric field analysis. First, as illustrated in Fig. 6.1(b), the width of each electrode w is assumed to be the same as the gap d. Hence, the compartment has transverse length $4d$. Second, since the thickness of the electrodes δ_e is up to two orders of magnitude smaller than their width, their thickness is ignored, $\delta_e = 0$. Consequently, the upper surface of the electrodes lies in the same plane, $y = 0$, as the glass slide. The potential applied to electrodes is shown in the full, unabbreviated form $V_o \cos(\omega t + \theta)$, $\theta = 0, \pi$ for completeness. To avoid unnecessary detail, and without loss of generality, one considers $m = 0$. Hence, the transverse boundary simplified in Fig. 6.1(b), $\{x : 0 \le x \le 4d\}$.

6.1.1 General features of the electric potential

The approach for electric field analysis develops the methods used in earlier work (see *List of Publications* at the end of this dissertation, specifically by Morgan *et al.*, 2001) where the DEP force for an interdigitated electrode array was analysed. The approach is to start with Maxwell's equations in quasi-electrostatic form, apply the charge continuity condition, and write the time varying electric potential Φ with angular frequency ω as

$$\Phi(x,y,t) = \Phi(x,y)\cos\omega t \tag{6.1.1}$$

where $\Phi(x,y)$ denotes the non-time varying, or stationary, potential. Assuming, for simplicity, there is no free charge[1] within the compartment shown in Fig. 6.1(b), $\Phi(x,y)$ satisfies Laplace's equation

$$\nabla^2 \Phi(x,y) = 0 \tag{6.1.2}$$

An example of a numerical solution to the Laplace equation (6.1.2), for the compartment in Fig. 6.1(b), is shown in Fig. 6.1(c). The solution was obtained using the FlexPDE 2.15 finite element solver with $V_o = 1$, $d = 10$, $\delta_e = 0.1$ (the program is listed, CD-R:/FlexPDE/*Epot2D3ElTh.pde*). The details of the BCs are given in the forthcoming section. The contour density reveals that the potential $\Phi(x,y)$ varies markedly around the electrodes and variation is significant until $y = 20$ (a.u.) or $y = 2d$. The green contour labelled 'k' shows $\Phi(10,y) = 0 = \Phi(30,y)$. Closer inspection of the contours (all alphabetical character and colour coded) reveals symmetry about these lines.

---

[1] In general, the potential satisfies the Poisson equation (Jackson, 1975, p. 39). However, to solve this equation would require knowledge of the spatial-temporal distribution of charge density. This issue is discussed further in Chapter 7.

6.1.2 Electric field boundary conditions (BCs)

The following (electrical) BCs are applied to each perimeter segment in the compartment shown in Fig. 6.1(b).

1) Since the thickness of the two electrodes is extremely small (δ_e = 0.1 μm), the potential of the lower barrier at $y = 0$ for the boundary line covering the two electrodes shown in Fig. 6.1(b), is

$$\Phi(x,0,t) = \begin{cases} V_0\cos(\omega t), & 0 \le x < \frac{d}{2} \\ V_0\cos(\omega t + \pi), & \frac{3d}{2} < x < \frac{5d}{2} \\ V_0\cos(\omega t), & \frac{7d}{2} < x \le 4d \end{cases} \qquad (6.1.3a)$$

where V_o is the peak sinusoidal electric potential. It is convenient to separate the time dependence according to the relation given by (6.1.1). Thus, the Dirichlet BC is,

$$\Phi(x,0) = \begin{cases} +V_0, & 0 \le x < \frac{d}{2} \\ -V_0, & \frac{3d}{2} < x < \frac{5d}{2} \\ +V_0, & \frac{7d}{2} < x \le 4d \end{cases} \qquad (6.1.3b)$$

Note that the choice of open sub-intervals (that excludes end points), rather than closed, does not affect the analysis [2].

2) Continuity of the normal component of the electric flux density[3] (C m^{-2}) (Jackson, 1975, p.146; Von Hippel, 1954) across the aqueous-glass cover-slip interface at $y = h$ means the electric field in the aqueous medium is much smaller (*ca.* ×30) than in the glass cover-slip. This leads to the Neumann BC approximation (Washizu, 1990),

$$\left.\frac{\partial\Phi(x,y)}{\partial y}\right|_{y=h} = 0,\ 0 \le x \le 4d \qquad (6.1.4)$$

3) The aqueous medium-glass interface along the inter-electrode spaces, or gaps, is also modelled in the *first instance* as a Neumann BC,

---

[2] Subsequent analyses use the potentials inside integrals where singular points do not contribute to the interval, or are said to have zero measure (Sokolnikoff and Redheffer, 1966, p. 716-19).

[3] The electric flux density is also known as the electric displacement (Jackson, 1975, p. 14; Von Hippel, 1954, p. 6).

$$\left.\frac{\partial\Phi(x,y)}{\partial y}\right|_{y=0} = 0, \left\{\begin{matrix}\frac{d}{2} < x < \frac{3d}{2} \\ \frac{5d}{2} < x < \frac{7d}{2}\end{matrix}\right\} \qquad (6.1.5a)$$

This BC (6.1.5a), in conjunction with the aforementioned BCs (6.1.3b) and (6.1.4), is used in the *numerical* solution to Laplace's equation (6.1.2) shown in Fig. 6.1(c). The Neumann inter-electrode gap BCs are denoted by 'N' in the figure. The combination of Dirichlet and Neumann BCs specified for the perimeter of the compartment illustrated in Fig. 6.1(c) forms a *mixed* BC (Jackson, 1975, p. 42).

The use of the Neumann BC for the gaps, however, is known to be problematic for developing *analytical* solutions for the electric field (Wang *et al.*, 1996). Instead, for the analytical approach, the gaps are modelled by a Dirichlet BC that suitably 'mimics' the Neumann BC. Initial work (see *List of Publications* at the end of this dissertation) and by others (Wang *et al.*, 1996) assumed a Dirichlet gap potential profile that is a linear interpolation between the electrode potentials at each gap endpoint. This is a good, first order approximation but it can be made more flexible and subsequently optimised by varying the values of the endpoints. This procedure is illustrated in Fig. 6.1(d). The bold, red curve, is an elevation view of the contour plot Fig. 6.1(c) for the transverse gap segment, $5 < x < 15$ (or $\frac{d}{2} < x < \frac{3d}{2}$) at $y = 0$ between points '1' and '2'. The numerical solution extends between 1 and –1 in accordance with the example value, $V_o = 1$. The line-of-best-fit to the bold red profile, performed using Origin 4.1 ™ (Microcal, MA, USA), is shown by the green dot-dash (· – · – · –) line. It has endpoint values ± 0.78 as shown. The blue dotted (·····) line is the linear interpolation used by the abovementioned authors. Introducing a parameter γ that defines the gradient, where $0 \le \gamma \le 1$, the line-of-best-fit is labelled by $\gamma = 0.78$, the blue dotted (·····) line by $\gamma = 1$, and the horizontal brown dashed line (– – –) by $\gamma = 0$, as shown.

The $\Phi(x,0)$ for $\frac{d}{2} < x < \frac{3d}{2}$ shown in Fig. 6.1(d) is representative of all gap segments. Inspecting the contours in Fig.6.1(c) it is clear $\Phi(x,0)$ for $\frac{5d}{2} < x < \frac{7d}{2}$ is the mirror reflection of Fig. 6.1(d) (about $x = d$). Thus, the Dirichlet BC for the gaps in the compartment is constructed as,

$$\Phi(x,0) = \left\{\begin{matrix}+2\gamma V_0(1-\frac{x}{d}), & \frac{d}{2} < x < \frac{3d}{2} \\ -2\gamma V_0(3-\frac{x}{d}), & \frac{5d}{2} < x < \frac{7d}{2}\end{matrix}\right\}, \{\gamma : 0 \le \gamma \le 1\} \qquad (6.1.5b)$$

It is understood that setting $\gamma = 1$ yields the same BC used in earlier work (see *List of Publications* at the end of this dissertation, specifically by Morgan *et al.*, 2001). An improved value predicted numerically is $\gamma = 0.78$.

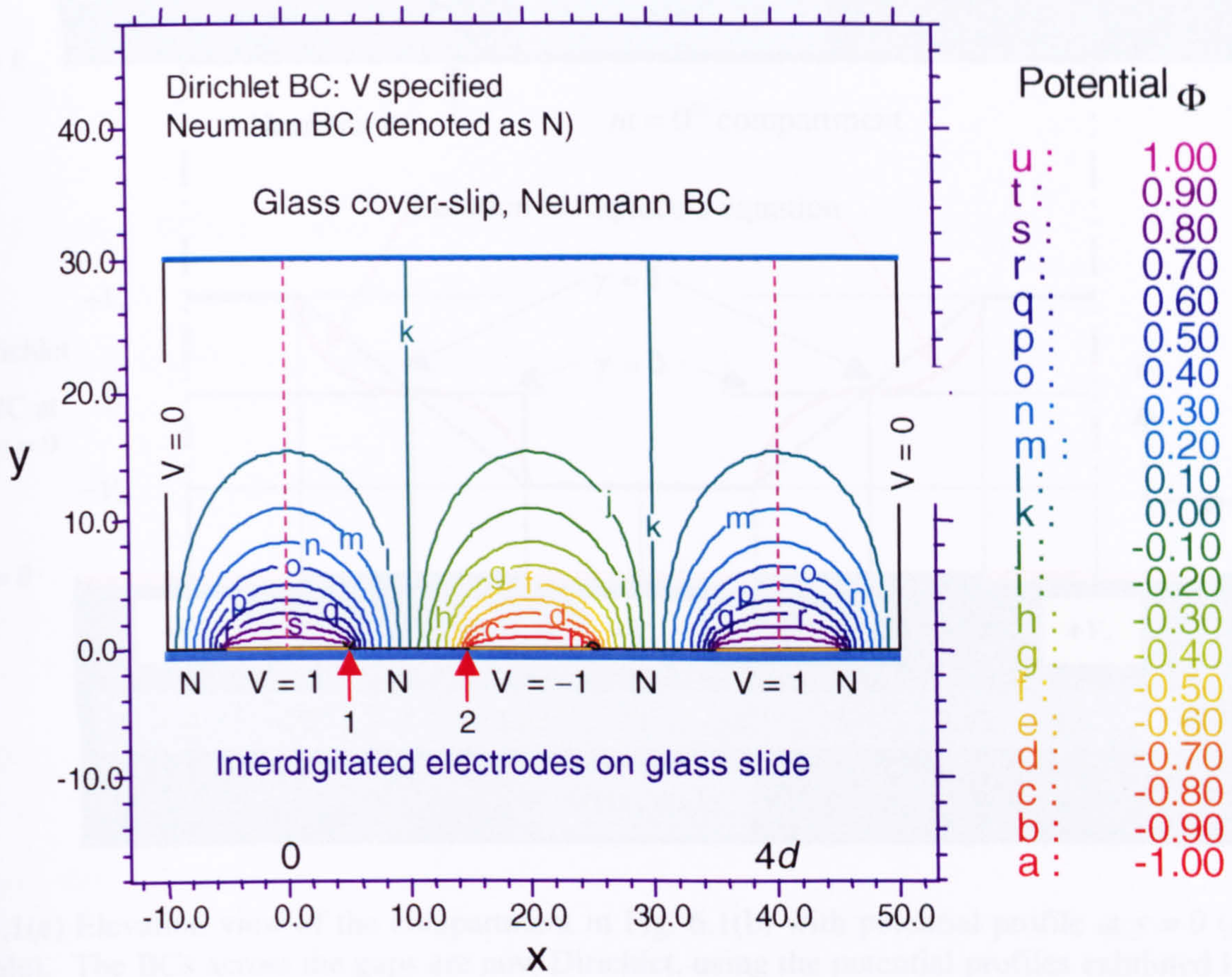

Fig. 6.1(c) Electric potential contour plot obtained by numerically solving Laplace's equation (6.1.2) for the compartment in Fig. 6.1(b) scaled with $\delta_e = 0.1$, $d = 10$, $h = 30$ and $V_o = 1$ (a.u.). The BCs are as shown, see text for details.

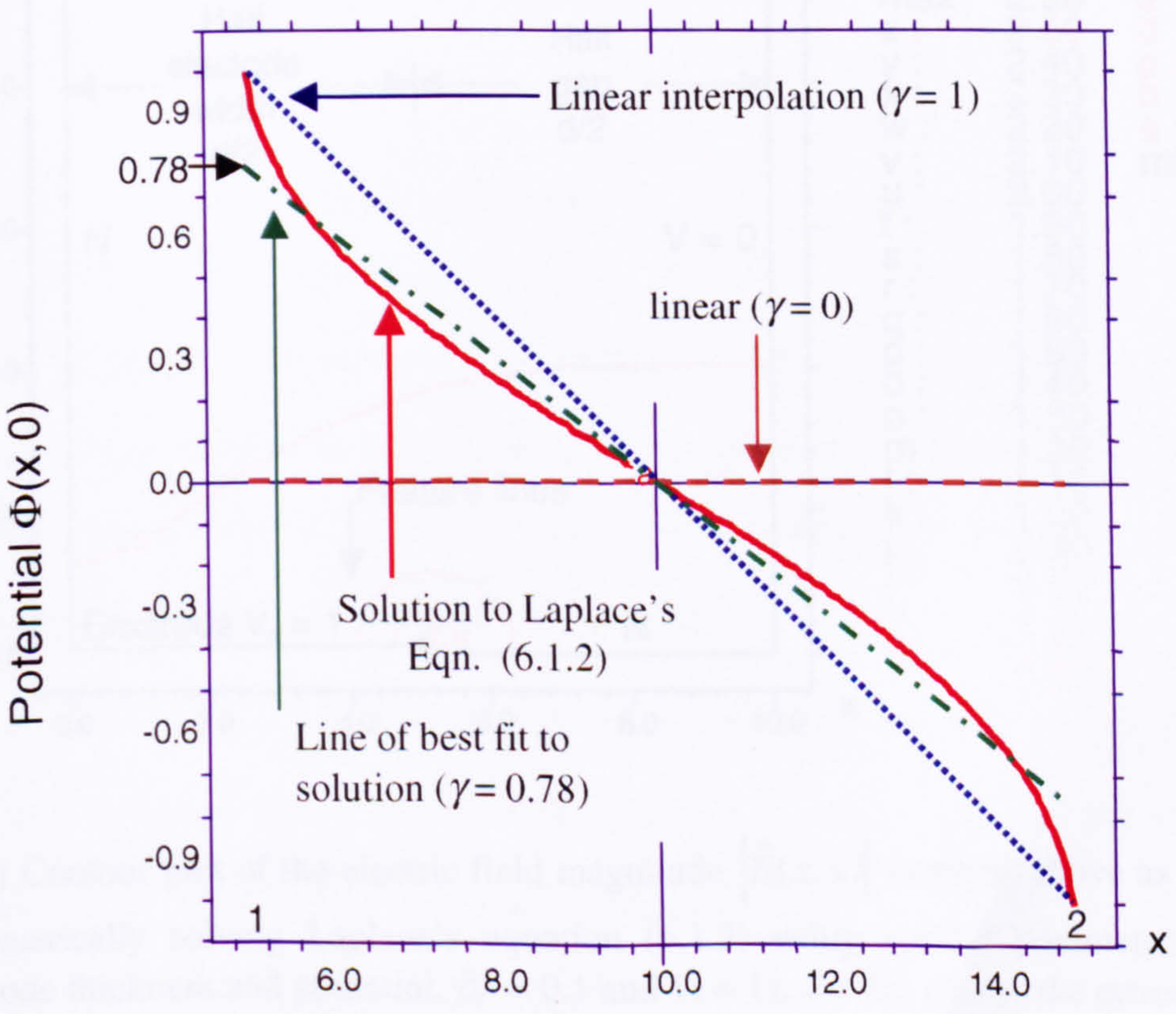

Fig. 6.1(d) Elevation view of the potential in Fig. 6.1(c) between arrows labelled '1' and '2' at $y = 0$ (red —), line of best fit (green, – · – ·) and approximations (blue, ·····) and brown (– – –).

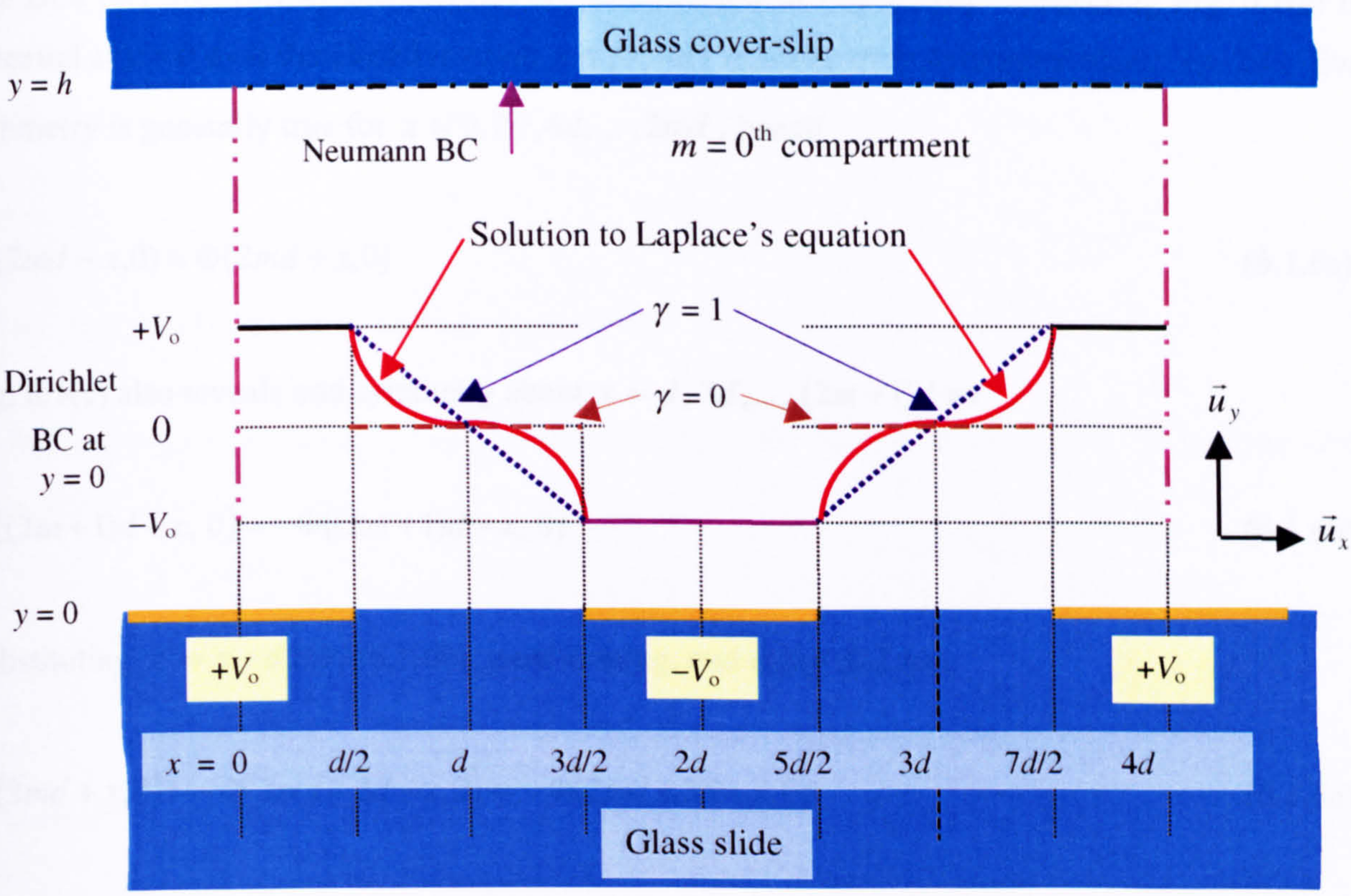

Fig. 6.1(e) Elevation view of the compartment in Fig. 6.1(b) with potential profile at $y = 0$ (*not* to scale). The BCs across the gaps are now Dirichlet, using the potential profiles exhibited in Fig. 6.1(d).

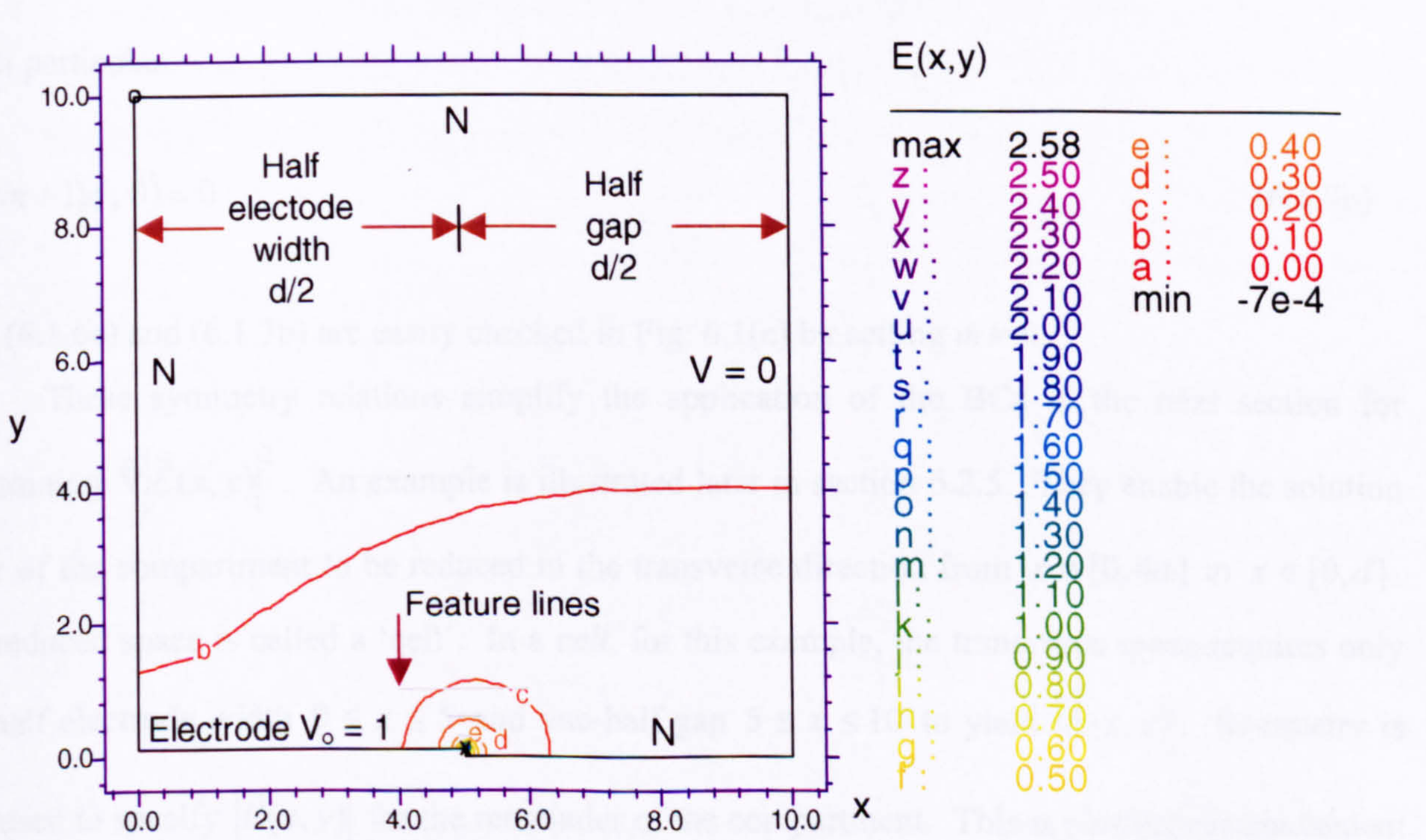

Fig. 6.1(f) Contour plot of the electric field magnitude $\left|\vec{E}(x, y)\right|$ (written above as E(x,y)) obtained by numerically solving Laplace's equation (6.1.2) using similar parameters as Fig. 6.1(c) (electrode thickness and potential, $\delta_e = 0.1$ and $V_o = 1$), $d = 10$, except the cover-slip is placed at $y = 10$ (a.u.). The Dirichlet BCs have potential (V) as specified, the Neumann BCs are denoted as 'N'.

The BCs (6.1.3b), (6.1.4) and (6.1.5b) are summarized in Fig. 6.1(e). Inspecting Fig. 6.1(e) the potential at $y = 0$ over the closed interval $x \in [0, 4d]$ exhibits even symmetry about $x = 2d$. Even symmetry is generally true for $x = 0, 2d, 4d, \ldots, 2md$, hence

$$\Phi(2md - x, 0) = \Phi(2md + x, 0) \tag{6.1.6a}$$

Fig. 6.1(e) also reveals odd symmetry about $x = d, 3d, \ldots, (2m+1)d$ so

$$\Phi\big((2m+1)d + x,\, 0\big) = -\Phi\big((2m+1)d - x,\, 0\big) \tag{6.1.6b}$$

Substituting $x' = x + d$ into (6.1.6b), transforming, and using (6.1.6a),

$$\Phi\big(2md + x, 0\big) = -\Phi\big(2md + 2d - x, 0\big) = -\Phi\big(2md + 2d + x, 0\big) \tag{6.1.6c}$$

The periodicity of the potential is expressed,

$$\Phi\big(4d(m+1) + x, 0\big) = \Phi\big(4md + x, 0\big) \tag{6.1.7a}$$

and in particular,

$$\Phi\big((2m+1)d,\, 0\big) = 0 \tag{6.1.7b}$$

Both (6.1.6c) and (6.1.7b) are easily checked in Fig. 6.1(e) by setting $m = 0$.

These symmetry relations simplify the application of the BCs in the next section for determining $\vec{\nabla}\left|\vec{E}(x,y)\right|^2$. An example is illustrated later in section 6.2.5. They enable the solution space of the compartment to be reduced in the transverse direction from $x \in [0, 4d]$ to $x \in [0, d]$. The reduced space is called a 'cell'. In a *cell*, for this example, the transverse space requires only one-half electrode width $0 \le x \le 5$ and one-half gap $5 \le x \le 10$ to yield $\left|\vec{E}(x,y)\right|$. Symmetry is then used to specify $\left|\vec{E}(x,y)\right|$ for the remainder of the compartment. This is particularly convenient for numerical evaluations of the electric field using (6.1.2). An example of this reduced space is a contour plot of the electric field magnitude $\left|\vec{E}(x,y)\right|$ shown in Fig. 6.1(f). The potential was solved using the same parameters as Fig. 6.1(c) except the cover-slip height h has been reduced to $h = 10$ (a. u.) for clarity. The contour density is shown to be particularly high about the electrode edge at $x = 5$ and 'features' were written in the program CD-R:/FlexPDE/*Epot2D0.5ElTh.pde* to

increase local finite element mesh density and maintain accuracy. These features were set up near the electrode edge and are marked in Fig. 6.1(f). The contour plot is discussed further in the next section where a comparison is made with evaluations from analytical expressions.

6.1.3 Analytical solution to Laplace's equation

Using rectangular coordinates, the potential is cast in the form of eigenfunction expansion and is separable,

$$\Phi(x,y)=\sum_{m=0}^{\infty}\Phi_m(x,y)=\sum_{m=0}^{\infty}g_m(x)h_m(y) \tag{6.1.8}$$

Substituting Laplace's equation (6.1.2) into (6.1.8),

$$\sum_{m=0}^{\infty}\frac{\partial^2\left(g_m(x)h_m(y)\right)}{\partial x^2}+\frac{\partial^2\left(g_m(x)h_m(y)\right)}{\partial y^2}=0 \tag{6.1.9}$$

the PDE is split into two ODEs and these are integrated separately. The details can be found in Appendix I. Imposing BCs (6.1.3) – (6.1.5), symmetry properties (6.1.6) and periodic condition (6.1.7) results in the potential being expressed as a Fourier cosine series,

$$\Phi(x,y)=\sum_{n=1,3,5\ldots}^{\infty}\left(A_n e^{-\kappa_n y}+B_n e^{+\kappa_n y}\right)\cos\kappa_n x \tag{6.1.10}$$

where

$$\kappa_n=\frac{\pi n}{2d} \tag{6.1.11}$$

$n=2m+1=1,3,5,\ldots$,

and Fourier coefficients A_n and B_n,

$$A_n=\frac{4V_0(1-\gamma)\pi n\sin(\pi n/4)+16V_0\gamma\cos(\pi n/4)}{\pi^2 n^2(1+e^{-\pi nh/d})} \tag{6.1.12}$$

$$B_n = A_n \exp(-2\kappa_n h) = A_n e^{-\pi n h/d} \tag{6.1.13}$$

For the case where $h = d$, $e^{-\pi n}\big|_{\max} = e^{-\pi} \cong 0.043 << 1$ so the exponential term in the denominator of (6.1.12) can be ignored. The approximation improves markedly for values of $n > 1$, particularly for the experimental arrangements where $h \geq 2d$. Thus, (6.1.12) simplifies,

$$A_n = \underbrace{\frac{4V_0(1-\gamma)}{\pi n}\sin\left(\frac{\pi n}{4}\right)}_{Sq} + \underbrace{\frac{16V_0\gamma}{\pi^2 n^2}\cos\left(\frac{\pi n}{4}\right)}_{T} \tag{6.1.14}$$

Combining (6.1.10), (6.1.11) and (6.1.13) the potential is written,

$$\Phi(x,y) = \sum_{n=1,3,5\ldots}^{\infty} A_n \left(\underbrace{e^{-\frac{\pi n y}{2d}}}_{\infty} + \underbrace{e^{\frac{\pi n(y-2h)}{2d}}}_{H} \right) \cos\left(\frac{\pi n x}{2d}\right) \tag{6.1.15}$$

The Fourier coefficient A_n expressed in (6.1.14) consists of two terms labelled, 'Sq' and T'. These terms are labelled according to their contribution to the potential via (6.1.15). When $\gamma = 0$, the gap (or inter-electrode) potentials are zero and the electrode potentials are $\pm V_o$. Therefore, the potential along the array (at $y = 0$) exhibits a type of 'square' waveform. Since $\gamma = 0$ means only the first term contributes to A_n, it is accordingly labelled 'Sq'. Conversely, when $\gamma = 1$, the potentials along the gaps are a linear interpolation between neighbouring electrode potentials at $+V_o$ and $-V_o$. Therefore, the potential along the array surface exhibits a clipped 'triangular' waveform. Since, the second term only contributes to A_n, it is accordingly labelled 'T'.

Two further components of the potential (6.1.15) inside the bracket ( ) are labelled as '∞' and 'H' according to the status of the cover-slip height h. As $h \to \infty$, the second, 'H' term $\to 0$ and only the first term contributes to the potential. Consequently, the first term is labelled '∞'. On the other hand, when $h = H$ a finite value then both terms contribute, and therefore the second term is labelled 'H'. In the next section, first and second partial derivatives are taken of the potential to determine $\nabla\left|E(x,y)\right|^2$. To determine closed form expressions amenable for FlexPDE it is convenient to consider the four components of the potential separately. Thus, (6.1.15) is re-written,

$$\Phi(x,y) = \Phi_{\infty,T}(x,y) + \Phi_{\infty,Sq}(x,y) + \Phi_{H,T}(x,y) + \Phi_{H,Sq}(x,y) \tag{6.1.16}$$

where each potential is labelled according to each combination of the above-mentioned four terms:

$$\Phi_{\infty,T}(x,y) = \sum_{n=1,3,5\ldots}^{\infty} \frac{16V_0\gamma}{\pi^2 n^2}\cos\left(\frac{\pi n}{4}\right)e^{-\frac{\pi n y}{2d}}\cos\left(\frac{\pi n x}{2d}\right) \tag{6.1.17a}$$

$$\Phi_{\infty,Sq}(x,y) = \sum_{n=1,3,5\ldots}^{\infty} \frac{4V_0(1-\gamma)}{\pi n}\sin\left(\frac{\pi n}{4}\right)e^{-\frac{\pi n y}{2d}}\cos\left(\frac{\pi n x}{2d}\right) \tag{6.1.17b}$$

$$\Phi_{H,T}(x,y) = \sum_{n=1,3,5\ldots}^{\infty} \frac{16V_0\gamma}{\pi^2 n^2}\cos\left(\frac{\pi n}{4}\right)e^{\frac{\pi n(y-2h)}{2d}}\cos\left(\frac{\pi n x}{2d}\right) \tag{6.1.17c}$$

$$\Phi_{H,Sq}(x,y) = \sum_{n=1,3,5\ldots}^{\infty} \frac{4V_0(1-\gamma)}{\pi n}\sin\left(\frac{\pi n}{4}\right)e^{\frac{\pi n(y-2h)}{2d}}\cos\left(\frac{\pi n x}{2d}\right) \tag{6.1.17d}$$

The expression in (6.1.17a) is the same expression as derived in earlier work (see *List of Publications* at the end of this dissertation, specifically by Morgan *et al.*, 2001) for interdigitated electrode arrays where the potential was assumed to be zero as $y \to \infty$, i.e. the effect of the cover-slip was ignored, or $h \to \infty$. This is essentially valid when h is very large, for example, in DEP levitation experiments. It is less accurate for simulations where the effect of varying h on the particle collection and relaxation profiles is being explored.

6.2 Determining the electric field intensity gradient

The expressions for the 2-D potential, (6.1.16) and (6.1.17), enables the electric field to be determined. For an irrotational electric field (Jackson, 1975, chs. 1 and 6; Morse and Feshbach, 1953, Ch. 2),

$$\begin{aligned}\vec{E}(x,y) &= -\vec{\nabla}\Phi(x,y) = -\partial_x\Phi(x,y)\vec{u}_x - \partial_y\Phi(x,y)\vec{u}_y \\ &= -E_x\vec{u}_x - E_y\vec{u}_y\end{aligned} \tag{6.2.1a}$$

where the electric field is represented in terms of components E_x and E_y in respective x and y directions with unit vectors $\vec{u}_x$ and $\vec{u}_y$. The magnitude of the electric field (6.2.1a) is written as,

$$\left|\vec{E}(x,y)\right| = \sqrt{E_x^2 + E_y^2} \tag{6.2.1b}$$

The 2-D DEP force is determined using (6.0.2), and the electric field intensity gradient can be expressed in terms of components $\partial_x\left|\vec{E}\right|^2$ and $\partial_y\left|\vec{E}\right|^2$,

$$\begin{aligned}\vec{\nabla}\left|\vec{E}(x,y)\right|^2 &= \vec{\nabla}\left(E_x^2+E_y^2\right)=\partial_x\left|\vec{E}\right|^2\vec{u}_x+\partial_y\left|\vec{E}\right|^2\vec{u}_y \\ &=2(E_xE_{x,x}+E_yE_{y,x})\vec{u}_x+2(E_xE_{x,y}+E_yE_{y,y})\vec{u}_y\end{aligned} \tag{6.2.2}$$

where it is understood $E_{x,x}=\partial E_x/\partial x=\partial_x E_x$, $E_{x,y}=\partial E_x/\partial y=\partial_y E_x$, etc. Since the potential (6.1.16) has four identifiable parts, each of the electric field components is comprised of four parts.

6.2.1 Expressions for the electric field

The component of the electric field in the x-direction, $\vec{u}_x$, is

$$E_x(x,y)=-\partial_x\Phi(x,y)=-\partial_x\Phi_{\infty,T}-\partial_x\Phi_{\infty,Sq}-\partial_x\Phi_{H,T}-\partial_x\Phi_{H,Sq} \tag{6.2.3}$$

where the explicit dependence on x and y is removed for brevity and is assumed. Closed form expressions for each of the E_x parts are derived in Appendix J.1. The parts of E_x are labelled concisely in terms of the derivatives of expressions (6.1.17a) to (6.1.17d),

$$E_{x_a}=-\frac{\partial\Phi_{\infty,T}}{\partial x}=\frac{2\gamma V_o}{\pi d}\left[\tan^{-1}\left(\frac{\sin\hat{x}}{\sinh\hat{y}}\right)-\tan^{-1}\left(\frac{\cos\hat{x}}{\sinh\hat{y}}\right)\right] \tag{6.2.4a}$$

$$E_{x_b}=-\frac{\partial\Phi_{\infty,Sq}}{\partial x}=\frac{(1-\gamma)V_o\sinh\hat{y}}{d}\left[\frac{\sin\hat{x}}{\cosh 2\hat{y}+\cos 2\hat{x}}-\frac{\cos\hat{x}}{\cosh 2\hat{y}-\cos 2\hat{x}}\right] \tag{6.2.4b}$$

$$E_{x_c}=-\frac{\partial\Phi_{H,T}}{\partial x}=\frac{2\gamma V_o}{\pi d}\left[\tan^{-1}\left(\frac{\sin\hat{x}}{\sinh\hat{\mathcal{y}}}\right)-\tan^{-1}\left(\frac{\cos\hat{x}}{\sinh\hat{\mathcal{y}}}\right)\right] \tag{6.2.4c}$$

$$E_{x_d}=-\frac{\partial\Phi_{H,Sq}}{\partial x}=\frac{(1-\gamma)V_o\sinh\hat{\mathcal{y}}}{d}\left[\frac{\sin\hat{x}}{\cosh 2\hat{\mathcal{y}}+\cos 2\hat{x}}-\frac{\cos\hat{x}}{\cosh 2\hat{\mathcal{y}}-\cos 2\hat{x}}\right] \tag{6.2.4d}$$

where $\hat{y}=\pi y/2d$, $\hat{\mathcal{y}}=\pi h/d-\pi y/2d=2\hat{h}-\hat{y}$ and $\hat{x}=\pi x'/2d=\pi x/2d+\pi/4$ and are valid $\forall\ x$, $0<y\le h$, $h>0$.

Similarly, the component of the electric field in the y-direction, $\vec{u}_y$, is,

$$E_y(x,y) = -\partial_y\Phi(x,y) = -\partial_y\Phi_{\infty,T} - \partial_y\Phi_{\infty,Sq} - \partial_y\Phi_{H,T} - \partial_y\Phi_{H,Sq} \tag{6.2.5}$$

and closed form expressions for each of the E_y component are derived in Appendix J.2. These are

$$E_{y_a} = -\frac{\partial\Phi_{\infty,T}}{\partial y} = \frac{\gamma V_o}{\pi d}\ln\left(\frac{\cosh\hat{y}+\cos\hat{x}}{\cosh\hat{y}-\cos\hat{x}}.\frac{\cosh\hat{y}+\sin\hat{x}}{\cosh\hat{y}-\sin\hat{x}}\right) \tag{6.2.6a}$$

$$E_{y_b} = -\frac{\partial\Phi_{\infty,Sq}}{\partial y} = \frac{(1-\gamma)V_o\cosh\hat{y}}{d}\left[\frac{\sin\hat{x}}{\cosh 2\hat{y}-\cos 2\hat{x}} + \frac{\cos\hat{x}}{\cosh 2\hat{y}+\cos 2\hat{x}}\right] \tag{6.2.6b}$$

$$E_{y_c} = -\frac{\partial\Phi_{H,T}}{\partial y} = \frac{-\gamma V_o}{\pi d}\ln\left(\frac{\cosh\hat{y}+\cos\hat{x}}{\cosh\hat{y}-\cos\hat{x}}.\frac{\cosh\hat{y}+\sin\hat{x}}{\cosh\hat{y}-\sin\hat{x}}\right) \tag{6.2.6c}$$

$$E_{y_d} = -\frac{\partial\Phi_{H,Sq}}{\partial y} = \frac{-(1-\gamma)V_o\cosh\hat{y}}{d}\left[\frac{\sin\hat{x}}{\cosh 2\hat{y}-\cos 2\hat{x}} + \frac{\cos\hat{x}}{\cosh 2\hat{y}+\cos 2\hat{x}}\right] \tag{6.2.6d}$$

6.2.2 Comparison with numerical solution

Substituting (6.2.4a) – (6.2.4d) into (6.2.3), (6.2.6a) – (6.2.6d) into (6.2.5), and subsequently these two expressions into (6.2.1b), yields the electric field magnitude $\left|\vec{E}(x,y)\right|$ (abbreviated $\left|\vec{E}\right|$). This is evaluated for parameter values $V_o = 1$, $\gamma = 0.78$, $d = 10$, and $h = 10$ (a.u.). A contour plot is shown in Fig. 6.2(a). Since the parameters are chosen to be the same as the numerical solution Fig. 6.1(f), a comparison between the two contour plots can be made if differences in the solution space of the two figures 6.1(f) and 6.2(a) can be accommodated. The first issue concerns the electrode thickness δ_e. In Fig. 6.1(f), $\delta_e = 0.1$ whereas the analytical expressions assume $\delta_e = 0$ and this is evident in Fig. 6.2(a).

The second issue concerns the singularity in the expression for $\left|\vec{E}\right|$ that occurs at the electrode 'edge' where $x = \frac{d}{2}$, $y = 0$ (or $\hat{x} = 0$, $\hat{y} = 0$). The singularity arises from discontinuity in the gradient of the potential at these coordinate values. The non-zero finite element size in the numerical solution helps avoid the problem, although dependency of the maximum value on mesh localized about the electrode edge is not particularly satisfactory. However, the situation is worse

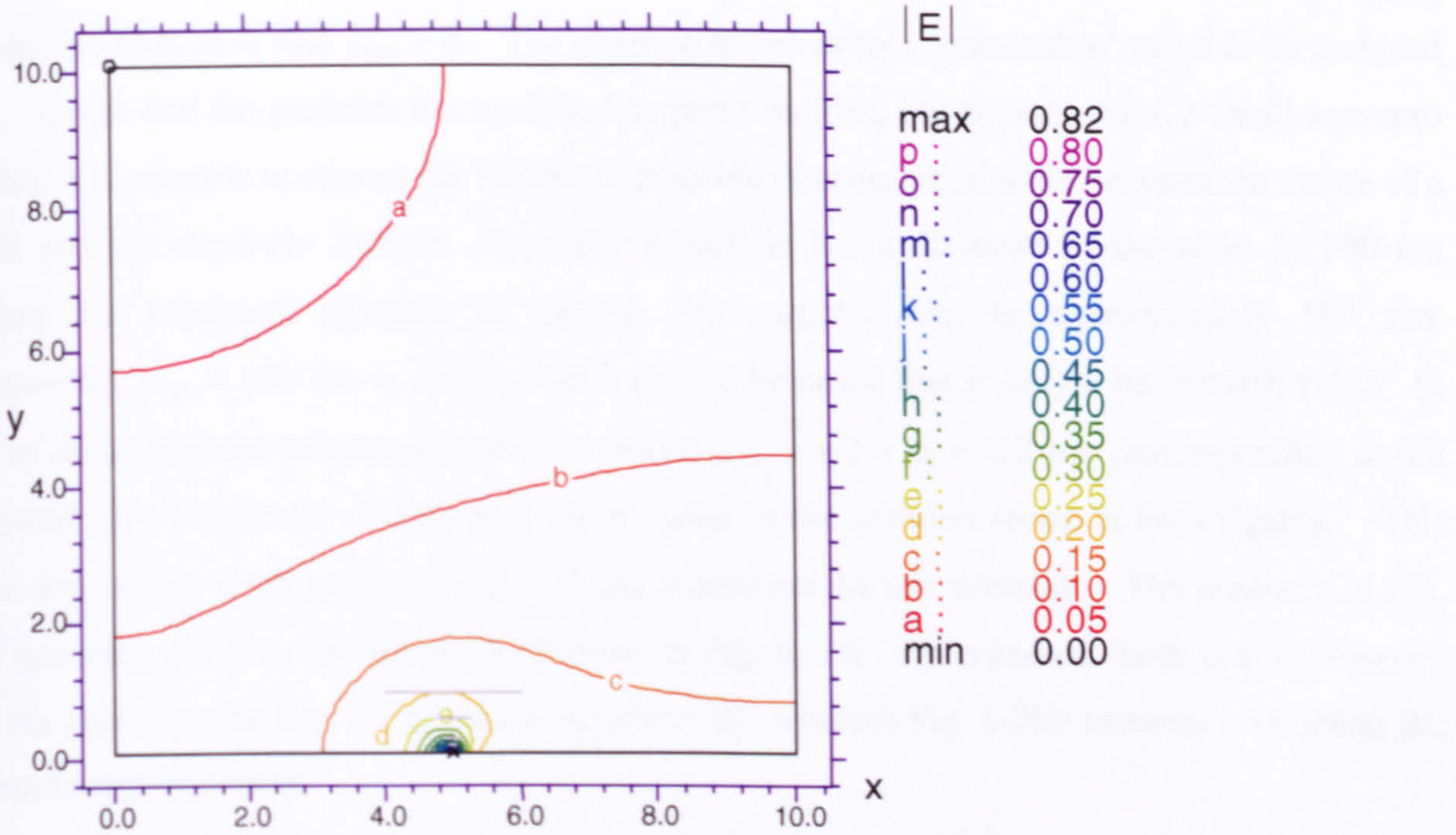

Fig. 6.2(a) Electric field magnitude $\left|\vec{E}(x,y)\right|$ contour plot generated from (6.2.3) – (6.2.6) using parameter values $d = 10$, $V_o = 1$, $h = 10$ (a.u.), and $\gamma = 0.78$. The lower boundary has been offset by the thickness of electrode $\delta_e = 0.1$, thus enabling a comparison with Fig. 6.1(f).

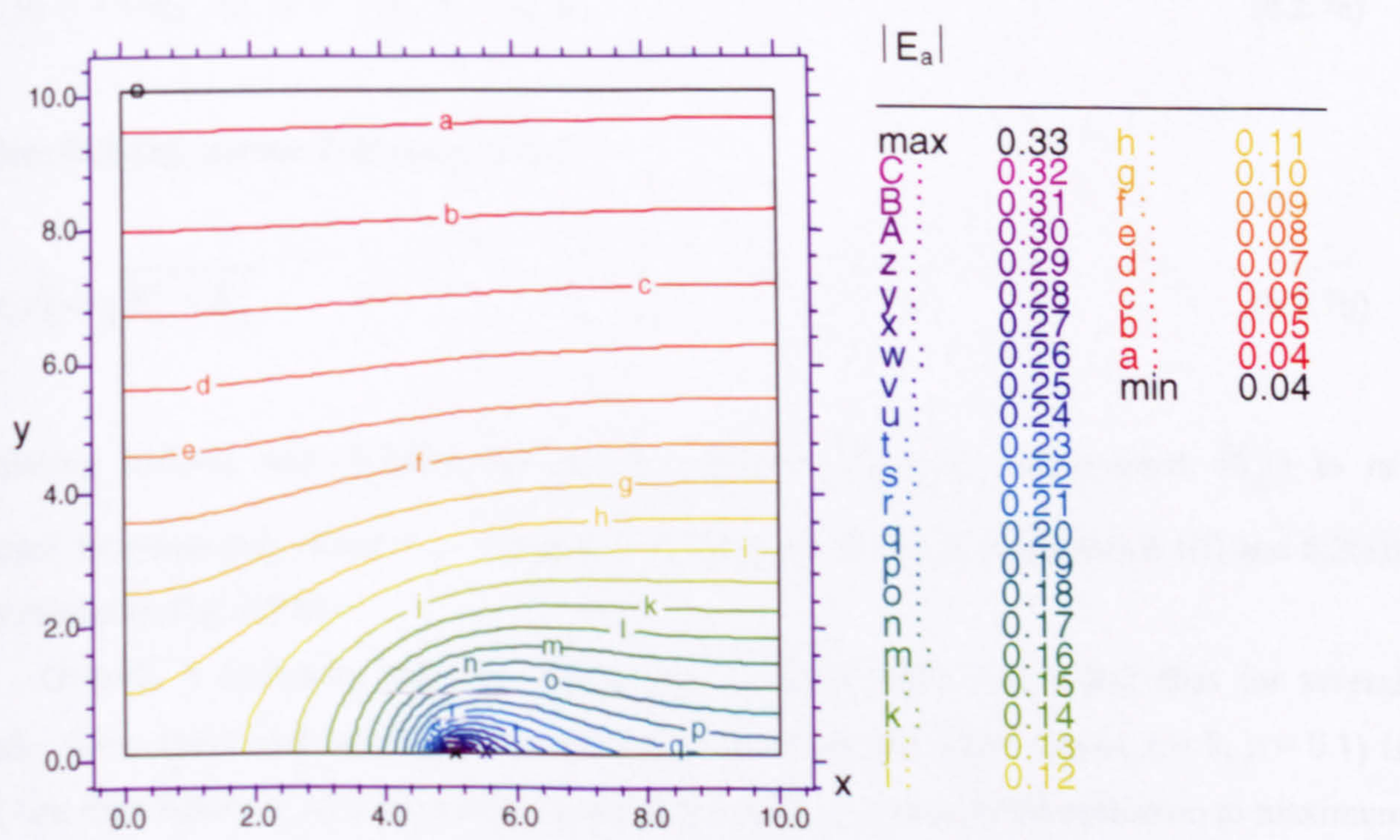

Fig. 6.2(b) Electric field magnitude $\left|\vec{E}_a(x,y)\right|$ contour plot generated using (6.2.7b) using parameter values $d = 10$, $V_o = 1$, $h = 10$ (a.u.), and $\gamma = 1.00$. The lower boundary has been offset by value of electrode thickness $\delta_e = 0.1$, thus enabling a comparison with Fig. 6.1(f).

with the analytical solution for $\left|\vec{E}(x,y)\right|$ that tends to infinity. To avoid the singularity, the lower boundary is offset such that $y_{\min} > 0$. The question arises as to a 'reasonable' value to be assigned to y_{min}. Given that the particles are modelled as point entities, but actually have a small non-zero diameter, it is sensible to choose the minimum possible distance obtainable between the centre of a particle and the electrode surface. Typically a particle has a diameter of the order of 200 nm therefore the minimum distance is limited, by particle size, to approximately 100 nm. Consequently, $y_{\min} = 100$ nm is chosen, but it should be noted this is only a benchmark value. In terms of modelling sub-micron particle movement, $y_{\min} = r/2 + \delta_e = 0.2$ μm (corresponding to 0.2 a.u.) could be alternatively chosen as a lower value in the solution space in both figures. This implies for micron sized particles, $y_{\min} \approx 1$ μm would not be unreasonable. The contours in Fig. 6.2(a) generally compare favourably with those in Fig. 6.1(f). As expected, there is a discrepancy along the gap since the Fig. 6.1(f) uses a Neumann BC whereas Fig. 6.2(a) assumes a Dirichlet BC – as previously discussed.

One is also interested in the simplest expression for the electric field $\vec{E}_a(x,y)$ where the effect of the cover-slip is ignored and assumes $\gamma = 1$. This means only the first terms in (6.2.3) and (6.2.5) are substituted into (6.2.1a), therefore

$$\vec{E}_a(x,y) = -\vec{\nabla}\Phi_{\infty,T}(x,y) = -E_{x_a}\vec{u}_x - E_{y_a}\vec{u}_y \qquad (6.2.7a)$$

and from (6.2.1b), electric field magnitude is

$$\left|\vec{E}_a(x,y)\right| = \sqrt{E_{x_a}^2 + E_{y_a}^2} \qquad (6.2.7b)$$

Substituting (6.2.4a) and (6.2.6a) into (6.2.7b) enables $\left|\vec{E}_a(x,y)\right|$ (abbreviated $\left|\vec{E}_a\right|$) to be evaluated for parameter values $V_o = 1$ and $d = 10$ (that are the same as figures 6.1(f) and 6.2(a)) and is plotted in Fig. 6.2(b).

Overall, it compares with Fig. 6.1(f) less favourably than Fig. 6.2(a) does for several reasons. First, the overall density of contours near the 'electrode edge' (about $x = 5$, $y = 0.1$) is much less then figures 6.1(f) and 6.2(a). Second, the range of values from minimum to maximum is 2 to 3 times less than the latter (compare upper potential value of 0.33 with 0.82). Third, the contours that are almost parallel to the upper boundary contrast distinctly with the contour in Fig. 6.2(a) that is perpendicular. This is not unexpected, and is indicative of ignoring the effect of the cover-slip that would otherwise impose a Neumann BC. As for Fig. 6.2(a), the assumption of a Dirichlet BC along the gap means the contours contrast with those in Fig. 6.1(f). In terms of a basic profile for the electric field magnitude, however, $\left|\vec{E}_a\right|$ as illustrated Fig. 6.2(b), is remarkably

good given its simplicity. The consequences of the contour plots in terms of gradient components is discussed later in section 6.2.4.

6.2.3 Expressions for the electric field intensity gradient

Evaluation of the electric field intensity gradient (6.2.2) requires the partial derivative,

$$E_{x,x} = \partial_x E_{x_a} + \partial_x E_{x_b} + \partial_x E_{x_c} + \partial_x E_{x_d} \tag{6.2.8}$$

The expression for each part of $E_{x,x} = \partial_x E_x$ is found by differentiation of (6.2.4a) – (6.2.4d) with respect to x:

$$E_{x,x_a} = \frac{\partial E_{x_a}}{\partial x} = \frac{2\gamma V_o \sinh\hat{y}}{d^2}\left[\frac{\cos\hat{x}}{\cosh 2\hat{y} - \cos 2\hat{x}} + \frac{\sin\hat{x}}{\cosh 2\hat{y} + \cos 2\hat{x}}\right] = -\frac{\partial E_{y_a}}{\partial y} = -E_{y,y_a} \tag{6.2.9a}$$

$$E_{x,x_b} = \frac{\partial E_{x_b}}{\partial x} = \frac{\pi(1-\gamma)V_o \sinh\hat{y}}{4d^2}\left[\begin{array}{l}\dfrac{\sin\hat{x}(\cosh^2\hat{y} + \cos^2\hat{x})}{(\sinh^2\hat{y} + \sin^2\hat{x})^2} \\ \quad + \dfrac{\cos\hat{x}(\cosh^2\hat{y} + \sin^2\hat{x})}{(\sinh^2\hat{y} + \cos^2\hat{x})^2}\end{array}\right] = -\frac{\partial E_{y_b}}{\partial y} = -E_{y,y_b} \tag{6.2.9b}$$

$$E_{x,x_c} = \frac{\partial E_{x_c}}{\partial x} = \frac{2\gamma V_o \sinh\hat{y}}{d^2}\left[\frac{\cos\hat{x}}{\cosh 2\hat{y} - \cos 2\hat{x}} + \frac{\sin\hat{x}}{\cosh 2\hat{y} + \cos 2\hat{x}}\right] = -\frac{\partial E_{y_c}}{\partial y} = -E_{y,y_c} \tag{6.2.9c}$$

$$E_{x,x_d} = \frac{\partial E_{x_b}}{\partial x} = \frac{\pi(1-\gamma)V_o \sinh\hat{y}}{4d^2}\left[\begin{array}{l}\dfrac{\sin\hat{x}(\cosh^2\hat{y} + \cos^2\hat{x})}{(\sinh^2\hat{y} + \sin^2\hat{x})^2} \\ \quad + \dfrac{\cos\hat{x}(\cosh^2\hat{y} + \sin^2\hat{x})}{(\sinh^2\hat{y} + \cos^2\hat{x})^2}\end{array}\right] = -\frac{\partial E_{y_d}}{\partial y} = -E_{y,y_d} \tag{6.2.9d}$$

An alternative method, by differentiating the infinite series sum, is given in Appendix J.3 for E_{x,x_a}. It is also shown in (J.3.12) $E_{x,x_a} = -E_{y,y_a}$.

Equation (6.2.2) also requires the partial derivative,

$$E_{x,y} = \partial_y E_{x_a} + \partial_y E_{x_b} + \partial_y E_{x_c} + \partial_y E_{x_d} \tag{6.2.10}$$

and each term is found by differentiation of (6.2.4a) – (6.2.4d) with respect to y:

$$E_{x,y_a} = \frac{\partial E_{x_a}}{\partial y} = \frac{2\gamma V_o \cosh\hat{y}}{d^2}\left[\frac{\cos\hat{x}}{\cosh 2\hat{y} + \cos 2\hat{x}} - \frac{\sin\hat{x}}{\cosh 2\hat{y} - \cos 2\hat{x}}\right] = \frac{\partial E_{y_a}}{\partial x} = E_{y,x_a} \qquad (6.2.11a)$$

$$E_{x,y_b} = \frac{\partial E_{x_b}}{\partial y} = \frac{\pi(1-\gamma)V_o \cosh\hat{y}}{4d^2}\left[\begin{array}{l}\dfrac{\cos\hat{x}(\sinh^2\hat{y} - \sin^2\hat{x})}{(\sinh^2\hat{y} + \sin^2\hat{x})^2} \\ \quad + \dfrac{\sin\hat{x}(\cos^2\hat{x} - \sinh^2\hat{y})}{(\sinh^2\hat{y} + \cos^2\hat{x})^2}\end{array}\right] = \frac{\partial E_{y_b}}{\partial x} = E_{y,x_b} \qquad (6.2.11b)$$

$$E_{x,y_c} = \frac{\partial E_{x_c}}{\partial y} = \frac{-2\gamma V_o \cosh\hat{y}}{d^2}\left[\frac{\cos\hat{x}}{\cosh 2\hat{y} + \cos 2\hat{x}} - \frac{\sin\hat{x}}{\cosh 2\hat{y} - \cos 2\hat{x}}\right] = \frac{\partial E_{y_c}}{\partial x} = E_{y,x_c} \qquad (6.2.11c)$$

$$E_{x,y_d} = \frac{\partial E_{x_d}}{\partial y} = \frac{-\pi(1-\gamma)V_o \cosh\hat{y}}{4d^2}\left[\begin{array}{l}\dfrac{\cos\hat{x}(\sinh^2\hat{y} - \sin^2\hat{x})}{(\sinh^2\hat{y} + \sin^2\hat{x})^2} \\ \quad + \dfrac{\sin\hat{x}(\cos^2\hat{x} - \sinh^2\hat{y})}{(\sinh^2\hat{y} + \cos^2\hat{x})^2}\end{array}\right] = \frac{\partial E_{y_d}}{\partial x} = E_{y,x_d} \qquad (6.2.11d)$$

The alternative differentiation; the infinite series sum, is given in Appendix J.3 for E_{x,y_a}. It is also shown in (J.3.10) $E_{x,y_a} = E_{y,x_a}$.

Inspecting the *lhs* and *rhs* of the partial derivatives of equations (6.2.9a) – (6.2.9d) and (6.2.11a) – (6.2.11d), and superposition properties of (6.2.8) and (6.2.10) it is generally true $E_{x,y} = E_{y,x}$ and $E_{x,x} = -E_{y,y}$, and the latter is expected from Laplace's equation (6.1.2). Thus, the general expression for the electric field intensity gradient $\vec{\nabla}|E|^2$, (6.2.2), is written more conveniently,

$$\begin{aligned}\vec{\nabla}|E(x,y)|^2 &= \vec{\nabla}\left(E_x^2 + E_y^2\right) = \partial_x\left|\vec{E}\right|^2\vec{u}_x + \partial_y\left|\vec{E}\right|^2\vec{u}_y \\ &= 2(E_xE_{x,x} + E_yE_{x,y})\vec{u}_x + 2(E_xE_{x,y} - E_yE_{x,x})\vec{u}_y\end{aligned} \qquad (6.2.12)$$

For the forthcoming discussion in the next section, it is useful to label the components separately,

$$\partial_x\left|\vec{E}\right|^2 = 2(E_xE_{x,x} + E_yE_{x,y}) \qquad (6.2.12a)$$

$$\partial_y\left|\vec{E}\right|^2 = 2(E_xE_{x,y} - E_yE_{x,x}) \qquad (6.2.12b)$$

Each of the terms $E_x, E_y, E_{x,x}$ and $E_{x,y}$ in (6.2.12) is evaluated by substituting (6.2.4a) – (6.2.4d) into (6.2.3), (6.2.6a) – (6.2.6d) into (6.2.5), (6.2.9a) – (6.2.9d) into (6.2.8), and (6.2.11a) – (6.2.11d) into (6.2.10). A typical value is $\gamma = 0.78$.

A simpler version of (6.2.12), ignores the effect of the cover-slip and assumes the potentials along the gaps are a linear interpolation between neighbouring electrode potentials at $+V_o$ and $-V_o$. As discussed in the previous sections, $\gamma = 1$. Thus,

$$\begin{aligned}\vec{\nabla}\left|E_a(x,y)\right|^2 &= \vec{\nabla}\left(E_{x_a}^2 + E_{y_a}^2\right) = \partial_x\left|\vec{E}_a\right|^2\vec{u}_x + \partial_y\left|\vec{E}_a\right|^2\vec{u}_y \\ &= 2(E_{x_a}E_{x,x_a} + E_{y_a}E_{x,y_a})\vec{u}_x + 2(E_{x_a}E_{x,y_a} - E_{y_a}E_{x,x_a})\vec{u}_y\end{aligned} \tag{6.2.13}$$

Again, for the discussion in the next section, the components are labelled separately,

$$\partial_x\left|\vec{E}_a\right|^2 = 2(E_{x_a}E_{x,x_a} + E_{y_a}E_{x,y_a}) \tag{6.2.13a}$$

and

$$\partial_y\left|\vec{E}_a\right|^2 = 2(E_{x_a}E_{x,y_a} - E_{y_a}E_{x,x_a}) \tag{6.2.13b}$$

the four terms $E_{x_a}, E_{y_a}, E_{x,x_a}$ and E_{x,y_a} are given by respective equations (6.2.4a), (6.2.6a), (6.2.9a) and (6.2.11a) with $\gamma = 1$.

6.2.4 Comparison of evaluations of the electric field intensity gradient

Contour plots of the analytical expressions for $\partial_x\left|\vec{E}\right|^2$ and $\partial_y\left|\vec{E}\right|^2$ components can be compared with a FlexPDE 2.15 finite element evaluation in a similar way to comparisons for $\left|\vec{E}\right|$ described in section 6.2.2. However, contour plots for the electric field gradients are so dense near the electrode 'edge' where $x = \frac{d}{2}$, $y = 0$ and sparse elsewhere, that carefully placed 'elevation' views are more useful. The 'elevation' views for $\partial_x\left|\vec{E}\right|^2$ along the transverse x-axis are compared in Fig. 6.2(c). For convenience, the shorthand labelling is used, and it is understood $\partial_x E^2 = \partial_x\left|\vec{E}\right|^2$, etc. The plots span half-electrode width, half-electrode gap, $0 \le x \le 10$, and are all positioned at $y_{\min} = 0.2$ (a.u.). The three comparisons are similar to those in section 6.2.2, with the same values $V_o = 1$, $d = 10$, and are as follows:

(1) the red bold (———) plot of $\partial_x E^2$ is computed numerically (via Laplace's equation (6.1.2)) using electrode thickness $\delta_e = 0.1$ in the author's program *Epot2D0·5ElTh.pde*

(2) the green dot-dash ($\cdot - \cdot -$) plot of $\partial_x E^2$ is (6.2.12a) with $\gamma = 0.78$ and $h = 10$ (a.u.) and is implemented in *EpotPl0·5ElTh.pde*

(3) the blue dotted (·····) plot $\partial_x E_a^{\,2}$ is (6.2.13a) with $\gamma = 1$ and is implemented in *EpotPl0·5ElTh.pde*

All three plots exhibit extrema at similar x-ordinates but it is clear the analytic electric field intensity gradient component $\partial_x E^2$, $\gamma = 0.78$ ($\cdot - \cdot -$) is closer to the numerically computed $\partial_x E^2$ (——) than $\partial_x E_a^{\,2}$ (6.2.13a) with $\gamma = 1$ (·····). The main problem with $\partial_x E_a^{\,2}$ is its scale, the extrema are approximately an order of magnitude smaller than the numerically computed $\partial_x E^2$. However, the actual magnitude of the extrema are themselves somewhat arbitrary in the sense that they depend on $y_{\min}$ chosen. As discussed in section 6.2.2 this can vary, 0.1 – 1 μm. Thus, if one is willing to compromise accuracy for simplicity then (6.2.13a) can arguably be used. In fact, as becomes evident later in sections 6.4 and 6.5, the extrema are themselves problematic so simulations of DEP collections that suppress the peaks of $\partial_x E^2$ are useful.

Similar conclusions can reached for 'elevation' views of $\partial_y \left|\vec{E}\right|^2$ along the transverse x-axis plotted in Fig. 6.2(d). The plots are dual (line and colour) coded as in Fig. 6.2(c) and labelled accordingly. They are evaluated using the same parameter values as stated above and implemented in the same programs. The three plots exhibit minima at similar x-ordinates and $\partial_y E^2$, $\gamma = 0.78$ ($\cdot - \cdot -$) (6.2.12b) is closer to the numerically computed $\partial_y E^2$ (——) than $\partial_y E_a^{\,2}$ (6.2.13b) with $\gamma = 1$ (·····). Alike $\partial_x E_a^{\,2}$ in Fig. 6.2(c), the minimum of $\partial_y E_a^{\,2}$ is at least an order of magnitude smaller than the numerically computed $\partial_x E^2$ minima. A final point worth noting is that both numerically computed $\partial_x E^2$ and $\partial_y E^2$ plots are not smoothed and exhibit small-scale fluctuations.

The log-linear plots for $\partial_x \left|\vec{E}\right|^2$ and $\partial_y \left|\vec{E}\right|^2$ at $x = 4.9$ (a.u.) along the 'vertical' y-axis (orthogonal to the transverse axis) are compared in figures 6.2(e), 6.2(f) and 6.2(g). The plots are coded as in the previous figures 6.2(c) and 6.2(d) and are evaluated using the same parameter values and same equations (the analytic electric field intensity gradients). In Fig. 6.2(e) $\partial_x E^2$ (with $\gamma = 0.78$) crosses the x-axis (marked by ⇔) manifesting suppressions in the logarithmic plots at approximately $y = 0.4$ and 1.2 (a.u.). Clearly, $\partial_x E^2$ ($\gamma = 0.78$ green $\cdot - \cdot -$) deviates more from the numerically computed $\partial_x E^2$ red (——) than $\partial_x E_a^{\,2}$ ($\gamma = 1$ blue ·····) does up to *ca.* $y = 3.3$ (a.u). However, above this value, $\partial_x E^2$ and the numerically computed $\partial_x E^2$ concur whereas $\partial_x E_a^{\,2}$ differs from these gradients. This difference is attributed to the finite cover-slip height $h = 10$ (a.u.) that is not taken into account in the expression for $\partial_x E_a^{\,2}$. In Fig. 6.2(f) $\partial_y E^2$ ($\gamma = 0.78$ green $\cdot - \cdot -$) and the numerically computed $\partial_x E^2$ (red ——) agree closely for all y values. This contrasts with $\partial_x E_a^{\,2}$ (with $\gamma = 1$ blue ·····) that deviates from the numerical $\partial_x E^2$ near $y = 0.2$ and 10 (a.u.) but agrees

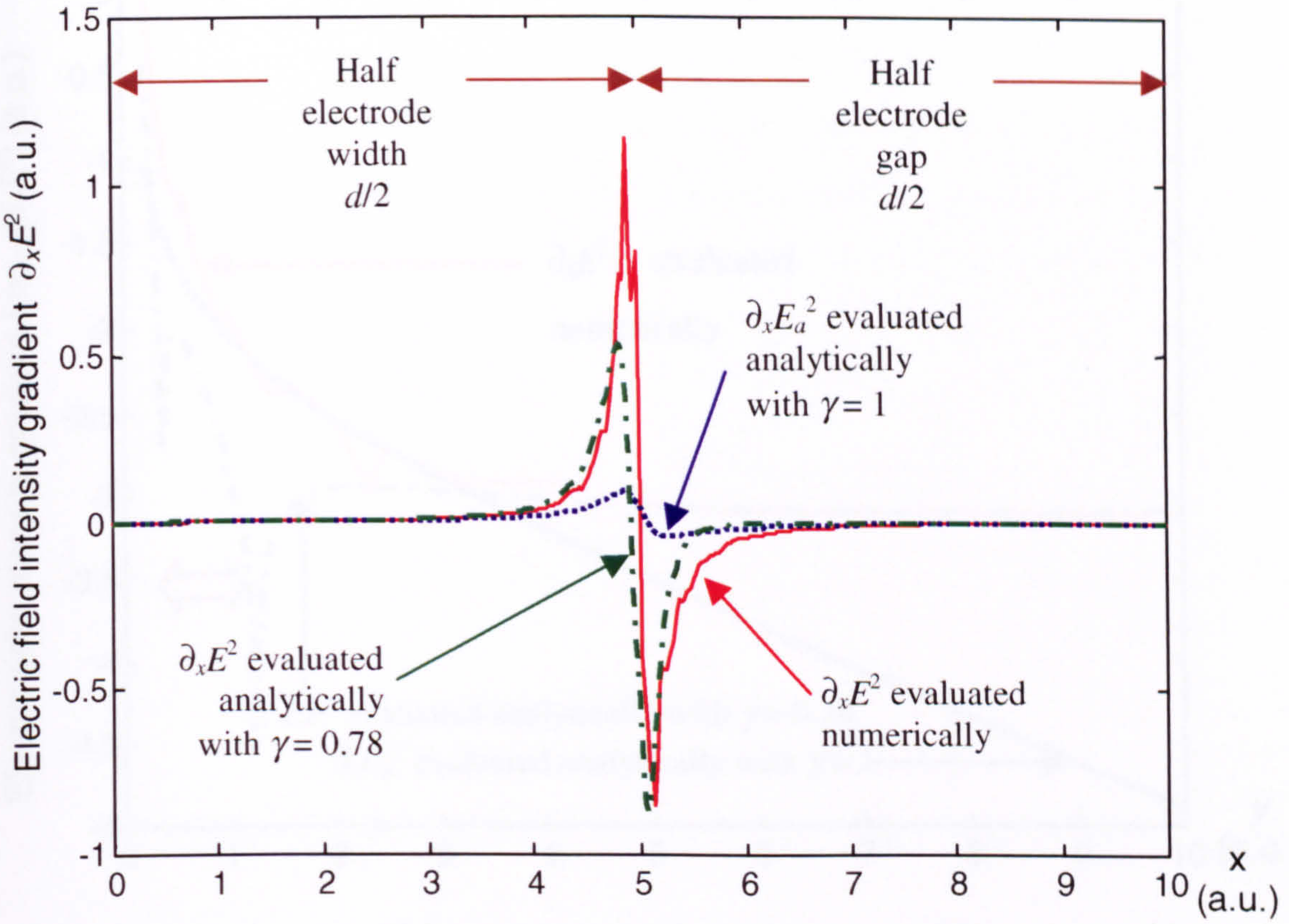

Fig. 6.2(c) A comparison of $\partial_x \left|\vec{E}\right|$ profiles (written above as $\partial_x E^2$) at $y = 0.2$ for $x = 0$ to 10 generated using values $\delta_e = 0.1$, $d = 10$, $h = 10$ and $V_o = 1$ (a.u.). See text for details.

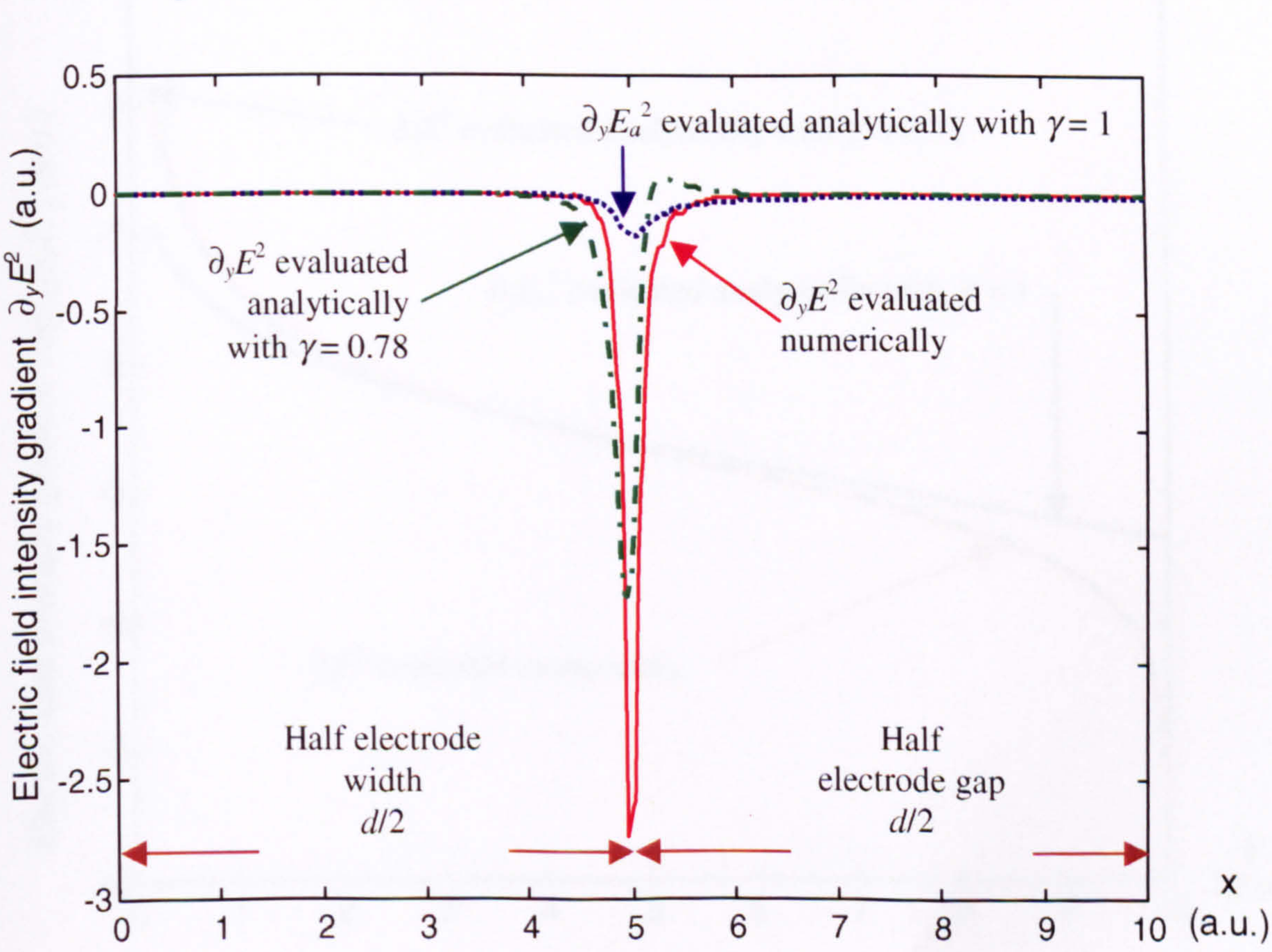

Fig. 6.2(d) A comparison of $\partial_y \left|\vec{E}\right|$ profiles (written above as $\partial_y E^2$) at $y = 0.2$ for $x = 0$ to 10 generated using values $\delta_e = 0.1$, $d = 10$, $h = 10$ and $V_o = 1$ (a.u.). See text for details.

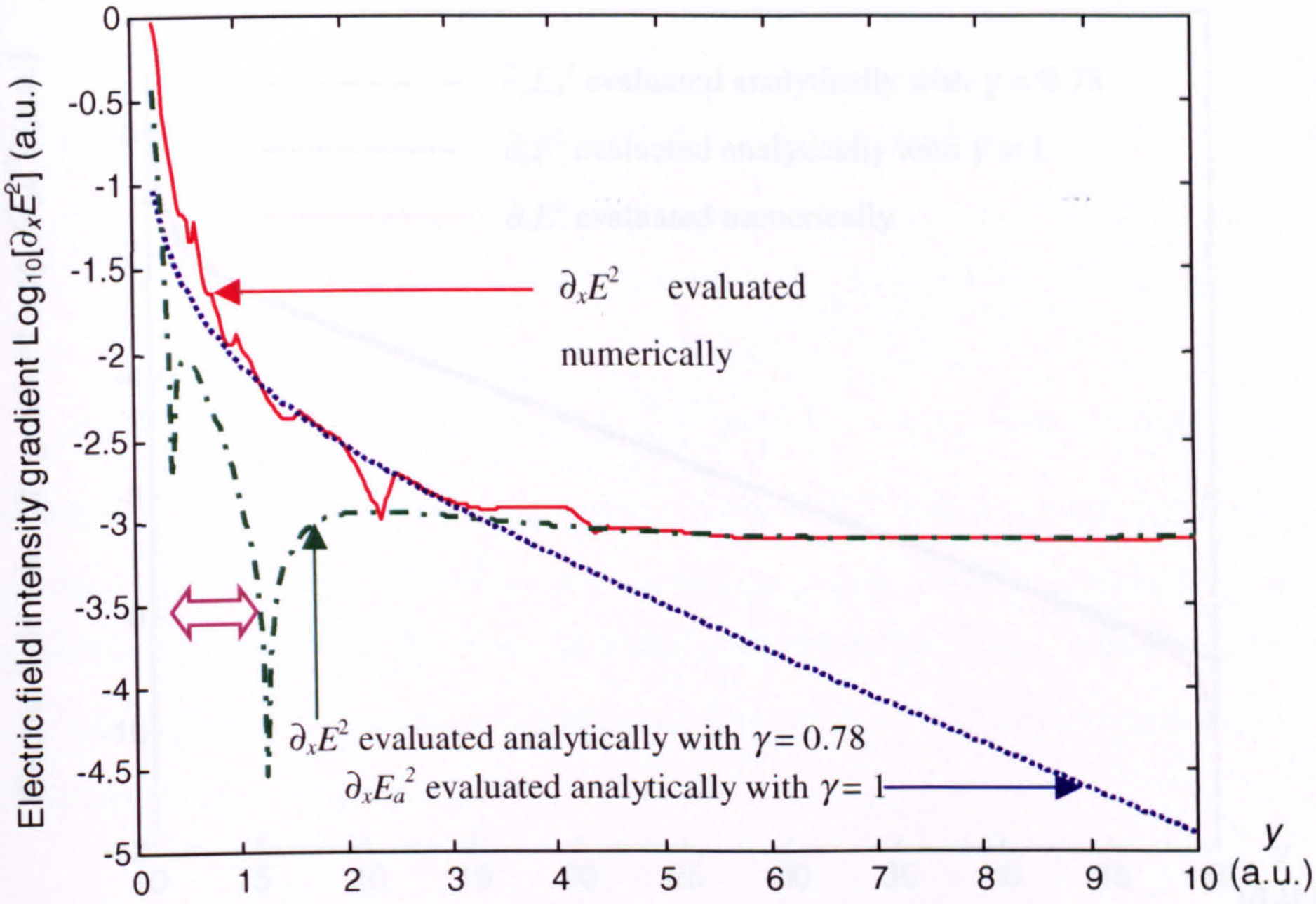

Fig. 6.2(e) Log-linear plots of $\partial_x \left|\vec{E}\right|$ (written above as $\partial_x E^2$) at $x = 4.9$ for $y = 0.2$ to 10 generated using values $\delta_e = 0.1$, $d = 10$, $h = 10$ and $V_o = 1$ (a.u.). See text for further details.

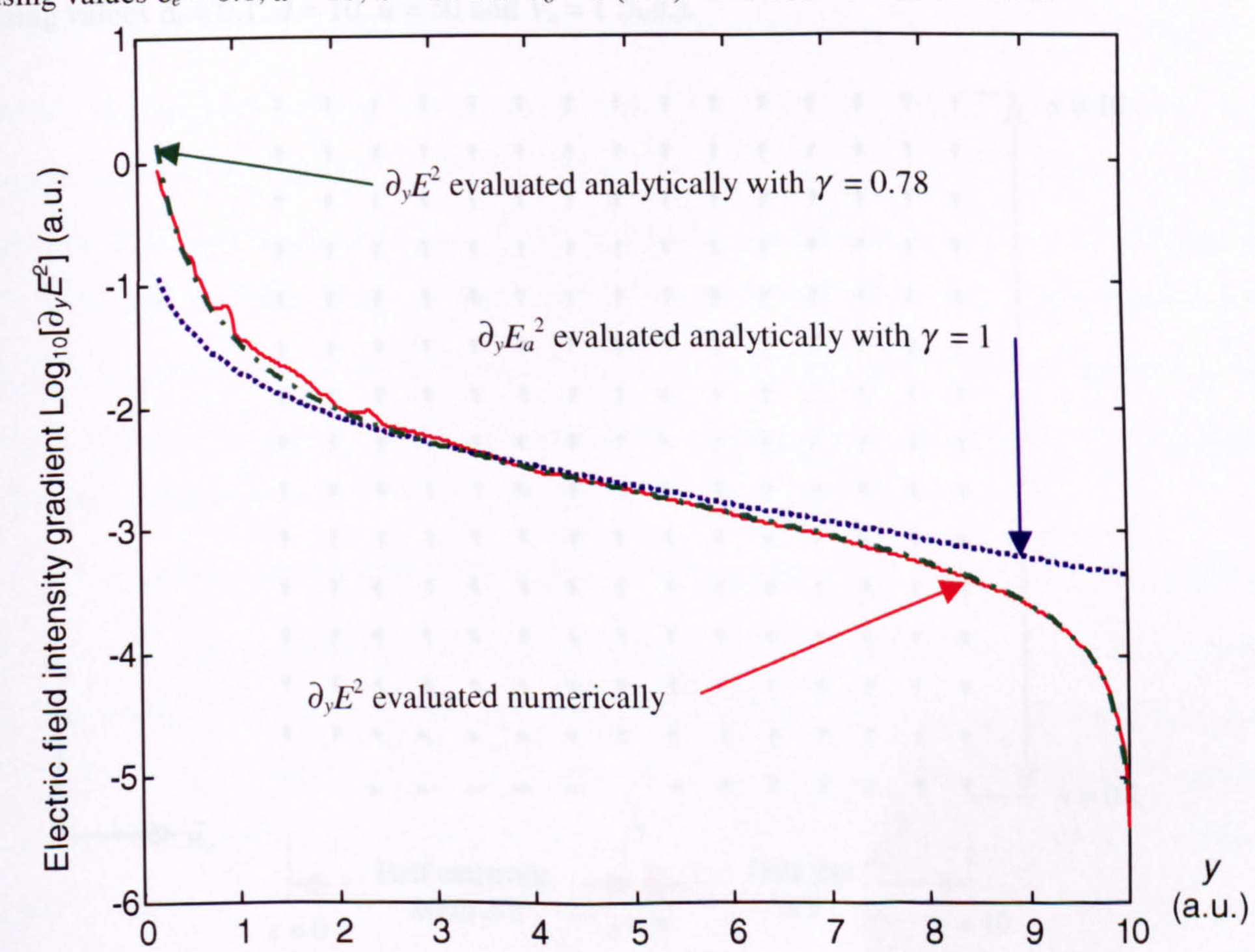

Fig. 6.2(f) Log-linear plots of $\partial_y \left|\vec{E}\right|$ (written above as $\partial_y E^2$) at $x = 4.9$ for $y = 0.2$ to 10 generated using values $\delta_e = 0.1$, $d = 10$, $h = 10$ and $V_o = 1$ (a.u.). See text for further details.

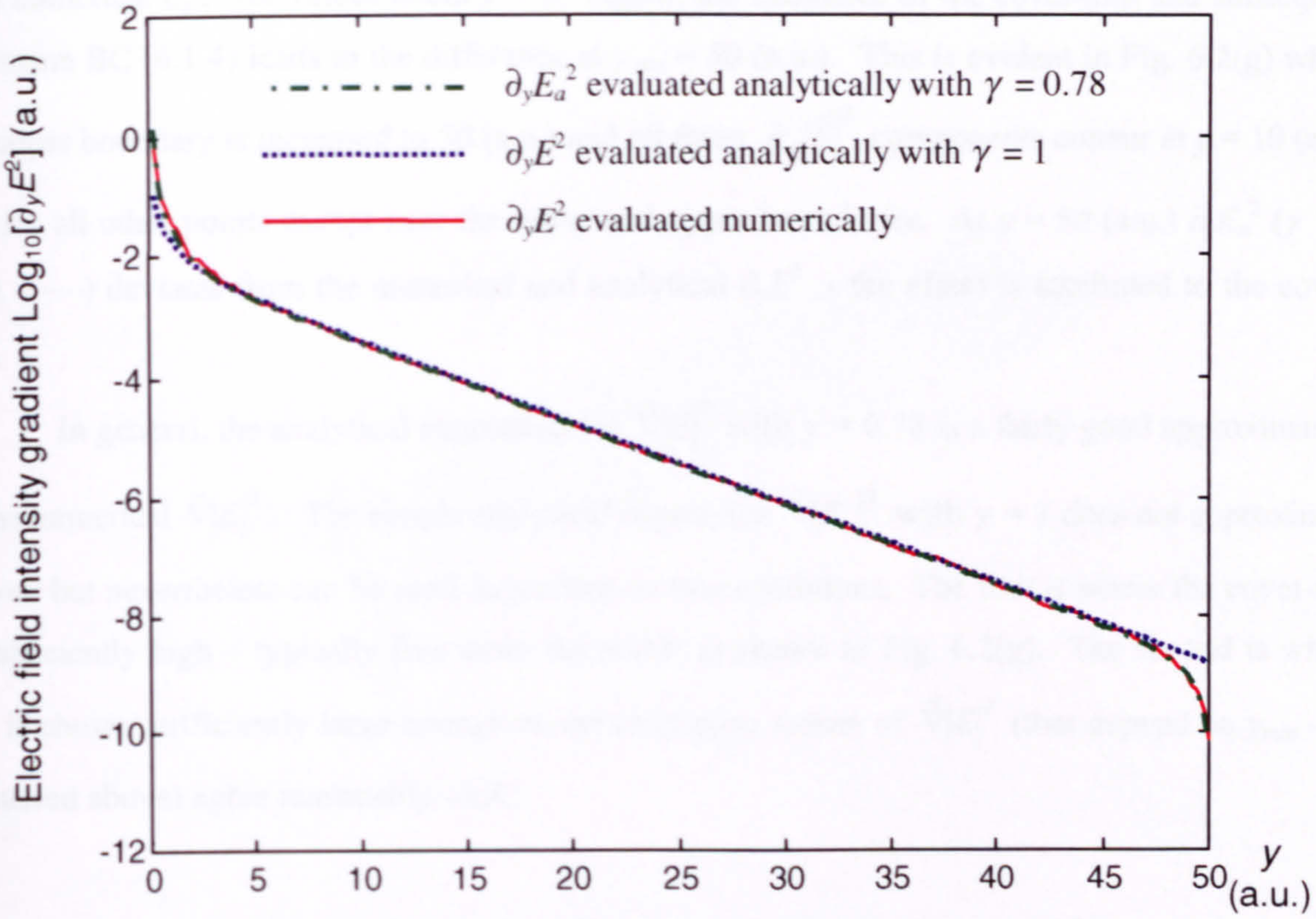

Fig. 6.2(g) Log-linear plots of $\partial_y \left|\vec{E}\right|$ (written above as $\partial_y E^2$) at $x = 4.9$ for $y = 0.2$ to 50 generated using values $\delta_e = 0.1$, $d = 10$, $h = 50$ and $V_o = 1$ (a.u.).

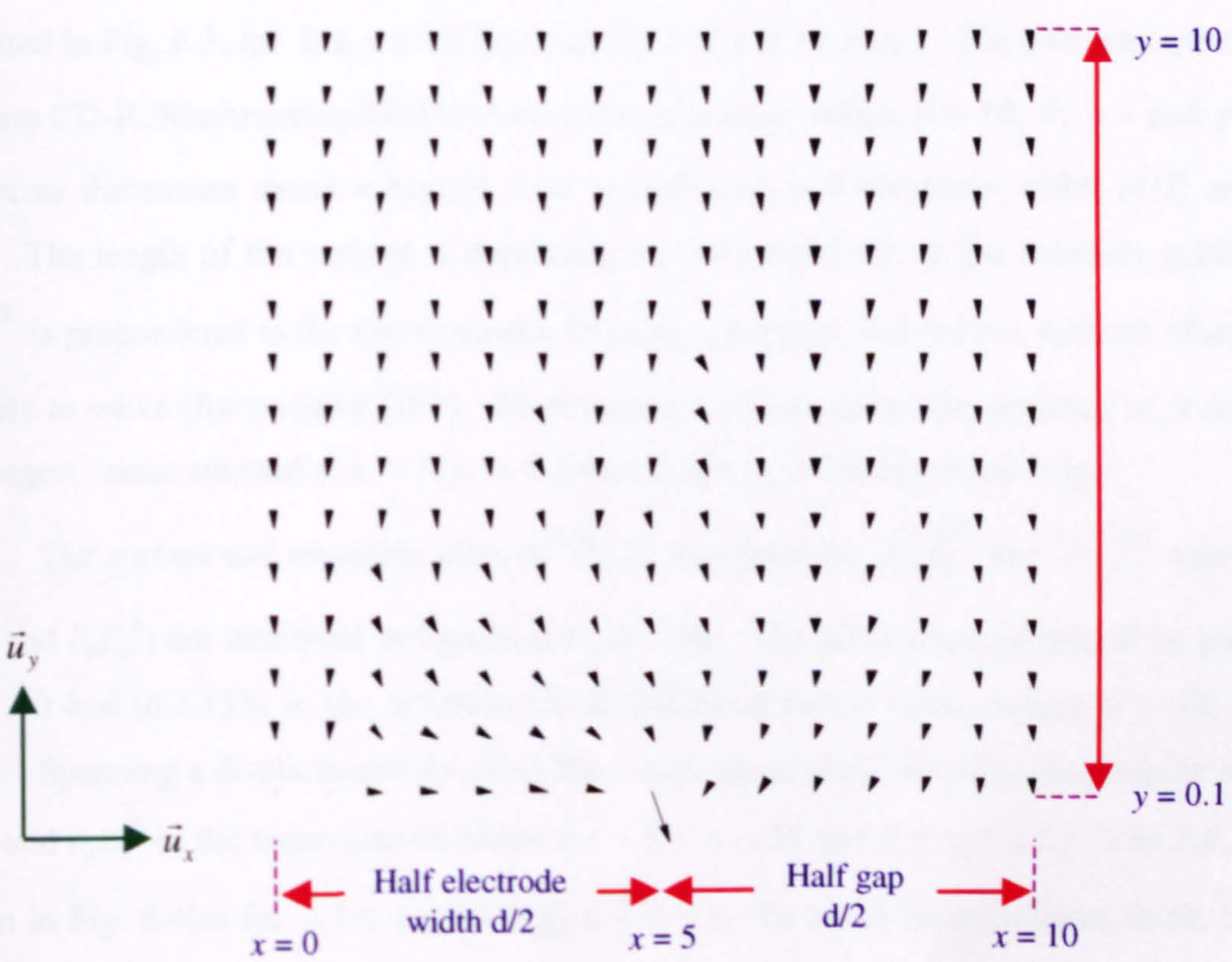

Fig. 6.3 Vector field plot of electric field intensity gradient $\nabla\left|\vec{E}_a\right|^2 = \partial_x\left|\vec{E}_a\right|^2 \vec{u}_x + \partial_y\left|\vec{E}_a\right|^2 \vec{u}_y$ for $0 \le x \le 10$, $0.1 \le y \le 10$ generated using $d = 10$ (a.u.), $\gamma = 1$ and $V_o = 1$ (a.u.).

with numerical $\partial_x E^2$ for values about $y = 5$. Again, the influence of the cover-slip and subsequent Neumann BC (6.1.4) leads to the difference at $y_{max} = 50$ (a.u.). This is evident in Fig. 6.2(g) where the upper boundary is increased to 50 (a.u.) and all three $\partial_y \left|\vec{E}\right|^2$ components concur at $y = 10$ (a.u.) and for all other points except near the lower and upper boundaries. At $y = 50$ (a.u.) $\partial_y E_a^{\,2}$ ($\gamma = 1$ blue .....) deviates from the numerical and analytical $\partial_y E^2$ - the effect is attributed to the cover-slip.

In general, the analytical expression for $\vec{\nabla}\left|E\right|^2$ with $\gamma = 0.78$ is a fairly good approximation to the numerical $\vec{\nabla}\left|E\right|^2$. The simple analytical expression $\vec{\nabla}\left|E_a\right|^2$ with $\gamma = 1$ does not approximate as well but nevertheless can be used depending on two conditions. The first is where the cover-slip is sufficiently high – typically five times the width as shown in Fig. 6.2(g). The second is where y_{min} is chosen sufficiently large enough so the extremum values of $\vec{\nabla}\left|E\right|^2$ (that depend on y_{min} – as discussed above) agree reasonably well.

6.2.5 Plots of the electric field intensity gradient given by (6.2.13a) and (6.2.13b)

A vector field plot of the electric field intensity gradient $\vec{\nabla}\left|E_a\right|^2 = \partial_x \left|\vec{E}_a\right|^2 \vec{u}_x + \partial_y \left|\vec{E}_a\right|^2 \vec{u}_y$ is exhibited in Fig. 6.3. for $0 \le x \le 10$ (a.u.) and $0.1 \le y \le 10$ (a.u.). The plot was generated in the program CD-R:/Mathematica/*Grd3dTh.nb* with parameter values, $d = 10$, $V_o = 1$ and $\gamma = 1$. The transverse dimension spans a typical 'cell' comprising half-electrode width (d/2) and half-gap (d/2). The length of the vectors is dependent on the magnitude or the intensity gradient. Since $\vec{\nabla}\left|E_a\right|^2$ is proportional to the electrokinetic force on a particle, the vectors indicate where a particle is likely to move (for positive DEP). Most particles will therefore be attracted to, a drift towards, the longest vector situated at $x = 5, y = 0.1$ (a.u.), that is, at the electrode 'edge'.

The surface and elevation plots of $\vec{\nabla}\left|E_a\right|^2$ components $\partial_x \left|\vec{E}\right|^2$ and $\partial_y \left|\vec{E}\right|^2$ (also written as $\partial_x E_a^{\,2}$ and $\partial_y E_a^{\,2}$) are exhibited in figures 6.4 (a) – (d). The plots were generated by implementing (6.2.13a) and (6.2.13b) in the program CD-R:/Matlab/*E3dth.m* using values, $d = 10$, $V_o = 1$ and $\gamma = 1$. Spanning a displacement $4d$ along the x-axis, these plots visualize the periodic structures of $\partial_x E_a^{\,2}$ and $\partial_y E_a^{\,2}$ in the transverse direction for $-5 \le x \le 35$ (or $0 \le \hat{x} \le 2\pi$). The $\partial_x E_a^{\,2}$ surface is shown in Fig. 6.4(a) for $0.1 \le y \le 10$ ($\frac{\pi}{200} \le \hat{y} \le \frac{\pi}{2}$). To assist interpretation, thick, bold orange lines along the $y = 0$ axis have been added in to show the placement of the electrodes and '$\pm V_o$' denotes the potentials. Values of the $\partial_x E_a^{\,2}$ are scaled as shown and have been colour coded to assist visualization. It is clear $\partial_x E_a^{\,2}$ extrema are located near the plane $y = 0.1$ (a.u.) at the electrode

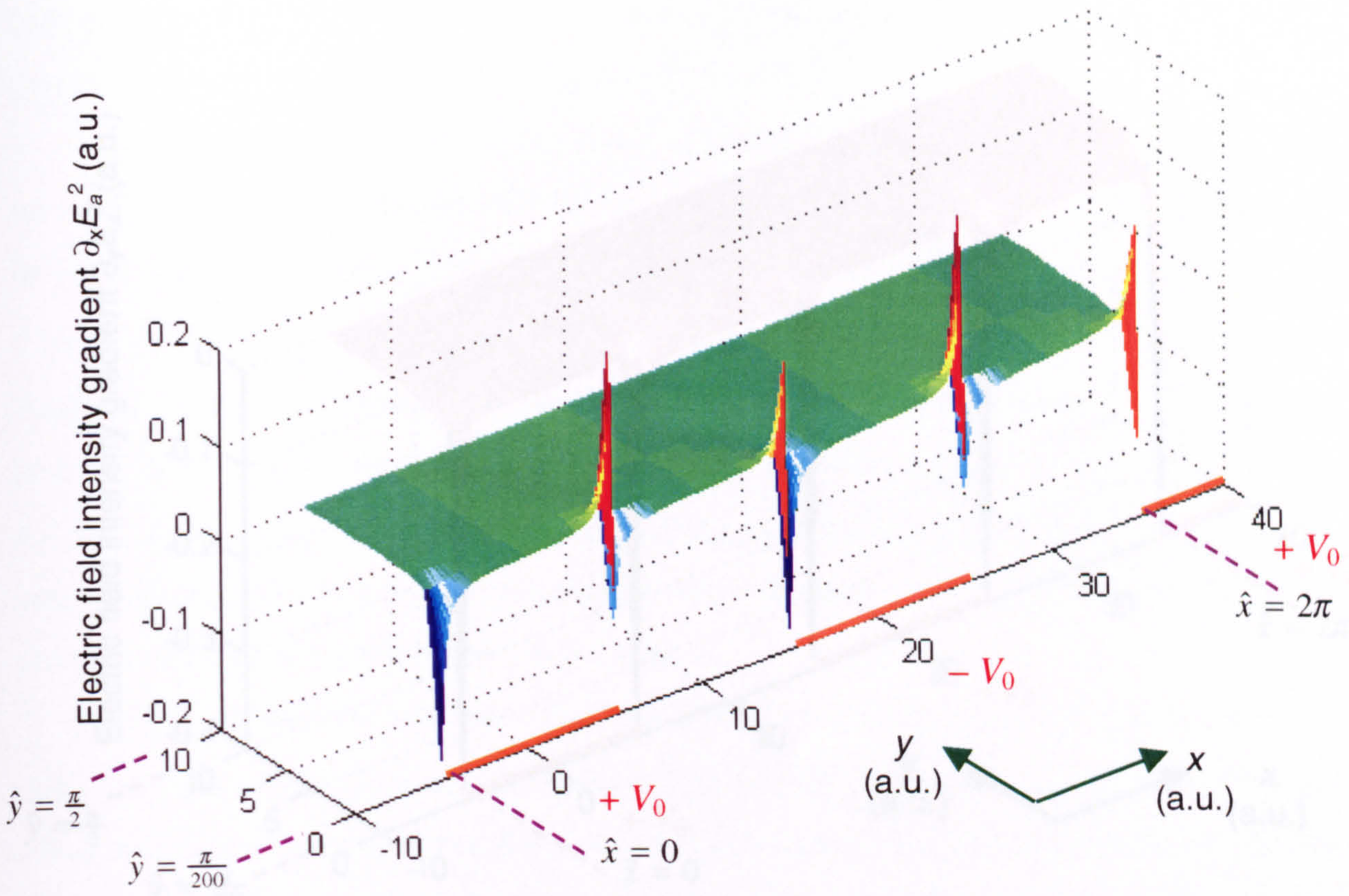

Fig. 6.4(a) Orthographic view of a $\partial_x\left|\vec{E}_a\right|^2$ ($\partial_x E_a^2$) surface generated using $d = 10$, $\gamma = 1$ and $V_o = 1$ (a.u.) in (6.2.13a) for the region $-\frac{d}{2} \le x \le \frac{7d}{2}$ and $\frac{d}{100} \le y \le d$ ($0 \le \hat{x} \le 2\pi$ and $\frac{\pi}{200} \le \hat{y} \le \frac{\pi}{2}$).

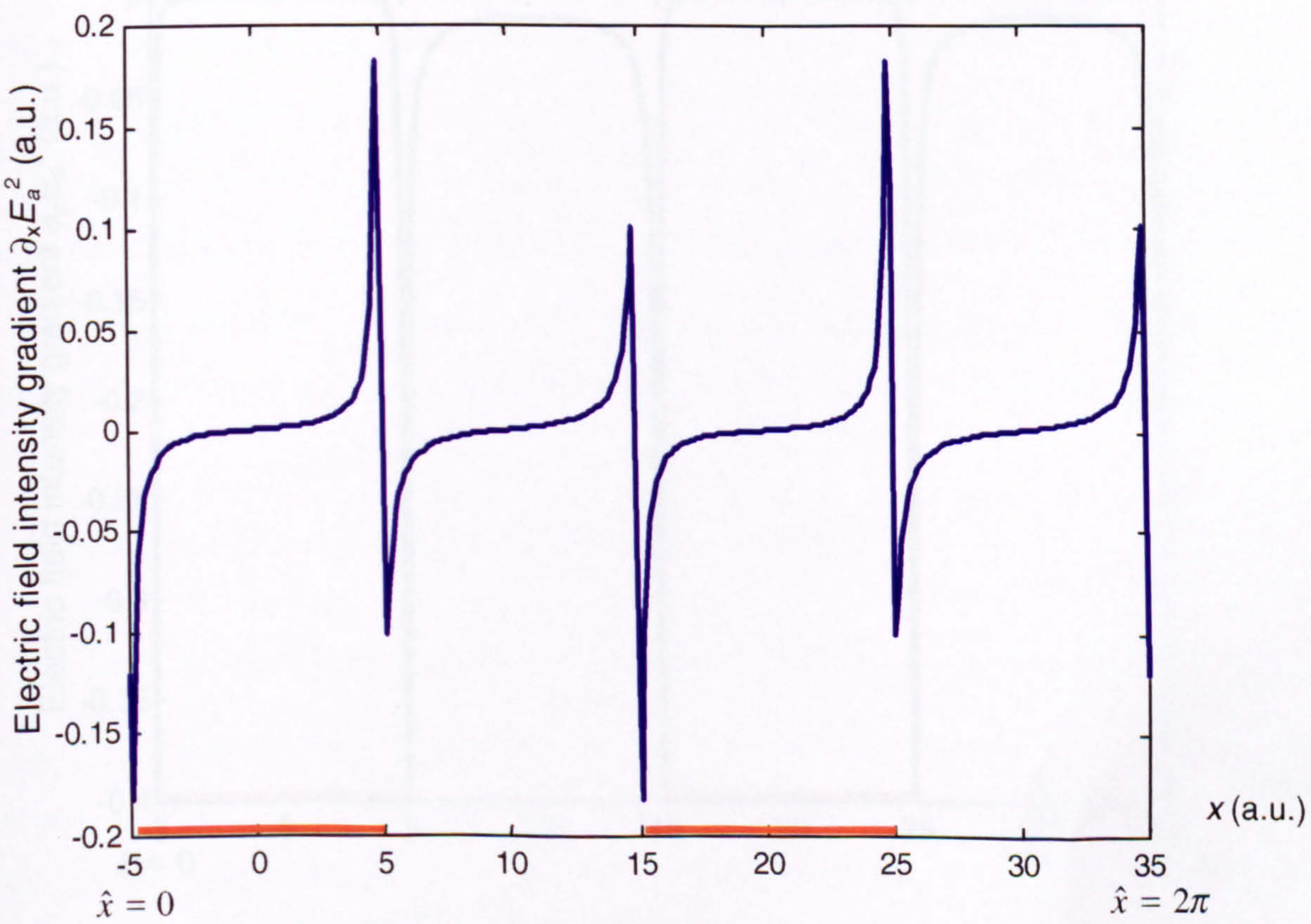

Fig. 6.4(b) A plot of $\partial_x\left|\vec{E}_a\right|^2$ (written as $\partial_x E_a^2$) at $y = \frac{d}{100}$ ($\hat{y} = \frac{\pi}{200}$) for $-\frac{d}{2} \le x \le \frac{7d}{2}$ ($0 \le \hat{x} \le 2\pi$) generated using the same parameters as Fig. 6.4(a) above, $d = 10$ (a.u.), $\gamma = 1$ and $V_o = 1$ (a.u.).

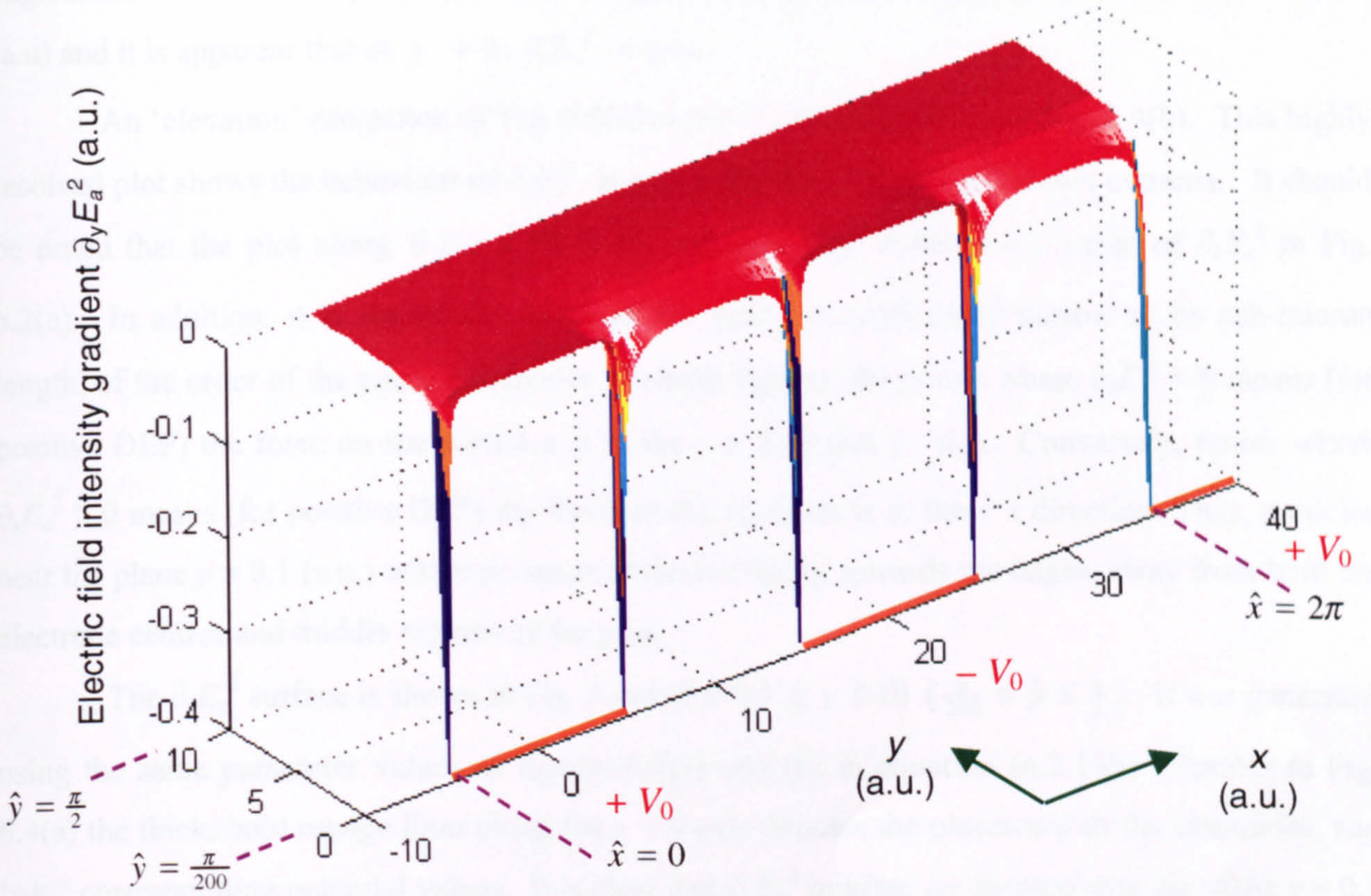

Fig. 6.4(c) Orthographic view of $\partial_y \left|\vec{E}_a\right|^2$ $(\partial_y E_a^2)$ surface generated using $d = 10$, $\gamma = 1$ and $V_o = 1$ (a.u.) in (6.2.13b) for the region $-\frac{d}{2} \le x \le \frac{7d}{2}$ and $\frac{d}{100} \le y \le d$ $(0 \le \hat{x} \le 2\pi$ and $\frac{\pi}{200} \le \hat{y} \le \frac{\pi}{2})$.

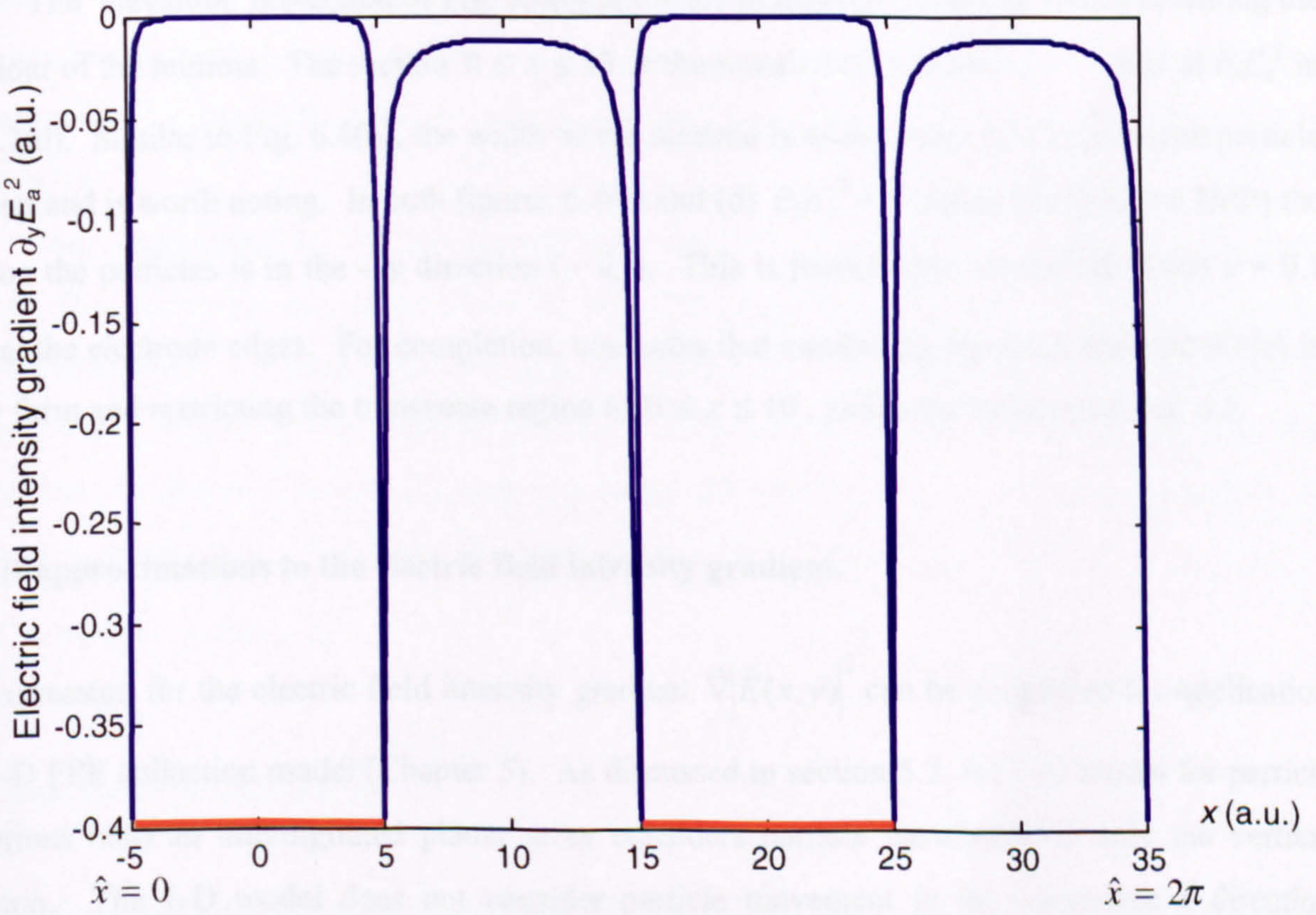

Fig. 6.4(d) A plot of $\partial_y \left|\vec{E}_a\right|^2$ (written as $\partial_y E_a^2$) at $y = \frac{d}{100}$ $(\hat{y} = \frac{\pi}{200})$ for $-\frac{d}{2} \le x \le \frac{7d}{2}$ $(0 \le \hat{x} \le 2\pi)$ generated using the same parameters as Fig. 6.4(c) above, $d = 10$, $\gamma = 1$ and $V_o = 1$ (a.u.).

edge ordinates $x = -5$, 5, 15, 25, and 35 (a.u.). The extrema of $\partial_x E_a^2$ are shown to be near $\pm$ 0.2 (a.u) and it is apparent that as $y \to 0$, $\partial_x E_a^2 \to \pm\infty$.

An 'elevation' projection of Fig. 6.4(a) at $y = 0.1$ (a.u.) is given in Fig. 6.4(b). This highly resolved plot shows the behaviour of $\partial_x E_a^2$, in particular, at inflexion points and extrema. It should be noted that the plot along $0 \le x \le 10$ is the rescaled blue dotted (·····) plot of $\partial_x E_a^2$ in Fig. 6.2(c). In addition, it is shown the width of the peaks is sufficiently narrow to be sub-micron length, of the order of the particle diameter. In both figures, the points where $\partial_x E_a^2 < 0$ means (for positive DEP) the force on the particles is in the $-x$ direction ($-\vec{u}_x$). Conversely, points where $\partial_x E_a^2 > 0$ means (for positive DEP) the force on the particles is in the $+x$ direction. Thus, particles near the plane $y = 0.1$ (a.u.) will experience attractive forces towards the edges, away from both the electrode centres and middle regions of the gaps.

The $\partial_y E_a^2$ surface is shown in Fig. 6.4(c) for $0.1 \le y \le 10$ ($\frac{\pi}{200} \le \hat{y} \le \frac{\pi}{2}$). It was generated using the same parameter values as figures 6.4(a) and (b) in equation (6.2.13b). Similar to Fig. 6.4(a) the thick, bold orange lines along the $y = 0$ axis denotes the placement of the electrodes, and '$\pm V_o$' corresponding potential values. It is clear that $\partial_y E_a^2$ minima are located near the plane $y = 0.1$ (a.u.) at the edge ordinates $x = -5$, 5, 15, 25, and 35 (a.u.). The minima of $\partial_x E_a^2$ are shown to be near $-$ 0.4 (a.u) and it is apparent that as $y \to 0$, $\partial_y E_a^2 \to -\infty$.

The 'elevation' projection of Fig. 6.4(c) at $y = 0.1$ (a.u.) is given in Fig. 6.4(d) revealing the behaviour of the minima. The section $0 \le x \le 10$ is the rescaled blue dotted (·····) plot of $\partial_y E_a^2$ in Fig. 6.2(d). Similar to Fig. 6.4(b), the width of the minima is of the order of a sub-micron particle diameter and is worth noting. In both figures 6.4(c) and (d) $\partial_y E_a^2 < 0$ means (for positive DEP) the force on the particles is in the $-y$ direction ($-\vec{u}_y$). This is particularly so near the plane $y = 0.1$ (a.u.) at the electrode edges. For completion, one notes that combining figures 6.4(a) and 6.4(c) in vector form and restricting the transverse region to $0 \le x \le 10$, yields the vector plot Fig. 6.3.

6.3 1-D approximations to the electric field intensity gradient.

The expression for the electric field intensity gradient $\vec{\nabla}\left|\vec{E}(x,y)\right|^2$ can be simplified for application in a 1-D FPE collection model (Chapter 5). As discussed in section 5.2, the 1-D model for particle collections onto an interdigitated planar array considers particle movement in only the vertical direction. The 1-D model does not consider particle movement in the transverse x direction because the electric field is assumed to be spatially invariant. As fig. 6.4(b) illustrates in the previous section, the component of electric field intensity gradient in the transverse x-direction, $\partial_x\left|\vec{E}_a\right|^2$, exhibits asymmetric characteristics that indicate the average over the closed

interval $x \in [0,4d]$, or period, is zero. This is generally true; the average of $\partial_x \left|\vec{E}\right|^2$ over a (compartment) period is,

$$\overline{\partial_x \left|\vec{E}\right|^2} = \frac{1}{4d}\int_0^{4d} \partial_x \left|\vec{E}\right|^2 dx = \frac{1}{4d}\int_0^{4d} d\left|\vec{E}\right|^2 = \frac{1}{4d}\left[\ \left|\vec{E}\right|^2\right]_0^{4d} = \frac{1}{4d}\left[E_x^2 + E_y^2\ \right]_0^{4d} = 0 \qquad (6.3.1)$$

where the last step arises from periodicity of E_x and E_y, $E_x(0,y) = E_x(4d,y)$ and $E_y(0,y) = E_y(4d,y)$. Therefore, the average $\vec{\nabla}\left|\vec{E}(x,y)\right|^2$ over the period $x \in [0,4d]$, denoted $\overline{\vec{\nabla}\left|\vec{E}\right|^2}$, simplifies

$$\begin{aligned}\overline{\vec{\nabla}\left|\vec{E}(x,y)\right|^2} &= \frac{1}{4d}\int_0^{4d} \vec{\nabla}(E_x^2 + E_y^2)\,dx = \frac{1}{4d}\int_0^{4d} \left(\partial_x \left|\vec{E}\right|^2 \vec{u}_x + \partial_y \left|\vec{E}\right|^2 \vec{u}_y\right) dx \\ &= \frac{\vec{u}_y}{4d}\int_0^{4d} \partial_y \left|\vec{E}\right|^2\, dx = \overline{\partial_y \left|\vec{E}\right|^2}\vec{u}_y\end{aligned} \qquad (6.3.2)$$

and is valid for $0 < y \le h$. Thus, spatial invariance in the transverse x direction for $0 < y \le h$ can be achieved by averaging over a $4d$ period. One may note that averaging in this way guarantees transverse invariance but it is not always a necessary requirement, in particular for making field approximations. It depends of the domain of y values considered, and will be discussed later in section 6.3.2.

Two approximations for the electric field intensity gradient are considered in the next section. The first is the less straightforward near field approximation, and the second is the far field approximation. For simplicity, both approximations are specific for the case where height of the cover-slip is infinite so the effect on the electric field is negligible. Both approximations also assume that the potential across the gap is a linear interpolation of the electrode potentials, as described in section 6.1. Thus, only the potential $\Phi_{\infty,T}(x,y)$ and subsequently E_{x_a}, E_{y_a}, E_{x,x_a}, and E_{x,y_a} need be considered.

6.3.1 Near field approximations

The near field properties of electric field intensity gradient, for the case $\gamma = 1$, are evident in Figs. 6.4(a) – (d). The plots show $\vec{\nabla}\left|\vec{E}_a(x,y)\right|^2$ is salient for $y \to 0$ at the electrode edges

$x=(2m+1)d/2$. To understand the general behaviour of the intensity gradient very close to the edges, it is sufficient to examine $\vec{\nabla}\left|\vec{E}_a(x,y)\right|^2$ at just one edge.

6.3.1.1 Near field approximation at an electrode edge

For convenience, the edge corresponding to $x=-d/2$ (or $\hat{x}=0$) is chosen. In Appendix K.1, a series expansion of equations (6.2.4a), (6.2.6a), (6.2.9a) and (6.2.11a) is taken for $\hat{x}=0$ $\{\hat{y}: 0<\hat{y}\leq\frac{\pi}{200}\}$. This yields an approximation for the electric field intensity gradient components in the near field, written as $\partial_x\left|\vec{E}_a\right|^2_{\hat{x}=0,\hat{y}\to 0}$ and $\partial_y\left|\vec{E}_a\right|^2_{\hat{x}=0,\hat{y}\to 0}$. Expressions for these components are given in (K.1.10) and (K.1.12). Substituting into (6.2.13),

$$\begin{aligned}\vec{\nabla}\left|\vec{E}_a(x,y)\right|^2_{\hat{x}=0,\hat{y}\to 0} &= \vec{u}_x\,\partial_x\left|\vec{E}_a\right|^2_{\hat{x}=0,\hat{y}\to 0}+\vec{u}_y\,\partial_y\left|\vec{E}_a\right|^2_{\hat{x}=0,\hat{y}\to 0}\\ &= -\frac{2\gamma^2V_o^2}{\hat{y}d^3}\vec{u}_x+\frac{4\gamma^2V_o^2\ln(\hat{y}/2)}{\pi\hat{y}d^3}\vec{u}_y\end{aligned} \qquad (6.3.3)$$

Clearly, as $y\to 0$, $\partial_x\left|\vec{E}_a\right|^2_{\hat{x}=0}\to-\infty$ and $\partial_y\left|\vec{E}_a\right|^2_{\hat{x}=0}\to-\infty$. Elsewhere for x values corresponding to the electrode width and inter-electrode gap (i.e. excluding the edges), the gradient of the electric field intensity, $\vec{\nabla}\left|\vec{E}_a(x,y)\right|^2$ is finite as $y\to 0$.

The singularities at the electrode edges raises a question about the choice of a minimum y value that results in a meaningful expression for a 'near field' approximation. If one selects a minimum value of y, y_{min} = 0.1 μm then for d = 10 μm, $\hat{y}_{\min}=\pi/200$. The choice of y_{max} is somewhat arbitrary but an order of magnitude increase, y_{max} = 1 μm, is reasonable. Thus, the term 'near field' for d = 10 μm implies the y values ranging from 0.1 μm to 1 μm, or $\{\hat{y}: \frac{\pi}{200}\leq\hat{y}\leq\frac{\pi}{20}\}$.

6.3.1.2 Average near field approximation

The average electric field intensity gradient close to the electrode surface, $\{d/100\leq y\leq d/10\}$, is denoted $\overline{\vec{\nabla}\left|\vec{E}_a\right|^2}_{near}$ where it is understood the 'a' sub-script denotes the case where the height of the cover-slip is infinite and the potential across the gap is a linear interpolation of the electrode potentials. One may note in passing that the method can be extended for the other three cases

discussed in section 6.1 that include the effect of the cover-slip and zero 'gap' potential. A good approximation to the expression for $\overline{\vec{\nabla}\left|\vec{E}_a\right|^2}_{near}$ is called the *average near field* approximation.

To find an analytical expression for this parameter, it is useful to develop the result given by (6.3.2) that is generally applicable for all $y > 0$. Consider (6.3.2) again,

$$\overline{\vec{\nabla}\left|\vec{E}_a\right|^2} = \overline{\partial_y\left|\vec{E}_a\right|^2}\,\vec{u}_y = \frac{\vec{u}_y}{4d}\int_0^{4d}\partial_y\left|\vec{E}_a\right|^2 dx \tag{6.3.4}$$

From (6.2.13b), using the relations from (J.3.10) $E_{x,y_a} = E_{y,x_a}$ and from (J.3.12) $E_{y,y_a} = -E_{x,x_a}$, the integral for the gradient of electric field intensity in the y direction is

$$\int_0^{4d}\partial_y\left|\vec{E}_a\right|^2 dx = 2\left(\int_0^{4d} E_{x_a}\,E_{y,x_a}\,dx - \int_0^{4d} E_{y_a}\,E_{x,x_a}\,dx\right) \tag{6.3.5}$$

Integrating each term in (6.3.5) by parts,

$$\int_0^{4d} E_{x_a}\,E_{y,x_a}\,dx = [E_{x_a}E_{y_a}]_0^{4d} - \int_0^{4d} E_{y_a}\,E_{x,x_a}\,dx = -\int_0^{4d} E_{y_a}\,E_{x,x_a}\,dx \tag{6.3.6a}$$

$$\int_0^{4d} E_{y_a}\,E_{x,x_a}\,dx = [E_{y_a}E_{x_a}]_0^{4d} - \int_0^{4d} E_{y,x_a}\,E_{x_a}\,dx = -\int_0^{4d} E_{y,x_a}E_{x_a}\,dx \tag{6.3.6b}$$

where periodicity of the product of E_{x_a} and E_{y_a}, over the closed interval $x \in [0,4d]$ results in the [] definite integral terms being zero. Hence, combining (6.3.5) and (6.3.6a) and (6.3.6b)

$$\int_0^{4d}\partial_y\left|\vec{E}_a\right|^2 dx = -4\int_0^{4d} E_{y_a}\,E_{x,x_a}\,dx = 4\int_0^{4d} E_{x_a}\,E_{y,x_a}\,dx \tag{6.3.7}$$

The choice of the two integrals, for evaluating the integral is arbitrary. Both expressions in (6.3.7) are not straightforward to integrate analytically, in particular, when a simple analytical solution is desired. Linear approximations of the integrand often provide a route for a simple solution, and in this respect, the $E_{y_a}E_{x,x_a}$ integrand is the most convenient to linearise. In terms of the integration interval in (6.3.7), advantage is taken of the periodic and symmetric properties of $\partial_y|E_a|^2$ shown in Fig. 6.4(d). These properties stem from the properties of the electric potential described in the

previous section. Hence, only a quarter of the integration interval is needed. Thus, substituting (6.3.7) into (6.3.4)

$$\overline{\vec{\nabla}\left|\vec{E}_a\right|^2} = \frac{\vec{u}_y}{4d}\int_0^{4d} \partial_y\left|\vec{E}_a\right|^2 dx = \frac{\vec{u}_y}{d}\int_0^{d} \partial_y\left|\vec{E}_a\right|^2 dx = -\frac{4\vec{u}_y}{d}\int_0^{d} E_{y_a} E_{x,x_a}\, dx \qquad (6.3.8)$$

The independent variable is transformed $\hat{x} = \frac{\pi x}{2d} + \frac{\pi}{4}$ as given in (6.2.4). Thus (6.3.8) becomes

$$\overline{\vec{\nabla}\left|\vec{E}_a\right|^2} = \frac{\vec{u}_y}{d}\frac{2d}{\pi}\int_{\pi/4}^{3\pi/4} \partial_y\left|\vec{E}_a\right|^2 d\hat{x} = -\frac{8\vec{u}_y}{\pi}\int_{\pi/4}^{3\pi/4} E_{y_a} E_{x,x_a}\, d\hat{x} \qquad (6.3.9)$$

It is convenient to linearise E_{y_a} and E_{x,x_a} about $\hat{x} = 0$. Since, $\partial_y\left|E_a\right|^2$ is symmetric about $\hat{x} = \frac{\pi}{4}$, (6.3.9) is invariant to a translation in the integration interval, $\hat{x} \in [\frac{\pi}{4}, \frac{3\pi}{4}] \rightarrow [-\frac{\pi}{4}, \frac{\pi}{4}]$. Hence,

$$\overline{\vec{\nabla}\left|\vec{E}_a\right|^2} = -\frac{8\vec{u}_y}{\pi}\int_{-\pi/4}^{+\pi/4} E_{y_a} E_{x,x_a}\, d\hat{x} \qquad (6.3.10)$$

The linear approximations are detailed in Appendix K.2. The product $E_{y_a} E_{x,x_a}$ applicable for $\{\hat{y}: \frac{\pi}{200} \le \hat{y} \le \frac{\pi}{20}\}$, from (K.2.14) is

$$E_{y_a} E_{x,x_a} \cong \widetilde{E}_{y_a} \widetilde{E}_{x,x_a} = \frac{\gamma^2 V_o^{\,2} \hat{y}}{\pi d^3}\left[\ln 4 - 2\ln\hat{y} - \frac{2\hat{x}^2/\hat{y}^2}{2+\hat{x}^2/\hat{y}^2} + 2\hat{x}\right]\left[\frac{1}{\hat{y}^2+\hat{x}^2} + \frac{\hat{x}}{1-\hat{x}^2}\right] \qquad (6.3.11)$$

The product $E_{y_a} E_{x,x_a}$ and approximation $\widetilde{E}_{y_a} \widetilde{E}_{x,x_a}$ are plotted in Fig. 6.5. They compare closely near their maximum and less well at the tail ends. Hence, the area under both curves is expected to be nearly the same.

Rewriting (6.3.10), the *average near field* approximation is given by

$$\overline{\vec{\nabla}\left|\vec{E}_a\right|^2}_{near} = -\frac{8\vec{u}_y}{\pi}\int_{-\pi/4}^{+\pi/4} E_{y_a} E_{x,x_a}\, d\hat{x} \cong -\frac{8\vec{u}_y}{\pi}\int_{-\pi/4}^{+\pi/4} \widetilde{E}_{y_a} \widetilde{E}_{x,x_a}\, d\hat{x} \qquad (6.3.12a)$$

Substituting (6.3.11) into (6.3.12a) the integration is evaluated in equations (K.2.15) - (K.2.19). They show

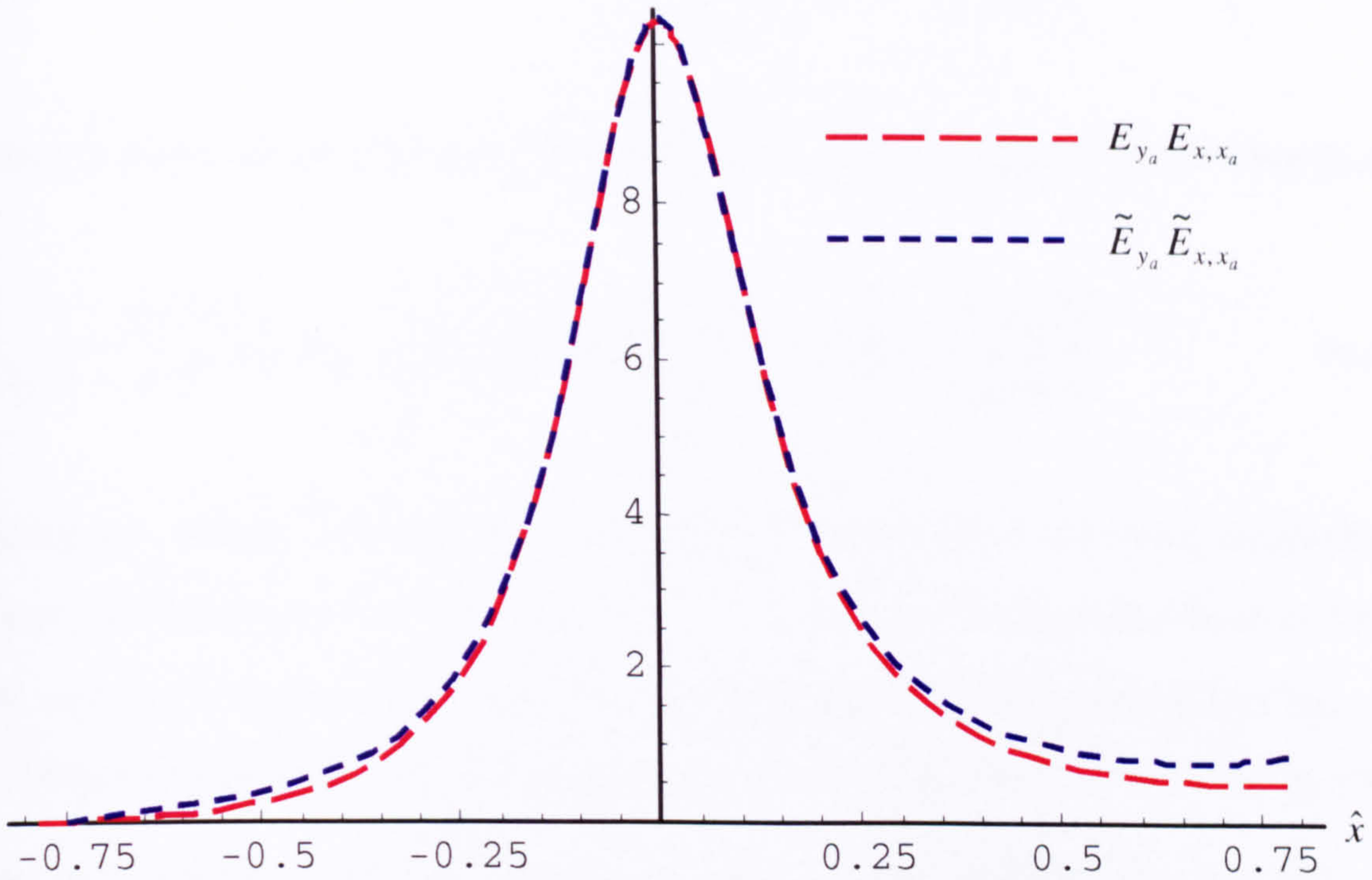

Fig. 6.5 Component of the electric field intensity gradient $E_{y_a} E_{x,x_a}$ and approximation $\tilde{E}_{y_a} \tilde{E}_{x,x_a}$ versus normalised transverse displacement $\hat{x}$ at $\hat{y} = \frac{\pi}{20}$ (or y = d/10) using (normalised) values $d = 1$, $\gamma = 1$ and $V_o = 1$.

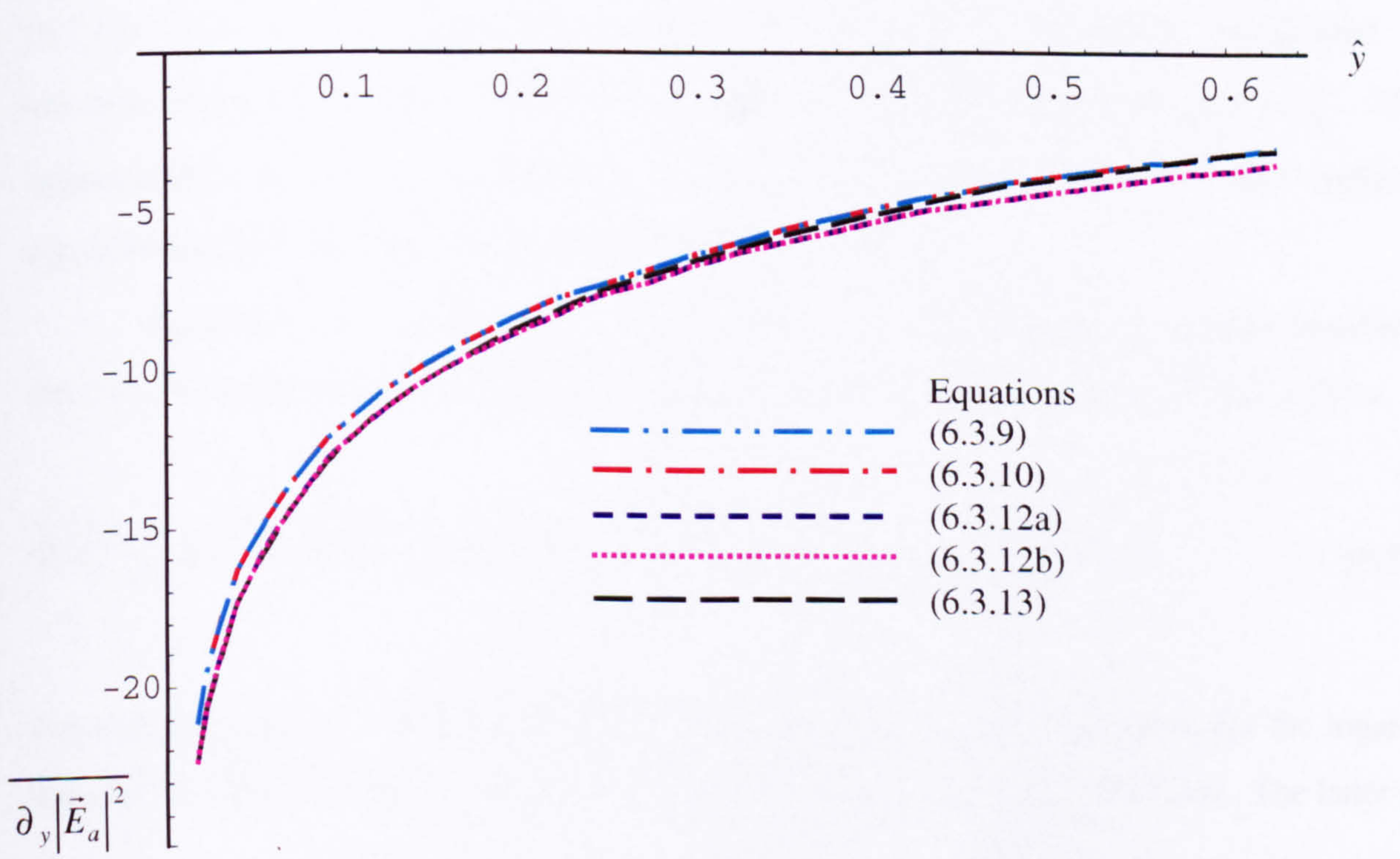

Fig. 6.6 A comparison of numerical and analytical approximations of the electric field intensity gradient magnitude $\overline{\partial_y \left|\vec{E}_a\right|^2}_{near}$ versus normalised displacement $\hat{y}$. The profiles are plotted for $\{\pi / 200 \le \hat{y} \le \pi / 5\}$ and used normalised values $d = 1$, $\gamma = 1$ and $V_o = 1$.

$$\overline{\vec{\nabla}\left|\vec{E}_a\right|^2}_{near} \cong -\frac{8\gamma^2 V_o^2}{\pi^2 d^3}\left[2[\ln(4)-2\ln(\hat{y})+2]\tan^{-1}\left(\frac{\pi/4}{\hat{y}}\right)-4\sqrt{2}\tan^{-1}\left(\frac{\pi/4}{\hat{y}\sqrt{2}}\right)+1.096\hat{y}\right] \qquad (6.3.12b)$$

Appendix K.2 shows the last term in (6.3.12b) can be neglected for $\{\frac{\pi}{200}\le\hat{y}\le\frac{\pi}{5}\}$, yielding (K.2.20),

$$\overline{\vec{\nabla}\left|\vec{E}_a\right|^2}_{near} \cong -\frac{8\gamma^2 V_o^2}{\pi^2 d^3}\left[2[\ln(4)-2\ln(\hat{y})+2]\tan^{-1}\left(\frac{\pi/4}{\hat{y}}\right)-4\sqrt{2}\tan^{-1}\left(\frac{\pi/4}{\hat{y}\sqrt{2}}\right)\right] \qquad (6.3.13)$$

The relations are plotted in Figure 6.6 for a range of $\hat{y}$ values about four times longer than the above *near field* expressions assume, $\{\frac{\pi}{200}\le\hat{y}\le\frac{\pi}{5}\}$. The first expression on the *rhs* of (6.3.9), and (6.3.10), were each numerically integrated using Mathematica 4.0™ (Mathematica Inc., USA, 1999). Numerical integration of (6.3.9) required sub-dividing the interval $\hat{x}\in[\frac{\pi}{4},\frac{3\pi}{4}]$ to maintain accuracy. A comparison of the $\overline{\vec{\nabla}\left|\vec{E}_a\right|^2}$ plots shows they agree extremely closely. This is expected, and helps to cross-check the expressions. The numerical integration of (6.3.10) over the interval $\hat{x}\in[-\frac{\pi}{4},\frac{\pi}{4}]$ is viable, it is used as a basis or 'reference' for comparing the near field approximations (6.3.12) – (6.3.13). The plots using equations (6.3.12a) and (6.3.12b) concur, as expected. They are close to the (6.3.10) curve with about a 5% error for the near field region, $\frac{\pi}{200}\le\hat{y}\le\frac{\pi}{20}$. The last approximation (6.3.13) is very close to (6.3.12a) and (6.3.12b) in near field and interestingly approximates (6.3.12) better for higher $\hat{y}$ values, $\frac{\pi}{10}\le\hat{y}\le\frac{\pi}{5}$.

Since (6.3.13) is valid one can approximate the inverse tan terms by a series expansion for the case where the magnitude of the argument is greater than unity. Equation (K.2.21) gives,

$$\overline{\vec{\nabla}\left|E_a\right|^2}_{near} \cong \frac{-8\gamma^2 V_o^{\,2}\vec{u}_y}{\pi^2 d^3}\left[[2\ln(2)-2\ln(\hat{y})+2]\left(\pi-\frac{8\hat{y}}{\pi}\right)-2\pi\sqrt{2}+\frac{32\hat{y}}{\pi}\right] \qquad (6.3.14)$$

Equation (6.3.14) is further simplified by choosing a suitable series expansion for the logarithmic term, $\ln(\hat{y})$. The expansions are developed in Appendix K.2, (K.2.22) – (K.2.24). The latter yields

$$\overline{\vec{\nabla}\left|E_a\right|^2}_{near} \cong \frac{-8\gamma^2 V_o^{\,2}\vec{u}_y 2\pi}{\pi^2 d^3(1+\hat{y}/A)}\left[\begin{array}{l}\ln\left(\frac{2}{A}\right)+3-\sqrt{2}+\frac{\hat{y}}{A}\left[\ln\left(\frac{2}{A}\right)-1-\sqrt{2}\right]\\ -\frac{8\hat{y}}{\pi^2}\left[\ln\left(\frac{2}{A}\right)+1\right]-\frac{8\hat{y}^2}{\pi^2 A}\left[\ln\left(\frac{2}{A}\right)-3\right]\end{array}\right] \qquad (6.3.15)$$

where for $\hat{y}$ values of interest, suitable values of the constant A are $\pi/35 \le A \le \pi/25$.

Selecting a value $A = 1/10 \cong \pi/31.42$, (6.3.15) gives

$$\overline{\vec{\nabla}|E_a|^2}_{near} \cong \frac{-16\gamma^2 V_o{}^2 \vec{u}_y}{\pi d^3(1+10\hat{y})}\left[4.582 + 2.576\hat{y} - 0.03460\hat{y}^2\right] \qquad (6.3.16)$$

As described in (K.2.25), the first term in the bracket [ ] is dominant for near field $\hat{y}$ values. Hence, (6.3.16) approximates to a hyperbolic relation

$$\overline{\vec{\nabla}|E_a|^2}_{near} \cong \frac{-16\gamma^2 V_o{}^2 \vec{u}_y 4.582}{\pi d^3(1+10\hat{y})} \cong \frac{-23.33\gamma^2 V_o{}^2 \vec{u}_y}{d^3(1+10\hat{y})}, \text{ for } \frac{\pi}{200} \le \hat{y} \le \frac{\pi}{20} \qquad (6.3.17)$$

and is plotted in Fig. 6.7. It compares reasonably well with the numerically integrated reference (6.3.10) with a relative error of up to about 10% over $\pi/200 \le \hat{y} \le \pi/5$. Transforming $\hat{y}$ for application as a 1-D DEP model in Chapter 5, Appendix K.2 (K.2.26) - (K.2.28) shows,

$$\overline{\vec{\nabla}|E_a|^2}_{near} \cong \frac{-1.485\gamma^2 V_o{}^2 \vec{u}_y}{d^2 y'} \quad \text{for} \quad \frac{d}{100}+\frac{d}{5\pi} \le y' \le \frac{d}{10}+\frac{d}{5\pi} \qquad (6.3.18)$$

Substituting $d = 10$ μm and $\gamma = 1$ into (6.3.18) gives,

$$\overline{\vec{\nabla}|E_a|^2}_{near} \cong \frac{-1.485\cdot 10^{10} V_o{}^2 \vec{u}_y}{y'} \quad \text{for } 0.737\ \mu\text{m} \le y' \le 1.637\ \mu\text{m} \qquad (6.3.19)$$

Alternatively, a lower value of the logarithmic approximation constant, $A = \pi/25$ can be used in (6.3.15). Neglecting the first and second order terms, $\hat{y}$ and $\hat{y}^2$, terms, (K.2.30) – (K.2.32) yield,

$$\overline{\vec{\nabla}|E_a|^2}_{near} \cong \frac{-16\gamma^2 V_o{}^2 \vec{u}_y 4.353}{\pi d^3(1+25\hat{y}/\pi)} \cong \frac{-22.17\gamma^2 V_o{}^2 \vec{u}_y}{d^3(1+25\hat{y}/\pi)}, \text{ for } \frac{\pi}{200} \le \hat{y} \le \frac{\pi}{20} \qquad (6.3.20)$$

and is also plotted in Fig. 6.7. Both $\overline{\vec{\nabla}|E_a|^2}_{near}$ approximations, (6.3.17) and (6.3.20), fit closely with the abovementioned 'reference' (6.3.10) integrated numerically. Deciding which of (6.3.17) and (6.3.20) gives the 'best fit' to (6.3.10) depends on the $\hat{y}$ interval considered. Equation (6.3.17),

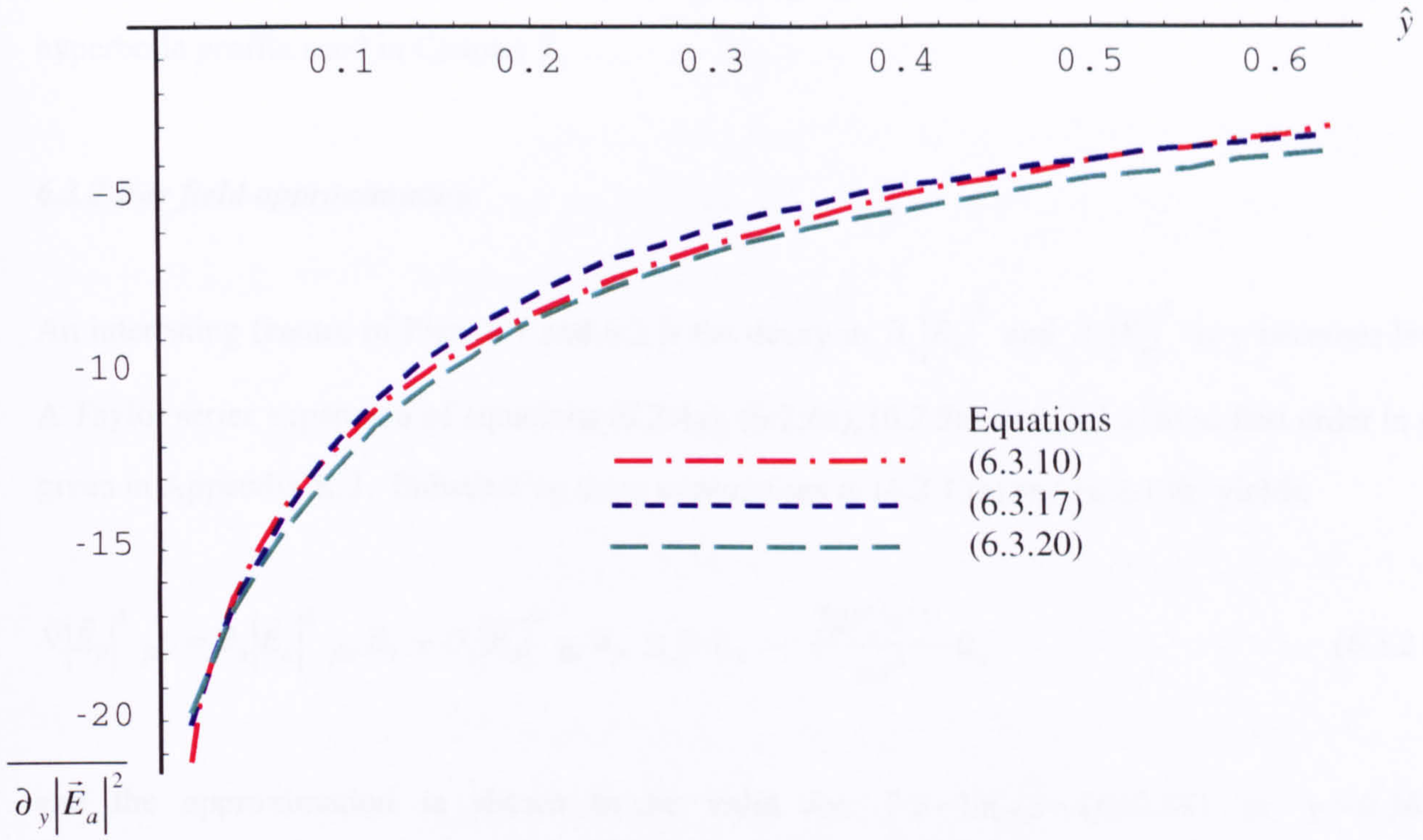

Fig. 6.7 A comparison of numerical and analytical approximations of the electric field intensity gradient magnitude $\overline{\partial_y \left|\vec{E}_a\right|^2}_{near}$ versus normalised displacement $\hat{y}$. The profiles are plotted for $\{\pi / 200 \leq \hat{y} \leq \pi / 5\}$ using values $d = 1$, $\gamma = 1$ and $V_o = 1$.

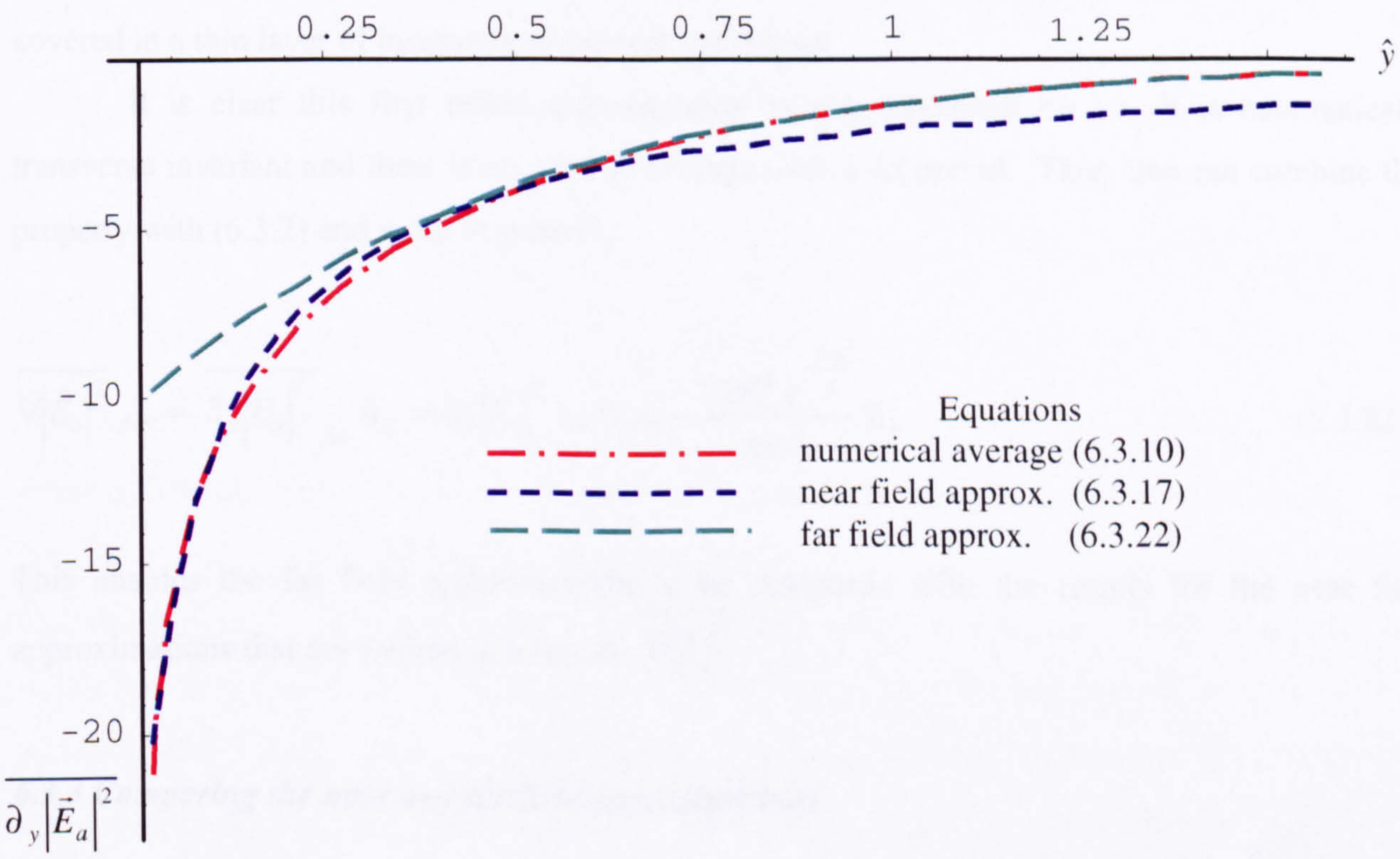

Fig. 6.8 A comparison of near and far field analytical approximations of the electric field intensity gradient magnitude $\overline{\partial_y \left|\vec{E}_a\right|^2}$ versus normalised displacement $\hat{y}$. The profiles are plotted for $\{\pi / 200 \leq \hat{y} \leq \pi / 2\}$ using values $V_o = 1$, $\gamma = 1$ and $d = 1$.

with $A = 1/10$, is marginally closer for low and high $\hat{y}$ values, and therefore constitutes the 1-D hyperbolic profile used in Chapter 5.

6.3.2 Far field approximation

An interesting feature of Figs. 6.1 and 6.2 is the decay in $\partial_x\left|\vec{E}_a\right|^2$ and $\partial_y\left|\vec{E}_a\right|^2$ as y becomes large. A Taylor series expansion of equations (6.2.4a), (6.2.6a), (6.2.9a) and (6.2.11a) to first order in $\hat{y}$ is given in Appendix K.3. Substituting these expressions in (6.2.13a) and (6.2.13b) yields,

$$\vec{\nabla}\left|\vec{E}_a\right|^2_{far} = \partial_x\left|\vec{E}_a\right|^2_{far}\vec{u}_x + \partial_y\left|\vec{E}_a\right|^2_{far}\vec{u}_y \cong 0\cdot\vec{u}_x - \frac{32V_o^2e^{-2\hat{y}}}{\pi d^3}\vec{u}_y \tag{6.3.21}$$

and the approximation is shown to be valid for $\hat{y} > -\ln(\sqrt{2}-1) \cong 0.881$ or $y > 0.561d$. Consequently, (6.3.21) is called the *far field approximation*. Equation (6.3.21) concurs with Cui *et al.* (2001) and the general exponential form given by Markx *et al.* (1997) and Rousselet *et al.* (1998). It validates the use of a simple, exponential decay in a 1-D DEP model in this far field regime. The approximation is useful for investigations on dielectrophoretic field flow fractionation (FFF) and DEP levitation where particle movement in the far field region is considered. The simple exponential decay is also useful in DEP FFF studies where the planar electrodes have been covered in a thin layer of insulation to prevent hydrolysis.

It is clear this first order approximation is not dependent on x. It is automatically transverse invariant and there is no need to average over a $4d$ period. Thus, one can combine this property with (6.3.2) and write in general,

$$\overline{\vec{\nabla}\left|\vec{E}_a\right|^2}_{far} = \overline{\partial_y\left|\vec{E}_a\right|^2}_{far}\vec{u}_y = \partial_y\left|\vec{E}_a\right|^2_{far}\vec{u}_y \cong -\frac{32V_o^2e^{-\frac{\pi y}{d}}}{\pi d^3}\vec{u}_y \tag{6.3.22}$$

This enables the far field approximation to be compared with the results for the near field approximations that are written in terms of $\overline{\vec{\nabla}\left|\vec{E}_a\right|^2}$.

6.3.3 Comparing the near and far field approximations

The near and far field $\overline{\vec{\nabla}\left|\vec{E}\right|^2}$ analytic approximations, (6.3.17) and (6.3.22), are extended to cover two orders of magnitude, $\frac{\pi}{200} \le \hat{y} \le \frac{\pi}{2}$. This enables a comparison to be made with the abovementioned numerically integrated reference equation (6.3.10). The plots are shown in Fig.

6.8 and show the near and far field approximations overlap at about $\hat{y} \cong 0.4$. The near field closely approximates (6.3.10) for an interval $\frac{\pi}{200} \leq \hat{y} \leq \frac{\pi}{5}$. The far field is observed to approximate (6.3.10) very closely for $\hat{y} > 0.4$; that is, with a limit lower than $\hat{y} = 0.881$ quoted in the previous section. The near and far field approximations can therefore be superposed to give a 1-D model valid for $\hat{y} \geq \frac{\pi}{200}$ should such a model be required.

6.3.4 Summary and outline of the next two sections

General expressions for the 2-D electric field and electric (field) intensity gradient, $\vec{\nabla}\left|\vec{E}(x,y)\right|^2$, have been derived in sections 6.1 and 6.2 for a periodic planar interdigitated electrode array with finite cover-slip height, h. The solution for $\vec{\nabla}\left|\vec{E}\right|^2$ was found by replacing the Neumann BC along the inter-electrode gap that interfaces the aqueous medium with glass, by a linear Dirichlet BC. This linear BC approximated the electric potential determined numerically by solving Laplace's equation. The gradient of the line of best-fit to the potential across the gap was $\gamma = 0.78$.

Approximations for the electric field intensity gradient were found for both near and far fields to the electrode plane. The approximations assumed the above mentioned Dirichlet BC was a simple linear interpolation with $\gamma = 1$, and the effect of the cover-slip was ignored ($h \to \infty$). That is, only a special case of the general solution $\vec{\nabla}\left|\vec{E}\right|^2$ was considered, the component being $\vec{\nabla}\left|\vec{E}_a\right|^2$. The reason for this was largely a matter of convenience, and because in many cases the influence of the cover-slip can be ignored.

In the following sections 6.4 and 6.5, expressions are derived for the particle 2-D probability density $p(x,y,t)$ based on $\vec{\nabla}\left|\vec{E}_a\right|^2$. That is, the abovementioned Dirichlet BC is assumed to be a linear interpolation with $\gamma = 1$ and the effect of the cover-slip is ignored ($h \to \infty$). The predicted steady state probability density when the DEP collection has reached steady state, $p(x,y,\infty) \equiv p(x,y)$, is derived and simulated in Section 6.4. The expression for the surface of the probability density $p(x,y)$ is subsequently simplified by considering just two points, one in the near field close to the electrode edge, and one in the far field. This is based on the near and far field approximations described above and it should be remembered these assume $\gamma = 1$ and $h \to \infty$. Particle collections, $p(x,y,t)$, simulated by the 2-D FPE are described in section 6.5.

6.4 2-D FPE steady state solution

Before considering the time evolution of the probability density $p(x,y,t)$ described by the FPE (6.0.1) and (6.0.2) it is useful to consider the steady state solution that occurs as $t \to \infty$. This is particularly important when the steady state solution $p(x,y)$ can be expressed in compact analytical form. An independent evaluation of $p(x,y)$ enables verification of the final step of the numerical integration of the FPE system. It also gives the final density distribution in advance of the simulation (or integration) and is useful for assigning values to system parameters, such as, the peak applied voltage V_o. This sub-section develops the analytical expression for the steady state probability. It discusses the sensitivity of the solution to variations in V_o for electrode dimensions and particles sizes relevant to experimental measurements in the following chapter.

6.4.1 General expression for the steady state probability density

Substituting (6.2.2) into (6.0.2), the small-time averaged DEP force can be written as

$$\vec{F}_{DEP}(x,y) = k_f\,\partial_x|E|^2\,\vec{u}_x + k_f\,\partial_y|E|^2\,\vec{u}_y = F_x(x,y)\vec{u}_x + F_y(x,y)\vec{u}_y \tag{6.4.1a}$$

where the DEP force coefficient k_f is given by

$$k_f = \frac{\alpha V}{4} = \pi r^3 \varepsilon_m \,\mathrm{Re}\{f_{CM}\} \tag{6.4.1b}$$

and all other symbols have been previously defined. It is understood the force components and coefficient are due to DEP; for brevity, the 'DEP' subscript has not been used. Thus, the FPE (6.0.1) is written in terms of J_x and J_y the flux magnitudes in x and y directions,

$$\begin{aligned}\partial_t p(x,y,t) &= -\vec{\nabla}\cdot\vec{J}(x,y,t) = -\left(\vec{u}_x\partial_x + \vec{u}_y\partial_y\right)\cdot\left(J_x(x,y,t)\vec{u}_x + J_y(x,y,t)\vec{u}_y\right)\\ &= -\partial_x J_x(x,y,t) - \partial_y J_y(x,y,t)\end{aligned} \tag{6.4.2a}$$

where

$$\begin{Bmatrix}J_x(x,y,t)\\ J_y(x,y,t)\end{Bmatrix} = \begin{Bmatrix}p(x,y,t)F_x(x,y)/\zeta - D\,\partial_x p(x,y,t)\\ p(x,y,t)F_y(x,y)/\zeta - D\,\partial_y p(x,y,t)\end{Bmatrix} \tag{6.4.2b}$$

The condition for steady state is $\partial_t p(x,y,t) = 0$. Setting the *lhs* to zero in (6.4.2a) leads to

$$\partial_x J_x + \partial_y J_y = 0 \tag{6.4.3}$$

where the independent variables, x and y, are implicit. Combining (6.4.1a), (6.4.2b) and (6.4.3),

$$D\frac{\partial^2 p}{\partial x^2} - \frac{k_f}{\zeta}\frac{\partial|\bar{E}|^2}{\partial x}\frac{\partial p}{\partial x} - \frac{k_f}{\zeta}p\frac{\partial^2|\bar{E}|^2}{\partial x^2} + D\frac{\partial^2 p}{\partial y^2} - \frac{k_f}{\zeta}\frac{\partial|\bar{E}|^2}{\partial y}\frac{\partial p}{\partial y} - \frac{k_f}{\zeta}p\frac{\partial^2|\bar{E}|^2}{\partial y^2} = 0 \tag{6.4.4}$$

From (6.2.1b), $|\bar{E}|^2 = E_x^2(x,y) + E_y^2(x,y)$ and the diffusion coefficient $D = k_B T/\zeta$.

By inspection, the general solution of (6.4.4) is

$$p(x,y) = Ce^{\frac{k_f}{k_B T}\left(E_x^2(x,y) + E_y^2(x,y)\right)} \tag{6.4.5a}$$

where C is an arbitrary integration constant. Essentially, the exponent of (6.4.5a) is the ratio of the DEP energy to the randomizing thermal energy. From Chapter 2 (2.4.18a), the joint probability density $p(x,y)$ has the axiomatic property $\iint p(x,y)dxdy = 1 \ \forall\, x$ and y where $p(x,y) \neq 0$.

Consequently, for a 2-D compartment over the intervals $0 \le x \le 4d$ and $a \le y \le b$, $a > 0$, $b > a$, the integration constant is evaluated

$$C = \left[\int_a^b \int_0^{4d} e^{\frac{k_f}{k_B T}\left(E_x^2(x,y) + E_y^2(x,y)\right)} dxdy\right]^{-1} \tag{6.4.5b}$$

The combination of (6.4.5a) and (6.4.5b) is the particular solution of (6.4.4). It should be noted the GS (6.4.5a) also satisfies the joint condition

$$\partial_x J_x = 0 \text{ and } \partial_y J_y = 0 \tag{6.4.6}$$

which is a particular case of (or is less general than) the condition for steady state given by (6.4.3). In fact, the GS of (6.4.4) was found by investigating (6.4.6). The details are given in Appendix L. The PS (6.4.5) can be verified by numerical integration of (6.4.4) using typical values for the DEP force and diffusion coefficients.

6.4.2 Plots of the steady state probability density

Consider the evaluation of the 2-D steady state probability density stated in (6.4.5a) and (6.4.5b) for a range of parameter values. For convenience the case is chosen where the height of the cover-slip is infinite, $h \to \infty$, and the potential across the gap is a linear interpolation of the electrode potentials with $\gamma = 1$. This is the familiar case used in the previous section where the electric field components E_{x_o} and E_{y_o} were only considered in the analysis.

The term of particular interest is the argument of the exponent that can vary considerably in value. Using equations for the DEP force coefficient k_f (6.4.1b), and electric field components (6.2.4a) and (6.2.6a), the argument of the exponential term in (6.4.5a) is cast,

$$\frac{k_f}{k_B T}\left(E_{x_o}^2 + E_{y_o}^2\right) = \frac{\pi r^3 \varepsilon_m \mathrm{Re}\{f_{CM}\}}{k_B T}\frac{V_o'^2}{\pi^2 d^2}\left[4\Theta_T^{\,2} + \Theta_L^{\,2}\right] \tag{6.4.7}$$

where the dimensionless functions are

$$\Theta_T = \tan^{-1}\left(\frac{\sin\hat{x}}{\sinh\hat{y}}\right) - \tan^{-1}\left(\frac{\cos\hat{x}}{\sinh\hat{y}}\right) \text{ and } \Theta_L = \ln\left(\frac{\cosh\hat{y}+\cos\hat{x}}{\cosh\hat{y}-\cos\hat{x}}\cdot\frac{\cosh\hat{y}+\sin\hat{x}}{\cosh\hat{y}-\sin\hat{x}}\right)$$

Some of the parameters in front of the bracket [ ] in (6.4.7) can be assumed to remain constant. For example, the dielectric constant of water (medium) at 25 °C is $\varepsilon_m = 78.4\times8.854\times10^{-12}$ (F m^{-1}) and the Boltzmann temperature is $k_B T = 1.38\times298\times10^{-23}$ (J).

Other terms have a limited range of experimentally relevant values, so they can be conveniently re-scaled. For example, the particle radius r is typically ~ 100 nm and electrode width $d \geq 10$ μm. Consequently, these parameters are rescaled, $r = \hat{r}10^{-6}$(m) and $d = \hat{d}10^{-6}$(m). The real part of the Clausius-Mossotti factor (for positive DEP) is bounded, $0 < \mathrm{Re}\{f_{CM}\} \leq 1$. It will be recalled in Chapter 2 that this factor constitutes the frequency dependent polarisability, and subsequently is a key determinant of the DEP force. Thus, (6.4.7) is re-written,

$$\frac{k_f}{k_B T}\left|\bar{E}_o\right|^2 = \frac{5.373\times10^4 \hat{r}^3 \mathrm{Re}\{f_{CM}\}V_o^2}{\hat{d}^2}\left[4\Theta_T^{\,2} + \Theta_L^{\,2}\right] \tag{6.4.8a}$$

Consider a DEP collection experiment using 10 μm width and gap electrodes and a suspension of 216 nm diameter latex beads in water at 25°C with unit Claussius-Mossotti factor, $\Rightarrow$ $\hat{d} = 10.0\,(\mu\text{m})$, $\hat{r} = 0.108\,(\mu\text{m})$, and frequency, such that, $\text{Re}\{f_{CM}\} = 1.00$. Substituting these values, equation (6.4.8a) simplifies,

$$\frac{k_f}{k_B T}\left|\vec{E}_o\right|^2 = 0.676 V_o^2\left[4\Theta_r^2 + \Theta_i^2\right] \tag{6.4.8b}$$

Suppose the probability density is considered for the 2-D cell region $0 \le x \le d$, $\frac{d}{100} \le x \le d$. It is shown in the author's program CD-R:/Mathematica/*GrdE2NrEdgeTh.nb* the maximum of the bracket [] term in (6.4.8b) is $4\Theta_r^2 + \Theta_i^2\big|_{\max} \cong 105.84$ and occurs at $x \cong \frac{d}{2}$ and $y = \frac{d}{100}$. Using a low value of $V_o = 0.1$ (V), (6.4.8b) yields $k_f\left|\vec{E}_o\right|^2 / k_B T \le 0.7163$. Since the exponent is less than unity, the surface of $p(x,y)$ given by (6.4.5a) and (6.4.5b) is relatively smooth and the integration constant C is easily determined numerically.

The 2-D steady state probability density $p(x,y)$ is plotted in Fig. 6.9(a) and clearly depicts the particle density over the regions where $\left|\vec{E}_o\right|^2$ is maximal. The surface was evaluated in the program CD-R:/Matlab/*sidepth.m* where the integration constant, $C = 106.2\ \mu\text{m}^{-2}$ was computed for a cell with dimensions $x \in [0, \text{d}]$, $y \in [a, b]$. The maximum is shown to be located at (x, y) coordinate (5 μm , 0.1 μm) in the *near* field region. The relative variation in $p(x,10)$ along the line $y = 10$ μm is extremely small (5×10^{-4}) so the minimum in the *far* field region can be considered to be independent of the x-ordinate and lies along the line $y = 10$ μm. The ratio of the two probability densities is 0.019/0.0095 = 2.0 – a detail that will be referred to in the next section 6.4.3.

In cases where the DEP force is much higher, such as $V_o = 0.5$, the steady state probability density $p(x,y)$ becomes increasingly singular at the electrode edges and $p(x,y) \cong 0$ elsewhere. Consequently, it is more useful to plot the logarithm of steady state probability density. In fact, taking the natural logarithm of $p(x,y)$ in (6.4.5a), and subtracting the constant $\ln C$, yields the exponent stated in (6.4.7),

$$\ln(p(x,y)) - \ln C = \ln\left(C\exp\left(\frac{k_f}{k_B T}\left|\vec{E}_o\right|^2\right)\right) - \ln C = \frac{k_f}{k_B T}\left|\vec{E}_o\right|^2 \tag{6.4.9}$$

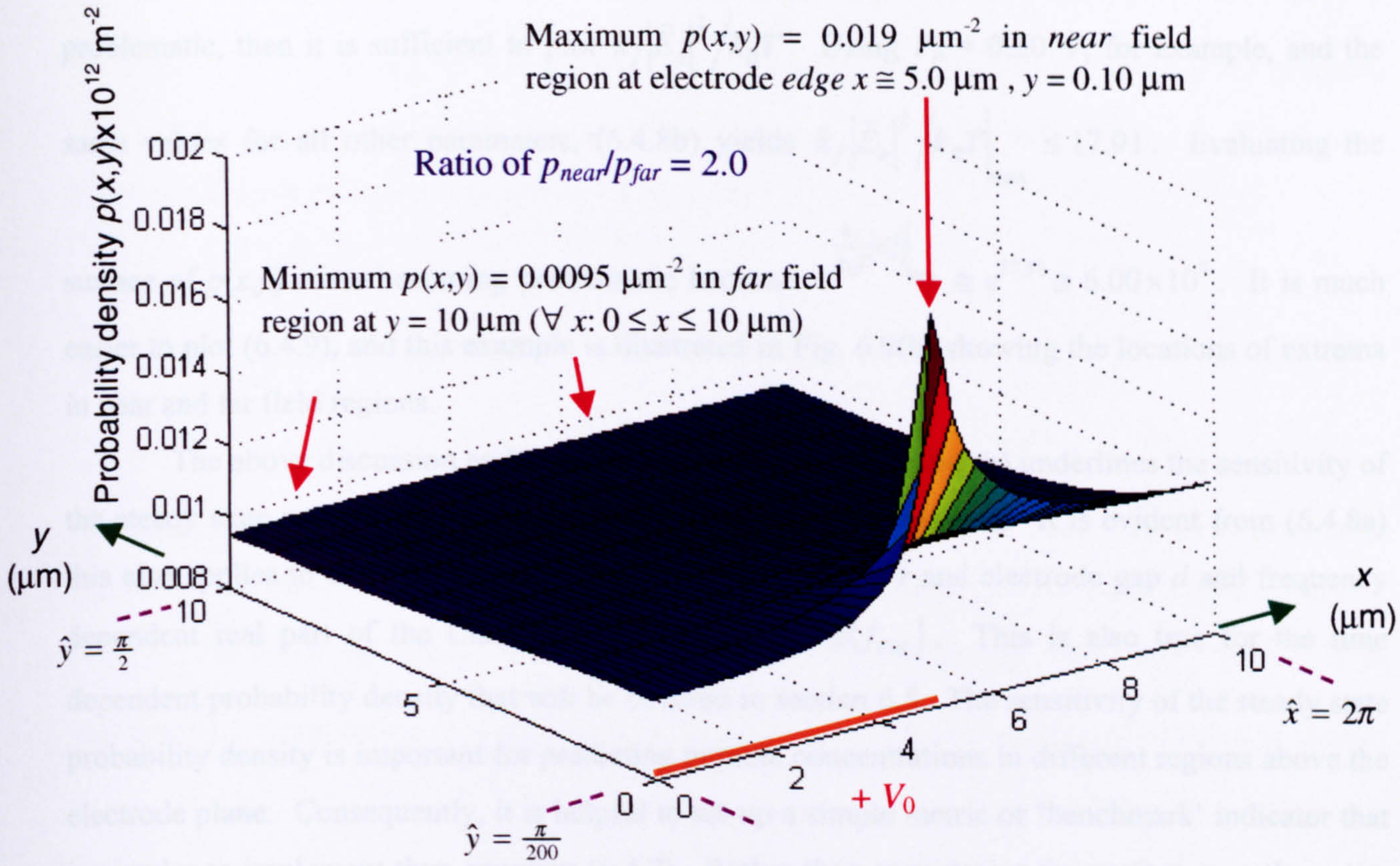

Fig. 6.9(a) Orthographic projection of the steady state probability density $p(x,y)$ for $0 \le \hat{x} \le 2\pi$ and $\frac{\pi}{200} \le \hat{y} \le \frac{\pi}{2}$ generated from (6.4.5) and (6.4.8b) using $V_o = 0.1$ V. See text.

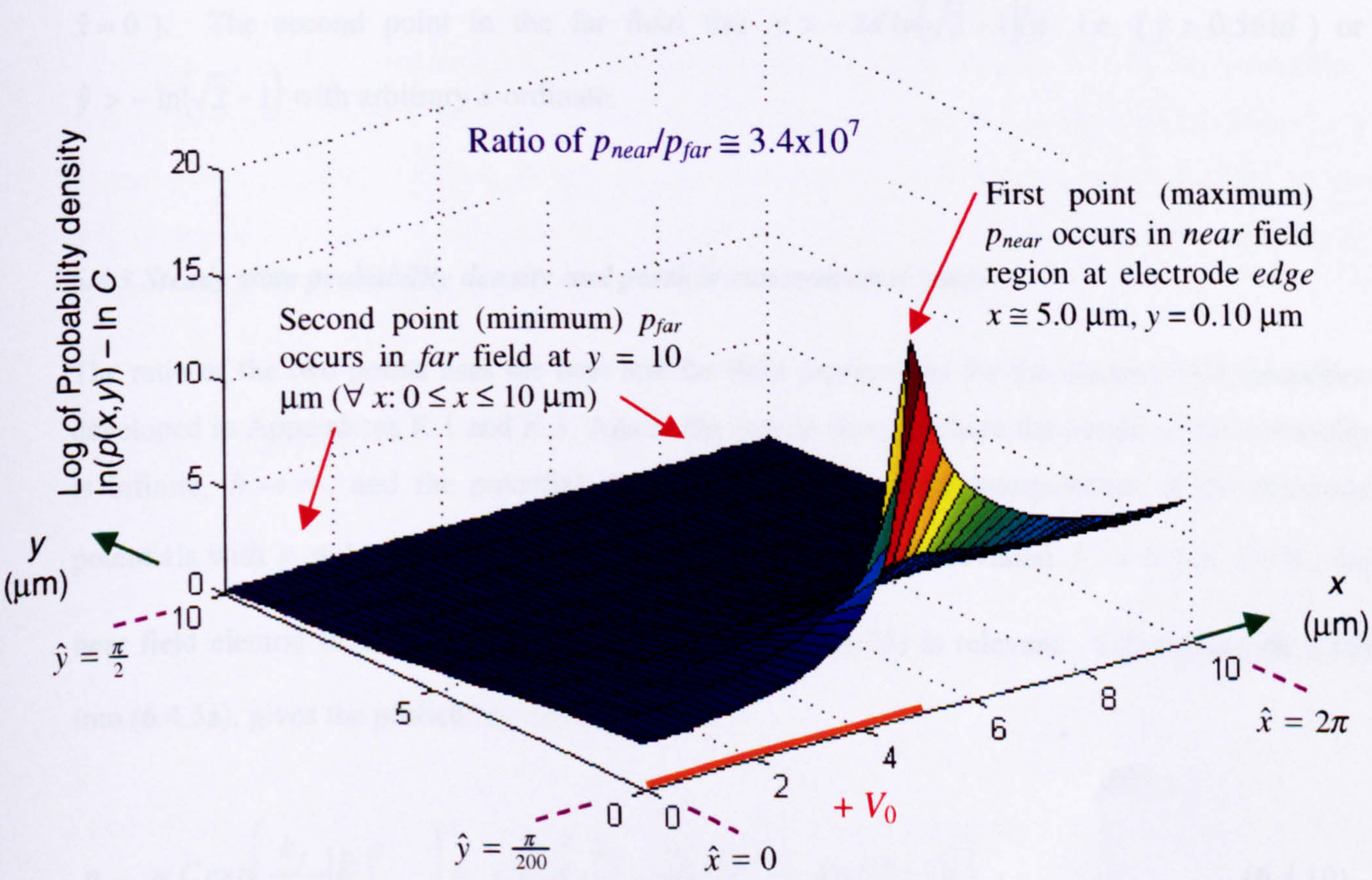

Fig. 6.9(b) Log-linear orthographic projection of the steady state probability density $\ln(p(x,y)) - \ln(C)$ for $0 \le \hat{x} \le 2\pi$ and $\frac{\pi}{200} \le \hat{y} \le \frac{\pi}{2}$ generated from (6.4.8b) and (6.4.9) using $V_o = 0.5$ V. See text for further details.

If the DEP force is so high that numerical integration of the integration constant C in (6.4.5b) is problematic, then it is sufficient to plot $k_f\left|\vec{E}_a\right|^2/k_BT$. Using $V_o = 0.50$ V, for example, and the same values for all other parameters, (6.4.8b) yields $k_f\left|\vec{E}_a\right|^2/k_BT\Big|_{\max} \le 17.91$. Evaluating the surface of $p(x,y)$ starts becoming problematic because $e^{\frac{k_f}{k_BT}\left|E_a^2\right|_{\max}} \cong e^{17.91} \cong 6.00\times10^7$. It is much easier to plot (6.4.9), and this example is illustrated in Fig. 6.9(b) showing the locations of extrema in near and far field regions.

The above discussion and illustrations in figures 6.9(a) and (b) underlines the sensitivity of the steady state probability density to values of the peak potential V_o. It is evident from (6.4.8a) this also applies to other parameters including particle radius r and electrode gap d and frequency dependent real part of the Clausius-Mossotti factor, $\mathrm{Re}\{f_{CM}\}$. This is also true for the time dependent probability density that will be covered in section 6.5. The sensitivity of the steady state probability density is important for predicting particle concentrations in different regions above the electrode plane. Consequently, it is helpful to set-up a simple metric or 'benchmark' indicator that is simpler to implement than equation (6.4.7). Rather than considering the surface over the entire 2-D region, a comparison of $p(x,y)$ is made at *two* points as illustrated in figures 6.9 (a) and (b). The first point is in the near field $0 < y \le \frac{d}{100}$ ($0 < \hat{y} \le \frac{\pi}{200}$) at the electrode edge $x = \frac{d}{2}$ (or $\hat{x} = 0$). The second point in the far field lies $y > -2d\ln\left(\sqrt{2}-1\right)/\pi$ i.e. ($y > 0.561d$) or $\hat{y} > -\ln\left(\sqrt{2}-1\right)$ with arbitrary x-ordinate.

6.4.3 Steady state probability density and particle concentration ratio

The ratio of the two points uses the near and far field expressions for the electric field intensities developed in Appendices K.1 and K.3. Again, the case is chosen where the height of the cover-slip is infinite, $h \to \infty$, and the potential across the gap is a linear interpolation of the electrode potentials with $\gamma = 1$. Since the first point lies $0 < \hat{y} \le \frac{\pi}{200}$ (abbreviated $\hat{y} \to 0$) at $\hat{x} = 0$, the near field electric field expression for $\left|\vec{E}_a\right|^2$ given by (K.1.15) is relevant. Substituting (K.1.15) into (6.4.5a), gives the probability density p_{edge} as

$$p_{edge} = C\exp\left(\frac{k_f}{k_BT}\left|\vec{E}_a\right|^2_{\substack{\hat{x}=0\\ \hat{y}\to 0}}\right) = C\exp\left(\frac{k_f}{k_BT}\frac{V_o^2}{\pi^2 d^2}\left[\pi^2 + 4\ln^2(2/\hat{y})\right]\right) \tag{6.4.10}$$

It should be noted that the maximum of the electric field intensity $\left|\vec{E}_a\right|^2$ does not occur *exactly* at $\hat{x}=0$ but is very close to it at $\hat{y}=\frac{\pi}{200}$. In fact, comparing (6.4.10) with the terms in the exponent in (6.4.7) the terms in front of the bracket [ ] are the same. Those terms inside the [ ] approximate to the numerically evaluated maximum, c.f. (6.4.8b),

$$\underbrace{4\Theta_T^2+\Theta_L^2\big|_{max}}_{105.84} \cong \pi^2 + 4\ln^2\left(2/\hat{y}\right)\Big|_{y=\frac{\pi}{200}} \cong \underbrace{\pi^2 + \overbrace{4\ln^2\left(400/\pi\right)}^{93.963}}_{103.83} \tag{6.4.11}$$

As expected, the *rhs* of (6.4.11) approximates the *lhs* to within 2%. Hence, (6.4.10) is a useful expression, or 'benchmark' for the maximum steady state probability density that is positioned very close to the electrode edge. Consider the second point in the far field $\hat{y} > -\ln\left(\sqrt{2}-1\right)$ or $\hat{y} > 0.8814$. Substituting $\left|\vec{E}_a\right|^2_{far}$ stated in (K.3.14) into (6.4.5a), yields the probability density p_{far},

$$p_{far} = C\exp\left(\frac{k_f}{k_BT}\left|\vec{E}_a\right|^2_{far}\right) = C\exp\left(\frac{k_f}{k_BT}\frac{V_o^2 32\, e^{-2\hat{y}}}{\pi^2 d^2}\right) \tag{6.4.12}$$

In Chapter 2 equation (2.4.20), the particle concentration is shown to be the probability density multiplied by the number of particles, N, in the system – essentially the latter is a normalisation constant. Hence, it follows that the particle concentration ratio is equal to the probability density ratio. Combining (6.4.10) and (6.4.12) the ratio of the probability densities or concentrations at the two points is written,

$$\begin{aligned} c_{cf} = p_{cf} = \frac{p_{edge}}{p_{far}} &= Ce^{\frac{k_f}{k_BT}\left|\vec{E}_a\right|^2_{edge}} \Big/ Ce^{\frac{k_f}{k_BT}\left|\vec{E}_a\right|^2_{far}} \\ &= \exp\left(\frac{k_f}{k_BT}\frac{V_o^2}{\pi^2 d^2}\left[\pi^2 + 4\ln^2\left(2/\hat{y}_{min}\right) - 32e^{-2\hat{y}_{min}}\right]\right) \\ &= \exp\left(\frac{r^3\varepsilon_m \mathrm{Re}\{f_{CM}\}}{k_BT}\frac{V_o^2}{\pi d^2}\left[\pi^2 + 4\ln^2\left(2/\hat{y}_{min}\right) - 32e^{-2\hat{y}_{min}}\right]\right) \end{aligned} \tag{6.4.13}$$

where $0 < \hat{y}_{min} \le \frac{\pi}{200}$ and $\hat{y}_{max} > 0.8814$. The terms in front of the bracket are the same as those in (6.4.7). For consistency, the same parameter values and scaling factors are used as those in (6.4.8a), i.e. $\varepsilon_m = 78.4\times8.854\times10^{-12}$ (Fm^{-1}), $k_BT = 1.38\times298\times10^{-23}$ (J), $r = \hat{r}10^{-6}$ (m), $d = \hat{d}10^{-6}$ (m) and $0 < \mathrm{Re}\{f_{CM}\} \le 1$. Consider the terms in the square bracket, [ ]. Suppose the

minimum value of y chosen is $\hat{y}_{min} = \frac{\hat{r}}{200}$ or $y_{min} = \frac{d}{100}$. This is the minimum value used in sections 6.2 and 6.3. Regarding the maximum $\hat{y}_{max}$: a value of the y ordinate needs to be selected that is significantly further away from the electrode than the first point, $\hat{y}_{min}$, but preferably not 'too' far away, i.e. not $100d$ or infinity! A reasonable choice, two orders of magnitude higher than the first point, is $\hat{y}_{max} = \frac{\hat{r}}{2}$ (or $y = d$). Using these values, (6.4.13) is simplified,

$$c_{df} = p_{df} = \exp\left(\frac{5.373\times10^{4}\,\hat{r}^{3}\,\mathrm{Re}\{f_{CM}\}V_{o}^{2}}{\hat{d}^{2}}\left[\underbrace{\pi^{2} + 4\ln^{2}(400/\pi)}_{102.45} - \underbrace{32e^{-\pi}}_{1.38}\right]^{103.83}\right) \qquad (6.4.14)$$
$$= \exp\left(\frac{5.505\times10^{6}\,\hat{r}^{3}\,\mathrm{Re}\{f_{CM}\}V_{o}^{2}}{\hat{d}^{2}}\right)$$

Equation (6.4.14) shows the sensitivity of particle concentration ratio c_{df} to four key parameters: particle size, electrode width (or gap), frequency dependent polarisability, and electrode potential.

Consider a *simulated* DEP collection experiment with parameter values c.f. (6.4.8b) using 10 μm width and gap electrodes, $\hat{d} = 10.0\,(\mu m)$ and a suspension of 216 nm diameter latex beads, $\hat{r} = 0.108\,(\mu m)$. Initially, before particles collect at the electrode edges, they are uniformly distributed. So by definition, $c_{df} = p_{df} = 1$ exactly. Suppose an AC electrode potential is applied with $V_o = 0.5$ V and frequency such that, $\mathrm{Re}\{f_{CM}\} = 0.04$ (the reason for using a value of $0.04 = 1/5^2$ becomes clear below). After the particles have collected and the system is steady state, (6.4.14) predicts (using the above parameter values) $c_{df} = p_{df} = e^{0.6934} = 2.00$. In fact, the DEP force and electrode geometry is equivalent to the case where $V_o = 0.1$ V and $\mathrm{Re}\{f_{CM}\} = 1.00$, as in the previous section 6.4.2. So Fig. 6.9(a) illustrates the steady state probability density. The concentration ratio is only ×2 of that before the DEP collection started.

Suppose the simulated DEP collection experiment is repeated with a different AC frequency such that $\mathrm{Re}\{f_{CM}\} = 1.00$. Increasing the Clausius-Mossotti factor by a factor of 25 means the DEP force is increased by the same factor, and (6.4.14) yields $c_{df} = p_{df} = e^{17.33} \cong 3.36\times10^{7}$. A concentration ratio of about 33 million upwards means that almost all particles will have accumulated near the electrode edges and there will be virtually no particles elsewhere in the far field. This is illustrated in the log-linear plot of the probability density, Fig. 6.9(b). Increasing the frequency dependent DEP force, therefore, results in a very large change in the steady state concentration ratio and this should be easily observed experimentally.

The simulated experiment gives different concentration ratios if, for example, 93 nm diameter latex beads are used. In this case the particle diameter is approximately halved to 46.5 nm $\Rightarrow \tilde{r} = 0.0465$ (μm). This causes a ×12.5 decrease in the DEP force. Using the same values for the other parameters as above, with $\mathrm{Re}\{f_{CM}\} = 0.04$, (6.4.14) predicts $c_{ef} = p_{ef} = e^{0.05535} \cong 1.06$. Changing the frequency so $\mathrm{Re}\{f_{CM}\} = 1.00$ results in $c_{ef} = p_{ef} = e^{1.384} \cong 4.0$. In this case, the frequency dependency of the DEP force results in only a *modest* increase in the predicted steady state concentration ratio. The effect is much less than that with the larger 216 nm diameter particle. A larger change in concentration ratio could be achieved by increasing V_o' to accommodate the ×12.5 decrease in the simulated DEP force. This adjustment in V_o' would effectively restore the DEP system to an appropriate 'operating regime'.

Further comparisons in predicted steady state concentrations or probability densities can in theory also be made using larger electrodes. The key point is that (6.4.13) – (6.4.14) enables prediction of a 'reasonable set' of parameter values for DEP collections. This is important, particularly in view of the highly nonlinear exponential dependence on parameters that can be controlled by experiment. In principle, therefore, variations in values can be used to explore, for example, frequency dependent polarisability, or support the development of the 2-D FPE model.

6.5 2-D FPE time dependent solution

Combining the expressions for the 2-D FPE and DEP force, (6.0.1) and (6.4.1), the FPE to be numerically solved is,

$$\frac{\partial p}{\partial t} = -k_v\left(\frac{\partial(p.\partial_x|E|^2)}{\partial x} + \frac{\partial(p.\partial_y|E|^2)}{\partial y}\right) + D\left(\frac{\partial^2 p}{\partial x^2} + \frac{\partial^2 p}{\partial y^2}\right) \qquad (6.5.1a)$$

where the DEP velocity coefficient k_v is

$$k_v = \frac{k_f}{\zeta} = \frac{\alpha V'}{4\zeta} = \frac{\pi r^3 \varepsilon_m \mathrm{Re}\{f_{CM}\}}{\zeta} = \frac{r^2 \varepsilon_m \mathrm{Re}\{f_{CM}\}}{6\eta} \qquad (6.5.1b)$$

The last line in (6.5.1b) assumes the drag coefficient is for a sphere, $\zeta = 6\pi\eta r$, and all other symbols have been previously defined and the dimensions are in S.I. units. As in the previous sections, the electric field intensity gradients are chosen for the case where height of the cover-slip is infinite and the potential across the gap is a linear interpolation of the electrode potentials. Thus,

the FPE solution is restricted to $\partial_x|\vec{E}_o|^2$ and $\partial_y|\vec{E}_o|^2$ components. Numerical integration of (6.5.1a) requires careful consideration of the coefficient values and scale of the variables. Typical values for the velocity and diffusion coefficients are applicable for a 100nm radius sphere suspended in water at 25.0 °C. Assuming $\mathrm{Re}\{f_{CM}\}=1$, and using $\varepsilon_m = 78.4\varepsilon_0 = 6.942\times10^{-10}$ (Fm^{-1}) and $\eta = 9.00\times10^{-4}$ (kg $m^{-1}s^{-1}$) in (6.5.1b), the velocity coefficient is $k_v = 12.86\times10^{-22}$ (F m^2 s kg^{-1}) and the diffusion coefficient is $D = k_BT/\zeta = 2.424\times10^{-12}$ ($m^2\,s^{-1}$). In addition, the scale of the solution independent variables, x and y, is typically in terms of microns (10^{-6} m). Consequently, for (6.5.1a) to be amenable to numerical integration, the terms need to be re-scaled, or normalised.

6.5.1 Normalisation of the FPE

Normalisation is achieved by re-scaling $x=10^{-6}x'$, $y=10^{-6}y'$ where x' and y' are in (μm). The 2-D probability density function p, which is probability per unit area (m^2), is also rescaled, $p=10^{12}p'$ μm^{-2}. Thus, (6.5.1a) transforms,

$$10^{12}\frac{\partial p'}{\partial t} = 10^{12}\left[-\frac{k_v}{10^{-6}}\left(\frac{\partial(p'.\partial_x|E|^2)}{\partial x'}+\frac{\partial(p'.\partial_y|E|^2)}{\partial y'}\right)+\frac{D}{10^{-12}}\left(\frac{\partial^2 p'}{\partial x'^2}+\frac{\partial^2 p'}{\partial y'^2}\right)\right] \qquad (6.5.2)$$

Consider the $\partial_x|\vec{E}_o|^2$ and $\partial_y|\vec{E}_o|^2$ components. To achieve appropriate scaling, they are cast with the dimensionless, explicit x, y dependent functions separated from the constants that have dimensions.

6.5.1.1 Dimensionless intensity gradient

Substituting (6.2.4a), (6.2.6a), (6.2.9a) and (6.2.11a) into (6.2.13) (or (6.2.2)),

$$\begin{aligned}\partial_x|\vec{E}_o(x,y)|^2 &= 2(E_{x_o}E_{x,x_o}+E_{y_o}E_{y,x_o}) = 2(E_{x_o}E_{x,x_o}+E_{y_o}E_{x,y_o})\\ &= 2\left(\frac{2\gamma V_o}{\pi d}\Theta_T\frac{2\gamma V_o}{d^2}\Xi_+ + \frac{\gamma V_o}{\pi d}\Theta_L\frac{2\gamma V_o}{d^2}\Xi_-\right)\\ &= \frac{4\gamma^2V_o^2}{\pi d^3}\underbrace{(2\Theta_T\Xi_+ + \Theta_L\Xi_-)}_{\Gamma_x} = \frac{4\gamma^2V_o^2}{\pi d^3}\Gamma_x(x,y)\end{aligned} \qquad (6.5.3)$$

$$\partial_y\left|\vec{E}_a(x,y)\right|^2 = 2(E_{x_a}E_{x,y_a} + E_{y_a}E_{y,y_a}) = 2(E_{x_a}E_{x,y_a} - E_{y_a}E_{x,x_a})$$
$$= \frac{4\gamma^2 V_o^2}{\pi\, d^3}\underbrace{(2\Theta_T\,\Xi_- - \Theta_L\,\Xi_+)}_{\Gamma_y} = \frac{4\gamma^2 V_o^2}{\pi\, d^3}\Gamma_y(x,y) \qquad (6.5.4)$$

where the dimensionless functions Θ_T and Θ_L are as defined in (6.4.7),

$$\Theta_T = \tan^{-1}\left(\frac{\sin\hat{x}}{\sinh\hat{y}}\right) - \tan^{-1}\left(\frac{\cos\hat{x}}{\sinh\hat{y}}\right),\ \Theta_L = \ln\left(\frac{\cosh\hat{y}+\cos\hat{x}}{\cosh\hat{y}-\cos\hat{x}}\cdot\frac{\cosh\hat{y}+\sin\hat{x}}{\cosh\hat{y}-\sin\hat{x}}\right),$$

$$\Xi_+ = \frac{\sinh\hat{y}\cos\hat{x}}{\cosh 2\hat{y} - \cos 2\hat{x}} + \frac{\sinh\hat{y}\sin\hat{x}}{\cosh 2\hat{y} + \cos 2\hat{x}}\ ,\ \Xi_- = \frac{\cosh\hat{y}\cos\hat{x}}{\cosh 2\hat{y} + \cos 2\hat{x}} - \frac{\cosh\hat{y}\sin\hat{x}}{\cosh 2\hat{y} - \cos 2\hat{x}}$$

$\hat{y} = \pi y/2d$, and $\hat{x} = \pi x/2d + \pi/4$. Before using the results of (6.5.3) and (6.5.4) it is important to briefly investigate the range of values Γ_x and Γ_y exhibit.

Expressions for the dimensionless parts of the electric field intensities Γ_x and Γ_y can be simplified by considering expressions for $\partial_x\left|\vec{E}_a\right|^2$ and $\partial_y\left|\vec{E}_a\right|^2$ in the near field at the electrode edges, and far field. Consider Γ_x at $\hat{x}=0$ and $0<\hat{y}\le\frac{\pi}{200}$ (abbreviated $\hat{y}\to 0$). Equating (6.5.3) with (K.1.9) – (K.1.10),

$$\Gamma_x\Big|_{\substack{\hat{x}=0\\ \hat{y}\to 0}} = -\frac{\pi}{2\hat{y}} + \ln 2/\hat{y} + 1 + O(\hat{y}) \cong -\frac{\pi}{2\hat{y}} \qquad (6.5.5a)$$

Similarly, equating (6.5.4) with (K.1.11) – (K.1.12),

$$\Gamma_y\Big|_{\substack{\hat{x}=0\\ \hat{y}\to 0}} = \frac{\ln\hat{y}/2}{\hat{y}} - \frac{\pi}{2} + O(\hat{y}) \cong \frac{\ln\hat{y}/2}{\hat{y}} \qquad (6.5.5b)$$

For example, at $\hat{x}=0$ and $\hat{y}=\frac{\pi}{200}$ (or $y=\frac{d}{100}$), $\Gamma_x \cong -100$ and $\Gamma_y \cong -309$. It should be remembered these are not the extremum values of the intensity gradient, but are good estimates of it (within a factor of 2). In fact, the plots of in Fig. 6.4(b) and (d) at $\hat{y}=\frac{\pi}{200}$, show the extrema of $\partial_x\left|\vec{E}_a\right|^2$ and $\partial_y\left|\vec{E}_a\right|^2$. Inverting the relation (6.5.3), $\Rightarrow \Gamma_x = \frac{\pi\, d^3}{4\gamma^2 V_o^2}\partial_x\left|\vec{E}_a\right|^2$ and (6.5.4)

$\Rightarrow \Gamma_y = \frac{\pi d^3}{4\gamma^2 V_o^2}\partial_y\left|\vec{E}_o\right|^2$ gives, $\Gamma_{x\min} \cong -175$, $\Gamma_{x\max} \cong +175$ and $\Gamma_{y\min} \cong -319$. The extrema are listed in the program CD-R:/Mathematica/*GrdE2NrEdgeTh.nb*.

In the far field, equating (6.5.3) with (K.3.11), and (6.5.4) with (K.3.12)

$$\Gamma_x\big|_{far} \cong 0 \tag{6.5.5c}$$

$$\Gamma_y\big|_{far} \cong -8e^{-2\hat{y}} \cong -8e^{-\pi y/d} \tag{6.5.5d}$$

Hence, for $\hat{y} > \frac{\pi}{2}$ (or $y > d$), $-0.35 < \Gamma_{x_{far}} < 0$. Thus, the approximate range of values Γ_x and Γ_y can take over the two dimensional space $0 \le x \le 4d$ and $y \ge \frac{d}{100}$ can be summarized as, $-175 < \Gamma_x < 175$ and $-319 < \Gamma_y < 0$.

6.5.1.2 Normalised FPE - general expression

Using (6.5.3) and (6.5.4), and substituting (6.5.1b) the velocity terms of the FPE (6.5.2) are

$$k_v\begin{Bmatrix}\partial_x|E|^2\\ \partial_y|E|^2\end{Bmatrix} = k_v\frac{4\gamma^2 V_o^2}{\pi d^3}\begin{Bmatrix}\Gamma_x(x,y)\\ \Gamma_y(x,y)\end{Bmatrix} = \frac{r^2\varepsilon_m \operatorname{Re}\{f_{CM}\}}{6\eta}\frac{4\gamma^2 V_o^2}{\pi d^3}\begin{Bmatrix}\Gamma_x(x,y)\\ \Gamma_y(x,y)\end{Bmatrix} \tag{6.5.6}$$

It is understood variables x and y are specified now in microns (μm) and p in (μm^{-2}) and the dashes are dropped in (6.5.2).

Some of the parameters values can be assumed to be constant for most experiments, $\varepsilon_m = 78.4\varepsilon_o = 6.942\times10^{-10}\,(Fm^{-1})$, $T = 298$ (K), and $\eta = 9.00\times10^{-4}\,(kg\ m^{-1}s^{-1})$ In addition, the particle radius and electrode gap are scaled, $r = \hat{r}10^{-6}$ (m) and $d = \hat{d}10^{-6}$ (m) – as performed in the previous section 6.4.2. Assuming $\gamma = 1$ and the above parameters, (6.5.6) simplifies to

$$k_v\begin{Bmatrix}\partial_x|E|^2\\ \partial_y|E|^2\end{Bmatrix} = \frac{0.1637\hat{r}^2 \operatorname{Re}\{f_{CM}\} V_o^2}{\hat{d}^3}\begin{Bmatrix}\Gamma_x(x,y)\\ \Gamma_y(x,y)\end{Bmatrix} \tag{6.5.7a}$$

The diffusion coefficient D in (6.5.2) is also scaled,

$$D=\frac{k_BT}{\zeta}=\frac{1.38\cdot10^{-23}298}{6\pi9.00\hat{r}\times10^{-4-6}}=\frac{0.2424\times10^{-12}}{\hat{r}} \tag{6.5.7b}$$

Substituting (6.5.7a) and (6.5.7b) into (6.5.2),

$$\frac{\partial p}{\partial t}=-\frac{1.637\times10^{5}\hat{r}^{2}\,\mathrm{Re}\{f_{CM}\}V_o^{2}}{\hat{d}^{3}}\left(\frac{\partial(p.\Gamma_x)}{\partial x}+\frac{\partial(p.\Gamma_y)}{\partial y}\right)+\frac{0.2424}{\hat{r}}\left(\frac{\partial^2 p}{\partial x^2}+\frac{\partial^2 p}{\partial y^2}\right) \tag{6.5.8}$$

Assuming a typical 100 nm radius sphere, $\hat{r}=0.100\,(\mu\mathrm{m})$, and 10 μm electrode width $\hat{d}=10.0$ (μm) and the upper value $\mathrm{Re}\{f_{CM}\}=1.00$,

$$\frac{\partial p}{\partial t}=-1.637\,V_o^{2}\left(\frac{\partial(p.\Gamma_x)}{\partial x}+\frac{\partial(p.\Gamma_y)}{\partial y}\right)+2.424\left(\frac{\partial^2 p}{\partial x^2}+\frac{\partial^2 p}{\partial y^2}\right) \tag{6.5.9}$$

For a typical 2-D solution space $0\le x\le 4d$ and $y\ge\frac{d}{100}$, the previous section 6.5.1.2 has shown $-175<\Gamma_x<175$ and $-319<\Gamma_y<0$. In regions near the extrema, $\Gamma_x\approx\pm175$ and $\Gamma_y\cong-319$, the first (velocity drift) term in (6.5.9) is *prima facie* two orders of magnitude higher than the second (diffusion) term that tends to stabilise the numerical solver. Consequently, integration of (6.5.9) may be problematic for $V_o\approx0.5\,\mathrm{V}$ and higher. A thorough assessment should, of course, take into account the partial derivatives of $p(x,y)$ and Γ_x and Γ_y. Notwithstanding this, experience shows numerical integration is in fact problematic for values $V_o\approx0.5\,\mathrm{V}$ and higher.

6.5.2 2-D solution space for FlexPDE finite element program

The 2-D FPE (6.5.8) was solved numerically using FlexPDE (PDE Solutions, CA, USA) version 2.15 finite element software. This is the same numerical package used to integrate the 1-D FPE (5.2.1) and the approach taken to obtain a satisfactory solution has been described in Chapter 5, section 5.2.3. One of the key issues of finite element integration is that the accuracy of the solution increases with the number of elements but this also increases the computation time. In this respect, to minimise the computation time and number of elements, advantage is taken of the periodic and symmetry properties of the gradient of the electric field intensity $\vec{\nabla}\left|\vec{E}\right|^2$. The properties are illustrated in figures 6.4(a) – (d) for the simplest case $\vec{\nabla}\left|\vec{E}_a\right|^2$ and show the compartment solution

space can be reduced in the transverse direction from $0 \le x \le 4d$ to a cell $0 \le x \le d$. Since the particle force (and velocity) is proportional to $\vec{\nabla}|\vec{E}|^2$ it follows the solution space for the FPE (6.5.8) can also be reduced to a cell. To find the PS for (6.5.8) requires specification of the BCs and IC for a cell.

6.5.2.1 Specification of BCs and IC

Boundary conditions are applied to all four boundaries of the cell at $x = 0, d$ and $y = a, b$. The impenetrable (or reflecting), or zero flux, BC is applied at each boundary in a direction normal to the boundary (line). The BC is written,

$$\vec{n} \cdot \vec{J}(x,y) = 0 \tag{6.5.10}$$

where $\vec{n}$ is unit vector normal to the line (or in three dimensions, plane) of each boundary and $\vec{J}(x,y) = J_x \vec{u}_x + J_y \vec{u}_y$. More explicitly,

$$J_x(0,y) = 0 = J_x(d,y) \quad \text{for} \quad a \le y \le b \tag{6.5.12a}$$

and

$$J_y(x,a) = 0 = J_y(x,b) \quad \text{for} \quad 0 \le x \le d \tag{6.5.12b}$$

The FlexPDE language enables the BCs to be imposed using the 'natural' boundary condition statement, "natural(p) = 0" in a similar manner to that described for the 1-D case in section 5.2.3. The cell boundaries are sketched in Fig. 6.10.

The IC is uniformly distributed and has the same dimensions as $p(x,y,t)$ in (μm^{-2}),

$$p(x,y,0) = \frac{1}{(b-a)(d-0)} \tag{6.5.13}$$

where it is understood a, b, and d are all in μm.

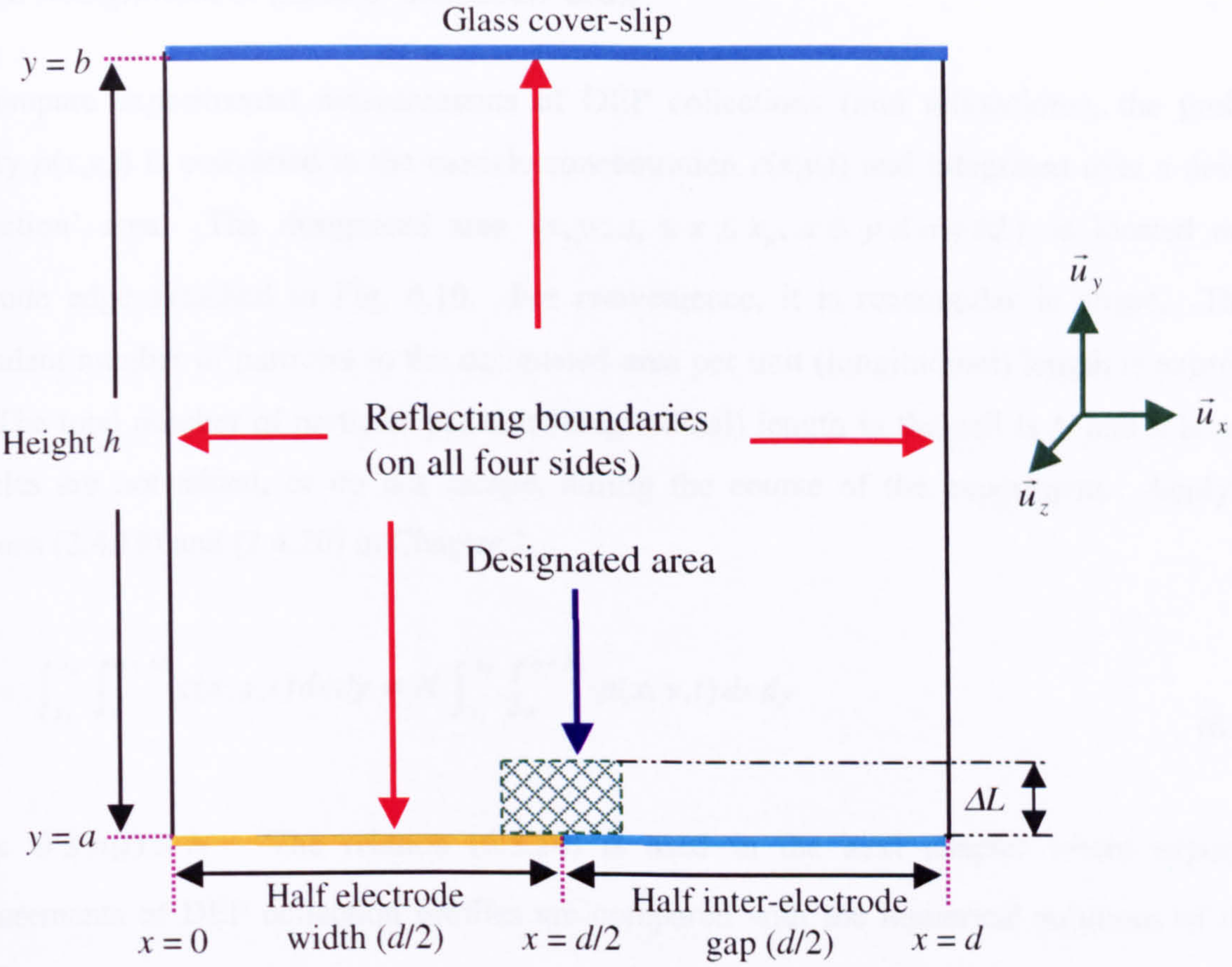

Fig. 6.10 FPE solution cell $0 \le x \le d$, $a \le y \le b$ showing reflecting boundaries and designated 'collection area' region $x_l \le x \le x_u$ and $a \le y \le a + \Delta L$.

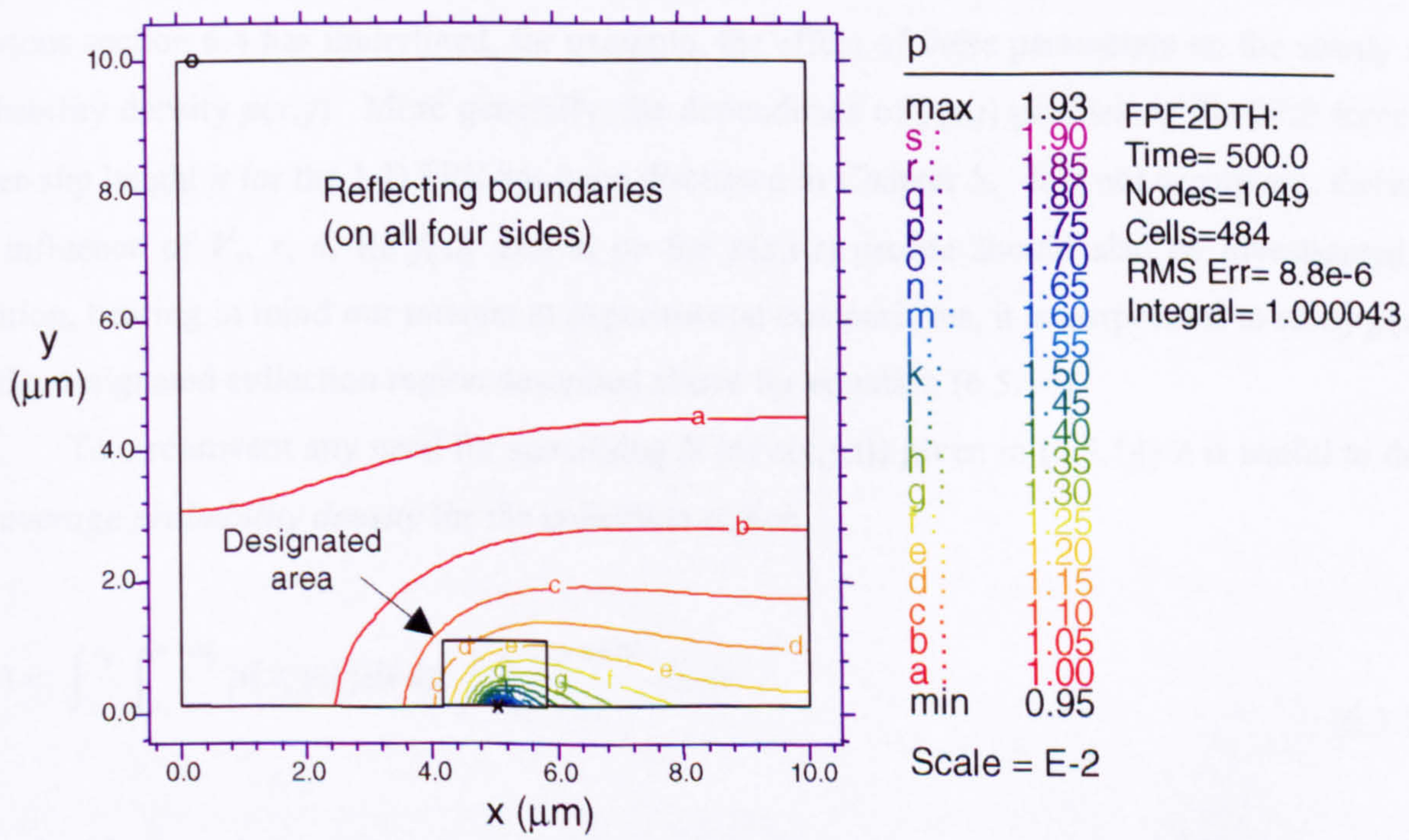

Fig. 6.11 Contour plot of the probability density $p(x,y,500)$ μm^{-2} (essentially at steady state) generated using parameter values $V_o = 0.5$ (V), $\hat{r} = 0.108$, $\hat{d} = 10.0$ and $\mathrm{Re}\{f_{CM}\} = 0.04$ in (6.5.8).

6.5.2.2 Assignment of particle 'collection' area

To compare experimental measurements of DEP collections (and relaxations), the probability density $p(x,y,t)$ is converted to the particle concentration $c(x,y,t)$ and integrated over a designated 'collection' area. The designated area $\{x,y: x_l \le x \le x_u, a \le y \le a+\Delta L\}$ is located near the electrode edge sketched in Fig. 6.10. For convenience, it is rectangular in shape. The time dependent number of particles in the designated area per unit (longitudinal) length is expressed as $n(t)$. The total number of particles per unit (longitudinal) length in the cell is N and it is assumed particles are not added, or do not escape, during the course of the experiment. Applying the relations (2.4.19) and (2.4.20) in Chapter 2,

$$n(t) = \int_{x_l}^{x_u}\int_{a}^{a+\Delta L} c(x,y,t)\,dx\,dy = N\int_{x_l}^{x_u}\int_{a}^{a+\Delta L} p(x,y,t)\,dx\,dy \qquad (6.5.14)$$

where $0 \le n(t) \le N$. The relation (6.5.14) is used in the next chapter where experimental measurements of DEP collection profiles are compared with the numerical solutions of the FPE (6.5.8).

A key intermediate step in making comparisons involves interpretation of the simulation results. That is, it is important to understand how different parameter values, such as, electrode potential V_o, particle radius r, and electrode gap width d affect simulation predictions. The previous section 6.4 has underlined, for example, the effect of these parameters on the steady state probability density $p(x,y)$. More generally, the dependence of $p(y,t)$ profiles on the DEP force and cover-slip height h for the 1-D FPE has been discussed in Chapter 5. It is not surprising, therefore, the influence of V_o, r, d, $\mathrm{Re}\{f_{CM}\}$ and h, on the $p(x,y,t)$ profile should also be investigated. In addition, bearing in mind our interest in experimental comparisons, it is purposeful to study $p(x,y,t)$ for the designated collection region described above for equation (6.5.14).

To circumvent any need for specifying N (or $c(x,y,t)$) given in (6.5.14) it is useful to define the *average probability density* for the collection region,

$$\bar{\bar{p}}(t) = \int_{x_l}^{x_u}\int_{a}^{a+\Delta L} p(x,y,t)\,dx\,dy \Big/ \int_{x_l}^{x_u}\int_{a}^{a+\Delta L} dx\,dy \qquad (6.5.15)$$

The double bar (=) over $p(t)$ indicates spatial averaging in both directions, $\vec{u}_x$ and $\vec{u}_y$. Furthermore, since the extremum of the steady state densities $p(x,y)$ in section 6.4 varies considerably on V_o, r, $\mathrm{Re}\{f_{CM}\}$ it is useful to consider the relative probability density (or simply, '*relative probability*' since it is dimensionless),

$$\hat{p}(t) = \frac{\bar{\bar{p}}(t) - \bar{\bar{p}}(0)}{\bar{\bar{p}}(\infty) - \bar{\bar{p}}(0)}, \quad 0 \le \hat{p}(t) \le 1 \tag{6.5.16}$$

It is understood $\bar{\bar{p}}(0)$ is the initial average probability density and $\bar{\bar{p}}(\infty)$ is the steady state average density. It is clear from (6.5.16) that the initial relative probability $\hat{p}(0) = 0$, and $\hat{p}(\infty) = 1$ so different profiles can be easily compared for a range of parameters. The average densities are easily computed in FlexPDE 2.15. An immediate consequence of the definition is that for a uniform distribution the average is the same as the density, e.g. for the IC (6.5.13), $\bar{\bar{p}}(0) = p(x,y,0)$. Before discussing case examples of time dependent DEP particle collections, it helpful to introduce two important error measures, or 'yardsticks'. These are important for monitoring errors in the 2-D cell solution space in addition to those internally generated within the FlexPDE 2.15 software package.

6.5.2.3 Error measures

A prominent source of error for the 2-D PDE model arises from a finite mesh size (or finite number of mesh nodes) and the reflecting BCs not being exactly obeyed. As discussed in section 5.2.3, the implementation of the 'firstparts' command means the BCs are satisfactorily implemented. However, under extreme conditions (such as a very large DEP force) the area integral of the probability density, that should ideally be always unity, appears to 'leak' particle probability flux. This means the axiomatic property applicable for the cell, $\int_a^b \int_0^d p(x,y,t)\,dx\,dy = 1$ is violated. Consequently, a useful measure of 'error performance' is the deviation of the probability density area integral from unity. This is written for a 2-D cell,

$$\int_a^b \int_0^d p(x,y,t)\,dx\,dy = 1 \pm \varepsilon_A(t) \tag{6.5.17}$$

where the error $\varepsilon_A(t)$ is the deviation from unity and subscript 'A' denotes the 'area integral'. The performance is optimal when $\varepsilon_A(t) = 0$.

Another route for validating numerical integration of the FPE is to compare the probability density, as the system approaches steady state, with analytical predictions from (6.4.5a) and (6.4.5b). The relative error is a useful measure, and is written,

$$\varepsilon(x,y,t) = \frac{p_{num}(x,y,t) - p_{anl}(x,y)}{p_{anl}(x,y)} \quad \forall\, x,y \text{ within the cell} \tag{6.5.18a}$$

where $p_{anl}(x,y)$ is the analytical steady state probability density (from (6.4.5a) and (6.4.5b), and $p_{num}(x,y,t)$ is the probability density as the numerical integrated FPE approaches steady state, for times $t \geq T$. The former, $p_{anl}(x,y)$, is implemented in the FlexPDE program so a contour plot of $\varepsilon(x,y,t)$ is displayed and monitored during the simulation.

To record the error performance, it is helpful to simplify $\varepsilon(x,y,t)$ by selecting the maximum of the error magnitude within the 2-D cell region. This measure is defined as,

$$\varepsilon_{max}(T) = \left| \frac{p_{num}(x,y,T) - p_{anl}(x,y)}{p_{anl}(x,y)} \right|_{max} \tag{6.5.18b}$$

6.5.3. Examples of time dependent FPE solutions

Comparisons of time dependent relative densities $\hat{p}(t)$ are made for the same set of parameter values considered for the steady state $p(x,y)$ examples described in section 6.4.3. The set of parameters yield four $\hat{p}(t)$ profiles for a comparison.

6.5.3.1 2-D FPE simulation

These four collection relative density profiles are generated using the FPE (6.5.8) in the program CD-R:/FlexPDE/*Fpe2dTh.pde*. The parameters held constant are $\hat{d} = 10.0$ and $V_o = 0.5$ V. The first example profile uses the same values as adopted in the previous sections 6.4.2 and 6.4.3; $\hat{r} = 0.108$ and $\mathrm{Re}\{f_{CM}\} = 0.04$. A contour plot of $p(x,y,t)$ at $t = 500$ seconds is shown in Fig. 6.11. The value of the cover-slip height is chosen to be small to illustrate the contours, $h = 10 - 0.1 = 9.9$ μm. The probability density is essentially at steady state since it is practically identical to the steady state density $p(x,y)$ computed from (6.4.5) and (6.4.8b); the orthographic projection is illustrated in Fig. 6.9(a). The listed contour values shows the maximum of the density $p(x,y,500) = 0.0193$ and minimum $p(x,y,500) = 0.0095$. These values concur with those steady state values in Fig. 6.9(a).

A contour plot of the relative error (not shown) in the cell exhibited $\varepsilon_{max}(t) = 5.7 \times 10^{-4}$ for $48 \leq t \leq 500$ seconds and the relative error within the designated collection area was an order of magnitude smaller. This means the FlexPDE numerical integration, for the entire solution space, concurs with the steady state analytical solution determined from (6.4.5) and (6.4.8b), i.e. $p_{num}(x,y,t) = p_{anl}(x,y)$ for $t \geq 48$ secs. Features (too small to be viewed in Fig. 6.11) were

implemented (by the author in the program *Fpe2dTh.pde*) to increase mesh density near coordinates corresponding to the electrode edge (5.0,0.1); the number of cells is listed as 484. The accuracy of the numerical solution is also verified by $\varepsilon_A(t)$ given by (6.5.17). The statement in Fig. 6.11, 'Integral = 1.000043' implies $\varepsilon_A(t) = 4.3\times10^{-5}$ which is extremely small. This indicates the 'leakage' particle probability flux through the boundaries, as described in section 5.2.3, is negligible.

The designated 'collection' region is outlined in Fig. 6.11. It comprised, in the transverse direction, $x_l = \hat{d}/2 - 0.83 = 4.17$ μm and $x_u = \hat{d}/2 + 0.83 = 5.83$ μm, and $y_l = \hat{a} = 0.10$ μm and $y_u = \hat{a} + 1.00 = 1.10$ μm in the vertical direction. The transverse values correspond to typical pixel locations used in image processing, as described in Chapter 3, where small particles accumulate at the electrode edges. The vertical values accommodate the ΔL = 1.00 μm depth of field characteristic of the microscope objective described in sections 3.3.3 and 3.3.4. Data values of the designated region average probability $\bar{\bar{p}}(t)$ were generated in *Fpe2dTh.pde* using (6.5.15), exported into separate files, and imported and assembled by the program CD-R:/Matlab/*ch6flx.m*.

6.5.3.2 Results of simulation and discussion

The time dependent relative probability $\hat{p}(t)$ for the collection region, computed by programming (6.5.16) in *ch6flx.m*, for this first profile is exhibited as 'Profile I' (blue - - -) in Fig. 6.12. The steady state average density in the collection region is $\bar{\bar{p}}(\infty) = \bar{\bar{p}}(t \geq 48) = 0.0128$ (since it remains constant). The profile exhibits a characteristic typical of diffusion limited DEP accumulation described for the 1-D FPE model in Chapter 5. The rise time is τ_{rise} = 1.2 secs and was evaluated by determining t such that $\hat{p}(t) = (1-e^{-1}) \cong 0.632$ using a built-in MATLAB interpolation routine. The values of $\bar{\bar{p}}(\infty)$ and τ_{rise} that are key indictors of FPE system dynamics, are listed (with greater accuracy) in Table 6.1.

The second example of $\hat{p}(t)$, is plotted as 'Profile II' (red - · - ·) in Fig. 6.12 and uses the same parameter values as the first example ($\hat{d}$ = 10.0 and V_o = 0.5 V) and $\hat{r} = 0.108$ except $\mathrm{Re}\{f_{CM}\}$ = 1.00. Profile II was generated and assembled using the same programs (*Fpe2dTh.pde* and *ch6flx.m*) described for Profile I. Using $\mathrm{Re}\{f_{CM}\}$ = 1.00 represents a ×25 increase in DEP force compared with the first example, and results in high value for steady state average density in the collection region, $\bar{\bar{p}}(\infty) = \bar{\bar{p}}(t \geq 84) = 0.58363$. Contour and elevation plots (not shown) indicated a low probability density in all regions of the cell except near the coordinates corresponding to the

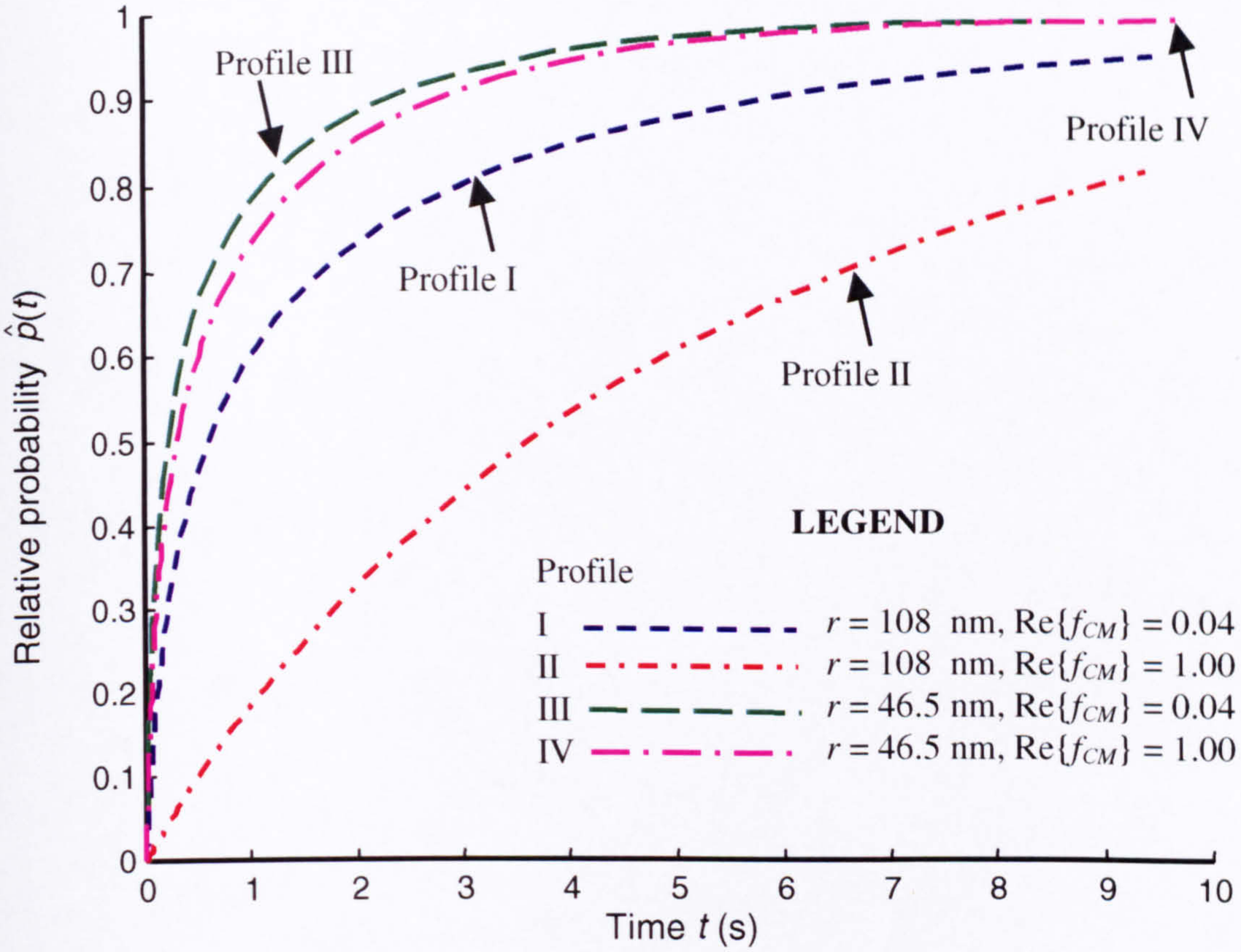

Fig. 6.12 DEP collection relative probability $\hat{p}(t)$ profiles for the designated region and cell shown in Fig. 6.11. The profiles were generated using the FPE (6.5.8) combined with (6.5.15) and (6.5.16) with parameter values $\hat{d} = 10.0$, $V_o = 0.5$ V, $h = 9.9$ μm, and r and Re$\{f_{CM}\}$ as shown.

Profile in Fig. 6.12	Particle radius r (μm)	Real part of the Claussius-Mossotti factor Re$\{f_{CM}\}$	Profile rise time τ_{rise} (s)	Steady state average probability density $\bar{\bar{p}}(\infty)$	Steady state $\varepsilon_{\max}(t)$	Steady state $\varepsilon_A(t)$
I	0.108	4.0×10^{-2}	1.183	0.012799	5.72×10^{-4}	4.3×10^{-5}
II	0.108	1.0	5.377	0.583631	0.840	4.96×10^{-2}
III	0.0465	4.0×10^{-2}	0.4398	0.010292	1.18×10^{-4}	3×10^{-6}
IV	0.0465	1.0	0.6029	0.016263	1.30×10^{-3}	1.11×10^{-4}

Table 6.1 Data for profiles in Fig. 6.12 listing rise times, steady state average probability densities and error measures (see text for details).

electrode edge (5.0,0.1) as the system approached steady state. This distribution is in general agreement with the analytical steady state density described in Fig. 6.9(b). Physically, the salient probability density near the electrode edge means most of the particles accumulate well within the designated collection region. The movement of particles towards the 'electrode edge' can account for the significant increase in rise time $\tau_{rise} = 5.4$ seconds compared with Profile I.

Several simulations for the parameter values were run with times extending to 10,000 seconds to ascertain steady state conditions. Due to the high DEP force, $\varepsilon_A(t) = 0.0496$, which is much larger than Profile I but still within acceptable limits. Contour plots of the relative error showed a significant variation $\varepsilon_{max}(t) = 0.84$ for $84 \le t \le 10000$ seconds though most of the extreme relative errors were outside the designated region. However, in the region very close to the electrode edge where the probability density was greatest, $\left| p_{num}(x,y,t) / p_{anl}(x,y) - 1 \right| \le 0.05$ for $84 \le t \le 10000$. This means the FlexPDE numerical integration concurs within 5% to the steady state analytical solution where the density is highest, but prone to numerical errors elsewhere. Thus, Profile II is accurate for our purposes but could possibly be improved by deploying more feature lines to force a higher mesh density.

In the third example, Profile III (green — —), $\mathrm{Re}\{f_{CM}\} = 0.04$ as in the first example, but the particle radius is reduced to $\tilde{r} = 0.0465$. This means the DEP force is reduced to $(\frac{46.5}{108})^3 \cong 0.08$ compared to Profile I, and the drag coefficient ζ is also halved (*ca.* ×0.43). Physically, this means the particle movement is minimal and the system rapidly approaches steady state as indicated by $\bar{p}(\infty) = \bar{p}(t \ge 21) = 0.0103$ and $\tau_{rise} = 0.44$ secs. The FPE simulation was run for the short time interval up to 50 secs. The error measures were $\varepsilon_A(t) = 3 \times 10^{-6}$ and $\varepsilon_{max}(t) = 1.18 \times 10^{-4}$ for $21 \le t \le 50$.

Maintaining $\tilde{r} = 0.0465$ and increasing the real part of the Claussius-Mossotti factor to $\mathrm{Re}\{f_{CM}\} = 1.00$ yields Profile IV (magenta — · — ·). In this fourth example, the DEP force is $0.08 \times 25 = 2$ about twice that of the first example (profile I). This is indicated by $\bar{p}(\infty) = \bar{p}(t \ge 27) = 0.0163$ that is greater than $\bar{p}(\infty) = 0.0128$ for Profile I, as summarised in Table 6.1. It is very interesting, however, that the rise time is short, $\tau_{rise} = 0.6$ secs. This is half the rise time for Profile I ($\tau_{rise} = 1.2$ secs). Clearly, a higher DEP force that causes more particles to be transported into the collection region does not imply a larger rise time (as observed with Profile II). The short rise time is attributed to the drag coefficient that is about half (×0.43) of profile I. This results in the particle velocity being ×0.46 of Profile I and a diffusion coefficient that is more than doubled. Further comparisons of DEP collection profiles are made in the next chapter in conjunction with experimental results.

6.6 Concluding remarks

As summarised in 6.3.4, sections 6.1 to 6.3 of this chapter described the development of the general expression for the electric field intensity gradient, $\vec{\nabla}\left|\vec{E}\right|^2$, for a periodic planar interdigitated electrode array with finite cover-slip height, h. To simplify the analysis the electrode width was assumed to be equal to the inter-electrode gap ($w = d$) – a valid assumption in practice. One of the components of $\vec{\nabla}\left|\vec{E}\right|^2$ that adequately describes the intensity in many cases is $\vec{\nabla}\left|\vec{E}_a\right|^2$. It assumes a linearly interpolated Dirichlet BC across the electrode gap with $\gamma = 1$ and ignores the effects of the cover-slip ($h \to \infty$). Near and far field approximations for the electric field intensity gradient, based on $\vec{\nabla}\left|\vec{E}_a\right|^2$, were found and shown to agree with $\vec{\nabla}\left|\vec{E}_a\right|^2$ over the appropriate values of y.

In sections 6.4 and 6.5, expressions were derived for the particle 2-D probability density based on $\vec{\nabla}\left|\vec{E}_a\right|^2$. An expression for the probability density when the DEP collection has reached steady state, $p(x,y)$, was derived and evaluated in Section 6.4. The expression for the surface of the probability density $p(x,y)$ was subsequently simplified by considering just two points, one in the near field close to the electrode edge, and one in the far field. The ratio of the densities at the two points is the same as the particle concentration. This 'steady state' metric was shown to be responsive to changes in parameters, such as, peak potential V_o, particle radius r, electrode gap d (or width w), and applied frequency (via the real part of the Claussius-Mossotti $\mathrm{Re}\{f_{CM}\}$ function).

The set up for a numerical simulation of particle collections, $p(x,y,t)$, using the 2-D FPE was described in section 6.5. This included normalisation of the FPE, designation of a 2-D collection area, and establishment of error measures for the simulation. The simulation was used to generate time dependent particle collection profiles for typical values of V_o, r, d, and $\mathrm{Re}\{f_{CM}\}$. The dependency of the time-profiles on these parameters was briefly investigated using $\bar{\bar{p}}(\infty)$ and the τ_{rise} parameters as used in the 1-D FPE simulations in Chapter 5.

Finally, it is worth remarking that the field approximations and expressions for $p(x,y)$ and $p(x,y,t)$ developed in sections 6.3 - 6.5 could be extended for the more general case where $\gamma = 0.78$ and with a finite cover-slip height, h. However, since this is likely to be complicated, it is a subject for further work and should be considered in the light of the experimental findings discussed in the next chapter.

7 DEP collection experiments and comparisons with theory

7.0 Introduction

Chapters 5 and 6 have predicted the DEP collection and relaxation profiles of sub-micron particles on planar surfaces. In particular, Chapter 6 has described the use of the 2-D FPE to predict particle collections onto the edges of interdigitated electrode arrays. In this chapter, the particle collection predictions are compared with measurements of sub-micron particle collections using fluorescence microscopy. The experimental apparatus and methods have been detailed in Chapter 3. The first comparison is made with 216 nm diameter latex micro-spheres (or beads) and the second with pTA250 DNA plasmids described in Chapter 4.

The comparison of theoretical predictions with experiments using 216 nm diameter beads is quantitative and more rigorous since individual beads are well defined and can, in most instances, be counted. Essentially, the key time dependent parameters for comparison are the particle number *predicted*, $n_p(t)$, and the number determined from *experiment*, $n_e(t)$. In this respect, the chapter starts with a review and description of $n_p(t)$ and $n_e(t)$ in section 7.1. The comparison of theory with experiments using 216 nm diameter latex micro-spheres is described in the next section 7.2. The comparison between theoretical predictions and experiments using DNA plasmids is described in the following section 7.3. The comparison is more qualitative than for the beads because, as described in sections 3.3.4 and 3.3.5, the plasmids are less well defined and tend to aggregate. All measurements used the same set of 10 μm width, 10 μm gap separately addressable interdigitated electrode arrays.

7.1 Background – comparing experiments and simulations

The particle movement over interdigitated electrode arrays that exhibit periodic and symmetric geometry is represented by the characteristic half-width plus half-gap ($w/2 + d/2$) 'cell' described previously in chapters 3 and 6. The key parameters for comparison, $n_e(t)$ and $n_p(t)$, refer to particle collections within a *designated* volume in a characteristic cell. The following sections describe how $n_e(t)$ is determined from experiments that measure fluorescence intensity $I(x, z, t)$ over the 2-D surface of the array. The computation of $n_p(t)$ from the probability density is developed further from the introduction given in section 6.5.2.2.

7.1.1 Determining DEP collections from changes in normalised fluorescence

Chapter 3 has introduced the normalised fluorescence intensity $F(t)$ that describes fluorophore accumulation within a designated region about the electrode edge in a characteristic cell. This is the starting point for determining $n_e(t)$ and indeed the change of the number of particles collected over given time interval $t-t_0$, $\Delta n_e(t)$.

7.1.1.1 Time dependent normalised fluorescence intensity: a brief review

The profiles of the normalised fluorescence intensity about the electrode edge $F(t)$ are calculated from the time dependent 2-D image intensity $I(x,z,t)$ using (3.5.10)

$$F(t) = \frac{\bar{\bar{I}}_E(t)}{\bar{\bar{I}}_{LU}(t)} \tag{7.1.1}$$

where $\bar{\bar{I}}_E(t)$ is the characteristic $w/2 + d/2$ intensity $\tilde{I}(x,t)$ spatially averaged in the transverse direction $\vec{u}_x$ over $x_l \le x \le x_u$ encompassing the *electrode edge* positioned at $x_e = \frac{w}{2} = \frac{d}{2}$. The *lower* limit x_l and *upper* limit x_u are bounded $0 \le x_l < x_e$ and $x_e < x_u \le x_c$ where the cell transverse length is $x_c = \frac{w+d}{2} = d$ for the electrode array geometry of interest. The $\bar{\bar{I}}_{LU}(t)$ intensity is the characteristic intensity $\tilde{I}(x,t)$ spatially averaged over the cell length *not* covered by $\bar{\bar{I}}_E(t)$, that is, over both the *lower* and *upper* intervals, $0 \le x < x_l$ and $x_u < x \le x_c$. These average intensities are evaluated, using the trapezoidal rule, from (3.5.7), (3.5.8) and (3.5.11), where i_l and i_u are the integer values corresponding to x_l and x_u: $x_l = (i_l - 1)(\frac{w+d}{2})/(n_c - 1)$ and $x_u = (i_u - 1)(\frac{w+d}{2})/(n_c - 1)$, and n_c is the number of sample points for each $w/2 + d/2$ characteristic (a typical value chosen is $n_c = 100$).

The *characteristic* intensity $\tilde{I}(x,t)$ is described in Chapter 3 as a *periodic* and *symmetric* average of a larger x-domain intensity $\bar{I}(x,t)$ comprising the array of n_{pr} electrode and gap pairs. The averaging process is described in equations (3.5.2) to (3.5.5). $\bar{I}(x,t)$ is the spatial average of the image intensity $I(x,z,t)$ over a displacement $z_2 - z_1$ in the longitudinal $\vec{u}_z$ direction, and is evaluated from (3.5.1b) where r and c are respective pixel values for each row r and column c that constitute the x-z 2-D image, and $c_{max} = 720$.

In addition to detailing the computation of the $\bar{\bar{I}}_E(t)$ and $\bar{\bar{I}}_{LU}(t)$ from the image intensity $I(x,z,t)$, models of $\bar{\bar{I}}_E(t)$ and $\bar{\bar{I}}_{LU}(t)$ were derived in chapter 3 that described the fluorescence in the vertical direction parallel to the microscope optical axis, $\vec{u}_y$. The fluorescence arising from particles within a small displacement ΔL within the plane of focus, near the electrode surface, was distinguished from fluorescence attributed to particles above the focal plane in the bulk solution. These models were expressed by (3.6.1) and (3.6.4) and both were linearly dependent on the microscope source intensity $I_s(t)$. However, the normalisation ratio cancelled the $I_s(t)$ dependency, thus yielding a smoother time dependent intensity profile,

$$F(t) = \frac{\bar{\bar{I}}_E(t)}{\underbrace{\bar{\bar{I}}_{LU}(t)}_{evaluation}} = \frac{k_l \bar{\bar{c}}_E(t) + \bar{\bar{B}}_E(t)}{\underbrace{k_l \bar{\bar{c}}_{LU}(t) + \bar{\bar{B}}_{LU}(t)}_{structure}} \tag{7.1.2}$$

where the constant $k_l = k_{op}\, k_{ra}\, \eta_q\, k_a\, k_{ea}\, \Delta L$ accounts for a number optical parameters including numerical aperture of the microscope objective, re-absorption of emitted light, fluorophore quantum efficiency, absorption, scattering and excitation absorbance. The particle concentrations within the vertical displacement ΔL, $\bar{\bar{c}}_E(t)$ and $\bar{\bar{c}}_{LU}(t)$, are spatially averaged in directions $\vec{u}_x$ and $\vec{u}_z$ analogous to $I_E(t)$ and $I_{LU}(t)$. Expressions for these concentrations are given by (3.6.2) and (3.6.5) where a weighting has been given to the constants r_{el} and r_{gp} that describe the reflectivity of the electrode and glass interface to the aqueous solvent. As before, the subscript 'E' corresponds to x-values about electrode *edge* $\{x: x_l \le x \le x_u\}$, and 'LU' to *lower* and *upper* intervals, $\{x: 0 \le x \le x_l\} \cup \{x: x_u \le x \le x_c\}$. Likewise, $\bar{\bar{B}}_E(t)$ and $\bar{\bar{B}}_{LU}(t)$ account for *background* fluorescence from particles in the bulk above the focal plane.

This completes the discussion of the normalised fluorescence $F(t)$ given by (7.1.2), in terms of both *evaluation* by image processing (section 3.5) and *structure* (section 3.6.1). In the subsequent section 3.6.2.1, the structure was exploited to eliminate background fluorescence $\bar{\bar{B}}_E$ by considering the difference in $F(t)$ over a given time interval $t - t_0$. The difference in fluorescence is,

$$\Delta F(t) = F(t) - F(t_0) = k[n_e(t) - n_e(t_0)] + \varepsilon_f(t) = k\Delta n_e(t) + \varepsilon_f(t) \tag{7.1.3a}$$

where $n_e(t)$ is the *experimentally* determined number of particles about an electrode *edge* with designated volume weighted by the reflection constants,

$$n_e(t) = r_{el}\underbrace{\int_{x_l}^{x_e}\int_{z_1}^{z_2}\int_{a}^{a+\Delta L} c(x,y,z,t)dydzdx}_{\text{particle number from } x_l \text{ to edge}} + r_{gp}\underbrace{\int_{x_e}^{x_u}\int_{z_1}^{z_2}\int_{a}^{a+\Delta L} c(x,y,z,t)dydzdx}_{\text{particle number from edge to } x_u} \qquad (7.1.3b)$$

$$\text{with fluorescence constant } k = \frac{k_{op}k_{ra}\,\eta_q\,k_a\,k_{ea}}{(x_u - x_l)(z_2 - z_1)[k_l \overline{\overline{c}}_{LU}(t_0) + \overline{\overline{B}}_{LU}(t_0)]} \qquad (7.1.3c)$$

The error is $\varepsilon_f(t) = k\delta_f\, n_e(t)$ where δ_f accounts for small temporal deviations in background fluorescence, $0 \le \delta_f << 1$ and is typically 10% or less. In most cases $\varepsilon_f(t)$ is sufficiently small, so

$$\Delta n_e(t) \cong \frac{\Delta F(t)}{k} \qquad (7.1.3d)$$

Consequently, from section 3.6.2.2, the time derivative (or rate) of particle collection is

$$\dot{n}_e(0) = \frac{\dot{F}(0)}{k} \qquad (7.1.4)$$

7.1.1.2 Measuring the initial collection rate

The initial rate of fluorescence increase can be estimated simply be measuring F over small increments in time immediately before and after the DEP force is applied, $\dot{F}(0) \cong \delta F / \delta t$. This is not always satisfactory, however, if there is a minor perturbation in measurement. These perturbations include, for example, small corrections in (microscope) focus that are often required after fluorescent sub-micron particles start collecting.

An alternative method, far less susceptible to perturbations in measurement, is to deduce $\dot{F}(0)$ from the entire collection characteristic, $F(t)$. The characteristic is fitted to an analytical function, and the function is differentiated with respect to time. As shown in the next section 7.2, collection profiles are fitted with single or, more commonly, with double exponential functions. The equation for the double exponential fitted in Origin 4.1™ has the form

$$F(t) = F_0 - F_1 \exp[-(t-t_0)/\tau_1] - F_2 \exp[-(t-t_0)/\tau_2] \qquad (7.1.5)$$

where $F_1 > 0$ and $F_2 > 0$. Differentiating,

$$\dot{F}(t) = dF/dt = F_1/\tau_1 \exp[-(t-t_0)/\tau_1] + F_2/\tau_2 \exp[-(t-t_0)/\tau_2] \qquad (7.1.6)$$

Hence, setting $t = t_0 = 0$

$$\dot{F}(0) = F_1/\tau_1 + F_2/\tau_2 \qquad (7.1.7)$$

To confirm validity of the method, values of $\dot{F}(\gamma)$ determined from (7.1.6) can be compared against $\delta F/\delta t$ about $t = \gamma$. The difference between the two divided by $\delta F/\delta t$ is the relative error $\varepsilon_{\dot{F}}(\gamma)$,

$$\varepsilon_{\dot{F}}(\gamma) = \left|\frac{\dot{F}(\gamma) - \delta F/\delta t}{\delta F/\delta t}\right| = \left|\frac{F_1/\tau_1 \exp(-\gamma/\tau_1) + F_2/\tau_2 \exp(-\gamma/\tau_2) - \delta F/\delta t}{\delta F/\delta t}\right| \qquad (7.1.8)$$

Substituting (7.1.7) into (7.1.4), the initial collection rate is given by

$$\dot{n}_e(0) = \frac{F_1/\tau_1 + F_2/\tau_2}{k} \qquad (7.1.9)$$

7.1.2 Predicting DEP collections from simulations of the FPE

The *predicted* number of particles $n_p(t)$ collected over a designated 3-D volume $x_l \le x \le x_u$, $a \le y \le a+\Delta L$, $z_1 \le z \le z_2$, is given by (2.4.25),

$$n_p(t) = N\int_{z_1}^{z_2}\int_{a}^{a+\Delta L}\int_{x_l}^{x_u} p(x,y,z,t)\,dx\,dy\,dz = N\int_{a}^{a+\Delta L}\int_{x_l}^{x_u} p(x,y,t)\,dx\,dy \quad 0 \le n(t) \le N \qquad (7.1.10a)$$

where the joint probability density, $p(x,y,t)$ is the solution of the 2-D FPE (6.5.8),

$$\frac{\partial p(x,y,t)}{\partial t} = -\frac{1.637\times10^5 \hat{r}^2\,\mathrm{Re}\{f_{CM}\}\,V_o^{\,2}}{\hat{d}^3}\left(\frac{\partial[p(x,y,t)\Gamma_x(x,y)]}{\partial x} + \frac{\partial[p(x,y,t)\,\Gamma_y(x,y)]}{\partial y}\right) + \frac{0.2424}{\hat{r}}\left(\frac{\partial^2 p(x,y,t)}{\partial x^2} + \frac{\partial^2 p(x,y,t)}{\partial y^2}\right) \qquad (7.1.10b)$$

and the dimensionless parts of the electric field intensity gradients $\Gamma_x = 2\Theta_T\ \Xi_+ + \Theta_L\ \Xi_-$ and $\Gamma_y = 2\Theta_T\ \Xi_- - \Theta_L\ \Xi_+$ are given by (6.5.3) and (6.5.4). The transcendental functions Θ_T and Θ_L are as defined in (6.4.7),

$$\Theta_T = \tan^{-1}\left(\frac{\sin\hat{x}}{\sinh\hat{y}}\right) - \tan^{-1}\left(\frac{\cos\hat{x}}{\sinh\hat{y}}\right),\ \Theta_L = \ln\left(\frac{\cosh\hat{y}+\cos\hat{x}}{\cosh\hat{y}-\cos\hat{x}}.\frac{\cosh\hat{y}+\sin\hat{x}}{\cosh\hat{y}-\sin\hat{x}}\right), \qquad (7.1.10c)$$

$$\Xi_+ = \frac{\sinh\hat{y}\cos\hat{x}}{\cosh 2\hat{y} - \cos 2\hat{x}} + \frac{\sinh\hat{y}\sin\hat{x}}{\cosh 2\hat{y} + \cos 2\hat{x}}\ ,\ \Xi_- = \frac{\cosh\hat{y}\cos\hat{x}}{\cosh 2\hat{y} + \cos 2\hat{x}} - \frac{\cosh\hat{y}\sin\hat{x}}{\cosh 2\hat{y} - \cos 2\hat{x}}$$

with $\hat{y} = \pi y/2d$, and $\hat{x} = \pi x/2d + \pi/4$. It is understood the dimensions of independent variables x and y are in microns (μm), and similarly for the radius, $\hat{r}$, of the spherical particle and electrode gap, $\hat{d}$ (the over-bracket, $\overline{\ }$, indicates numerical values substituted for these constants should be in microns). The real part of the frequency dependent Claussius-Mossotti factor, $\mathrm{Re}\{f_{CM}\}$, is given by (2.2.4), and V_o is the peak electrode potential (V). It should be remembered the expressions given by (7.1.10c) apply to the simplest case where the electric field components assume the height of the cover-slip is infinite and the potential across the gap is a linear interpolation of the electrode potentials. That is, the electric field components considered in the analysis are solely given by (6.2.4a) and (6.2.6a), $E_x = E_{x_a}$ and $E_y = E_{y_a}$, with $\gamma = 1$.

As described in Chapter 6, the 2-D (7.1.10b) is solved numerically using FlexPDE 2.15 program *Fpe2dth.pde*. The key parameter of the simulation is the average density over the designated area,

$$\overline{\overline{p}}(t) = \frac{1}{(x_u - x_l)\Delta L}\int_a^{a+\Delta L}\int_{x_l}^{x_u} p(x,y,t)\,dx\,dy \qquad (7.1.11)$$

and the predicted particle number is,

$$n_p(t) = (x_u - x_l)\Delta L\, N\,\overline{\overline{p}}(t) \qquad 0 \le n(t) \le N \qquad (7.1.12)$$

7.1.2.1 Initial collection rate (at $t = 0$)

Initially, before DEP collections begin at $t = 0$, the joint probability density is uniformly distributed and is therefore a constant value over the solution space, so $\overline{\overline{p(x,y,0)}} = p(0) = 1/(d(b-a))$. This implies the spatial partial derivatives are zero; $\frac{\partial p(x,y,0)}{\partial x} = 0 = \frac{\partial p(x,y,0)}{\partial y}$ and $\frac{\partial^2 p(x,y,0)}{\partial x^2} = 0 = \frac{\partial^2 p(x,y,0)}{\partial y^2}$. Approximating (7.1.10b) by allowing these relations to apply for times *very soon* after the onset of DEP, i.e., $t = 0^+$,

$$\left.\frac{\partial p(x,y,t)}{\partial t}\right|_{t=0^+} = \dot{p}(x,y,0) \cong -\frac{1.637\times10^5 \hat{r}^2 \,\mathrm{Re}\{f_{CM}\} V_o^{\,2} p(0)}{\hat{d}^3}\left(\frac{\partial \Gamma_x(x,y)}{\partial x} + \frac{\partial\, \Gamma_y(x,y)}{\partial y}\right) \quad (7.1.13a)$$

$$\cong -1.637\times10^5\left(\hat{r}^2/\hat{d}^3\right)\mathrm{Re}\{f_{CM}\} V_o^{\,2}\left(\Gamma_{x,x} + \Gamma_{y,y}\right)p(0)$$

where it is understood the time derivative of interest is in the $+t$ direction about $t = 0$. Since, $\overline{\overline{\partial_t p(x,y,t)}} = \partial_t \overline{\overline{p(x,y,t)}} \equiv \dot{\bar{\bar{p}}}(t)$, the initial derivative of the average probability density (over the designated region) is written,

$$\dot{\bar{\bar{p}}}(0) = \overline{\overline{\dot{p}(x,y,0)}} \cong -1.637\times10^5\left(\hat{r}^2/\hat{d}^3\right)\mathrm{Re}\{f_{CM}\} V_o^{\,2}(\overline{\overline{\Gamma_{x,x}}} + \overline{\overline{\Gamma_{y,y}}})p(0) \quad (7.1.13b)$$

7.1.3 Comparing predictions of DEP collections from experimental data

7.1.3.1 Comparing initial collection rates

There are two key results from (7.1.13) that can enable comparisons with experimental data. First, applying (7.1.12) and (7.1.13b) results in

$$\frac{\dot{n}_p(0)}{n_p(0)} = \frac{(x_u - x_l)\Delta L\, \dot{\bar{\bar{p}}}(0)}{(x_u - x_l)\Delta L\, p(0)} = \frac{\dot{\bar{\bar{p}}}(0)}{p(0)} = -1.637\times10^5\left(\hat{r}^2/\hat{d}^3\right)(\overline{\overline{\Gamma_{x,x}}} + \overline{\overline{\Gamma_{y,y}}})\mathrm{Re}\{f_{CM}\} V_o^{\,2} \quad (7.1.14)$$

The ratio $\dot{n}_p(0)/n_p(0)$ *predicted* theoretically is evaluated numerically. This can be compared with $\dot{n}_e(0)/n_e(0)$ from experiment, either by direct particle counts, or by combining (7.1.4) and (7.1.9),

$$\frac{\dot{n}_e(0)}{n_e(0)} = \frac{\dot{F}(0)}{k\,n_e(0)} = \frac{F_1/\tau_1 + F_2/\tau_2}{k\,n_e(0)} \tag{7.1.15}$$

Note that $n_e(0) \neq F(0)/k$ since the background fluorescence must be subtracted.

The second result concerns the *ratio* of the collection rates. Consider two Gedanken DEP collection experiments where only two parameters, applied peak voltage V_0 and frequency f (via $\mathrm{Re}\{f_{CM}\}$) are allowed to vary and all other parameters remain the same. The ratio of the initial collection rates from (7.1.14) is,

$$\frac{\dot{n}_{p_2}(0)}{\dot{n}_{p_1}(0)} = \frac{\dot{\overline{\overline{p}}}_2(0)}{\dot{\overline{\overline{p}}}_1(0)} = \frac{-1.637\times10^5\,\hat{r}^2\,\mathrm{Re}\{f_{CM_2}\}\,V_{o_2}{}^2\,p(0)\left(\overline{\overline{\Gamma_{x,x}}} + \overline{\overline{\Gamma_{y,y}}}\right)/\hat{d}^3}{-1.637\times10^5\,\hat{r}^2\,\mathrm{Re}\{f_{CM_1}\}\,V_{o_1}{}^2\,p(0)\left(\overline{\overline{\Gamma_{x,x}}} + \overline{\overline{\Gamma_{y,y}}}\right)/\hat{d}^3} \tag{7.1.16}$$

$$= \frac{\mathrm{Re}\{f_{CM_2}\}\,V_{o_2}{}^2}{\mathrm{Re}\{f_{CM_1}\}\,V_{o_1}{}^2}$$

This can be compared with the experimental ratio found directly from fluorescence measurements. Using (7.1.15), and assuming $n_{e_2}(0) = n_{e_1}(0)$,

$$\frac{\dot{n}_{e_2}(0)}{\dot{n}_{e_1}(0)} = \frac{\dot{F}_2(0)}{\dot{F}_1(0)} \tag{7.1.17}$$

Note that the ratio is independent of k and $n_e(0)$.

7.1.3.2 Comparing collections over a time interval

Using (7.1.12) the predicted collections over a given time interval $t - t_0 = t - 0$, can be evaluated

$$\frac{\Delta n_p(t)}{n_p(0)} = \frac{n_p(t) - n_p(0)}{n_p(0)} = \frac{[\overline{\overline{p}}(t) - \overline{\overline{p}}(0)](x_u - x_l)\Delta L}{\overline{\overline{p}}(0)(x_u - x_l)\Delta L} = \frac{\Delta\overline{\overline{p}}(t)}{\overline{\overline{p}}(0)} \tag{7.1.18}$$

and compared directly with experimental values over the same interval. From (7.1.3d),

$$\frac{\Delta n_e(t)}{n_e(0)} = \frac{n_e(t) - n_e(0)}{n_e(0)} \cong \frac{\Delta F(t)}{k\,n_e(0)} \tag{7.1.19}$$

The predicted ratio between different experiments with different peak voltage V_0 and frequency f, and all other constants being the same, is

$$\frac{\Delta n_{p_2}(t)}{\Delta n_{p_1}(t)} = \frac{\Delta \bar{\bar{p}}_2(t)}{\Delta \bar{\bar{p}}_2(t)} \qquad (7.1.20)$$

and can be compared with experimental measurements,

$$\frac{\Delta n_{e_2}(t)}{\Delta n_{e_1}(t)} = \frac{\Delta F_2(t)}{\Delta F_1(t)} \qquad (7.1.21)$$

where it is assumed $n_{e_2}(0) = n_{e_1}(0)$. Again, similar to (7.1.17), the ratio is independent of k and does not require $n_e(0)$.

7.2 DEP collections and relaxations of colloidal particles

All DEP experiments on colloidal particles used 216 nm diameter carboxy-modified polystyrene fluorescent micro-spheres with emission wavelength λ_e = 515 nm, FluoSpheres® (Molecular Probes, USA, F-8811). The experiments were performed on a separately addressable 8 array interdigitated electrode device with transverse width $w = d$ = 10 μm. This device is described in section 3.2.1.1 and is illustrated in Fig. 3.1(b). Cover-slips (18×18 mm^2) were used to reduce evaporation and enabled the height h (of the cover-slip) above the electrode plane to be well controlled. The volume of bead suspension required to adequately fill the well with 200 mm^2 planar area was 40 μl, hence, h = 200 μm.

The DEP collections and relaxations were investigated for two *independent* variables, applied DEP frequency, f, and peak potential, V_0. Three different frequencies were applied using $V_o = 2$ V; f = 500 kHz, 1 MHz, and 2 MHz. No collections were observed for $f \geq 3$ MHz. Collections using three peak voltages, V_0 = 1, 2 and 4 V were conducted at f = 2 MHz. In each experiment the particle *collection* was observed for 2 – 3 minutes, followed by particle *relaxation* (DEP switched off, V_0 = 0 V), which was observed for 30 – 60 seconds.

7.2.1 Preparations of latex micro-spheres and experimental measurements

Stock preparations of latex micro-spheres consisted of 1 μl of 2% solids added to 99 μl distilled RO water. In each experiment, 4 μl of this stock was added to 36 μl dilute KCl solution with measured conductivity, σ_m = 1.7 mS/m (Jenway 4701, RS Components, U.K.). This gave a final bead dilution of 1:1000. Using (3.4.2) with parameter values, $\hat{d}_s$ = 0.216 μm, $\hat{S}$ = 0.02, $\hat{\rho}_s$ = 1.05 g/cm^3 and V_r = 1/1000, yields the number of spheres per unit volume (or concentration) used in each DEP experiment, c_v = 3.61×10^{15} m^{-3} or c_v = 3.61×10^{-3} (μm)$^{-3}$. The AC potentials to the electrodes mounted on PCB were supplied by a computer controlled DDS as described in section 3.1 and Fig. 3.1(a). The DEP potentials were switched on/off manually by a nearby switch. An oscilloscope was used to monitor the peak voltage and frequency on each channel separately. The CCD camera was set with automatic gain control turned off and the microscope source was maintained at approximately the same intensity. The video frames were cropped for TV viewing with length ratio 4:3, and typically spanned an *x*-*z* planar electrode array area of 186 × 248 μm.

Since particle collections tended to vary over the area of an array, collections and relaxations were performed in *sets* of *three* experiments. In each set, the same area of the array was used to record particle collections (and relaxations) for all of the three possible *states* of the independent variable (f or V_o). This enabled the collections to be compared with each other to avoid, as much as possible, any anomalies. Furthermore, the collection for the first experiment tended to be slightly less than the following ones but the evidence is not at all conclusive. As a precaution against bias, the *ordering* of the experiments in each set was such that all states were used in the 'initial' collection (before any DEP had perturbed the system of particles).

For example, one set of experiments started with f = 500 kHz (with V_o held constant at 2V), followed by f = 2 MHz, then f = 1 MHz. This set is written concisely as $\{V_o = 2; f = 0.5, 2, 1\}$. The five other sets were: $\{V_o = 2; f = 2, 1, 0.5\}$, $\{V_o = 2; f = 1, 2, 0.5\}$, $\{f = 2; V_o = 2, 4, 1\}$, $\{f = 2; V_o = 4, 1, 2\}$, and $\{f = 2; V_o = 1, 2, 4\}$. The original collection and relaxation data are listed in Appendix M, tables M.1 and M, grouped in six sets $\mathcal{A}$ to $\mathcal{F}$, with experiments, $\mathscr{E}$ = 1, 2 and 3, in chronological order.

7.2.2 Experimental results

Profiles for the time dependent normalised fluorescence $F(t)$ were determined using equations (3.5.1b) - (3.5.8), (3.5.11) and (3.6.7) referred to in section 7.1.1.1. These expressions were evaluated by the program *depint* as described in chapter 3.5. Unless otherwise stated, it is assumed each DEP collection starts at t_0 = 0. The number of sample points for each (w/2 + d/2) characteristic was n_c = 100, and number of electrode pairs was n_{pr} = 8. The image processing

parameters all had the property, $i_u - i_l = 16$. This implies the transverse length of the *x-y* cross-section designated collection area, using the expressions for (3.5.7b) with $w = d = 10$ μm, is $\Delta x = x_u - x_l = 1.62$ μm. Typically, the integer values ranged from $i_l = 43$ to $i_l = 49$ and $i_u = 59$ to $i_u = 65$, respectively. The integer values depended on the transverse alignment of the frames used for set-up (or 'templates') described in section 3.5.

All collections, except for the $V_o = 1$, $f = 2$ MHz case, were best fitted by a double exponential (7.1.5) using Origin 4.1™. The relaxation after collection was best fitted by a single exponential, with fall amplitude and time, F_3 and τ_{e3}. Values of the rise amplitudes F_1 and F_2 and times τ_{e1} and τ_{e2}, are shown in Table 7.1(a). It is important to note that each of these values is an average of *three* experimental values compiled from the six sets (of three experiments) listed in Appendix M, tables M.1 and M.2. In this respect, the values have been purposefully rounded to two significant figures except $F(0)$ and $F(120)$[1].

Collection									Relaxation	
V_o (V)	f (MHz)	$F(0)$ (a.u.)	$F(120)$ (a.u.)	F_1 $\times 10^{-2}$	τ_{e1} (s)	F_2 $\times 10^{-2}$	τ_{e2} (s)	$\delta F/\delta t$ $\times 10^{-2}$	F_3 $\times 10^{-2}$	τ_{e3} (s)
2	0.5	0.988	1.189	12	4.1	22	220	1.8	19	1.2
2	1	0.982	1.149	7.9	2.9	9.1	35	1.5	19	1.6
2	2	0.980	1.081	3.4	2.9	4.8	17	0.79	9.5	1.4
4	2	0.984	1.201	13	2.3	6.6	17	3.3	22	1.4
2	2	0.985	1.095	6.1	5.8	7.1	88	0.91	11	1.5
1	2	0.993	1.007	1.6	3.5	0	--	0.29	1.5	2.5

Table 7.1(a): Experimental frequency and voltage dependent DEP normalised fluorescence collection and relaxation data. The values are averages of the data tabulated in Appendix M.

Values of the normalised fluorescence at the start of each collection, $F(0)$ and 120 seconds later $F(120)$ are also listed in Table 7.1(a). The final column in the table shows the 'initial' rate of increase in normalised fluorescence, $\delta F/\delta t$ during the first 4 to 5 seconds. The values were found by a linear fit to $F(t)$ using Origin 4.1™. High values of $F(120)$ and $\delta F/\delta t$, for example, for the experiment where $V_o = 4$ and $f = 2$ MHz, clearly indicate a strong DEP collection of micro-spheres. Conversely, low values of $F(120)$ and $\delta F/\delta t$, such as, for the experiment where $V_o = 1$ and $f = 2$ MHz, clearly indicate very weak DEP forces acting on the beads. Another interesting feature is that the relaxation times τ_{e3} are generally smaller than the rise times, except after very weak collections where the data was relatively scattered. Another aspect of the weak collections is that they attracted sufficiently low number of particles that measurements were degraded by interference from fluorescence due to aggregations of beads.

---

[1] These are used in section 7.2.2.2, Table 7.1(b), for computing $\Delta F(120)$ and $\Delta F_r(120)$ where round-off error needs to be avoided in order for the reader to follow the calculations if desired.

7.2.2.1 A case example of DEP collection and relaxation

A typical characteristic $w/2 + d/2$ intensity $\tilde{I}(x,t)$ is illustrated in Fig. 7.1(a) for experimental conditions $V_o = 2$ V; $f = 1$ MHz. The corresponding data in App. M, Table, M.1 is set $\mathcal{A}$, $\mathcal{E} = 3$. There are a number of features worth highlighting. The first feature of $\tilde{I}(x,t)$ is that 2 minutes after the onset of DEP, the collection over the electrode edge is substantially at steady state. The video was frame grabbed at rate of 1 frame per second, so the entire collection and relaxation required *ca.* 200 frames to image process. This took several hours using a PC. A faster technique developed was to select frames for image processing on a non-uniform basis. This involved high density selection (1 frame/s) before and after the onset of DEP, at 120 seconds, and before and after the DEP force was turned off. A lower density (2 – 8 frames/s) was used elsewhere. This enabled a 3 – 4 minute collection and relaxation experiment to be described by ~ 70 frames that could be processed in about half-an hour.

The second feature of Fig. 7.1(a) is that a rather rapid decrease in fluorescence occurs over the lower and upper transverse intervals after the onset of DEP (frame 21), at points located near P_1 and P_2. The precise cause of this reduction in not entirely clear but it generally occurs with all DEP experiments so it is *not* attributed to fluctuations in the source intensity, $I_s(t)$. Restoration of the fluorescence also occurs after the DEP is switched off, as shown near points P_3 and P_4. The fluorescence reduction (and restoration) phenomena tend to be more pronounced when the DEP force is strong, so it is likely to be due to DEP induced depletion of particles within and above the focal plane (thickness ΔL). Fig. 7.1 (a) also shows a gradual decline in fluorescence over the course of the collection. Other experiments have shown, however, that the fluorescence increases during collection. Since $I_s(t)$ fluctuates over a wide range of times this gradual decline is attributed to $I_s(t)$ but could also include particle depletion. Fluorescence depletion and restoration affects no more than about 10 % of the intensity $\tilde{I}(x,t)$ so the effect is easily accommodated by the deviation parameter δ_f (or error $\varepsilon_f(t)$), in (7.1.3c) and leads to the approximation (7.1.3d). As discussed in section 7.1, the effect of $I_s(t)$ can be minimised or cancelled by normalisation.

Spatially averaging and normalising $\tilde{I}(x,t)$ led to a piecewise continuous collection and relaxation normalised fluorescence profile, $F_{\mathcal{A}3}$(t), shown in Fig. 7.1(b). The subscript denotes the data of the profile, as in Table M.1, set $\mathcal{A}$, $\mathcal{E} = 3$. The data points (coded blue '+') constituting the collection, or 'rise', were fitted with Origin 4.1™ for 120 seconds yielding $\tau_{e1} = 3.2$ and $\tau_{e2} = 44.6$ seconds. Data for the relaxation, or 'fall', was fitted to a single exponential $\tau_{e3} = 1.8$ seconds. The double and single exponential fits have been superposed on the data points as shown (brown - - -).

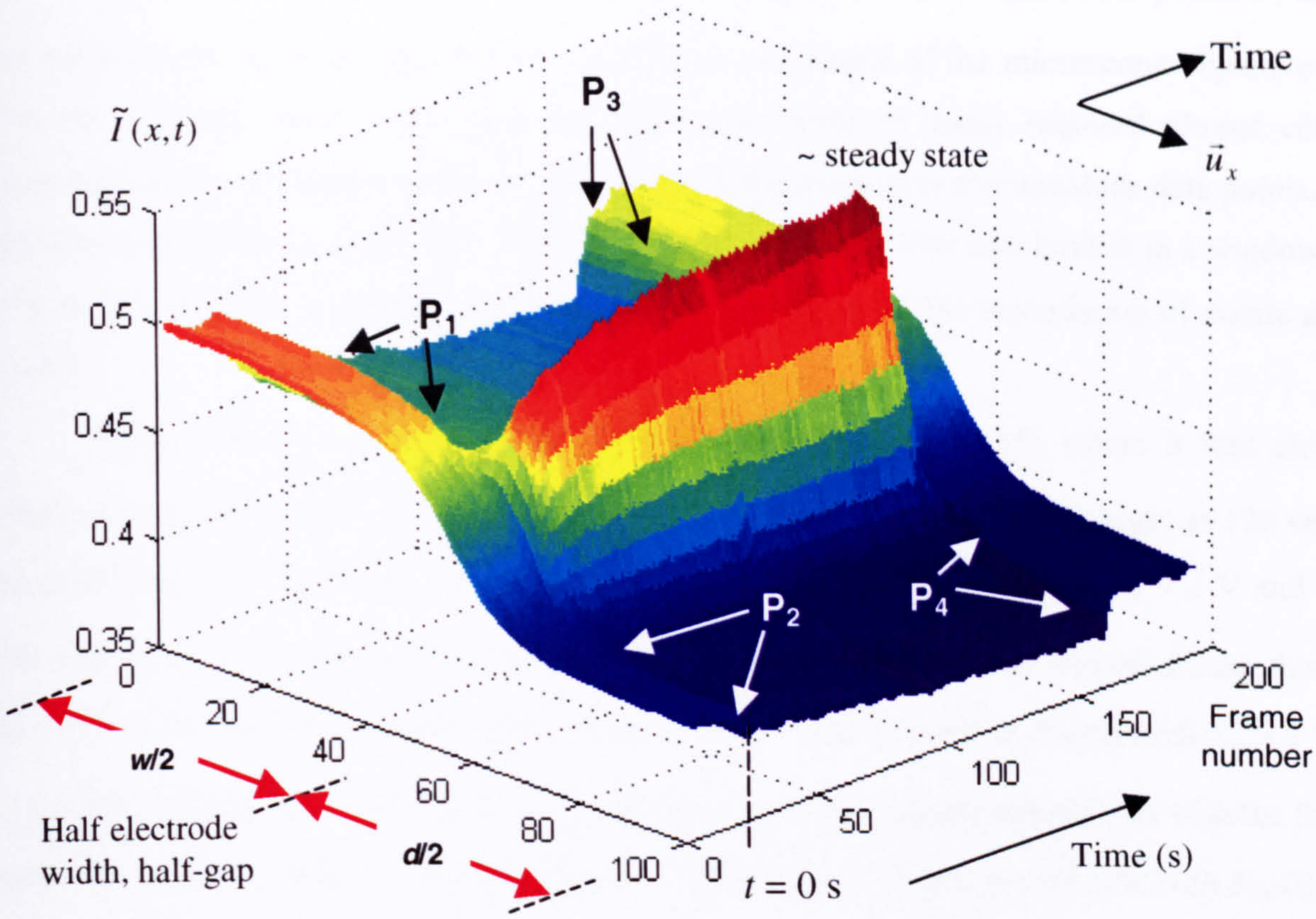

Fig. 7.1(a) Example of a characteristic $w/2 + d/2$ fluorescence intensity $\tilde{I}(x,t)$ that shows DEP particle collections and relaxations from a representative electrode edge. See text.

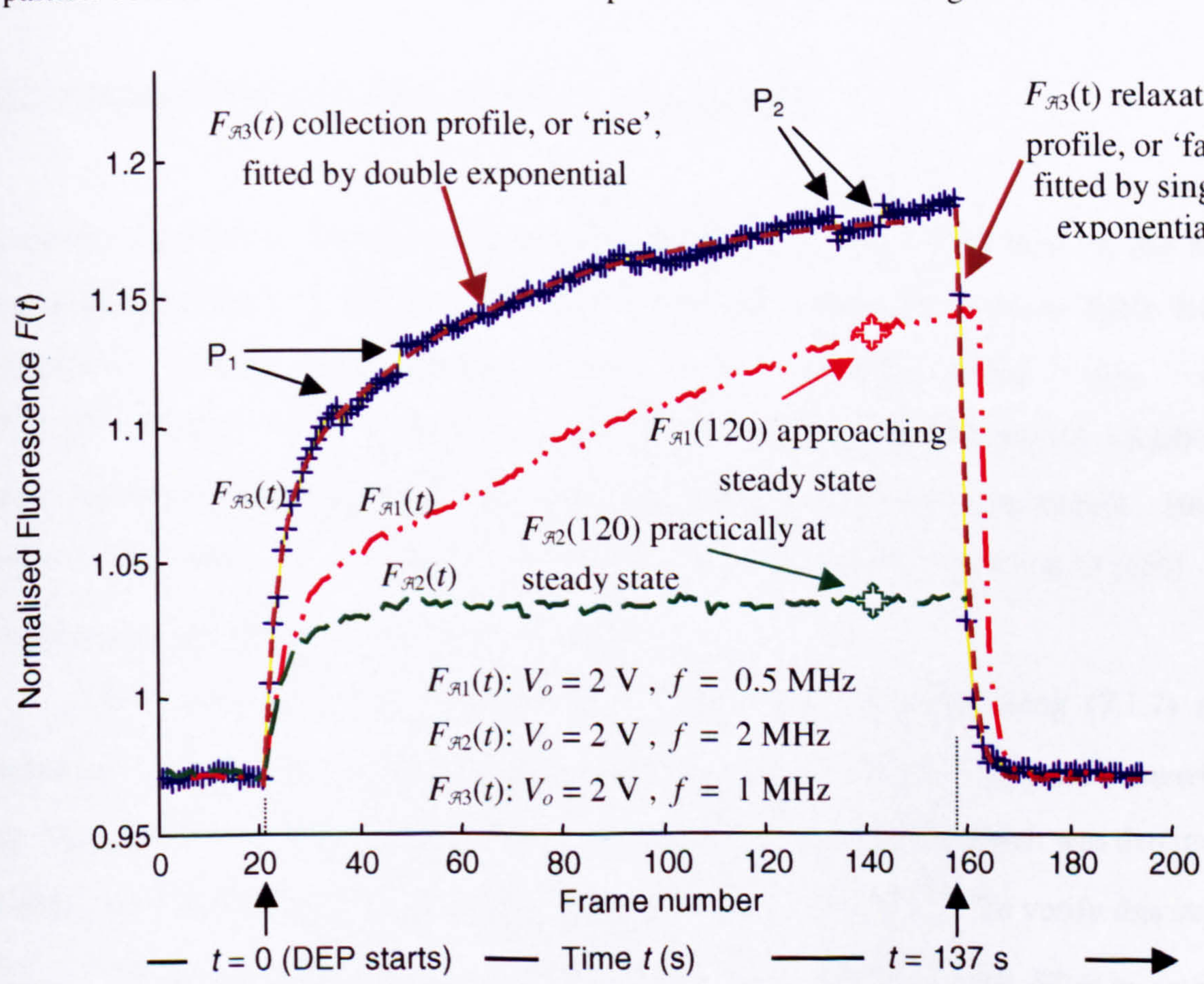

Fig. 7.1(b) Examples of normalised fluorescence F(t). The F_{A3}(t) collection and relaxation profile was calculated from $\tilde{I}(x,t)$ illustrated in Fig. 7.1(a) above. See text for details.

Fig. 7.1(b) also shows a small suppression followed by a recovery of $F_{\mathcal{A}3}(t)$ near points P_1 and P_2. The suppressions were due to minor defocusing, or movement of the microscope objective away from the electrode plane. To keep the bead collections in focus required almost constant monitoring during the experiments. In plots where defocusing caused anomalous data points, these were removed during curve fitting. The curve fitting of the rise was also limited to a window from $t = 0$ to 120 seconds, or slightly more (125 secs), depending on the smoothness of points around $F(120)$.

Many collections resembled the 'well rounded' form of $F_{\mathcal{A}3}(t)$, where it was clear the collection was substantially at steady state (zero time rate of fluorescence change) at 120 seconds and exhibited short rise times. An example of this is $F_{\mathcal{A}2}(t)$ with parameters $V_o = 2$ V and $f = 1$ MHz where $\tau_{e1} = 2.9$ and $\tau_{e2} = 8.6$ seconds. Other collections however, deviated from this form and continued to approach steady state at 120 seconds. One example is $F_{\mathcal{A}1}(t)$ with $V_o = 2$ V and $f = 0.5$ MHz where $\tau_{e1} = 4.6$ and $\tau_{e2} = 172$ seconds. To enable a clear comparison with the form of $F_{\mathcal{A}3}(t)$, the origins of both $F_{\mathcal{A}1}(t)$ and $F_{\mathcal{A}2}(t)$ at $F(0)$ have been shifted to coincide with $F_{\mathcal{A}3}(t)$. The relaxation profiles of both $F_{\mathcal{A}1}(t)$ and $F_{\mathcal{A}2}(t)$ have also been removed for clarity. The possible reason for these variations in rise times is discussed later in section 7.2.5.

7.2.2.2 Determining bead collections from fluorescence

To enable quantitative comparisons with theoretical predictions, differences in the normalised fluorescence $\Delta F(120) = F(120) - F(0)$, were calculated. These are listed in Table 7.1(b). The normalised relative fluorescence, given by (3.6.15), was also computed, $\Delta F_r(120) = F(120)/F(0) - 1$ This was done in view of the abovementioned variations in the values chosen for the integers i_l and i_u, between imaged-processed experiments. However, as shown in the table, the $F(0)$ values are all close to unity and $\Delta F_r(120) \cong \Delta F(120)$ so it was satisfactory to base collections on $\Delta F(120)$ values.

Values for the initial collection rates $F(0)$ were computed using (7.1.7) and listed amplitudes F_1 and F_2 and times τ_1 and $\tau_{2,}$. The rates, listed in Table 7.1(b), are somewhat higher than those for $\delta F/\delta t$ in Table 7.1(a). This is not surprising since $\delta F/\delta t$, which was determined over the first 4 to 5 seconds, would be a closer estimate of $\dot{F}(2)$ than $\dot{F}(0)$. To verify this supposition, values of $\dot{F}(2)$ were computed using $t = 2$ in (7.1.6) and substituted with $\delta F/\delta t$ to determine the relative error, $\varepsilon_{\dot{F}}(2)$ via (7.1.8). The relative errors, $\varepsilon_{\dot{F}}(2)$, listed in Table 7.1(b), are mostly

small. Thus, one can be reasonably confident that $\dot{F}(0)$ values are in the correct range and concur with rise amplitudes and times.

The parameters $\dot{n}_e(0)/n_e(0)$ and $\Delta n_e(120)/n_e(0)$ were evaluated using equations (7.1.15) and (7.1.19). The fluorescence constant k was estimated by mapping the average change in number of beads, Δn_e, counted along 248 μm long electrode edges versus fluorescence intensity change ΔF for selected frames (or times t_j). The relation between ΔF and Δn_e is mapped in Fig. 7.2(a) for two sets of data as listed, and was fitted to a second order polynomial using Origin 4.1™. The relationship between Δn_e and ΔF is linear for low Δn_e. For high ΔF, however, individual beads lying on the electrode edges in groups or clusters are practically impossible to distinguish. Therefore, the value of the constant was taken from the linear term in the polynomial, $k = 1/860$. The clustering of beads is shown in video frame in Fig. 7.2(b). The frame corresponds to the largest data point P_1 in Fig. 7.2(a).

V_o (V)	f (MHz)	$\Delta F(120)$ $\times 10^{-2}$	$\Delta F_r(120)$ %	$\dot{F}(0)$ $\times 10^{-2}$	$\varepsilon_{\dot{F}}(2)$ %	$\frac{\dot{n}_e(0)}{n_e(0)}$	$\frac{\Delta n_e(120)}{n_e(0)}$	τ_{e1} (s)	τ_{e2} (s)
2	0.5	20.1	20.3	3.1	5.3	9.4	55	4.1	220
2	1	16.7	17.0	2.9	7.6	8.9	48	2.9	35
2	2	10.1	10.3	1.5	4.7	4.6	29	2.9	17
4	2	21.6	22.0	5.9	10	18	62	2.3	17
2	2	11.0	11.2	1.3	7.2	4.1	32	5.8	88
1	2	1.47	1.48	0.51	20	1.6	4.2	3.5	--

Table 7.1(b) Experimental frequency and voltage dependent DEP particle collections.

Clearly, there are also edge segments where there is an absence of beads. The statistics of the positions of beads has not been analysed though it would be interesting to do so. At this stage, from repeated observation, it appears there are variations in bead density due to variations in electrode edge definition during micro-fabrication.

The number of beads counted along the electrode edges, before DEP experiments were started, varied from $n_e(0) = 2.6$ to 4.2 beads per 248 μm edge. Assuming a depth-of-focus $\Delta y = 1$ μm and transverse interval $\Delta x = 1.6$ μm the expected number of beads observed along a 248 μm electrode edge, before and immediately when DEP collection starts, is $n = c_V \Delta V = c_V \Delta x \Delta y \Delta z = 3.6 \times 1.6 \times 248 \cong 1.4$ beads. Thus, the above counts were up to twice to three times the theoretical value. Such variation is not unusual so a nominal value of $n_e(0) = 2.8$ beads was used for evaluating $\dot{n}_e(0)/n_e(0)$ and $\Delta n_e(120)/n_e(0)$ in Table 7.1(b).

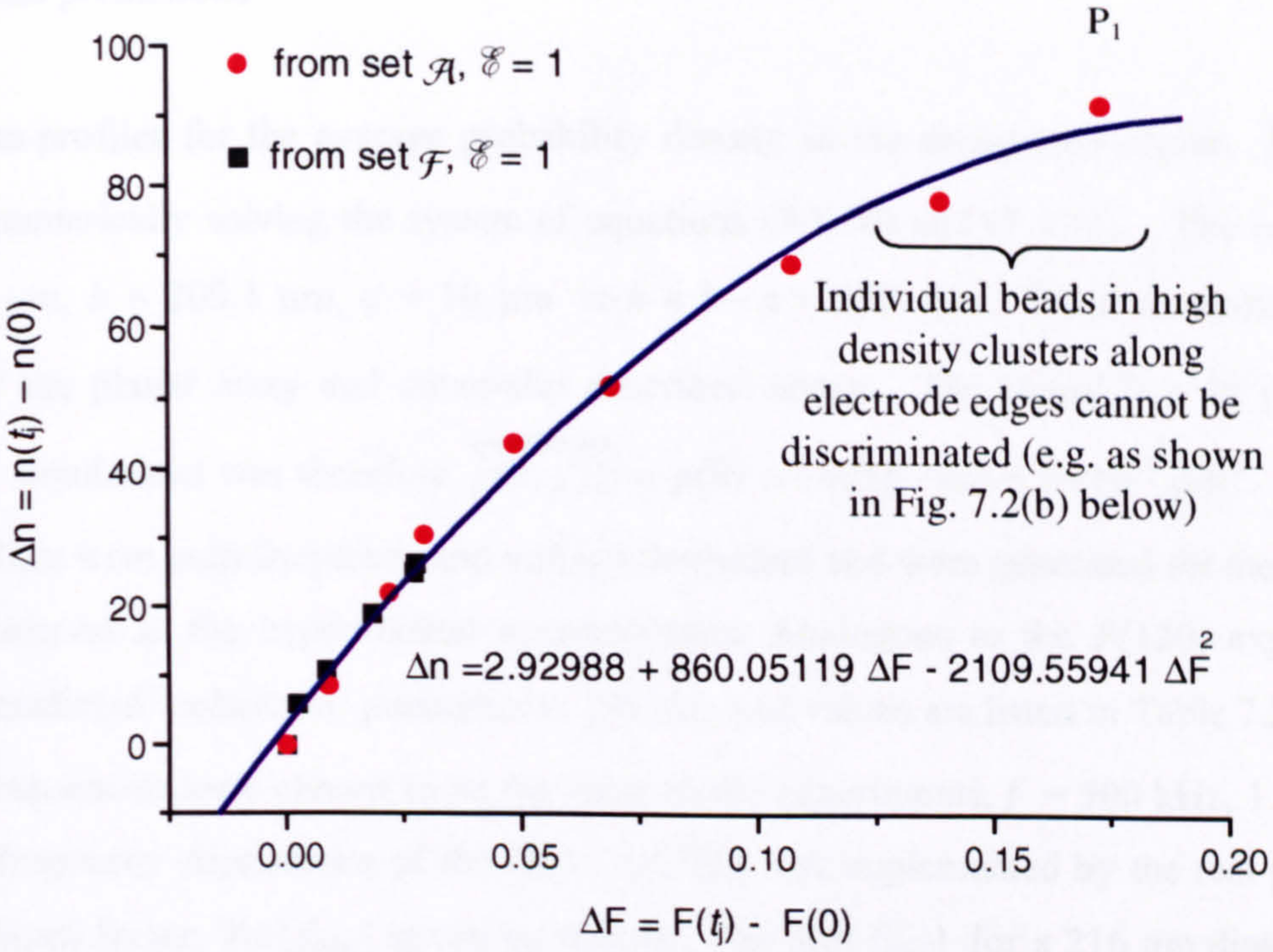

Fig. 7.2(a) Relationship between change in average bead number Δn_e (collected on electrode edges) and change in fluorescence ΔF.

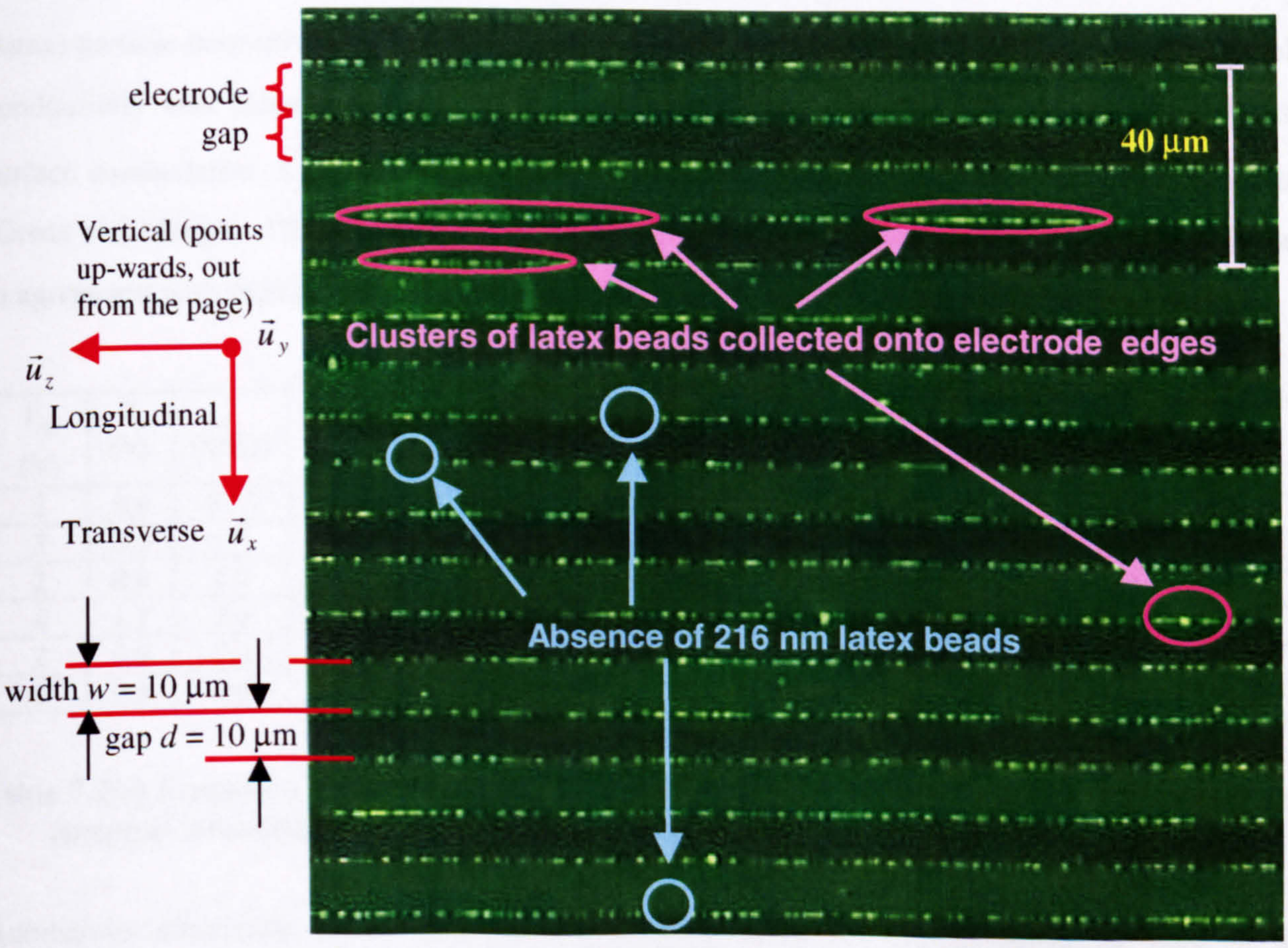

Fig. 7.2(b) A video frame of 216 nm diameter beads collecting 133 seconds after onset of DEP - corresponding to data point P_1 in Fig. 7.2(a) above. The image shows variation in bead distribution along electrode edges. Individual beads are indistingishable along high density segments.

7.2.3 Theoretical predictions

Collection time-profiles for the average probability density in the designated region, $\overline{\overline{p}}(t)$, were generated by numerically solving the system of equations (7.1.10) and (7.1.11). The cell lengths were a = 0.1 μm, b = 200.1 μm, d = 10 μm $\Rightarrow h = b-a$ = 200 μm. These correspond to the dimensions of the planar array and cover-slip described above. The *initial* (t = 0) probability density for all simulations was therefore $\overline{\overline{p(x,y,0)}} = p(0) = 1/(d(b-a)) = 5\times10^{-4}$ μm^{-2}. The $\overline{\overline{p}}(t)$ collection profiles were both frequency and voltage dependent and were generated for the same 120 second time interval as the experimental measurements. Analogous to the $F(120)$ experimental values, a key predicted 'collection' parameter is $\overline{\overline{p}}(120)$, and values are listed in Table 7.2(a).

The frequencies were chosen to be the same as the experiments, f = 500 kHz, 1 MHz, and 2 MHz. The frequency dependence of the FPE (7.1.10b) was implemented by the real part of the Claussius-Mossotti factor, Re$\{f_{CM}\}$ given by (2.2.4). The Re$\{f_{CM}\}$ for a 216 nm diameter latex micro-sphere is plotted in Fig. 7.3(a) using r = 108 nm, medium conductivity σ_m = 1.7 mS/m, particle conductivity σ_p = 18.5 mS/m, medium permittivity for water at 25°C, $\varepsilon_m = 78.4\varepsilon_o$, and (latex) particle permittivity, $\varepsilon_p = 2.55\varepsilon_o$ where ε_o = 8.854×10^{-12} F m^{-1}. The value for the particle conductivity was calculated from (2.2.10) with conductivity of the bulk (latex) σ_b = 0, and surface conductance, K_s = 1.0 nS. This value is reduced slightly from the value determined by (Green and Morgan, 1997a). It yields a cross-over frequency slightly above 3 MHz in Fig. 7.3(a), in agreement with experimental observations that no DEP collections occurred for $f \geq 3$ MHz.

V_{o_e} (V)	V_o (V)	f (MHz)	Re$\{f_{CM}\}$	$\overline{\overline{p}}(120)$ (a.u.)	A_{p1} × 10^{-2}	τ_{p1} (s)	A_{p2} × 10^{-2}	τ_{p2} (s)	$\dot{\overline{\overline{p}}}_{lin}(0)$ × 10^{-2}	$\dot{\overline{\overline{p}}}_{Ar}(0)$ × 10^{-2}
2	0.6	0.50	0.7185	0.07424	2.134	4.41	6.638	80.7	0.660	0.566
2	0.6	1.0	0.5925	0.06713	1.865	4.98	6.178	83.6	0.544	0.448
2	0.6	2.0	0.2756	0.01011	0.338	2.38	0.612	39.0	0.253	0.158
4	1.2	2.0	0.2756	0.08016	2.405	3.31	6.626	71.0	1.017	0.820
2	0.6	2.0	0.2756	0.01011	0.338	2.38	0.612	39.0	0.253	0.158
1	0.3	2.0	0.2756	0.00102	0.023	0.914	0.021	17.1	0.063	0.026

Table 7.2(a) Frequency and voltage dependent particle collection probability density predicted by computer simulation.

Anomalous simulation results were obtained when using the same voltage as used in the experiments. That is, the simulated DEP force was so strong as to cause the numerical FlexPDE solver to become unstable and prone to error. This situation has been discussed in 6.4 and 6.5. A much better fit to the experimental data was obtained by reducing the electrode potential in the

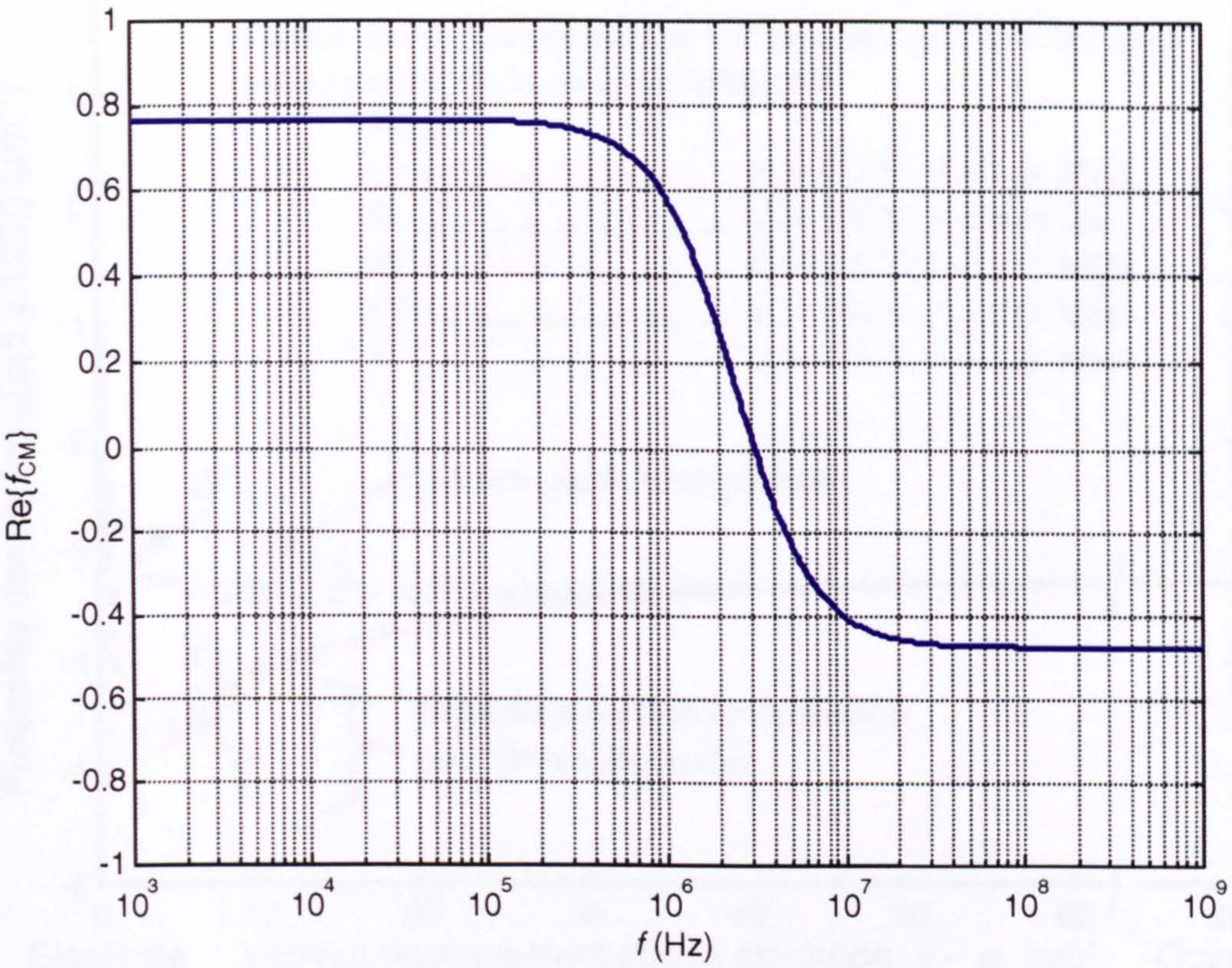

Fig. 7.3(a) Frequency dependent real part of the Claussius-Mossotti function Re{f_{CM}) used for predicting the polarisability of 216 nm diameter latex micro-spheres in low conductivity medium.

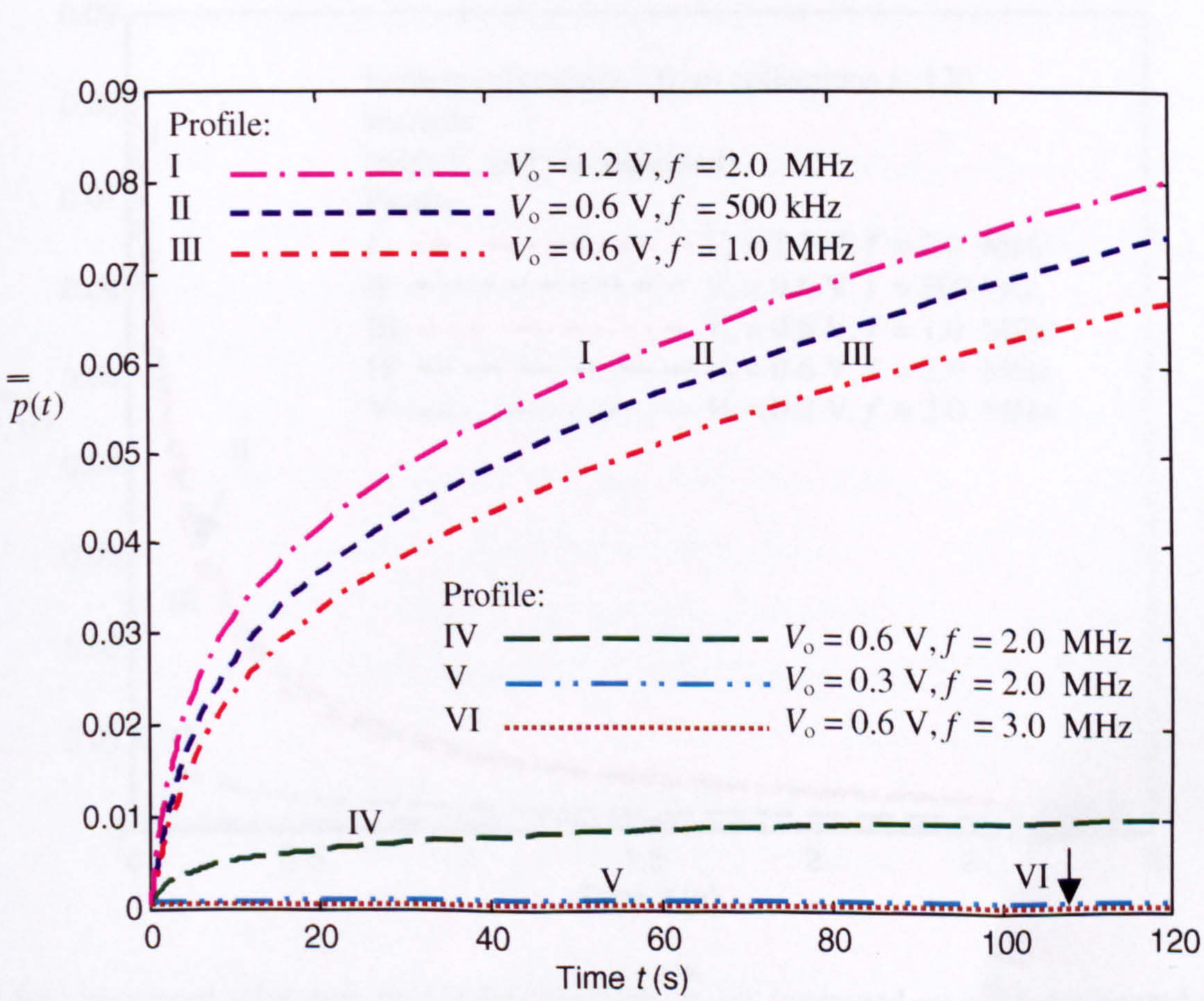

Fig. 7.3(b) Probability density (spatially averaged over a 2-D designated 'collection' region), $\overline{p(t)}$ predicted by computer simulation for peak potential V_o and frequency f as listed.

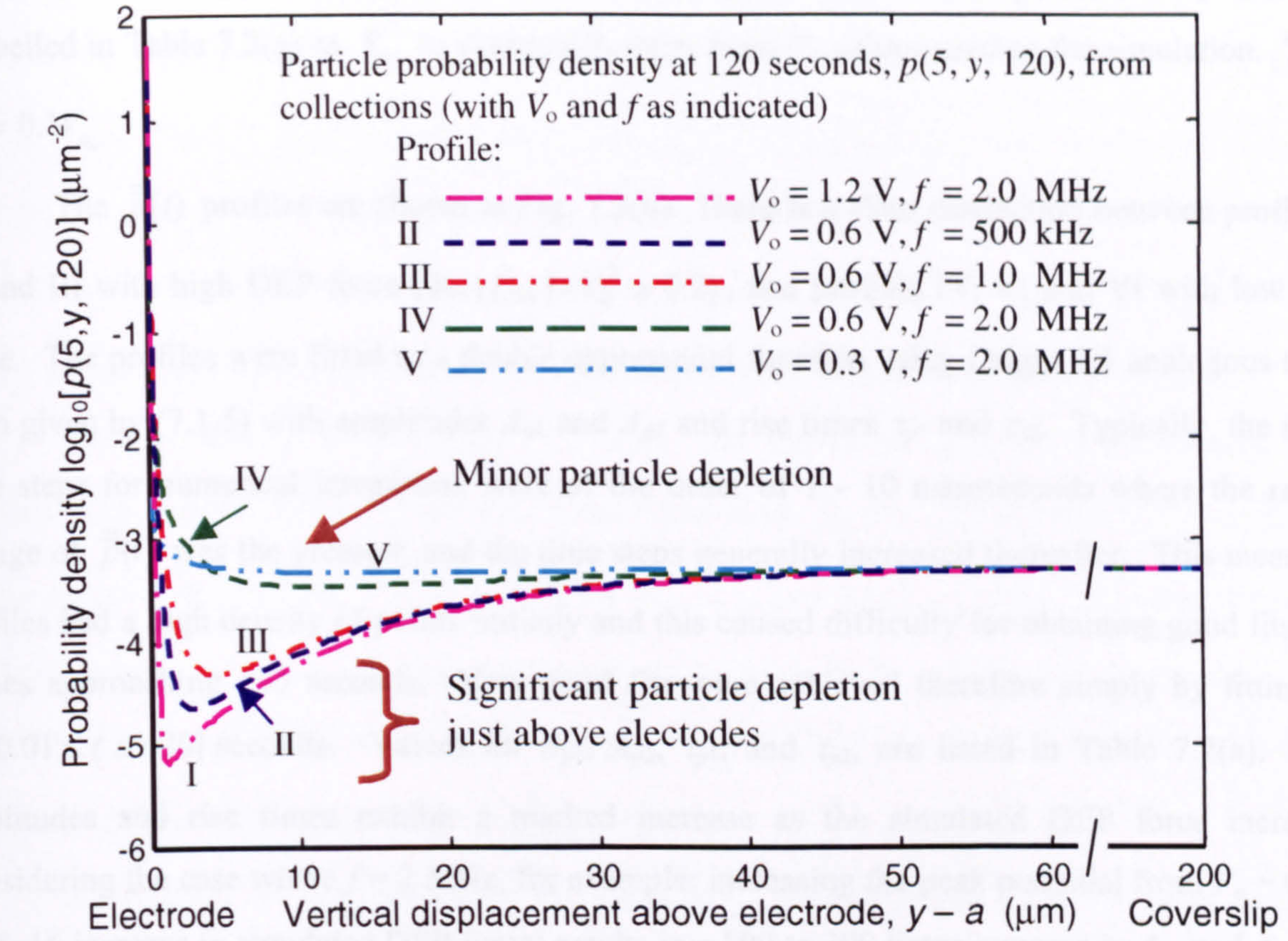

Fig. 7.3(c) Cross-section of particle probability density at transverse position $x = 5$ μm, in direction $\vec{u}_y$, at $t = 120$ seconds from start of collection with potential V_o and frequency f as listed.

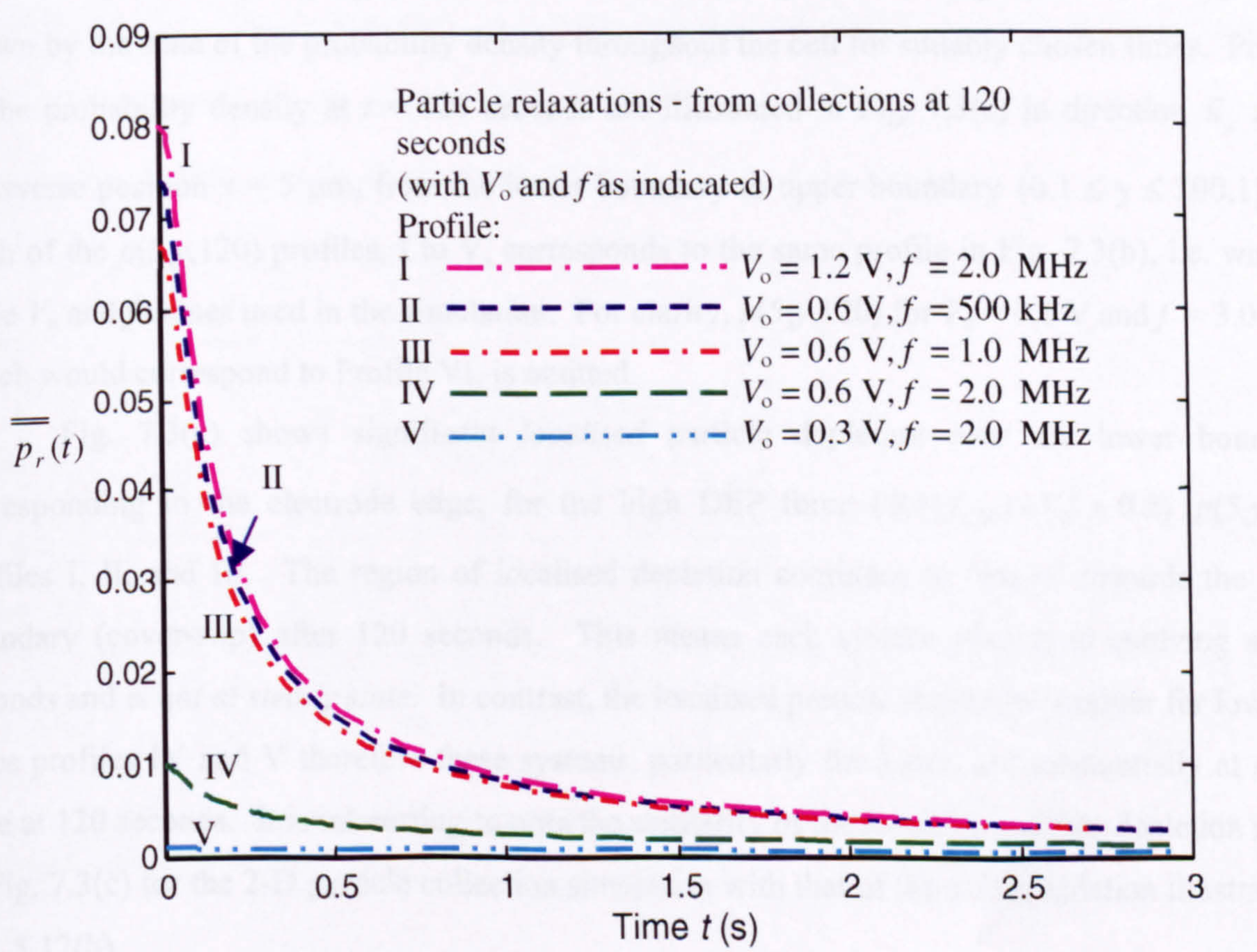

Fig. 7.3(d) Simulated relaxation probability densities $\overline{\overline{p}}_r(t)$ (averaged over the designated region) with initial condition $\overline{\overline{p}}_r(0) = \overline{\overline{p}}(120)$, resulting from collections with V_o and f as listed.

FPE simulation to approximately 30 % of the experimental value. The experimental V_o values are relabelled in Table 7.2(a) as V_{o_e} to distinguish them from V_o values used in the simulation. Thus, $V_o = 0.3V_{o_e}$.

The $\bar{\bar{p}}(t)$ profiles are shown in Fig. 7.3(b). There is a clear distinction between profiles I, II, and III with high DEP force ($\mathrm{Re}\{f_{CM}\}\times V_0^2 > 0.2$), and profiles IV, V, and VI with low DEP force. The profiles were fitted to a double exponential function using Origin 4.1 analogous to the form given by (7.1.5) with amplitudes A_{p1} and A_{p2} and rise times τ_{p1} and τ_{p2}. Typically, the initial time steps for numerical integration were of the order of 1 - 10 nanoseconds where the rate of change of $\bar{\bar{p}}(t)$ was the greatest, and the time steps generally increased thereafter. This meant the profiles had a high density of points initially and this caused difficulty for obtaining good fits for t values approaching 120 seconds. Very good fits were achieved therefore simply by fitting for $\{t : 0.01 \le t \le 120\}$ seconds. Values for A_{p1}, A_{p2}, τ_{p1}, and τ_{p2}, are listed in Table 7.2(a). Both amplitudes and rise times exhibit a marked increase as the simulated DEP force increases. Considering the case where $f = 2$ MHz, for example: increasing the peak potential from $V_o = 0.3$ to 1.2 (×16 increase in simulated DEP force) results in a 100 to 300 times increase in A_{p1} and A_{p2}, and a three to four fold increase in τ_{p1} and τ_{p2}.

The effect of varying the simulated DEP force, by values assigned to V_o and f, is also shown by the state of the probability density throughout the cell for suitably chosen times. Profiles of the probability density at t = 120 seconds are illustrated in Fig. 7.3(c) in direction $\vec{u}_y$ at the transverse position x = 5 μm, from the lower boundary to upper boundary $\{0.1 \le y \le 200.1\}$ μm. Each of the $p(5,y,120)$ profiles, I to V, corresponds to the same profile in Fig. 7.3(b), i.e. with the same V_o and f values used in the simulation. For clarity, $p(5,y,120)$ for $V_o = 0.6$ V and $f = 3.0$ MHz which would correspond to Profile VI, is omitted.

Fig. 7.3(c) shows significant *localised* particle depletion near the lower boundary, corresponding to the electrode edge, for the high DEP force ($\mathrm{Re}\{f_{CM}\}\times V_0^2 > 0.2$) $p(5,y,120)$ profiles I, II, and III. The region of localised depletion continues to 'move' towards the upper boundary (cover-slip) after 120 seconds. This means each system $p(x,y,t)$ is evolving at 120 seconds and is *not at steady state*. In contrast, the localised particle depletion is minor for low DEP force profiles IV and V therefore these systems, particularly the latter, are substantially at steady state at 120 seconds. It is interesting to note the similarity of the *localised* particle depletion region in Fig. 7.3(c) for the 2-D particle collection simulation with that of the 1-D simulation illustrated in Fig. 5.12(b).

The initial time rate of change of the probability density was determined by a very good linear fit of $\bar{\bar{p}}(t)$ using Origin 4.1™ over the initial time interval up to nearly 0.01 second, $0 \le t < 0.01$. The estimation of $\dot{\bar{\bar{p}}}(0)$ using this method is denoted by $\dot{\bar{\bar{p}}}_{lin}(0)$. As a check, $\dot{\bar{\bar{p}}}(0)$

values were also determined using predicted amplitudes and times in the derivative of the double exponential, $\dot{\bar{\bar{p}}}_{A\tau}(0) = A_{p1}/\tau_{p1} + A_{p2}/\tau_{p2}$, analogous to (7.1.7). Comparing the values of $\dot{\bar{\bar{p}}}_{lin}(0)$ and $\dot{\bar{\bar{p}}}_{A\tau}(0)$ in Table 7.2(a), it is clear they generally agree particularly for simulations with high DEP forces. This is not surprising given that profiles with low forces were more difficult to fit. As expected from (7.1.16), the numerically generated ratios of $\dot{\bar{\bar{p}}}_{lin}(0)$ concurred with ratios of the product, $\mathrm{Re}\{f_{CM}\}\times V_0^2$. On the other hand the ratios of $\dot{\bar{\bar{p}}}_{A\tau}(0)$ did not agree as closely.

Using relations (7.1.14) and (7.1.18), the predicted particle number parameters $\dot{n}_p(0)/n_p(0)$ and $\Delta n_p(120)/n_p(0)$ were determined from $\dot{\bar{\bar{p}}}_{lin}(0)$, $\bar{\bar{p}}(120)$ and $p(0)$ values. The values are compiled in Table 7.2(b) along with V_{o_e}, V_o, f and $\mathrm{Re}\{f_{CM}\}\times V_0^2$. The latter determines the DEP force – given that all other parameters are held constant. Table 7.2(b) shows clearly how the particle rate parameter, $\dot{n}_p(0)/n_p(0)$, predicted by simulation, changes proportionally to the DEP force governed by the product $\mathrm{Re}\{f_{CM}\}\times V_0^2$.

In contrast, the particle collection parameter, $\Delta n_p(120)/n_p(0)$, is far more sensitive. Considering the case where $f = 2$ MHz, for example: increasing the peak potential from $V_o = 0.3$ to 1.2 results in a ×16 increase in $\dot{n}_p(0)/n_p(0)$ and approximately ×154 increase in $\Delta n_p(120)/n_p(0)$. This is true for V_o values that coincide, as much as possible, to the experimental values ranging over a couple of volts. This sensitivity of $\Delta n_p(120)/n_p(0)$ is much less, however, when the range of V_o is reduced to several millivolts (mV) in the simulation.

Collection								Relaxation			
V_{o_e} (V)	V_0 (V)	f (MHz)	$\mathrm{Re}\{f_{CM}\}\times V_0^2$	$\frac{\dot{n}_p(0)}{n_p(0)}$	$\frac{\Delta n_p(120)}{n_p(0)}$	τ_{p1} (s)	τ_{p2} (s)	$A_{p3}\times 10^{-2}$	τ_{p3} (s)	$A_{p4}\times 10^{-2}$	τ_{p4} (s)
2	0.6	0.50	0.2587	13.2	147.5	4.41	80.7	6.64	0.223	0.745	2.93
2	0.6	1.0	0.2133	10.9	133.3	4.98	83.6	5.92	0.217	0.759	2.68
2	0.6	2.0	0.0992	5.06	19.21	2.38	39.0	0.708	0.208	0.237	2.63
4	1.2	2.0	0.3969	20.3	159.3	3.31	71.0	7.23	0.208	0.922	2.43
2	0.6	2.0	0.0992	5.06	19.21	2.38	39.0	0.708	0.208	0.237	2.63
1	0.3	2.0	0.0248	1.27	1.037	0.914	17.1	0.031	0.292	0.019	6.11

Table 7.2(b) Frequency and voltage dependent particle collections and relaxations predicted by computer simulation.

The particle probability density relaxations corresponding to each collection profile I to V are illustrated in Fig. 7.3(d). Most of the profiles were fitted best by a double, rather than a single, exponential function using Origin 4.1™. The values for amplitudes A_{p3} and A_{p4}, and fall times τ_{p3} and τ_{p4}, are listed in Table 7.2(b). The relaxations started immediately after the collections stopped

at 120 seconds, hence, the relaxation IC was $p_r(x,y,0) = p(x,y,120)$. The τ_{p3} and τ_{p4} values relaxing from collections with a weak DEP force are *greater* than those from a strong DEP force. As expected A_{p3} and A_{p4} resulting from simulating the strong force are greater than those values arising from the weak DEP force. Compare the relaxation data, for example, from the collections with f = 2 MHz where the peak potential increased from V_o = 0.3 to 1.2 V (×16 increase in simulated DEP force). The fall times decrease from τ_{p3} = 0.292 to 0.208 s, and τ_{p4} = 6.11 to 2.43, seconds.

Comparing the collection data with the relaxation data, the rise times, τ_{p1} and τ_{p2}, are longer than the fall times τ_{p3} and τ_{p4}, respectively. This is particularly so when the simulated DEP force is high. For example, the case where f = 2 MHz and V_o = 1.2 V collection and subsequent relaxation shows $\tau_{p1} > 10\times\tau_{p3}$ and similarly $\tau_{p2} > 10\times\tau_{p4}$. In contrast, when the DEP force is low, the rise times are much closer to the fall times. Compare, for example, the collection with f = 2 MHz and V_o = 0.3 V and subsequent relaxation: $\tau_{p1} \cong 3\times\tau_{p3}$ and $\tau_{p2} \cong 3\times\tau_{p4}$. This observation is interesting because similar dynamics are exhibited for the 1-D dielectrophoretic collection and relaxation system discussed in Chapter 5, section 5.6. Simulated particle collections under the action of *strong* DEP force exhibited a 'state transition' of the probability density with respect to the relaxed uniform distribution of particles, with large density changes near the boundaries and $\tau_{rise} >> \tau_{fall}$. On the other hand particle collections under *weak* DEP forces exhibited a perturbation of the probability density with respect to the relaxed uniform distribution of particles, with small density changes near the boundaries, and $\tau_{rise} \approx \tau_{fall}$.

7.2.4 Comparison of experiments and predictions

The data from experiments, Table 7.1(b), and simulations, Table 7.2(b), is combined into Table 7.3(a) for comparison (the simulation values have been reduced to two significant figures). Inspection of columns 3 and 8 shows the values for the experimental initial particle rates $\dot{n}_e(0)/n_e(0)$ generally concur with those predicted $\dot{n}_p(0)/n_p(0)$ for f and V_o as stated.

f (MHz)	Experiment					2-D FPE simulation				
	V_{o_e} (V)	$\frac{\dot{n}_e(0)}{n_e(0)}$	$\frac{\Delta n_e(120)}{n_e(0)}$	τ_{e1} (s)	τ_{e2} (s)	V_o (V)	$\frac{\dot{n}_p(0)}{n_p(0)}$	$\frac{\Delta n_p(120)}{n_p(0)}$	τ_{p1} (s)	τ_{p2} (s)
0.5	2	9.4	58	4.1	220	0.6	13	150	4.4	81
1	2	8.9	48	2.9	35	0.6	11	130	5.0	84
2	2	4.6	29	2.9	17	0.6	5.1	19	2.4	39
2	4	18	62	2.3	17	1.2	20	160	3.3	71
2	2	4.1	32	5.8	88	0.6	5.1	19	2.4	39
2	1	1.6	4.2	3.5	--	0.3	1.3	1.0	0.91	17

Table 7.3(a) Comparison of experimental and predicted particle collections.

It is important to note that the ratios $\dot{n}_e(0)/n_e(0)$ for the experiments are not exactly proportional to $\mathrm{Re}\{f_{CM}\}\times V_o^2$ in contrast to the predicted $\dot{n}_p(0)/n_p(0)$. Consider the data in rows 1 and 3, for example, where the frequency increases from 0.5 MHz to 2 MHz, and the peak potential remains constant ($V_{o_e} = 2$, $V_o = 0.3$ V). The $\dot{n}_e(0)/n_e(0)$ value reduces from 9.4 to 4.6, a factor of 2.0 whereas $\dot{n}_p(0)/n_p(0)$ reduces by 2.5. Similarly, with the above example where $f = 2$ MHz and V_o increases by a factor of four; $\dot{n}_e(0)/n_e(0)$ increases ×11 whereas $\dot{n}_p(0)/n_p(0)$ increases by ×15. Further comparisons show the same trend.

The simulation predictions of particle collection rates are more sensitive to changes in the DEP force than exhibited by the experimental data. Nonetheless, the general agreement between the experimental and predicted values for potentials, V_o, confirms the voltage and frequency dependence of the collection rates. Furthermore, since the frequency dependence stems from the induced polarisability via the Claussius-Mossotti factor, by implication, the initial collection rates are dependent on the dielectric polarisability of the 216 nm diameter micro-spheres.

The previous section highlighted the sensitivity of $\Delta n_p(120)/n_p(0)$ in comparison to $\dot{n}_p(0)/n_p(0)$ for $1 \le V_o \le 4$ V. This is also the case when comparisons are made with the data from experimental collections at 120 seconds $\Delta n_e(120)/n_e(0)$. In the example where the frequency increases, 0.5 → 2 MHz (so $\mathrm{Re}\{f_{CM}\}$ decreases by ×2.6) and V_o remains constant, $\Delta n_p(120)/n_p(0)$ reduces from 150 to 19, i.e. ×8 reduction. By contrast, $\Delta n_e(120)/n_e(0)$ reduces only by a factor of two. Similarly, for the previous case where $f = 2$ MHz and V_o reduces from 1.2 → 0.3 V, $\Delta n_p(120)/n_p(0)$ reduces by ×160 whereas $\Delta n_e(120)/n_e(0)$ reduces ×15. That is, the relative increases in particle number predicted by simulation can be more than an order of magnitude more sensitive than those experimentally observed.

Arguably this disparity can be reduced by choosing a lower set of peak potentials in the simulation; for example $V_o = 0.23V_{o_e}$ so $V_o = \{0.23, 0.46, 0.92\}$ is used instead of $V_o = \{0.3, 0.6, 1.2\}$. However, this would then compromise the agreement between values with medium strength DEP force, such as, for the case where $f = 2$ MHz, $V_o = 0.6$ that results in $\Delta n_p(120)/n_p(0) = 19$. Since, this value compares with $\Delta n_e(120)/n_e(0) = 32$, further reducing V_o would increase the disparity between these two values. The current agreement between $\dot{n}_p(0)/n_p(0)$ and $\dot{n}_p(0)/n_p(0)$ values would also be compromised. In general, the trends in relative collections at 120 seconds determined from experiments, is attributed to the frequency dependent polarisation and voltage. This adds to the evidence provided by the collection rates.

The experimental τ_{e1} rise times broadly agree with those predicted by simulation τ_{p1} but they are less sensitive and the trends are not consistent. The τ_{e1} values for the set (rows 1 to 3), for

example, $\{V_{oe} = 2; f = 0.5, 1, 2\}$, decrease with frequency (DEP force). This trend, however, is clearly not true for $\{f = 2; V_{oe} = 4, 2, 1\}$. On the other hand, τ_{p1} increases with increasing DEP force – notwithstanding minor errors in fitting a double exponential to profiles before t approaches steady state. Similar characteristics apply to the comparison between τ_{e2} and τ_{p2}, except there is less agreement between the values. Thus, one can conclude at this stage, the experimental rise time data do not yield any conclusive evidence regarding the physical mechanisms attributed to the collection rates.

The experimental data for the bead relaxations was fitted best by a single exponential whereas the optimal fit for simulated relaxations was a double exponential. Therefore, to facilitate comparisons between experimental and predicted fall times the amplitudes for the double exponential (simulation data) have been included in Table 7.3(b) below (2 sig. figs.). In cases where $A_{p3} >> A_{p4}$ our interest lies essentially with τ_{p3} and it is clear the experimental fall times, $\tau_{e3} \gtrsim 5\times\tau_{p3}$. That is, the experimental fall times are at least five times longer than predicted by the FPE simulation. This occurs for particle relaxations from collections with high DEP force. Relaxations from collections with low force, on the other hand, exhibit $\tau_{p3} < \tau_{e3} < \tau_{p4}$, so the experimental values are closer to the predicted values from theory. In general, τ_{e3} are not as consistent as the predicted fall times, however, as remarked in section 7.2.2, the experimental fall times are all *less* than the rise times in agreement with the trends predicted by the FPE simulation.

f (MHz)	Experiment				2-D FPE simulation					
	V_{o_e} (V)	$\frac{\Delta n_e(120)}{n_e(0)}$	F_3 $\times 10^{-2}$	τ_{e3} (s)	V_o (V)	$\frac{\Delta n_p(120)}{n_p(0)}$	A_{p3} $\times$ 10^{-2}	τ_{p3} (s)	A_{p4} $\times$ 10^{-2}	τ_{p4} (s)
0.5	2	58	19	1.2	0.6	150	6.6	0.22	0.75	2.9
1	2	48	19	1.6	0.6	130	5.9	0.22	0.76	2.7
2	2	29	9.5	1.4	0.6	19	0.71	0.21	0.24	2.6
2	4	62	22	1.4	1.2	160	7.2	0.21	0.92	2.4
2	2	32	11	1.5	0.6	19	0.71	0.21	0.24	2.6
2	1	4.2	1.5	2.5	0.3	1.0	0.031	0.29	0.019	6.1

Table 7.3(b) Comparison of experimental and predicted particle relaxations.

7.2.5 Discussion

The comparison of the experimental data with predictions from simulations generally confirms the frequency (or effective polarisability) and electrode voltage dependence of dielectrophoretic collections. However, the sensitivity of the initial collection rates, and collections 2 minutes after the onset of DEP, is predicted to be much higher than experimentally observed. This is highlighted by the fact that agreement between the particle numbers is obtained with the electrode potential in

the simulation being ~ 30 % of the experimental value. In addition, the experimentally measured rise times do not show the consistent trend of the predicted rise times that generally increase with DEP force.

In many respects these findings are similar to a preliminary investigation by the author (referenced in *List of publications*) of DEP collections with 216 nm diameter latex spheres suspended in aqueous solution over planar interdigitated electrodes with a 10 μm width and 10 μm gap. These electrodes, described in section 3.2.1.1, were a prototype of those used in this investigation. The peak potential used in the experiments was $V_o = 2$ V and the frequencies were the same as those above. They showed the experimentally determined relative collections over a 40 second observation period, $\Delta n_e(40)/n_e(0)$, also followed the same trend as those predicted by computer simulation. Using a peak potential in the simulation, $V_o = 0.45$ V (or about 23% of the experimental value) the range of experimental collections fell within the range predicted $\Delta n_p(40)/n_p(0)$. The simulation was clearly more sensitive to changes in the DEP force than the experimental data, and the single rise times τ_e did not increase with force as τ_p exhibited. Thus, the anomalies in rise times and sensitivity encountered in this investigation are similar to the preliminary study.

The difference in voltage between theory and experiment leads to about an order of magnitude difference in the forces. The reasons for these disparities are not entirely clear, however, there are at least two attributable effects. The first is that both colloidal particles and DNA contain charge and associated layers of counterions – as described in Chapter 2. The presence of the charges can disturb the local electric field surrounding the particles, and therefore the spatial distribution of charged species within the solution 'cell' should be included in the model of the electric field presented in Chapter 6. In this respect, the use of Laplace's equation (6.1.2) is a first approximation to Poisson's equation (Jackson, 1975) that would otherwise model the electric field more comprehensively by inserting a (non-zero, finite) charge density term on the *rhs* of (6.1.2).

If Poisson's equation was used, the spatially distributed charge density term would require solving the FPE to determine the positions of the particles[2] at a specific instance in time. Since the FPE itself requires the spatial distribution of the electric field, then Poisson's equation and the FPE would need to be coupled together and be mutually consistent. To obtain the temporal evolution of particle concentration would require a step-by-step numerical solution of the coupled PDEs - thus considerably increasing computational complexity. In the current model, the use of Laplace's equation with the *rhs* in (6.1.2) set to zero effectively decouples it from the FPE. This enables a simpler prediction of the spatial-temporal dependent particle concentration, but at the cost of

---

[2] The assignment of 'charges' to particles (colloidal particles or DNA macromolecules) would also need consideration of the effects of counterion screening described in section 2.2.

accuracy since the influence of particle charge on the electric field and subsequent distortion of the DEP force, is ignored.

Particle levitation experiments by Markx *et al.*, (1997) and Cui *et al.*, (2001) have shown that the actual field experienced by the particles is close to the theoretical value in the far field. This indicates that the electric field, without particles in close proximity to the edges of the interdigitated electrodes[3], behaves as predicted and effects, such as, electrode polarisation are unlikely to be the cause of the discrepancy between simulation and experiment. It is interesting to note that the parameter where theoretical predictions and experiments disagree the least is the initial particle collection rate. The measurement of the initial collection rate occurs when the particle concentration around the electrode edges is uniform and in terms of the temporal collection, a minimum. Therefore the distortion of the electric field (and subsequently the DEP force) would also be minimal compared with the system after particles have collected. This suggests that the abovementioned coupling of the FPE with Poisson's equation may lead to a better agreement between simulations and experiment. Parenthetically, the FPE model (7.1.10b) ignores interactions between particles, but this is unlikely to lead directly to the large discrepancies since many beads collected individually on the electrodes and the bead concentration was low. The situation where there are particle-particle interactions is more applicable to DNA plasmid collections and is described in the next section.

The second possible reason for the disparity is due to fluid motion over the surface of the electrodes. Inspection of bead trajectories has indicated the presence of vertical circular fluid motion in the transverse plane. This tends to drag beads down (from the suspension above the electrodes) into the centre of each electrode gap, propel them away from the electrode edge towards the centre of the electrodes, and thence upwards (Ramos *et al.*, 1998; Ramos *et al.*, 1999; Green *et al.*, 2000a; Green *et al.*, 2000b). It is possible that the effect of fluid motion reduces the net accumulation of beads at the electrode edges.

7.3 DEP collections and relaxations of pTA250 DNA

The collections and relaxations of pTA250 DNA were performed using essentially the same experimental set-up as described in section 7.2 for the 216 nm diameter micro-spheres. The DDS, amplifier, microscope, and video processing arrangements, etc., were the same but the experiments predated those reported in section 7.2 and were less developed in terms of stringency in parameters and buffering from mechanical vibrations. After the plasmids had collected and appeared not to be collecting any further, other regions of the array were visually inspected to verify that the

---

[3] Particle levitation experiments use negative DEP. Hence, particles move away from the regions of greatest electric field intensity gradient - located at the interdigitated electrode edges - up to a plane significantly far above the array.

collections recorded were typical of the entire array. The plane of focus was also raised up to the plane of the cover-slip to verify the presence of suspended plasmids. This meant that the relaxations, after the DEP force was switched off, were not as comprehensively measured compared with latex beads.

In addition, the microscope arrangement was susceptible to vibrations up to a second after manually switching on (and off) the electrode potentials. This resulted in a small amount of overshoot at the beginning of collection (and undershoot at the start of relaxation) of the fluorescence arising from micron-scale mechanical perturbation of the mounted array with respect to the microscope objective. For most experiments this was not a major hindrance but it did limit the number of experiments that could be appropriately analysed. The vibration problem was later eradicated for the latex micro-sphere collections by suitable cushioning of the microscope and electrical switching apparatus.

The 8 separately addressable interdigitated array was of the same design as described in section 3.2.1.1 and illustrated in figures 3.1(b) and 3.2(b). It had the same longitudinal and transverse electrode dimensions, $w = d = 10$ μm. However, the height h of the 18 mm × 18 mm cover-slip (used to reduce solvent evaporation) above the electrode plane was not as well controlled as described for the micro-sphere experiments.

7.3.1 Preparations of DNA and experimental measurements

The purification and preparation of pTA250 DNA plasmids for DEP experiments has been described in section 3.3. Each set of experiments used 2 μl of stock DNA stored in double distilled water ($pDNA_{ddw}$, as described in section 3.3.1) added to 2 μl of anti-bleaching agent (10% 2-Mercaptoethanol, section 3.3.6) and 2 μl of fluorescent dye (1 mg/ml DAPI stock, section 3.3.3). The 6 μl suspension of fluorescently stained pTA250 DNA was diluted with 14 μl of RO water and the 20 μl droplet was viewed briefly under a UV lamp to confirm DNA content (described in section 3.3.5.2). The 20 μl aliquot was transferred to the interdigitated electrode array and enclosed by a glass cover-slip, 18 mm × 18 mm. The final height of the cover-slip above the electrode array was calculated, $h = 20/18^2 = 0.062$ mm $\cong 60$ μm.

As for the micro-spheres, the plasmid collections tended to vary over the area of an array observed, so collections and relaxations were performed in *sets* of experiments. As described in chapter 3, however, the DNA tends to aggregate and the content is less reliable. Consequently the dependency of the collections was investigated for one independent variable, frequency f. In each set, *approximately* the same area of the array was used to record particle collections (and relaxations) for as many different frequencies as possible. In contrast to the micro-sphere collections, however, the *precise* region of the array imaged under the microscope was changed from experiment-to-experiment to avoid fluorescence quenching that occurred over the timescale of

several minutes. The potential was held constant for each set of experiments $V_o \sim 4.5$ V and frequencies ranged from 100 kHz to 20 MHz. In each experiment, a particle *collection* was observed for 1 – 2 minutes, followed by particle *relaxation* (DEP force switched off, $V_o = 0$ V), observed for 30 – 60 seconds.

In most DEP experiments, particularly at low frequencies, $f \leq 500$ kHz, the plasmid collections tended to fill the entire gap between the electrodes, as shown in Fig. 7.4. Figures 7.4(a) and (b) are half-width video images, of exactly the same array area, juxtaposed to show the movement of DNA away from the electrode surfaces to the inter-electrode gaps after the onset of DEP. The reason for using half-width frames is simply to give enough clarity and emphasise the contrast in fluorescence due to the movement of the DNA. The frames have also been cropped vertically for layout. The plasmids tended to be amorphous or cloudy in appearance. During this experiment there was minor movement of DNA mainly in the longitudinal direction due to fluid movement. The bridging of the plasmids across the gap for frequencies in the range $f = 100 - 200$ kHz indicates the presence of pearl chains that are likely to form for moderately high DEP forces (Llamas *et al.*, 1998; Giner *et al.*, 1999).

7.3.2 Experimental results

To adequately characterise DNA accumulation, the designated transverse interval was chosen from the electrode edge, x_e, to the maximum length of the cell (midway across the gap), x_c. Hence, the designated collection region in the transverse direction spanned from *lower* limit $x_l \cong x_e = w/2 = 5$ μm to the *upper* limit $x_u = x_c = w/2 + d/2 = 10$ μm. The designated transverse interval characterising the collections was therefore, $\Delta x = x_u - x_l \cong 5$ μm. One of the consequences of $\Delta x \cong 5$ μm for these collections is that the deviation of the fluorescence, δ_f, over the time interval $t - t_0$ used in deriving equation (3.6.8), (c.f. Appendix E.3) is much higher than the 10% maximum. This means that it is more appropriate to base the approximation for the experimentally determined change in particle number, $\Delta n_e(t) \cong \Delta F(t)/k$ using the alternative definition for the normalised fluorescence intensity stated in equation (3.5.9). This is

$$F(t) = I_N(t) = \frac{\bar{\bar{I}}_E(t)}{\bar{\bar{I}}_T(t)} \tag{7.3.1}$$

where $\bar{\bar{I}}_T(t)$ is the characteristic $w/2 + d/2$ intensity $\tilde{I}(x,t)$ spatially averaged in the direction $\vec{u}_x$ over the entire or *total* transverse interval $0 \leq x \leq x_c$, and $\bar{\bar{I}}_E(t)$ has been described in 7.1.1.1 and is defined in (3.5.7).

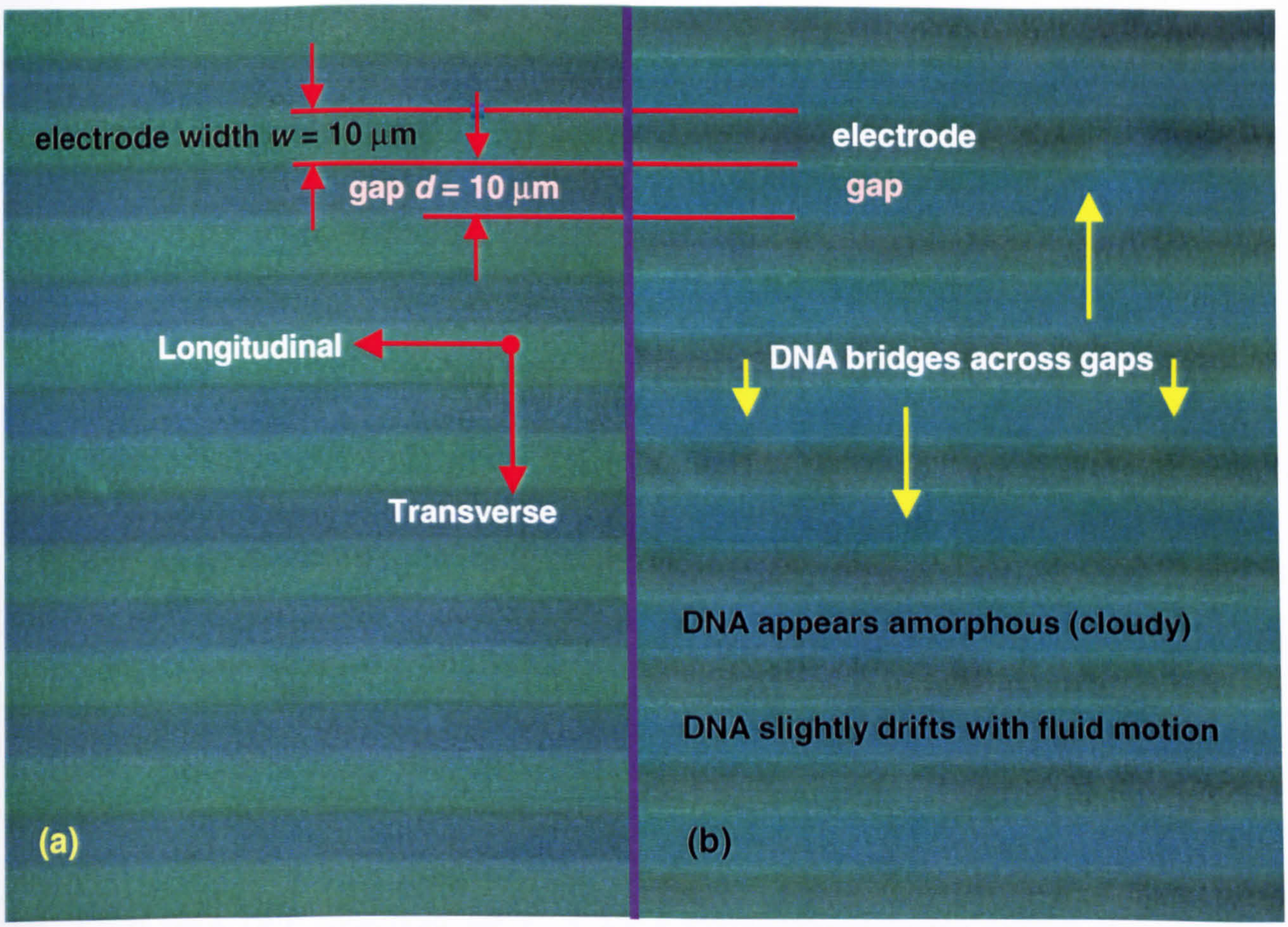

Fig. 7.4 DAPI labelled DNA plasmid suspension – half-frame width video images: (a) before onset of DEP and (b) 4.2 seconds after onset of DEP with $V_o = 4.5$ V, $f = 200$ kHz.

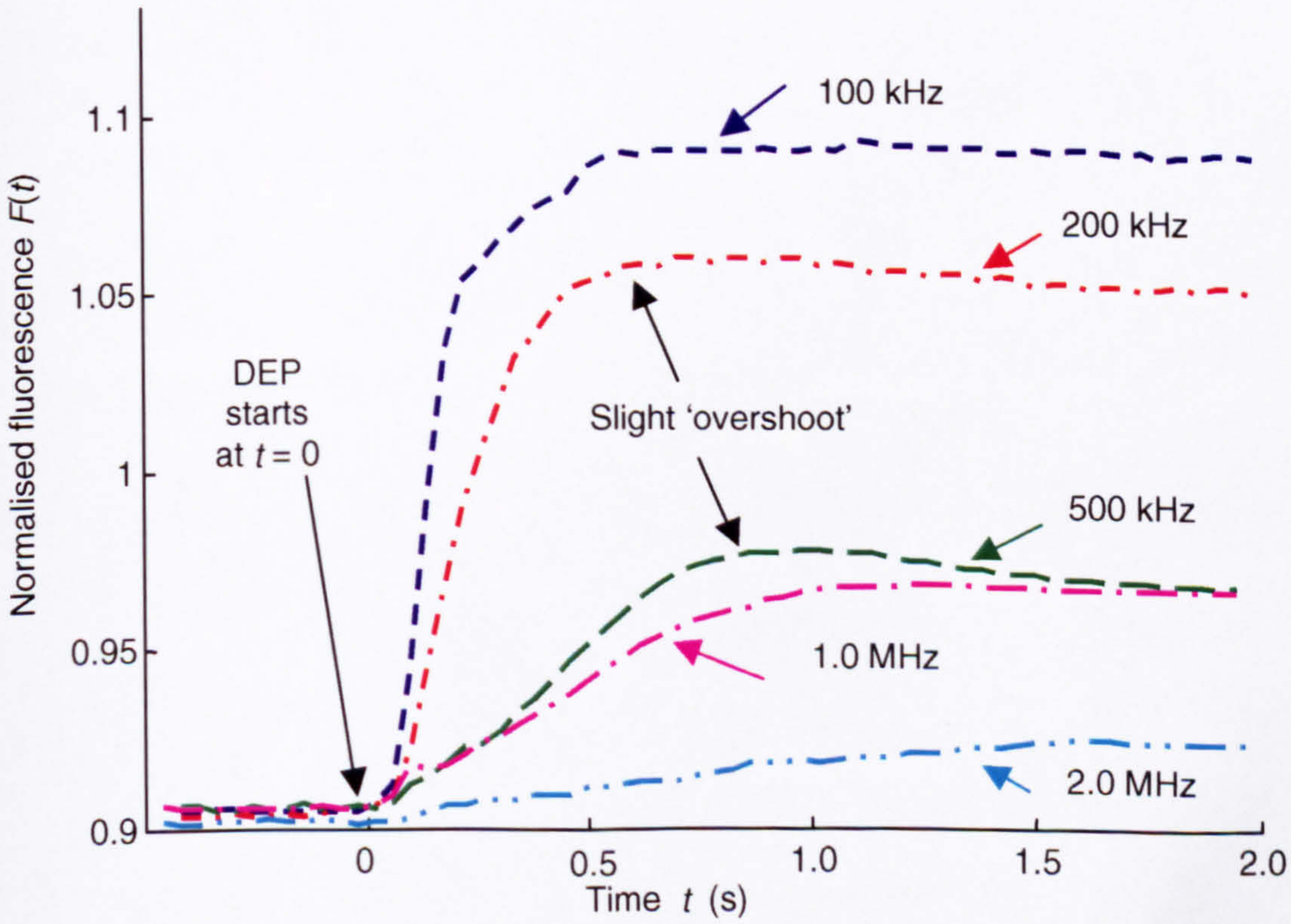

Fig. 7.5(a) DNA DEP collections for $V_o = 4.5$ V (2 ½ second window): profiles of normalised fluorescence $F(t)$ illustrating frequency dependence of initial collection rates (gradients).

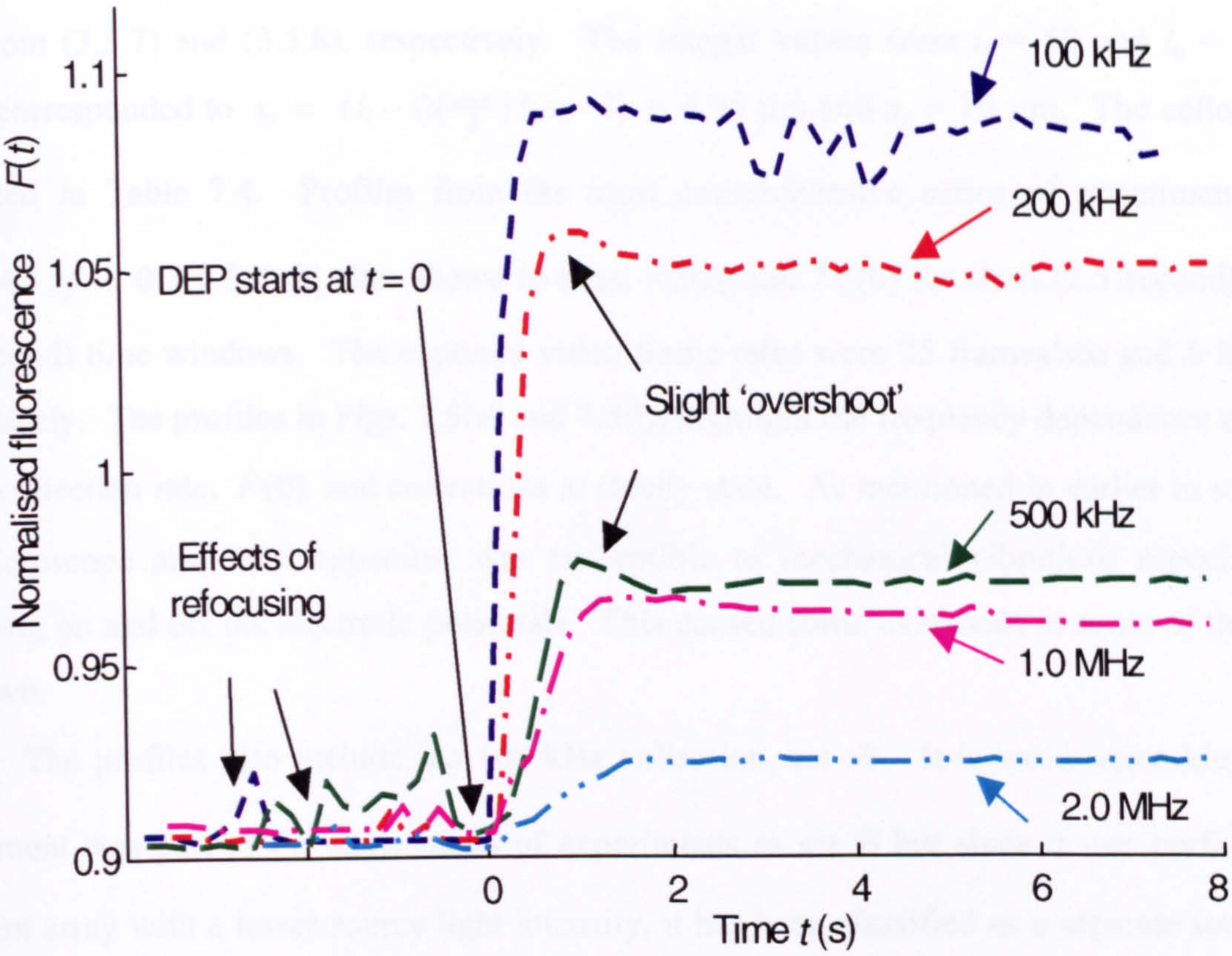

Fig. 7.5(b) DNA DEP collections for V_o = 4.5 V (12 second window): profiles of normalised fluorescence F(t) illustrating the frequency dependence of collections at steady state.

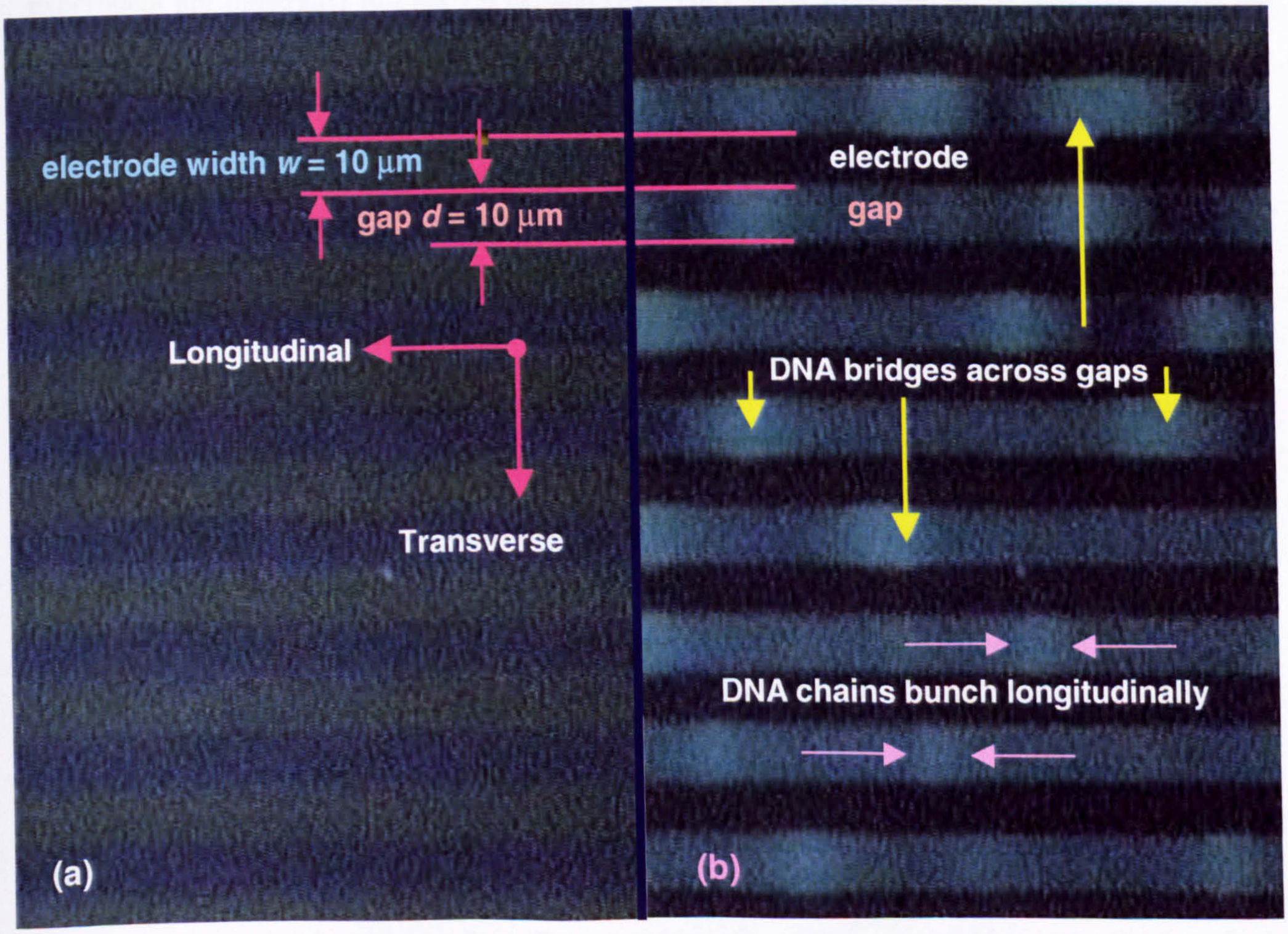

Fig. 7.6 DAPI labelled DNA plasmid suspension: half-frame width images: (a) before the onset of DEP and (b) 0.13 seconds after the onset of DEP with V_o = 4.5 V, f = 100 kHz.

The spatially averaged intensities $\bar{\bar{I}}_E(t)$ and $\bar{\bar{I}}_T(t)$ were evaluated, using the trapezoidal rule, from (3.5.7) and (3.5.8), respectively. The integer values were $i_l = 50$ and $i_u = 100 = n_c$. These corresponded to $x_l = (i_l - 1)(\frac{w+d}{2})/(n_c - 1) = 4.95$ μm and $x_u = 10$ μm. The collection data are listed in Table 7.4. Profiles from the most comprehensive series of experiments, set $\mathcal{B}$ $\{V_o = 4.5; f = 0.2, 0.5, 1, 2\}$, are shown in Figs. 7.5(a) and 7.5(b) for short (2.5 second) and long (12 second) time windows. The captured video frame rates were 25 frames/sec and 5 frames/sec, respectively. The profiles in Figs. 7.5(a) and 7.5(b) highlight the frequency dependence of both the initial collection rate, $F(0)$ and collections at steady state. As mentioned in earlier in section 7.3, the microscope and DEP apparatus was susceptible to mechanical vibrations especially when switching on and off the electrode potentials. This caused some overshoot in some of the profiles, as shown.

The profiles also include the 100 kHz collection, set $\mathcal{A}$. It is worth remarking that this experiment was part of the same series of experiments as set $\mathcal{B}$ but since it was performed on a different array with a lower source light intensity, it has been classified as a separate set. The 100 kHz profiles in Figs. 7.5 (a) and (b) were adjusted (×0.9378) so they matched the $F(0)$ values of set $\mathcal{B}$; the original data is listed in Table 7.4. Two juxtaposed half-width video frames for the 100 kHz experiment are illustrated in Figs 7.6 (a) and (b). They show the build up of plasmids across the inter-electrode gaps after the onset of DEP. Fig. 7.6(b) is similar to Fig. 7.4(b) ($f = 200$ kHz) except the plasmids tend to bunch together, as shown. The experiment was also the last in a series so the chains tended to drift longitudinally due to evaporation of solvent near the cover-slip edges.

Each of the tabulated normalised fluorescence values $F(0)$, was averaged over 3 frames of the 25 frames/sec sequence just before the onset of DEP. The steady state fluorescence $F(\mathrm{T})$ for each set of experiments $\mathcal{A}$ and $\mathcal{B}$ is an average of three $F(t)$ values for each 5 frames/sec sequence, between 6 – 7 seconds after the onset of DEP. As shown in Fig. 7.5(b) this window is suitable for comparing the collections for all frequencies. The results from other sets of experiments, C and $\mathcal{D}$, are also given in Table 7.4. It should be noted that the precise time values T chosen for determining the steady state $F(t)$ are only important in so far as the collection profile has zero gradient, is smooth, and not affected by overshoot. Consequently, the variation in T values listed for sets C and $\mathcal{D}$ is not important and is tabulated essentially for completeness. The chronological order of each experiment $\mathscr{E}$ in each set {} did not appear to have a significant affect and is similarly listed for completeness.

Since all time profiles rapidly reached steady state, one can write $F(T) = F(\infty)$. The tabulated fluorescence changes from initial to steady state were evaluated by the relations, $\Delta F = F(\infty) - F(0)$ and $\Delta F_r = F(\infty)/F(0) - 1$. The values listed in Table 7.4 for the relative change

ΔF_r are close to ΔF so that the latter is a satisfactory metric for comparing DNA collections. As mentioned earlier in section 7.3, the microscope and DEP apparatus incurred some mechanical vibrations especially switching on and off the electrode potentials. The presence of overshoot and limited data meant that fitting of the double exponential function given by (7.1.6) tended to be problematic. Fitting the time profiles to a single exponential function was more successful. However, the most robust method was to find the *experimental rise* time τ_e by finding t such that

$$F(t) = F(0) + \left(F(\infty) - F(0)\right)\left(1 - e^{-1}\right) = F_\tau \qquad (7.3.2)$$

The fluorescence data points at discrete 0.04 second time intervals in the vicinity of F_τ were interpolated using Origin 4.1™ and the τ_e values are listed in Table 7.4.

{}	$\mathscr{E}$	V_o (V)	f (MHz)	$F(0)$ (a.u.)	T (s)	$F(T)$ (a.u.)	$\Delta F(T)$ (a.u.)	ΔF_r %	$\dot{F}(0)$ $\times 10^{-1}$	τ_e (s)
$\mathscr{A}$	-	4.5	0.1	0.96530	6 - 7	1.15220	0.18690	19.4	11.1	0.108
$\mathscr{B}$	4	4.5	0.2	0.90435	6 - 7	1.05062	0.14627	16.2	5.72	0.179
	2	4.5	0.5	0.90615	6 - 7	0.97059	0.06444	7.11	1.00	0.438
	1	4.5	1	0.90609	6 - 7	0.95972	0.05363	5.92	0.737	0.496
	3	4.5	2	0.90210	6 - 7	0.92448	0.02238	2.48	0.155	0.782
$\mathscr{C}$	2	4.4	0.1	0.94125	1.5 - 1.7	1.12243	0.18118	19.2	4.05	0.288
	1	4.4	1	0.93016	6 - 11	0.99406	0.06390	6.87	0.817	0.520
$\mathscr{D}$	1	4.5	0.5	0.93707	2.5 - 3	1.01422	0.07715	8.23	1.80	0.477
	2	4.5	1	0.94835	2.5 - 3	1.00205	0.05370	5.66	0.431	0.810

Table 7.4 Frequency dependent DNA plasmid collections. The fluorescence values are listed to 5 decimal places for completeness.

The values show an interesting increase with frequency or reduction in polarisability. There was less data for the fall times and these are not listed. Three values from set $\mathscr{B}$ were evaluated using the same method as the rise times. They also showed an interesting increase with increasing frequency: from τ_{fall} = 0.31 seconds at 200 kHz to 0.88 seconds at 500 kHz, and 1.0 seconds at 1 MHz. The initial rate of increase of fluorescence for each experiment, $\delta F/\delta t$, was also determined by linear interpolation using Origin 4.1™. Since the data values were very close (0.04 seconds apart) this technique was a good estimator for the initial fluorescence rate,

$$\dot{F}(0) \cong \delta F / \delta t \qquad (7.3.3)$$

and the values are shown in Table 7.4.

Two features are immediately clear from the profiles in Fig. 7.5 and data in Table 7.4. First, the gradient of the initial fluorescence increase, $\dot{F}(0)$, decreases by about an order of

magnitude as the frequency increases by a decade from 100 kHz to 1 MHz. In Table 7.4 there are statistical variations in the data but since the potential is approximately $V_o = 4.5$ V average values can be taken for repeated experiments. Taking the average of two values for the 100 kHz and 500 kHz collections and three values for 1 MHz as listed, the ratios of the initial rates of fluorescence are, $\dot{F}_{100\,\mathrm{kHz}}(0)/\dot{F}_{500\,\mathrm{kHz}}(0) \cong 5.4$ and $\dot{F}_{100\mathrm{kHz}}(0)/\dot{F}_{1\mathrm{MHz}}(0) \cong 11$. The ratios of the fluorescence changes are $\Delta F_{100\ \mathrm{kHz}}/\Delta F_{500\ \mathrm{kHz}} = 2.6$ and $\Delta F_{100\ \mathrm{kHz}}/\Delta F_{1\ \mathrm{MHz}} = 3.2$. The rise time ratios were $\tau_{100\ \mathrm{kHz}}/\tau_{500\ \mathrm{kHz}} = 0.43$ and $\tau_{100\ \mathrm{kHz}}/\tau_{1\ \mathrm{MHz}} = 0.33$ seconds. The collections in the range at 10 - 20 MHz yielded collections along the longitudinal edges too small to be analysed quantitatively and confirmed the trend of a decreasing DEP response with increasing frequency. At 20 MHz, for example, plasmids tended to be attracted to the end edge corners of each interdigitated electrode where the electric field intensity gradient is higher than the longitudinal edges.

The most likely reason for these trends is the reduction in effective polarisability of the plasmid DNA as found using dielectric spectroscopy described in Chapter 4. Values for the effective polarisability per DNA macromolecule were determined for three dispersions lying within the frequency range of these DEP experiments. This enables a comparison of experimental collections with those predicted by simulation - analogous to the latex micro-spheres in section 7.2.4. However, the amorphous, cloudy appearance of the DNA, as illustrated in figures 7.4 and 7.6, means values for the fluorescence constant $k = \Delta F(t)/\Delta n_e(t)$ and initial plasmid number count $n_e(0)$ are difficult to determine. Consequently, values for the experimentally determined plasmid numbers, $\Delta n_e(\infty)/n_e(0)$ and $\dot{n}_e(0)/n_e(0)$, cannot be readily obtained. This limits the comparisons that can be made between experiments and predictions to general trends and sensitivity to electrode potential V_o.

As pointed out in the previous sections, ratios of these parameters corresponding to different experiments (labelled as '1' and '2') as expressed by equations (7.1.17) and (7.1.21), $\dot{n}_{e_2}(0)/\dot{n}_{e_1}(0) = \dot{F}_2(0)/\dot{F}_1(0)$ and $\Delta n_{e_2}(t)/\Delta n_{e_1}(t) = \Delta F_2(t)/\Delta F_1(t)$, do not require explicit values of the fluorescence constant k nor initial plasmid number count $n_e(0)$. The ratios apply provided k remains constant across experiments and $n_{e_2}(0) = n_{e_1}(0)$ - which should be the case since the DNA and DAPI preparations remained the same. This means that comparing ratios of fluorescence ΔF and $F(0)$ for different experiments leads to the same ratios of plasmid number changes and collection rates. Consequently, the results in Table 7.4 imply that as the frequency changes from 100 kHz to 1 MHz, then $\Delta n_{e\,100\mathrm{kHz}}/\Delta n_{e\,1\mathrm{MHz}} \cong 3$ and $\dot{n}_{e\,100\mathrm{kHz}}(0)/\dot{n}_{e\,1\mathrm{MHz}}(0) \cong 10$ or an order of magnitude. These experimentally determined 'benchmarks' can be compared with predicted changes Δn_p and $\dot{n}_p(0)$.

7.3.3 Theoretical predictions

A simple comparison of predicted collections using the 2-D FPE model can be made using the effective polarisability per DNA macromolecule (or plasmid), α_m, values found in Chapter 4. The polarisability per unit volume, α, of a single DNA macromolecule with volume V_{1dna} is related to α_m by $\alpha V_{1dna} = \alpha_m$. Substituting this relation into (6.0.2a) and (6.0.1) and performing the same scaling relations described in section 6.5, yields the 2-D FPE for the joint probability density, $p(x,y,t)$,

$$\frac{\partial p(x,y,t)}{\partial t} = -\frac{18.763\tilde{\alpha}_m V_o^{\,2}}{\hat{r}\,\hat{d}^3}\left(\frac{\partial[p(x,y,t)\Gamma_x(x,y)]}{\partial x} + \frac{\partial[p(x,y,t)\,\Gamma_y(x,y)]}{\partial y}\right) + \frac{0.2424}{\hat{r}}\left(\frac{\partial^2 p(x,y,t)}{\partial x^2} + \frac{\partial^2 p(x,y,t)}{\partial y^2}\right) \tag{7.3.4}$$

where $\tilde{\alpha}_m = \alpha_m \times 10^{30}$ (F m^2), and the dimensionless parts of the electric field intensity gradients Γ_x and Γ_y are given in (7.1.10c). As for (7.1.10c), it is understood the dimensions of independent variables x and y, and the spherical particle radius, $\hat{r}$, and electrode gap, $\hat{d}$, are in microns (μm). The geometry of the DNA for calculating the drag coefficient can be approximated to a sphere (Hermans, 1955; Nagasawa, 1974; Ajdari and Prost, 1991). As described in section 2.3.2 for 12 kbp pTA250 DNA, the extremum values of the radius are r = 20 nm and r = 200 nm, $0.020 \le r \le 0.20$ μm. These extremum values correspond respectively to the radius of tightly coiled DNA and to the hydrodynamic radius of a plasmid in aqueous suspension. It is not clear at this stage which value of r is most likely to represent the experiment, although r = 200 nm yields a value for the diffusion coefficient D close to that expected for 12 kbp DNA at room temperature (Smith *et al.*, 1996). In this context, it should be noted that varying the value of r in (7.3.4) is largely for dealing with uncertainty and using the relation $\alpha_m = \alpha V_{1dna}$ means that the DEP force is *independent* of r. This is a simplistic model relating DEP force to effective polarisability based on counterion fluctuations. The model is less developed than the frequency dependent Maxwell-Wagner interfacial polarisation model used for latex spheres where the DEP force has a dependence on the particle volume, i.e. r^3. In Chapter 4, values for the effective polarisability per DNA macromolecule were calculated to be, α_m = 7.9, 1.9, and 0.20×10^{-30} (F m^2) at dielectric dispersion frequencies of 0.14, 2.0 and 12 MHz, respectively.

Time profiles for the average probability density in the designated region, $\bar{\bar{p}}(t)$, were generated by numerically solving (7.3.4), (7.1.10c) and (7.1.11) implemented in FlexPDE 2.15™ program CD-R:/FlexPDE/*Fpde2dThDNA.pde*. The cell lengths were a = 0.1 μm, b = 60.1 μm, d = 10 μm $\Rightarrow h = b - a$ = 60.0 μm. These correspond to the dimensions of the planar array and

cover-slip described in section 7.3.1. The *initial* spatially averaged probability density for all simulations was therefore $\overline{\overline{p(x,y,0)}} = p(0) = 1/(d(b-a)) = 1.66\dot{6}\times10^{-3}\ \mu m^{-2}$. The designated collection region for spatially averaging the probability density in the cell was $4.95 \le x \le 10.0$ μm and $0.10 \le y \le 1.10$ μm that corresponds to the experimental dimensions described in section 7.2.2. The $\overline{\overline{p}}(t)$ collection profiles were generated for eight cases corresponding to the two extremum values of the radius r and polarisability α_m, and two potentials: $\tilde{\alpha}_m = \{0.2, 7.9\}$, $\tilde{r} = \{0.020, 0.20\}$ and $V_o = \{0.1, 0.45\}$ V. An additional two profiles were generated for $\alpha_m = 1.9\times10^{-30}$ (corresponding to the second dispersion at $f_R = 2$ MHz) assuming $r = 200$ nm and $V_o = \{0.1, 0.45\}$.

The five predicted collection profiles for $V_o = 0.45$ V (10 % of the experimental value) are plotted for 10 second and a half-hour time windows in Figs. 7.7 (a) and (b). The other five profiles for $V_o = 0.1$ V are shown in Fig. 7.8 and clearly have shorter rise times than the case where $V_o = 0.45$ V. As expected, the steady state values of the probability density are independent of the radius r in (7.3.4) since these r terms originated from the spherical drag coefficient, ζ. Furthermore, (7.3.4) shows that the time independent variable scales as the radius r, so the rise times are predicted to increase by an order of magnitude as the radius is increased from 20 nm to 200 nm.

The steady state values of the spatially averaged probability density $\overline{\overline{p}}(\infty)$, respective differences, $\Delta\overline{\overline{p}} = \overline{\overline{p}}(\infty) - \overline{\overline{p}}(0)$, and predicted rise times τ_p are listed in Table 7.5 for all 10 cases. The τ_p values were calculated by the same method as for the experiments, that is, by finding t such that

$$\overline{\overline{p}}(t) = p(0) + \left(\overline{\overline{p}}(\infty) - p(0)\right)\left(1 - e^{-1}\right) = \overline{\overline{p}}_\tau \qquad (7.3.5)$$

The initial time rate of change of the probability density, spatially averaged over the designated region, $\dot{\overline{\overline{p}}}(0)$, was determined for each case by a good linear fit of $\overline{\overline{p}}(t)$ using Origin 4.1™,

$$\dot{\overline{\overline{p}}}(0) \cong \dot{\overline{\overline{p}}}_{lin}(0) = \delta\,\overline{\overline{p}}/\delta t \qquad (7.3.6)$$

The data values used for linear fitting ranged $0 \le t < 0.01$ s for the simulation with $r = 20$ nm and $0 \le t < 0.1$ s for the $r = 200$ nm case. Using the same approach as described in sections 7.1.2.1 and 7.1.3.1 that led to (7.1.13b) and (7.1.16), it can be shown $\dot{\overline{\overline{p}}}(0)/p(0) \propto \alpha_m V_o^2/r$ and

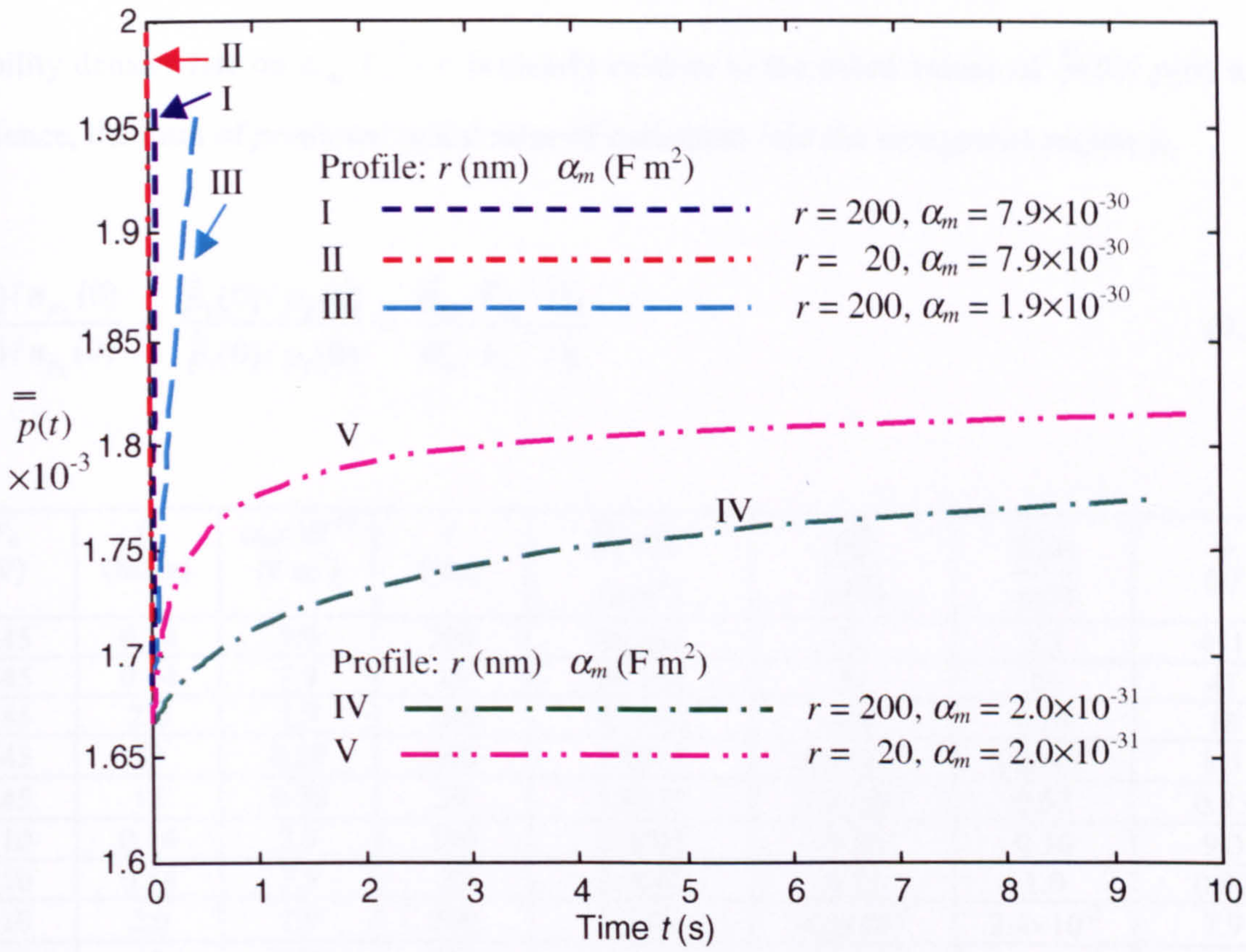

Fig. 7.7(a) Probability density (spatially averaged over the designated 'collection' region), $\bar{p}(t)$, predicted by computer simulation for $V_o = 0.45$ V and particle radius r and polarisability α_m as shown.

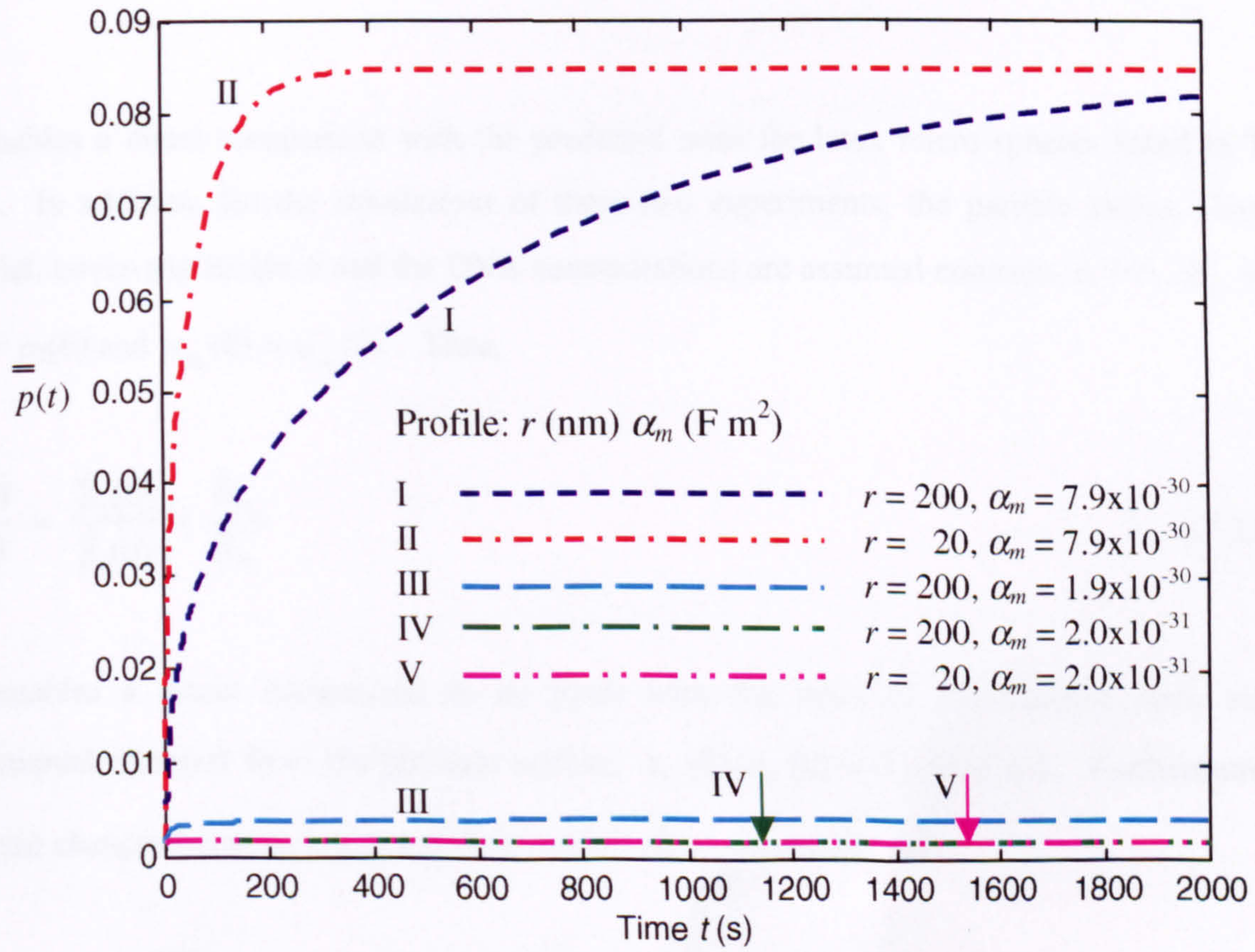

Fig. 7.7(b) Probability density (spatially averaged over the designated 'collection' region), $\bar{p}(t)$, predicted by computer simulation for $V_o = 0.45$ V and particle radius r and polarisability α_m as shown.

$\dot{n}_p(0)/n_p(0) = \dot{\bar{\bar{p}}}(0)/p(0)$ where $\propto$ denotes proportionality. The dependency of the initial probability density rate on $\alpha_m V_o^2/r$ is clearly evident in the listed values of $\dot{\bar{\bar{p}}}(0)/p(0)$ in Table 7.5. Hence, the ratio of *predicted* initial rates of collection into the designated region is,

$$\frac{\dot{n}_{p_2}(0)/n_{p_2}(0)}{\dot{n}_{p_1}(0)/n_{p_1}(0)} = \frac{\dot{\bar{\bar{p}}}_2(0)/p_2(0)}{\dot{\bar{\bar{p}}}_1(0)/p_1(0)} = \frac{\tilde{\alpha}_{m_2} V_{o_2}^2/\hat{r}_2}{\tilde{\alpha}_{m_1} V_{o_1}^2/\hat{r}_1} \qquad (7.3.7)$$

V_o (V)	f_R (MHz)	$\alpha_m \times 10^{-30}$ (F m^2)	r (nm)	$\bar{\bar{p}}_s \times 10^{-3}$ (μm^{-2})	$\frac{\Delta\bar{\bar{p}}}{p(0)}$	$\frac{\dot{\bar{\bar{p}}}(0)}{p(0)}$	τ_p (s)
0.45	0.14	7.9	200	86.161	51	2.3	411
0.45	0.14	7.9	20	86.161	51	23	41
0.45	2.0	1.9	200	4.1552	1.5	0.54	18
0.45	12	0.20	200	1.8317	9.9×10^{-2}	5.2×10^{-2}	8.3
0.45	12	0.20	20	1.8317	9.9×10^{-2}	0.52	0.83
0.10	0.14	7.9	200	2.0045	0.20	0.10	9.0
0.10	0.14	7.9	20	2.0045	0.20	1.0	0.90
0.10	2.0	1.9	200	1.7421	4.5×10^{-2}	2.4×10^{-2}	7.9
0.10	12	0.20	200	1.6744	4.7×10^{-3}	2.5×10^{-3}	7.7
0.10	12	0.20	20	1.6744	4.7×10^{-3}	2.5×10^{-2}	0.77

Table 7.5 Polarisation and voltage dependent DNA probability densities predicted by computer simulation.

and enables a direct comparison with the predicted rates for latex micro-spheres listed in Table 7.2(b). In addition, for the *simulations* of these two experiments, the particle radius, electrode potential, cover-slip height h and the DNA concentrations are assumed constant, $r_2 = r_1$, $V_{o_2} = V_{o_1}$, $p_2(0) = p_1(0)$ and $n_{p_2}(0) = n_{p_1}(0)$. Thus,

$$\frac{\dot{n}_{p_2}(0)}{\dot{n}_{p_1}(0)} = \frac{\dot{\bar{\bar{p}}}_2(0)}{\dot{\bar{\bar{p}}}_1(0)} = \frac{\tilde{\alpha}_{m_2}}{\tilde{\alpha}_{m_1}} \qquad (7.3.8)$$

This enables a direct comparison to be made with the ratio of fluorescence rates via the experimental relations from the previous section, $\dot{n}_{e_2}(0)/\dot{n}_{e_1}(0) = \dot{F}_2(0)/\dot{F}_1(0)$. Furthermore, the predicted changes between initial and final (steady state) values are,

$$\underbrace{\frac{\Delta n_{p_2}/n_{p_2}(0)}{\Delta n_{p_1}/n_{p_1}(0)} = \frac{\Delta\bar{\bar{p}}_2/p_2(0)}{\Delta\bar{\bar{p}}_1/p_1(0)}}_{\text{Compare with latex beads}} = \underbrace{\frac{\Delta n_{p_2}}{\Delta n_{p_1}} = \frac{\Delta\bar{\bar{p}}_2}{\Delta\bar{\bar{p}}_1}}_{\text{Compare with DNA } \Delta F} \qquad (7.3.9)$$

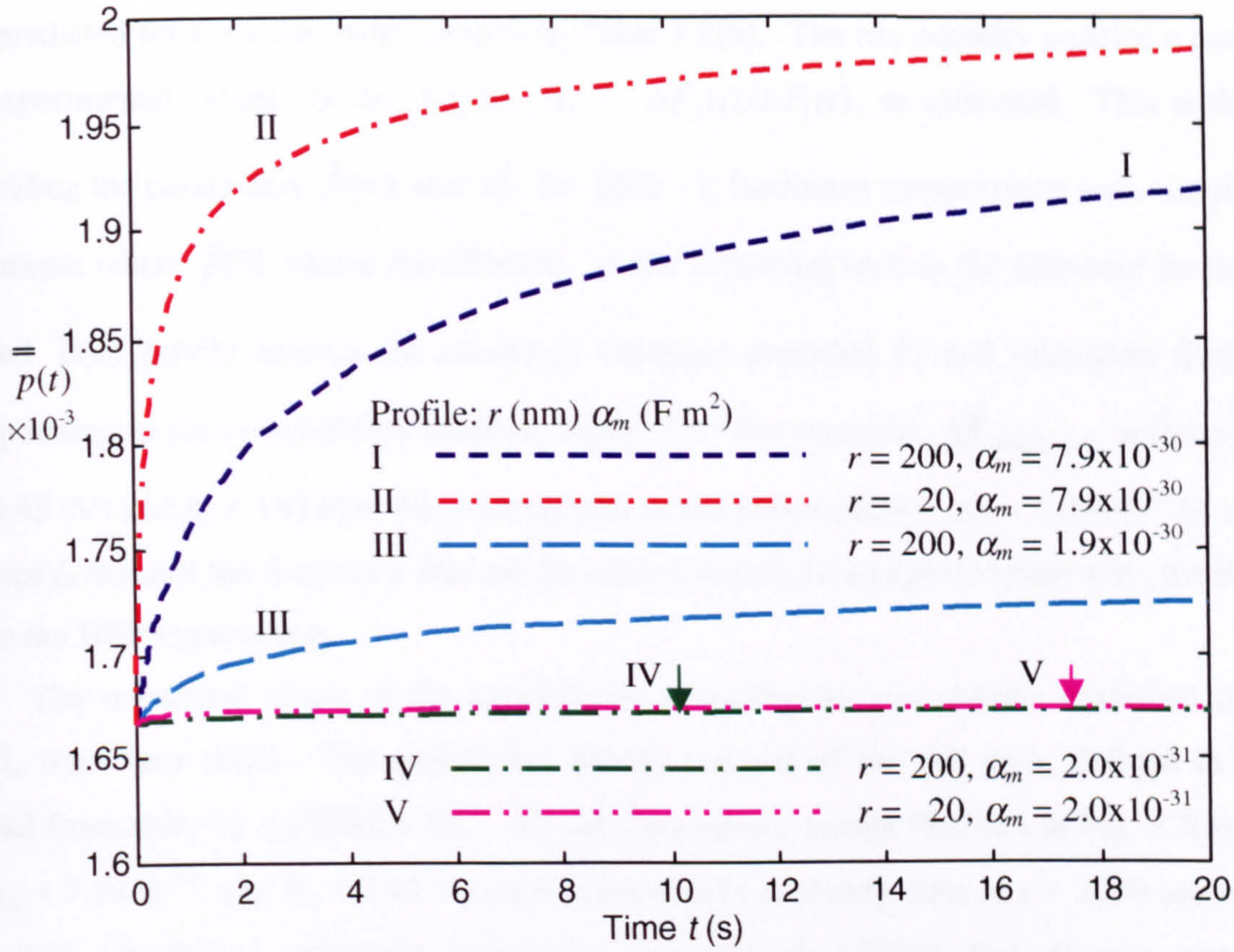

Fig. 7.8 Probability density (spatially averaged over designated 'collection' region), $\bar{p}(t)$, predicted by computer simulation for $V_o = 0.1$ V and particle radius r and polarisability α_m as shown.

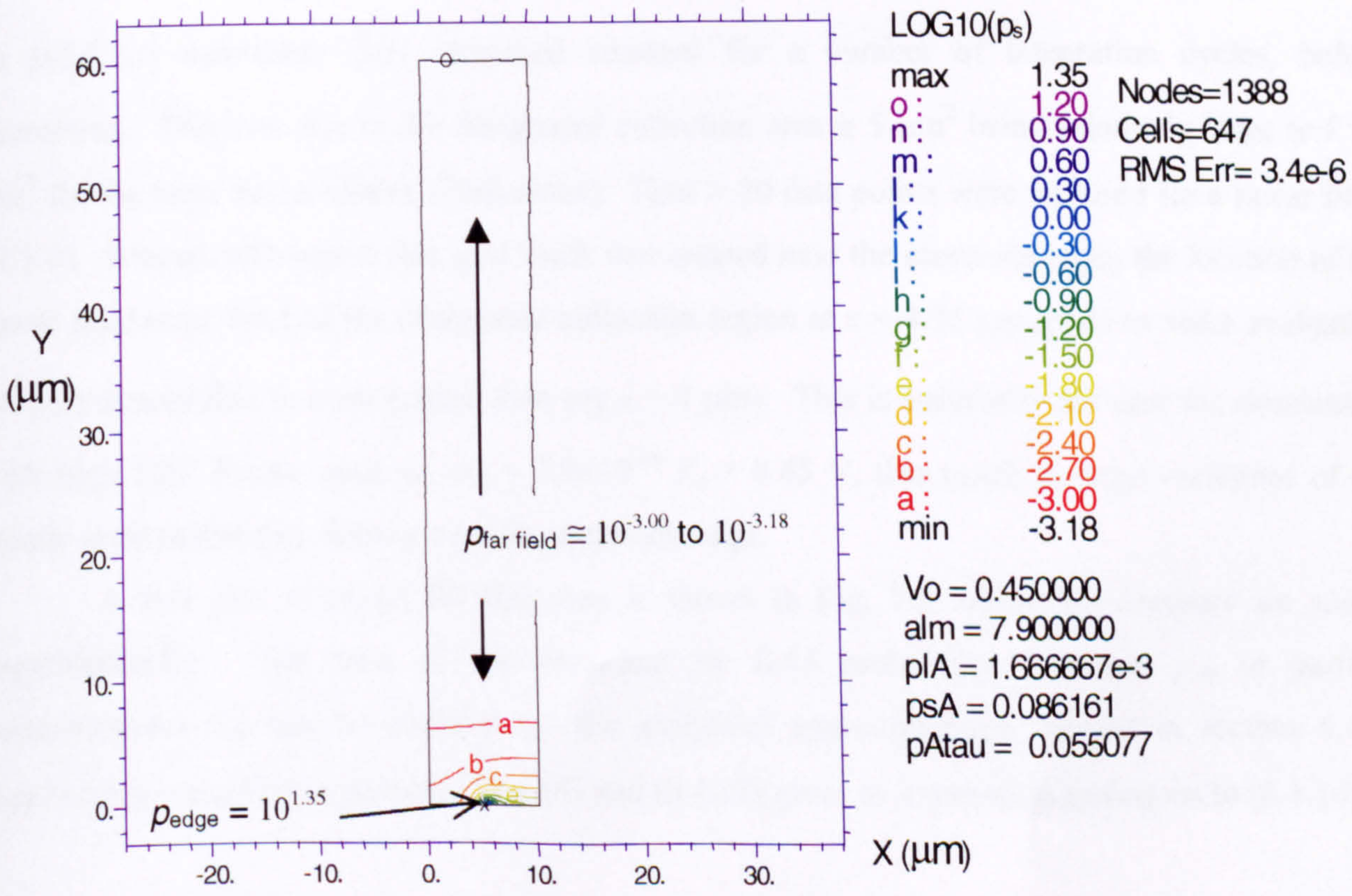

Fig. 7.9 Contour plot of the steady state probability density $\log_{10}[p(x,y)]$ for simulation conditions of experiment: $V_o = 0.45$ V, $a = 0.1$ μm, $d = 10$ μm, $h = 60$ μm, and $\alpha_m = 7.9\times10^{-30}$ F m^2.

The *lhs* equality of (7.3.9), as labelled, enables a comparison of values listed in Table 7.5 with those predicted for the latex micro-spheres in Table 7.2(b). The *rhs* equality enables a comparison with experimental values via $\Delta n_{e_2}(t)/\Delta n_{e_1}(t) = \Delta F_2(t)/\Delta F_1(t)$, as indicated. This is the reason for dividing the parameters $\bar{\bar{p}}(\infty)$ and $\Delta\bar{\bar{p}}$ by $\bar{\bar{p}}(0)$ - it facilitates comparisons with simulations of experiments where $\bar{\bar{p}}(0)$ values are different. In the following section the subscript on parameters $\Delta\bar{\bar{p}}$ and $\dot{\bar{\bar{p}}}(0)$ jointly denotes the *simulated* electrode potential V_o and relaxation frequency f_R corresponding to the polarisability listed in Table. 7.5. For example, $\Delta\bar{\bar{p}}_{140kHz,0.45}$ refers to $\Delta\bar{\bar{p}}$ for $V_o = 0.45$ (V) and $f_R = 140$ kHz that corresponds to the polarisability, $\alpha_m = 7.9\times10^{-30}$ (F m^2). The subscript f_R denotes the frequency that can be used to match, in an approximate way, the frequency used in the DEP experiments.

The numerical errors in the simulations, according to two metrics described in section 6.5.2.3, were very small. The probability density integral of the cell area, defined in (6.5.17), deviated from unity by $\varepsilon_A(2000) \leq 10^{-4}$. All ten simulations, except Profile I in Fig. 7.7(a) ($r = 200$ nm, $\alpha_m = 7.9\times10^{-30}$, and $V_o = 0.45$ V) were substantially at steady state at $t = 2000$ seconds. The nine other simulations exhibited probability densities $p(x,y,2000)$ that closely matched the analytical solution with maximum relative error defined in (6.5.18b), $\varepsilon_{max}(2000) \leq 4$ %. However, there are two points worth noting.

First, the density at the electrode edge, $p(5,0.1,t)$, was monitored throughout the simulations and tended to reach steady state before $\dot{\bar{\bar{p}}}(t)$. During the initial time steps (~ 10^{-7} secs) as $p(5,0.1,t)$ increased, $\dot{\bar{\bar{p}}}(t)$ remained constant for a number of integration cycles, before increasing. This was due to the designated collection area $\cong 5$ μm^2 being relatively large (c.f 1.6 μm^2 for the latex micro-sphere simulations). Thus > 20 data points were required for a linear fit in (7.3.6). Second, although a fine grid mesh was created near the electrode edge, the location of the lower transverse limit of the designated collection region at $x = 4.95$ μm tends to make evaluation of $\dot{\bar{\bar{p}}}(t)$ susceptible to error (rather than say $x = 4$ μm). This is especially the case for simulations with high DEP forces, such as, $\alpha_m = 7.9\times10^{-30}$ $V_o = 0.45$ V, that result in large variations of the steady state probability density near the electrode edge.

A 2-D plot of $p(x,y)$ for this case is shown in Fig. 7.9 where the contours are scaled logarithmically. The ratio of the near and far field probability densities, p_{ef}, or particle concentrations c_{ef}, can be checked by the analytical approximations derived in section 6.4.3. Applying $k_f = \alpha_m/4$ into equations (6.4.10) and (6.4.12) gives an expression analogous to (6.4.14),

$$c_{ef} = p_{ef} = \exp\left(\frac{6.1695\tilde{\alpha}_m V_o^2}{\hat{d}^2}\left[\underbrace{\overbrace{\pi^2 + 4\ln^2(400/\pi)}^{103.83} - \overbrace{32e^{-\pi}}^{1.38}}_{102.45}\right]\right) \qquad (7.3.10)$$

Substituting $\hat{d} = 10$, $\tilde{\alpha}_m = 7.9$, and $V_o = 0.45$, $p_{ef} = e^{10.095} \cong 2.4\times10^4$. This is close to the ratio that can be obtained from Fig. 7.9, $p_{ef} = 10^{1.35}/10^{-3.00} = 10^{4.35} \cong 2.2\times10^4$. This means that, under these operating conditions, very few plasmids should be observed in the far field. The issue of uniformity of $p(x,y)$ is discussed further in the next section.

7.3.4 Comparison of experiments and predictions

Consider the data in Table 7.5 with $V_o = 0.45$ V. The ratio of the probability density changes, $\Delta\bar{\bar{p}}_{140\text{kHz},0.45} / \Delta\bar{\bar{p}}_{2\text{ MHz},0.45} = 51/1.5 \cong 34$. This means that an approximate ×4 increase in polarisability from $\alpha_m = 1.9\times10^{-30}$ to $\alpha_m = 7.9\times10^{-30}$ results in a ×34 increase in the predicted $\Delta\bar{\bar{p}}$. This ratio is much greater than the ratio of experimentally measured fluorescence changes over approximately the same frequency range. Comparing 100 kHz to 1 MHz discussed in section 7.3.2, for example, $\Delta F_{100\text{kHz}}(t)/\Delta F_{1\text{MHz}}(t) \cong 3.2$. One should remark that the increase in polarisability from $\alpha_m = 0.2\times10^{-30}$ to $\alpha_m = 7.9\times10^{-30}$ (i.e. *ca.* ×40) yields a greater disparity, $\Delta\bar{\bar{p}}_{140\text{kHz},0.45} / \Delta\bar{\bar{p}}_{12\text{ MHz},0.45}$ 51/0.099 ≅ 515.

This means that the chosen value for the potential in the simulation $V_o = 0.45$ V (that is 10 % of the experimental potential) is too high, at least in terms of the steady state $\bar{\bar{p}}(\infty)$. A lower value $V_o = 0.1$ V (2.2 % of the experimental value) for the simulation gives a closer comparison. The values in Table 7.5 show, $\Delta\bar{\bar{p}}_{140\text{kHz},0.1} / \Delta\bar{\bar{p}}_{2\text{ MHz},0.1} = 0.2/0.045 \cong 4.5$ that is close to the above fluorescence ratio value of 3.2. The decrease in $\Delta\bar{\bar{p}}$ sensitivity is highlighted by $\Delta\bar{\bar{p}}_{140\text{kHz},0.1} / \Delta\bar{\bar{p}}_{12\text{ MHz},0.1}$ $0.2/4.7\times10^{-3} \cong 43$ which is an order of magnitude lower than predicted by the $V_o = 0.45$ V simulation. Another indication that $V_o = 0.45$ V is too high stems from $c_{ef} = p_{ef} \cong 2\times10^4$ as shown in Fig. 7.9. However, inspection of the suspension at focal planes up to the cover-slip (after the collections at the electrodes appeared to be at steady state) indicated a sufficiently high plasmid concentration suggesting it is much more uniform then predicted. Decreasing the potential in the simulation to $V_o = 0.1$ V and substituting $\hat{d} = 10$, $\tilde{\alpha}_m = 7.9$ into (7.3.10) predicts a much more uniform concentration, $c_{ef} = p_{ef} = e^{0.5} \cong 1.6$.

As expected from equation (7.3.8), the ratios for $\dot{\bar{\bar{p}}}(0)$ are *not* dependent on the electrode potential (in so far as $V_{o_2} = V_{o_1}$). Thus, $\dot{\bar{\bar{p}}}_{140\text{kHz}}(0) / \dot{\bar{\bar{p}}}_{2\text{ MHz}}(0) = 7.9/1.9 \cong 4$. This is *less* than the

ratio of the fluorescence rates over approximately the same frequency range described in section 7.3.2, $\dot{F}_{100\text{kHz}}(0)/\dot{F}_{1\text{MHz}}(0) \cong 11$. On the other hand, $\dot{\bar{\bar{p}}}_{140\text{kHz}}(0)/\dot{\bar{\bar{p}}}_{12\,\text{MHz}}(0) = 7.9/0.2 \cong 40$. Thus, at this stage, the experimental collection rates of plasmids lie within the range predicted by the FPE simulation.

Clearly, the predicted rise times τ_p in Table 7.5 for $r = 200$ nm are one to two orders of magnitude larger than those experimentally observed. Averages of τ_e values listed in Table 7.3 range from $\tau_e \cong 0.20$ secs at 100 kHz, $\tau_e \cong 0.45$ secs at 500 kHz and $\tau_e \cong 0.61$ secs at 1 MHz. The only cases where the rise times are commensurate, $\tau_e \approx \tau_p$, are for $r = 20$ nm accompanied with a low DEP force, i.e. excluding the $\alpha_m = 7.9\times10^{-30}$ and $V_o = 0.45$ V case. Furthermore, as pointed out in section 7.3.2, the experimental rise times exhibit a consistent increase with frequency or reduction in polarisability. This trend is contrary to the trend predicted by the FPE simulation. For example, using listed values in Table 7.5, $\tau_{p\,140\text{kHz},\,0.45}/\tau_{p\,2\,\text{MHz},\,0.45} = 411/18 \cong 23$ and $\tau_{p\,140\text{kHz},\,0.1}/\tau_{p\,2\,\text{MHz},\,0.1} = 9.0/7.9 \cong 1.1$. Both of these ratios are above unity whereas $\tau_{e\,100\,\text{kHz}}/\tau_{e\,1\,\text{MHz}} = 0.33 < 1$.

7.3.5 Discussion

In broad qualitative terms, the simulated collection profiles predicted by the FPE model agree with those observed for fluorescently labelled plasmid DNA. The predicted response of the DEP collection profiles, in terms of initial collection rates and steady state values, decreases with frequency dependent polarisability α_m. This correlates with the experimentally measured responses. However, there are clear quantitative differences, especially with respect to the electrode potential V_o where the closest agreement between theory and experiment occurred when $V_o \cong 2$ % of the experimental value. In addition, the values of the rise times and general trend with frequency did not agree.

There are a number of reasons for the variations between theory and experiment. The first is due to the simplifying assumption that the charge associated with the DNA and associated counterions has no effect on the electric field generated by the interdigitated electrodes - as discussed earlier in section 7.2.5 for the DEP collections of 216 nm diameter latex micro-spheres. It is interesting to note that the DNA plasmids formed pearl chains at the lower frequencies and this indicates the presence of induced dipole-dipole interactions (Jones, 1995; Llamas *et al.*, 1998). It is possible, therefore, if the influence of the charges on the electric field was included via a non-zero charge density term on the *rhs* of (6.1.2) (i.e. Laplace's equation replaced by Poisson's equation) then the analysis would not be complete without further consideration of these dipole-dipole

interactions. In addition, one can remark that plasmid-plasmid interactions are not directly modelled by the FPE (Doi and Edwards, 1986) and the FPE model also assumes the particles have a point like size and do not exclude each other volumetrically.

The second reason, also discussed in section 7.2.5, is due to fluid movement over the surface of the electrodes. This is particularly the case when the electrode potential and minimum frequency for the DEP collections of DNA were 4.5 V and 100 kHz, compared with 2 V and 500 kHz for the latex micro-spheres. The lower frequency and higher potentials produce greater fluid movement (Ramos *et al.*, 1998; Ramos *et al.*, 1999; Green *et al.*, 2000a; Green *et al.*, 2000b).

A third possible reason for the disparity between theory and experiments is that the induced dipole arising from counterion fluctuations may in fact saturate, or reach a limiting value, at high field strengths (Manning, 1993). This was suggested by Asbury (1999) as a possible reason for the DEP trapping efficiency being lower than predicted by dielectric spectroscopy. There is experimental evidence from studies of electric dichroism and birefringence of DNA that the induced dipole given by equation (2.1.4) reaches a limiting value in high electric field strengths (Elias and Eden, 1981; Fixman, 1980b; Stellwagen, 1981; Diekmann *et al.*, 1982; Porschke, 1985; Mohanty and Zhao, 1996). This means the DNA plasmids may not experience the high DEP forces near the electrode edges as predicted by the linear model (2.1.4) relating the DEP force to electric field intensity. If this is the case then the relation, $\alpha_m = \alpha V_{1dna}$ used in the FPE (7.3.4) would need amendment. It is questionable, however, whether the same phenomenon of dipole saturation accounts for the disparity between theory and experiment of the latex beads - as discussed in section 7.2. This is in view of the uniform surface charge density being three orders of magnitude higher that the induced surface charge density (Pethig, 1991).

General investigations of DEP using 12 kbp pTA250 DNA on both polynomial and interdigitated electrodes, as described in section 3.2, appeared to require higher electrode potentials - *ca.* 2 to 4 times those needed for 216 nm diameter micro-spheres - to obtain significant DEP collections. One set of published results by the author (listed at the end of this thesis) of pTA250 DNA DEP collections at 1 MHz on the prototype interdigitated electrodes described in section 3.2.1.1, for example, used $V_o = 9$ V. The plasmids collected on the electrode edges, with the same $w = d = 10$ μm geometry, in a manner similar to those exhibited in Fig. 3.3(b). The polarisability of a 216 nm diameter sphere at 140 kHz, assuming the same values for parameters as described in section 7.2.3 with $\mathrm{Re}\{f_{CM}\} = 0.7633$, is calculated from (2.2.3) to be $\alpha_{sphere} = \alpha V_{sphere} \cong 8.4\times10^{-30}$ F m^2. This is only slightly higher than the value of the macromolecular plasmid DNA polarisability, $\alpha_m = 7.9\times10^{-30}$ F m^2 for the first dispersion at the same frequency, 140 kHz. This is interesting: one would therefore expect the DEP response of a pTA250 DNA macromolecule in low conductivity medium to be the same as a 216 nm diameter sphere, except the former has a hydrodynamic radius of about twice the latter.

A good starting point for clarifying the quantitative observation of DNA would be to further investigate how frequency dependent macromolecular polarisability, based on counterion fluctuations described in section 2.2.3.2, gives rise to a DEP force in a non-uniform electric field. Another improvement would be to find estimates for plasmid numbers $n_e(0)$ and fluorescence constant k as described for the latex spheres in section 7.2.2.2. This would enable direct comparisons between experimentally observed plasmid numbers $\Delta n_e(t)/n_e(0)$ with those predicted $\Delta n_p(t)/n_p(0)$, and similarly $\dot{n}_e(0)/n_e(0)$ with $\dot{n}_p(0)/n_p(0)$. This would be more satisfactory rather than merely determining ratios of these parameters, and assist cross-comparisons with results for the latex micro-spheres. A more immediate improvement would be to perform the same collection experiments of pTA250 DNA at different electrode potentials with the most recent apparatus that has a controlled sample chamber (or cover-slip) height and is not hindered by mechanical vibrations.

7.4 Concluding remarks

Quantitative measurements of model colloidal particles (216 nm latex micro-spheres) and 12 kbp pTA250 DNA exhibit frequency dependent DEP collections on interdigitated electrode arrays. Comparisons with simulated collections using a 2-D FPE model indicates broad agreement with experiments. However, the FPE model predicts collections that have a greater sensitivity with respect to the applied electrode voltage and frequency dependent polarisability. The initial rate of collection parameter generally gives the best agreement between theory and experiment, followed by the parameter for steady state values.

There are a number of reasons for the differences between the theoretical FPE model and experiments, particularly for the steady state collections and rise times. The first is that the electric field intensity gradient (and DEP force) is determined from Laplace's equation that does not take into account the effect of electric charge on the micro-spheres or plasmid DNA and associated counterions. It would be more accurate to use Poisson's equation but this would involve further analysis and considerable computation. The second reason is that the fluid motion over the surface on the interdigitated electrodes could disrupt the particle collections. The other reasons also point to assumptions made in the FPE model in varying ways. These include, particle-particle interactions not being taken into account and assumption of point size particles, and induced dipole saturation for the DNA.

8 Summary, outlook, and future work

8.0 Summary of research

Chapters 2 to 7 have described investigations of the high frequency dielectrophoretic movement of polarisable sub-micron diameter particles suspended in aqueous solution. The two types of sub-micron sized particles considered in this dissertation were 216 nm diameter micro-spheres and 12 kbp plasmid DNA (pTA250). Chapter 2 laid the theoretical foundations for the thesis, introducing the basic theory of dielectrophoresis (distinguishing between positive and negative DEP) and discussing Maxwell-Wagner interfacial and counterion fluctuation polarisation mechanisms for these bioparticles. The forces acting on bioparticles were discussed and the dielectrophoretic, Stokes' drag, and thermal stochastic (Brownian) forces were shown to be dominant. The equation encapsulating these forces for a single particle is the Langevin equation. The motion of a sufficiently large ensemble of non-interacting particles, however, can be characterised by the continuity equation, or Fokker-Planck equation.

Chapter 3 described the experimental apparatus for measuring DEP collections and relaxations using epi-fluorescence microscopy, micro-fabrication of polynomial and interdigitated planar electrodes on glass substrates, and purification and preparation of pTA250 DNA. In particular, section 3.5 described the image processing software written in MATLAB 5.0™ for quantifying video images of fluorescently labelled DNA and micro-spheres collecting onto, or diffusing away from, the surfaces of interdigitated planar electrode arrays. Chapter 4 described the time domain dielectric spectroscopic measurements of pTA250 DNA suspensions and identified three dispersions at 140 kHz, 2 MHz and 12 MHz; corresponding to effective polarisability values of 80, 20, and 2×10^{-31} ($F\ m^2$) per DNA macromolecule, respectively. The mechanism responsible for the polarisability was concluded to be counterion fluctuation along subunits of the DNA double-helical longitudinal axis, although Maxwell-Wagner interfacial polarisation could not be ruled out for the third dispersion.

In chapters 5 and 6 theoretical 1-D and 2-D simulations of particle movement by positive DEP were performed using the FPE and including the effect of diffusion. Chapter 5 introduced the diffusion limited motion of harmonically bound particles and considered in detail particle accumulation on an electrode boundary where the positive DEP force was modelled by a hyperbolic function. This hyperbolic dependency was later shown in Chapter 6 to be valid for planar interdigitated arrays of interest, albeit for a limited range of values in the near field. The FPE was solved for a range of forces and cover-slip (or sample chamber) heights using a Fourier-Bessel series eigenfunction expansion. The structure of the solutions for the probability density

shows particle collections and relaxations can be best approximated by a single exponential function and more generally by a multiple-exponential series. The solutions confirm results obtained by a finite element method written in FlexPDE 2.15™ code. Finite element solutions assuming a 1-D exponential positive DEP force relation were also given with time-profiles of relaxations. A distinction was made between weak DEP force collections followed by relaxation-by-diffusion with comparable rise and fall times, $\tau_{rise} \approx \tau_{fall}$, and strong DEP collections with $\tau_{rise} >> \tau_{fall}$. In the former, the distribution of particles after a collection has reached steady state can be considered to be a *perturbation* of the distribution of particles before the collection started. In contrast, the steady state particle collection under strong a DEP force is sufficiently different compared with distribution before the collection commenced, that the process of particle movement can be viewed as a *state transition*.

The 2-D FPE model presented in Chapter 6 simulated pseudo 3-D sub-micrometre particle collection onto interdigitated electrodes in a way that corresponds to a typical experimental situation. Starting with Laplace's equation and applying boundary conditions, expressions for the gradient of the electric field intensity were derived and shown to approximate to hyperbolic and exponential relations in near and far fields, respectively. The former was further simplified to a simple inverse DEP force relation used in Chapter 5. The ratio of steady state probability density in near and far field locations was also determined and shown to exhibit a wide range of values, depending on the frequency and particle size dependent induced polarisability, and electrode potential. Chapter 6 also included analytical solutions for the electric field assuming a finite sample chamber height.

The experimental and theoretical research on positive DEP sub-micron particle collections and relaxations, described in previous chapters, was brought together in Chapter 7. Experiments of DEP collections of 216 nm diameter latex micro-spheres and 12 kbp pTA250 DNA, for 100 kHz – 20 MHz frequencies, onto planar interdigitated electrodes were analysed using the software described in Chapter 3. The collections showed broad agreement with data predicted from computer simulations of the 2-D FPE developed in Chapter 6. Initial collections rates and steady state values agreed with trends predicted by the effective polarisability for both examples of sub-micron sized particles.

However, it is clear that predictions of the FPE model are far more sensitive with respect to variations in the effective polarisability, and in particular, peak electrode potential V_o. In particular, at steady state, the model predicts that particles with moderate values for polarisability, $\alpha_{particle} \approx 10^{-29}$ (F m^2), attracted by DEP forces to 10 μm width and gap interdigitated electrodes with $V_o \cong 2 - 4$ (V), should be strong enough to attract almost all particles on to the edges of the electrodes leaving the remaining regions up to the cover-slip $h \approx 60$ - 200 μm above the electrode plane practically depleted. However, under these conditions experiments indicated an abundance of particles up to the cover-slip capping the chamber.

As pointed out in section 7.4, there are a number of possible reasons for the discrepancies between theory and experiment. The first is that electric field intensity gradient (and DEP force) is determined from Laplace's equation that does not take into account the effect of the electric charge on the micro-spheres, or plasmid DNA, and surrounding counterions. The second reason is attributed to electrohydrodynamic fluid motion in the vertical-transverse plane that disrupts particle DEP collections. The other reasons include particle-particle interactions not being taken into account, assumption of point size particles, and possible induced dipole saturation for the DNA.

8.1 Outlook

The theoretical and experimental investigations of dielectrophoretic time-dependent sub-micron particle collections, described in this dissertation, may be useful in several areas of future research. This work has shown that DEP collection rates are dependent on particle polarisability. This means that DEP collection profiles can be used to investigate the dielectric properties of particles suspended in solution, thus complementing conventional dielectric spectroscopic techniques. An attractive feature of DEP is that the sample suspension volumes required for analysis can be three orders of magnitude (from millilitres to microlitres) less than needed for dielectric spectroscopy.

The second area of scientific and technological interest where the results of this work may be useful lies in a general understanding of the macroscopic movement of particles in potential energy wells influenced by Brownian motion. This has been of long-standing theoretical interest (Kramers, 1940; Brinkman, 1956; Doering and Gadoua, 1992) and in recent years thermal fluctuations have been used to achieve macroscopic particle motion by means of Brownian ratchets (Magnasco, 1993; Rousselet *et al.*, 1994; Slater *et al.*, 1997; Duke and Austin, 1998; Ertas, 1998; Hammond *et al.*, 2000) for colloids and polyelectrolytes including DNA. DEP forces have been used as asymmetric trapping potentials in Brownian ratchets (Gorre-Talini *et al.*, 1997) and in other devices combined with electrophoresis (Ajdari and Prost, 1991) and hydrodynamic fluid flow (Washizu *et al.*, 1994) to achieve particle separation. Currently there is considerable interest in using non-contact particle manipulation devices that can be functionally integrated and miniaturised for applications in 'lab-on-a chip' technology and DNA diagnostics and for wider use in genomics and proteomics (Abramowitz, 1996). It is likely that success of using DEP as an electrokinetic force for colloids and polyelectrolytes in these future devices will depend on the time-dependent particle flux it can generate.

8.2 Future work

The research on DEP of DNA and colloidal particles reported in this dissertation could be improved and extended in a number of ways. First, as evident from the previous section and

findings in Chapter 7, there is a need to elucidate the mechanisms leading to the quantitative differences between the experimentally measured collection time-profiles and those predicted using the 2-D FPE theory. As a starting point, it would be useful to examine if the presence of the micro-spheres or plasmid DNA collected onto the electrode edge distorts the electric field. As discussed in sections 7.2.5 and 7.3.5 the effect of electric charge on these particles and surrounding counterions is ignored in the Laplace equation model that is used to predict the electric field generated by the interdigitated electrodes. Including charge density in a more general Poisson equation model would be more accurate but requires coupling with the FPE, thus increasing computational complexity.

One way to minimize the computation required would be to start by solving the Poisson-FPE model when the DEP particle collections have approached steady state (i.e. the *lhs* of 6.0.1 is set to zero). As stated in section 8.0, the steady state particle concentration (or probability density) predicted by theory for moderate values of the induced polarisability and electrode potentials predicts that almost all particles in the suspension will be attracted to the electrode edges. However, the DEP experiments under these conditions demonstrated the converse – an abundance of particles far above the interdigitated array up to the cover-slip. The steady state particle concentration distribution is a clearly a sensitive measure of agreement between theory and experiment – as discussed in section 6.4.3. In view of these issues of computation and sensitivity, it would be reasonable to examine the probability density distribution predicted by the Poisson-FPE model at steady state. Furthermore, since the steady state particle collection (probability density or concentration) is identical to the *initial condition* for particle *relaxation*, the temporal response of the model could be evaluated for the particle relaxation regime and compared with experiment. The relaxation simulation should be straightforward since the DEP potential is switched off and there is no external electric field, so particle movement is governed solely by diffusion.

The other effect that should be included in the 2-D FPE is electrohydrodynamic fluid motion above the electrode surface that is not included but has been observed in experiments. Again, for the abovementioned reasons of computation and sensitivity, it might be useful to solve and evaluate this modified 2-D FPE model at steady state. Other approaches to understanding the discrepancies between theory and experiment include examining the possibility of induced dipole saturation. The latter investigation could be extended to further clarify the polarisation mechanisms for DNA – particularly a closer examination of the Maxwell-Wagner polarisation model for DNA by Grosse (1989) presented in chapters 2 and 4.

The second aspect of future work relates to the size and type of colloidal and polyelectrolyte particles used in experiments. The results in Chapter 7 so far are limited to 216 nm polystyrene micro-spheres (beads) and 12 kbp plasmid DNA, and a more complete characterisation should include a range of particle sizes. Other parameters that could be varied include the medium conductivity, electrode width, gap and length, and using a wider range of electrode potentials and

frequencies. The temporal application of the high frequency AC electrode potential has also been essentially a switched step 'off/on' function and more novel experiments could include a ramp or other suitable function. The same applies to the switched 'on/off' relaxations.

A third area of work needed lies in improving the quality of the particle collection experiments. As mentioned in section 7.2.2.2 there were variations in bead density attributed to variations in electrode edge definition during micro-fabrication process described in Chapter 3. Since the sharpness of electrode edge influences the electric field non-uniformity, particle collection measurements could benefit from a greater control of the edge definition during micro-fabrication. The collections and relaxations would also benefit from a more stable light source. In general experimental analyses would be facilitated by improvements in the image processing program *depint* particularly with regard to robustness to vibrations and accidental movements in the electrode alignment with respect to the optical viewing axis of the microscope. Furthermore, it would be very useful to combine the program, *depint*, and data post-processing by Origin 4.1™ or similar software into a fully automated system run on a PC. Apart from the saving in labour, this would facilitate a larger number of replications of DEP collections and relaxations enabling a more rigorous statistical analysis of particle movement. The DDS, for example, could be programmed to generate a periodic train of potentials that are applied to each of the separately addressable interdigitated electrodes described in chapters 3 and 7. This would enable a series of particle collection and relaxation experiments to be conducted for each array for a selected frequency and peak voltage. The resultant collection and relaxation profiles could be analysed to give values for fluorescence amplitudes and rise/fall times in terms of both mean values and variances, and possibly tests of significant differences in these DEP responses using Analysis-of-Variance and related statistical methods.

The experimental evidence in Chapter 7 indicates, from a system viewpoint, positive DEP particle motion for 2-D arrays is observed to be a perturbation rather than a state transition (that would otherwise lead to entire particle depletion in the far field – as discussed in Chapter 7 and section 8.1 above). That is, the DEP force is short ranged so particle transport over distances orthogonal to the electrode plane is limited. Rather than seeing this as 'limiting' the possibilities for particle transport devices, advantage could be taken of these short range attractive forces using a 3-D electrode structure consisting of separately addressable planar interdigitated arrays tiered on top of each other, as shown in Fig. 8.1.

The interelectrode gaps would be either perforated non-conducting substrate or simply the suspending medium (as shown), thus allowing particles to move to in an orthogonal direction from plane-to-plane. An AC potential applied to each selected interdigitated array in a tier would attract particles to the electrode edges. By consecutively switching 'on' the AC potential at each layer (and 'off' for the other layers), the particles could be shunted through the 3-D tiers. This method of

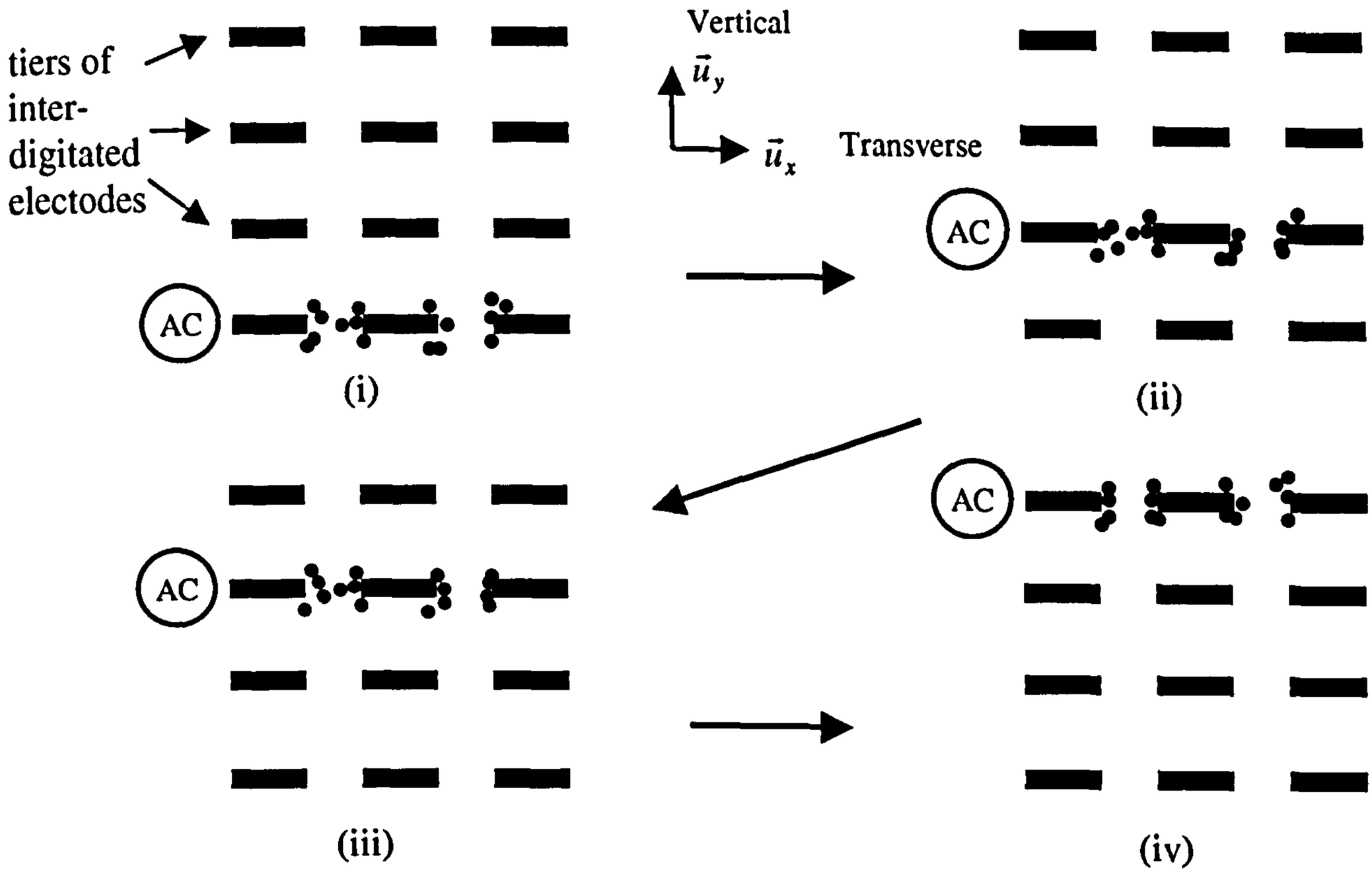

Fig. 8.1 Particles being dielectrophoretically 'shunted' through a 3-D 4-tier interdigitated electrode array structure. An AC potential (indicated by 'AC') is applied consecutively to each tier from bottom (i) to top (iv) attracting nearby particles to the edges at each stage.

dielectrophoretically shunting particles could be an alternative to using long-range electrophoretic forces or travelling wave DEP. It is worth remarking that the electrodes in Fig. 8.1 are illustrated as planar but this is not necessary and they could be, for example, cylindrical. Simulations of movement could be simplified by taking advantage of geometric symmetry – as mentioned in the introduction to Chapter 5.

Bearing in mind the technological interest in particle separations according to particle size and dielectric properties, and the research performed by groups mentioned in the previous section 8.1, it may be worthwhile investigating the particle separation properties of this proposed dielectrophoretic shunt. In more abstract viewpoint, the research discussed in this dissertation has focused on the movement of colloidal particles and DNA subjected to deterministic DEP forces and stochastic Brownian motion. The DEP forces are *spatially* deterministic – in terms of the interdigitated electrodes that generate periodic and symmetric DEP forces as described in chapters 3, 6, and 7, and *temporally* deterministic in terms of the applied electrode potential. In this context, it may be worth examining the particle separation properties by superposing the deterministic electrical potential with a stochastic component.

8.3 Concluding remarks

The experimental and theoretical investigations of the dielectrophoretic movement of colloidal particles and polyelectrolytes suspended in aqueous solution have been summarised. The experiments used fluorescence microscopy to image DEP collections of fluorescently labelled 216 nm diameter carboxyl-modified polystyrene micro-spheres and 12 kbp pTA250 DNA plasmids onto 10 μm width and 10 μm gap interdigitated Ti/Pd/Au electrode arrays. The dielectrophoretic collections (and subsequent relaxations) for AC frequencies, $100\,\text{kHz} \le f \le 20\,\text{MHz}$ and applied peak electrode potentials, $1.0 \le V_o \le 4.5$ V, exhibited collection and relaxation profiles in qualitative agreement to those predicted by theoretical simulation using a 2-D FPE. However there were significant quantitative differences, particularly in terms of the voltage required to generate DEP particle collections. The FPE model consisted of DEP-induced particle flux, governed by the frequency dependent effective particle polarisability, and thermally driven diffusion flux that is significant for sub-micron sized particles at room temperature.

There are a number of reasons for the experimentally measured dielectrophoretic response to be less than predicted by theory. These include electric field distortion due to the collections of colloidal particles or plasmid DNA near the electrode edges, and electrohydrodynamically induced fluid motion that was not included in the relatively simple FPE model. It is possible that fluid motion disrupts the particle movement so that the DEP particle flux is spatially shorter ranged than expected. Other factors that may also reduce the experimental DEP response include possible

induced dipole saturation and the inherent assumption that the particles have point size (zero volume).

It is recommended for future theoretical work that the effects of electric field distortion and fluid motion be incorporated into a more general FPE model and the other possibilities for the disparities between theory and experiment be examined in closer detail. Suggested improvements include electrode edge definition during microfabrication and developments of existing software for image processing and data post-processing. In general, quantitative measurements of DEP experiments would benefit from higher replications made possible by automating image and data processing. This would be useful for future experiments of particle collections and relaxations on interdigitated electrode arrays including those that explore the effects of changing particle size, electrode features, and potential waveforms applied to the electrodes. Given the technological interest in sub-micron particle movement and the evidence about DEP collections gathered in the course of this work, a brief proposal of a dielectrophoretic shunt is outlined.

Appendix A Development of the Langevin equation

A.1 General

The Newtonian one-dimensional equation of motion, from Ch. 2 (2.4.3) can be rearranged,

$$\begin{aligned} &\frac{dx}{dt} = v \\ &m\frac{dv}{dt} + \zeta v = F_{Ext}(x,t) + F_{Therm}(t) \end{aligned} \tag{A.1.1}$$

where x is assumed to vary slowly with respect to the fast variable v, and all other symbols have been previously defined. The solution of the first order ordinary differential equation (ODE) yields the velocity (Kreyszig, 1967),

$$\begin{aligned} v(x,t) &= v(t_0)e^{-(t-t_0)/\tau} + e^{-t/\tau}\int_{t_0}^{t}\frac{e^{t'/\tau}}{m}F_{ext}(x,t')dt' + e^{-t/\tau}\int_{t_0}^{t}\frac{e^{t'/\tau}}{m}F_{Therm}(x,t')dt' \\ &= v(t_0)e^{-(t-t_0)/\tau} + v_{Ext}(x,t) + v_{Therm}(t) \end{aligned} \tag{A.1.2}$$

where $\tau = m/\zeta$ is the relaxation decay time, t_0 is the initial time and x, t dependence is made explicit for use in the following sections. Typically for 12 kbp DNA and 216 nm diameter latex spheres, values of m and ζ_{sphere} yield $\tau \approx 10^{-11}$ and $\tau \approx 10^{-9}$ sec. This means that without the external and thermal forces applied to the particle, the velocity rapidly decreases over nanosecond timescales. Since our interest lies with time intervals greater than 10^{-9} seconds, $t >> \tau + t_0$. Hence, $e^{-(t-t_0)/\tau} \to 0$ and the initial velocity in (A.1.2) can be ignored,

$$v(x,t) = v_{Ext}(x,t) + v_{Therm}(t) \tag{A.1.3}$$

To explain the particle dynamics, the components of velocity arising from the 'external' deterministic forces are treated separately from the stochastic 'thermal' force.

A.2 Solution of external forces

Substituting (2.3.8) into the form for the external velocity given by (A.1.2),

$$v_{Ext}(x,t) = e^{-t/\tau}\int_0^t \frac{e^{t'/\tau}}{m} F_{Ext}(x,t')dt = e^{-t/\tau}\int_0^t \frac{e^{t'/\tau}}{m}\left(F_{DEP}(x,t') + F_{EP}(x,t') + F_{Const}\right)dt' \qquad \text{(A.2.1)}$$

where, for convenience and without loss of generality, $t_0 = 0$. Consider the dielectrophoretic (DEP) velocity first. Substituting (2.3.9) into (A.2.1), and segregating x and t dependence,

$$v_{DEP}(x,t) = e^{-t/\tau}\int_0^t \frac{e^{t'/\tau}}{m} F_{DEP}(x,t')\,dt' = F_{DEP}(x)e^{-t/\tau}\int_0^t \frac{e^{t'/\tau}}{m}\left(1+\cos(2\omega t' + 2\theta)\right)dt' \qquad \text{(A.2.2)}$$

where $F_{DEP}(x) = \frac{\alpha V}{4}\frac{\partial E(x)^2}{\partial x} = \pi r^3 \varepsilon_m \,\mathrm{Re}\{f_{CM}\}\frac{\partial E(x)^2}{\partial x}$. Integrating by parts (Gröbner und Hofreiter, 1965, p. 133), and after some algebra,

$$\frac{v_{DEP}(x,t)}{F_{DEP}(x)} = \frac{\left(1-e^{-t/\tau}\right)}{\zeta} + \left\{\frac{\cos(2\omega t + 2\theta) + 2\omega\tau\sin(2\omega t + 2\theta) - e^{-t/\tau}\left(\cos(2\theta) + 2\omega\tau\sin(2\theta)\right)}{\zeta[1+(2\omega\tau)^2]}\right\} \qquad \text{(A.2.3)}$$

Two approximations are made. First, as before, we consider time intervals greater than 10^{-9} seconds, $t >> \tau$, hence, $e^{-t/\tau} \to 0$. This corresponds to an almost instantaneous time response of the particle to applied forces. This is true for the relatively long (μsec – msec) periods of the applied electric field, and even longer experimental observation times (> 10 msec). Secondly, the applied AC electric fields are bandlimited, for frequencies, 20 kHz $\le f \le$ 20 MHz; hence $2\omega\tau < 1$. Parenthetically, we note that for the extreme case, f = 20 MHz using a 216 nm latex bead with relaxation time, $\tau = 2.7\text{x}10^{-9}$ s, $(2\omega\tau)^2 = 0.46$ so the approximation may not strictly be valid. However, for much lower frequencies, clearly $2\omega\tau << 1$. It should be noted, this approximation is largely for a matter of convenience, and does not affect the final result after time integration of the velocity in the next section. Approximating (A.2.3),

$$v_{DEP}(x,t) = \frac{F_{DEP}(x)}{\zeta}\left[1+\cos(2\omega t + 2\theta)\right] \qquad \text{(A.2.4)}$$

Similarly, substituting (2.3.10) into (A.2.1), the electrophoretic (EP) velocity term is

$$v_{EP}(x,t) = e^{-t/\tau}\int_0^t \frac{e^{t'/\tau}}{m} F_{EP}(x,t')dt' \\ = F_{EP}(x)e^{-t/\tau}\int_0^t \frac{e^{t'/\tau}}{m}\cos(\omega t'+\theta)\,dt' \tag{A.2.5}$$

where $F_{EP}(x) = \mu\zeta E(x)$ and all symbols have been previously defined. After some algebra,

$$v_{EP}(x,t) = \mu\zeta E(x)\left[\frac{\cos(\omega t+\theta)+\omega\tau\sin(\omega t+\theta)-e^{-t/\tau}\left(\cos(\theta)+\omega\tau\sin(\theta)\right)}{\zeta[1+\omega^2\tau^2]}\right] \tag{A.2.6}$$

Again, the similar approximations, $e^{-t/\tau} \to 0$ and $\omega\tau < 1$ can be made,

$$v_{EP}(x,t) = \frac{F_{EP}(x)\cos(\omega t+\theta)}{\zeta} = \mu E(x)\cos(2\pi f t+\theta) \tag{A.2.7}$$

The constant velocity term is,

$$v_{Const}(t) = e^{-t/\tau}\int_0^t \frac{e^{t'/\tau}}{m} F_{Const}\,dt' = \frac{F_{Const}}{\zeta}\left(1-e^{-t/\tau}\right) \tag{A.2.8}$$

and the approximation $e^{-t/\tau} \to 0$ leaves it time invariant,

$$v_{Const} = F_{Const}/\zeta \tag{A.2.9}$$

A.3 Solution of thermal forces

Using (2.3.16) the thermal velocity is written,

$$v_{Therm}(x,t) = e^{-t/\tau}\int_{t_0}^t \frac{e^{t'/\tau}}{m} F_{Therm}(x,t')dt' = e^{-t/\tau}\int_{t_0}^t \frac{e^{t'/\tau}}{m}\sqrt{2\zeta\,k_B T}\,\xi(t')\,dt' \\ = \sqrt{\frac{2k_B T}{\zeta}}\int_{t_0}^t \frac{e^{-(t-t')/\tau}}{\tau}\xi(t')\,dt' \tag{A.3.1}$$

Following the approach by Gardiner (1985, p. 80-1 and 195-6) the above integral can be approximated by letting $t_0 \to -\infty$ without 'significant error' and taking the limit $\tau \to 0$. This means the first term in the integrand product has the properties of the Dirac-δ function that can be written,

$$\lim_{\tau \to 0}\left\{\frac{e^{-|t'-t|/\tau}}{2\tau}\right\} = \delta(t'-t) \tag{A.3.2}$$

Hence, (A.3.1) simplifies

$$v_{Therm}(x,t) \to \sqrt{\frac{2k_BT}{\zeta}} \int_{-\infty}^{t} \lim_{\tau \to 0}\left\{\frac{e^{-(t-t')/\tau}}{\tau}\right\}\xi(t')\,dt' = \sqrt{\frac{2k_BT}{\zeta}}\,\xi(t) \tag{A.3.3}$$

A.4 Integration and ensemble average

Combining equations (A.2.1), (A.2.4), (A.2.7), (A.2.9), (A.3.3) and (A.1.3), the particle velocity is

$$v(x,t) = v_{DEP}(x,t) + v_{EP}(x,t) + v_{Const} + v_{Therm}(t) \tag{A.4.1}$$

$$= F_{DEP}(x)\left[\frac{1+\cos(2\omega t+2\theta)}{\zeta}\right] + \frac{F_{EP}(x)\cos(\omega t+\theta)}{\zeta} + \frac{F_{Const}}{\zeta} + \sqrt{\frac{2k_BT}{\zeta}}\xi(t)$$

The aim is to simplify (A.4.1) by identifying the most significant terms. The most straightforward approach is to consider displacements x that are small enough so the dielectrophoretic and electrophoretic forces are approximately constant: $F_{DEP}(x) = \hat{F}_{DEP}$ and $F_{EP}(x) = \hat{F}_{EP}$. Thus, (A.4.1) is separable and can be integrated,

$$\int dx = \int_{t_1}^{t}\left\{\hat{F}_{DEP}\left[\frac{1+\cos(2\omega t')}{\zeta}\right] + \frac{\hat{F}_{EP}\cos(\omega t')}{\zeta} + \frac{F_{Const}}{\zeta} + \sqrt{\frac{2k_BT}{\zeta}}\xi(t')\right\}dt' \tag{A.4.2}$$

where the initial time t_1 is considered to be sufficiently 'long' after the relaxation time, so $t_1 > \tau + t_0$. To simplify the following analysis and without loss of generality the phase of the electric field is set to zero, $\theta = 0$. Hence,

$$x(t)=\underbrace{x^*(t_1)+\left(\frac{\hat{F}_{DEP}}{\zeta}+\frac{F_{Const}}{\zeta}\right)t+\frac{\hat{F}_{DEP}\sin(2\omega t)}{\zeta 2\omega}+\frac{\hat{F}_{EP}\sin(\omega t)}{\zeta\omega}}_{\text{deterministic}}+\underbrace{\sqrt{\frac{2k_BT}{\zeta}}\int_{t_1}^{t}\xi(t')\,dt'}_{\text{stochastic}} \qquad \text{(A.4.3)}$$

where the initial displacement terms are grouped together for convenience,

$$x^*(t_1)=x(t_1)-\left(\frac{\hat{F}_{DEP}}{\zeta}+\frac{F_{Const}}{\zeta}\right)t_1-\frac{\hat{F}_{DEP}\sin(2\omega t_1)}{2\zeta\omega}-\frac{\hat{F}_{EP}\sin(\omega t_1)}{\zeta\omega}$$

For the dielectrophoretic and electrophoretic forces to be constant, the maximum integration time t is limited, $t = T_p + t_1$ where the epoch T_p, is large with respect to the electric field time period $1/f$. Choosing, for example, the video frame period $T_p = 40$ msec; since 20 kHz $\le f \le$ 20 MHz, then $50\,\text{ns} \le 1/f \le 50\,\mu\text{s}$. Hence, $T_p >> 1/f$.

To simplify the expression for displacement $x(t)$ it is convenient to examine, separately, the deterministic and stochastic terms as labelled in (A.4.3). Consider the two deterministic DEP terms. The maximum ratio of the AC oscillating component compared with the DC component is,

$$X_{AC/DC}=\left|\frac{\hat{F}_{DEP}[\sin(2\omega t)-\sin(2\omega t_1)]/(2\zeta\omega)}{\hat{F}_{DEP}(t-t_1)/\zeta}\right|_{\max}\cong\frac{2}{(t-t_1)2\omega_{\min}}=\frac{1}{2\pi f_{\min}T_p} \qquad \text{(A.4.4)}$$

where it assumed, for conciseness of argument, $\left|\sin(2\omega t)-\sin(2\omega t_1)\right|_{\max}=2$. Letting $T_p = 40$ msec and $f_{\min} = 20$ kHz, $X_{AC/DC} = 1/(1600\pi)$. Thus, the magnitude of the displacement due to the AC oscillating component of the DEP force is negligible compared with the DC component.

Similarly, to compare the oscillatory EP and 'DC' DEP displacements requires an estimate of the maximum ratio

$$X_{EP/DEP}=\left|\frac{\hat{F}_{EP}[\sin(\omega t)-\sin(\omega t_1)]/(\zeta\omega)}{\hat{F}_{DEP}(t-t_1)/\zeta}\right|_{\max}\cong\frac{2\hat{F}_{EP}}{\hat{F}_{DEP}(t-t_1)\omega_{\min}}=\frac{\hat{F}_{EP}/\hat{F}_{DEP}}{\pi f_{\min}T_p} \qquad \text{(A.4.5)}$$

Assuming Maxwell-Wagner polarisation for a latex bead, the DEP force is

$$\hat{F}_{DEP}=\frac{\alpha V}{4}\frac{\partial E(x)^2}{\partial x}\cong\pi a^3\varepsilon_m\,\text{Re}\{f_{CM}\}\frac{\Delta\Phi^2}{\Delta x^3} \qquad \text{(A.4.6)}$$

and the EP force is

$$\hat{F}_{EP} = 6\pi a \varepsilon_m Z_\phi E = 6\pi a \varepsilon_m Z_\phi \Delta\Phi / \Delta x \qquad \text{(A.4.7)}$$

where, for a typical DEP experiment, $\Delta\Phi$ = 10 V_{peak} potential difference across inter-electrode space Δx = 10 μm leads to $E = 1.0\times10^6$ V/m. For a 216 nm diameter bead, with $\text{Re}\{f_{CM}\} = 1$, Z_ϕ = 50 mV, in medium with $\varepsilon_m = 78.4\times8.854\times10^{-12}$ F/m, the DEP and EP forces are approximately, $\hat{F}_{DEP}=0.2747\times10^{-12}$N = 0.275 pN and $\hat{F}_{EP}=70.66$ pN ≅ 71 pN, respectively. Choosing the minimum frequency, f = 20 kHz, and T_p = 40 msec video frame period, a reasonable lower bound of the ratio of the DEP and EP displacements is

$$X_{EP/DEP} = \frac{\hat{F}_{EP}/\hat{F}_{DEP}}{\pi f_{\min} T_p} = \frac{257.2}{800\pi} = 0.1023 \cong 0.1 \qquad \text{(A.4.8)}$$

The ratio $X_{EP/DEP}$ is proportionally smaller as f increases, and indeed T_p (provided the EP and DEP forces remain constant). Hence, the DEP displacement is at least an order of magnitude greater then the EP component.

Thus, the deterministic DEP and EP oscillating terms can be discarded for these high frequencies, and (A.4.1) simplifies

$$x(t) \cong \left(\frac{\hat{F}_{DEP}}{\zeta} + \frac{F_{Const}}{\zeta}\right)(t - t_1) + \sqrt{\frac{2k_BT}{\zeta}} \int_{t_1}^{t} \xi(t')\,dt' \qquad \text{(A.4.9)}$$

If the frequency is much lower, $f \sim$ Hz, then AC oscillatory components would need to be included in the model. This prediction agrees with experimental observations where latex spheres have exhibited oscillatory motion at low AC frequencies.

A suitable method of determining the significance of the stochastic noise term is by considering the statistics of displacement x for an *ensemble* of experiments. Assuming the noise to be Gaussian, it is sufficient to find the average (or mean) and variance of x. The ensemble average, from (2.3.14)

$$\langle x(t)\rangle = \lim_{N\to\infty}\left\{\frac{1}{N}\sum_{n=1}^{N} x_n(t)\right\} \tag{A.4.10}$$

$$\begin{aligned}\langle x(t)\rangle &= \left\langle \left(\frac{\hat{F}_{DEP}}{2\zeta}+\frac{F_{Const}}{\zeta}\right)(t-t_1)\right\rangle + \left\langle \sqrt{\frac{2k_BT}{\zeta}}\int_{t_1}^{t}\xi(t')\,dt'\right\rangle \\ &= \left(\frac{\hat{F}_{DEP}}{2\zeta}+\frac{F_{Const}}{\zeta}\right)(t-t_1)+\sqrt{\frac{2k_BT}{\zeta}}\int_{t_1}^{t}\langle\xi(t')\rangle\,dt'\end{aligned} \tag{A.4.11}$$

Since $\langle\xi(t)\rangle = \lim_{N\to\infty}\left\{\frac{1}{N}\sum_{n=1}^{N}\xi_n(t)\right\} = 0$,

$$\langle x(t)\rangle = \left(\frac{\hat{F}_{DEP}}{2\zeta}+\frac{F_{Const}}{\zeta}\right)(t-t_1) \tag{A.4.12}$$

which justifies the inclusion of the *deterministic* term in (A.4.9).

The variance of $x(t)$, from (2.3.15) is

$$\mathrm{var}\{x(t)\} = \left\langle\left[x(t)-\langle x(t)\rangle\right]^2\right\rangle$$

Using (A.4.9) and (A.4.12),

$$\begin{aligned}\mathrm{var}\{x(t)\} &= \left\langle\left[\left(\frac{\hat{F}_{DEP}}{2\zeta}+\frac{F_{Const}}{\zeta}\right)(t-t_1)(1-1)+\sqrt{\frac{2k_BT}{\zeta}}\int_{t_1}^{t}\xi(t')\,dt'\right]^2\right\rangle \\ &= 2k_BT/\zeta\left\langle\int_{t_1}^{t}\int_{t_1}^{t}\xi(t')\xi(t'')\,dt'dt''\right\rangle = 2k_BT/\zeta\int_{t_1}^{t}\int_{t_1}^{t}\langle\xi(t')\xi(t'')\rangle\,dt'dt''\end{aligned} \tag{A.4.13}$$

and since $\langle\xi(t')\xi(t'')\rangle = \delta(t'-t'')$ then

$$\mathrm{var}\{x(t)\} = 2k_BT/\zeta\int_{t_1}^{t}\int_{t_1}^{t}\delta(t'-t'')dt'dt'' = 2k_BT/\zeta\int_{t_1}^{t}1\,dt'' = 2k_BT(t-t_1)/\zeta \tag{A.4.14}$$

It is clear, therefore, knowledge of var$\{x(t)\}$ (or how the distribution of x varies with time t) requires the inclusion of the *stochastic* term in (A.4.9). Thus, (A.4.1) requires the non-time varying deterministic term, and stochastic term

$$v(x,t) = \frac{dx}{dt} = \frac{F_{DEP}(x)}{\zeta} + \frac{F_{Const}}{\zeta} + \sqrt{\frac{2k_BT}{\zeta}}\xi(t) \qquad \text{(A.4.15)}$$

and (2.4.5) follows.

Appendix B Development of the Fokker-Planck equation

The incremental change in the probability distribution, from (2.4.13), is

$$\Delta p(x,t)=\underbrace{\left\langle -\left[\left(v_{dtm}(x(t))\Delta t+\Delta v_{stch}(t)\right)\right]\frac{d\,\delta(x-x(t))}{dx}\right\rangle}_{term\,1}+\underbrace{\frac{1}{2}\left\langle\left[v_{dtm}(x(t))\Delta t+\Delta v_{stch}(t)\right]^2\frac{d^2\,\delta(x-x(t))}{dx^2}\right\rangle}_{term\,2} \tag{B.1}$$

Consider *term* 1 on the right hand side (*rhs*). Since the events leading up to $x(t)$ are independent of events after t, (that is, the increment Δt), the sum of products can be split. Following the approach taken by Haken (1978), p. 158-164,

$$\begin{aligned}&\left\langle -\left[\left(v_{dtm}(x(t))\Delta t+\Delta v_{stch}(t)\right)\right]\frac{d\,\delta(x-x(t))}{dx}\right\rangle\\&=\left\langle -\Delta t\frac{d\left[\delta(x-x(t))v_{dtm}(x)\right]}{dx}\right\rangle-\left\langle\Delta v_{stch}(t)\right\rangle\left\langle\frac{d\,\delta(x-x(t))}{dx}\right\rangle\end{aligned} \tag{B.2}$$

$$\Rightarrow\ term\,1=-\Delta t\frac{d\left[\left\langle\delta(x-x(t))\right\rangle v_{dtm}(x)\right]}{dx}-\sqrt{\frac{2kT}{\zeta}}\left\langle\Delta\xi(t)\right\rangle\frac{d\left\langle\delta(x-x(t))\right\rangle}{dx}$$

Since $\langle\xi(t)\rangle=0$, then $\langle\Delta\xi(t)\rangle=\left\langle\int^{t+\Delta t}\xi(t)\,dt\right\rangle=\int^{t+\Delta t}\langle\xi(t)\rangle dt=0$, hence

$$rhs\ term\ 1=-\Delta t\frac{d\left[p(x,t)v_{dtm}(x)\right]}{dx}=-\Delta t\frac{d\left(pv_{dtm}\right)}{dx} \tag{B.3}$$

Consider term 2,

$$\begin{aligned}&\frac{1}{2}\left\langle\left[v_{dtm}(x(t))\Delta t+\Delta v_{stch}(t)\right]^2\frac{d^2\,\delta(x-x(t))}{dx^2}\right\rangle\\&=\frac{1}{2}\left\langle\left[{v_{dtm}}^2(x(t))\Delta t^2+2v_{dtm}(x(t))\Delta t\Delta v_{stch}(t)+\Delta v_{stch}(t)^2\right]\frac{d^2\,\delta(x-x(t))}{dx^2}\right\rangle\end{aligned} \tag{B.4}$$

$$\therefore term\,2 = \frac{1}{2}\left\langle v_{dtm}{}^2(x(t))\Delta t^2 \frac{d^2\,\delta(x-x(t))}{dx^2}\right\rangle + 2\Delta t\left\langle v_{dtm}(x(t))\frac{d^2\,\delta(x-x(t))}{dx^2}\right\rangle\sqrt{\frac{2k_BT}{\zeta}}\underbrace{\langle\Delta\xi(t)\rangle}_{\to 0}$$

$$+\frac{2k_BT}{2\zeta}\langle\Delta\xi(t)\Delta\xi(t')\rangle\left\langle\frac{d^2\,\delta(x-x(t))}{dx^2}\right\rangle$$

and since $\langle\xi(t)\xi(t')\rangle = \delta(t-t')$ then, (B.5)

$$\langle\Delta\xi(t)\Delta\xi(t')\rangle = \int_t^{t+\Delta t}\int_{t'}^{t'+\Delta t}\delta(t-t')dt\,dt' = \int_t^{t+\Delta t}1dt' = \Delta t$$

$$\therefore rhs\ term\,2 = \frac{k_BT}{\zeta}\Delta t\frac{d^2\langle\delta(x-x(t))\rangle}{dx^2} + \frac{\Delta t^2}{2}\left\langle v_{dtm}{}^2(x(t))\frac{d^2\,\delta(x-x(t))}{dx^2}\right\rangle$$

$$= \frac{k_BT}{\zeta}\Delta t\frac{\partial^2 p(x,t)}{\partial x^2} + \frac{\Delta t^2}{2}\left\langle v_{dtm}{}^2(x(t))\frac{d^2\,\delta(x-x(t))}{dx^2}\right\rangle \quad (B.6)$$

Combining (B.1), (B.3) and (B.6),

$$\Delta p(x,t) = -\Delta t\frac{\partial(p(x,t)v_{dtm}(x))}{\partial x} + \frac{k_BT}{\zeta}\Delta t\frac{\partial^2 p(x,t)}{\partial x^2} + \frac{\Delta t^2}{2}\left\langle v_{dtm}{}^2(x(t))\frac{d^2\,\delta(x-x(t))}{dx^2}\right\rangle \quad (B.7)$$

dividing both sides by Δt and taking the limit $\Delta t \to 0$

$$\lim_{\Delta t\to 0}\left\{\frac{\Delta p(x,t)}{\Delta t}\right\} = \lim_{\Delta t\to 0}\left\{-\frac{\partial(p(x,t)v_{dtm}(x))}{\partial x} + \frac{k_BT}{\zeta}\frac{\partial^2 p(x,t)}{\partial x^2} + \frac{\Delta t}{2}\left\langle v_{dtm}{}^2(x(t))\frac{d^2\,\delta(x-x(t))}{dx^2}\right\rangle\right\}$$

the term with Δt vanishes, thus yielding the FPE

$$\frac{\partial p(x,t)}{\partial t} = -\frac{\partial(p(x,t)v_{dtm}(x))}{\partial x} + \frac{k_BT}{\zeta}\frac{\partial^2 p(x,t)}{\partial x^2} \quad (B.8)$$

Appendix C Fabrication of microelectrodes

The following is a brief summary of steps used by the author for positive resist fabrication of micro-electrodes onto glass microscope slides and is illustrated in Fig. 3.3(a). The positive[1] resist S1818 coated onto the slides consisted of a Novolac polymer and photoactive compound (PAC) that broke down when exposed to Ultra-Violet (UV) light at 364 nm. Immersed in a developer at high pH, patterned glass areas of UV exposed photo-resist became soluble and were washed away. In contrast, immersing areas of non-exposed photo-resist in the developer caused the Novolac and PAC to bind into an insoluble, structurally stable film. Evaporation of titanium, and consecutive metals, resulted in UV exposed patterned areas to be coated with metals that bound with the glass substrate. The non-exposed areas of film were also coated. However, these non-exposed areas were then dissolved by immersing the metallic coated slide in acetone. This final process, called 'lift-off' thus left the metallic layers bound onto glass opposite to the original pattern of the mask.

1. The glass slides were checked for scratches and scrubbed to remove debris. To remove grease the slides were then bathed in Opticlear® for 5 minutes (mins.) followed by acetone and methanol then treated with ultrasound (5 mins). A more rigorous alternative was to bath slides for 5 – 10 mins. in hydrogen peroxide/sulphuric acid ($7\times H_2SO_4$: $1\times H_2O_2$) maintaining temperature 70 – 80 °C (using a water bath in a fume-hood cabinet). The slides were rinsed with RO water, and blow-dried with nitrogen (N_2)
2. The cleaned slides were coated with positive resist (≈ 1.8 μm thickness). This involved a 1 minute (min.) pre-spin to remove any dust, a 30 second spin with primer (especially under conditions of relatively high humidity), and a 30 second spin 4000 rpm with S1818 resist. The coated slides were left to dry.
3. The resist coated glass slides were then baked in an oven at 90°C for 30 minutes. To improve pattern edge definition quality during lift-off (step 8), they were baked for 15 mins., soaked in chlorobenzene for 15 mins. (in fumehood cabinet), and baked for another 15 mins.
4. A pattern of UV light was exposed onto the slides using a prepared Cr/Fe mask pattern. To ensure correct exposure the instrument was carefully adjusted to ensure an even contact was established between the surface of the coated slide and the Cr/Fe mask, Fig. 3.3(a). The mask was cleaned before use by immersing in acetone and subjecting to ultrasound. Frequently, it was inspected under the microscope to check there was no debris to hinder an even contact with the resist coating. The UV source intensity was rated at 4 mW/cm^2. Double UV exposures were often performed, where a small UV filter covered the electrode area for the second exposure. The electrode areas received typically 5.8 seconds exposure, and electrode buses and bonding pads received 5.5 + 7.2 = 13 seconds.

---

[1] The term 'positive' resist refers to the type of polymeric compound that is *more* soluble (in a suitable solvent) after being irradiated than areas of unexposed resist (Pacansky and Lyerla, 1979).

5. The UV 'patterned' slides were immersed in photo-developer (150 ml developer suitable for S1818 resist diluted with 150 ml water) usually from 90 to 150 seconds.
6. Each slide was carefully inspected under the microscope to ascertain if the pattern of resist ('positive' or the same as the mask) had been coated onto the glass, Fig. 3.3(a)(ii). Optimal UV exposure and development times were achieved by trial-and-error. They depended on the patterned (or designed) size of electrodes and minimum inter-electrode spacing. For example, over-development resulted in areas resist being etched that should otherwise remain. This was particularly problematic for polynomial interelectrode spaces of 2 μm. On the other hand, under-development left smears of resist on glass substrate areas that should otherwise be free.
7. Metallic layers were consecutively deposited onto the (negative) developed resist pattered slides using a Plassys evaporator, Fig. 3.3(a)(iii). The aim was to deposit gold (Au) onto the glass, since gold is an excellent electrical conductor. However, gold does not bond to glass very well. Thus, the first metal evaporated was Titanium (Ti) typically 10 nm that forms a strong bond to the glass. The second metal evaporated onto Ti was Palladium (Pd), usually from 10 - 20 nm. The final metal evaporated onto palladium was gold 100 nm. The reason for using the palladium layer was to prevent the gold from oxidising the titanium.
8. The coated slides were immersed in acetone and treated with ultrasound for about 5 minutes to assist the lift-off process, Fig. 3.3(a)(iv). The pattern of electrodes ('negative' or opposite to the original mask design) was washed and dried.

Appendix D Production, testing, and analysis of pTA250 DNA

This appendix describes the growth, harvesting, purification and sample testing of plasmid DNA. These processes followed published standard protocols and procedures in the literature Sambrook *et al.* (1989); Maniatis *et al.* (1982, p. 86-95); QIAGEN Plasmid purification Handbook, January 1997; Brown (1995, chs. 3 and 5). The analysis of plasmid DNA recovered from DEP experiments is also described.

D.1 Growth, harvesting and purification of plasmid DNA

D.1.1 Growth of bacterial culture

1. A 2 litre solution of Luria Bertani (LB) broth was prepared by adding 20 g tryptone, 10 g yeast extract and 10g NaCl to 1900 ml to Reverse Osmosis (RO) purified water. The pH was adjusted to 7.5 by adding 25 ml NaOH (2g/100 ml) and the remaining 75 ml with RO water (Sambrook *et al.*, 1989, Book 3, Appendix A).
2. 100 ml of media was decanted and added to 1.5g agar powder.
3. Both the 100 ml agar solution and 1900 ml of media were autoclaved for about 20 minutes.
4. 40 mg of ampicillin antibiotic was measured directly into an Eppandorf® micro-tube, 1000 µl of double distilled water (ddH_2O) was further added, and vortexed. The reason for using the antibiotic was to improve growth selectivity by destroying bacteria that did not have ampicillin resistance conferred by the pTA250 plasmids.
5. The 1 ml ampicillin solution was added to 100 ml agar gel, mixed and poured into four petri dishes (25 ml each).
6. Two of four dishes (other remaining in storage for further use) were inoculated with pTA250 plasmid DNA (in storage at -70 °C). The inoculation procedure involved careful cross-pattern scraping over the agar gel. The dishes were incubated, upside down to prevent water condensation affecting bacteria, at 37 °C, and stored overnight at 4 °C.
7. Single colonies of *Eschericha coli* bacteria were picked from the gels and carefully placed into flasks containing the 1900 ml of autoclaved broth. The reason that single colonies were chosen is that they, rather than groups of colonies, indicate strength and resistance and hence would contain the ampicillin marker DNA.
8. The flasks were incubated overnight at 37 °C in a rotary shaker, shaking at 150 revolutions per minute (rpm).

D.1.2 Harvesting bacterial culture

1. The 1900 ml of bacterial culture was centrifuged for 20 minutes at 2 °C at 10000 rpm. Care was taken to ensure the total mass of each centrifuge tube was the same, to within ± 0.25 g, and centrifugation occurred in a vacuum.
2. The culture medium supernatant was discarded from the centrifuge tubes.
3. The pellet of bacterial cells at the bottom of each container was re-suspended in ice-cold TE buffer (and stirred with a glass pipette rod).

D.1.3 Plasmid purification

Purification of the mitochondrial plasmid DNA from bacterial cells was performed in accordance with protocol for Qiagen® tip 2500 for plasmids with medium copy number, Purification Handbook, p. 18-21 and 45-61. The purification is based on optimised alkaline lysis method, *op. cit.* p. 45. A detergent, sodium dodecyl sulphate (SDS) was used to lyse bacterial cell walls releasing plasmid and genomic (chromosomal) DNA, ribonucleic acid (RNA), protein and other cell debris. Additional NaOH and RNase denatured the chromosomal DNA, protein, and RNA. A positively charged anion exchange resin separated plasmid DNA from the debris by binding it, then the plasmid DNA was eluted and desalted by isopropanol precipitation.

D.2 Plasmid sample testing

Two simple tests of the pTA250 plasmid DNA purity were optical spectrophotometry and non-denaturing agarose gel electrophoresis. Agarose gel electrophoresis was also performed on pTA250 cut by restriction enzymes.

D.2.1 Optical spectrophotometry

To quantify concentrations of DNA and RNA, the readings of the optical spectrophotometer are based on units of optical density (OD) at wavelength (λ) of 260 nm OD_{260} (Davis *et al.*, 1994, p. 23), or expressed otherwise as absorption A_{260}. An OD_{260} = 1.0 (or 1 A_{260} unit) corresponds to approximately 50 µg/ml for double stranded DNA, 40 µg/ml for single stranded DNA and RNA, and ~ 20 µg/ml for single stranded oligonucleotides (Sambrook *et al.*, 1989, Appendix E, p. 5).

The concentrations of 1200 µl stock DNA, described in section 3.3.1, were measured using a scanning spectrophotometer (Shimadzu, Japan, UV-2101PC) with the direction and assistance of Dr. P. Dominy. The first set of measurements used three samples of freshly prepared pTA250 stored in TE buffer ($pDNA_{TE}$). Each sample was diluted in 1 ml of TE buffer in a quartz cuvette and shaken. The usual precautions were taken to avoid contamination, such as, temporarily sealing the cuvette with Nescofilm® (Azwell Inc., Japan) before shaking, etc. The reference was filled with 1 ml of TE buffer, and both cuvettes mounted for measurement. Absorption readings A_{260} and A_{280} were taken at separate wavelengths $\lambda = 260$ nm and $\lambda = 280$ nm, respectively. The values for each sample are listed for each sample in Table D.1. The readings were taken with respect to the reference so that absorption values above $\lambda = 320$ nm were zero.

The DNA concentration in the cuvette (µg/ml) is expressed,

$$C_{DNA\,cuvette} = (A_{260} - A_{320}) \times OD_{260} = A_{260} \times OD_{260} \qquad (D.1)$$

hence, the concentration of the prepared stock DNA C_{DNA} (µg/µl) is written,

$$C_{DNA} = \frac{C_{DNA\,cuvette} V_{cuvette}}{V_{sample}} = \frac{A_{260}\ OD_{260} V_{cuvette}}{V_{sample}} = \frac{A_{260}\ OD_{260}}{V_{sample}} \qquad (D.2)$$

where V_{sample} is the sample volume (µl) and $V_{cuvette} = 1$ ml is the dilution volume (that was the same in all measurements). For example, the stock DNA concentration calculated from measurements of the first sample is,

$C_{DNA} = A_{260} \times OD_{260} / V_{sample} = 0.064 \times 0.050/1.0 = 3.2$ µg/µl

Similarly, the ratio A_{260}/A_{280} for the first sample is calculated, $A_{260}/A_{280} = 0.064/0.043 = 1.9$

Sample	Sample vol. (µl)	A_{260}	A_{280}	C_{DNA} (µg/µl)	A_{260}/A_{280}
1	1.0	0.064	0.034	3.2	1.9
2	1.0	0.067	0.038	3.4	1.8
3	1.0	0.053	0.031	2.6	1.7
Average	1.0	0.061	0.034	3.1	1.8

Table D.1. Results of optical spectrophotometry measurements for freshly purified pTA250 plasmid

The results are summarised in Table D.1. The A_{260}/A_{280} ratios are all above 1.6 indicating the sample absorption is due to nucleic acids, and is free of protein and contaminants, including phenol or other organic compounds (Davis *et al.*, 1994, p. 23). Note, that pure preparations of DNA and RNA have respective absorption ratios of 1.8 and 2.0 (Sambrook *et al.*, 1989, p. E.5). Hence the A_{260}/A_{280} ratios indicate the presence of DNA rather than RNA.

A second set of optical spectrophotometry measurements, taken approximately 20 months later, using samples from three separate aliquots (from the same 1200 µl stock DNA preparation) gave similar results. The three samples were from pTA250 diluted in 10 % TE ($pDNA_{10\%TE}$) buffer and had been frozen at – 20 °C (for *ca.* 20 months). The $pDNA_{10\%TE}$ sample volumes are listed below in Table D.2. Each sample was diluted in 1 ml of RO water and the reference cuvette also contained 1 ml of RO water. The concentration of each DNA sample was calculated using equation (D.2) and is summarised in Table D.2 together with the A_{260}/A_{280} ratios. The results are similar to the first table, in particular the $A_{260}/A_{280} = 1.8$ indicates the sample is pure.

Trial	Sample vol. (µl)	A_{260}	A_{280}	C_{DNA} (µg/µl)	A_{260}/A_{280}
4	5.0	0.25	0.13	2.5	1.9
5	5.0	0.20	0.11	2.0	1.8
6	3.0	0.14	0.082	2.3	1.7
Average	-	-	-	2.3	1.8

Table D.2. Results of the second optical spectrophotometry measurements for purified pTA250 plasmid

The 'stringy' viscous appearance of the stock DNA during micro-pipetting indicated it had not been denatured during freezing. The DNA concentration C_{DNA} values are slightly lower than in the first table but with respect to the variation discussed in section 3.3.4, this is not significant. The benchmark value for the 1200 µl DNA stock concentration throughout the course of DEP (and dielectric) measurements is therefore the average, $C_{DNA} = (3.1 + 2.3)/2 = \underline{2.7\ \mu g/\mu l}$.

D.2.2 Agarose gel electrophoresis

The preparation of a 1% (w/v) 8 lane agarose mini-gel (10×10×1 cm i.e. 100 ml) followed the instructions stated in Sambrook *et al.* (1989): Book 1, Ch. 6. For a high molecular weight DNA where gel pore size needs to be larger, a lower percentage, 0.6 - 0.8 % (w/v) of agarose should be used.

1. 100 ml 0.5 TBE (Tris-Borate EDTA) was prepared by adding 5 ml 10×TBE to 95 ml ddH_2O.
2. 1 g of agarose gel powder was measured, added to 100 ml 0.5×TBE, and mixed in a 500 ml flask (that was large enough to prevent spillage).
3. The contents of the flask were heated in a microwave oven until it started to boil.
4. A gel tray was set-up by fixing masking tape at both ends ensuring there would be no leaks.
5. 5 µl of (10 µg/µl) of ethidium bromide ($C_{21}H_{20}N_3Br$, Sigma™ E1510) was dissolved into the warm-hot 100 ml gel (resulting in an ethidium bromide concentration = 0.5 µg/ml).
6. When the ethidium bromide gel had cooled further, the solution was poured into the tray (the edges of the mould were sealed first). A plastic comb for loading the DNA was inserted once the solution had sufficiently cooled (so the comb would not deform).
7. The gel was left for a half-hour to set, and checked for leakages.
8. Once the gel had set, the tray was placed in a bath and filled with electrophoresis (TBE) buffer until it covered the gel by several millimetres.
9. The gel wells (slots) were carefully micro-pipetted with DNA and buffer. The aim was to fill each well with 30 – 300 ng DNA taking care to avoid puncturing the bottom of the gel.
10. At least one well was filled marker (or 'ladder') DNA.
11. The potential supplied for electrophoresis was usually 50 or 100 V (run for ½ - 1 hour). Electrolysis occurred at the electrodes and the DNA moved from negative to positive electrodes.
12. The gel was carefully handled and inspected under UV light at 30 minute intervals to monitor movement of the DNA. A UV camera recorded the location of the bands.

D.2.3 Restriction enzyme preparation and analysis

D.2.3.1 Preparation

The details of the restriction enzyme digestions of pTA250 were as follows:

1. 4 µl from a 10 µl aliquot of pTA250 in ddH_2O (i.e. 10 µl $pDNA_{ddw}$) was added to 28 µl of distilled water and divided into 4 × 8 µl aliquots.
2. The first aliquot was a control sample, and was added to 2 µl of distilled water, and mixed (pulse micro-fuged) and left in ice.
3. The three other samples were added to 1 µl of buffer and 1 µl of restriction enzymes, *Bam*H1, *Eco*R1, and *Hin*dIII .
4. The three 10 µl solutions were mixed (pulse micro-fuged), and incubated at 37 °C for two hours.

D.2.3.2 Electrophoresis analysis

5. A 1% agarose mini-gel was prepared (as described in Appendix D.2.2)
6. 5 µl of each *Bam*H1, *Eco*R1, and *Hin*dIII restriction digest was added to 1 µl of loading buffer (Promega E, Promega H, and BRL respectively).
7. The remaining 5 µl of each sample was left on ice for use in DEP experiments (described below section D.2.3.3).
8. 10 kb Marker DNA was loaded into the first, far left, lane (lane 1), the control (or uncut sample) was loaded into lane 2, and samples digested with *Bam*H1, *Eco*R1, and *Hin*dIII were loaded into lanes 3, 4 and 5, respectively
9. A 100 V potential was used in the mini-gel electrophoresis, and after 30 minutes it was inspected under UV light. The DNA appeared to be migrating satisfactorily, and smears that may indicate low molecular weight protein, were absent.
10. Electrophoresis was resumed for another half hour and the mini-gel photographed again, Fig. 3.6(a).

D.2.3.3 Dielectrophoresis experiments

11. 5 µl aliquots of the four samples (control pTA250, and digests *Bam*H1, *Eco*R1, and *Hin*dIII) remaining from gel electrophoresis (step 7, D.2.3.2), were used for DEP experiments after a two day storage at +4°C.
12. 1 µl DAPI stock and 1 µl 2-Mercaptoethanol was added to each aliquot, and each of the 4 7 µl samples was micro-pipetted onto polynomial DEP electrodes (5, 7.5 and 10 µm centre diagonal).
13. Each sample was enclosed with a cover-slip and a variable AC potential applied to the electrodes.
14. The only aliquot which exhibited DEP was the undigested *control* DNA solution. Very curiously, large structures of DNA were not as prevalent.
15. All three samples which had been incubated with restriction enzyme clearly exhibited particles in solution, however, very little DEP movement or accumulation occurred.
16. This may be due to very high conductivities of the solutions since,

- the oscilloscope recorded about three-quarters the DDS voltage (14 $V_{p\text{-}p}$) and
- hydrolysis occurred at 1 MHz which is very unusual at this frequency.

D.3 Analysis of plasmid DNA recovered from DEP experiments

Three 10 µl aliquots of $pDNA_{TE}$, $pDNA_{10\%TE}$, and $pDNA_{ddw}$ were used to prepare samples as follows:

- Sample Type (I): 2 µl of $pDNA_{TE}$ was added to 2 µl of ethidium bromide stock (500 µg/ml Sigma ™, E1385) and further diluted in 10 µl of RO water.
- Sample Type (II): as above except using $pDNA_{10\%TE}$ instead of $pDNA_{TE}$
- Sample Type (III): as above except using $pDNA_{ddw}$

Each 14 µl labelled DNA solution sample was micro-pipetted onto a polynomial design electrode set and enclosed with a 7×22 mm cover-slip to reduce evaporation. Under epi-fluorescence microscopy, ethidium bromide labelled samples I and III did not exhibit 'specs' or particles; they appeared to 'form' out of solution only when AC frequencies of the order of 20 V_{p-p} (peak-to-peak) were applied to polynomial electrodes with centre diagonal sizes 5, 7.5 and 10 µm. Sample III appeared very cloudy & it was queried whether it may be degraded. Sample II exhibited particles that were thought to be plasmid, though the solution also appeared cloudy. Each DEP experiment was terminated in less than 10 minutes (since they did not appear to be very successful). After removing the cover-slip, each fluorescently labelled solution was pipetted off the electrode/glass surface and temporally stored; for convenience they have been labelled I′, II′ and III′ the (dash) ′ denoting the solution type that has been *recovered* from *DEP experiment*.

A 1% agarose gel was prepared, as described in Appendix D.2.2. 1 µl aliquots of samples I, II, and III were each diluted in 100 µl of RO water, mixed, and 10 µl of each sample added to 2 µl of gel loading buffer (the remaining 90 µl was stored for other DEP experiments). The same procedure was applied to *recovered* samples I′, II′ and III′. The 6 individual 12 µl samples were then loaded into lanes 2-7 of a gel. Lane 1 was used to establish a size base pair metric: 5µl of 1 kbp marker, added with 2 µl of loading buffer, was loaded into this lane. After electrophoresis, the gel was inspected under UV light, and subsequently photographed, Fig. 3.6(b). Unfortunately, as the Marker lane Fig. 3.6(b) reveals, the ladder DNA in the far left hand lane 1 degraded, resulting in a smear rather than the usual series of bands. Nonetheless, the gel analysis indicated all samples in lanes 2 - 7 contained two bands of DNA, and most likely these correspond to the same plasmid DNA in two different topological or isomeric states.

Appendix E A model for the normalised fluorescence image intensity

This appendix develops a phenomenological model of the time dependent normalised fluorescence intensity and how this relates to particle collection.

Appendix E.1 The form of the fluorescence image intensity

The light intensity, $I(l_2)$ emitted with by a suspension of fluorescent particles with concentration $c(y)$ over a length $l_2 - l_1$ is given by

$$I(l_2) = \eta_q I_{absorbed}(l_2) = \eta_q \left(1 - e^{-k_a \int_{l_1}^{l_2} c(y)\,dy}\right) I_{Incident}(l_1) \qquad \text{(E.1.1)}$$

where η_q is the quantum efficiency of the fluorophore, k_a is the absorption coefficient, and $I_{Incident}(l_1)$ is the initial optical intensity before absorption and re-emission with λ_e (Born and Wolf, 1999; Ploem and Tanke, 1987, ch. 5). In the usual case where the concentration of particles is low, $k_a \int_{l_1}^{l_2} c(y)\,dy < 1$ and (E.1.1) approximates,

$$I(l_2) \cong \eta_q k_a \int_{l_1}^{l_2} c(y)\,dy\; I_{Incident}(l_1) \qquad \text{(E.1.2)}$$

The intensity becomes proportional to particle concentration and is the basis of a simple model for quantitative measurements of DEP collections using fluorescence microscopy.

The light intensity, introduced in Chapter 3.5, $I(x,z,t)$ detected by the microscope CCD camera, of a suspension of fluorescent sub-micron particles includes light emitted over a considerable displacement along the optical axis. The axis is orthogonal to the electrode plane and parallel to the (vertical) y-axis, and the suspension lies $\{a \le y \le b\}$ where $y = a$, b are the respective positions of the electrode plane and cover-slip as described in chapters 5 and 6. In terms of physical size, the intensity consists of particle fluorescence essentially up to the height h of the cover-slip so $b - a = h$ where typically $20 \le h \le 200$ μm. The emitted light includes fluorescence emission parallel to $\vec{u}_y$ in both directions through the suspension: from cover-slip to electrodes, $b \to a$, and reverse, $a \to b$. This is particularly so when the electrodes significantly reflect light – and this effect is clearly evident in experimental observations.

Recording the DEP particle collection onto electrode edges requires the focal plane of the microscope to be adjusted so that it is close to the plane of the electrodes. This means the image

intensity $I(x,z,t)$, located optically at the plane of the camera detector, can be cast as the sum of two components

$$I(x,z,t) = I_{fp}(x,z,t) + I_b(x,z,t) \qquad \text{(E.1.3)}$$

where $I_{fp}(x,z,t)$ is the fluorescence from particles within a small displacement about the focal plane, and $I_b(x,z,t)$ is the fluorescence from the bulk suspension above the focal plane. The focal plane is assumed to have a small thickness or *length* ΔL where particles are in focus. At this stage it is convenient to describe two simplifications that can be made concerning the independent variables x and z.

As described in equation (3.5.1a), processing of the CCD images (or video frames) involved pixel averaging along a displacement in the longitudinal $\vec{u}_z$ direction given by $z_2 - z_1$. Therefore, the intensity in (E.1.3) can be written as having spatial dependence only in the transverse x direction (the over-bar denotes it is a spatial average),

$$\bar{I}(x,t) = \int_{z_1}^{z_2} I(x,z,t)\, dz \Big/ \int_{z_1}^{z_2} dz = \frac{1}{z_2 - z_1} \int_{z_1}^{z_2} I(x,z,t)\, dz \qquad \text{(E.1.4a)}$$

Furthermore, as detailed in Chapter 3 (and Chapter 6), the periodic and reflection symmetry properties of the electrode array in the $\vec{u}_x$ direction enabled the images to be 'averaged' in a periodic and symmetric sense or *transformed*. The process is detailed in equations (3.5.2) to (3.5.5). This means the $\vec{u}_x$ displacement is reduced from $x_1 \le x \le x_2$ to the *reduced* x-interval $0 \le x \le x_c$, where the 'cell' length is $x_c = \frac{w+d}{2}$. For brevity, the transformation is written as

$$\bar{I}(x,t) \rightarrow \tilde{I}(x,t) \qquad \text{(E.1.4b)}$$

where $\tilde{I}(x,t)$ is the transformed intensity. For the electrode arrangement previously described with ½ electrode and ½ gap cell length, $w = d = 10$ μm.

The source (excitation) intensity before absorption at $y = b$ is expressed as $I_s(\underline{x},t)\big|_{y=b}$. Since the source intensity is constant over the 2-D x-z image for the dimensions of interest, it is understood $I_s(x,b,z,t) \equiv I_s(t)$. Consider the first component. The incident excitation intensity at the focal plane $y = a + \Delta L$ is written,

$$I_{Incident}(x, a+\Delta L, z, t) = k_{ea}\, I_s(t) \qquad \text{(E.1.5)}$$

where k_{ea} accounts for the attenuation of incident light travelling in the direction $b \rightarrow a$ by *excitation absorbance* in the bulk suspension. Three other optical processes are included in the model. *Re-absorption* of the light emitted by the in-focus fluorophores, in the direction $a \rightarrow b$, can also occur in the bulk suspension before the light enters the microscope objective; this is expressed by k_{ra}. The interdigitated gold-electrode glass-gap interface also reflects incident (excitation) and emitted light with spatial variation in the x-direction,

$$r(x) = r_{el} - (r_{el} - r_{gp})\,u(x - x_e) \text{ for } 0 \le x \le x_c \qquad \text{(E.1.6a)}$$

where constants r_{el} and r_{gp} express the reflectivity of electrodes and glass, respectively, and $u(x-x_e)$ is the unit step function,

$$u(x-x_e) = \begin{cases} 1, & x > x_e \\ 0, & x < x_e \end{cases} \qquad \text{(E.1.6b)}$$

and x_e is the position of the electrode edge. Finally, optical parameters such as the numerical aperture of the microscope objective, are included in the *optical* constant k_{op}. Thus, substituting (E.1.5) into (E.1.2) and including the (x, t) independent variables, the first component is written,

$$I_{fp}(x,z,t) = k_{op} k_{ra}\, r(x) \eta_q k_a\; k_{ea} \int_a^{a+\Delta L} c(x,y,z,t)\,dy\, I_s(t) = k_l\, r(x) c(x,z,t) I_s(t) \qquad \text{(E.1.7)}$$

For convenience, the concentration is cast as being constant over the small length $l_2 - l_1 = \Delta L$ the particles are in focus, and the constant k_l is written to include ΔL, $k_l = k_{op}\, k_{ra}\; \eta_q\, k_a\; k_{ea}\, \Delta L$.

The second component of the intensity detected is the 'background' fluorescence from the bulk solution above the focal plane. It has similar features to the first component, though the concentration cannot be generally assumed to be constant in the y direction. The dashes $'$ denote different values assigned to the constants k_a, k_{ra}, etc., compared with the first component. The intensity is comprised of fluorescence processes in both directions ($b \rightarrow a$ and $a \rightarrow b$) and is written as a non-linear function $f(\,)$

$$I_b(x,z,t) = f\left(k_{op}\, k'_{ra}, k_a^{'}, k_{ea}, r(x), \eta_q, a, \Delta L, b, \int c(\underline{x},t)\,dy\right) I_s(t) \cong r(x)\; B(x,z,t)\, I_s(t) \qquad \text{(E.1.8)}$$

It is not essential to know the precise form of $f(\ )$ since the background fluorescence is essentially eliminated when the relative change in fluorescence is considered. It is sufficient to encapsulate most of the optical processes in the bulk suspension as $B(x,z,t)$. In the approximation, the spatial variation in reflection $r(x)$ is separated, although video images indicate the glass-electrode reflection transition is more gradual than the step function defined in (E.1.6b). Nonetheless, for the following argument, this does not matter. It should be noted light scattering is likely to occur so the constants are 'bulk' constants and scattering losses can be lumped with k'_a (Jenkins and White, 1981, p. 459).

Thus, combining (E.1.8), (E.1.7), (E.1.4a) and (E.1.3), the total intensity, spatially averaged along the longitudinal z-direction is

$$\bar{I}(x,t) = \frac{1}{z_2 - z_1}\int_{z_1}^{z_2}\Big(I_{fp}(x,z,t) + I_b(x,z,t)\Big)dz = \underbrace{k_l\, r(x)\bar{c}(x,t)I_s(t)}_{\bar{I}_{fp}(x,t)} + \underbrace{r(x)\bar{B}(x,t)I_s(t)}_{\bar{I}_b(x,t)} \qquad \text{(E.1.9a)}$$

where

$$\bar{c}(x,t) = \frac{1}{z_2 - z_1}\int_{z_1}^{z_2} c(x,z,t)\, dz \qquad \text{(E.1.9b)}$$

and

$$\bar{B}(x,t) = \frac{1}{z_2 - z_1}\int_{z_1}^{z_2} B(x,z,t)\, dz \qquad \text{(E.1.9c)}$$

To determine the temporal change in collections about the electrode edges, the intensity $\bar{I}(x,t)$ is averaged in the transverse direction $\vec{u}_x$ over the entire array, $x_1 \le x \le x_2$. The first 'average' uses the periodic and symmetric properties of the array described in the transformation (E.1.4b), so $\bar{I}(x,t) \to \tilde{I}(x,t)$ and $0 \le x \le x_c$. This also implies $\bar{c}(x,t) \to \tilde{c}(x,t)$ and $\bar{B}(x,t) \to \tilde{B}(x,t)$ on the *rhs* of (E.1.9a).

The second average is taken over a suitably chosen cell interval, $x_l \le x \le x_u$ where x_l denotes the *lower* limit bounded by $0 < x_l < x_e$, and x_u denotes the *upper* limit, $x_e < x_u < x_c$. For the electrode array geometry of interest, the edge position, $x_e = \frac{d}{2}$ and cell length is $x_c = d$. Averaging the *lhs* of (E.1.9a),

$$\bar{\bar{I}}_E(t) = \frac{1}{x_u - x_l}\int_{x_l}^{x_u} \tilde{I}(x,t)\,dx \qquad \text{(E.1.10)}$$

where the double over-bar denotes the spatial average in *both* $\vec{u}_x$ and $\vec{u}_z$ directions of the image plane. Consider the average of the first term on the *rhs* of (E.1.9a) and (E.1.9b), using (E.1.6)

$$\bar{\bar{I}}_{fp}(t) = \frac{1}{x_u - x_l}\int_{x_l}^{x_u} \tilde{I}_{fp}(x,t)\,dx = \frac{k_l I_s(t)}{x_u - x_l}\int_{x_l}^{x_u} \left(r_{el} - (r_{el} - r_{gp})u(x - x_e)\right)\tilde{c}(x,t)\,dx \qquad \text{(E.1.11a)}$$

$$= \frac{k_l I_s(t)}{x_u - x_l}\left(r_{el}\int_{x_l}^{x_u} \tilde{c}(x,t)\,dx - (r_{el} - r_{gp})\int_{x_e}^{x_u} \tilde{c}(x,t)\,dx\right) = k_l I_s(t)\bar{\bar{c}}_E(t)$$

where the second line results from the properties of the step function defined in (E.1.6b) and $\bar{\bar{c}}_E(t)$ is the average concentration 'weighted' by the reflection constants,

$$\bar{\bar{c}}_E(t) = \frac{1}{x_u - x_l}\left(r_{el}\int_{x_l}^{x_e} \tilde{c}(x,t)\,dx + r_{gp}\int_{x_e}^{x_u} \tilde{c}(x,t)\,dx\right) \qquad \text{(E.1.11b)}$$

Similarly, the average of the second term on the *rhs* of (E.1.9a) and (E.1.9c) is,

$$\bar{\bar{\bar{I}}}_b(t) = \frac{1}{x_u - x_l}\int_{x_l}^{x_u} \tilde{I}_b(x,t)\,dx = \bar{\bar{\bar{B}}}_E(t)I_s(t) \qquad \text{(E.1.12a)}$$

where

$$\bar{\bar{\bar{B}}}_E(t) = \frac{1}{x_u - x_l}\left(r_{el}\int_{x_l}^{x_e} \tilde{B}(x,t)\,dx + r_{gp}\int_{x_e}^{x_u} \tilde{B}(x,t)\,dx\right) \qquad \text{(E.1.12b)}$$

Combining (E.1.10) – (E.1.12), the spatial average of the intensity about the electrode edge is

$$\bar{\bar{I}}_E(t) = \left(k_l\bar{\bar{c}}_E(t) + \bar{\bar{\bar{B}}}_E(t)\right)I_s(t) \qquad \text{(E.1.13)}$$

Microscope CCD camera video images enables the time profile of $\bar{\bar{I}}_E(t)$ to be measured. These profiles are further manipulated to yield the collection of particles on electrode edges. This is described in the following appendices E.2 and E.3.

Appendix E.2 Normalisation of the fluorescence intensity

The normalised fluorescence intensity reduces the effect of temporal fluctuations in the source intensity, and is written,

$$F(t) = \frac{\bar{\bar{I}}_E(t)}{\bar{\bar{I}}_{LU}(t)} = \frac{\bar{\bar{I}}_E(t)}{\bar{\bar{I}}_T(t) - \bar{\bar{I}}_E(t)} \tag{E.2.1}$$

where $\bar{\bar{I}}_E(t)$ is given by (E.1.13) and $\bar{\bar{I}}_{LU}(t)$ is the complement of the total intensity (*excludes* the intensity contribution about the edge),

$$\bar{\bar{I}}_{LU}(t) = \frac{\int_0^{x_c} \tilde{I}(x,t)\,dx - \int_{x_l}^{x_u} \tilde{I}(x,t)\,dx}{x_c - 0 - (x_u - x_l)} = \frac{\int_0^{x_l} \tilde{I}(x,t)\,dx + \int_{x_u}^{x_c} \tilde{I}(x,t)\,dx}{x_c - x_u + x_l} \tag{E.2.2}$$

Substituting (E.1.9) and (E.1.6) into (E.2.2) and performing algebraic manipulations similar to those in Appendix E.1,

$$\bar{\bar{I}}_{LU}(t) = \left(k_l \bar{\bar{c}}_{LU}(t) + \bar{\bar{B}}_{LU}(t)\right) I_s(t) \tag{E.2.3a}$$

where

$$\bar{\bar{c}}_{LU}(t) = \frac{r_{el}\int_0^{x_l} \tilde{c}(x,t)\,dx + r_{gp}\int_{x_u}^{x_c} \tilde{c}(x,t)\,dx}{x_c - x_u + x_l} \tag{E.2.3b}$$

and

$$\bar{\bar{B}}_{LU}(t) = \frac{r_{el}\int_0^{x_l} \tilde{B}(x,t)\,dx + r_{gp}\int_{x_u}^{x_c} \tilde{B}(x,t)\,dx}{x_c - x_u + x_l} \tag{E.2.3c}$$

Substituting (E.1.13) and (E.2.3) into (E.2.1), $F(t)$ becomes independent of the source intensity $I_s(t)$,

$$F(t) = \frac{\bar{\bar{I}}_E(t)}{\bar{\bar{I}}_{LU}(t)} = \frac{[k_l \bar{\bar{c}}_E(t) + \bar{\bar{B}}_E(t)]I_s(t)}{[k_l \bar{\bar{c}}_{LU}(t) + \bar{\bar{B}}_{LU}(t)]I_s(t)} = \frac{k_l \bar{\bar{c}}_E(t) + \bar{\bar{B}}_E(t)}{k_l \bar{\bar{c}}_{LU}(t) + \bar{\bar{B}}_{LU}(t)} \tag{E.2.4}$$

Appendix E.3 Relative change in fluorescence image intensity

The difference between the normalised fluorescence, given by (E.2.4), over a given time interval $t-t_0$ is

$$\Delta F(t) = F(t) - F(t_0) = \frac{k_l \bar{\bar{c}}_E(t) + \bar{\bar{B}}_E(t)}{k_l \bar{\bar{c}}_{LU}(t) + \bar{\bar{B}}_{LU}(t)} - \frac{k_l \bar{\bar{c}}_E(t_0) + \bar{\bar{B}}_E(t_0)}{k_l \bar{\bar{c}}_{LU}(t_0) + \bar{\bar{B}}_{LU}(t_0)} \tag{E.3.1}$$

Repeated measurements indicate the background fluorescence, away from the electrode edge, decreases *slightly* over $t-t_0$, so $k_l \bar{\bar{c}}_{LU}(t) + \bar{\bar{B}}_{LU}(t) = (1-\delta_f)[k_l \bar{\bar{c}}_{LU}(t_0) + \bar{\bar{B}}_{LU}(t_0)]$ where δ_f tends to increase with time especially at the beginning but is always small, $0 \le \delta_f << 1$ and is typically 10% or less. In general, the background fluorescence over the electrode edge is significantly smaller than the fluorescence from the bead concentration for the time interval, $\Rightarrow$ $\bar{\bar{B}}_E(t) - \bar{\bar{B}}_E(t_0) < k_l[\bar{\bar{c}}_E(t) - \bar{\bar{c}}_E(t_0)]$ and indications are that $\bar{\bar{B}}_E(t) = (1-\delta_f)\bar{\bar{B}}_E(t_0)$. Therefore, substituting these relations into (E.3.1) and approximating $1/(1-\delta_f) \cong 1 + \delta_f$

$$\Delta F(t) = F(t) - F(t_0) = \frac{k_l \bar{\bar{c}}_E(t) + (1-\delta_f)\bar{\bar{B}}_E(t_0)}{(1-\delta_f)[k_l \bar{\bar{c}}_{LU}(t_0) + \bar{\bar{B}}_{LU}(t_0)]} - \frac{k_l \bar{\bar{c}}_E(t_0) + \bar{\bar{B}}_E(t_0)}{k_l \bar{\bar{c}}_{LU}(t_0) + \bar{\bar{B}}_{LU}(t_0)}$$

$$\cong \underbrace{\frac{1}{k_l \bar{\bar{c}}_{LU}(t_0) + \bar{\bar{B}}_{LU}(t_0)}}_{\textit{constant}} k_l[(1+\delta_f)\bar{\bar{c}}_E(t) - \bar{\bar{c}}_E(t_0)] \tag{E.3.2}$$

Thus, the normalised fluorescence change is approximately proportional to the change in average particle concentration about the electrode edge. Moreover, recalling (E.1.7) and (E.1.11b) the first term in the numerator of (E.3.2) is,

$$k_l \bar{\bar{c}}_E(t) = \frac{k_{op} k_{ra} \eta_q k_a k_{ea} \Delta L}{x_u - x_l}\left(r_{el} \int_{x_l}^{x_e} \tilde{c}(x,t)\, dx + r_{gp} \int_{x_e}^{x_u} \tilde{c}(x,t)\, dx \right) \tag{E.3.3}$$

The reverse transformations $\tilde{c}(x,t) \to \bar{c}(x,t)$ and $\tilde{B}(x,t) \to \bar{B}(x,t)$ are invoked simply by stipulating $k_l \bar{\bar{c}}_E(t)$ as *per unit cell*, $0 \le x \le x_c$ that is representative of all electrodes on the array considered in the image. Applying (E.1.9b)

$$\overline{\overline{k_l c_E}}(t) = \frac{k_{op} k_{ra}\ \eta_q k_a\ k_{ea}\,\Delta L}{x_u - x_l}\left(r_{el} \int_{x_l}^{x_e} \bar{c}(x,t)\,dx + r_{gp} \int_{x_e}^{x_u} \bar{c}(x,t)\,dx \right)$$

$$= \frac{k_{op} k_{ra}\ \eta_q k_a\ k_{ea}\Delta L}{(x_u - x_l)(z_2 - z_1)}\left(r_{el} \int_{x_l}^{x_e} \int_{z_1}^{z_2} c(x,z,t)\,dzdx + r_{gp} \int_{x_e}^{x_u} \int_{z_1}^{z_2} c(x,z,t)\,dzdx \right)$$

and invoking the assumptions leading to (E.1.7),

$$\overline{\overline{k_l c_E}}(t) = \frac{k_{op} k_{ra}\ \eta_q k_a\ k_{ea}}{(x_u - x_l)(z_2 - z_1)}\left(r_{el} \int_{x_l}^{x_e} \int_{z_1}^{z_2} \int_{a}^{a+\Delta L} c(x,y,z,t)dydzdx + r_{gp} \int_{x_e}^{x_u} \int_{z_1}^{z_2} \int_{a}^{a+\Delta L} c(x,y,z,t)dydzdx \right)$$

$$= \frac{k_{op} k_{ra}\ \eta_q k_a\ k_{ea} n_E(t)}{(x_u - x_l)(z_2 - z_1)} \qquad \text{(E.3.4a)}$$

where $n_E(t)$ is the number particles at an electrode edge of a representative 'cell' weighted by the reflection constants, and

$$n_E(t) = r_{el} \underbrace{\int_{x_l}^{x_e} \int_{z_1}^{z_2} \int_{a}^{a+\Delta L} c(x,y,z,t)dydzdx}_{\text{particle number from } x_l \text{ to edge}} + r_{gp} \underbrace{\int_{x_e}^{x_u} \int_{z_1}^{z_2} \int_{a}^{a+\Delta L} c(x,y,z,t)dydzdx}_{\text{particle number from edge to } x_u} \qquad \text{(E.3.4b)}$$

The same analysis is applied to the second term in the numerator of (E.3.2). Applying (E.3.4) to (E.3.2), the normalised fluorescence increase is approximately proportional to the increase in average particle number about the electrode edges,

$$\Delta F(t) = F(t) - F(t_0) \cong k[(1+\delta_f)n_E(t) - n_E(t_0)] \cong k[n_E(t) - n_E(t_0)] + \underbrace{k\delta_f\, n_E(t)}_{\text{error}} \qquad \text{(E.3.5)}$$

$$\cong k\Delta n_E(t) + \varepsilon_f(t)$$

where $k = \dfrac{k_{op} k_{ra}\ \eta_q k_a\ k_{ea}}{(x_u - x_l)(z_2 - z_1)[\overline{\overline{k_l c_{LU}}}(t_0) + \overline{\overline{B_{LU}}}(t_0)]}$ and the small error in fluorescence is $\varepsilon_f(t) = k\delta_f\, n_E(t)$.

Finally, since the experimental values of ΔF are small, a useful 'benchmark' is the *relative* change in normalised fluorescence ΔF_r,

$$\Delta F_r = \frac{F(t) - F(t_0)}{F(t_0)} \cong \frac{k_l\,[(1+\delta_f)\bar{\bar{c}}_E(t) - \bar{\bar{c}}_E(t_0)]}{k_l\,\bar{\bar{c}}_{LU}(t_0) + \bar{\bar{B}}_{LU}(t_0)} \Bigg/ \frac{k_l\,\bar{\bar{c}}_E(t_0) + \bar{\bar{B}}_E(t_0)}{k_l\,\bar{\bar{c}}_{LU}(t_0) + \bar{\bar{B}}_{LU}(t_0)}$$

$$\cong \frac{k_l\,[(1+\delta_f)\bar{\bar{c}}_E(t) - \bar{\bar{c}}_E(t_0)]}{k_l\,\bar{\bar{c}}_E(t_0) + \bar{\bar{B}}_E(t_0)} \cong k_r\,[n_E(t) - n_E(t_0)] + \underbrace{k_r\,\delta_f\,n_E(t)}_{error} \qquad \text{(E.3.6)}$$

$$\cong k_r \Delta n_E(t) + \varepsilon_r(t)$$

where $k_r = \dfrac{k_{op}\,k_{ra}\,\eta_q\,k_a\,k_{ea}}{(x_u - x_l)(z_2 - z_1)[k_l\,\bar{\bar{c}}_E(t_0) + \bar{\bar{B}}_E(t_0)]}$ and the relative error is $\varepsilon_r(t) = k_r \delta_f\,n_E(t)$.

Appendix F O-U solution with rectangular function IC

This appendix finds the solution of the Ornstein–Uhlenbeck (O-U) process with a rectangular function IC given by (5.1.7). The motivation for continuing the approach by Gardiner (1985) stems from being able to immediately use the expression for the GS of the PDE (5.1.2),

$$\frac{\partial p}{\partial t} = -\frac{\partial (pv)}{\partial x} + \frac{k_B T}{\zeta}\frac{\partial^2 p}{\partial t^2} = \frac{k}{\zeta}\frac{\partial (xp)}{\partial x} + \frac{k_B T}{\zeta}\frac{\partial^2 p}{\partial x^2} \tag{F.1}$$

where $p = p(x, t)$ and $v = v(x) = -kx/\zeta$. The GS is given conveniently in transform space s. The characteristic 'C' transform, and the inverse transform 'C^{-1}' are defined,

$$\phi(s) = C\{p(x)\} = \int_{-\infty}^{+\infty} p(x) e^{jsx}\, dx \tag{F.2}$$

$$p(x) = C^{-1}\{\phi(s)\} = \frac{1}{2\pi}\int_{-\infty}^{+\infty} \phi(s) e^{-jsx}\, ds \tag{F.3}$$

and it is understood $\leftrightarrow$ denotes C-transform pairs, $p(x) \leftrightarrow \phi(s)$. It is not difficult to generate transform pairs in Table F.1, with guidance from closely related Fourier pairs (Erdélyi, 1954; Stark and Tuteur, 1979). They can be verified, by replacing the Fourier pair variable time t with C-displacement x, and radian frequency ω with $-s$. The C-transform of the PDE (F.1), using properties in Table F.2,

$$\frac{\partial \phi}{\partial t} = -\hat{k}s\frac{\partial \phi}{\partial s} - Ds^2\phi \tag{F.4}$$

where $\phi = \phi(s, t)$, $\hat{k} = k/\zeta$ and $D = k_B T/\zeta$ is the diffusion coefficient. The transform of the IC given by (5.1.7) is

$$\begin{aligned}\phi(s,t) &= C\left\{\frac{1}{L}\mathrm{rect}\left(\frac{x-x_0}{L}\right)\right\} = \frac{1}{L}\int_{-\infty}^{+\infty}\mathrm{rect}\left(\frac{x-x_0}{L}\right)e^{jsx}\,dx = \frac{1}{\mathrm{L}}\int_{x_0-L/2}^{x_0+L/2} e^{jsx}\,dx \\ &= \left[\frac{e^{jsx}}{jsL}\right]_{x_0-L/2}^{x_0+L/2} = \frac{1}{jsL}\left(e^{jsL/2} - e^{-jsL/2}\right)e^{jsx_0}\end{aligned} \tag{F.5}$$

The GS of (F.4) is equation (3.8.68) in Gardiner (1985)

$$\phi(s,t) = e^{\frac{Ds^2}{2\hat{k}}} h\left(se^{-\hat{k}t}\right) \tag{F.6}$$

where the function h is not yet specified. It is found by equating the IC with the GS at $t = 0$,

$$\begin{aligned}
\phi(s,0) &= e^{\frac{Ds^2}{2\hat{k}}} h(s) \equiv \frac{\left(e^{js(x_0 + L/2)} - e^{js(x_0 - L/2)}\right)}{jsL} \\
\therefore h(s) &\equiv e^{\frac{Ds^2}{2\hat{k}}} \frac{\left(e^{js(x_0 + L/2)} - e^{js(x_0 - L/2)}\right)}{jsL} \\
\therefore h\left(se^{-\hat{k}t}\right) &= e^{\frac{Ds^2 e^{-2\hat{k}t}}{2\hat{k}}} \frac{\left(e^{jse^{-\hat{k}t}(x_0 + L/2)} - e^{jse^{-\hat{k}t}(x_0 - L/2)}\right)}{jse^{-\hat{k}t}L}
\end{aligned} \tag{F.7}$$

Hence, using (F.6)

$$\phi(s,t) = e^{-\frac{Ds^2}{2\hat{k}}\left(1 - e^{-2\hat{k}t}\right)} e^{\hat{k}t} \frac{\left(e^{jse^{-\hat{k}t}(x_0 + L/2)} - e^{jse^{-\hat{k}t}(x_0 + L/2)}\right)}{jsL} \tag{F.8}$$

Equating terms for convenience, $A \equiv D(1 - e^{-2\hat{k}t})/(2\hat{k}) \equiv k_B T(1 - e^{-2kt/\zeta})/(2k)$, $B \equiv \hat{k}t$, $C_+ \equiv (x_0 + \frac{L}{2})e^{-\hat{k}t}$ and $C_- \equiv (x_0 - \frac{L}{2})e^{-\hat{k}t}$

$$\phi(s,t) = \frac{e^{-s^2 A + B + jsC_+} - e^{-s^2 A + B + jsC_-}}{jsL} \tag{F.9a}$$

and letting $\tilde{\phi}(s) = \frac{1}{L} e^{-s^2 A + B}$ then (F.9a) is written succinctly,

$$\phi(s,t) = \frac{\tilde{\phi}(s)e^{jsC_+}}{js} - \frac{\tilde{\phi}(s)e^{jsC_-}}{js} \tag{F.9b}$$

Introducing *ansatz* the Dirac-δ function term and regrouping,

$$\therefore \phi(s,t) = \left(\frac{j\tilde{\phi}(s)e^{jsC_-}}{s} + \tilde{\phi}(s)\pi\delta(s)\right) - \left(\frac{j\tilde{\phi}(s)e^{jsC_+}}{s} + \tilde{\phi}(s)\pi\delta(s)\right) \tag{F.10}$$

Since the Dirac-δ function has the property for any continuous function $\phi(s)$, $\phi(s)\delta(s) = \phi(0)\delta(s)$ (Stark and Tuteur, 1979, p. 62), then

$$\phi(s,t) = \tilde{\phi}(s)e^{jsC_-}\left(\frac{j}{s} + \pi\delta(s)\right) - \tilde{\phi}(s)e^{jsC_+}\left(\frac{j}{s} + \pi\delta(s)\right) \qquad \text{(F.11)}$$

From Table F.2, (F.11) has recognisable form $\tilde{\phi}(s)\left(\pi\delta(s) + \frac{j}{s}\right) \leftrightarrow \int_{-\infty}^{x} \tilde{p}(\chi)d\chi$ hence,

$$p(x,t) = \int_{-\infty}^{x} \tilde{p}(\chi - C_-)d\chi - \int_{-\infty}^{x} \tilde{p}(\chi - C_+)d\chi \qquad \text{(F.12)}$$

Furthermore, from Gaussian delayed function C-transform pair, Table F-1, $\tilde{\phi}(s) = \frac{1}{L}e^{-s^2A + B + jsC_+} \leftrightarrow$ $\frac{1}{2L}\sqrt{\frac{\pi}{A}}e^{-(x-C_+)^2/4A}e^{B} \equiv \tilde{p}(x)$ hence,

$$p(x,t) = \frac{e^{B}}{2L\sqrt{\pi A}}\left[\int_{-\infty}^{x} e^{-\frac{(\chi - C_+)^2}{4A}}d\chi - \int_{-\infty}^{x} e^{-\frac{(\chi - C_+)^2}{4A}}d\chi\right] \qquad \text{(F.13)}$$

The integrals of the Gaussian functions in (F.13), can be written in terms of the error function $\text{erf}(z) = \frac{2}{\sqrt{\pi}}\int_0^z e^{-\gamma^2}d\gamma$ in (5.1.11) that is readily evaluated using software such as MATLAB 5.0 (Mathworks Inc., 1996). Transforming (F.13); for the first integral let $\gamma = \frac{\chi}{2\sqrt{A}} - \frac{C_-}{2\sqrt{A}} \Rightarrow$ $\chi = 2\sqrt{A}\gamma + C_-$, $d\chi = 2\sqrt{A}d\gamma$, $\gamma_1 = \frac{\chi_1 - C_-}{2\sqrt{A}} = \frac{-\infty - C_-}{2\sqrt{A}} = -\infty$, and $\gamma_2 = \frac{\chi_2 - C_-}{2\sqrt{A}} = \frac{x - C_-}{2\sqrt{A}}$. Similarly with the second integral, (F.13) is re-written

$$p(x,t) = \frac{e^{B}2\sqrt{A}}{2L\sqrt{\pi A}}\left[\int_{-\infty}^{(x-C_-)/2\sqrt{A}} e^{-\gamma^2}d\gamma - \int_{-\infty}^{(x-C_+)/2\sqrt{A}} e^{-\gamma^2}d\gamma\right] \qquad \text{(F.14)}$$

$$\therefore p(x,t) = \frac{e^{B}}{L\sqrt{\pi}}\left[\int_{-\infty}^{0} e^{-\gamma^2}d\gamma + \int_{0}^{(x-C_-)/2\sqrt{A}} e^{-\gamma^2}d\gamma - \left(\int_{-\infty}^{0} e^{-\gamma^2}d\gamma + \int_{-\infty}^{(x-C+)/2\sqrt{A}} e^{-\gamma^2}d\gamma\right)\right] \text{(F.15)}$$

where $\int_{-\infty}^{0} e^{-\gamma^2}d\gamma = \sqrt{\pi}/2$. Thus,

$$p(x,t)=\frac{e^{B}}{L\sqrt{\pi}}\frac{\sqrt{\pi}}{2}\left[\frac{2}{\sqrt{\pi}}\int_{0}^{(x-C_{-})/2\sqrt{A}}e^{-\gamma^{2}}d\gamma-\frac{2}{\sqrt{\pi}}\int_{-\infty}^{(x-C_{+})/2\sqrt{A}}e^{-\gamma^{2}}d\gamma\right] \tag{F.16}$$

$$\therefore p(x,t)=\frac{e^{B}}{2L}\left[\operatorname{erf}\left(\frac{x-C_{-}}{2\sqrt{A}}\right)-\operatorname{erf}\left(\frac{x-C_{+}}{2\sqrt{A}}\right)\right] \tag{F.17a}$$

or, using the above definitions for A, B, C_0, and C_L,

$$p(x,t)=\frac{e^{kt/\zeta}}{2L}\left[\operatorname{erf}\left(\frac{x-(x_0-\frac{L}{2})e^{-kt/\zeta}}{2\sqrt{\frac{D}{2k/\zeta}\left(1-e^{-2kt/\zeta}\right)}}\right)-\operatorname{erf}\left(\frac{x-(x_0+\frac{L}{2})e^{-kt/\zeta}}{2\sqrt{\frac{D}{2k/\zeta}\left(1-e^{-2kt/\zeta}\right)}}\right)\right] \tag{F.17b}$$

The mid-point of the rectangular function at x_0 assists in algebraically checking (F.17). Otherwise, for the computer simulations of the O-U process, $x_0 = L/2$ and (5.1.10) follows. To partly substantiate the above result, the PS for IC as a rectangular function is labelled $p_{rc}(x, t)$. The PS (5.1.6), that uses the Dirac-δ function as an IC, is labelled $p_{\delta}(x, t)$. Partial verification of (F.17b) can be achieved by showing the stationary solutions ($t \to \infty$) are the same, $p_{rc}(x) = p_{\delta}(x)$.

It is instructive to note the Dirac-δ function can be defined (Stark and Tuteur, 1979, p. 58)

$$\delta(x)=\lim_{a\to\infty}\{a\ \operatorname{rect}(ax)\} \tag{F.18}$$

$$\Rightarrow\ \delta(x-x_0)=\lim_{L\to 0}\left\{\frac{1}{L}\operatorname{rect}\left(\frac{x-x_0}{L}\right)\right\} \tag{F.19}$$

Furthermore, it needs to be recognised the PS entails the 'history' or 'evolution' of combined PDE, associated BCs, and IC. It follows, therefore, that by showing $p_{rc}(x,t)\to p_{\delta}(x,t)$ as $L\to 0$ assists in verifying (F.17b). The demonstration is assisted using a Taylor series expansion of the error function (Abramowitz and Stegun, 1965, p. 304),

$$\operatorname{erf}(z+a)=\operatorname{erf}(z)+\frac{2}{\sqrt{\pi}}e^{-z^{2}}\left(a-a^{2}z+O(a^{3})\right) \tag{F.20}$$

where $O(a^3)$ means terms of order a^3 and higher (and includes polynomials in z).

Equating $z \equiv \dfrac{x - x_0 e^{-kt/\zeta}}{2\sqrt{A}}$ and in the first and second error functions, $a_+ \equiv \dfrac{+\frac{L}{2} e^{-kt/\zeta}}{2\sqrt{A}}$

$a_- \equiv \dfrac{-\frac{L}{2} e^{-kt/\zeta}}{2\sqrt{A}}$, (F.17) is expanded

$$p_{rc}(x,t) = \frac{e^B}{2L}\left[\begin{array}{l} \operatorname{erf}(z) + \dfrac{2}{\sqrt{\pi}} e^{-z^2}\left(a_+ - a_+{}^2 z + O(a_+{}^3)\right) \\ \quad - \left(\operatorname{erf}(z) + \dfrac{2}{\sqrt{\pi}} e^{-z^2}\left(a_- - a_-{}^2 z + O(a_-{}^3)\right)\right) \end{array}\right] \tag{F.21}$$

taking the limit $L \to 0$

$$\begin{aligned} \{p_{rc}(x,t)\}_{L\to 0} &= \left\{\frac{e^{kt/\zeta}}{2L}\left[\frac{2}{\sqrt{\pi}} e^{-z^2}\left(\frac{L e^{-kt/\zeta}}{2\sqrt{A}}\right) - 0 - O\left(\frac{L^3 e^{-kt/\zeta}}{\sqrt{A}}\right)^3\right]\right\}_{L\to 0} \\ &= \left\{\left[\frac{1}{2\sqrt{A\pi}} e^{-z^2} - \left(\frac{e^{kt/\zeta}}{2L}\right) O\left(\frac{-L^3 e^{-3kt/\zeta}}{\left(2\sqrt{A}\right)^3}\right)\right]\right\}_{L\to 0} = \frac{1}{2\sqrt{A\pi}} e^{-z^2} \end{aligned} \tag{F.22}$$

since $a_+ - a_- = \dfrac{L e^{-kt/\zeta}}{2\sqrt{A}}$ and $a_+{}^2 - a_-{}^2 = \dfrac{(\frac{L^2}{4} - \frac{L^2}{4}) e^{-2kt/\zeta}}{4A} = 0$ and all other L dependent terms vanish as $L \to 0$. Comparing (5.1.6),

$$\begin{aligned} \{p_{rc}(x,t)\}_{L\to 0} &= \frac{1}{2\sqrt{A\pi}} e^{-z^2} = \frac{1}{\sqrt{2\pi k_B T(1 - e^{-2kt/\zeta})/k}} \exp\left(-\frac{(x - x_0 e^{-kt/\zeta})^2}{2\, k_B T(1 - e^{-2kt/\zeta})/k}\right) \\ &= \frac{1}{\sqrt{2\pi\sigma^2(t)}} \exp\left(-\frac{(x - \bar{x}(t))^2}{2\sigma^2(t)}\right) = p_\delta(x,t) \end{aligned} \tag{F.23}$$

This assists in confirming the validity of (F.17b). Finally, (F.22) also shows the PS using the rectangular function IC, $p_{rc}(x, t)$, converges to the same steady state solution as the PS using the Dirac-δ function IC. That is, $p_{rc}(x,t) \to p(x)$ as $t \to \infty$,

$$\{p_{rc}(x,t)\}_{t\to\infty} = \left\{\frac{e^{kt/\zeta}}{2L}\left[\frac{2}{\sqrt{\pi}}e^{-z^2}\left(\frac{Le^{-kt/\zeta}}{2\sqrt{A}}\right) - 0 - O\left(\frac{L^3e^{-kt/\zeta}}{\sqrt{A}}\right)^3\right]\right\}_{t\to\infty}$$

$$= \left\{\frac{1}{2\sqrt{A\pi}}e^{-z^2}\right\}_{t\to\infty} = \left\{\frac{1}{\sqrt{2\pi k_B T(1-e^{-2kt/\zeta})/k}}\exp\left(-\frac{(x-x_0e^{-kt/\zeta})^2}{2k_BT(1-e^{-2kt/\zeta})/k}\right)\right\}_{t\to\infty} \qquad \text{(F.24)}$$

$$= \frac{1}{\sqrt{2\pi k_B T/k}}\exp\left(-\frac{kx^2}{2k_BT}\right) = p(x)$$

where the last line results from a comparison with (5.1.4).

Name	$p(x)$	$\phi(s)$
1. Constant	1	$2\pi\delta(s)$
2. Sign function	$\operatorname{sgn}(x) = \begin{cases} +1, & x>0 \\ -1, & x<0 \end{cases}$	$\frac{2j}{s}$
3. Unit step function	$u(x) = \frac{1}{2} + \frac{1}{2}\operatorname{sgn}(x)$	$\pi\delta(s) + \frac{j}{s}$
4. Rectangular function (normalised)	$\frac{1}{L}\operatorname{rect}\left(\frac{x-x_0}{L}\right)$	$\frac{1}{jsL}\left(e^{jsL/2} - e^{-jsL/2}\right)e^{jsx_0}$
5. Gaussian function	$\frac{1}{2\pi}\sqrt{\frac{\pi}{a}}e^{-x^2/4a}$	e^{-as^2}
6. Delayed Gaussian function	$\frac{1}{2\pi}\sqrt{\frac{\pi}{a}}e^{-(x-b)^2/4a}$	e^{-as^2+jsb}

Table F.1 *C*-transform pairs

Name	Displacement function (x)	C-transform space (s)
1. Linearity	$ap(x)+bp(x)$	$a\phi(s)+b\phi(s)$
2. Displacement shift	$p(x+a)$	$\phi(s)e^{-jsa}$
3. Partial differentiation I	$\frac{\partial p(x,t)}{\partial t}$	$\frac{\partial \phi(s,t)}{\partial t}$
4. Partial n-th differentiation II	$\frac{\partial^n p(x,t)}{\partial x^n}$	$(-js)^n\phi(s,t)$
5. Multiplication by x (also called s differentiation)	$xp(x)$	$\frac{1}{j}\frac{d\phi(s)}{ds}$
6. Partial differentiation III (combining 4 and 5)	$\frac{\partial(xp(x,t))}{\partial x}$	$-s\frac{\partial\phi(s,t)}{\partial s}$
7. Integration I	$\int_{-\infty}^{x} p(\chi)d\chi$	$\phi(s)\left(\pi\delta(s)+\frac{j}{s}\right)$
8. Integration II (combining 2 and 7)	$\int_{-\infty}^{x} p(\chi-a)d\chi$	$\phi(s)e^{+jsa}\left(\pi\delta(s)+\frac{j}{s}\right)$

Table F.2 C-transform properties

Appendix G Solution of 1D-FPE with hyperbolic DEP force

Restating the main relations; the FPE with hyperbolic DEP force characteristic (5.3.6b) is

$$g_m''(y) + \frac{(1-2\alpha)}{y} g_m'(y) + \left(\beta_m{}^2 + \frac{\alpha^2-\mu^2}{y^2}\right) g_m(y) = 0 \qquad \text{(G.1)}$$

has GS (5.3.8a),

$$g_m(y) = y^{\alpha}\left(C_{1_m} J_{-\mu}(y\beta_m) + C_{2_m} J_{+\mu}(y\beta_m)\right) \qquad \text{(G.2)}$$

where $\alpha = \frac{1}{2} - \frac{k}{2k_BT}$, $\beta_m = \sqrt{\frac{\rho_m{}^2\zeta}{k_BT}}$, $\mu = \frac{1}{2} + \frac{k}{2k_BT}$, C_{1_m} and C_{2_m} are arbitrary integration constants. The zero flux BC at $y = a$ and $y = b$, requires (5.3.10)

$$g_m'(y) + (1-2\alpha) g_m(y)/y\Big|_{y=a,b} = 0 \qquad \text{(G.3)}$$

Differentiating $g(y)$ in (G.2) with respect to y,

$$g_m'(y) = \frac{\alpha y^{\alpha}}{y}\left(C_{1_m} J_{-\mu}(y\beta_m) + C_{2_m} J_{+\mu}(y\beta_m)\right) + y^{\alpha}\left(C_{1_m} \frac{dJ_{-\mu}(y\beta_m)}{dy} + C_{2_m} \frac{dJ_{+\mu}(y\beta_m)}{dy}\right) \qquad \text{(G.4)}$$

and substituting into (G.3),

$$g_m'(y) + \frac{(1-2\alpha)}{y} g_m(y)\Big|_{y=a,b} = y^{\alpha}\left\{\begin{array}{l} C_{1_m}\left[\frac{\mu}{y} J_{-\mu}(y\beta_m) + \frac{dJ_{-\mu}(y\beta_m)}{dy}\right] \\ + C_{2_m}\left[\frac{\mu}{y} J_{+\mu}(y\beta_m) + \frac{dJ_{+\mu}(y\beta_m)}{dy}\right] \end{array}\right\}\Bigg|_{y=a,b} \qquad \text{(G.5)}$$

where the identity has been used, $\alpha + 1 - 2\alpha = 1 - \alpha = \mu$. The relations (Gradshteyn and Ryzhik, 1994, p. 979) for a generalised Bessel function Z of order ν

$$z\frac{d}{dz} Z_{\nu}(z) + \nu Z_{\nu}(z) = z Z_{\nu-1}(z) \qquad \text{(G.6a)}$$

$$z\frac{d}{dz}Z_\nu(z) - \nu Z_\nu(z) = -z\,Z_{\nu+1}(z) \tag{G.6b}$$

These are particularized for (G.4), where $Z = J$. Letting $z = y\beta_m$, (G.6a) and (G.6b) lead to

$$\frac{d}{dy}J_\nu(y\beta_m) + \frac{1}{y}\nu J_\nu(y\beta_m) = \beta_m J_{\nu-1}(y\beta_m) \tag{G.7a}$$

$$\frac{d}{dy}J_\nu(y\beta_m) - \frac{1}{y}\nu J_\nu(y\beta_m) = -\beta_m J_{\nu+1}(y\beta_m) \tag{G.7b}$$

Carefully considering the form of (G.5); letting $\nu = +\mu$, (G.7a) becomes

$$\frac{d}{dy}J_{+\mu}(y\beta_m) + \frac{1}{y}\mu J_{+\mu}(y\beta_m) = \beta_m J_{+\mu-1}(y\beta_m) \tag{G.8a}$$

and $\nu = -\mu$, so (G.7b) becomes

$$\frac{d}{dy}J_{-\mu}(y\beta_m) + \frac{1}{y}\mu J_{-\mu}(y\beta_m) = -\beta_m J_{-\mu+1}(y\beta_m) \tag{G.8b}$$

Equations (G.8a) and (G.8b) enable the general form for the BC (G.5) to be concisely written,

$$g_m'(y) + \frac{(1-2\alpha)}{y}g_m(y) = y^\alpha\left[-C_{1_m}\beta_m J_{-\mu+1}(y\beta_m) + C_{2_m}\beta_m J_{+\mu-1}(y\beta_m)\right] \tag{G.9}$$

Recalling the BC at $y = a$, $g_m'(a) + (1-2\alpha)g_m(a)/a = 0$ and applying (G.9)

$$a^\alpha\left[-C_{1_m}\beta_m J_{-\mu+1}(a\beta_m) + C_{2_m}\beta_m J_{+\mu-1}(a\beta_m)\right] = 0 \tag{G10.a}$$

Since, $a^\alpha \neq 0$, then

$$C_{1_m}\underbrace{\left(-\beta_m J_{-\mu+1}(a\beta_m)\right)}_{[1a]} + C_{2_m}\underbrace{\beta_m J_{+\mu-1}(a\beta_m)}_{[2a]} = 0 \tag{G.10b}$$

Similarly the BC at $y = b$, $g_m'(b) + (1-2\alpha)g_m(b)/b = 0$, implies since $b^\alpha \neq 0$

$$C_{1_m}\underbrace{\left(-\beta_m J_{-\mu+1}(b\beta_m)\right)}_{[1b]} + C_{2_m}\underbrace{\beta_m J_{+\mu-1}(b\beta_m)}_{[2b]} = 0 \qquad \text{(G.10c)}$$

where the [ ] terms have been labelled in accordance with C-subscript and y-value. Otherwise, the two simultaneous equations (G.10b) and (G.10c) are solved in matrix form,

$$\begin{pmatrix}[1a] & [2a]\\ [1b] & [2b]\end{pmatrix}\begin{pmatrix}C_{1_m}\\ C_{2_m}\end{pmatrix} = \begin{pmatrix}0\\ 0\end{pmatrix} \qquad \text{(G.10d)}$$

and for nontrivial $C_{1_m}, C_{1_m} \neq 0$, the determinant $\begin{vmatrix}[1a] & [2a]\\ [1b] & [2b]\end{vmatrix} = 0 \Rightarrow [1a][2b]-[1b][2a]=0$ or,

$$\left(-\beta_m J_{-\mu+1}(a\beta_m)\right)\beta_m J_{+\mu-1}(b\beta_m)-\left(-\beta_m J_{-\mu+1}(b\beta_m)\right)\beta_m J_{+\mu-1}(a\beta_m)=0 \qquad \text{(G.11)}$$

For nonzero eigenvalues $\beta_m \neq 0$, (G.11) establishes the condition for evaluating β_m,

$$J_{-\mu+1}(b\beta_m)J_{+\mu-1}(a\beta_m)-J_{-\mu+1}(a\beta_m)J_{+\mu-1}(b\beta_m) = 0 \qquad \text{(G.12)}$$

The special case where $\beta_0 = 0$ is considered in Appendix H. Using (G.12) in either (G.10b) or (G.10c) establishes the ratio of the C-constants as,

$$C_{R_m} \triangleq \frac{C_{2_m}}{C_{1_m}} = \frac{-[1a]}{[2a]} = \frac{J_{1-\mu}(a\beta_m)}{J_{\mu-1}(a\beta_m)} = \frac{-[1b]}{[2b]} = \frac{J_{1-\mu}(b\beta_m)}{J_{\mu-1}(b\beta_m)} \qquad \text{(G.13)}$$

The procedure is to determine a set of eigenvalues β_m unique for each integer m, $\{\beta_0, \beta_1, \beta_2, \beta_3, \ldots\}$ satisfying (G.12). The set C_{R_m} corresponding to each m $\{C_{R_0}, C_{R_1}, C_{R_2}, C_{R_3}, \ldots\}$ can then be evaluated from (G.13). To determine C_{1_m}, $g_m(y)$ is re-written,

$$g_m(y) = C_{1_m} y^{\alpha}\underbrace{(J_{-\mu}(y\beta_m)+C_{R_m}J_{+\mu}(y\beta_m))}_{\hat{g}_m(y)} = C_{1_m} y^{\alpha}\hat{g}_m(y) \qquad \text{(G.14)}$$

where $\hat{g}_m(y) \triangleq J_{-\mu}(y\beta_m)+C_{R_m}J_{+\mu}(y\beta_m)$ is defined. From (5.2.9), (5.2.12) and (G.14), the GS is,

$$p(y,t) = \sum_{m=0}^{\infty} g_m(y)h_m(t) = \sum_{m=0}^{\infty} C_{1_m} y^{\alpha}\underbrace{(J_{-\mu}(y\beta_m)+C_{R_m}J_{+\mu}(y\beta_m))}_{\hat{g}_m(y)}e^{-\rho_m^2 t} \qquad \text{(G.15)}$$

To find C_{1_m}, an orthogonal basis is established using an IC valid for restricted domain $\{y : a \le y \le b\}$. The IC is imposed on (G.15) by setting $t = 0 \Rightarrow h_m(0) = \exp(0) = 1 \; \forall \; m$,

$$\therefore \; p(y,0) = \sum_{m=0}^{\infty} g_m(y) = \sum_{m=0}^{\infty} C_{1_m} y^{\alpha} \hat{g}_m(y) = \sum_{m=0}^{\infty} C_{1_m} y^{\alpha} \underbrace{\left(J_{-\mu}(y\beta_m) + C_{R_m} J_{+\mu}(y\beta_m)\right)}_{\hat{g}_m(y)} \tag{G.16}$$

Since $p(y,0)$ is known, and β_m and C_{R_m} determine $\hat{g}_m(y)$, values of C_{1_m} can be found for each m. The procedure to find C_{1_m} requires a function $q_m(y)$ that is orthogonal to $g_m(y)$. It has been shown (Gardiner, 1985) for the analysis of the *reverse* FPE that

$$q_m(y) = g_m(y) / p(y) \tag{G.17a}$$

where $p(y)$ is the stationary solution of $p(y, t)$, and from (5.3.5),

$$p(y) = p_c y^{(2\alpha - 1)} \text{ with } p_c = \begin{cases} 2\alpha / \left(b^{2\alpha} - a^{2\alpha}\right), & \alpha \neq 0 \\ 1 / \ln(b/a), & \alpha = 0 \end{cases} \tag{G.17b}$$

Hence, the form for the orthogonal function is established in terms of $g_m(y)$,

$$\begin{aligned} q_m(y) &= g_m(y) / p_s(y) = g_m(y) y^{1-2\alpha} / p_c \\ &= C_{1_m} y^{\alpha} \hat{g}_m(y) y^{1-2\alpha} / p_c = C_{1_m} y^{1-\alpha} \hat{g}_m(y) / p_c \end{aligned} \tag{G.18}$$

Multiplying *rhs* and *lhs* of (G.16) by q_n(y), integrating over the interval $y \in [a,b]$, and summing,

$$\sum_{n=0}^{\infty} \int_a^b p(y,0) q_n(y) dy = \sum_{n=0}^{\infty} \int_a^b q_n(y) \sum_{m=0}^{\infty} g_m(y) dy = \sum_{n=0}^{\infty} \sum_{m=0}^{\infty} \int_a^b g_m(y) q_n(y) dy \tag{G.19}$$

Substituting (G.18) into (G.19),

$$\sum_{n=0}^{\infty} \int_a^b p(y,0) C_{1_n} y^{1-\alpha} \hat{g}_n(y) / p_c \, dy = \sum_{n=0}^{\infty} \sum_{m=0}^{\infty} \int_a^b \underbrace{C_{1_m} y^{\alpha} \hat{g}_m(y)}_{g_m(y)} \underbrace{C_{1_n} y^{1-\alpha} \hat{g}_n(y) / p_c}_{q_n(y)} dy \tag{G.20}$$

By definition an orthogonal pair of functions has properties,

$$\int_a^b g_n(y)\,q_m(y)\,dy \;= c_n\delta_{mn} = \begin{cases} c_n, & n = m \\ 0, & n \neq m \end{cases} \tag{G.21}$$

where c_n is a normalization constant and δ_{mn} is the Kronecker delta function. Using the property $\mu = 1-\alpha$ and factoring C_{1_m} and p_c, (G.20) simplifies for $m = n$,

$$\sum_{n=0}^{\infty}\int_a^b p(y,0)\,y^{\mu}\hat{g}_n(y)\,dy \;=\; \sum_{n=0}^{\infty} C_{1_n}\int_a^b y\,\hat{g}_n(y)\hat{g}_n(y)\,dy \tag{G.22a}$$

$\therefore$

$$C_{1_m} = \frac{\int_a^b p(y,0)\,y^{\mu}\hat{g}_m(y)dy}{\int_a^b y\,\hat{g}_m{}^2(y)\,dy} \tag{G.22b}$$

The denominator of (G.22b) is evaluated by expanding $\hat{g}_m(y)$ given in (G.14),

$$\begin{aligned}\int_a^b y\,\hat{g}_m{}^2(y)\,dy &= \int_a^b y\left(J_{-\mu}(y\beta_m) + C_{R_m}J_{+\mu}(y\beta_m)\right)^2 dy \\ &= \underbrace{\int_a^b y J_{-\mu}{}^2(y\beta_m)\,dy}_{I_I} + \underbrace{2C_{R_m}\int_a^b y J_{-\mu}(y\beta_m)J_{+\mu}(y\beta_m)dy}_{I_{II}} + \underbrace{C_{R_m}{}^2\int_a^b y J_{\mu}{}^2(y\beta_m)\,dy}_{I_{III}}\end{aligned} \tag{G.23}$$

Expressions for the integrals *I and III* are listed in Prudnikov *et al.*, 1986, Vol. 2, pp. 40-41, and the expression for integral *II* can be deduced

$$I_I = \int_a^b y J_{-\mu}{}^2(y\beta_m)\,dy \;=\; \frac{1}{2}\left[y^2 J'^2_{-\mu}(y\beta_m) + \left(y^2 - \frac{\mu^2}{\beta_m^2}\right)J^2_{-\mu}(y\beta_m)\right]_a^b \tag{G.24a}$$

$$\begin{aligned} I_{II} &= 2C_{R_m}\int_a^b y\,J_{-\mu}(y\beta_m)J_{+\mu}(y\beta_m)\,dy \\ &= \frac{2C_{R_m}}{2}\left[y^2 J'_{-\mu}(y\beta_m)J'_{+\mu}(y\beta_m) + \left(y^2 - \frac{\mu^2}{\beta_m^2}\right)J_{-\mu}(y\beta_m)J_{+\mu}(y\beta_m)\right]_a^b \end{aligned} \tag{G.24b}$$

$$I_{III} = C_{R_m}^2 \int_a^b y J_\mu{}^2(y\beta_m)\,dy = \frac{C_{R_m}^2}{2}\left[y^2 J_\mu'^2(y\beta_m) + \left(y^2 - \frac{\mu^2}{\beta_m^2}\right) J_\mu^2(y\beta_m)\right]_a^b \qquad \text{(G.24c)}$$

In each of the integrals *I, II, and III* the derivatives of the Bessel functions, shown as superscript ′, are with respect to the argument $y\beta_m$ as given in (G.6), i.e. $J'_m(y\beta_m) = \partial_{y\beta_m} J(y\beta_m)$. The denominator (sum of integrals *I, II, and III*) can be written concisely,

$$\int_a^b y\,\hat{g}_m{}^2(y)\,dy = I_I + I_{II} + I_{III} = \frac{1}{2}\left[y^2 \hat{g}_m'^2(y) + \left(y^2 - \frac{\mu^2}{\beta_m^2}\right)\hat{g}_m^2(y)\right]_a^b \qquad \text{(G.25)}$$

where $\hat{g}'_m(y) = \partial_{y\beta_m}\,\hat{g}(y) = J'_{-\mu}(y\beta_m) + C_{R_m} J'_{+\mu}(y\beta_m)$ is the derivative of $\hat{g}_m(y)$ with respect to the argument $y\beta_m$. Using the recursion relations (G.5), integrals *I, II, and III* can be rewritten without derivatives and in a form suitable for numerical evaluation by MATLAB 5.0™,

$$I_I = \left[\left(\frac{y^2}{2}\right)\left(J_{-\mu}^2(y\beta_m) - J_{-\mu+1}(y\beta_m) J_{-\mu-1}(y\beta_m)\right)\right]_a^b \qquad \text{(G.26a)}$$

$$I_{II} = 2C_{R_m}\left[\left(\frac{y^2}{2}\right)\left(J_{-\mu}(y\beta_m) J_{+\mu}(y\beta_m) + J_{-\mu-1}(y\beta_m) J_{+\mu-1}(y\beta_m)\right)\right]_a^b \qquad \text{(G.26b)}$$

$$I_{III} = C_{R_m}^2\left[\left(\frac{y^2}{2}\right)\left(J_\mu^2(y\beta_m) - J_{\mu+1}(y\beta_m) J_{\mu-1}(y\beta_m)\right)\right]_a^b \qquad \text{(G.26c)}$$

and can be summed

$$\begin{aligned}\int_a^b y\,\hat{g}_m{}^2(y)\,dy &= I_I + I_{II} + I_{III} \\ &= \left[\frac{y^2}{2}\left\{\hat{g}_\mu^2(y) + J_{1-\mu}(y\beta_m)\left(J_{-\mu-1}(y\beta_m) - \frac{J_{1-\mu}(y\beta_m)}{J_{\mu-1}(y\beta_m)} J_{\mu+1}(y\beta_m)\right)\right\}\right]_a^b \qquad \text{(G.27)} \\ &= I_\Sigma(b,\mu,\beta_m) - I_\Sigma(a,\mu,\beta_m)\end{aligned}$$

where $I_\Sigma(b,\mu,\beta_m) = \frac{b^2}{2}\left[\hat{g}_\mu^2(b) + J_{1-\mu}(b\beta_m)\left(J_{-\mu-1}(b\beta_m) - C_{R_m} J_{\mu+1}(b\beta_m)\right)\right]$ and similarly for $I_\Sigma(a,\mu,\beta_m)$ using the relations for C_{R_m} in (G.13).

The expression for the denominator can be validated by casting the ODE (G.1) and BC (G.3) in terms of the Sturm-Liouville problem (Kreyszig, 1967, p. 476-85) for finding orthogonal eigenfunctions and corresponding eigenvalues. Only a brief explanation is needed. The ODE (G.1) is cast in terms of the Sturm-Liouville equation, and can also be written in terms of the index n as well as m. Thus the two, coupled ODEs are set up with solutions $g_m(y)$ and $g_n(y)$, and it can be shown,

$$\left(\beta_m^2-\beta_n^2\right)\int_a^b y^{1-2\alpha} g_m(y) g_n(y)\,dy = \left[y^{1-2\alpha}\left(g_n'(y)g_m(y)-g_m'(y)g_n(y)\right)\right]_a^b \tag{G.28}$$

Imposing BCs given by (G.3), $g_m'(a)=(2\alpha-1)g_m(a)/a$ and $g_m'(b)=(2\alpha-1)g_m(b)/b$ on the *rhs*, and using (G.14), (G.28) becomes,

$$\begin{aligned}\left(\beta_m^2-\beta_n^2\right)C_{1_m}C_{1_n}\int_a^b y\,\hat{g}_m(y)\hat{g}_n(y)\,dy = &\left[b^{-2\alpha}(2\alpha-1)\left(g_n(b)g_m(b)-g_m(b)g_n(b)\right)\right]\\ &-\left[a^{-2\alpha}(2\alpha-1)\left(g_n(a)g_m(a)-g_m(a)g_n(a)\right)\right]\\ &=0-0=0\end{aligned} \tag{G.29}$$

In nontrivial cases $C_{1_m}\neq 0$, $C_{1_n}\neq 0$. Hence if $\mathrm{m}\neq\mathrm{n} \Rightarrow \beta_m^2-\beta_n^2\neq 0$, then (G.29) implies

$$\int_a^b y\,\hat{g}_m(y)\hat{g}_n(y)\,dy\Big|_{n\neq m} = 0 \tag{G.30}$$

If $\mathrm{m}=\mathrm{n} \Rightarrow C_{1_m}^2\int_a^b y\,\hat{g}_m(y)\hat{g}_m(y)\,dy = \dfrac{0}{\beta_m^2-\beta_m^2}=\dfrac{0}{0}$ and is indeterminate. Following the approach taken by Lebedev (1965, p. 128-30), L' Hopital's rule is applied,

$$C_{1_m}^2\int_a^b y\,\hat{g}_m^2(y)\,dy = \frac{\lim\limits_{\beta_n\to\beta_m}\{\partial_{\beta_n} f(\beta_n,\beta_m)\}}{\lim\limits_{\beta_n\to\beta_m}\{\partial_{\beta_n}(\beta_m{}^2-\beta_n{}^2)\}} \tag{G.31}$$

where $f(\beta_n,\beta_m)=\left[y^{1-2\alpha}\left(g_n'(y)g_m(y)-g_m'(y)g_n(y)\right)\right]_a^b$ and ∂_{β_n} means $\frac{\partial}{\partial\beta_n}$ (the derivative with respect to β_n). Since the m, n subscript is cumbersome, for the following argument let $\chi=\beta_m$ and $\beta=\beta_n$, so the *rhs* of (G.31) becomes,

$$\frac{\lim\limits_{\beta_n\to\beta_m}\{\partial_{\beta_n} f(\beta_n,\beta_m)\}}{\lim\limits_{\beta_n\to\beta_m}\{\partial_{\beta_n}(\beta_m{}^2-\beta_n{}^2)\}} \equiv \frac{\lim\limits_{\beta\to\chi}\{\partial_{\beta} f(\beta,\chi)\}}{\lim\limits_{\beta\to\chi}\{\partial_{\beta}(\chi^2-\beta^2)\}} \tag{G.32a}$$

Also, for convenience let $\underline{J}(y\beta) = C_{1_n}\hat{g}_n(y)$ and $\underline{J'}(y\beta) = \partial_{y\beta}J(y\beta) = C_{1_n}\hat{g}'_n(y)$, so that $\underline{J}(y\beta) = C_{1_n}\left(J_{-\mu}(y\beta)+C_{R_n}J_{+\mu}(y\beta)\right)$, $\underline{J'}(y\beta) = C_{1_n}\left(J'_{-\mu}(y\beta) + C_{R_n}J'_{+\mu}(y\beta)\right)$, and furthermore, $\underline{J}(y\chi) = C_{1_m}\left(J_{-\mu}(y\chi) + C_{R_m}J_{+\mu}(y\chi)\right)$ and $\underline{J'}(y\chi) = C_{1_m}\left(J'_{-\mu}(y\chi) + C_{R_m}J'_{+\mu}(y\chi)\right)$ (G.32b)

The denominator of (G.32a) is evaluated simply,

$$\lim_{\beta\to\chi}\{\partial_\beta(\chi^2-\beta^2)\} = \lim_{\beta\to\chi}\left\{\frac{\partial(\chi^2-\beta^2)}{\partial\beta}\right\} = -2\beta|_{\beta\to\chi} = -2\chi \tag{G.33}$$

Consider the numerator in (G.31), using the notation in (G.32a) and (G.32b)

$$\begin{aligned} f(\beta,\chi) &= \left[y^{1-2\alpha}\left(\partial_y\left(y^\alpha\underline{J}(y\beta)\right)y^\alpha\underline{J}(y\chi) - \partial_y\left(y^\alpha\underline{J}(y\chi)\right)y^\alpha\underline{J}(y\beta)\right)\right]_a^b \\ &= \left[y^{1-2\alpha}\begin{pmatrix}\left[\alpha y^{\alpha-1}\underline{J}(y\beta) + y^\alpha\partial_y\underline{J}(y\beta)\right]y^\alpha\underline{J}(y\chi)\\ -\left[\alpha y^{\alpha-1}\underline{J}(y\chi) + y^\alpha\partial_y\underline{J}(y\chi)\right]y^\alpha\underline{J}(y\beta)\end{pmatrix}\right]_a^b \\ &= \begin{bmatrix}\left[\alpha\underline{J}(y\beta) + y\beta\underline{J'}(y\beta)\right]\underline{J}(y\chi)\\ -\left[\alpha\underline{J}(y\chi) + y\chi\underline{J'}(y\chi)\right]\underline{J}(y\beta)\end{bmatrix}_a^b \end{aligned} \tag{G.34}$$

since $\partial_y\underline{J}(y\beta) = \beta\partial_{y\beta}\underline{J}(y\beta) = \beta\underline{J'}(y\beta)$ and $\partial_y\underline{J}(y\chi) = \chi\partial_{y\chi}\underline{J}(y\chi) = \chi\underline{J'}(y\chi)$. Furthermore, $\partial_\beta\underline{J}(y\beta) = y\partial_{y\beta}\underline{J}(y\beta) = y\underline{J'}(y\beta)$ and $\partial_\beta\underline{J'}(y\beta) = y\partial_{y\beta}\underline{J'}(y\beta) = y\underline{J''}(y\beta)$. These relations are simply deduced from the rules of differential calculus. Hence,

$$\begin{aligned} \partial_\beta f(\beta,\chi) &= \begin{bmatrix}\left[\alpha\partial_\beta\underline{J}(y\beta) + \partial_\beta\left(y\beta\underline{J'}(y\beta)\right)\right]\underline{J}(y\chi)\\ -\left[\alpha\underline{J}(y\chi) + y\chi\underline{J'}(y\chi)\right]\partial_\beta\underline{J}(y\beta)\end{bmatrix}_a^b \\ &= \begin{bmatrix}\left[\alpha y\underline{J'}(y\beta) + y\underline{J'}(y\beta) + y^2\beta\underline{J''}(y\beta)\right]\underline{J}(y\chi)\\ -\left[\alpha\underline{J}(y\chi) + y\chi\underline{J'}(y\chi)\right]y\underline{J'}(y\beta)\end{bmatrix}_a^b \end{aligned} \tag{G.35}$$

Acknowledging $g_n(y) = y^\alpha\underline{J}(y\beta)$, etc., and combining (G.1) and (G.2) it can be shown,

$$\begin{aligned} \underline{J''}(y\beta) &= -\frac{\underline{J'}(y\beta)}{y\beta} - \left(1-\frac{\mu^2}{y^2\beta^2}\right)\underline{J}(y\beta) \\ \therefore\ y^2\beta\underline{J''}(y\beta) &= -y\underline{J'}(y\beta) + \left(\frac{\mu^2}{\beta} - y^2\beta\right)\underline{J}(y\beta) \end{aligned} \tag{G.36}$$

Substituting (G.36) into (G.35),

$$\partial_\beta f(\beta,\chi)=\left[\begin{array}{l}\left[\alpha y\,\underline{J'}(y\beta)+\left(\frac{\mu^2}{\beta}-y^2\beta\right)\underline{J}(y\beta)\right]\underline{J}(y\chi)\\ -\left[\alpha\underline{J}(y\chi)+y\chi\,\underline{J'}(y\chi)\right]y\,\underline{J'}(y\beta)\end{array}\right]_a^b \qquad \text{(G.37)}$$

Hence,

$$\lim_{\beta\to\chi}\{\partial_\beta f(\beta,\chi)\}=\left[\left(\frac{\mu^2}{\beta}-y^2\beta\right)\underline{J}(y\beta)\underline{J}(y\chi)-y\chi\,\underline{J'}(y\chi)y\,\underline{J'}(y\beta)\right]_a^b\Bigg|_{\beta\to\chi}$$
$$=-\chi\left[y^2\underline{J'^2}(y\chi)-\left(\frac{\mu^2}{\chi^2}-y^2\right)\underline{J}^2(y\chi)\right]_a^b \qquad \text{(G.38)}$$

Thus combining (G.32), (G.33) and (G.38)

$$\frac{\lim_{\beta\to\chi}\{\partial_\beta f(\beta,\chi)\}}{\lim_{\beta\to\chi}\{\partial_\beta(\chi^2-\beta^2)\}}=\frac{-\chi}{-2\chi}\left[y^2\underline{J'^2}(y\chi)-\left(\frac{\mu^2}{\chi^2}-y^2\right)\underline{J}^2(y\chi)\right]_a^b$$
$$=\frac{1}{2}\left[y^2\underline{J'^2}(y\chi)+\left(y^2-\frac{\mu^2}{\chi^2}\right)\underline{J}^2(y\chi)\right]_a^b \qquad \text{(G.39)}$$

Since $\underline{J}(y\chi)=C_{1_m}\hat{g}_m(y)$ and $\underline{J'}(y\chi)=C_{1_m}\partial_{y\chi}\left(\hat{g}_m(y)\right)=C_{1_m}\hat{g}'_m(y)$, (G.39) is rewritten using sum index notation enabling (G.31) to be included

$$C_{1_m}^2\int_a^b y\,\hat{g}_m^2(y)\,dy=\frac{\lim_{\beta_n\to\beta_m}\{\partial_{\beta_n}f(\beta_m,\beta_n)\}}{\lim_{\beta_n\to\beta_m}\{\partial_{\beta_n}(\beta_m{}^2-\beta_n{}^2)\}}=\frac{C_{1_m}^2}{2}\left[y^2\hat{g}'_m{}^2(y)+\left(y^2-\frac{\mu^2}{\beta_m{}^2}\right)g_m{}^2(y)\right]_a^b$$

$$\therefore\ \int_a^b y\,\hat{g}_m^2(y)\,dy=\frac{1}{2}\left[y^2\hat{g}'_m{}^2(y)+\left(y^2-\frac{\mu^2}{\beta_m{}^2}\right)g_m{}^2(y)\right]_a^b \qquad \text{(G.40)}$$

Equation (G.40) is the same as (G.25) found using tabulated integrals.

Appendix H Verifying the $m = 0^{th}$ Fourier-Bessel series term is steady state

The PS from (5.3.16) is written,

$$p(y,t) = \overbrace{C_{1_0} y^{\alpha} \underbrace{\left(J_{-\mu}(y\beta_m) + C_{R_0} J_{+\mu}(y\beta_m)\right)}_{\hat{g}_0(y)} \underbrace{e^{-\rho_0^2 t}}_{h_0(t)}}^{m=0 \text{ term}} + \sum_{m=1}^{\infty} C_{1_m} y^{\alpha} \hat{g}_m(y)\, e^{-\rho_m^2 t} \tag{H.1}$$

The behaviour of the $m = 0^{th}$ term of the expansion (H.1) is of interest since as $\beta_0 \to 0 \Rightarrow \rho_0 \to 0$ $\therefore\ h_0(t) \to 1\ \forall\ t$. This contrasts with the other $m = 1, 2, \ldots$ terms of the expansion (H.1) with the separation constant $\rho^2\big|_{m=1,2,\ldots} > 0$ that are time dependent. In particular, they approach zero as $t \to \infty$. The $m = 0$ term $g_0(y)$ is the only one that remains, and is in effect, the steady state term. In summary,

$$p(y,t \to \infty) = g_0(y).1 + \sum_{m=1}^{\infty} g_m(y) \underbrace{e^{-\rho_m^2 t \to \infty}}_{\to 0} = g_0(y) \tag{H.2}$$

To evaluate $g_0(y)$,

$$g_0(y) = \lim_{\beta_0 \to 0} \left\{ C_{1_0} y^{\alpha} \underbrace{\left(J_{-\mu}(y\beta_m) + C_{R_0} J_{+\mu}(y\beta_m)\right)}_{\hat{g}_0(y)} \right\} = C_{1_0} y^{\alpha} \hat{g}_0(y)\Big|_{\beta_0 \to 0} \tag{H.3}$$

recall the series expansion for Bessel functions of the first kind (Gradshteyn and Ryzhik, 1994, p. 960; Lebedev, 1965, pp. 102-4),

$$J_{\mu}(y\beta_m) = \sum_{k=0}^{\infty} \frac{(-1)^k (y\beta_m/2)^{\mu+2k}}{\Gamma(k+1)\Gamma(k+\mu+1)},\ \ |y\beta_m| < \infty \tag{H.4}$$

where one is considering solutions with an order that is real and non-integer value, $\mu \in R$ and $\mu \notin J$, as stated in (5.3.8a). Noting y is bounded $\{y : a \le y \le b,\ a > 0\}$ our interest lies solely in $\beta_0 \to 0$, and it sufficient to consider the first couple of terms in the expansion of (H.3). This leads to

$$J_{+\mu}(y\beta_0) = \frac{(y\beta_0/2)^{\mu}}{\Gamma(1+\mu)} - \frac{(y\beta_0/2)^{2+\mu}}{\Gamma(2+\mu)} + \ldots. = \frac{(y\beta_0/2)^{\mu}}{\Gamma(1+\mu)}\left(1 - \frac{(y\beta_0/2)^2}{(1+\mu)} + \ldots.\right) \tag{H.5a}$$

$$J_{-\mu}(y\beta_0) = \frac{(y\beta_0/2)^{-\mu}}{\Gamma(1-\mu)} - \frac{(y\beta_0/2)^{2-\mu}}{\Gamma(2-\mu)} + ... = \frac{(y\beta_0/2)^{-\mu}}{\Gamma(1-\mu)}\left(1 - \frac{(y\beta_0/2)^2}{(1-\mu)} + ...\right) \qquad \text{(H.5b)}$$

where factorisation is assisted by the properties of the gamma function, $\Gamma(n+\mu) = (n-1+\mu)\Gamma(n-1+\mu) \Rightarrow \Gamma(2+\mu) = (1+\mu)\Gamma(1+\mu)$ and $\Gamma(2-\mu) = (1-\mu)\Gamma(1-\mu)$, etc., (Abramowitz and Stegun, 1965, p. 255-6; Gradshteyn and Ryzhik, 1994, p. 946-7). The approximations are applied to expressions for $J_{-\mu}(y\beta_0)$, $J_{+\mu}(y\beta_0)$, C_{R_0} and C_{I_0} that comprise $g_0(y)$ as shown in (H.1).

The first step for evaluating $g_0(y)$ given by (H.3) is to determine

$$\hat{g}_0(y) = J_{-\mu}(y\beta_0) + C_{R_0} J_{+\mu}(y\beta_0) \qquad \text{(H.3')}$$

with

$$C_{R_0} = \frac{J_{1-\mu}(a\beta_0)}{J_{\mu-1}(a\beta_0)} = \frac{\frac{(a\beta_0/2)^{1-\mu}}{\Gamma(1+1-\mu)}\left(1 - \frac{(a\beta_0/2)^2}{(2-\mu)} + ...\right)}{\frac{(a\beta_0/2)^{\mu-1}}{\Gamma(1+\mu-1)}\left(1 - \frac{(a\beta_0/2)^2}{\mu} + ...\right)} = \left(\frac{a\beta_0}{2}\right)^{2\alpha} \frac{\Gamma(\mu)[1+O(\beta_0)^2]}{\Gamma(2-\mu)[1+O(\beta_0)^2]} \qquad \text{(H.6)}$$

where the last line results from the relation (5.3.8b), $\alpha + \mu = 1$, and $O(\beta_0{}^n)$ means β_0 terms of order n and higher ($\geq n$). Generally, our interest lies in terms up to first order, and second order $\beta_0{}^2$ terms and higher are grouped as $O(\beta_0{}^2)$. Substituting (H.5a), (H.5b) and (H.6) into (H.3'),

$$\hat{g}_0(y) = \frac{(y\beta_0/2)^{-\mu}[1+O(y\beta_0)^2]}{\Gamma(1-\mu)} + \left(\frac{a\beta_0}{2}\right)^{2\alpha} \frac{\Gamma(\mu)[1+O(\beta_0)^2](y\beta_0/2)^{\mu}[1+O(y\beta_0)^2]}{\Gamma(2-\mu)[1+O(\beta_0)^2]\Gamma(1+\mu)}$$

$$= \frac{(\beta_0/2)^{-\mu} y^{-\mu}[1+O(y\beta_0)^2]}{\Gamma(1-\mu)} + \frac{a^{2\alpha}(\beta_0/2)^{2\alpha+\mu}\Gamma(\mu) y^{\mu}[1+O(\beta_0)^2][1+O(y\beta_0)^2]}{(1-\mu)\Gamma(1-\mu)[1+O(\beta_0)^2]\,\mu\,\Gamma(\mu)} \qquad \text{(H.7)}$$

$$= \frac{(\beta_0/2)^{-\mu}}{\Gamma(1-\mu)}\left[y^{-\mu}\left(1+O(y\beta_0)^2\right) + \frac{a^{2\alpha}(\beta_0/2)^2\, y^{\mu}[1+O(\beta_0)^2][1+O(y\beta_0)^2]}{(1-\mu)\,\mu\,[1+O(\beta_0)^2]}\right]$$

The second step for evaluating $g_0(y)$ given by (H.3) is to determine C_{I_0} given by (5.3.15),

$$C_{1_0} = \frac{\int_a^b p(y,0)\, y^{\mu} \hat{g}_0(y) dy}{\int_a^b y\, \hat{g}_0{}^2(y) dy} = \frac{\int_a^b p(y,0)\, y^{\mu} \hat{g}_0(y) dy}{I_\Sigma(b,\mu,\beta_0) - I_\Sigma(a,\mu,\beta_0)} \tag{H.8}$$

Consider first the numerator of C_{1_0}. Substituting (H.7),

$$\int_a^b p(y,0)\, y^{\mu} \hat{g}_0(y) dy = \int_a^b p(y,0)\, y^{\mu} \frac{(\beta_0/2)^{-\mu}}{\Gamma(1-\mu)} \left[\begin{array}{c} y^{-\mu} + y^{-\mu} O(y\beta_0)^2 + \\ \frac{a^{2\alpha}(\beta_0/2)^2\, y^{\mu}[1+O(\beta_0)^2]}{(1-\mu)\mu[1+O(\beta_0)^2]} \\ \times\left(1+O(y\beta_0)^2\right) \end{array} \right] dy$$

$$= \frac{(\beta_0/2)^{-\mu}}{\Gamma(1-\mu)} \left(\underbrace{\int_a^b p(y,0)\, dy}_{=1} + \frac{(\beta_0/2)^2\, a^{2\alpha}}{\mu(1-\mu)} \int_a^b p(y,0)\, y^{2\mu}\, dy + ... \right) \tag{H.9}$$

$$= \frac{(\beta_0/2)^{-\mu}[1+O(\beta_0^2]}{\Gamma(1-\mu)}$$

Note that the numerator of C_{1_0} given by (H.9) becomes *independent* of the IC as the second and higher order terms $\to 0$ as $\beta_0 \to 0$. The denominator of C_{1_0} in (H.8) can be evaluated directly,

$$\int_a^b y\, \hat{g}_0{}^2(y) dy = \int_a^b y \frac{(\beta_0/2)^{-2\mu}}{[\Gamma(1-\mu)]^2} \left[\begin{array}{c} y^{-\mu} + y^{-\mu} O(y\beta_0)^2 + \\ \frac{a^{2\alpha}(\beta_0/2)^2\, y^{\mu}[1+O(\beta_0)^2]}{(1-\mu)\mu[1+O(\beta_0)^2]} \left(1+O(y\beta_0)^2\right) \end{array} \right]^2 dy$$

$$= \frac{(\beta_0/2)^{-2\mu}}{[\Gamma(1-\mu)]^2} \left(\int_a^b y^{1-2\mu}\, dy + \frac{(\beta_0/2)^2\, a^{2\alpha}}{\mu(1-\mu)} \int_a^b y\, dy + ... \right) \tag{H.10}$$

$$= \frac{(\beta_0/2)^{-2\mu}}{[\Gamma(1-\mu)]^2} \left(\int_a^b y^{2\alpha-1}\, dy + O(\beta_0)^2 \right)$$

Evaluating the integral in (H.10) using the result from (5.3.4b) for the general case where $\alpha \neq 0$,

$$\int_a^b y\, \hat{g}_0{}^2(y) dy = \frac{(\beta_0/2)^{-2\mu}}{[\Gamma(1-\mu)]^2} \left(\frac{b^{2\alpha} - a^{2\alpha}}{2\alpha} + O(\beta_0)^2 \right), \alpha \neq 0 \tag{H.11}$$

Alternatively, the denominator is evaluated using $I_\Sigma(b,\mu,\beta_0) - I_\Sigma(a,\mu,\beta_0)$. The algebra is more tedious and the manipulations have been performed using Mathematica 4.0™ where the integrals

are evaluated using expressions (G.24) – (G.27). The manipulations are listed in CD-R:/Mathematica/*BesFourZero.nb*. Substituting (H.9) and (H.11) into (H.8),

$$C_{1_0} = \frac{\dfrac{(\beta_0/2)^{-\mu}[1+O(\beta_0^2]}{\Gamma(1-\mu)}}{\dfrac{(\beta_0/2)^{-2\mu}}{[\Gamma(1-\mu)]^2}\left(\dfrac{b^{2\alpha}-a^{2\alpha}}{2\alpha}+O(\beta_0)^2\right)} = \frac{(\beta_0/2)^{\mu}\Gamma(1-\mu)[1+O(\beta_0^2]}{\left(\dfrac{b^{2\alpha}-a^{2\alpha}}{2\alpha}+O(\beta_0)^2\right)}, \alpha \neq 0 \qquad \text{(H.12)}$$

Substituting (H.7) and (H.12) into (H.3) and letting $\beta_0 \to 0$,

$$g_0(y) = \lim_{\beta_0 \to 0}\left\{\frac{(\beta_0/2)^{\mu}\Gamma(1-\mu)[1+O(\beta_0^2]}{\left(\dfrac{b^{2\alpha}-a^{2\alpha}}{2\alpha}+O(\beta_0)^2\right)} y^{\alpha}\frac{(\beta_0/2)^{-\mu}}{\Gamma(1-\mu)}\times \right.$$
$$\left.\left[y^{-\mu}\left(1+O(y\beta_0)^2\right)+\frac{a^{2\alpha}(\beta_0/2)^2\, y^{\mu}[1+O(\beta_0)^2][1+O(y\beta_0)^2]}{(1-\mu)\mu[1+O(\beta_0)^2]}\right]\right\} \qquad \text{(H.13)}$$

$$= \frac{2\alpha y^{\alpha-\mu}}{b^{2\alpha}-a^{2\alpha}} = \frac{2\alpha y^{2\alpha-1}}{b^{2\alpha}-a^{2\alpha}}, \alpha \neq 0$$

Thus, from (H.2) as expected, as $t \to \infty$ yields the steady state solution $p(y)$ concurring with (5.3.5),

$$p(y,t\to\infty) = g_0(y).1 = \frac{2\alpha y^{2\alpha-1}}{b^{2\alpha}-a^{2\alpha}}, \alpha \neq 0 \qquad \text{(H.14)}$$
$$\equiv p(y)$$

The same procedure can be easily applied for the case where $\alpha = 0$.

Appendix I Solution to the electric potential

Equation (6.1.9) is rewritten,

$$\sum_{m=0}^{\infty} g_m(x)\,h_m(y)\left(\frac{1}{g_m(x)}\frac{\partial^2(g_m(x))}{\partial x^2}+\frac{1}{h_m(y)}\frac{\partial^2(h_m(y))}{\partial y^2}\right)=0 \tag{I.1}$$

Adopting an integration constant κ_m for each mth eigenmode, (I.1) is split into two ODEs,

$$\frac{1}{g_m(x)}\frac{d^2 g_m(x)}{dx^2}=-\kappa_m^2 \tag{I.2a}$$

$$\frac{1}{h_m(y)}\frac{d^2 h_m(y)}{dy^2}=+\kappa_m^2 \tag{I.2b}$$

The sign of κ_m is governed by the conditions (6.1.3) – (6.1.7). The transverse periodicity means the $g_m(x)$ is a component of a trigonometric Fourier series with a GS satisfying (I.2a)

$$g_m(x)=G_{1_m}\cos\kappa_m x+G_{2_m}\sin\kappa_m x \tag{I.3a}$$

and the GS of (I.2b) is given by

$$h_m(y)=H_{1_m}\exp(-\kappa_m y)+H_{2_m}\exp(+\kappa_m y) \tag{I.3b}$$

where G_{1_m}, G_{2_m}, H_{1_m} and H_{2_m} are arbitrary integration constants. Substituting (I.3a) and (I.3b) into the series for the potential, (6.1.8), and letting $y=0$

$$\Phi(x,0)=\sum_{m=0}^{\infty}\left(G_{1_m}\cos\kappa_m x+G_{2_m}\sin\kappa_m x\right)\left(H_{1_m}+H_{2_m}\right) \tag{I.4}$$

Applying (I.4) to the evenness condition stated in (6.1.6a), $\Phi(-x,0)=\Phi(x,0)$, implies $G_{2_m}\equiv 0$ for the non-trivial cases $H_{1_m}+H_{2_m}\neq 0$ and $\sin\kappa_m x\neq 0$, and the expansion is restricted to a Fourier cosine series. Furthermore, $\Phi(x,0)=0$ when $x=d$ and $x=3d$. Hence, if $G_{1_m}\neq 0$ then the set of valid κ_m solutions is restricted,

$$\kappa_{2m+1}=\frac{\pi(2m+1)}{2d}\equiv\frac{\pi n}{2d}\equiv\kappa_n \tag{I.5}$$

where $n=2m+1=1,3,5,\ldots$. Thus, the expression for the potential is simplified and is written with two arbitrary constants A_n and B_n

$$\begin{aligned}\Phi(x,y)&=\sum_{m=0}^{\infty}\left(H_{1_{2m+1}}\exp(-\kappa_{2m+1}y)+H_{2_{2m+1}}\exp(+\kappa_{2m+1}y)\right)\left(G_{1_{2m+1}}\cos\kappa_{2m+1}x\right)\\&=\sum_{n=1,3,5\ldots}^{\infty}\left(A_n e^{-\kappa_n y}+B_n e^{+\kappa_n y}\right)\cos\kappa_n x\end{aligned} \tag{I.6}$$

$$\Rightarrow\Phi(x,0)=\sum_{n=1,3,5,\ldots}^{\infty}\left(A_n+B_n\right)\cos\kappa_n x \tag{I.7}$$

The constants A_n and B_n are determined by establishing orthogonality of $\Phi(x,y)$ over $x\in[0,4d]$ and applying BCs (I.3) – (I.5) at $y=0$ and $y=h$. To achieve this, (I.7) is multiplied by $\cos\frac{\pi n'x}{2d}$ and integrated,

$$\sum_{n=1,3,5,..}^{\infty}\left(A_n+B_n\right)\int_0^{4d}\cos\left(\frac{\pi n x}{2d}\right)\cos\left(\frac{\pi n'x}{2d}\right)dx=\int_0^{4d}\Phi(x,0)\cos\left(\frac{\pi n'x}{2d}\right)dx \tag{I.8}$$

Evaluation of (I.8) is facilitated by symmetry properties of $\cos\frac{\pi n'x}{2d}$ over $x\in[0,4d]$,

$$\cos\left(\frac{\pi n'(2d+x)}{2d}\right)=(-1)^{n'}\cos\left(\frac{\pi n'x}{2d}\right)=-\cos\left(\frac{\pi n'x}{2d}\right)\ \forall\ n'=1,3,5\ldots \tag{I.9a}$$

$$\cos\left(\frac{\pi n'(2d-x)}{2d}\right)=(-1)^{n'}\cos\left(\frac{-\pi n'x}{2d}\right)=-\cos\left(\frac{\pi n'x}{2d}\right)\ \forall\ n'=1,3,5\ldots \tag{I.9b}$$

The relation (I.9a) together with symmetry properties of the potential, (6.1.6c), enables the integration interval to be halved,

$$\begin{aligned}\int_0^{4d}\Phi(x,0)\cos\left(\frac{\pi n'x}{2d}\right)dx&=\int_0^{2d}\Phi(x,0)\cos\left(\frac{\pi n'x}{2d}\right)dx+\int_{2d}^{4d}\Phi(x,0)\cos\left(\frac{\pi n'x}{2d}\right)dx\\&=\int_0^{2d}\Phi(x,0)\cos\left(\frac{\pi n'x}{2d}\right)dx+\int_0^{2d}\Phi(x+2d,0)\cos\left(\frac{\pi n'(x+2d}{2d}\right)dx\\&=2\int_0^{2d}\Phi(x,0)\cos\left(\frac{\pi n'x}{2d}\right)dx\end{aligned} \tag{I.10}$$

The integration interval can be further halved by transforming and applying (6.1.6c) and (I.9b),

$$\begin{aligned}\int_0^{2d}\Phi(x,0)\cos\left(\frac{\pi n'x}{2d}\right)dx &= \int_0^{d}\Phi(x,0)\cos\left(\frac{\pi n'x}{2d}\right)dx+\int_d^{2d}\Phi(x,0)\cos\left(\frac{\pi n'x}{2d}\right)dx\\ &= \int_0^{d}\Phi(x,0)\cos\left(\frac{\pi n'x}{2d}\right)dx+\int_{-d}^{0}\Phi(2d+x,0)\cos\left(\pi n'+\frac{\pi n'x}{2d}\right)dx\\ &= \int_0^{d}\Phi(x,0)\cos\left(\frac{\pi n'x}{2d}\right)dx--\int_0^{d}\Phi(2d-x,0)\cos\left(\pi n'-\frac{\pi n'x}{2d}\right)dx\\ &= 2\int_0^{d}\Phi(x,0)\cos\left(\frac{\pi n'x}{2d}\right)dx\end{aligned} \tag{I.11}$$

Using (I.10) and (I.11) it can be shown, for $n = 1, 3, 5, \ldots$, the *lhs* integral of (I.8) becomes

$$\int_0^{4d}\cos\left(\frac{\pi nx}{2d}\right)\cos\left(\frac{\pi n'x}{2d}\right)dx = 4\int_0^{d}\cos\left(\frac{\pi nx}{2d}\right)\cos\left(\frac{\pi n'x}{2d}\right)dx = 2d\delta_{nn'} = \begin{cases}2d, & n=n'\\ 0, & n\neq n'\end{cases} \tag{I.12}$$

Substituting (I.12) into the *lhs* of (I.8), and (I.10) and (I.11) into the *rhs* of (I.8),

$$\begin{aligned}&\sum_{n=1,3,\ldots}^{\infty}(A_n+B_n)\int_0^{d}\cos\left(\frac{\pi nx}{2d}\right)\cos\left(\frac{\pi n'x}{2d}\right)dx = 4\int_0^{d}\Phi(x,0)\cos\left(\frac{\pi n'x}{2d}\right)dx\\ &\Rightarrow \sum_{n=1,3,\ldots}^{\infty}(A_n+B_n)2d\,\delta_{nn'} = 4\int_0^{d}\Phi(x,0)\cos\left(\frac{\pi n'x}{2d}\right)dx\\ &\Rightarrow A_n+B_n = \frac{2}{d}\int_0^{d}\Phi(x,0)\cos\left(\frac{\pi nx}{2d}\right)dx\end{aligned} \tag{I.13}$$

Applying the two BCs (6.1.3b) and (6.1.5b)

$$\begin{aligned}A_n+B_n &= \frac{2}{d}\int_0^{d}\Phi(x,0)\cos\left(\frac{\pi nx}{2d}\right)dx\\ &= \frac{2}{d}\int_0^{d/2}V_0\cos\left(\frac{\pi nx}{2d}\right)dx+\frac{4V_0\gamma}{d}\int_{d/2}^{d}\left(1-\frac{x}{d}\right)\cos\left(\frac{\pi nx}{2d}\right)dx\end{aligned} \tag{I.14}$$

After some algebra,

$$A_n+B_n = \frac{4V_0(1-\gamma)}{\pi n}\sin\left(\frac{\pi n}{4}\right)+\frac{16V_0\gamma}{\pi^2n^2}\cos\left(\frac{\pi n}{4}\right) \tag{I.15}$$

Applying the BC at the cover-slip (6.1.4) into (I.6),

$$\left.\frac{\partial\Phi(x,y)}{\partial y}\right|_{y=h} = \sum_{n=1,3,5\ldots}^{\infty} \partial_y\left(A_n e^{-\kappa_n y} + B_n e^{+\kappa_n y}\right)\cos\kappa_n x\Big|_{y=h}$$
$$= \sum_{n=1,3,5\ldots}^{\infty}\left(-A_n e^{-\kappa_n h} + B_n e^{+\kappa_n h}\right)\kappa_n \cos\kappa_n x \;= 0 \qquad \text{(I.16)}$$

Generally, $\kappa_n \cos\kappa_n x \neq 0$ hence (I.16) implies,

$$B_n = A_n \exp(-2\kappa_n h) = A_n e^{-\pi n h/d} \qquad \text{(I.17)}$$

Combining (I.15) and (I.17),

$$A_n = \frac{4V_0(1-\gamma)\pi n\sin(\pi n/4) + 16V_0\gamma\cos(\pi n/4)}{\pi^2 n^2(1+e^{-\pi n h/d})} \qquad \text{(I.18)}$$

Appendix J Expressions for the electric field intensity gradient

J.1 Electric field in the x direction, E_x

The electric field component E_{x_a} is found by partial differentiation of equation (6.1.17a),

$$E_{x_a}(x,y) = -\frac{\partial \Phi_{\infty,T}}{\partial x} = --\sum_{n=1,3..}^{\infty} \frac{16\gamma V_o}{2\pi n d} e^{\frac{\pi n y}{2d}} \cos\left(\frac{\pi n}{4}\right)\sin\left(\frac{\pi n x}{2d}\right) \tag{J.1.1}$$

Translating the x-ordinate to $x' = x + d/2 \Leftrightarrow x = x' - d/2$, (J.1.1) is recast as

$$E_{x_a}(x,y) = \sum_{n=1,3,5....}^{\infty} \frac{4\gamma V_o}{\pi n d} e^{-k_n y}\left[\sin\left(\frac{\pi n x'}{2d}\right) - \sin\left(\frac{\pi n}{2}\right)\cos\left(\frac{\pi n x'}{2d}\right)\right] \tag{J.1.2}$$

$$= \frac{4\gamma V_o}{\pi d}\sum_{m=1}^{\infty} \frac{e^{\frac{\pi(2m-1)}{2d}y}}{(2m-1)}\left[\sin\left(\frac{\pi(2m-1)x'}{2d}\right) - (-1)^{m-1}\cos\left(\frac{\pi(2m-1)x'}{2d}\right)\right]$$

Using tabulations of sums infinite sums (Gradshteyn and Ryzhik, 1994, section 1.448),

$$E_{x_a}(x,y) = \frac{2\gamma V_o}{\pi d}\left[\tan^{-1}\left(\frac{2e^{-\hat{y}}\sin\hat{x}}{1-e^{-2\hat{y}}}\right) - \tan^{-1}\left(\frac{2e^{-\hat{y}}\cos\hat{x}}{1-e^{-2\hat{y}}}\right)\right] \tag{J.1.3}$$

$$= \frac{2\gamma V_o}{\pi d}\left[\tan^{-1}\left(\frac{\sin\hat{x}}{\sinh\hat{y}}\right) - \tan^{-1}\left(\frac{\cos\hat{x}}{\sinh\hat{y}}\right)\right]$$

where $\hat{y} = \pi y/2d$, and $\hat{x} = \pi x'/2d = \pi x/2d + \pi/4$ and all other symbols are as previously defined. The component E_{x_b} is found by partial differentiation of equation (6.1.17b). Recognizing (6.1.17b) has a similar form to (J.1.1),

$$\Phi_{\infty,Sq}(x,y) = \sum_{n=1,3,5...}^{\infty} \frac{4V_0(1-\gamma)}{\pi n}\sin\left(\frac{\pi n}{4}\right)e^{-\frac{\pi n y}{2d}}\cos\left(\frac{\pi n x}{2d}\right) \tag{J.1.4}$$

$$= \frac{4V_0(1-\gamma)}{\pi}\sum_{m=1}^{\infty}\frac{e^{-\frac{\pi(2m-1)y}{2d}}}{2(2m-1)}\left[\sin\left(\frac{\pi(2m-1)x'}{2d}\right) + (-1)^{m-1}\cos\left(\frac{\pi(2m-1)x'}{2d}\right)\right]$$

Hence, the infinite series for the potential is written

$$\Phi_{\infty,Sq}(x,y) = \frac{(1-\gamma)V_o}{\pi}\left[\tan^{-1}\left(\frac{\sin\hat{x}}{\sinh\hat{y}}\right) + \tan^{-1}\left(\frac{\cos\hat{x}}{\sinh\hat{y}}\right)\right] \qquad \text{(J.1.5)}$$

where all symbols are as previously defined. Differentiating (J.1.5) using the chain rule, and after some algebra

$$\begin{aligned} E_{x_b} &= -\frac{\partial\Phi_{\infty,Sq}}{\partial x} = -\frac{\partial\Phi_{\infty,Sq}}{\partial\hat{x}}\cdot\frac{\partial\hat{x}}{\partial x} = -\frac{\partial\Phi_{\infty,Sq}}{\partial\hat{x}}\cdot\frac{\pi}{2d} \\ &= \frac{(1-\gamma)V_o\sinh\hat{y}}{d}\left[\frac{\sin\hat{x}}{\cosh 2\hat{y}+\cos 2\hat{x}} - \frac{\cos\hat{x}}{\cosh 2\hat{y}-\cos 2\hat{x}}\right] \end{aligned} \qquad \text{(J.1.6)}$$

The component E_{x_c} is found by partial differentiation of equation (6.1.17c),

$$E_{x_c}(x,y) = -\frac{\partial\Phi_{H,T}}{\partial x} = --\sum_{n=1,3..}^{\infty}\frac{16\gamma V_o}{2\pi n d}e^{-n\left(\frac{\pi h}{d}-\frac{\pi y}{2d}\right)}\cos\left(\frac{\pi n}{4}\right)\sin\left(\frac{\pi n x}{2d}\right) \qquad \text{(J.1.7)}$$

It is clear (J.1.7) is same as (J.1.1) with $\hat{y}$ replaced by $\hat{\mathcal{y}} = \pi h/d - \pi y/2d = 2\hat{h} - \hat{y}$. Hence, from (J.1.3),

$$E_{x_c} = -\frac{\partial\Phi_{H,T}}{\partial x} = \frac{2\gamma V_o}{\pi d}\left[\tan^{-1}\left(\frac{\sin\hat{x}}{\sinh\hat{\mathcal{y}}}\right) - \tan^{-1}\left(\frac{\cos\hat{x}}{\sinh\hat{\mathcal{y}}}\right)\right] \qquad \text{(J.1.8)}$$

Comparing (6.1.17d) with (6.1.17b), $\Phi_{H,Sq}(x,y)$ is the same as $\Phi_{\infty,Sq}(x,y)$ with $\hat{y}$ replaced by $\hat{\mathcal{y}}$. Therefore, from (J.1.5)

$$\Phi_{H,Sq}(x,y) = \frac{(1-\gamma)V_o}{\pi}\left[\tan^{-1}\left(\frac{\sin\hat{x}}{\sinh\hat{\mathcal{y}}}\right) + \tan^{-1}\left(\frac{\cos\hat{x}}{\sinh\hat{\mathcal{y}}}\right)\right] \qquad \text{(J.1.9)}$$

and by inspection of (J.1.6),

$$E_{x_d} = -\frac{\partial\Phi_{H,Sq}}{\partial x} = \frac{(1-\gamma)V_o\sinh\hat{\mathcal{y}}}{d}\left[\frac{\sin\hat{x}}{\cosh 2\hat{\mathcal{y}}+\cos 2\hat{x}} - \frac{\cos\hat{x}}{\cosh 2\hat{\mathcal{y}}-\cos 2\hat{x}}\right] \qquad \text{(J.1.10)}$$

The expressions (J.1.3), (J.1.6), (J.1.8) and (J.1.10) are valid $\forall\, x,\ 0<y\le h\,,\ h>0.$

J.2 Electric field in the y direction, E_y

The electric field component E_{y_a} is found by partial differentiation of (6.1.17a) with respect to the independent variable y and translating the x-ordinate to $x' = x + d/2 \ \Leftrightarrow x = x' - d/2$,

$$E_{y_a}(x,y) = -\frac{\partial \Phi_{\infty,T}}{\partial y} = --\sum_{n=1,3..}^{\infty} \frac{16\gamma V_o}{2\pi n d} e^{\frac{\pi n}{2d}y} \cos\left(\frac{\pi n}{4}\right)\cos\left(\frac{\pi n x}{2d}\right)$$
$$= \frac{4\gamma V_o}{\pi d}\sum_{m=1}^{\infty} \frac{e^{\frac{\pi(2m-1)}{2d}y}}{(2m-1)}\left[\cos\left(\frac{\pi(2m-1)x'}{2d}\right) + (-1)^{m-1}\sin\left(\frac{\pi(2m-1)x'}{2d}\right)\right] \qquad \text{(J.2.1)}$$

The closed form sum of the infinite series is (Gradshteyn and Ryzhik, 1994, section 1.448),

$$E_{y_a} = -\frac{\partial \Phi_{\infty,T}}{\partial y} = \frac{\gamma V_o}{\pi d}\left[\ln\left(\frac{1+\Theta_{c+}}{1+\Theta_{c-}}\right) + \ln\left(\frac{1+\Theta_{s+}}{1+\Theta_{s-}}\right)\right] \qquad \text{(J.2.2a)}$$

where $\begin{Bmatrix}\Theta_{c\pm}\\ \Theta_{s\pm}\end{Bmatrix} = \begin{Bmatrix}\pm 2e^{-\hat{y}}\cos\hat{x} + e^{-2\hat{y}}\\ \pm 2e^{-\hat{y}}\sin\hat{x} + e^{-2\hat{y}}\end{Bmatrix}$, and $\hat{x}$ and $\hat{y}$ are as previously defined. Since, $\frac{1+e^{-2\hat{y}}}{2e^{-\hat{y}}} = \cosh\hat{y}$, (J.2.2a) simplifies,

$$E_{y_a} = -\frac{\partial \Phi_{\infty,T}}{\partial y} = \frac{\gamma V_o}{\pi d}\ln\left(\frac{\cosh\hat{y}+\cos\hat{x}}{\cosh\hat{y}-\cos\hat{x}}\cdot\frac{\cosh\hat{y}+\sin\hat{x}}{\cosh\hat{y}-\sin\hat{x}}\right) \qquad \text{(J.2.2b)}$$

The field component E_{y_b} is found by partial differentiation, with respect to y, of the closed form expression for $\Phi_{\infty,Sq}(x,y)$, (J.1.5). Thus,

$$E_{y_b} = -\frac{\partial \Phi_{\infty,Sq}}{\partial y} = \frac{(1-\gamma)V_o\cosh\hat{y}}{d}\left[\frac{\sin\hat{x}}{\cosh 2\hat{y} - \cos 2\hat{x}} + \frac{\cos\hat{x}}{\cosh 2\hat{y} + \cos 2\hat{x}}\right] \qquad \text{(J.2.3)}$$

The component E_{y_c} is determined by the method similar to that for finding E_{x_c},

$$E_{y_c}(x,y) = -\frac{\partial \Phi_{H,T}}{\partial y} = -\sum_{n=1,3..}^{\infty} \frac{16\gamma V_o}{2\pi n d} e^{-n\left(\frac{\pi h}{d} - \frac{\pi y}{2d}\right)} \cos\left(\frac{\pi n}{4}\right) \cos\left(\frac{\pi n x}{2d}\right) \qquad \text{(J.2.4)}$$

Recognizing (J.2.4) has a form similar to (J.2.1) except a minus sign in front of the sum and $\hat{y} \to \hat{y}$, then

$$E_{y_c} = -\frac{\partial \Phi_{H,T}}{\partial y} = \frac{-\gamma V_o}{\pi d} \ln\left(\frac{\cosh \hat{y} + \cos \hat{x}}{\cosh \hat{y} - \cos \hat{x}} \cdot \frac{\cosh \hat{y} + \sin \hat{x}}{\cosh \hat{y} - \sin \hat{x}}\right) \qquad \text{(J.2.5)}$$

Equation (J.2.4) can be verified by noting

$$E_{y_c} = -\frac{\partial \Phi_{H,T}}{\partial y} = -\frac{\partial \Phi_{H,T}}{\partial \hat{y}} \cdot \frac{\partial \hat{y}}{\partial y} = -\frac{\partial \Phi_{H,T}}{\partial \hat{y}} \cdot \frac{-\pi}{2d} \qquad \text{(J.2.6)}$$

Similarly, E_{y_d} has the same form as E_{y_b} except there is a minus sign in front of the sum and $\hat{y} \to \hat{y}$. Using (J.1.9)

$$E_{y_d} = -\frac{\partial \Phi_{H,Sq}}{\partial y} = -\frac{\partial \Phi_{H,Sq}}{\partial \hat{y}} \cdot \frac{\partial \hat{y}}{\partial y} = -\frac{\partial \Phi_{H,Sq}}{\partial \hat{y}} \cdot \frac{-\pi}{2d}$$

$$= \frac{-(1-\gamma)V_o \cosh \hat{y}}{d}\left[\frac{\sin \hat{x}}{\cosh 2\hat{y} - \cos 2\hat{x}} + \frac{\cos \hat{x}}{\cosh 2\hat{y} + \cos 2\hat{x}}\right] \qquad \text{(J.2.7)}$$

J.3 Derivatives of the electric field

Rewriting (J.1.2) with the summing index beginning at $m = 0$,

$$E_{x_a}(x,y) = \frac{4\gamma V_o}{\pi d} \sum_{m=0}^{\infty} \frac{e^{\frac{\pi(2m+1)}{2d}y}}{(2m+1)}\left[\sin\left(\frac{\pi(2m+1)x'}{2d}\right) - (-1)^m \cos\left(\frac{\pi(2m+1)x'}{2d}\right)\right] \qquad \text{(J.3.1)}$$

where $x' = x + d/2$. Differentiating (J.3.1) with respect to x,

$$E_{x,x_a}(x,y)=\frac{\partial E_{x_a}}{\partial x}=\frac{2\gamma V_o}{d^2}\sum_{m=0}^{\infty}e^{-\frac{\pi(2m+1)}{2d}y}\left[\cos\left(\frac{\pi(2m+1)x'}{2d}\right)+(-1)^m\sin\left(\frac{\pi(2m+1)x'}{2d}\right)\right] \quad \text{(J.3.2)}$$

Using tabulations of infinite sums (Prudnikov *et al.*, 1986, Vol. 1, section 5.4.9, p. 736),

$$E_{x,x_a}=\frac{2V_o\gamma e^{-\hat{y}}(1-e^{-2\hat{y}})}{d^2}\left[\frac{\cos\hat{x}}{1+e^{-4\hat{y}}-2e^{-2\hat{y}}\cos 2\hat{x}}+\frac{\sin\hat{x}}{1+e^{-4\hat{y}}+2e^{-2\hat{y}}\cos 2\hat{x}}\right] \quad \text{(J.3.3)}$$

Since, $\frac{1-e^{-2\hat{y}}}{2e^{-\hat{y}}}=\sinh\hat{y}$ and $\frac{1+e^{-4\hat{y}}}{2e^{-2\hat{y}}}=\cosh 2\hat{y}$, then

$$E_{x,x_a}=\frac{\partial E_{x_a}}{\partial x}=\frac{2\gamma V_o\sinh\hat{y}}{d^2}\left[\frac{\cos\hat{x}}{\cosh 2\hat{y}-\cos 2\hat{x}}+\frac{\sin\hat{x}}{\cosh 2\hat{y}+\cos 2\hat{x}}\right] \quad \text{(J.3.4)}$$

Similarly, differentiating (J.3.1) with respect to y,

$$\begin{aligned}E_{x,y_a}(x,y)&=\frac{\partial E_{x_a}}{\partial y}\\&=-\frac{2\gamma V_o}{d^2}\sum_{m=0}^{\infty}e^{-\frac{\pi(2m+1)}{2d}y}\left[\sin\left(\frac{\pi(2m+1)x'}{2d}\right)-(-1)^m\cos\left(\frac{\pi(2m+1)x'}{2d}\right)\right]\end{aligned} \quad \text{(J.3.5)}$$

Equating with expressions for infinite sums (Prudnikov *et al.*, 1986, Vol. 1, section 5.4.9, p. 736),

$$E_{x,y_a}=\frac{-2V_o\gamma e^{-\hat{y}}(1+e^{-2\hat{y}})}{d^2}\left[\frac{\sin\hat{x}}{1+e^{-4\hat{y}}-2e^{-2\hat{y}}\cos 2\hat{x}}-\frac{\cos\hat{x}}{1+e^{-4\hat{y}}+2e^{-2\hat{y}}\cos 2\hat{x}}\right] \quad \text{(J.3.6)}$$

Using $\frac{1+e^{-2\hat{y}}}{2e^{-\hat{y}}}=\cosh\hat{y}$ etc.,

$$E_{x,y_a}=\frac{\partial E_{x_a}}{\partial y}=\frac{2\gamma V_o\cosh\hat{y}}{d^2}\left[\frac{\cos\hat{x}}{\cosh 2\hat{y}+\cos 2\hat{x}}-\frac{\sin\hat{x}}{\cosh 2\hat{y}-\cos 2\hat{x}}\right] \quad \text{(J.3.7)}$$

In addition, rewriting (J.2.1) with the summing index beginning at $m = 0$,

$$E_{y_a}(x,y) = \frac{4\gamma V_o}{\pi d}\sum_{m=0}^{\infty}\frac{e^{\frac{\pi(2m+1)}{2d}y}}{(2m+1)}\left[\cos\left(\frac{\pi(2m+1)x'}{2d}\right) + (-1)^m \sin\left(\frac{\pi(2m+1)x'}{2d}\right)\right] \qquad \text{(J.3.8)}$$

and differentiating (J.3.8) with respect to x,

$$E_{y,x_a}(x,y) = \frac{\partial E_{y_a}}{\partial x}$$

$$= \frac{2\gamma V_o}{d^2}\sum_{m=0}^{\infty} e^{-\frac{\pi(2m+1)}{2d}y}\left[-\sin\left(\frac{\pi(2m+1)x'}{2d}\right) + (-1)^m \cos\left(\frac{\pi(2m+1)x'}{2d}\right)\right] \qquad \text{(J.3.9)}$$

Comparing (J.3.9) with (J.3.5),

$$E_{x,y_a} = \frac{\partial E_{x_a}}{\partial y} = \frac{\partial E_{y_a}}{\partial x} = E_{y,x_a} \qquad \text{(J.3.10)}$$

Finally, differentiating (J.2.1) with respect to y,

$$E_{y,y_a}(x,y) = \frac{\partial E_{y_a}}{\partial y}$$

$$= -\frac{2\gamma V_o}{d^2}\sum_{m=0}^{\infty} e^{-\frac{\pi(2m+1)}{2d}y}\left[\cos\left(\frac{\pi(2m+1)x'}{2d}\right) + (-1)^m \sin\left(\frac{\pi(2m+1)x'}{2d}\right)\right] \qquad \text{(J.3.11)}$$

Comparing (J.3.11) with (J.3.2),

$$E_{x,x_a} = \frac{\partial E_{x_a}}{\partial x} = -\frac{\partial E_{y_a}}{\partial y} = -E_{y,y_a} \qquad \text{(J.3.12)}$$

Appendix K Electric field intensity gradient approximations

K.1 Near field approximations at an electrode edge

Consider the electric field intensity gradient for y values very close to one electrode edge. For convenience, the edge at $x=-d/2$, or $\hat{x}=0$, is chosen. The domain of 'very close' y values is considered is $\{\hat{y}: 0<\hat{y}\le\frac{\pi}{200}\}$ and is abbreviated $\hat{y}\to 0$. Expanding the expression for E_{x_a} given in (J.1.3) or (6.2.4a)

$$E_{x_a}(x,y)\Big|_{\substack{\hat{x}=0\\ \hat{y}\to 0}} = \frac{2\gamma V_o}{\pi d}\left[\tan^{-1}\left(\frac{\sin\hat{x}}{\sinh\hat{y}}\right)-\tan^{-1}\left(\frac{\cos\hat{x}}{\sinh\hat{y}}\right)\right]\Bigg\|_{\substack{\hat{x}=0\\ \hat{y}\to 0}}$$

$$=-\frac{2\gamma V_o}{\pi d}\tan^{-1}\left(\frac{1}{\sinh\hat{y}}\right)\Bigg|_{\hat{y}\to 0} \qquad (K.1.1)$$

$$=-\frac{2\gamma V_o}{\pi d}\left[\frac{\pi}{2}-\sinh\hat{y}+\frac{\sinh^3\hat{y}}{3}-....\right]=\frac{\gamma V_o}{\pi d}\left[2\hat{y}-\pi+O(\hat{y}^3)\right]$$

where the inverse tan function expansion (in the second line) applies for the case where argument is greater than unity (Abramowitz and Stegun, 1972, p. 81, relation 4.4.42; Gradshteyn and Ryzhik, 1994, p. 60, 1.643) and $O(\hat{y}^n)$ means $\hat{y}$ terms of order n and higher ($\ge n$). Generally, our interest lies in terms up to first order for these electric field components, and second order and terms $\hat{y}^2$ terms and higher are grouped as $O(\hat{y}^2)$.

Similarly, from (J.2.2b) or (6.2.6a)

$$E_{y_a}(x,y)\Big|_{\substack{\hat{x}=0\\ \hat{y}\to 0}} =\frac{\gamma V_o}{\pi d}\ln\left(\frac{\cosh\hat{y}+\cos\hat{x}}{\cosh\hat{y}-\cos\hat{x}}\frac{\cosh\hat{y}+\sin\hat{x}}{\cosh\hat{y}-\sin\hat{x}}\right)\Bigg|_{\substack{\hat{x}=0\\ \hat{y}\to 0}}$$

$$=\frac{\gamma V_o}{\pi d}\ln\left(\frac{1+\frac{\hat{y}^2}{2!}+\frac{\hat{y}^4}{4!}+....+1}{1+\frac{\hat{y}^2}{2!}+\frac{\hat{y}^4}{4!}+....-1}\right)\Bigg|_{\hat{y}\to 0} =\frac{\gamma V_o}{\pi d}\ln\left(\frac{2(1+\frac{\hat{y}^2}{2\cdot 2!}+\frac{\hat{y}^4}{2\cdot 4!}+....)}{\frac{\hat{y}^2}{2}(1+\frac{2\hat{y}^2}{4!}+\frac{2\hat{y}^4}{6!}+....)}\right)\Bigg|_{\hat{y}\to 0} \qquad (K.1.2)$$

$$=\frac{\gamma V_o}{\pi d}\left[\ln(4)-2\ln(\hat{y})+\ln\left(1+\frac{\hat{y}^2}{2\cdot 2!}+\frac{\hat{y}^4}{2\cdot 4!}+...\right)-\ln\left(1+\frac{2\hat{y}^2}{4!}+\frac{2\hat{y}^4}{6!}+...\right)\right]\Bigg\|_{\hat{y}\to 0}$$

Both logarithm functions can be expanded in the form (Abramowitz and Stegun, 1972, p. 68, 4.1.24; Gradshteyn and Ryzhik, 1994, p. 52, 1.511),

$$\ln(1+\Theta) = \Theta - \frac{\Theta^2}{2} + \frac{\Theta^3}{3} - \ldots\ldots \qquad -1 < \Theta \le 1 \qquad \text{(K.1.3)}$$

By equating the argument of both functions in the last line of (K.1.2) with Θ in (K.1.3), the condition $-1 < \Theta \le 1$ is shown to be satisfied. Therefore,

$$E_{y_a}(x,y)\Big|_{\substack{\hat{x}=0\\ \hat{y}\to 0}} = \frac{\gamma V_o}{\pi d}\left[\ln 4 - 2\ln\hat{y} + O(\hat{y}^2)\right] \qquad \text{(K.1.4)}$$

Expanding the electric field derivative E_{x,x_a} from (J.3.3) with $X_{\mp} = e^{-4\hat{y}} \mp 2e^{-2\hat{y}}\cos 2\hat{x}$,

$$\begin{aligned} E_{x,x_a}(x,y)\Big|_{\substack{\hat{x}=0\\ \hat{y}\to 0}} &= \frac{2\gamma V_o e^{-\hat{y}}(1-e^{-2\hat{y}})}{d^2}\left(\frac{\cos\hat{x}}{1+X_-} + \frac{\sin\hat{x}}{1+X_+}\right)\Bigg|_{\substack{\hat{x}=0\\ \hat{y}\to 0}} \\ &= \frac{2\gamma V_o e^{-\hat{y}}(1-e^{-2\hat{y}})}{d^2}\left(\frac{1}{(1-e^{-2\hat{y}})^2} + 0\right)\Bigg|_{\hat{y}\to 0} = \frac{\gamma V_o}{d^2\sinh\hat{y}}\Bigg|_{\hat{y}\to 0} \end{aligned} \qquad \text{(K.1.5)}$$

Using the series approximation for $\operatorname{cosech}\hat{y}$, valid for $|\hat{y}|<\pi$ (Abramowitz and Stegun, 1972, p. 85, 4.5.65; Gradshteyn and Ryzhik, 1994, p. 42, 1.411)

$$E_{x,x_a}(x,y)\Big|_{\substack{\hat{x}=0\\ \hat{y}\to 0}} = \frac{\gamma V_o}{d^2}\left[\frac{1}{\hat{y}} - \frac{\hat{y}}{6} + O(\hat{y}^3)\right] \qquad \text{(K.1.6)}$$

Expanding the electric field derivative E_{x,y_a} from (J.3.6)

$$\begin{aligned} E_{x,y_a}(x,y)\Big|_{\substack{\hat{x}=0\\ \hat{y}\to 0}} &= \frac{2\gamma V_o e^{-\hat{y}}(1+e^{-2\hat{y}})}{d^2}\left(\frac{\cos\hat{x}}{1+X_+} - \frac{\sin\hat{x}}{1+X_-}\right)\Bigg|_{\substack{\hat{x}=0\\ \hat{y}\to 0}} \\ &= \frac{2\gamma V_o e^{-\hat{y}}(1+e^{-2\hat{y}})}{d^2}\left(\frac{1}{(1+e^{-2\hat{y}})^2} + 0\right)\Bigg|_{\hat{y}\to 0} = \frac{\gamma V_o}{d^2\cosh\hat{y}}\Bigg|_{\hat{y}\to 0} \end{aligned} \qquad \text{(K.1.7)}$$

Using the approximation for $\operatorname{sech}\hat{y}$, valid for $|\hat{y}|<\pi/2$ (Abramowitz and Stegun, 1972, p. 85, 4.5.66)

$$E_{x,y_a}(x,y)\Big|_{\substack{\hat{x}=0\\ \hat{y}\to 0}} = \frac{\gamma V_o}{d^2}\left[1-\frac{\hat{y}^2}{2}+\frac{5\hat{y}^4}{24}+....\right] \cong \frac{\gamma V_o}{d^2}\left[1+O(\hat{y}^2)\right] \qquad \text{(K.1.8)}$$

Also, from (J.3.12) $E_{y,y_a}(x,y)\Big|_{\substack{\hat{x}=0\\ \hat{y}\to 0}} = -E_{x,x_a}(x,y)\Big|_{\substack{\hat{x}=0\\ \hat{y}\to 0}}$ and from (J.3.10) $E_{y,x_a}(x,y)\Big|_{\substack{\hat{x}=0\\ \hat{y}\to 0}} = E_{x,y_a}(x,y)\Big|_{\substack{\hat{x}=0\\ \hat{y}\to 0}}$.

Substituting equations (K.1.1), (K.1.4), (K.1.6) and (K.1.8) into (6.2.13a) and (6.2.13b),

$$\partial_x\left|\vec{E}_a\right|^2_{\substack{\hat{x}=0\\ \hat{y}\to 0}} = 2(E_{x_a}E_{x,x_a}+E_{y_a}E_{y,x_a})\Big|_{\substack{\hat{x}=0\\ \hat{y}\to 0}} = 2(E_{x_a}E_{x,x_a}+E_{y_a}E_{x,y_a})\Big|_{\substack{\hat{x}=0\\ \hat{y}\to 0}}$$

$$= \frac{2\gamma^2 V_o^2}{\pi d^3}\left[\begin{array}{l}\left(2\hat{y}-\pi+O(\hat{y}^3)\right)\left(\frac{1}{\hat{y}}-\frac{\hat{y}}{6}+O(\hat{y}^3)\right)+\\ \left(\ln 4-2\ln\hat{y}+O(\hat{y}^2)\right)\left(1+O(\hat{y}^2)\right)\end{array}\right] \qquad \text{(K.1.9)}$$

$$= \frac{2\gamma^2 V_o^2}{\pi d^3}\left[2-\frac{\pi}{\hat{y}}+\frac{\pi\hat{y}}{6}+\ln 4-2\ln\hat{y}+O(\hat{y}^2)\right]$$

For small values, $\{\hat{y}: 0<\hat{y}\le\frac{\pi}{200}\}$, the second term in [ ] (K.1.9) dominates, therefore

$$\partial_x\left|\vec{E}_a\right|^2_{\substack{\hat{x}=0\\ \hat{y}\to 0}} \cong -\frac{2\gamma^2 V_o^2}{\hat{y}d^3} \cong -\frac{4\gamma^2 V_o^2}{\pi y d^2} \qquad \text{(K.1.10)}$$

Similarly,

$$\partial_y\left|\vec{E}_a\right|^2_{\substack{\hat{x}=0\\ \hat{y}\to 0}} = 2(E_{x_a}E_{x,y_a} + E_{y_a}E_{y,y_a})\Big|_{\substack{\hat{x}=0\\ \hat{y}\to 0}} = 2(E_{x_a}E_{x,y_a} - E_{y_a}E_{x,x_a})\Big|_{\substack{\hat{x}=0\\ \hat{y}\to 0}}$$

$$= \frac{2\gamma^2 V_o^2}{\pi d^3}\left[\begin{array}{l}\left(2\hat{y}-\pi+O(\hat{y}^3)\right)\left(1+O(\hat{y}^2)\right)-\\ \left(\ln 4-2\ln\hat{y}+O(\hat{y}^2)\right)\left(\frac{1}{\hat{y}}-\frac{\hat{y}}{6}+O(\hat{y}^3)\right)\end{array}\right] \qquad \text{(K.1.11)}$$

$$= \frac{2\gamma^2 V_o^2}{\pi d^3}\left[2\hat{y}-\pi+\frac{\hat{y}}{6}\ln 4-\frac{\hat{y}\ln\hat{y}}{3}-\frac{\ln 4}{\hat{y}}+\frac{2\ln\hat{y}}{\hat{y}}+O(\hat{y})\right]$$

$$= \frac{2\gamma^2 V_o^2}{\pi d^3}\left[\frac{2\ln\hat{y}-\ln 4}{\hat{y}}-\pi+O(\hat{y})\right]$$

For small values, $\{\hat{y}: 0<\hat{y}\le\frac{\pi}{200}\}$, the first hyperbolic term in [ ] (K.1.11) dominates, therefore

$$\partial_y\left|\vec{E}_a\right|^2_{\substack{\hat{x}=0\\ \hat{y}\to 0}} \cong \frac{4\gamma^2 V_o^2\ln(\hat{y}/2)}{\pi\hat{y}d^3} \cong \frac{8\gamma^2 V_o^2}{\pi^2 y d^2}\ln(\pi y/(4d)) \qquad \text{(K.1.12)}$$

An expression for the electric field magnitude is useful in Chapter 6.4. Using the relations, (K.1.1) and (K.1.4), for the electric field components at $\hat{x}=0$ and $\{\hat{y}: 0<\hat{y}\le\frac{\pi}{200}\}$,

$$\left(E_{x_a}^2 + E_{y_a}^2\right)_{\substack{\hat{x}=0\\ \hat{y}\to 0}} = \frac{\gamma^2 V_o^2}{\pi^2 d^2}\left[\left(2\hat{y}-\pi+O(\hat{y}^3)\right)^2 + \left(2\ln(2/\hat{y})+O(\hat{y}^2)\right)^2\right]$$

$$= \frac{\gamma^2 V_o^2}{\pi^2 d^2}\left[\begin{array}{l}\pi^2 - 4\pi\hat{y} + 4\hat{y}^2 + O(\hat{y}^3) + 4\ln^2(2/\hat{y})\\ \quad + 4\ln(2/\hat{y})O(\hat{y}^2) + O(\hat{y}^4)\end{array}\right] \qquad \text{(K.1.13)}$$

At the upper limit $\hat{y}=\frac{\pi}{200}$,

$$\left(E_{x_a}^2 + E_{y_a}^2\right)_{\substack{\hat{x}=0\\ \hat{y}=\pi/200}} = \frac{\gamma^2 V_o^2}{\pi^2 d^2}\left[\begin{array}{l}\overbrace{\pi^2}^{\approx 10} - \overbrace{4\pi\hat{y}}^{\approx 0.2} + \overbrace{4\hat{y}^2}^{\cong 0.001} + O(\hat{y}^3) + \overbrace{4\ln^2(2/\hat{y})}^{\cong 94}\\ \quad + \underbrace{4\ln(2/\hat{y})}_{\cong 19}O(\hat{y}^2) + O(\hat{y}^4)\end{array}\right] \qquad \text{(K.1.14)}$$

and the terms $\ge$ first order $O(\hat{y})$ become smaller, relative to the first and fifth terms, as $\hat{y}\to 0$. Hence, a good approximation of (K.1.14) is

$$\left(E_{x_a}^2 + E_{y_a}^2\right)\Big|_{\substack{\hat{x}=0 \\ \hat{y}\to 0}} \cong \frac{\gamma^2 V_o^2}{\pi^2 d^2}\left[\pi^2 + 4\ln^2(2/\hat{y})\right] \tag{K.1.15}$$

Equations (K.1.1) – (K.1.15) have been developed and verified using Mathematica 4.0™ (Wolfram, 1999), and these can be viewed in CD-R:/Mathematica/*GrdE2NrEdgeThesis.nb*.

K.2 Average near field approximation

The first step for finding an expression for the average near field is to find an approximation for E_{y_a} in (6.3.8) that can be integrated analytically. The approximation is required to be valid for $\{\hat{x}: -\frac{\pi}{4} \le \hat{x} \le \frac{\pi}{4}\}$ and $\{\hat{y}: \frac{\pi}{200} \le \hat{y} \le \frac{\pi}{20}\}$. Rewriting (6.2.6a),

$$E_{y_a} = -\frac{\partial \Phi_{\infty,T}}{\partial y} = \frac{\gamma V_o}{\pi d}\ln\left(\frac{\cosh\hat{y}+\cos\hat{x}}{\cosh\hat{y}-\cos\hat{x}}\cdot\frac{\cosh\hat{y}+\sin\hat{x}}{\cosh\hat{y}-\sin\hat{x}}\right)$$

$$= \frac{\gamma V_o}{\pi d}\left[\overbrace{\ln(\cosh\hat{y}+\cos\hat{x})}^{E_{y1}} - \overbrace{\ln(\cosh\hat{y}-\cos\hat{x})}^{E_{y2}} + \overbrace{\ln\left(\frac{\cosh\hat{y}+\sin\hat{x}}{\cosh\hat{y}-\sin\hat{x}}\right)}^{E_{y3}}\right] \tag{K.2.1}$$

where the three terms have been consecutively labeled (with sub-sub-script 'a' omitted for brevity). Each term, E_{y1}, E_{y2}, and E_{y3} is approximated using series expansions for circular, hyperbolic and logarithmic functions (Abramowitz and Stegun, 1972, Ch.4).

$$E_{y1} = \ln(\cosh\hat{y}+\cos\hat{x}) = \ln\left(2\left[1+\frac{\hat{y}^2-\hat{x}^2}{2\cdot 2!}+\frac{\hat{y}^4+\hat{x}^4}{2\cdot 4!}+....\right]\right) \tag{K.2.2}$$

$$= \ln 2+\left(\frac{\hat{y}^2-\hat{x}^2}{2\cdot 2!}+\frac{\hat{y}^4+\hat{x}^4}{2\cdot 4!}+.....\right)-\frac{1}{2}\left(\frac{\hat{y}^2-\hat{x}^2}{2\cdot 2!}+\frac{\hat{y}^4+\hat{x}^4}{2\cdot 4!}+.....\right)^2+...$$

$\therefore$

$$E_{y1} \cong \ln 2 + \frac{\hat{y}^2-\hat{x}^2}{4} + ... \tag{K.2.3}$$

$$E_{y2} = \ln(\cosh\hat{y} - \cos\hat{x}) = \ln\left(1 - 1 + \frac{\hat{y}^2 + \hat{x}^2}{2!} + \frac{\hat{y}^4 - \hat{x}^4}{4!} + \ldots.\right)$$

$$= -\ln 2 + \ln\left(\hat{y}^2 + \hat{x}^2 + \frac{\hat{y}^4 - \hat{x}^4}{2 \cdot 3!} + \ldots..\right) = -\ln 2 + \ln(\hat{y}^2 + \hat{x}^2 + \ldots.) \qquad \text{(K.2.4)}$$

$$= -\ln 2 + \ln\left(\frac{\hat{y}^2}{A}\left[A + A\frac{\hat{x}^2}{\hat{y}^2} + \ldots\right]\right) = -\ln 2 + \ln\left(\frac{\hat{y}^2}{A}\right) + \ln\left(A + A\frac{\hat{x}^2}{\hat{y}^2} + \ldots.\right)$$

where A is an arbitrary approximation constant chosen to optimally linearise the logarithm function. An appropriate series approximation (Abramowitz and Stegun, 1972, p. 68, equation 4.1.27) for the $\ln(A + A\hat{x}^2/\hat{y}^2)$ term in (K.2.4) is,

$$\ln(z) = 2\left[\frac{z-1}{z+1} + \frac{1}{3}\left(\frac{z-1}{z+1}\right)^3 + \frac{1}{5}\left(\frac{z-1}{z+1}\right)^5 + \ldots.\right] \qquad \text{for } \mathrm{Re}\{z\} \geq 0,\ z \neq 0 \qquad \text{(K.2.5)}$$

and is valid for $(A + A\hat{x}^2/\hat{y}^2) > 0$. Thus, (K.2.4) is approximated as,

$$E_{y2} = -\ln 2 + \ln\left(\frac{\hat{y}^2}{A}\right) + 2\left[\frac{A + A\hat{x}^2/\hat{y}^2 - 1}{A + A\hat{x}^2/\hat{y}^2 + 1} + \frac{1}{3}\left(\frac{A + A\hat{x}^2/\hat{y}^2 - 1}{A + A\hat{x}^2/\hat{y}^2 + 1}\right)^3 + \ldots..\right] \qquad \text{(K.2.6)}$$

Since E_{y_a} is a maximum near the electrode edge $\hat{x} = 0$ and is multiplied by E_{x,x_a} that also peaks at the edge, then the most significant value of E_{y_a} is at $\hat{x} = 0$. Consequently, a suitable and valid value of the approximation constant for application in (K.2.6) is $A = 1$. Hence,

$$E_{y2} \cong -\ln 2 + 2\ln\hat{y} + \frac{2\hat{x}^2/\hat{y}^2}{2 + \hat{x}^2/\hat{y}^2} + \ldots.. \qquad \text{(K.2.7)}$$

The third term in (K.2.1) is approximated (James, 1996, p. 452; Abramowitz and Stegun, 1972, 4.1.28),

$$E_{y3} = \ln\left(\frac{1 + \dfrac{\sin\hat{x}}{\cosh\hat{y}}}{1 - \dfrac{\sin\hat{x}}{\cosh\hat{y}}}\right) = 2\left[\frac{\sin\hat{x}}{\cosh\hat{y}} + \frac{1}{3}\left(\frac{\sin\hat{x}}{\cosh\hat{y}}\right)^3 + \frac{1}{5}\left(\frac{\sin\hat{x}}{\cosh\hat{y}}\right)^5 + \ldots\right] = \frac{2\hat{x}}{1 + \hat{y}^2/2} + \ldots. \qquad \text{(K.2.8)}$$

Substituting (K.2.3), (K.2.7) and (K.2.8) into (K.2.1),

$$E_{y_a} = \frac{\gamma V_o}{\pi d}\left[\ln 2 + \frac{\hat{y}^2 - \hat{x}^2}{4} - \left(-\ln 2 + 2\ln \hat{y} + \frac{2\hat{x}^2/\hat{y}^2}{2+\hat{x}^2/\hat{y}^2}\right) + \frac{2\hat{x}}{1+\hat{y}^2/2} + \ldots.\right]$$
$$= \frac{\gamma V_o}{\pi d}\left[\ln 4 - 2\ln \hat{y} \; - \frac{2\hat{x}^2/\hat{y}^2}{2+\hat{x}^2/\hat{y}^2} + \frac{2\hat{x}}{1+\hat{y}^2/2} + \frac{\hat{y}^2 - \hat{x}^2}{4} + \ldots.\right] \qquad \text{(K.2.9)}$$

Since $\hat{y}^2 \le \frac{\pi^2}{20^2} \cong \frac{1}{40}$ and $\hat{x}^2 \le \frac{\pi^2}{4^2} \cong \frac{3}{5}$, the last term in (K.2.9) is ignored, and second last simplifies, hence

$$E_{y_a} \cong \frac{\gamma V_o}{\pi d}\left[\ln 4 - 2\ln \hat{y} - \frac{2\hat{x}^2/\hat{y}^2}{2+\hat{x}^2/\hat{y}^2} + 2\hat{x}\right] = \widetilde{E}_{y_a} \qquad \text{(K.2.10)}$$

Both E_{y_a} and the linear approximation $\widetilde{E}_{y_a}$ are plotted in Fig. K.2(a). As expected, the approximation is excellent near the electrode edge $\hat{x}=0$. The approximation is poor near the 'tail ends' at $\hat{x}=\pm\frac{\pi}{4}$ and can be improved, for example, by considering the third order term in (K.2.6). However, as discussed above, this is not important because $\widetilde{E}_{y_a}$ is multiplied by $\widetilde{E}_{x,x_a}$ that is relatively small in the tail regions $\hat{x}\approx\pm\frac{\pi}{4}$.

The second step for finding an expression for the average near field is to approximate E_{x,x_a} in (6.3.8) where, as before, $\{\hat{x}: -\frac{\pi}{4}\le\hat{x}\le\frac{\pi}{4}\}$ and $\{\hat{y}: \frac{\pi}{200}\le\hat{y}\le\frac{\pi}{20}\}$. Expanding (6.2.9a),

$$E_{x,x_a} = \frac{\partial E_{x_a}}{\partial x} = \frac{2\gamma V_o \sinh \hat{y}}{d^2}\left[\frac{\cos\hat{x}}{\cosh 2\hat{y} - \cos 2\hat{x}} + \frac{\sin\hat{x}}{\cosh 2\hat{y} + \cos 2\hat{x}}\right]$$

$$= \frac{2\gamma V_o\left(\hat{y} + \frac{\hat{y}^3}{3!} + \ldots\right)}{d^2}\left[\frac{1 - \frac{\hat{x}^2}{2!} + \frac{\hat{x}^4}{4!} - \ldots..}{1 + \frac{(2\hat{y})^2}{2!} + \ldots - \left(1 - \frac{(2\hat{x})^2}{2!} + \ldots\right)} + \frac{\hat{x} - \frac{\hat{x}^3}{3!} + \frac{\hat{x}^5}{5!} + \ldots..}{1 + \frac{(2\hat{y})^2}{2!} + \ldots + \left(1 - \frac{(2\hat{x})^2}{2!} + \ldots\right)}\right] \qquad \text{(K.2.11)}$$

$\therefore$

$$E_{x,x_a} = \frac{2\gamma V_o \hat{y}}{d^2}\left[\frac{1}{2}\left(\frac{1-\hat{x}^2/2}{\hat{y}^2+\hat{x}^2}\right) + \frac{1}{2}\left(\frac{\hat{x}}{1+\hat{y}^2-\hat{x}^2}\right) + \ldots.\right] \qquad \text{(K.2.12)}$$

Since, $1/(\hat{y}^2+\hat{x}^2)\big|_{\hat{x}=0} = \hat{y}^{-2} > 40$, $\hat{x}^2{}_{\max} = \frac{\pi^2}{4^2} = 5^2\frac{\pi^2}{20^2} = 25\,\hat{y}^2{}_{\max}$, and $\hat{x}^2/(\hat{y}^2+\hat{x}^2)\big|_{\hat{x}=\pm\pi/4} \cong 1$,

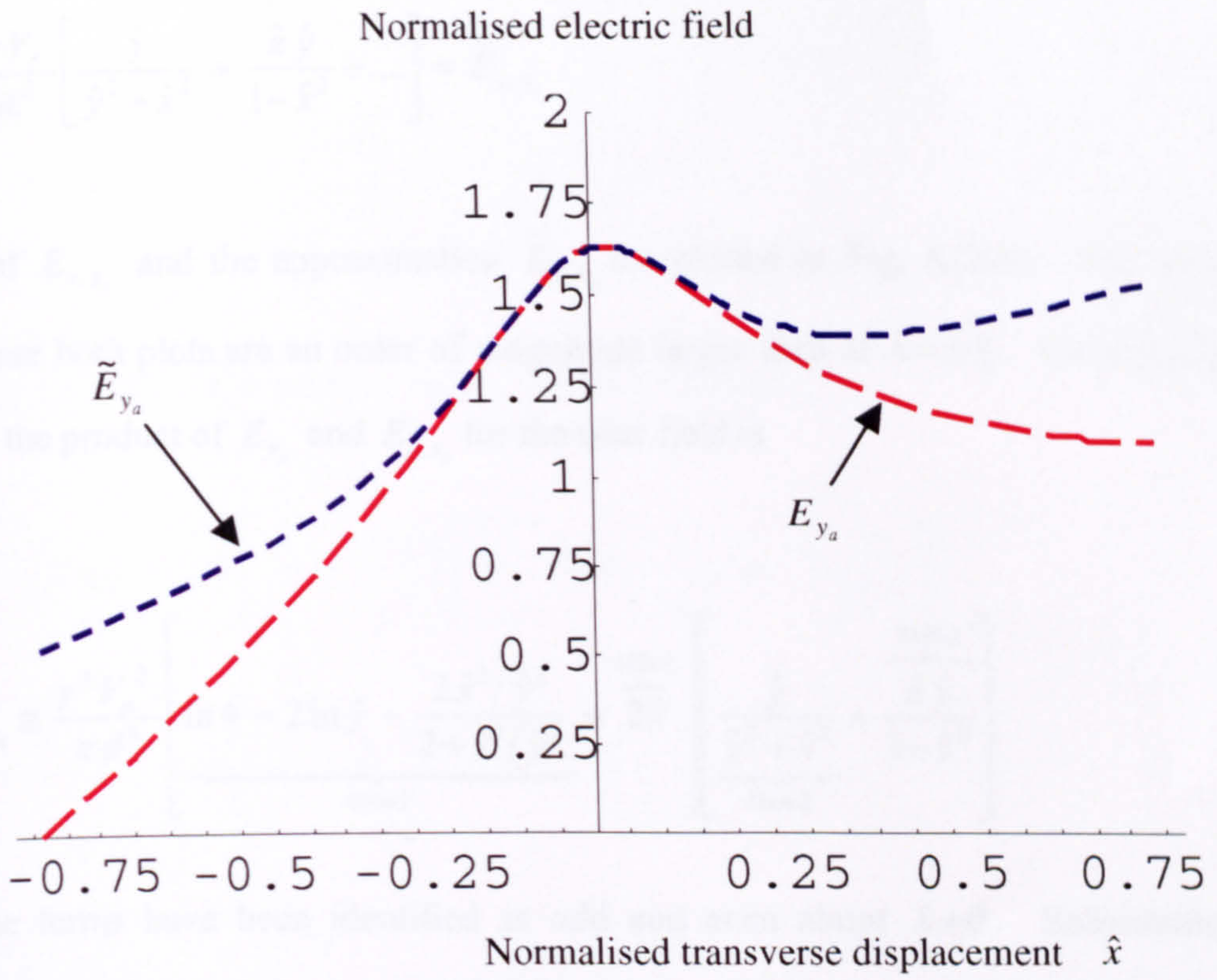

Fig. K.2(a) Electric field E_{y_a} and approximation $\tilde{E}_{y_a}$ at $\hat{y}=\frac{\pi}{20}$ (or y = 1 μm for d = 10 μm)

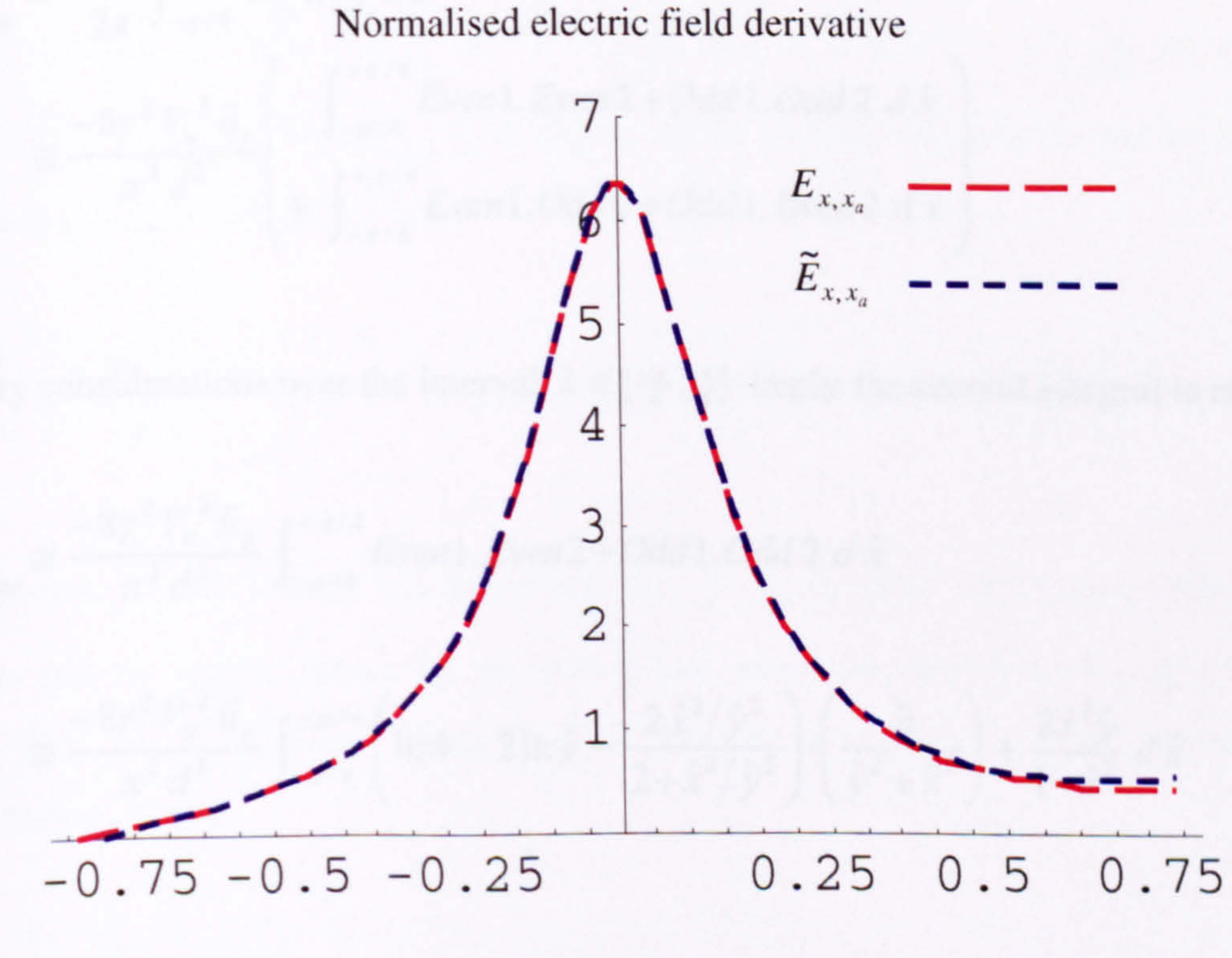

Fig. K.2(b) Electric field derivative E_{x,x_a} and approximation $\tilde{E}_{x,x_a}$ at $\hat{y}=\frac{\pi}{20}$

$$E_{x,x_a} \cong \frac{\gamma V_o}{d^2}\left[\frac{\hat{y}}{\hat{y}^2+\hat{x}^2}+\frac{\hat{x}\,\hat{y}}{1-\hat{x}^2}+....\right]=\widetilde{E}_{x,x_a} \qquad \text{(K.2.13)}$$

Profiles of E_{x,x_a} and the approximation $\widetilde{E}_{x,x_a}$ are plotted in Fig. K.2(b). The plots concur near $\hat{x}=0$ where both plots are an order of magnitude larger than at $\hat{x}=\pm\frac{\pi}{4}$. Combining (K.2.10) and (K.2.13), the product of E_{y_a} and E_{x,x_a} for the near field is

$$E_{y_a}E_{x,x_a} \cong \frac{\gamma^2 V_o^{\,2}}{\pi d^3}\left[\underbrace{\ln 4-2\ln\hat{y}-\frac{2\hat{x}^2/\hat{y}^2}{2+\hat{x}^2/\hat{y}^2}}_{Even\,1}+\overbrace{2\hat{x}}^{Odd\,1}\right]\left[\underbrace{\frac{\hat{y}}{\hat{y}^2+\hat{x}^2}}_{Even\,2}+\frac{\overbrace{\hat{x}\,\hat{y}}^{Odd\,2}}{1-\hat{x}^2}\right] \qquad \text{(K.2.14)}$$

where the terms have been identified as odd and even about $\hat{x}=0$. Substituting the product $E_{y_a}E_{x,x_a}$ (K.2.14) into the expression for the average of the electric field intensity (6.3.10)

$$\overline{\vec{\nabla}\left|\vec{E}_a\right|^2}_{near}=-\frac{16}{2\pi}\int_{-\pi/4}^{+\pi/4}E_{y_a}E_{x,x_a}\,d\hat{x}$$

$$\cong \frac{-8\gamma^2 V_o^{\,2}\vec{u}_y}{\pi^2 d^3}\begin{pmatrix}\int_{-\pi/4}^{+\pi/4}Even1.Even2+Odd1.Odd2\;d\hat{x}\\+\int_{-\pi/4}^{+\pi/4}Even1.Odd2+Odd1.Even2\;d\hat{x}\end{pmatrix} \qquad \text{(K.2.15)}$$

Symmetry considerations over the interval $\hat{x}\in[\frac{-\pi}{4},\frac{\pi}{4}]$ imply the second integral is zero. Therefore

$$\overline{\vec{\nabla}\left|\vec{E}_a\right|^2}_{near}\cong\frac{-8\gamma^2 V_o^{\,2}\vec{u}_y}{\pi^2 d^3}\int_{-\pi/4}^{+\pi/4}Even1.Even2+Odd1.Odd2\;d\hat{x} \qquad \text{(K.2.16)}$$

$$\cong\frac{-8\gamma^2 V_o^{\,2}\vec{u}_y}{\pi^2 d^3}\int_{-\pi/4}^{+\pi/4}\left(\ln 4-2\ln\hat{y}-\frac{2\hat{x}^2/\hat{y}^2}{2+\hat{x}^2/\hat{y}^2}\right)\cdot\left(\frac{\hat{y}}{\hat{y}^2+\hat{x}^2}\right)+\frac{2\hat{x}^2\hat{y}}{1-\hat{x}^2}\,d\hat{x}$$

Using partial fractions,

$$\overline{\vec{\nabla}\left|\vec{E}_a\right|^2}_{near} \cong \frac{-8\gamma^2 V_o{}^2 \vec{u}_y}{\pi^2 d^3}\left[\underbrace{\int_{-\pi/4}^{+\pi/4} \frac{(\ln 4 - 2\ln\hat{y} + 2)\hat{y}}{(\hat{x}^2+\hat{y}^2)} - \frac{4\hat{y}}{(\hat{x}^2+2\hat{y}^2)}\, d\hat{x}}_{I_1} + \underbrace{\int_{-\pi/4}^{+\pi/4} 2\hat{y}\left(\frac{1}{1-\hat{x}^2}-1\right) d\hat{x}}_{I_2}\right] \tag{K.2.17}$$

Evaluating each integral separately using standard relations,

$$I_1 = (\ln 4 - 2\ln\hat{y} + 2)\hat{y}\left[\frac{1}{\hat{y}}\tan^{-1}\left(\frac{\hat{x}}{\hat{y}}\right)\right]_{-\pi/4}^{+\pi/4} - 4\hat{y}\left[\frac{1}{\hat{y}\sqrt{2}}\tan^{-1}\left(\frac{\hat{x}}{\hat{y}\sqrt{2}}\right)\right]_{-\pi/4}^{+\pi/4} \tag{K.2.18}$$

$$= 2(\ln 4 - 2\ln\hat{y} + 2)\tan^{-1}\left(\frac{\pi}{4\hat{y}}\right) - 4\sqrt{2}\tan^{-1}\left(\frac{\pi/4}{\hat{y}\sqrt{2}}\right)$$

$$I_2 = 2\hat{y}\left[\frac{1}{2}\ln\left|\frac{1+\hat{x}}{1-\hat{x}}\right| - \hat{x}\right]_{-\pi/4}^{+\pi/4} = 2\hat{y}\left[\ln\left(\frac{4+\pi}{4-\pi}\right) - \frac{\pi}{2}\right] \cong 1.096\,\hat{y} \tag{K.2.19}$$

Considering the maximum and minimum values of the domain $\{\hat{y}: \frac{\pi}{200} \le \hat{y} \le \frac{\pi}{20}\}$ and substituting into (K.2.18) and (K.2.19): $\hat{y} = \frac{\pi}{20} \Rightarrow I_1 = 12.14$ and $I_2 = 0.1721$; $\hat{y} = \frac{\pi}{200} \Rightarrow I_1 = 27.54$ and $I_2 = 0.01721$. Hence, $\{70.56 \le I_1 / I_2 \le 1600\}$ and the second integral, I_2, can be ignored. Thus, substituting (K.2.18) into (K.2.17),

$$\overline{\vec{\nabla}\left|\vec{E}_a\right|^2}_{near} \cong \frac{-8\gamma^2 V_o{}^2 \vec{u}_y}{\pi^2 d^3}\left[2(\ln 4 - 2\ln\hat{y} + 2)\tan^{-1}\left(\frac{\pi}{4\hat{y}}\right) - 4\sqrt{2}\tan^{-1}\left(\frac{\pi/4}{\hat{y}\sqrt{2}}\right)\right] \tag{K.2.20}$$

The arguments of the inverse tan functions, for $\{\hat{y}: \frac{\pi}{200} \le \hat{y} \le \frac{\pi}{20}\}$, are greater than unity and the functions can be approximated by an appropriate series expansion given in Abramowitz and Stegun, 1972, p. 81, 4.4.42. Only the first two terms of the series are needed for a good approximation, hence

$$\overline{\vec{\nabla}\left|\vec{E}_a\right|^2}_{near} \cong \frac{-8\gamma^2 V_o{}^2 \vec{u}_y}{\pi^2 d^3}\left[[\ln(4) - 2\ln(\hat{y}) + 2]2\left(\frac{\pi}{2} - \frac{\hat{y}}{\pi/4} + \ldots\right) - 4\sqrt{2}\left(\frac{\pi}{2} - \frac{\hat{y}\sqrt{2}}{\pi/4} + \ldots\right)\right] \tag{K.2.21}$$

$$\cong \frac{-8\gamma^2 V_o{}^2 \vec{u}_y}{\pi^2 d^3}\left[[2\ln(2) - 2\ln(\hat{y}) + 2]\left(\pi - \frac{8\hat{y}}{\pi}\right) - 2\pi\sqrt{2} + \frac{32\hat{y}}{\pi}\right]$$

Equation (K.2.21) is further simplified by choosing (K.2.5) as a suitable series expansion for the logarithmic terms, $\ln(\hat{y})$. Renormalizing $\hat{y}$ by a judiciously chosen constant A, so sufficient accuracy is obtained using only the first term of the series,

$$\ln(\hat{y}) = \ln(A\hat{y}/A) = \ln(A) + \ln(\hat{y}/A) \cong \ln(A) + 2\left(\frac{\hat{y}/A-1}{\hat{y}/A+1}\right) \qquad \text{(K.2.22)}$$

For $\hat{y}$ values of interest, suitable values of the constant A are $\pi/35 \le A \le \pi/25$. Substituting (K.2.22) into (K.2.21)

$$\overline{\vec{\nabla}\left|\vec{E}_a\right|^2}_{near} \cong \frac{-8\gamma^2 V_o{}^2 \vec{u}_y}{\pi^2 d^3}\left[\begin{array}{l}\pi\left[2\ln\left(\frac{2}{A}\right)-4\left(\frac{\hat{y}/A-1}{\hat{y}/A+1}\right)+2(1-\sqrt{2})\right] \\ -\frac{8\hat{y}}{\pi}\left[2\ln\left(\frac{2}{A}\right)-4\left(\frac{\hat{y}/A-1}{\hat{y}/A+1}\right)-2\right]\end{array}\right] \qquad \text{(K.2.23)}$$

and after some algebra,

$$\overline{\vec{\nabla}\left|\vec{E}_a\right|^2}_{near} \cong \frac{-8\gamma^2 V_o{}^2 \vec{u}_y 2\pi}{\pi^2 d^3(1+\hat{y}/A)}\left[\begin{array}{l}\ln\left(\frac{2}{A}\right)+3-\sqrt{2}+\frac{\hat{y}}{A}\left[\ln\left(\frac{2}{A}\right)-1-\sqrt{2}\right] \\ -\frac{8\hat{y}}{\pi^2}\left[\ln\left(\frac{2}{A}\right)+1\right]-\frac{8\hat{y}^2}{\pi^2 A}\left[\ln\left(\frac{2}{A}\right)-3\right]\end{array}\right] \qquad \text{(K.2.24)}$$

Selecting a value $A = 1/10 \cong \pi/31.42$, yields the near field approximation as

$$\overline{\vec{\nabla}\left|\vec{E}_a\right|^2}_{near} \cong \frac{-16\gamma^2 V_o{}^2 \vec{u}_y}{\pi d^3(1+10\hat{y})}\left[\begin{array}{l}\ln 20+3-\sqrt{2}+10\hat{y}\left[\ln 20-1-\sqrt{2}\right] \\ -\frac{8\hat{y}}{\pi^2}\left[\ln 20+1\right]-\frac{80\hat{y}^2}{\pi^2}\left[\ln 20-3\right]\end{array}\right] \qquad \text{(K.2.25a)}$$

$$\overline{\vec{\nabla}\left|\vec{E}_a\right|^2}_{near} \cong \frac{-16\gamma^2 V_o{}^2 \vec{u}_y}{\pi d^3(1+10\hat{y})}\left[4.582 + 2.576\hat{y} - 0.03460\hat{y}^2\right] \qquad \text{(K.2.25b)}$$

Consider the values on the three terms inside the square bracket [ ] of (K.2.25b). The restriction on the $\hat{y}$ values, $\pi/200 \le \hat{y} \le \pi/20$, means both the second term $0.04047 \le 2.576\hat{y} \le 0.4047\ \hat{y}$ and third term $8.537\times10^{-6} \le 0.0346\hat{y}^2 \le 8.537\times10^{-4}$ can be ignored with respect to the first term. The maximum error incurred is 9 %. Thus, (K.2.25) approximates to a hyperbolic dependence,

$$\overline{\vec{\nabla}\left|\vec{E}_a\right|^2}_{near} \cong \frac{-16\gamma^2 V_o^{\,2}\vec{u}_y 4.582}{\pi d^3(1+10\hat{y})} \cong \frac{-23.33\gamma^2 V_o^{\,2}\vec{u}_y}{d^3(1+10\hat{y})}, \text{ for } \frac{\pi}{200} \le \hat{y} \le \frac{\pi}{20} \qquad \text{(K.2.26)}$$

and is written as (6.3.17) in Ch. 6.3. It is plotted in Fig. 6.7 and compares very closely with $\overline{\vec{\nabla}\left|E_a\right|^2}$ evaluated numerically using Mathematica 4.0™ (Wolfram, 1996) for $\pi/200 \le \hat{y} \le \pi/20$. Reconverting $\hat{y}$ defined in (6.2.4) $\Rightarrow 10\hat{y} = 5\pi y/d$ $\therefore$

$$\overline{\vec{\nabla}\left|\vec{E}_a\right|^2}_{near} \cong \frac{-23.33\gamma^2 V_o^{\,2}\vec{u}_y}{\frac{5\pi}{d}d^3(\frac{d}{5\pi}+y)} \cong \frac{-1.485\gamma^2 V_o^{\,2}\vec{u}_y}{d^2(\frac{d}{5\pi}+y)}, \text{ for } \frac{d}{100} \le y \le \frac{d}{10} \qquad \text{(K.2.27)}$$

For application as a 1-D DEP model in Chapter 5, it is convenient to recast the expression (K.2.27) using the transformation $y' = y + d/(5\pi)$,

$$\overline{\vec{\nabla}\left|\vec{E}_a\right|^2}_{near} \cong \frac{-1.485\gamma^2 V_o^{\,2}\vec{u}_y}{d^2 y'} \quad \text{for} \quad \frac{d}{100}+\frac{d}{5\pi} \le y' \le \frac{d}{10}+\frac{d}{5\pi} \qquad \text{(K.2.28)}$$

Substituting d = 10 μm into (K.2.28) gives,

$$\overline{\vec{\nabla}\left|\vec{E}_a\right|^2}_{near} \cong \frac{-1.485\cdot 10^{10}\gamma^2 V_o^{\,2}\vec{u}_y}{y'} \quad \text{for } 0.737\ \mu\text{m} \le y' \le 1.637\ \mu\text{m} \qquad \text{(K.2.29)}$$

Alternatively, selecting a lower value of the logarithmic approximation constant $A = \pi/25$, (K.2.24) yields

$$\overline{\vec{\nabla}\left|\vec{E}_a\right|^2}_{near} \cong \frac{-16\gamma^2 V_o^{\,2}\vec{u}_y}{\pi d^3(1+25\hat{y}/\pi)}\left[4.3531 - 0.2440\hat{y} + 1.501\hat{y}^2\right] \qquad \text{(K.2.30)}$$

Neglecting the second, $\hat{y}$, and third, $\hat{y}^2$, terms

$$\overline{\vec{\nabla}\left|\vec{E}_a\right|^2}_{near} \cong \frac{-16\gamma^2 V_o^{\,2}\vec{u}_y 4.353}{\pi d^3(1+25\hat{y}/\pi)} \cong \frac{-22.17\gamma^2 V_o^{\,2}\vec{u}_y}{d^3(1+25\hat{y}/\pi)}, \text{ for } \frac{\pi}{200} \le \hat{y} \le \frac{\pi}{20} \qquad \text{(K.2.31)}$$

and is also plotted in Fig. 6.7 and compares closely with the previous two $\overline{\vec{\nabla}|E_a|^2}$ profiles. Alternatively, transforming $1 + 25\hat{y}/\pi = \frac{25}{2d}\left(\frac{2d}{25} + y\right) = 25y'/(2d)$

$$\overline{\vec{\nabla}\left|\vec{E}_a\right|^2}_{near} \cong \frac{-22.17\gamma^2 V_o{}^2 \vec{u}_y}{\frac{25}{2d}d^3 y'} \cong \frac{-1.774\gamma^2 V_o{}^2 \vec{u}_y}{d^2 y'}, \text{ for } \frac{9d}{100} \le y' \le \frac{18d}{100} \qquad \text{(K.2.32)}$$

K.3 Electric field intensity gradient far field approximation

Expanding the expression for E_{x_a} given in (J.1.3),

$$E_{x_a} = \frac{2\gamma V_o}{\pi d}\left[\tan^{-1}(\Xi_s) - \tan^{-1}(\Xi_c)\right] = \frac{2\gamma V_o}{\pi d}\left[\Xi_s - \Xi_c - \frac{\Xi_s^3}{3} + \frac{\Xi_c^3}{3} + \ldots\right] \qquad \text{(K.3.1)}$$

where $\begin{Bmatrix}\Xi_s \\ \Xi_c\end{Bmatrix} = \frac{2e^{-\hat{y}}}{1-e^{-2\hat{y}}}\begin{Bmatrix}\sin\hat{x} \\ \cos\hat{x}\end{Bmatrix} = 2e^{-\hat{y}}(1 + e^{-2\hat{y}} + e^{-4\hat{y}} + \ldots)\begin{Bmatrix}\sin\hat{x} \\ \cos\hat{x}\end{Bmatrix}$ and $\hat{y} = \pi y/2d$ and $\hat{x} = \pi x/2d + \pi/4$. The expansions for both inverse tan functions are valid such that $|\Xi_s| < 1$ and $|\Xi_c| < 1$, implying $\exp(-\hat{y}) < \sqrt{2} - 1 \Rightarrow\ y > -2d\ln(\sqrt{2} - 1)/\pi$ or $y > 0.561d$. Hence, to first order in $\exp(-\hat{y})$, the expression for E_{x_a} in the far field,

$$E_{x_a}(x, y) \cong \frac{4\gamma V_o e^{-\hat{y}}}{\pi d}\left[\sin\hat{x} - \cos\hat{x}\right] \qquad \text{(K.3.2)}$$

One should remark that the approximation (K.3.2) is simply the first, $m = 1$ term, in the series for E_{x_a} given in (J.1.2). In this respect, the requirement $y > 0.561d$ is not absolutely necessary. It does, however, serve as a useful metric. This is particularly important given the divergence of E_{x_a} at the electrode edges as $y \to 0$. Expansions for inverse tan functions where $|\Xi_s| > 1$ and $|\Xi_c| > 1$ are better suited to the near field situation.

The series expansion for E_{y_a} given in (J.2.2a),

$$E_{y_a}(x,y)=\frac{\gamma V_o}{\pi d}\left[\ln\left(\frac{1+\Theta_{c+}}{1+\Theta_{c-}}\right)+\ln\left(\frac{1+\Theta_{s+}}{1+\Theta_{s-}}\right)\right]$$
$$=\frac{\gamma V_o}{\pi d}\left[\Theta_{c+}-\frac{\Theta_{c+}^{\,2}}{2}+..-\Theta_{c-}+\frac{\Theta_{c-}^{\,2}}{2}-..+\Theta_{s+}-\frac{\Theta_{s+}^{\,2}}{2}+..-\Theta_{s-}+\frac{\Theta_{s-}^{\,2}}{2}-..\right] \quad \text{(K.3.3)}$$

where $\begin{Bmatrix}\Theta_{c\pm}\\ \Theta_{s\pm}\end{Bmatrix}=\begin{Bmatrix}\pm 2e^{-\hat{y}}\cos\hat{x}+e^{-2\hat{y}}\\ \pm 2e^{-\hat{y}}\sin\hat{x}+e^{-2\hat{y}}\end{Bmatrix}$, and the logarithm expansions are only valid if each of the four arguments of Θ obey the criterion $|\Theta|<1$. This holds for the same condition for y as above, i.e. $y>0.561d$. Thus, to first order,

$$E_{y_a}(x,y)=\frac{\gamma V_o}{\pi d}\left[2e^{-\hat{y}}\cos\hat{x}+2e^{-\hat{y}}\sin\hat{x}+2e^{-\hat{y}}\cos\hat{x}+2e^{-\hat{y}}\sin\hat{x}+..\right] \quad \text{(K.3.4)}$$

therefore, in the far field region

$$E_{y_a}(x,y)\cong\frac{4\gamma V_o e^{-\hat{y}}}{\pi d}\left[\cos\hat{x}+\sin\hat{x}\right] \quad \text{(K.3.5)}$$

Again, one should remark that (K.3.5) can be found by considering the first, $m = 1$ term, in the series for E_{y_a} given in (J.2.1).

The approximations for the electric field derivatives E_{x,x_a} and E_{x,y_a} are found using (J.3.3) and (J.3.6). From (J.3.3),

$$E_{x,x_a}=-E_{y,y_a}=\frac{2V_o e^{-\hat{y}}(1-e^{-2\hat{y}})}{d^2}\left[\frac{\cos\hat{x}}{1+X_-}+\frac{\sin\hat{x}}{1+X_+}\right]$$
$$=\frac{2V_o e^{-\hat{y}}(1-e^{-2\hat{y}})}{d^2}\left[\cos\hat{x}(1-X_-+X_-^2-....)+\sin\hat{x}(1-X_++X_+^2-....)\right] \quad \text{(K.3.6)}$$

where $X_\mp=e^{-4\hat{y}}\mp 2e^{-2\hat{y}}\cos 2\hat{x}$ and the above condition $y>0.561d$ satisfies the requirement $|X_\mp|<1$. Thus, to a first order in $\exp(-\hat{y})$,

$$E_{x,x_a}=-E_{y,y_a}\cong\frac{2V_o e^{-\hat{y}}}{d^2}(\cos\hat{x}+\sin\hat{x}) \quad \text{(K.3.7)}$$

Equation (K.3.7) can also be deduced by considering the first, $m = 0$ term, in the series for E_{x,x_a} given in (J.3.2). Similarly, from (J.3.6),

$$E_{x,y_a} = E_{y,x_a} = \frac{2\gamma V_o e^{-\hat{y}}(1+e^{-2\hat{y}})}{d^2}\left[\frac{\cos\hat{x}}{1+X_+} - \frac{\sin\hat{x}}{1+X_-}\right]$$
$$= \frac{2\gamma V_o e^{-\hat{y}}(1-e^{-2\hat{y}})}{d^2}\left[\cos\hat{x}(1-X_+ + X_+^2 - ....) - \sin\hat{x}(1-X_- + X_-^2 - ....)\right] \quad \text{(K.3.8)}$$

$\therefore$

$$E_{x,y_a} = E_{y,x_a} \cong \frac{2\gamma V_o e^{-\hat{y}}}{d^2}(\cos\hat{x} - \sin\hat{x}) \quad \text{(K.3.9)}$$

As in the previous cases, the same result stems from considering the first, $m = 0$ term, in the series for E_{x,y_a} given in (J.3.9). From (6.2.13),

$$\vec{\nabla}\left|\vec{E}_a(x,y)\right|^2 = \vec{\nabla}\left(E_{x_a}^2 + E_{y_a}^2\right) = \partial_x\left|\vec{E}_a\right|^2\vec{u}_x + \partial_y\left|\vec{E}_a\right|^2\vec{u}_y \quad \text{(K.3.10)}$$

Substituting (K.3.2), (K.3.5), (K.3.7) and (K.3.9) into (6.2.13a) and (6.2.13b), the components are,

$$\partial_x\left|\vec{E}_a\right|^2\vec{u}_x = 2(E_{x_a}E_{x,x_a} + E_{y_a}E_{y,x_a})\vec{u}_x = 2(E_{x_a}E_{x,x_a} + E_{y_a}E_{x,y_a})\vec{u}_x$$
$$\cong \frac{16\gamma^2 V_o^{\,2} e^{-2\hat{y}}}{\pi d^3}\left[(\sin\hat{x}-\cos\hat{x})(\cos\hat{x}+\sin\hat{x}) + (\cos\hat{x}+\sin\hat{x})(\cos\hat{x}-\sin\hat{x})\right]\vec{u}_x \cong 0 \quad \text{(K.3.11)}$$

and

$$\partial_y\left|\vec{E}_a\right|^2\vec{u}_y = 2(E_{x_a}E_{x,y_a} + E_{y_a}E_{y,y_a})\vec{u}_y = 2(E_{x_a}E_{x,y_a} - E_{y_a}E_{x,x_a})\vec{u}_y$$
$$\cong \frac{16\gamma^2 V_o^{\,2} e^{-2\hat{y}}}{\pi d^3}\left[(\sin\hat{x}-\cos\hat{x})(\cos\hat{x}-\sin\hat{x}) + (\cos\hat{x}+\sin\hat{x})(-\cos\hat{x}-\sin\hat{x})\right]\vec{u}_y \quad \text{(K.3.12)}$$
$$\cong \frac{16\gamma^2 V_o^{\,2} e^{-2\hat{y}}}{\pi d^3}\left[2\left(-\sin^2\hat{x}-\cos^2\hat{x}\right)+(2-2)\sin\hat{x}\cos\hat{x}\right]\vec{u}_y \cong \frac{-32\gamma^2 V_o^{\,2} e^{-2\hat{y}}}{\pi d^3}\vec{u}_y$$

Applying (K.3.11) and (K.3.12) into (K.3.10), the far field approximation for the electric field intensity gradient is,

$$\vec{\nabla}\left|\vec{E}_a(x,y)\right|^2_{far} \cong -\frac{32\gamma^2 V_o^{\,2} e^{-2\hat{y}}}{\pi d^3}\vec{u}_y \cong -\frac{32\gamma^2 V_o^{\,2} e^{\frac{\pi y}{d}}}{\pi d^3}\vec{u}_y \quad \text{(K.3.13)}$$

A useful expression in Chapter 6.4 is the expression for the electric field in the 'far' region. Consequently, substituting (K.3.2) and (K.3.5) into the electric field magnitude,

$$\left|\vec{E}_a\right|^2_{far} = E^2_{x_a} + E^2_{y_a}\Big|_{far} \cong \frac{4^2\gamma^2 V_o{}^2 e^{-2\hat{y}}}{\pi^2 d^2}\left[(\sin\hat{x}-\cos\hat{x})^2 + (\sin\hat{x}+\cos\hat{x})^2\right] \tag{K.3.14}$$

$$\cong \frac{32\gamma^2 V_o{}^2 e^{-2\hat{y}}}{\pi^2 d^2}$$

As a final note, the far field approximation, (K.3.13), can be verified by substituting (K.3.14) into (K.3.10) and differentiating.

Appendix L Solution of the 2-D steady state PDE

Consider the joint condition (6.4.6),

$$\partial_x J_x = 0 \text{ and } \partial_y J_y = 0 \tag{L.1}$$

Integrating both equations (L.1) separately, $J_x = C_x$ and $J_y = C_y$ where C_x and C_y are arbitrary constants. The BCs require the flux in both directions to be zero at the edges, i.e. $J_x(0,y) = 0 = J_y(4d,y)$ and $J_y(x,a) = 0 = J_y(x,b)$. Hence, $C_x = 0 = C_y \Rightarrow J_x = 0 = J_y$. Hence, (L.1) is partitioned into two coupled, first order, homogeneous PDEs. Using the form for the flux stated in (6.4.2b), the coupled PDEs are written as

$$\begin{bmatrix} J_x(x,y) \\ J_y(x,y) \end{bmatrix} = \begin{bmatrix} D\partial_x p(x,y) - p(x,y)F_x/\zeta \\ D\partial_y p(x,y) - p(x,y)F_y/\zeta \end{bmatrix} = \begin{bmatrix} 0 \\ 0 \end{bmatrix} \tag{L.2}$$

The PDEs are solved separately,

$$p_1(x,y) = g_1(y)\exp\left(\frac{1}{D}\int\frac{F_x}{\zeta}dx\right) = g_1(y)\exp\left(\frac{k_f}{k_BT}\int\partial_x|E|^2dx\right) = g_1(y)e^{\frac{k_f}{k_BT}|E|^2} \tag{L.3a}$$

$$p_2(x,y) = g_2(x)\exp\left(\frac{1}{D}\int\frac{F_y}{\zeta}dy\right) = g_2(x)\exp\left(\frac{k_f}{k_BT}\int\partial_y|E|^2dy\right) = g_2(x)e^{\frac{k_f}{k_BT}|E|^2} \tag{L.3b}$$

where $g_1(y)$ and $g_2(x)$ are arbitrary functions (and include constants) arising from integration of the first order PDEs. Inspecting the analytic form of (L.3a) and (L.3b), it is clear $p(x,y) = p_1(x,y) = p_2(x,y)$ when $g_1(y) = g_2(x) = C$ where C is arbitrary. Thus,

$$p(x,y) = Ce^{\frac{k_f}{k_BT}\left(E_x^2(x,y) + E_y^2(x,y)\right)} \tag{L.4}$$

satisfies the joint condition (L.1) and is therefore the GS to (6.4.3) and (6.4.4). Equation (6.4.5a) subsequently follows.

Appendix M DEP collection and relaxation data for 216 nm diameter latex beads

Each *experiment* ($\mathscr{E}$) entailed a collection observed for more 2 – 3 minutes, followed by a relaxation, observed for 30 – 60 seconds. Two *independent* variables were used, applied DEP frequency f and potential peak potential V_o. The collection data (F_1, F_2, τ_{e1}, τ_{e2}) and relaxation data (F_3, τ_{e3}) resolved from curve fitting with Origin 4.1™ are shown in tables M.1 and M.2 below with respect to f and V_o.

Each table is comprised of three sets of experiments where each set {} is labelled alphabetically, $\mathcal{A}$ to $\mathcal{F}$. Each *set* consisted of *three* experiments where the independent variable (f or V_o) changed. The experiments in each set are numbered according to chronological order: the first experiment is labelled $\mathscr{E} = 1$, the second $\mathscr{E} = 2$, etc. The third column from the left on both tables shows the *corresponding* independent variable that is changed for each experiment. For example, in Table M.1, $V_o = 2$ V is held constant for all experiments. The set $\mathcal{A} = \{1,2,3\} \rightarrow \{V_o = 2\text{ V}; f = 0.5, 2, 1\}$ means the first experiment used $f = 0.5$ MHz applied to the electrodes; the second, $f = 2$ MHz; and the third, $f = 1$ MHz.

{}	$\mathscr{E}$	f (MHz)	$F(0)$ (a.u.)	$F(120)$ (a.u.)	F_1 $\times 10^{-2}$	τ_{e1} (sec)	F_2 $\times 10^{-2}$	τ_{e2} (sec)	F_3 $\times 10^{-2}$	τ_3 (sec)	$\delta F/\delta t$ $\times 10^{-2}$
$\mathcal{A}$	1	0.5	0.991	1.155	6.37	4.59	21.0	172	17.2	1.44	0.962
	2	2	0.975	1.039	2.91	2.14	3.18	8.61	6.35	1.70	0.77
	3	1	0.971	1.176	10.2	3.21	11.1	44.6	23.0	1.81	1.77
$\mathcal{B}$	1	2	0.981	1.104	1.66	1.72	5.34	15.0	10.58	1.01	0.636
	2	1	0.987	1.145	9.26	2.99	6.22	27.1	15.4	1.36	1.65
	3	0.5	0.990	1.179	11.3	3.12	7.62	37.9	18.4	1.25	1.91
$\mathcal{C}$	1	1	0.987	1.125	4.18	2.61	10.1	33.76	17.4	1.51	0.988
	2	2	0.985	1.100	5.61	4.69	5.91	27.1	11.6	1.35	0.955
	3	0.5	0.983	1.232	16.9	4.48	37.8	456.7	21.5	0.90	2.49

Table M.1 $V_o = 2$ V for all 3 sets {} of 3 experiments ($\mathscr{E}$) with different frequency f.

{}	$\mathscr{E}$	V_o (Volts)	$F(0)$ (a.u.)	$F(120)$ (a.u.)	F_1 $\times 10^{-2}$	τ_{e1} (sec)	F_2 $\times 10^{-2}$	τ_{e2} (sec)	F_3 $\times 10^{-2}$	τ_3 (sec)	$\delta F/\delta t$ $\times 10^{-2}$
$\mathcal{D}$	1	2	0.984	1.089	6.63	9.92	6.52	125	10.6	1.49	0.688
	2	4	0.984	1.201	7.56	1.97	8.41	7.51	22.0	1.91	2.26
	3	1	0.999	1.006	0.84	3.04	0	--	0.85	3.82	0.169
$\mathcal{E}$	1	4	0.983	1.216	17.82	2.63	4.3	9.5	24.7	1.11	4.48
	2	1	0.985	0.996	1.23	1.51	0	--	0.933	2.67	0.382
	3	2	0.987	1.071	5.84	3.87	2.77	37.7	8.75	1.58	0.941
$\mathcal{F}$	1	1	0.994	1.020	2.6	6.02	0	--	2.79	2.38	0.324
	2	2	0.983	1.125	5.88	3.65	12.1	101	14.8	1.52	1.11
	3	4	0.986	1.185	12.6	2.41	7.2	34.9	18.0	1.24	2.70

Table M.2 $f = 2$ MHz for all 3 sets {} of 3 experiments ($\mathscr{E}$) with different electrode potential V_o.

References

ABRAMOWITZ, M. and STEGUN, I. A. (1965) *Handbook of mathematical functions*. Ninth Printing, Dover Publications, New York, USA.

ABRAMOWITZ, S. (1996) Towards inexpensive DNA diagnostics. *TRIBECH*, **14**, October 1996, p. 397-401.

ADAMS, R. L. P. (1991) *DNA replication*. In Focus Series, Ed. D. Rickwood, IRL Press, Oxford University Press, Oxford, UK.

AJDARI, A. and PROST, J. (1991) Free-flow electrophoresis with trapping by a transverse inhomogeneous field. *Proc. Nat. Acad. Sci.*, **88**, p. 4468-4471.

AMES, W. F. (1969) *Numerical methods for partial differential equations*. Thomas Nelson, London, UK.

ANDERSON, C. F. and RECORD, M. T. Jr. (1982) Polyelectrolyte theories and their applications to DNA. *Ann. Rev. Phys. Chem.*, **33**, p. 191-222.

APPELS, R. and DVORÁK, J. (1982) The wheat ribosomal DNA spacer region: its structure and variation in populations and among species. *Theor. Appl. Genet.*, **63**, p. 337-348.

ARMSTRONG, R. W. and STRAUSS, U. P. (1969) Polyelectrolytes. **In**: *Encyclopedia of polymer science and engineering*. Vol. 10. John Wiley, New York, USA, p. 781-861.

ARNOLD, W. M., GESSNER, A. G. and ZIMMERMANN, U. (1993) Dielectric measurements on electro-manipulation media. *Biochem. Biophys. Acta*, **1157**, p. 32-44.

ASAMI, K., HANAI, T., and KOIZUMI, N. (1980) Dielectric approach to suspensions of ellipsoidal particles covered with a shell in particular reference to biological cells. *Jap. J. Appl. Phys.*, **19**, 2, p. 359-365.

ASBURY, C. L. and VAN DEN ENGH, G (1998) Trapping of DNA in nonuniform oscillating electric fields. *Biophys. J.*, **74**, 2, p. 1024-1030.

ASBURY, C. L. (1999) *Manipulation of DNA using nonuniform oscillating electric fields*. PhD dissertation, University of Washington, Seattle, USA.

BANGS (1997) *Technical notes #49 and #206* (1999) Bangs Laboratories Inc., USA.

BATES, A. D. and MAXWELL, A. (1993) *DNA topology*. In Focus Series, Ed. D. Rickwood, IRL Press, Oxford University Press, Oxford, UK.

BAYGENTS, J. C. (1994) Electrokinetic effects on the dielectric response of colloidal particles: dielectrophoresis and electrorotation. *Colloids and Surfaces A*, **92**, p. 67-77.

BECKER, F. F., WANG, X-B., HUANG, Y., PETHIG, R., VYKOUKAL, J. and GASCOYNE, P. R. C. (1994) The removal of human leukaemia cells from blood using interdigitated microelectrodes. *J. Phys. D: Appl. Phys.*, **27**, p. 2659-2662.

BENGUIGUI, L. and LIN., I. J. (1982) More about the dielectrophoretic force. *J. Appl. Phys.*, **53**, 2, p. 1141-1143.

BERG, H. C. (1983) *Random walks in biology*. Princeton University Press, Princeton, USA.

BLOOMFIELD, V. A., CROTHERS, D. M., and TINOCO Jr, I. (1974) *Physical chemistry of nucleic acids*. Harper and Row, New York.

BLOOMFIELD, V. A. (1991) Condensation of DNA by multivalent cations: considerations on mechanism. *Biopolymers*, **31**, p. 1471-1481.

BOEHRINGER MANNHEIM (1996) *Biochemicals Catalogue*.

BONE, S., and SMALL, C. A. (1995) Dielectric studies of ion fluctuation and chain bending in native DNA. *Biochim. Biophys. Acta*, **1260**, p. 85-93.

BONE, S., LEE, R. S. and HODGSON, C. E. (1996) Dielectric studies of intermolecular interactions in native DNA. *Biochim. Biophys. Acta*, **1306**, p. 93-97.

BONINCONTRO, A., CAMETTI, C., DI BIASIO, A. and PEDONE, F. (1984) Effect of ions on counterion fluctuation in low-molecular weight DNA dielectric dispersions. *Biophys. J.*, **45**, p. 495-501.

BORN, M. and WOLF, E. (1999) *Principles of optics*. 7th Ed., Cambridge University Press, Cambridge, UK.

BRINKMAN, H. C. (1956) Brownian motion in a field of force and the diffusion theory of chemical reactions. *Physica*, **XXII**, p. 29-34. Also Part II, p. 149-155.

BROWN, T. A. (1995) *Gene cloning – an introduction*. 3rd Ed., Chapman and Hall, London, UK.

BURT, J. P. H., AL-AMEEN, T. A. K., and PETHIG, R. (1989) An optical dielectrophoresis spectrometer for low-frequency measurements on colloidal particles. *J. Phys. E: Sci. Instrum.* **22**, p. 952-957.

BURT, J. P. H., CHAN, K. L., DAWSON, D., PARTON, A. and PETHIG, R. (1996) Assays for microbial contamination and DNA analysis based on electrorotation. *Ann. Biol. Clin.*, **54**, p. 253-257.

BUSTAMANTE, C. (1991) Direct observation and manipulation of single DNA molecules using fluorescence microscopy. *Ann. Rev. Biophys. Biochem.*, **20**, p. 415-446.

CALLADINE, C. R. and DREW, H. R. (1997) *Understanding DNA*. 2nd Ed., Academic Press, London, UK.

CHENG, J., SHELDON, E. L., WU, L., URIBE, A., GERRUE, L. O., CARRINO, J., HELLER, M. J., O'CONNELL, J. P. (1998) Preparation and hybridisation analysis of DNA/RNA from *E. Coli* on microfabricated bioelectronic chips. *Nature Biotech.*, **16**, p. 541-546.

COGGINS, L. (1987) Preparation of nucleic acids for electron microscopy. **In**: *Electron microscopy in molecular biology*. Ch. 1. Ed. J. Sommerville and U. Scheer, IRL Press, Oxford University Press, Oxford, UK, p. 1-29.

CRAN, A. and ROBERTSON, J. (Ed.) (1996) *Dictionary of Scottish quotations*. Mainstream Publishing, Edinburgh, UK.

CRIPPEN, S. M., HOLL, M. R., and MELDRUM, D. R. (2000) Examination of dielectrophoretic behaviour of DNA as a function of frequency from 30 Hz to 1 MHz using a flexible microfluidic test apparatus. *Proc. Micro Total Analysis Systems* (Ed. A. van den berg *et al.*) p. 529-532.

CUI, L., HOLMES, D. and MORGAN, H. (2001) The dielectrophoretic levitation and separation of latex beads in microchips. *Electrophoresis*, **22**, p. 3893-3901.

DAVIS, G. D., KUEHL, W. M. and BATTEY, J. F. (1994) *Basic methods in molecular biology*. Appleton and Lange, Norwalk, USA.

DELACEY, E. H. B. and WHITE, L. R. (1981) Dielectric response and conductivity of dilute suspensions of colloidal particles. *J. Chem. Soc. Faraday Trans. 2*, **77**, p. 2007-2039.

DIEKMANN, S., HILLEN, W., JUNG, M., WELLS, R. D. and PORSCHKE, D. (1982) Electric properties and structure of DNA restriction fragments from measurements of the electric dichroism. *Biophys. Chem.*, **15**, p. 157-167.

DOERING, C. R. and GADOUA, J. C. (1992) Resonant activation over a fluctuating barrier. *Phys. Rev. Lett.*, **69**, 16, p. 2318-2321.

DOI, M. and EDWARDS, S. F. (1986) *The theory of polymer dynamics*. Clarendon Press, Oxford, UK.

DUKE, T. A. and AUSTIN, R. H. (1998) Microfabricated sieve for the continuous sorting of macromolecules. *Phys. Rev. Lett.*, **80**, 7, p. 1552-1555.

DUKHIN, S. S. (1971) Dielectric properties of disperse systems. **In**: *Surface and colloid science*, **3**. Ed. E. Matijevic, John Wiley, New York, USA, p. 83-165.

EINSTEIN, A. (1924) *Investigations on the theory of Brownian movement*. Ed. R. Fürth, Translated by A. D. Cowper (1956), Dover Publications, New York, USA.

EISENBERG, H. (1976) *Biological macromolecules and polyelectrolytes in solution*. Clarendon Press, Oxford, UK.

ELIAS, J. G. and EDEN, J. (1981) Transient electric birefringence study of the persistence length and electrical polarizability of restriction fragments of DNA. *Macromolecules*, **14**, p. 410-419.

ERDÉLYI, A. (Ed.) (1954) *Tables of integral transforms*. Vol. 1. Bateman Manuscript Project, McGraw-Hill, New York, USA.

ERMOLINA, I. V., POLYGALOV, E. A., ROMANYCHEV, G. D., ZUEV Yu. F., FELDMAN Yu. D. (1991) Time domain dielectric spectroscopy with non-uniform signal sampling. *Rev. Sci. Instrum.*, **62**, p. 2262-2265.

ERMOLINA, I. V., IVOYLOV, I. N. and FEDOTOV, V. D. (1997) Dielectric relaxation, molecular motion and inter-protein interactions in myoglobin solution. *J. Biomol. Struct. & Dynamics*, **15**, p. 381-392.

ERTAS, D. (1998) Lateral separation of macromolecules and polyelectrolytes in microlithographic arrays. *Phys. Rev. Lett.*, **80**, 7, p. 1548-1551.

FELDMAN, Yu. and KOZLOVICH, N. (1995) Time-domain dielectric spectroscopy studies of macromolecular solutions. *Trends in Polymer Sci.*, **3**, p. 53-60.

FELDMAN, Yu. D, ANDRIANOV, A., POLYGALOV, E., ERMOLINA, I., ROMANYCHEV, G., ZUEV, Y., MILGOTIN B. (1996) Time domain dielectric spectroscopy: an advanced measuring system. *Rev. Sci. Instrum.*, **67**, p. 3208-3216.

FIXMAN, M. (1980a) Charged macromolecules in external fields. 1. The sphere. *J. Chem, Phys.* **72**, 9, p. 5177-5186.

FIXMAN, M. (1980b) Charged macromolecules in external fields. 2. Preliminary remarks on the cylinder. *Macromolecules*, **13**, p. 711-716.

GARDINER, C. W. (1985) *Handbook of stochastic methods for physics, chemistry, and the natural sciences*. Springer-Verlag, Berlin, Germany.

GASCOYNE, P. R. C., NOSHARI, J., BECKER, F. F. and PETHIG, R. (1994) Use of dielectrophoretic collection spectra for characterising differences between normal and cancerous cells. *IEEE Trans. Ind. Appl.*, **30**, no. 4, p. 829-833.

GERLACH, W. L. and BEDBROOK, J. R. (1979) Cloning and characterisation of ribosomal RNA genes from wheat and barley. *Nucleic Acids Res.*, **7**, p. 1869-1885.

GINER, V., Sancho, M., LEE, R. S., MARTINEZ, G. and PETHIG, R. (1999) Transverse dipolar chaining in binary suspensions induced by rf fields. *J. Phys. D: Appl. Phys.*, **32**, p. 1182-1186.

GOATER, A. D., BURT, J. P. H. and PETHIG, R. (1997) A combined travelling wave dielectrophoresis and electrorotation device: applied to the concentration and viability determination of *Cryptosporidium*. *J. Phys. D.: Appl. Phys.*, **30**, p. L65-69.

GORRE-TALINI, L., JEANJEAN, S. and SILBERZAN, P. (1997) Sorting of Brownian particles by the pulsed application of an asymmetric potential. *Phys. Rev. E*, **56**, 2, p. 2025-2034.

GRADSHTEYN, I. S. and RYZHIK, I. M. (1994) *Table of integrals, series, and products*. Ed. A. Jeffrey, 5th Ed., Academic Press, London, UK.

GRANT, E. H., SHEPPARD, R. J., and SOUTH, G. P. (1978) Dielectric behaviour of biological molecules in solution. **In**: *Monographs on physical biochemistry*. Eds. Harrington, W. F. and Peacocke, A. R., OUP.

GRATTAROLA, M. and MASSOBRIO, G. (1998) *Bioelectronics handbook*. McGraw-Hill, New York, USA.

GREEN, N. G. and MORGAN, H. (1997a) Dielectrophoretic investigations of sub-micrometre latex spheres. *J. Phys. D: Appl. Phys*. **30**, p. 2626-2633.

GREEN, N. G. and MORGAN, H. (1997b) Dielectrophoretic separation of nano-particles. *J. Phys. D: Appl. Phys*. **30**, p. L41-44.

GREEN, N. G. and MORGAN, H. (1998) Separation of submicrometre particles using a combination of dielectrophoretic and electrohydrodynamic forces. *J. Phys. D: Appl. Phys*. **31**, p. L25-30.

GREEN, N. G., RAMOS, A., GONZALEZ, A., MORGAN, H. and CASTELLANOS, A. (2000a) Fluid flow induced by non-uniform AC electric fields in electrolytic solutions on micro-electrodes. Part I: Experimental measurements. *Phys. Rev. E*, **61**, p. 4011-4018.

GREEN, N. G., RAMOS, A. and MORGAN, H. (2000b) AC electrokinetics: a survey of sub-micrometre particle dynamics. *J. Phys. D: Appl. Phys*., **33**, p. 632-641.

GROBNER, W. und HOFREITER, N. (1965) *Integraltafel* (*Unbestimmte Integrale*). Springer-Verlag, Vienna, Austria.

GROSSE, C., (1989) Microwave absorption of suspensions of DNA type particles in electrolyte solution. *Alta Frequenza*, **58**, p. 365-8.

HAGERMANN, P. J. (1998) Flexibility of DNA. *Ann. Rev. Biophys. Biophys. Chem*., **17**, p. 265-286.

HAKEN, H. (1978) *Synergetics – an introduction*. 2nd Ed., Springer-Verlag, Berlin, Germany.

HAKEN, H. (1983) *Advanced synergetics*. Springer-Verlag, Berlin, Germany.

HAMMOND, R. W., BADER, J. S., HENCK, S. A., DEEM, M. W., McDERMOTT, G. A., BUSTILLO, J. M. and ROTHBERG, J. M. (2000) Differential transport of DNA by a rectified Brownian motion device. *Electrophoresis*, **21**, p. 74-80.

HASKELL, B. G., PURI, A. and NETRAVALI, A. N. (1997) *Digital video: an introduction to MPEG-2*. Kluwer Academic Publishers, Boston, USA.

HERMANS, J. J. (1955) Sedimentation and electrophoresis of porous spheres. *J. Polymer Sci*., **XVIII**, p. 527-534.

HIEMENZ, P. C. (1986) *Principles of colloid chemistry*. 2nd Ed., Marcel Dekker, New York, USA.

HILFER, R., NØST, B., HASLUND, E., KAUTZSCH, VIRGIN, B. and HANSEN, B. D. (1994) Local porosity theory for the frequency dependent dielectric function of porous rocks and polymer blends. *Physica A*, **207**, p. 19-27.

HORSTHEMKE, W. and LEFEVER, R. (1984) *Noise-induced transitions*. Springer-Verlag, Berlin, Germany.

HOUSEAL, T. W., BUSTAMANTE, C., STUMP, R. F., and MAESTRE, M. F. (1989) Real-time imaging of single DNA molecules with fluorescence microscopy. *Biophys. J*., **56**, p. 507-516.

HUANG, Y. and PETHIG, R. (1991) Electrode design for negative dielectrophoresis. *Meas. Sci. Technol.* **2**, p. 1142-1146.

HUANG, Y., X-B WANG, TAME, J. A. and PETHIG, R. (1993) Electrokinetic behaviour of colloidal particles in travelling electric fields: studies using yeast cells. *J. Phys. D: Appl. Phys.*, **26**, p. 1528-1535.

HUGHES, M. P., MORGAN, H. and RIXON, F. J. (1997) Dielectrophoretic characterisation and separation of Herpes Simplex Virus particles. **In:** *Biophys. J. Abstracts.*, **72**, no. 2, part 2, p. A102 (41st Ann. Meeting, Biophys. Soc. New Orleans, USA)

HUGHES, M. P. and MORGAN, H. (1999) An evanescent field technique for dielectrophoresis studies of colloidal particles. *Meas. Sci. Technol.*, **10**, p. 759-762.

HUGHES, M. P., MORGAN, H. and FLYNN, M. F. (1999) The dielectrophoretic behaviour of sub-micrometre latex spheres: influence of surface conductance. *J. Colloid and Interface Sci.*, **220**, p. 454-457.

INOUE, T., PETHIG, R. AL-AMEEN, T. A. K., BURT, J. P. H., and PRICE, J. A. R. (1988) Dielectrophoretic behaviour of *Micrococcus lysodeikticus* and its protoplast. *J. Electrostatics*, **21**, p. 215-223.

JACKSON, J. D. (1975) *Classical Electrodynamics*. 2nd Ed., John Wiley, New York, USA.

JAMES, G. (1996) *Modern engineering mathematics*. 2nd Ed., Addison-Wesley, UK.

JENKINS, F. A. and WHITE, H. E. (1981) *Fundamentals of optics*. 4th Ed., McGraw-Hill, New York, USA.

JONES, T. B. (1995) *Electromechanics of particles*. Cambridge University Press, Cambridge, UK.

KABATA, H., KUROSAWA, O., ARAI, I., WASHIZU, M., MARGARSON, S. A., GLASS, R.E. and SHIMAMOTO, N. (1993) Visualisation of single molecules of RNA polymerase sliding along DNA. *Science*, **262**, p. 1561-1563.

KAMYSHNY, A., ERMOLINA, I., MAGDASSI, S., FELDMAN Yu. (2000) Study of the dynamic structure of native and hydrophobized glucose oxidase by time-domain dielectric spectroscopy. *J. Phys. Chem. B*, **104**, p. 7588-7594.

KAPUSCINSKI, J. (1995) DAPI: a DNA-specific fluorescent probe. *Biotechnic and Histochemistry*, **70**, 5, p. 220-233.

KRAMERS, H. A. (1940) Brownian motion in a field of force and the diffusion model of chemical reactions. *Physica*, **VII**, 4, p. 284-304.

KREYSZIG, E. (1967) *Advanced engineering mathematics*. 2nd Ed., John Wiley, New York, USA.

LEBEDEV, N. N. (1965) *Special functions and their applications*. Edited and translated by R. A. Silverman, Prentice-Hall, Englewood Cliffs, USA.

LEE, R. S. and BONE, S. (1998) Dielectric studies of chain melting and denaturation in native DNA. *Biochim. Biophys. Acta*, **1397**, p. 316-324.

LIDE, D. R. (Ed.) (1994) *CRC handbook of chemistry and physics*. CRC Press, Ann Arbor, USA.

LLAMAS, M., GINER, V. and SANCHO, M. (1998) The dynamic evolution of cell chaining in a biological suspension induced by an electric field. *J. Phys. D: Appl. Phys.*, **31**, p. 3160-3167.

LYKLEMA, J., DUKHIN, S. S., and SHILOV, V. N. (1983) The relaxation of the double layer around colloidal particles and the low-frequency dielectric dispersion: Part I. Theoretical considerations. *J. Electroanal. Chem.*, **143**, p. 1-21.

LYKLEMA, J., SPRINGER, M. M., SHILOV, V. N. and DUKHIN, S. S. (1986) The relaxation of the double layer around colloid particles and the low-frequency dielectric dispersion: Part III. Application of theory to experiments. *J. Electroanal. Chem.*, **198**, p. 19-26.

LYUBCHENKO, Y. L. and SHLYAKHTENKO, L. S. (1997) Visualisation of supercoiled DNA with atomic force microscopy *in situ*. *Proc. Natl. Acad. Sci. USA*, **94**, p. 496-501.

MAGNASCO, M. O. (1993) Forced thermal ratchets. *Phys. Rev. Lett.*, **71**, 10, p. 1477-1481.

MANDEL, M. (1961) The electric polarisation of rod-like, charged macromolecules. *Mol. Phys.* **4**, p. 489-496.

MANDEL, M. (1977) Dielectric properties of charged linear macromolecules with particular reference to DNA. *Ann. N. Y. Ac. Sci.*, **303**, p. 74-87.

MANDEL, M. and ODIJK, T. (1984) Dielectric properties of polyelectrolyte solutions. *Ann. Rev. Phys. Chem.*, **35**, p. 75-108.

MANDEL, M. (1988) Polyelectrolytes. **In:** *Encyclopedia of polymer science and engineering*. Vol. 11. John Wiley, New York, USA, p. 739-829.

MANIATIS, T., FRITSCH, E. F., and SAMBROOK, J. (1982) *Molecular cloning - a laboratory manual.* Cold Spring Harbour Laboratory.

MANNING, G. S. (1969) Limiting laws and counterion condensation in polyelectrolyte solutions I. colligative properties. *J. Chem. Phys.*, **51**, p. 924-933.

MANNING, G. S. (1978a) The molecular theory of polyelectrolyte solutions with applications to the electrostatic properties of polynucleotides. *Q. Rev. Biophys.*, **11**, 2, 1978, p. 179-246.

MANNING, G. S. (1978b) Limiting laws and counterion condensation in polyelectrolyte solutions V. Further development of the chemical model. *Biophys. Chem.*, **9**, 1978, p. 65-70.

MANNING, G. S. (1993) A condensed counterion theory for polarization of polyelectrolyte solutions in high fields. *J. Chem. Phys.*, **99**, 1, p. 477-486.

MARKX, G. H., HUANG, Y., ZHOU, X-F., and PETHIG, R. (1994) Dielectrophoretic characterisation and separation of micro-organisms. *Microbiology*, **140**, p. 585-591.

MARKX, G. H., PETHIG, R. and ROUSSELET, J. (1997) The dielectrophoretic levitation of latex beads, with reference to field-flow fractionation. *J. Phys. D: Appl. Phys.*, **30**, p. 2470-2477.

MASHIMO, S., UMEHARA, T. and KUWABURA, S. (1989) Dielectric study on dynamics and structure of water bound to DNA using a frequency range 10 MHz - 10 GHz. *J. Phys. Chem.*, **93**, p. 4963-4967.

MATHWORKS (1997) *PDE User's Guide.*

MATSUMOTO, S., MORIKAWA, K., and YANAGIDA, M. (1981) Light microscopic structure of DNA in solution studied by the 4', 6-diamidino-2-phenylindole staining method. *J. Mol.*, **152**, p. 501-516.

MELCHER, J. R. and TAYLOR, G. I. (1969) Electrohydrodynamics: A review of the role of interfacial shear stresses. *Ann. Rev. Fluid Mechanics*, **1**, p. 111-146.

MEL'NIKOV, S. M., SERGEYEV, V. G., and YOSHIKAWA, K. (1995) Discrete coil-globule transition of large DNA induced by cationic surfactant. *J. Am. Chem. Soc.*, **117**, p. 2401-2408.

MIZUNO, A., NISHIOKA, M., TANIZOE, T., and KATSURA, S. (1995) Handling of a single DNA molecule using electric field and laser beam. *IEEE Trans. Ind. Appl.*, **31**, no. 6, p. 1452-1457.

MOHANTY, U. and ZHAO, Y. (1996) Polarisation of counterions in polyelectrolytes. *Biopolymers*, **38**, p. 377-388.

MORIKAWA, K. and YANAGIDA, M. (1981) Visualisation of individual DNA molecules in solution by light microscopy: DAPI staining method. *J. Biochem.*, **89**, p. 693-696.

MORISHIMA, K., FUKUDA, T., ARAI, F., ISHIHARA, H., MATSUURA, H., and YOSHIKAWA, K. (1995) Noncontact transportation of DNA molecule by dielectrophoretic force. **In**: *Proc. IEEE Int. Symp. on Micro Machine and Human Sci.*, p. 145-152.

MORISHIMA, K., FUKUDA, T., ARAI, F., MATSUURA, H., and YOSHIKAWA, K. (1996) Noncontact transportation of DNA molecule by dielectrophoretic force for micro DNA flow system. **In**: *Proc. IEEE Int. Conf. on Robotics and Automation*, Minnesota, p. 2214-2219.

MORISHIMA, K., FUKUDA, T., ARAI, F., and YOSHIKAWA, K. (1997) Manipulation of DNA molecule utilizing the conformational transition in the higher order structure of DNA. **In**: *Proc. IEEE Int. Conf. on Robotics and Automation*, New Mexico, p. 1454-1459.

MORISHIMA, K., ARNOLD, D. W., WHEELER, A. R., RAKESTRAW, D. J., and ZARE, R. N. (2000) Novel separation method on a chip using capillary electrophoresis in combination with dielectrophoresis. **In**: *Proc. Micro Total Analysis Systems* (Ed. A. van den berg *et al.*), p. 269-272.

MORSE, P. M. and FESHBACH, H. (1953) *Methods of theoretical physics*. Part I. McGraw-Hill, New York, USA.

NAGASAWA, M. (1974) Ion-binding phenomena of polyelectrolytes. **In**: *Polyelectrolytes*. Vol. 1 Eds. E. Sélégny, M. Mandel, and U. P. Strauss, NATO Adv. Stud. Inst., France, 1972, D. Reidel Publishing, Holland, p. 57-77.

NEW ENGLAND BIOLABS (1999) *Biochemicals catalogue*.

NEWMAN, J. SWINNEY, H. L., BERKOWITZ, S. A., and DAY, L. A. (1974) Hydrodynamic properties and molecular weight of fd bacteriophage DNA. *Biochem.* **13**, 23, p. 4832-4838.

NISHIOKA, M., TANIZOE, T., KATSURA, S. and MIZUNO, A. (1995) Micromanipulation of cells and DNA molecules. *J. Electrostatics*, **35**, p. 83-91.

O'BRIEN, R. W. and WHITE, L. R. (1978) Electrophoretic mobility of a spherical colloidal particle, *J. Chem. Soc. Faraday Trans. 2*, **74**, p. 1607-1626.

O'BRIEN, R. W. (1986) The high-frequency dielectric dispersion of a colloid. *J. Colloid and Interface Sci.*, **113**, 1, p. 81-93.

ODIJK, T. (1979) Possible scaling relations for semidilute polyelectrolyte solutions. *Macromolecules*, **12**, p. 688-693.

OHSHIMA, H. (1997) Electrophoretic mobility of spherical colloidal particles in concentrated suspensions. *J. Colloid and Interface Sci.*, **188**, p. 481-485.

O'KONSKI, C. T. (1960) Electric properties of macromolecules. V. Theory of ionic polarisation in polyelectrolytes. *J. Phys. Chem.*, **64**, p. 605-619.

OOSAWA, F. (1970) Counterion fluctuation and dielectric dispersion in linear polyelectrolytes. *Biopolymers*, **9**, p. 677-688.

OOSAWA, F. (1971) *Polyelectrolytes*. Marcel Dekker, New York, USA.

PACANSKY, J. and LYERLA, J. R. (1979) Photochemical decomposition mechanisms for AZ-type photoresists. *IBM. Res. Develop.*, **23**, 1, p. 42-55.

PAPOULIS, A. (1984) *Probability, random variables, and stochastic processes*. McGraw-Hill (ISE), New York, USA.

PEDONE, F. and BONINCONTRO, A. (1991) Temperature dependence of DNA dielectric dispersion at radio frequency. *Biochim. Biophys. Acta*, **1073**, p. 580-584.

PENAFIEL, L. M. and LITOVITZ, T. A. (1992) High frequency dielectric dispersion of polyelectrolyte solutions and its relation to counterion condensation. *J. Chem. Phys.* **97**, p. 559-567.

PERBAL, B. (1988) *A practical guide to molecular cloning*. 2nd Ed., John Wiley, New York, USA.

PETHIG, R. (1979) *Dielectric and electronic properties of biological materials*. John Wiley, New York, USA.

PETHIG, R. (1991) Application of AC electrical fields to the manipulation and characterisation of cells. **In:** *Proc. 4th Toyota Conf.*, 21-24 October, 1990 (Ed. I. Karube *Automation in Biotechnology*) p. 159-185.

PETHIG, R., HUANG, Y., WANG, X-B., and BURT, J. P. H. (1992) Positive and negative dielectrophoretic collection of colloidal particles using interdigitated castellated microelectrodes. *J. Phys. D: Appl. Phys.*, **24**, p. 881-888.

PILLER, H. (1977) *Microscope photometry*. Springer-Verlag, Berlin, Germany.

PLOEM, J. S. and TANKE, H. J. (1987) *Introduction to fluorescence microscopy*. Oxford University Press, Oxford, UK.

POHL, H. A. (1951) The motion and precipitation of suspensoids in divergent electric fields. *J. Appl. Phys.*, **22**, 7, p. 869-871.

POHL, H. A. (1978) *Dielectrophoresis*. Cambridge University Press, Cambridge, UK.

PONTIGA, F., and CASTELLANOS, A. (1992) The onset of electrothermal convection in nonpolar liquids on the basis of a dissociation-injection conductivity model. *IEEE Trans. Ind. Appl.*, **28**, 3, p. 520-527.

PORSCHKE, D. (1985) Effects of electric fields on biopolymers. *Ann. Rev. Phys. Chem.*, **36**, p. 159-178.

PRESS, W. H., TEUKOLSKY, S. A., VETTERLING, W. T. and FLANNERY, B. P. (1986) *Numerical recipes*. Vol. 1. Cambridge University Press, Cambridge, UK.

PRICE, J. A. R., BURT, J. P. H., and PETHIG, R. (1988) Applications of a new optical technique for measuring the dielectrophoretic behaviour of micro-organisms. *Biochem. Biophys. Acta*, **964**, p. 221-230.

PRUDNIKOV, A. P., BRYCHKOV, Yu. A., and MARICHEV, O. I. (1986) *Integrals and series*. Vols. I and II. (Tr. N. M. Queen, Gordon and Breach, London, UK).

QIAGEN (1997) *Plasmid Purification Handbook*.

RAICU, V., RAICU, G. and TURCU, G. (1996) Dielectric properties of yeast cells as stimulated by the two-shell model. *Biochem. Biophys. Acta*, **1274**, p. 143-148.

RAINVILLE, E. D. (1960) *Special functions*. Macmillan, New York, USA.

RAMOS, A., MORGAN, H. GREEN, N. G. and CASTELLANOS, A. (1998) AC electrokinetics: a review of forces in microelectrode structures. *J. Phys. D: Appl. Phys.*, **31**, p. 2338-2353.

RAMOS, A., MORGAN, H. GREEN, N. G. and CASTELLANOS, A. (1999) AC electric-field-induced fluid flow in microelectrodes. *J. Colloid and Interface Sci.*, **217**, p. 420-422.

REESE, H. R. (1994) Effects of DNA charge and length on the electrophoretic mobility of intercalated DNA. *Biopolymers*, **34**, p. 1349 - 1358.

RISKEN, H. (1989) *The Fokker-Planck equation*. 2nd Ed., Springer-Verlag, Berlin, Germany.

ROUSSELET, J., SALOME, L., AJDARI, A. and PROST, J. (1994) Directional motion of Brownian particles induced by a periodic asymmetric potential. *Nature*, **370**, p. 446-448.

ROUSSELET, J., MARKX, G. H. and PETHIG, R. (1998) Separation of erythrocytes and latex beads by dielectrophoretic levitation and hyperlayer field-flow fractionation. *Colloids and Surfaces A: Physiochem. Eng. Aspects*, **140**, p. 209-216.

RUSSEL, W. B., SAVILLE., D. A., and SCHOWALTER., W. R. (1999) *Colloidal dispersions*. Cambridge University Press, Cambridge, UK.

RUSSELL, P. J. (1994) *Fundamentals of genetics*. Harper-Collins College Publishers, New York, USA.

SAIF, B., MOHR, R. K., MONTROSE, C. J., and LITOVITZ, T. A. (1991) On the mechanism of dielectric relaxation in aqueous DNA solutions. *Biopolymers*, **31**, p. 1171 - 1180.

SAMBROOK, J., FRITSCH, E. F., and MANIATIS, T. (1989) *Molecular cloning - a laboratory manual*. 2nd Ed., Cold Spring Harbour Laboratory Press, New York, USA.

SASAKI, S., ISHIKAWA, A. and HANAI, T. (1981) Dielectric properties of spherical macroion suspensions. I: Study on monodisperse polystyrene latex. *Biophys. Chem.*, **14**, p. 45-53.

SAUER, F. A. (1985) Interaction-forces between microscopic particles in an external electromagnetic field. **In**: *Interactions between electromagnetic fields and cells*. Eds. A. Chiabrera, C. Nicolini and H. P. Schwan, NATO Adv. Sci. Inst. Series, Plenum, New York, USA, p. 181-202.

SCHNELLE, T., HAGEDORN, R., FÜHR, G., FIEDLER, S. and MÜLLER, T. (1993) Three-dimensional electric field traps for manipulation of cells - calculation and experimental verification. *Biochem. Biophys. Acta*, **1157**, p. 127-140.

SCHWAN, H. P., SCHWARTZ, G., MACZUK, J., and PAULY, H. (1962) On the low-frequency dielectric dispersion of colloidal particles in electrolyte solution. *J. Chem.*, **66**, p. 2626-2635.

SCHWARZ, G. (1962) A theory of the low-frequency dielectric dispersion of colloidal particles in electrolyte solution. *J. Phys. Chem.*, **66**, p. 2636-2642.

SCHWARZ, G. (1963) General equation for the mean electrical energy of a dielectric body in an alternating electrical field. *J. Chem. Phys.*, **39**, p. 2387-2388.

SEGEL, I. H. (1976) *Biochemical calculations*. John Wiley, London, UK.

SHAW, D. J. (1992) *Introduction to colloid and surface chemistry*. 4th Ed., Butterworth Heinemann, Oxford.

SLATER, G. W., GUO, H. L. and NIXON, G. I. (1997) Bidirectional transport of polyelectrolytes using self-modulating entropic ratchets. *Phys. Rev. Lett.*, **78**, 6, p. 1170-1173.

SMITH, D. E., PERKINS, T. T. and CHU, S. (1996) Dynamical scaling of DNA diffusion coefficients. *Macromolecules*, **29**, p. 1372-1373.

SMITH, G. D. (1978) *Numerical solution of partial differential equations*. Clarendon Press, Oxford, UK.

SMITH, S. B. and BENDICH, A. J. (1990) Electrophoretic charge density and persistence length of DNA as measured by flourescence microscopy. *Biopolymers* **29**, p. 1167-1173.

SOKOLNIKOFF, I. S. and REDHEFFER, R. M. (1966) *Mathematics of physics and modern engineering*. 2nd Ed., McGraw-Hill, New York, USA.

SPRINGER, M. M., KORTEWEG, A., and LYKLEMA, J. (1983) The relaxation of the double layer around colloid particles and the low-frequency dielectric dispersion: Part II. Experiments. *J. Electroanal. Chem.*, **153**, p. 55-66.

STARK, H. and TUTEUR, F. B. (1979) *Modern electrical communications*. Prentice-Hall, New Jersey, USA.

STEINER and MILLAR (1970) The nucleic acids. **In**: *Biological polyelectrolytes*. Ed. A. Veis, Marcel Dekker, New York, USA.

STELLWAGEN, N. (1981) Electric birefringence of restriction enzyme fragments of DNA: Optical factor and electric polarizability as a function of molecular weight. *Biopolymers*, **20**, p. 399-434.

STRANG, G. (1986) *Introduction to applied mathematics*. Wellesley-Cambridge Press, Massachusetts, USA.

STRYER, L. (1995) *Biochemistry*. 4th Ed., W. H. Freeman, New York, USA.

STRZELECKA, T. E., DAVIDSON, M. W., and RILL, R. L. (1988) Multiple liquid crystal phases of DNA at high concentrations. *Nature*, **331**, p. 457-460.

SUZUKI, S., YAMANASHI, T., TAZAWA, S., KUROSAWA, O., and WASHIZU, M. (1995) Quantitative analysis of DNA orientation in stationary AC electric field using fluorescence anisotropy, *Conf. Rec. IEEE Ind. Appl. Con.*, **2**, p. 1374-1382.

TAKASHIMA, S., GABRIEL, C., SHEPPARD, R. J., and GRANT, E. H. (1984) Dielectric behaviour of DNA solution at radio and microwave frequencies (at $20^{o}C$). *Biophys. J.*, **46**, p. 29-34.

TAKASHIMA, S., CASALEGGIO, A., GIULIANO, F., MORANDO, M., ARRIGO, P. and RIDELLA, S. (1986) Study of bound water of poly-adenine using high frequency dielectric measurements. *Biophys. J.*, **49**, p. 1003-1008.

TAKASHIMA, S. (1989) *Electrical properties of biopolymers and membranes*. Adam Hilger, Philadelphia, USA.

TALARY, M. S. and PETHIG, R. (1994) Optical technique for measuring the positive and negative dielectrophoretic behaviour of cells and colloidal suspensions. *IEE Proc. Sci. Meas. Technol.*, Sept. 1994, **141**, no. 5, p. 395-399.

TALARY, M. S., BURT, J. P. H., and PETHIG, R. (1996) Electromanipulation and separation of cells using travelling electric fields. *J. Phys. D: Appl. Phys.*, **29**, p. 2198-2203.

TANFORD, C. (1961) *Physical chemistry of macromolecules*. John Wiley, USA.

TOLSTOV, G. P. (1962) *Fourier series*. Prentice-Hall, Englewood Cliffs, USA.

TRITTON, D. J. (1988) *Physical fluid dynamics*. Oxford University Press, Oxford, UK.

UHLENBECK, G. E. and ORNSTEIN, L. S. (1930) On the theory of Brownian motion. *Physical Review*, **36**, p. 823-841. Reprinted in: Wax, N. (Ed.) (1954) *Noise and stochastic processes*. Dover, UK.

VAN DER TOUW, F. and MANDEL, M. (1974) Dielectric increment and dielectric dispersion of solutions containing simple charged linear macromolecules. *Biophys. Chem.*, **2**, Parts I and II, p. 218-241.

VAN HOLDE, K. E. (1971) *Physical Biochemistry*. Prentice-Hall, Englewood Cliffs, USA.

VASILEVSKAYA, V. V., KHOKHLOV, A. R., MATSUZAWA, Y. and YOSHIKAWA, K. (1995) Collapse of single DNA molecule in poly(ethylene glycol) solutions. *J. Chem. Phys.*, **16**, p. 6595-6602.

VIOVY, J.-L. and DUKE, T. (1993) DNA electrophoresis in polymer solutions. *Electrophoresis*, **14**, p. 322-329.

VON HIPPEL, A. R. (1954) *Dielectrics and waves*. John Wiley, London, UK.

WANG, X-B., HUANG, Y., BURT, J. P. H., MARKX, G. H. and PETHIG, R. (1993a) Selective dielectrophoretic confinement of bioparticles in potential energy wells. *J. Phys. D: Appl. Phys.*, **26**, p. 1278-1285.

WANG, X-B., HUANG, Y., HÖLZEL, R., BURT J. P. H. AND PETHIG, R. (1993b) Theoretical and experimental investigations of the interdependence of the dielectric, dielectrophoretic and electrorotational behaviour of colloidal particles. *J. Phys. D: Appl. Phys.*, 1993, **26**, p. 312-322.

WANG, X-B, HUANG, Y., BECKER, F. F. and GASCOYNE, P. R. C. (1994) A unified theory of dielectrophoresis and travelling wave dielectrophoresis. *J. Phys. D: Appl. Phys.*, 1994, **27**, p. 1571-1572.

WANG, X., WANG, X-B, HUANG, Y., BECKER, F. F. and GASCOYNE, P. R. C. (1996) A theoretical method for dielectrophoretic electrode arrays using Green's theorem. *J. Phys. D: Appl. Phys.*, 1996, **29**, p. 1649-1660.

WANG, X., WANG, X.-B. AND GASCOYNE, P. R. C. (1997) General expressions for dielectrophoretic force and electrorotational torque derived using the Maxwell stress tensor method. *J. Electrostatics*, **39**, p. 277-295.

WASHIZU, M. (1990) Electrostatic manipulation of biological objects. *J. Electrostatics*, **25**, p. 109-123.

WASHIZU, M. and KUROSAWA, O. (1990) Electrostatic manipulation of DNA in microfabricated structures. *IEEE Trans. Industry Appl.*, **26**, no. 6, p. 1165-1172.

WASHIZU, M., SHIKIDA, M., AIZAWA, S. and HOTANI, H. (1992) Orientation and transformation of flagella in electrostatic field. *IEEE Trans. Ind. Appl.*, **28**, no. 5, p. 1194-1202.

WASHIZU, M., SUZUKI, S., KUROSAWA, O., NISHIZAKA, T. and SHINOHARA, T. (1994) Molecular dielectrophoresis of biopolymers. *IEEE Trans. Ind. Appl.*, **30**, no. 4, p. 835-843.

WASHIZU, M., KUROSAWA, O, ICHIRO, A., SUZUKI, S. and SHIMAMOTO, N. (1995) Applications of electrostatic stretch-and-positioning of DNA. *IEEE Trans. Ind. Appl.*, **31**, no. 3, p. 447-456.

WATARAI, H., SAKAMOTO, T. and TSUKAHARA, S. (1997) *In Situ* measurement of dielectrophoretic mobility of single polystyrene microparticles. *Langmuir*, **13**, p. 2417-2420.

WATSON, G. N. (1952) *A treatise on the theory of Bessel functions*. Cambridge University Press, Cambridge, UK.

WILLIAMS, W. E. (1980) *Partial differential equations*. Clarendon Press, Oxford, UK.

WISSENBURG, P., ODIJK, T., CIRKEL, P. and MANDEL, M. (1995) Multimolecular aggregation of mononucleosomal DNA in concentrated isotropic solutions. *Macromol.*, **28**, p. 2315-2328.

WOLFRAM, S. (1996) *The Mathematica book*. 3rd Ed., Cambridge University Press, Cambridge, UK.

XAMMAR ORO, J. R. DE and GRIGERA, J. R. (1984) Dielectric properties of aqueous solutions of sonicated DNA above 40 MHz. *Biopolymers*, **23**, p. 1457-1463.

YAMAMOTO, WASHIZU, M., KUROSAWA, O. and SHIMAMOTO, N. (1998) Molecular surgery of DNA. *Proc. SPIE Int. Soc. Opt. Eng.* USA, **2302**, p. 228-236.

YANAGIDA, M., HIRAOKA, Y. and KATSURA, I. (1983) Dynamic behaviours of DNA molecules in solution studied by fluorescence microscopy. *Cold Spring Harbour Symp Q. Biol.*, **47**, p. 177-187.

ZIENKIEWICZ, O. C. and TAYLOR, R. L. (1989) *The finite element method*. 4th Ed., McGraw-Hill, London, UK.

List of Publications

BAKEWELL, D., HUGHES, M., MILNER, J. J. and MORGAN, H. (1998) Dielectrophoretic manipulation of avidin and DNA. *Proc. 20th Int. Conf. IEEE/EMBS*, Hong Kong, p. 1079-1082.

BAKEWELL, D., MORGAN, H. and MILNER, J. J. (1999) Characterisation of the dielectrophoretic movement of DNA in micro-fabricated structures. **In:** *Inst. of Physics Ser. 163, Proc. 10th Int. Conf. Electrostatics*, 1999 (Bristol, Inst. Phys. Publishing, Bristol, UK) p. 73 - 76.

BAKEWELL, D., ERMOLINA, I., MORGAN, H., MILNER, J. and FELDMAN Y. (2000) Dielectric relaxation measurements of 12 kbp plasmid DNA. *Biochem. Biophys. Acta.*, **1493**, p. 151-158.

BAKEWELL, D. and MORGAN, H. (2000) Measuring the polarisability of sub-micrometre particles using AC electrokinetic methods. **In:** *Proc. 6th Int. Conf. Dielectric and Related Phenomena (DRP)*, Poland, p. 42.

BAKEWELL, D., ERMOLINA, I., MORGAN, H., MILNER, J. and FELDMAN Y. (2000) Dielectric Spectroscopy of Plasmid DNA. **In:** *Proc. 6th Int. Conf. Dielectric and Related Phenomena (DRP)*, Poland, p. 125.

BAKEWELL, D. J. and MORGAN, H. (2001) Measuring the frequency dependent polarisability of colloidal particles from dielectrophoretic collection data. *IEEE Trans. Dielect. and Elec. Ins.*, **8**, p. 566-571.

MORGAN, H., IZQUIERDOA. G., BAKEWELL, D., GREEN, N. G. and RAMOS, A. (2001) The dielectrophoretic and travelling wave forces for interdigitated electrode arrays: analytical solution using Fourier series. *J. Phys. D: Appl. Phys.*, **34**, p. 1553-1561.